University of Huddersfield Repository

Al-Hinai, Sulaiyam

Non-invasive velocity and volume fraction profile measurement in multiphase flows

Original Citation

Al-Hinai, Sulaiyam (2010) Non-invasive velocity and volume fraction profile measurement in multiphase flows. Doctoral thesis, University of Huddersfield.

This version is available at http://eprints.hud.ac.uk/id/eprint/9094/

NON-INVASIVE VELOCITY AND VOLUME FRACTION PROFILE MEASUREMENT IN MULTIPHASE FLOWS

SULAIYAM M. AL-HINAI
B.Eng., M.Sc.

A thesis submitted to the University of Huddersfield in Partial fulfilment of the requirement for the degree of Doctor of Philosophy.

University of Huddersfield

June 2010

DECLARATION

No portion of the work referred to in this thesis has been submitted in support of an application for another degree or qualification of this or any other university or other institute of learning.

ACKNOWLEDGEMENTS

ABSTRACT

Multiphase flow is the simultaneous flow of two or more phases, in direct contact, and is important in the oil industry, e.g. in production wells, in sub-sea pipelines and during the drilling of wells. The behaviour of the flow will depend on the properties of the constituent phases, the flow velocities and volume fractions of the phases and the geometry of the system. In solids-in-liquid flows, measurement of the local solids volume fraction distribution and the local axial solids velocity distribution in the flow cross section is important for many reasons including health and safety and economic reasons, particularly in oil well drilling operations. However upward inclined solids-liquid flows which are frequently encountered during oil well drilling operations are not well understood. Inclined solids-liquid flows result in non-uniform profiles of the solids volume fraction and axial solids velocity in the flow cross-section. In order to measure the solids volumetric flow rate in these situations it is necessary to measure the distributions of the local solids volume fraction and the local axial solids velocity and then to integrate the product of these local properties in the flow cross section.

This thesis describes the development of a non-intrusive Impedance Cross-Correlation (ICC) device to measure the local solids volume fraction distribution and the local solids axial solids velocity distribution in upward inclined solids-water flows in which these distributions are highly non-uniform. The ICC device comprises a non-conductive pipe section of 80mm internal diameter fitted with two arrays of electrodes, denoted 'array A' and 'array B', separated by an axial distance of 50mm. At each array, eight electrodes are equispaced over the internal circumference of the pipe. A control system consisting of a microcontroller and analogue switches is used such that, for arrays A and B, any of the eight electrodes can be configured as an 'excitation electrode' (V^+), a 'virtual earth measurement electrode' (Ve) or an 'earth electrode' (E) thus enabling the local mixture conductance in different regions of the flow cross-section to be measured and thereby allowing the local solids volume fraction in each region to be deduced. The conductance signals from arrays A and B are also cross-correlated to yield the local solids axial velocity in the regions of flow under interrogation.

A number of experiments were carried out in solids-in-water flows in a flow loop with an 80 mm inner diameter, 1.68m long Perspex test section which was inclined at three different inclination angle to the vertical ($0^o, 15^o$ and 30°). The obtained results show good quantitative agreement with previous work carried out using intrusive local probes. Integration of the flow profiles in the cross section also yielded excellent quantitative agreement with reference measurements of the mean solids volume fraction, the mean solids velocity and the solids volumetric flow rate. Furthermore, this study also showed good qualitative agreement with high speed film of the flow. It is believed that the method of velocity and volume fraction profile measurement described in this thesis is much simpler to implement, more accurate and less expensive than the currently very popular technique of dual-plane Electrical Resistance Tomography (ERT).

Finally, the thesis describes a mathematical model for predicting the axial velocity distribution of inclined solids-water flows using the solids volume fraction profiles measured by the ICC device. Good agreement was obtained between the predicted velocity profiles and the velocity profiles measured using the ICC device.

TABLE OF CONTENTS

LIST OF FIGURES

LIST OF TABLES

NOMENECLATURE LIST

Acronyms

DP	*Differential Pressure*
EFM	*Electromagnetic Flow Metering*
EIT	*Electrical Impedance Tomography*
ERT	*Electrical Resistance Tomography*
FEMLAB	*Finite Element Method Laboratory*
ICC	*Impedance Cross Correlation*
ID	*Inner Diameter*
LDA	*Laser Doppler Anemometry*
LED	*Light Emitting Diode*
LE	*Latch Enable*
Movf	*Mean oil volume fraction*
PDO	*Petroleum Development Oman*
PIV	*Particle Image Velocimetry*

V^+	'*Excitation Electrodes*'
Ve	'*Virtual Earth Measurement Electrodes*'
E	'*Earth Electrodes*'
Z	'*High Impedance*'

Symbols

A	The cross sectional area of the pipe.
C_D	The drag coefficient resisting the motion of a particle.
C(y)	The dispersed phase volume fraction.
D	The pipe diameter.
d	The particle diameter.
$\dfrac{du}{dx}$	The phase velocity in x direction.

$\dfrac{du}{dy}$	The phase velocity in y direction.
$\dfrac{du}{dz}$	The phase velocity in z direction.
$\dfrac{dp}{dx}$	The axial pressure gradient.
F	The frictional pressure loss along the length of pipe.
F_g	The downward force on a particle due to gravity.
f	Frequency.
f_s	The sampling frequency.
g	Gravity.
h	The length of the measuring working section over which the pressure gradient is measured.
I	Electrical current.
i^{th}	No. of hole (see Chapters 4&5).
j^{th}	The boundary voltage measurement.
K	The configuration constant gain (see Section 3.10).
K	The Turbine meter factor (see Section 6.3.2).
k	The conductance circuit gain (see Section 3.6).
L	The effective axial sensors separation. (see Section 3.3)
L	The length of pipe under consideration. (see Section 6.3.3)
M	The mass flow rate.
M_s	The mass solids flow rate.
M_w	The mass water flow rate.
m^{th}	No. of electrodes in both arrays A and B.
N	"Pixels".
n	The iteration number.
P	"Pixels" .

NOMENECLATURE LIST

P_1	The upstream pressure.
P_2	The downstream pressure.
Q	The volumetric flow rate.
Q_T	The total volumetric flow rate.
Q_i	The mean phase flow rate.
Q_s	The solids volumetric flow rate.
Q_w	The water volumetric flow rate.
$Q_{s,ref}$	The reference solids volumetric flow rate.
$Q_{w,ref}$	The reference water volumetric flow rate.
$\overline{Q}_{w,t,ref}$	The water volumetric flow rate from turbine.
$Q_{s,meas}$	The solids volumetric flow rate obtained by ICC.
R	The friction factor.
Ra	The feedback resistor (see Chapter 4).
R_f	The effective system resistance.
Re_p	The particle Reynolds number.
$R_{xy}(\tau)$	The Cross-correlation function.
S_{AM}	The set of electrodes in array A connected to the input of inverting amplifier Ve,A.
S_{BM}	The set of electrodes in array B connected to the input of inverting amplifier Ve,B.
$s_{i,j}$	The sensitivity coefficient relating changes in the jth boundary voltage measurement.
T	The total time period in cross-correlation.
t	Time.
U_{CC}	The mean flow velocity calculated from total volume flow (see Section 2.6.4.4).

U_h	The mean flow velocity calculated by cross correlation (see Section 2.6.4.4).
U_{WS}	The superficial water velocity.
$\bar{u}_i$	The mean flow velocity.
$\bar{u}_w$	The mean water velocity.
u_c	The critical velocity.
u_w	The local water velocity.
u_h	The homogenous flow velocity
u_s	The local axial solids velocity.
$\bar{u}_s$	The average solids velocity.
u_p	The particle velocity with respect to the fluid.
$u(y)$	The axial fluid velocity at coordinate y.
V	Voltage.
V_p	The particle velocity.
V_{slip}	The local axial slip velocity.
V_T	The terminal velocities.
V_s	The voltage response of the solids hopper load cell.
V_w	The voltage response of the water hopper load cell.
$V_{7,A}$	The output voltage from array A.
$V_{7,B}$	The output voltage from array B.
$V_{6,B,w}$	The output voltage from Array B when water only.
$V_{6,B,m}$	The output voltage when both water and solids flows.
$V_{6B,i}$	The output voltage from the detection circuitry associated with array B when the nylon rod is inserted into the ith hole.
$V_{6B,0}$	The output voltage when the nylon rod was absent.
$\delta V_{6B,i}$	Sensitivity parameter.

$\delta V_{6B,i,sta}$	The voltage difference obtained from static test.
$\delta V_{6B,i_{model}}$	The voltage difference obtained by COMSOL.
$x(t)$	The output signal form upstream sensor X.
$y(t)$	The output signal from downstream sensor Y.
Y_{meas}	The measurement values obtained from integrated local measurements obtained by the ICC.
Y_{ref}	The reference measurement obtained from the reference devices.
$[\Delta\sigma]$	The conductivity matrix.
$[\Delta\varphi]$	The potential difference matrix.
$[S]$	The sensitivity matrix.

Greek symbols

α_s	The local solids volume fraction.
$\bar{\alpha}_i$	The mean volume fraction.
$\bar{\alpha}_{ref}$	The reference mean volume fraction.
$\bar{\alpha}_{s,ref}$	The mean solids volume fraction in the working section.
$\bar{\alpha}_{s,meas}$	The mean solids volume fraction obtained by the ICC.
$\bar{\alpha}_{EIT}$	The mean volume fraction obtained by EIT system.
ε	The relative percentage error.
μ	The laminar viscosity.
μ_w	The water viscosity.
υ_T	The eddy viscosity.
ρ_m	The mean density.
ρ_w	The density of the water.

σ_m	The local mixture conductivity.
σ_s	The solids conductivity.
σ_w	The water conductivity.
τ	The transit time in cross-correlation.
θ	The phase angle.

Subscripts

B	Ball (see Chapter 5)
c	Continuous phase (see Section 8.4)
D	Drag (see Chapter 5)
d	dispersed phase (see Section 8.4)
ICC	Impedance Cross Correlation
i	Number of pixel (see Chapter 4)
j	boundary voltage measurement (see Chapter 4)
m	mixture
meas	measured value by the ICC
p	Practical
ref	Reference value
s	Solids
slip	Slip velocity (see Chapter 1)
T	Terminal (see Chapter 5)
t	Turbine (see Section 6.3.2)
w	Water

Chapter 1 INTRODUCTION

This chapter starts by explaining the motivation for choosing this particular research project. The problem of multiphase flow metering is discussed, as are possible applications for a non-intrusive, relatively simple and robust, solids-liquid flow metering device. Finally, the aims and research objectives are given, and the chapter ends by describing the layout of the thesis.

1.1 Motivation

In many industrial processes it is often of extreme importance to measure fluid flow rates accurately. Flow rate measurement may be essential for a variety of reasons including process control and on-line monitoring applications. Although many flows may consist of a single fluid flowing in pipe, multiphase flows are becoming increasingly important, particularly in the oil industry.

Multiphase flows, where two or three fluids, which may or may not carry solids, flow simultaneously in a pipe are important in many applications within the oil, mining, paper pulp, natural gas and other industries, even measuring the concentration of beans in tomato sauce Akagawa et al., (1989). It is vital for these industries to precisely monitor the flow properties, such as the mean volume fraction $\bar{\alpha}_i$ and mean velocity $\bar{u}_i$ of each phase to quantify the mean phase flow rate Q_i, as:

$$Q_i = \bar{\alpha}_i \, \bar{u}_i \, A \qquad\qquad 1\text{-}1$$

where: A is the cross-sectional area of the pipe.

Traditional commercial measuring techniques employ large, heavy and expensive separators to divide the mixture into its various components and meter them individually, which is time consuming and expensive (see Figure 1-1). Furthermore, such measurements can be unrepresentative because they do not operate continuously and sample only a fraction of the total production.
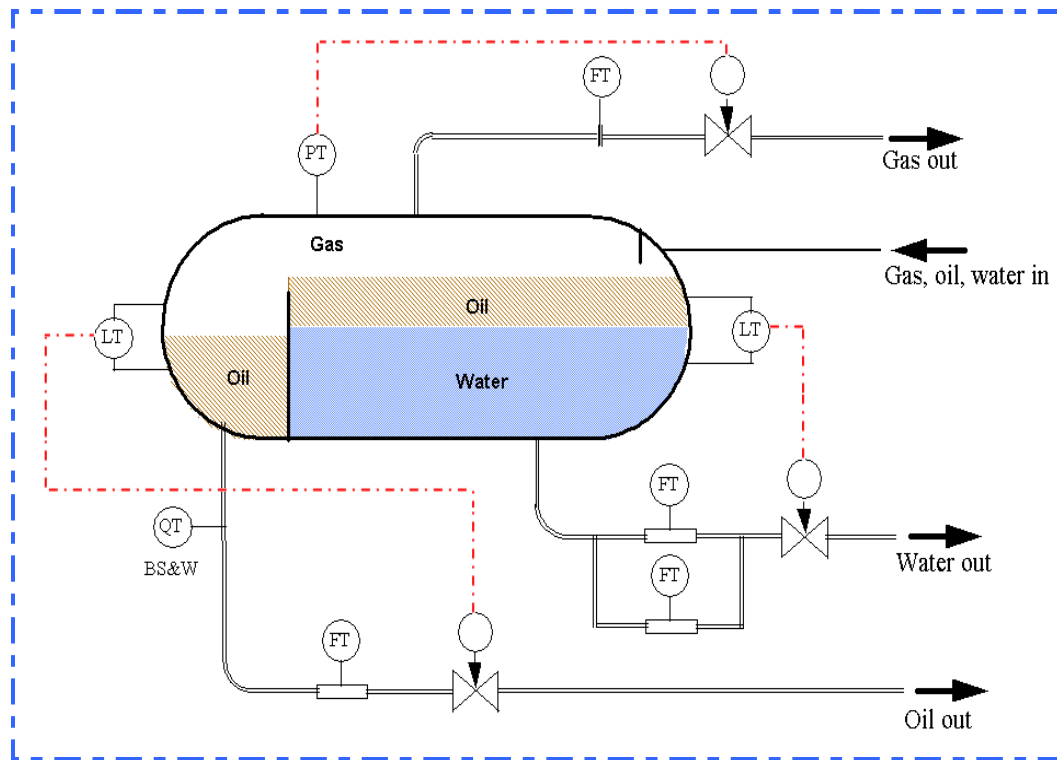
Figure 1-1: Test separator used in the oil industry [Al-Aufi and Al-Hinai, 2002]

A major problem for the measurement of multiphase flow is that it can occur in a number of different, not necessarily clearly defined, regimes such as stratified or dispersed or annular or slug Hewitt et al., (1986), which require different measurement techniques. For example for a homogeneous multiphase flow, a single phase flow measurement technique may sometimes be acceptable; however where the flow is transient and intermittent, such as in the slug regime, single phase techniques cannot be applied. Furthermore, complex coupling between the two phase flow pattern and the geometry of the containing pipe, which will change with changes of pipe geometry, complicate the measurement. Changes in pipe geometry due to the presence of bends, fittings and valves, can disrupt flow patterns over long distances (both upstream and downstream) before a stable pattern is again established.

Different fluid combinations, including gas-liquid flows, gas-solid flows, gas-liquid-solid flows, liquid-liquid flows and liquid-solid flows are all regarded as multiphase flows. The current investigation deals with solids-in-liquid flows, or to be more specific, with solids-water flows. The current research is restricted to multi-component flow in a pipe of cylindrical cross-section.

There are many commercial devices which are able to measure the velocity of a single phase flow which may also be used for the measurement of multiphase flow, but they will measure only the mean (homogeneous) velocity of the mixture and not the phase velocities of the components in the flow. There are also commercial devices capable of measuring volume fraction in oil-gas, oil-water, water-gas flow and solids-water flows. It can be said that while the problem of measuring volume fraction in multiphase flows is now largely solved when phases are uniformly distributed in cross-section. Techniques for accurate measurement of the local velocity of each flowing component require further investigation (Wei et al., (1998).

The development of techniques for measuring the flow of water-solids mixtures and monitoring the conditions of the flow remains an important multiphase flow problem. Inserting an intrusive measuring device into the pipeline is generally not acceptable with multiphase flows containing solids since it will be liable to damage by abrasion, and blockages may build up around it. Both problems are seriously exacerbated in small diameter pipelines. Thus, in recent years, advances in water-solids measurements have been based on the use of non-intrusive techniques. Optical, ultrasound, nuclear, conductance and electrostatic transducers are increasingly finding application in such metering devices.

In the oil and gas industry there are numerous instances when flow is in pipelines that are neither vertical nor horizontal but inclined at some arbitrary angle to the vertical. For example, when a single production platform drills a number of wells to maximise exploitation of a particular reservoir, most of those wells will have sections which are inclined to the vertical. In such circumstances it will be necessary to monitor the solids flow rates in solids-liquid flows, for example, to monitor the flow of drilling cuttings during drilling operations, for non-horizontal and non-vertical pipes.

Often in drilling operations, to remove the drilling cuttings produced by the bit at the base of the well, drilling mud is pumped into the well via the drill pipe, past the cutting bit, returning up the well bore. The returning mixture is a good example of solids-liquid flow. Knowing the rate at which an oil well is being drilled, it is theoretically possible to predict the volumetric flow rate, Q_S, at which the cuttings should return to the surface. If Q_S is less than the predicted value, rock cuttings

could be jammed in the well or the well bore, and this could lead to the drilling head becoming stuck in the well. On the other hand, if the value of Q_S is greater than predicted this could mean that the well is collapsing. Either of these scenarios would entail costs of millions of pounds sterling and need to be avoided. There is thus a need for a technology capable of monitoring solids-liquid flows.

The steady state volumetric flow rate Q_S of the cuttings in the pipe is given by:

$$Q_S = \int_A \alpha_S u_S dA \qquad\qquad 1\text{-}2$$

where: A represents the cross-sectional area of the pipe carrying the flow, α_S is the local solids volume fraction and u_S is the local axial solids velocity. Measurement of the distributions of α_S and u_S is particularly necessary in situations where their distributions are highly skewed (non-uniform), for example in horizontal and inclined flows.

At present, there are few commercially available devices for measuring both the local solids volume fraction and velocity distributions in water-solids flows in inclined pipes. Although the measurement of the solids volume fraction distribution in solids-in-water flows can be made using Electrical Resistance Tomography (ERT) - which can be very expensive – techniques for accurately measuring the axial solids velocity distribution are by no means so well developed. It should be noted that dual-plane ERT can be used to measure the solids axial velocity distribution. Moreover it must be also be noted that ERT is still in its infancy and is still essentially an experimental/ developing technique.

The purpose of this research is to develop a low cost device that measures the local solids volume fraction, α_S, and the local solids axial velocity, u_S, in highly non-uniform solids-liquid flows. One of the most widely used techniques for velocity measurement in multiphase flow is spatial cross-correlation, and the device proposed here to measure the local solids volume fraction distribution and the local axial solids velocity distribution in solids-water flows in which the distributions are highly non-uniform, is a non-intrusive Impedance Cross-Correlation (ICC) device.

The very nature of solids-liquid flows means that there will be non-uniform profiles

for the solids volume fraction and the axial solids velocity over the pipe cross-section. In such situations, to measure the solids volumetric or mass flow rate it is necessary to measure the profile of the local solids volume fraction and local axial solids velocity over the pipe cross-section and then obtain the relevant flow rate by integration.

Multiphase flows can contain any combination of gas, liquid and solid flows, and may contain more than one component of the same phase at the same time, for instance, water and oil. Thus to better understand the research aims and objectives, the properties of multiphase flows are discussed and explained in Section 1.2, possible industrial applications of the research are introduced in Section 1.3, and industrial implications, are discussed in Section 1.4.

1.2 Properties of multiphase flow

To understand the types of flows, and measurements that have been undertaken in this research, basic properties of the multiphase flows are described here. Figure 1-2 is a schematic representation of multiphase flow and depicts the flow of a mixture of liquid (water) and solid particles in a cylindrical pipe.

In Figure 1-2, Q_S represents the volumetric flow rate of the solid particles, and Q_W represents the volumetric flow rate of the water. For a steady state flow, Q_S and Q_W can be calculated using the following Equations:

$$Q_S = \int_A \alpha_S u_S dA \qquad\qquad 1\text{-}3$$

$$Q_W = \int_A u_W (1 - \alpha_S) dA \qquad\qquad 1\text{-}4$$

where:' A' represents the cross-sectional area of the pipe, α_S , u_S represent the local solids volume fraction and the local axial solids velocity respectively, and u_W represents the local axial water velocity. The local solids volume fraction α_S in the flow is defined as the volume of the solids in a local sample as a fraction of the total volume of the local sample.
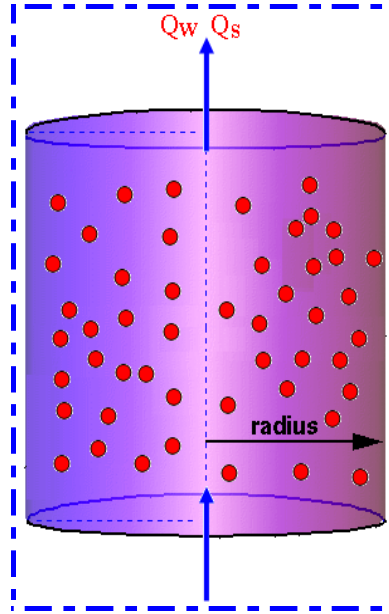
Figure 1-2: Schematic representation of a multiphase flow in a cylindrical pipe

The difference between the local velocities, u_S and u_W, is called the local axial slip velocity, V_{slip}, see Equation 1-5.

$$V_{slip} = u_W - u_S \qquad \text{1-5}$$

The average solids volume fraction $\bar{\alpha}_S$ in the flow cross-section is defined as in Equation 1-6:

$$\bar{\alpha}_S = \frac{1}{A} \int_A \alpha_S \, dA \qquad \text{1-6}$$

The average solids velocity $\bar{u}_S$ over the cross-sectional area, can be calculated as:

$$\bar{u}_S = \frac{\int_A \alpha_S u_S \, dA}{\int_A \alpha_S \, dA} = \frac{Q_S}{A\bar{\alpha}_S} \qquad \text{1-7}$$

And the average liquid velocity $\bar{u}_W$ over the cross-sectional area, can be calculated as:

$$\bar{u}_W = \frac{\int_A [1 - \alpha_s] u_W \, dA}{\int_A (1 - \bar{\alpha}_s) \, dA} = \frac{Q_W}{A(1 - \bar{\alpha}_W)} \qquad\qquad 1\text{-}8$$

The necessary basics of multiphase flows relevant to this thesis may be understood from these equations. Later in the thesis multiphase flows will be discussed in more detail.

1.3 The measurements needed for this research

In uniform flow in a pipe both the local solids volume fraction, $\alpha_{s,i}$ and the local axial solids velocity, $u_{s,i}$, would be constant across the pipe cross-section and Equation 1-6 would reduce to $\alpha_s = \alpha_{s,i}$. Similarly Equation 1.7 would reduce to $u_s = u_{s,i}$. In such conditions any global flow measuring device that measures the mean values of $\alpha_{s,i}$ and $u_{s,i}$ across a pipe cross-section would give a reasonably accurate measure of α_s and u_s. Equation 1-3 for the volumetric flow rate of the solid particles would simplify to:

$$Q_S = A \alpha_s u_s \qquad\qquad 1\text{-}9$$

However, local flow parameters are generally not uniformly distributed in the flow cross-section. A good example is upward solids-liquid flow in an inclined pipe, as shown schematically in Figure 1-3, where the distribution of the solids across the pipe cross-section is highly non-uniform. The distribution will depend on the density of the solids; the more dense the solids the less the net upward buoyancy force on its particles. Thus the more dense the particles the quicker they sink to the lower side of the inclined pipe – all other things being equal - causing a layer of solid particles to develop. If more than one solid was being transported the density and size of the particles would both vary and the layer of particles on the lower side of the inclined pipe would also be non-uniform.

If the layer of dense solid on the lower side of the inclined pipe becomes thick enough, it can slip/slide down the pipe against the fluid flow. Such reverse flow may be episodic or, under suitable circumstances, continuous.

Simultaneously the liquid is flowing upwards over the surface of the solid particles, and in so doing it entrains particles from the top of the layer back into the liquid flow, taking them further up the pipe. We may therefore see a kind of recycling process with particles being carried upstream sinking to the lower side of the inclined pipe being carried a distance downstream before being caught up by the fluid and carried upstream again. Of course, some solid particles could, depending on the fluid forces they experience, be carried up the pipe without ever sinking onto the solid layer. The process of entrainment is strong enough to ensure that there is a net upwards solids flow despite the downward motion of the solids bed at the lower side of the pipe.

There will be a dynamic balance between the conflicting forces and a flow will be established where the time averaged local solids volume fraction shows a variation across the pipe from a high value at the lower side of the inclined pipe to a much lower value at the upper side of the pipe. Naturally, the time averaged axial velocity profile for solids carried in multi-phase flow in an inclined pipe will be correspondingly complex with larger axial solids velocities in the forward direction at the upper side of the inclined pipe and smaller axial solids velocities in the reverse direction at the lower side.

In non-uniform flows it is accepted that complete profiles of α_S and u_S must be acquired in order to determine Q_S using Equation 1-3. One aim of the current investigation will be to develop a device that will measure the distribution of α_S and u_S in the flow cross-section.
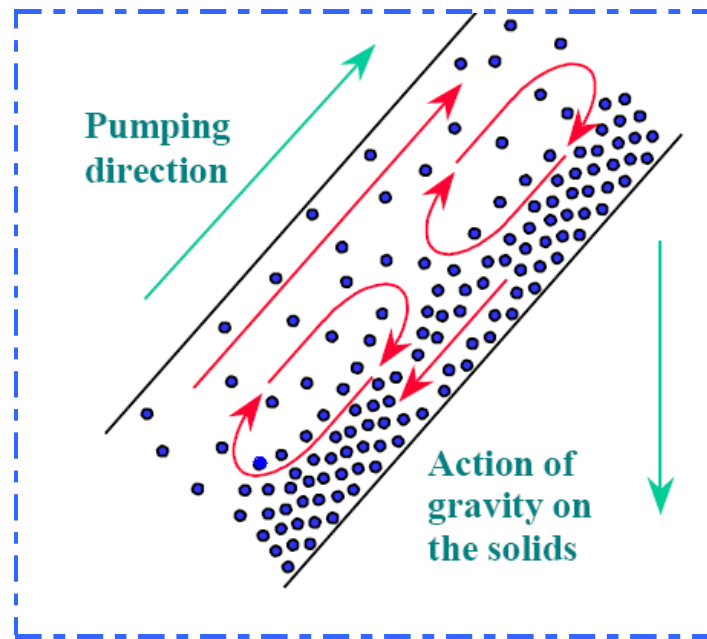
Figure 1-3: A solids-liquid flow in an inclined pipe

1.4 Possible applications for multiphase flow measurement

This section describes possible applications of a device capable of measuring the local properties of a solids-liquid pipe flow. This is not an exhaustive list, its purpose is to show the range of areas to which the current research could be applicable.

Before introducing possible applications of a solids-liquid flow measurement device, it is important to note the generic nature of much of the current investigation. The intended application is for a solids-water flow or more generally for a non-conducting dispersed phase in an electrically conducting continuous liquid. However, depending on the measurement method, the device could also have applications in such flows as gas-in-water and oil-in-water. It is intended that the device developed will be non-intrusive.

1.4.1 Oil and gas industry applications

Part of the original funding for this research came from the oil industry and the original intended application is within this field. An oil or gas well does not produce a single phase product. Often oil, gas, water and solids will be produced simultaneously from the same well, although for the majority of the time the predominant flow is two phases. Indeed oil and gas production probably is of the greatest interest in multiphase

flow measurement research and traditionally the oil and gas industry has been one of the largest funders of multiphase flow research. Much equipment developed within these industries is then subsequently devolved for other applications.

The following oil and gas industry applications are the ones for which this technology was originally intended. As such it has already attracted funding from both public and industrial sources which suggests that it is a viable market.

During oil well drilling operations a fluid, known as drilling mud, is pumped into the well. This fluid passes down the drill pipe, past the cutting bit, and then back up the well bore. As the fluid returns to the surface it carries with it the drilling cuttings produced at the base of the well. This returning mixture is a solids-liquid flow. This operation is shown schematically in Figure 1-4.
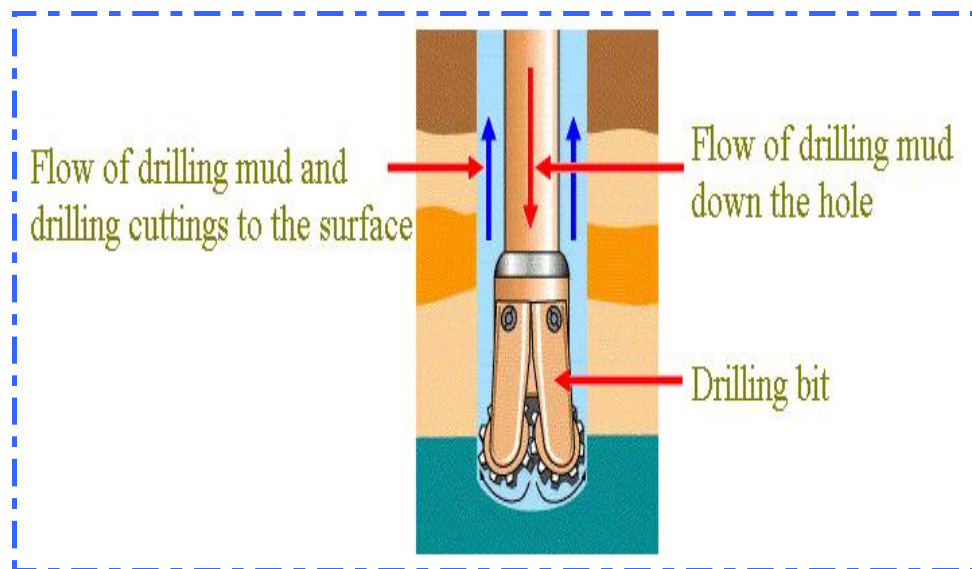
Figure 1-4: Representation of oil well drilling [http: //science.howstuffworks.com/oil-drilling4.htm., accessed 20/04/08]

As stated earlier in this chapter the rate at which an oil well is being drilled is known. Therefore it should be possible to predict the volumetric flow rate, Q_S, at which the rock cuttings will return to the surface. However this expected volumetric flow rate does not always occur. As state previously, if Q_S falls below the predicted value it is possible that rock cuttings are jammed in the well, which can lead to the entire drilling head becoming stuck in the well. Similarly if Q_S is higher than the predicted value then this could indicate that the well is collapsing. As either of these outcomes could

entail a cost of several million pounds they need to be avoided if possible. However, stopping drilling due to a false alarm is costly in terms of lost production, so a technology capable of accurately monitoring the solids flow rate would be of great assistance to the drilling team.

Although the thesis is primarily concerned with solids-in water flows, the technology that developed could also be used in a range of other applications in the oil industry in which water continuous multiphase flow occurs. Examples are given in (a) to (e) below:

(a) An area, in which considerable research into multiphase flow measurement is taking place, is well testing. As an oil well ages the relative fractions of oil, water and gas brought to the surface will vary. If the fraction of the desired product, whether oil or gas, drops too low the cost of operating the well will outweigh the income, so well testing needs to be carried out at regular intervals. At present the most common way to check the output from a well is to take a test separator to the well-head. The separator is attached to the production line, separates the phases and then individually meters each one. The test separators require the well to be off-line during testing and have reported that approximately 2% of production time is lost due to test separation procedures (Thorn et al., 1999). Possibly more importantly, test separators do not operate at flow conditions that are representative of those during production because they introduce a pressure drop of up to 100psi onto the well. Test separation is expensive, and Priddy (1999) has reported that for BP Exploration Operating Company Ltd. to carry out seventy-five well tests in a year on their Cusiana oil field in Colombia, which has eleven wells producing up to 500 thousand barrels of oil per day, costs £2.25million in operating costs. Jamieson (1999) reported that Shell UK Exploration and Production saved £40million in capital expenditure alone by installing four multiphase flow meters offshore in the North Sea. He also reported that Shell UK Exploration and Production expect to save between £180million and £280million in capital expenditure by 2010. Jamieson has also estimated that worldwide about 10000 multiphase flow meters, worth approximately £1billion, will be purchased between 2008 and 2010. Major oil companies such as Shell and BP calibrate multiphase flow meters at the well-head using test separators.

However, both Jamieson (1999) and Priddy (1999) consider that despite such precautions the measurements made by these devices are not satisfactory, and suggest that an increase in specialist laboratory facilities and instruments will be required as the need for multiphase flow meters increases. A relatively simple and robust non-intrusive device which could, for example, measure either the relative fractions or the proportion of gas present would be extremely valuable to the oil and gas industry.

(b) Another on-site application is downhole testing. Oil wells often produce oil and water from different strata along their length. Lowering a flow meter down the well hole allows the flow from each individual layer (stratum) to be monitored, and layers which are producing water can be found and sealed off. Jamieson (1999) has reported that the conditions downhole can reach a pressure of 850bar and a temperature of 150°C, which prevents dissolved gases from coming out of solution and can result in a two-phase flow which as compared to three phase flow is advantageous for multiphase metering (Zuber et al., (1965), making it more suitable for the technology which is expected to be developed in the current project.

(c) Another major application is allocation metering. Modern oil fields often produce relatively small amounts of oil so oil companies often combine production facilities and pipeline facilities to lower operating costs and manpower requirements to keep the field economically viable. Priddy (1999) has reported that the Eastern Trough Area Project in the North Sea, groups together seven oil and gas fields for these reasons. It is important in these types of situations to accurately meter each partner's allocation of oil or gas. Meter accuracies in this application must be higher because of the need for fiscal quality monitoring. Thorn et al suggest that while well testing requires an accuracy of ±10% allocation monitoring requires accuracies of better than ±5% (Thorn R.et.al, 1999). At the moment it is not known what will be the accuracy of the meter to be developed in this project, but the author is optimistic that it could be within ±5%.

(d) When drilling an oil well, there is the chance of bringing a pocket of natural gas from first entry in to the well through the mud out to the surface causing an eruption or explosion. This puts the staff on the oil rig in danger, destroys

expensive equipment, delays production and damages the environment around the oil well. Therefore, the understanding of multiphase flows is very important when developing control strategies to prevent explosions caused by the release of natural gas in the drilling process. Using a multiphase flow meter allows the driller to detect the presence of gas in the well and to determine the likely time the gas will take to reach the surface, which gives the driller the opportunity to take the necessary steps to prevent an explosion.

(e) To extract the oil from oil wells a pump has to be placed on the top of the well. This pump could stop operating if the oil is too heavy or too viscous to be pumped. To solve this problem steam (and sometimes water and gas) is pumped into the well, which helps move the oil towards the pump because of the increased temperature and pressure generated when the steam is pumped into the well. Using multiphase flow meters could facilitate this process by quantifying the properties of the multiphase flow in the pipe, which could provide the information needed to determine the quantity of steam needed to be pumped into the well to move the oil.

1.4.2 Other applications of multi-phase flow

In order to explain how this research relates to real world events, and how the results of this research could help solve current industrial issues, this section introduces some applications of multiphase flows, the emphasis here is on the need for metering.

Mining industry: Water is often used as a carrier medium for a range of different solids including such important materials as cement, coal, and iron ore, sometimes over long distances. After extraction, minerals usually need to be transported to other sites either for ongoing shipment or to be used. Traditionally this was done by road or rail transport, but now hydraulic transport is often a more attractive option. Constantini and Parsons (1974), Goosen and Cooke (1996), Asakura, et al., (1992), Seshadri, et al., (2001) and Ling, et al., (2003) have all argued that hydraulic transport usually results in a lower environmental impact and lower costs. For example, Constantini and Parsons (1974) estimate that a proposed 900 mile potash pipeline in Western Canada capable of transporting 6 million tons of potash per year would cost one third of the equivalent rail transport network. Therefore, hydraulic methods are attractive to the mining industry for transportation of raw materials. The resurgence of

coal as a major energy source been an impetus for substantial developmental effort devoted to transportation of coal slurry. The multiphase measuring device developed in this research project, if successful, could be applied to the measure of transportation of solids-in-liquids outside the gas and oil industry.

When using hydraulic transportation systems it is vital to ensure that the solids (minerals) are suspended in the flow. Thus, the speed of the suspension and the pressure drop along the pipe must be known and allowed for when designing the system and selecting the pumps which drive the system, so as to ensure the most economical and efficient operation - which is critical to ensure the cheapest running costs Lucas, et.al., (2004). As the size of hydraulic transport pipelines increases this becomes more important. For example, Constantini and Parsons (1974) have estimated that a proposed 1000 mile long coal pipeline in the USA capable of transporting 37 million tons of coal per year would cost $650 million to build with an operating cost of $137 million per annum. If improved knowledge of pumping loads could result in even a 1% saving in operating costs this would save $1.37 million per annum. However a survey of the literature showed that examples of local measurements acquired in these flows are uncommon.

Kakka (1974) has reported the case of a 53 mile long iron-ore pipeline in Tasmania used for transporting the mineral from the mine to waiting cargo ships. Here an instrument was required for measuring both the solids volume fraction and velocity in order to calculate the volumetric flow rate of ore into the ships. A number of existing devices have been developed and are in current use measuring the local properties of a multiphase flow (Lucas, et al., 1998; Dong, et al., 2003; Lucas and Mishra, 2005). These flow meters have different uses or applications such as when they are used to measure the local properties of multi-phase flows, however they generally suffer from either being intrusive, being limited to fluid-fluid flows being optical and unable to penetrate into a solids-liquid mix, or being complex, expensive and requiring a high level of technical support, see Chapter 2. The device to be developed here should be non-intrusive and relatively robust.

The study of two-phase flow is attracting more attention at present and the two-fluid model in which the fluid and the particle are regarded as two continuum materials fully filling the available space is widely used with the equations of state of the two

phases well established (Wang, et al., 2003). Concentrated solids/liquid flow occurs when the mean volume concentration of suspended solids exceeds 5-10% and is characterized by momentum transfer due to the collisions between particles and the movement of particles from one layer to another. Continuum descriptions require defining equations that relate the concentration of solids and the energy distribution and dissipation in the mixture to micro-mechanical aspects of particle motion and the material properties of the particles (Savage,1984; Campbell, 1990). Thus, research has concentrated on the less complex case of dilute two phase flow and avoided the complexities of dense two-phase flow which is usually met in reality (Takashi Hibiki, (2002). Key physical parameters that need to be controlled in any experiment are the ratio of solid and fluid densities, the shape, size and mechanical properties of the solid particles, and the viscosity of the fluid.

A further possible area of interest in this field is dredging and underwater mining. Ljubicic, et al., (1989) report an investigation into measuring the amounts of coal cut from the sea floor and being sucked onto a waiting vessel. Similar techniques, without the cutting tool, are used for the collection of aggregates at sea. What is important in both processes is to ensure that the solids are efficiently removed from the sea bed and it is clear that improved knowledge of the flow in the suction pipe would be valuable.

For example, the Palm Islands in Dubai are three large artificial islands, currently being constructed in the shape of palm trees and each will support residential communities and resorts. It is possible to make these islands due to the wide continental shelf off the Dubai coast and its relatively shallow depth. The islands are built from $80 \times 10^{6} \text{m}^3$ of sand dredged from the approach channel. Had suitable multiphase flow meters been available to measure the solids volumetric rates during dredging and during the spraying of the sand-water mixture, the process could have been much more efficiently managed.

It is likely that any device developed in the current investigation will be applicable in the areas of hydraulic transportation dredging and spraying of sand-water mixtures as described above.

Process industry: Within the process industries there are many examples of the need for the continuous measurement of solids in liquids, in particular water treatment processes where solids are removed from solids-liquid flows. Such removal can be achieved in a number of ways including centrifugal filtering and belt press separation. However, as Chu and Lee (1999) report, not all of the water can be removed by mechanical methods and to release this so-called bound water, a polymer flocculant is added to the process stream causing suspended particles in the water to aggregate, forming a floc. The quantity of polymer that must be added will vary with the type and volume fraction of the solids. If too little polymer is added the separated sludge will contain too high a water volume fraction. If too much polymer is added this not only incurs unnecessary costs but the resulting liquid stream can contain polluting levels of polymer (Abu-Orf, et al., 1997). Chu and Lee (1999) report that the process by which water is displaced out of the process stream (dewettability) will decrease if too much polymer is added. Abu-Orf, et al., (1988) have reported that the U.S.A. produced 5.3 million tons a day of dry solids from municipal wastewater treatment alone as long ago as 1993, and that to achieve that production approximately $130 million was spent each year on polymer flocculants. Even a 1% reduction in polymer usage could result in substantial saving. Traditionally, the quantity of flocculant to be added is assessed by visual inspection of the separated sludge, the condition of which can vary hourly (Abu-Orf, et al., 1979; Chu and Lee, 1999). Therefore there is a need for an instrument which gives on-line determination of the solids content of the flow.

Grieve, et al., (1999) report research into the application of solids-liquid measurement technology to level and moisture content measurements within water purification filters. As the operating filter and the resulting filter cake are both solids-liquid mixtures there is a possible application of new multiphase measurement technology here. The water treatment application described is, of course, analogous to many other solids-liquid pipeline flows within the process industries.

Within the field of separation there is a wide range of possible applications of multiphase measurement technology such as the measurement of the local solids volume fraction inside hydrocyclones, as reported by Bond, et al., (1999), or the measurement of component interface positions within a settling tank as reported by Schüller, et al., (1999). It is likely that there will be applications of the technology

presented in this thesis to these areas.

Modern manufacturing techniques have made possible the assembly and use of micro-chemical devices which are better than the commonly used batch reactors because they use only minimal amounts of fluids. Such devices have high heat and mass transfer rates, and shorter reaction times. In these micro-chemical reactors, multiphase flows are present and it is highly desirable to know the characteristics of these multiphase flows to ensure efficient operation and to develop new designs. For this, knowledge of flow patterns, volumetric content, pressure drop, liquid film thickness, and internal mixing quality is necessary (Halter, et al., 2004); Severin Waelchli, 2006; Feng, et.al., 2005).

Fermentation produces foams in both chemical and biochemical processes. Unfortunately, too much foam causes loss of sterility and so, to store the unwanted foam, oversized vessels are used which increases the cost of the process. Thus monitoring and controlling different foam phases that occur is important (Varley, et.al., 2004).

Because of their advantages over other reactors, bubble column multiphase reactors are used extensively in the chemical and biochemical industries. Their advantages include simplicity of construction because of the absence of mechanical moving parts, good mixing, good mass and heat transfer rates, high thermal stability, low power consumption and low operational costs. In these reactors gas is injected into a continuous liquid phase. The properties of the bubbles generated depend on how the gas is injected, reactor geometry, the operating conditions and on the physical and chemical properties of the two phases. These factors determine the shape, size, and velocity of the bubbles and whether or not the bubbles coalesce. It is necessary to measure the values of these parameters to construct an accurate model of bubble columns to obtain more efficient operation (Gourich, et al., 2006; Pradhan, et.al., 2008).

Many chemical processes require measurement of the rate of mass transfer and the interfacial area per unit volume in a multiphase flow in order to control or improve the overall performance of a chemical process. Examples include oxidation reactions, chlorination reactions, and aerobic fermentation (Steinemann and Buchholz, 1984). Generally in mass exchangers and in chemical reactors it is important to know bubble

diameters, volume fractions and the mass transfer rates. Reliable methods of measuring the properties of such complex flows are needed in order to maximise efficiency and to lower operational costs (Lucas, et al., 1999; Pohorecki, et al., 2005; Favelukis and Ly, 2005; Gao, et al., 2006; Pyung Seob Song, et al., 2005).

Geophysical applications: Although the current investigation aims to develop a device capable of making solids volume fraction measurements in pipe flows it may be applicable to other fields where a measurement of solids volume fraction is required. A number of these can be found within Geophysics. A good example is the measurement of sediment density on the sea bed as reported by Hulbert, et al., (1982). A similar application involving the measurement of sediment density in a bore-hole was reported by Lauer-Leredde, et, al., (1998). The density of a sediment is directly related to its solids volume fraction and therefore this is a possible application of the current research. A similar application is the detection of sediment height on the sea bed. The sediment level is usually measured by detecting the point at which the local sediment volume fraction drops to zero. An example of this application is reported by Ridd (1992). It is likely that any device developed in the current investigation will be applicable in these areas.

Many geophysical applications involve the measurement of conductivities, densities, or water volume fractions over large areas or the pinpointing of anomalous areas in an otherwise even material. A good introduction to this field is given by Griffiths, et al., (1983). Particular applications include the detection of layer interfaces within soils reported by Lagace, et al., (1996) and the detection of leaks from storage ponds or pipes reported by Binley, et al., (1999) and Jordana, et al., (1999). Although the current research is unlikely to be directly applicable in these areas it is possible that it could be developed for such applications.

Multiphase technology is also applicable to non-flowing mixtures. A device that can measure the volume fraction in a fluid mixture that is flowing may also be used with a mixture that is static. Thus, multiphase flow devices may be applicable to mixtures which are not contained in a pipe. For example, such sensors could be used in vessels and reactors with streams of bubbles, such as are present in many processes in industry. Thus, the results and conclusions of this research could be of use in a number of applications in different industries. To develop the uses of the multiphase flow meter,

the following subsections discuss some of the applications of multiphase flow meters in modern industries.

Nuclear industry: The understanding of multiphase flows is an important aspect in nuclear reactors where two-phase flow is used in the cooling process. The nuclear reactor generates steam by heating water using radioactive processes, the generated steam is then used to spin a turbine (the steam turbine) that generates electricity. After that, the steam is cooled and returned to the steam generator. The cooling process creates water vapour and a two-phase water-steam flow. Calculating the heat transfer in the nuclear reactor is important to ensure both efficient and safe operation (Lucas, et al., 2001). The heat transfer can be more accurately calculated if the diameter of the water droplets in the flow is known, and this can be achieved by measuring the size of the bubbles, and the volume fraction of the two-phase flow (Beggs and Brill, 1973).

Food Industry: The transportation of food within a plant often involves the flow of solid–liquid food mixtures within a pipe. However, such systems have specific requirements; they generally convey high solids fractions where the solids that have only a small density difference with the carrier liquid and the carrier liquid is usually highly viscous and non-Newtonian. The lack of a tested theory based on measured solids-liquid flows represents a major barrier in this industry to the extension of continuous aseptic processing technology (Holdsworth, 1992: Crilly and Fryer, 1993; Willhoft, 1993).

1.5   Research aims and objectives

The aim of this work is to design a novel non-intrusive impedance cross-correlation (ICC) flow meter. This device should be able to measure local volume fractions and local velocities in a non-uniform multiphase flow e.g solids-water flow. By taking measurements in each part of the flow cross-section, profiles of local volume fraction and local velocity will be extracted.

The data produced from the device can be used among other things for validating electrical resistance tomography (ERT) systems Lucas, et al., (1998). The ICC device will have similar features to an ERT system. It consists of two electrode arrays mounted around the pipe. It is intended that, the ICC device will be low cost

(compared to an ERT system) and will not required sophisticated algorithms to analyse the acquired data.

These aims are achieved by meeting the following objectives:

❖ Carrying out a literature review regarding multiphase flow measurement instrumentation and techniques.

❖ Designing and building an ICC flow meter with two axially separated electrode arrays A and B.

❖ Designing a conductance circuit to measure the mixture conductance at each array.

❖ Designing a switching circuit for the impedance cross-correlation flow meter controlled by computer via a LABJACK data acquisition and control unit to alternately take data at each electrode array.

❖ Performing a series of static bench tests in order to investigate spatial variations in the sensitivity of the electric sensing field for different electrode configurations in each array.

❖ Developing an ICC flow meter model in FEMLAB (COMSOL) to simulate the static bench test experiments.

❖ Installing the ICC device in a pipe inclined at 30º, 15° and 0° to the vertical in a real flow loop to measure the properties of solids-in water flows.

❖ Selecting the regions of flow to be interrogated by designing an electrode selection mechanism for both electrode arrays A and B.

❖ Determining the mean volume fraction in each region by measuring the mixture conductivity and invoking Maxwell's equation for mixtures of materials of different conductivities.

❖ Measuring the local solids velocity distribution by cross-correlating fluctuations of the measured mixture conductivity at corresponding regions of the flow cross-section in arrays A and B.

❖ Developing a mathematical model for inclined solids-water flow and checking the modelling results with the experimental results.

1.6   Thesis outline

In this section a brief outline is given of the contents and relative emphasis of the subsequent chapters in this thesis.

Chapter 2

This chapter presents a literature survey that discusses multiphase flow. It also introduces the different flow regime for vertical and horizontal multiphase flow. Section 2.4 gives different applications of multiphase flows and their measurement. Also it introduces two phase flow in an inclined pipe and introduces different measurement techniques for measuring solids-liquid flows. Finally, it reviews the different principles, techniques, and technologies for measuring multiphase flows in the real world of the oil and gas industry.

Chapter 3

In this chapter the design and construction of the measurement hardware and software are presented. It presents drawings of the ICC device and also presents the design and construction of the electrode selection circuits controlled by computer via a LABJACK data acquisition system and control device. The principle of operation for each electronic circuit is presented. The data acquisition system and control units are described.

Chapter 4

This chapter introduces the modelling of a single plane of the ICC flow meter. This includes a comprehensive guide to FEMLAB and how to set up the different parameters of the ICC flow meter model. It also familiarises the reader with the

FEMLAB software. Sensitivity distributions for different electrode configurations are presented. For each electrode configuration a Centre of Action for the relevant sensing field is defined.

Chapter 5

This chapter presents the results of static and dynamic experimental tests, using the ICC equipment described in Chapters 3 and 4. The static experimental testing was carried out to validate the finite element model presented in Chapter 3. Results are presented and interpretations are provided. Errors in the results are discussed and possible improvements are suggested.

Chapter 6

The multiphase flow loop that has been developed at the University of Huddersfield is described. All the reference measurement devices and their calibrations are presented in this chapter. In addition the experimental procedure is described covering the use of the ICC device and the reference measurement instruments.

Chapter 7

All experimental results are presented in this chapter. Including 3D plots of profiles for the local solids velocity and local solids volume fraction distributions. Measurement errors are also discussed.

Chapter 8

This chapter presents a mathematical model for inclined solids water flow bared on pervious models for inclined oil and water flows. The results obtained from the model compared it with the experimental results.

Chapter 9

This chapter draws conclusions about the results and achievements of the research. It starts by describing the achievements one by one and drawing relevant conclusions. A

summary of the novel features and the contribution to knowledge of this research is provided. Finally, the author addresses recommendations for future work on the ICC device.

Chapter 2   LITERATURE REVIEW

The aim of this chapter is to review recent relevant literature to provide a detailed background to this research project, to ensure the research is topical and up-to-date, and to ensure the research to be undertaken is relevant to the needs of the oil and gas industry. First the chapter reviews and describes the different two-phase flow regimes: gas-liquid, liquid-liquid and solid-liquid. Next the chapter discusses the principles, and reviews the techniques, and technologies for measuring solids-in-liquids flows. In particular, the final part of the chapter addresses the problems previously encountered with Electrical Resistance Tomography and conductivity probes before proposing a non-intrusive Impedance Cross-Correlation measurement system similar in principle to ERT for the measurement of solids axial velocity and solids volume fraction.

2.1   Introduction

The emphasis of the literature review is to provide the necessary background for the investigation to be undertaken. The project is derived from the declared needs of industry and the expertise, equipment and laboratory space available at the University of Huddersfield. After careful consideration the emphasis of the project will be on the measurement volume fraction and velocity distribution in two-phase solids-in-liquids flow. In the permitted time scale and resources available, interesting and useful phenomena concerned with the details of the flow such as turbulence intensities and eddy dimensions will not be considered.

2.2   Multiphase flow

A multiphase flow is where the flowing fluid consists of a mixture of two or more phases, and each phase has different characteristics. In the oil and gas industry; water, natural gas, oil and solids such as sand, are the typical components when dealing with multiphase flows. This research limits itself to two-phase flow: in particular solid-in-liquid flow through a pipe. In practical laboratory work the fluids tend to be air, water or oil, and the solids may be sand, mica or glass, see for example Goharzedeh and Rogers (2009) and Lucas and Panagiotopoulos (2009).

2.3   The Fluid Properties

Because multiphase mixtures contain different components with different properties, the overall properties of the multiphase mixture will depend on the properties and relative proportions of the different components. Unfortunately, the number of parameters which help determine flow characteristics is very large: of particular importance are density, viscosity, mean particle size, particle shape, pipe diameter, angle of pipe inclination to the vertical, phase velocities, expansibility and compressibility all of which can vary with changes in temperature and pressure. Lovick and Angeli (2004) have claimed that even the material from which the pipe is made will have an effect on droplet size in oil-water disperse flows.

The practical condition under which the work is carried out is important, for example, the work described in this thesis does not include consideration of heavy oils and is restricted to room temperatures, so viscous effects are not expected to introduce any

significant changes to the results obtained between different experiments. This is confirmed by Gysling and Loose (2005) who conducted an extensive review of the effect of viscosity on oil and gas flows in pipes. They confirmed the findings of Charles et al., (1961) that for viscosities, such as apply to this research, the liquid viscosity has little effect on flow pattern transition boundaries. The fluid components tend to separate from each other according to the differences in their densities that cause the different physical distribution for each component, and are largely the basis for the different flow regimes observed in multiphase flows.

However, the physics of multiphase flows is complex so that a large number of different descriptions have been used and are being used (Matsui G (1984)). This thesis attempts to be consistent in its use of terms and, where possible, to use common terms to describe common types of flow. This thesis follows the lead of Jana et al., (2006), that four main flow regimes are adequate to describe, for example, horizontal fluid-fluid multiphase flows and that these regimes may also be applied as descriptors to vertical and inclined flows. See Figure 2.1 which shows the four flow regimes: Stratified flow, Slug/plug flow, Dispersed "bubble" flow, and Annular flow.

Some of the key parameters used to quantify the behaviour of multiphase flows are: volume fraction, superficial velocity and actual velocity of a phase. Volume fraction is the time averaged fraction of the volume which is occupied by a phase. Superficial velocity is the velocity of a phase in the multiphase flow if it was flowing alone in a channel or pipe; superficial velocity may be defined as $\dfrac{Q_i}{A}$. Actual velocity is the velocity which would be measured if the velocity of a small volume of a phase could actually be determined.

Concentrated solids-liquid flow are those where the mean volume concentration of suspended solids exceeds 5-10% and here the momentum transfer due to collisions between particles and the movement of particles is an important consideration in both viscous forces and turbulence. Turbulent energy distribution and dissipation in such mixtures is related to micro-mechanical aspects of particle motion and the properties of the particle material. This is a demanding approach and as a consequence most research thus far has focused on dilute two-phase flow (Al-Aufi and Al-Hinai, 2002).

Key physical parameters that need to be controlled in any experiment are the ratio of solid and fluid densities, the shape, size and mechanical properties of the solid particles, and the viscosity of the fluid.

2.4   Fluid-fluid Flow Regimes

The workers who first laid the basis for the present descriptions of flow regimes did so over fifty years ago, Russell et al., (1959) and Charles et al., (1961). Being able to define the flow regime of a multiphase flow is crucial for the future development an accurate quantitative flow model, but there are, as yet, no standard classifications for flow regimes, and researchers have tended to refine and add to the classification of flow regimes according to their own analysis or understanding (Rodriguez and Oliemans, 2006). Because the classification of the flow regime often tends to be visual there is always some subjectivity in classifying the flow regime. Recently, however, it has been increasingly realised that the number of regimes used to describe a flow should be limited.

There are significant and substantial differences in flow patterns between vertical, inclined and horizontal pipe flow. As would be expected, because gravitational and buoyancy forces act parallel to pipe wall for vertical flow, radial symmetry exists and the flow patterns tend to be simpler. The lower the flow rates the greater the differences between vertical, inclined and horizontal pipe flows – all other things being equal. A brief, simplified review and description of the main regimes for upward vertical, inclined and horizontal two-phase flows taken from the available literature is presented in the following sections. To aid this rationalisation gas-liquid and liquid-flows have been combined, this follows the example of Bannwart et al., (2004), who worked to identify flow patterns in heavy crude oil-water flows and suggested strong correspondence with gas-liquid flows.

It needs to be mentioned that there is a marked lack of experimental data on liquid-liquid and liquid-solid, two-phase flows, particularly in inclined pipes. Some ten years ago Doran and Barnea (1996) and Doran et al., (1997) commented that – at that time – hardly any data could be found for solid-liquid flow in inclined pipes and none at all concerning solid layers at the bottom of the pipe. In 2006, Rodriguez and Oliemans (2006) had cause to remark on the very modest number of publications that addressed

liquid-liquid flow patterns in horizontal pipes and that they couldn't find any qualitative data on the effect of angle of inclination for oil-water flow patterns. Even more recently Yerrumshetty (2007) has claimed that little or no empirical data was available concerning the behaviour of solids in solid-liquid flows.

The reason is not hard to find, building the necessary and appropriate test-rigs is expensive, difficult and costly in terms of both time and laboratory space. One consequence of this is that a number of authors have used pipes of narrow diameter, e.g. Henthorn et al., (2005) who used a 25mm diameter pipe, and Grassi et al., (2008) who used a 21mm diameter pipe. With pipes of small diameter less than about 10mm, surface tension effects could be an important factor in the observed flow patterns, unless the liquid is very viscous, so the transfer of such results to pipes of 80mm diameter and larger must be treated with caution.

However, it appears that the situation is now changing, the author has found significant activity in the field of multi-phase flow with resurgent industrial/commercial interest and the funding of the development of new techniques, see Table 2-1 which presents a list of techniques used to investigate. This project is part of that development.

Table 2-1: Techniques used in the investigation of flow patterns and mixture/particle velocities

Authors	Technique	Phase(s)	Investigation
Lee, S. and Durst, F. (1982)	Laser-Doppler	Sand grains in air. Upward flow in vertical glass pipe 20.9mm ID	Particle velocity profiles
Vigneaux et al. (1988)	High frequency impedance probe	Kerosene–water and oil – water in 100mm and 200mm ID SS pipe	Flow patterns and mixture velocities at angles of inclination 0–65° to horizontal
Alajbegovic et al. (1994)	Single beam gamma-ray densitometer and laser-Doppler anemometer	Ceramic and polystyrene beads in water. Vertical 30.6mm ID FEP pipe	Volume fractions and velocity profiles
Angeli and Hewitt (2000)	Impedance probe	Oil - water in 24mm ID horizontal Perspex pipe	Stratified wavy/drops, three layer

Lucas, G.P. and Jin, N.D (2001)	Resistance cross-correlation flow meter	Oil – water in 150mm ID Perspex working section. Angles of inclination to the horizontal up to 75°	Flow velocities and flow patterns.
Matousek, V. (2002)	Differential pressure transducer, flow meter, radiometric density meter	Fine, medium and coarse sand particles in water, horizontal and vertical, 150mm ID. Plexiglass observation section	Concentration profiles
Wang et al. (2003)	Electrical impedance tomography	2mm diameter non-conducting beads in water. 50mm ID horizontal Perspex pipe	Solids distribution
Lovick and Angeli (2004)	Impedance, conductivity probe	Oil - water in 38mm ID horizontal SS pipe	Dual continuous flow, dispersion of oil in water
Lucas et al. (2004)	Dual sensor conductance probe	Air – water in 80mm ID vertical Perspex pipe	Local gas volume fraction and local gas velocity
Rodriguez O. and Oliemans, R. (2006)	Records of moving images	Oil – water in 82.8mm ID SS pipe. Horizontal and small positive inclinations	Flow patterns, water holdup, angle of inclination (0°, +2° and +5° to horizontal)
Jana et al. (2006)	Conductivity probe	Kerosene - water in 25mm ID vertical perspex pipe	Bubbly, dispersed, core annular flow (oil in the core)
Chakrabarti et al. (2007)	Non-intrusive optical probe	Kerosene – water in horizontal 25.4mm ID Perspex pipe	Stratified flow patterns
Goharzadeh and Rodgers (2009)	Particle image velocimetry and refractive index matching	Three phase oil-air-glass beads in 25.4mm ID horizontal Plexiglas pipe	Slug flow
Lucas, G.P. and Panagiotopoulos, N. (2009)	Dual sensor capacitance probe	Oil – water in 80mm ID vertical Perspex tube	Oil volume fraction and velocity profiles

2.4.1 Fluid-Fluid vertical flows

The classification and description of flow patterns begins with vertical flow. These are the simplest patterns found for two-phase fluid-fluid flows because gravitational and buoyancy forces act parallel to the flow and radial symmetry exists. Figure 2-1 shows a generic map of two-phase flows in vertical pipes issued by the Norwegian Society for Oil and Gas Measurement as recently as 2005 (Dahle, 2005).
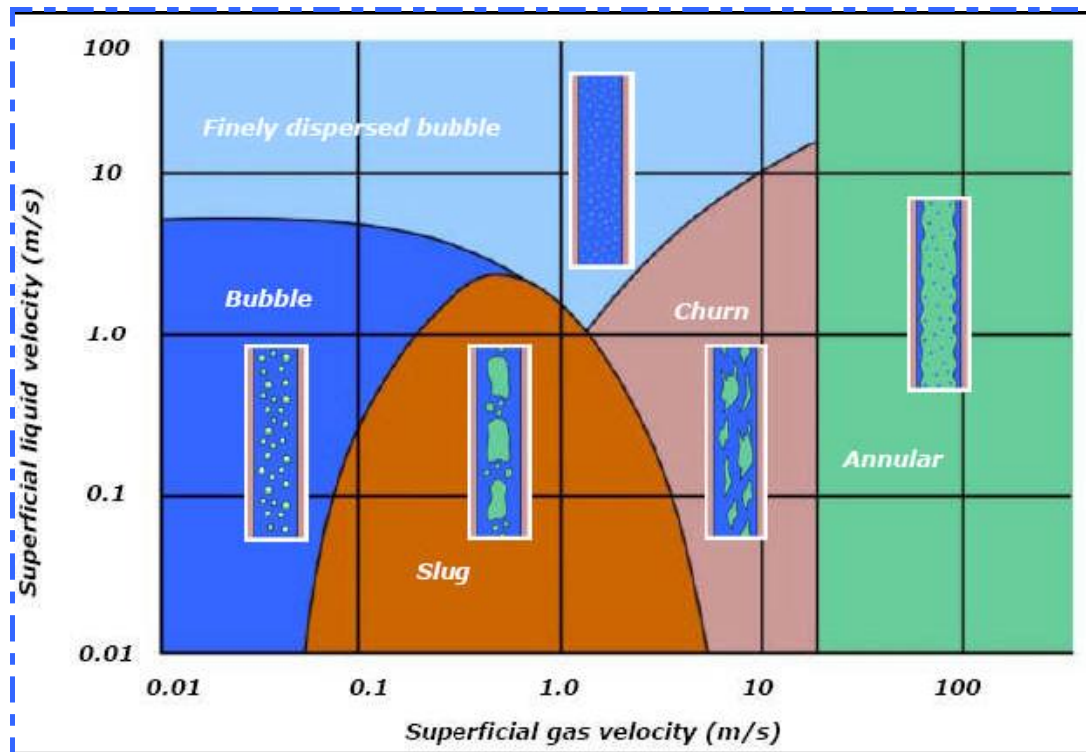
Figure 2-1: Generic map of two-phase flows for vertical pipe geometry [Dahle, 2005]
(Superficial phase velocity = Phase volume flow rate /cross-sectional area of pipe)

2.4.1.1 Bubbly flow

Bubbly flow happens when there is a liquid travelling upwards in a vertical pipe with bubbles of the lighter phase gas dispersed relatively uniformly in the heavier phase, e.g. air bubbles in water. Bubble flow occurs only when the superficial gas velocity is relatively low. The movement of these gas bubbles is very complex and they tend not to coalescence together. As the superficial liquid velocity increases, the bubbles become finer and more uniformly dispersed in the liquid flow. Because of gravitational and buoyancy effects the mean velocity of the bubbles tends to be higher than the mean velocity of the fluid. Lucas et al., (2004) performed extensive measurements on air-in-water flows. Their results tend to confirm those of previous workers but their technique – a dual sensor capacitance probe - was a radical step forward in giving 3D profile of the flow patterns, see Figure 2-2 below. The gas velocity profiles presented were typical for this kind of flow, a broad peak centred on the pipe axis decreasing to about 70% of the centreline velocity near to the pipe wall after which there is a sudden drop to zero at the wall. The local gas volume fraction

was a clear maximum (about 5%) on pipe centre-line falling away more or less linearly to 0% at the pipe wall.
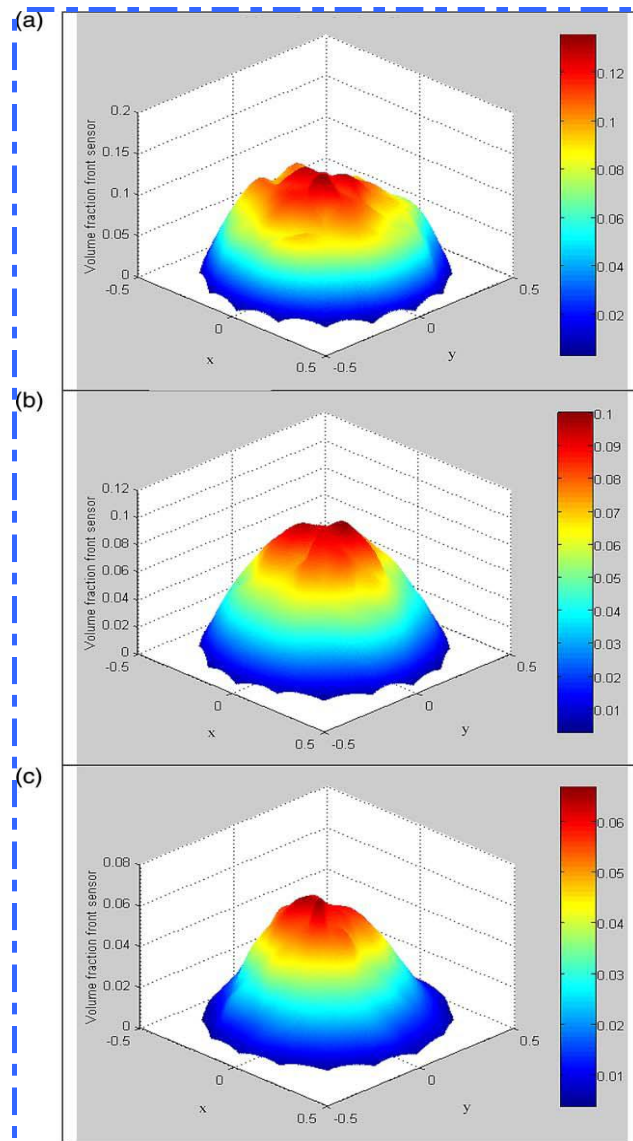
Figure 2-2: Local gas volume fraction distributions for vertical upflow in 80mm ID pipe: superficial gas velocity 0.033ms^{-1}, three water superficial velocities (a) 0.10ms^{-1}, (b) 0.38ms^{-1} and (c) 0.91ms^{-1} (Lucas et al., 2004)

The same phenomena has been observed with liquid-liquid flows. Both Vigneaux et al., (1988) and Jana et al., (2006) described the flow patterns of kerosene in water, that the kerosene forms oblate spheres within the continuous water medium, and strongly resemble the bubbly flow pattern with gas-liquid flows.

Lucas and Panagiotopoulos (2009) extended their earlier work to include oil-in-water flows. They found the same broad axial velocity distribution for oil as they had

previously found for air and concluded that the velocity profiles for gas in water and oil in water flows are very similar in shape notwithstanding that oil is over 600 times as dense as air. However they found that the oil volume fraction profiles across the pipe tend to be flatter than those for air, and change in character with volume flow rate much more so than those for air. For the values of the mean oil volume fraction (movf) investigated they found that over the range of $0.05 < movf < 0.2$ the oil volume fraction across the pipe changes dramatically. For a movf of 0.068 the oil volume fraction distribution across the pipe took the shape of a broad peak with its maximum on the centre-line and falling to near zero at the walls. But by the time the movf has reached just 0.121 the distribution had changed to being flat across the pipe with a sharp drop-off near the wall. With further increase in movf, to greater than 0.19, the distribution became slightly concave, again with a sharp drop-off near the wall.

2.4.1.2 Slug Flow

When the gas flow rate increases the smaller gas bubbles coalesce into plugs, which can occupy the majority of the cross-sectional area of the flow. The gas plugs are separated by regions containing predominantly liquid which are called slugs and will fill the cross-sectional area of the flow, see Figure 2.1. These large gas bubbles are so-called, Taylor bubbles and are described as having a bullet shape (Davies and Taylor, 1950). With further increase in the gas rate, the size and the velocity of the plugs/bubbles increases. The liquid between the bubbles will usually contain smaller scattered gas bubbles. The same general phenomena are observed with oil-in-water flow.

2.4.1.3 Churn Flow

With yet further increase in the gas superficial velocity, churn flow occurs. The flow acquires a more turbulent character, which destroys the liquid laminar film and so forms an unstable flow regime. This results in a churning movement of the liquid in the flow. Because churn flow is superficially similar to slug flow these two regimes are sometimes grouped together as slug flow. Churn flow normally occurs in larger diameter pipes rather than smaller diameter ones. The transition to annular flow is the

point where the liquid separating the gas bubbles disappears and the bubbles coalesce into a gas core.

For an immiscible liquid such as light oil flowing with water in a pipe of 25.4mm ID, as the superficial velocity of the water approaches about $1ms^{-1}$ the size of the oil drops decreases and they become dispersed as fine drops in the water probably due to the shearing forces created by the turbulence (Jana et al., 2006).

2.4.1.4 Annular Flow

With gas-water and light oil-water flows the transition between bubbly flow and core/annular flow occurs when the droplets of lighter phase begin to coalesce in the centre of the pipe to form a continuous core which pushes the water into an outer annulus. The transition appears to be a very chaotic with highly irregular flow patterns before settling down (Jana et al., 2006).

In annular gas-liquid flows, the liquid gathers and travels on the pipe wall while the gas travels in the centre of the pipe. However, a part of the liquid continues to travel as entrained drops in the centre of the pipe with the gas. In vertical annular upward flow, gravity has a greater effect on the more dense liquid, slowing it relative to the less dense gas. Thus gravity may be said to generate a difference between the liquid and gas velocities (slip).

When two fluids are forced to flow in opposite directions, e.g. when the liquid is descending and the gas rising, the relative velocity between the liquid and gas is high, so the annular regime dominates. When both fluids (gas and liquid) are descending, the liquid is likely to flow faster than the gas and the relative velocity between gas and liquid can be said to be against the direction of flow. Again this leads to larger relative velocities and this tends to lead to the annular flow regime being preferred.

2.4.2 Fluid-fluid horizontal flow

As would be expected the major differences between horizontal and with vertical flow regimes are at lower superficial liquid velocities because here there is greater opportunity for stratified flow to develop. In horizontal fluid-fluid flows, different

immiscible fluids separate from each other because of gravitational effects, and this allows distinct flow regimes to develop in the pipe system.

Figure 2-3 shows a generic map of two-phase flows in horizontal pipes issued by the Norwegian Society for Oil and Gas Measurement (Dahle, 2005). Seven regimes or sub-regimes are shown, but these can be reduced to four main types of horizontal flow regimes; Stratified flow, Slug/plug flow, Dispersed flow (where one phase becomes dispersed as drops in the other) and Annular flow (Gourich et al., 2006; Dahle, 2005; Carpentero-Rogero et al., (2009), Grassi et al., (2008). The similarity with the classifications for vertical flow is, of course, deliberate. A brief explanation for each of these flow regimes is provided in the following subsections.
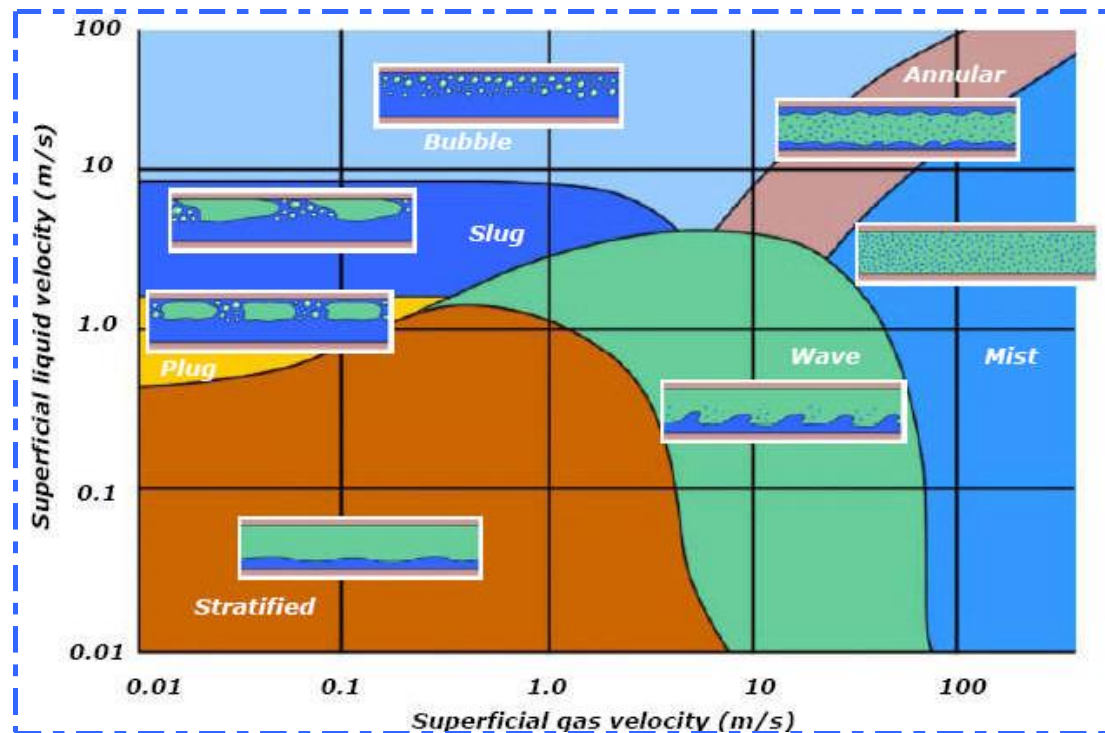
Figure 2-3: Generic map of two-phase flows for horizontal pipe geometry (Dahle, 2005)

In principle there is no theoretical difference between the mechanisms of oil-water flows and gas-water flows, but as Poesio et al., (2007) have pointed out the orders of magnitude differences in important quantities means the results obtained from gas-air flow are not always directly transferable to liquid-liquid flows. This is very unfortunate given the mass of literature that exists on gas-air flows and the relative little that has been written on liquid-liquid flows.

2.4.2.1 Stratified Flow

For low flows of both fluids, the less dense fluid tends to merge together and flow in the top part of the pipe, while the heavier fluid flows in the lower side of the pipe. At these low flow rates, the different phases share a smooth boundary, and each phase occupies a more or less constant proportion of the flow along the pipe. For gas-liquid flows the difference in densities of the two fluids is large and the flow ranges over which stratified flow is found is correspondingly larger.

2.4.2.2 Slug/Plug flow

Chakrabarti et al., (2007) have observed that for horizontal flows of air-water, stratified flow is not often seen in practice; the interface of the separated and stratified layers becomes wavy and slug/plug flow soon develops. They also observed that for kerosene-water flows the stratified flow patterns are more complicated and that degrees of separation can persist in the form of bubbles or large plugs of the lighter oil in the shape of "kerosene chunks" near the top of the pipe, not the uniform elongated Taylor bubbles found with air-water flows. Of course such a phenomenon will depend upon the relative densities and viscosities, but is generally seen only for superficial oil velocities of less than $0.5ms^{-1}$, see Figure 2-4 (Grassi et al., 2008).

If the superficial liquid velocity increases at lower gas flow rates the waves in the liquid at the gas-liquid boundary will touch the upper wall of the pipe creating gas plugs. The body of liquid filling the pipe and separating the plugs is called a slug. Slug dominated flow is very similar to plug flow, but contains bigger gas bubbles, and the liquid slugs themselves contain more bubbles. The term "sparkling waves" has been used to describe this flow when the liquid slugs contain many gas bubbles and "semi-slug" when the boundary waves do not entirely fill the pipe (Franca, L., et.al (1992) , Jones O.C, et.al (1976)). With oil-in-water, slug flow appears at very low oil flow-rates and when the superficial water velocity is low enough to avoid fragmentation of drops, thus the flow region over which slug/plug flow dominates is very limited, the water superficial velocity should be less than abut $1ms^{-1}$ and the oil superficial velocity less than about $0.2ms^{-1}$.
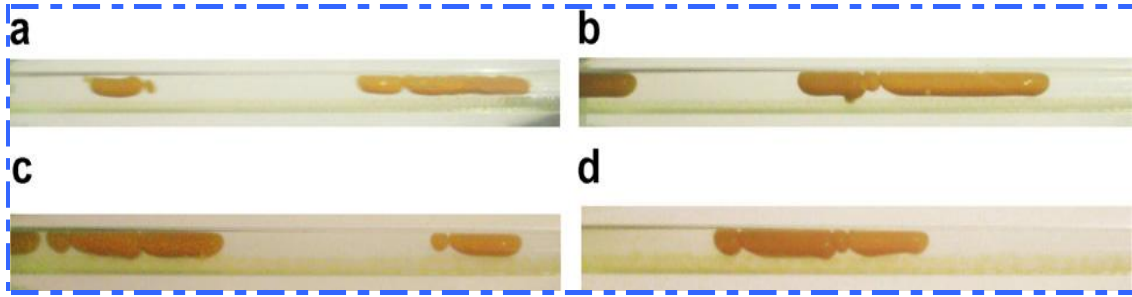
Figure 2-4: Oil plugs in water, after Grassi et al., (2008) (pipe ID 21mm, water superficial velocity 0.5ms^{-1}, oil superficial velocity 0.1ms^{-1})

Previous work by Marruaz et al., (2001) on an industrial rig and more recent laboratory work by Goharzadeh and Rodgers (2009) examined plug/slug flow for air-water mixtures. They found that for established and steady slug flow, increasing the velocity of either phase decreases the length of the liquid slugs. This would be expected given that increase in phase velocities would initiate transition to dispersed flow.

2.4.2.3 Dispersed Bubble Flow

For slug, plug or stratified gas-water flows if the superficial velocity of the water is further increased, and remains greater than that of the gas, dispersed bubble flow occurs. Here, gas bubbles are scattered throughout the body of the liquid just as with vertical bubble flows. Because of their lower density, the gas bubbles tend to gather at the upper wall of the pipe, however, and when the velocity of the liquid is high enough, turbulence effects disperse the gas bubbles into the liquid along the pipe.

An exactly corresponding phenomenon is observed with oil-in-water, with the oil drops becoming dispersed within the water. This phenomenon is observed from very dilute oil-in-water dispersions to more concentrated dispersions of larger oil drops. Rodriguez and Oliemans (2006) reported that they had observed dispersions of water in oil. However, on reading further these authors qualify their observation by saying that this did not necessarily mean the existence of an oil-continuous region, rather it meant very low water flow rates so that the observation of a continuous water phase was problematic.

Compared with the figure for gas-water flows (see Figure 2-3) the dispersed "bubble" region for oil-water flows occupies a much greater relative area. In fact it is the dominant mode of flow if the superficial water velocity is greater than three times the oil superficial velocity.
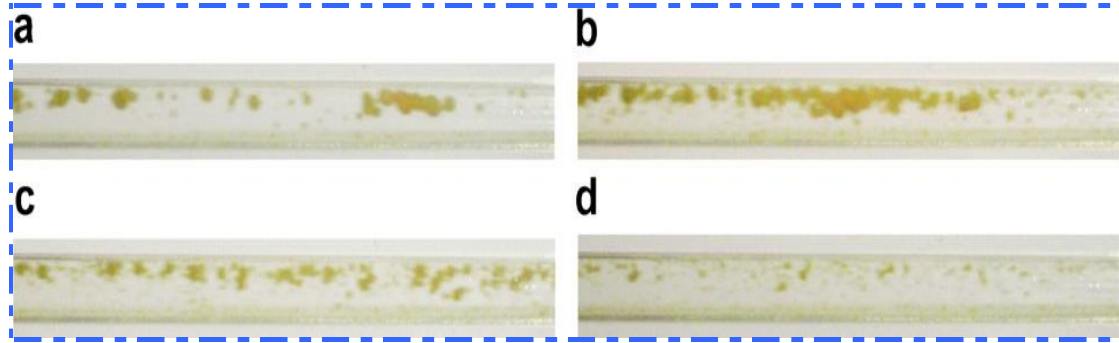
Figure 2-5: Oil dispersed in water, Grassi et al., (2008) (pipe ID 21mm, water superficial velocity 0.7-2.6 ms^{-1}, gas superficial velocity 0.03-0.1 ms^{-1})

The available literature on droplet size in pipe flow is exclusively for dispersed flow and agrees that the maximum diameter of the oil drops decreases with increase in continuous phase velocity, i.e. water flow rate (Lovick and Angeli, 2004, Chakrabarti et al., 2007). As the above Figure 2-5 suggests, and as confirmed by Lovick and Angeli (2004) even for fully dispersed flow the phase distribution across the pipe will be influenced by gravitational forces, and even where the oil fraction is as high as 80% there will be little or no oil present at the bottom of the pipe and no water present at the top.

2.4.2.4 Core Annular Flow

For gas-water flows if the gas superficial flow rate is increased such that the gas attains a much higher velocity than the liquid, then the boundary between the two phases takes on a wavy shape. The tips of these wavelets are blown off into the gas stream. As the gas flow continues to increase there comes a time at which the gas in the flow travels in the centre of the pipe while the liquid travels on the pipe walls and as droplets within the gas. The effect of gravity makes a thicker film of liquid in the lower side of the horizontal pipe, but if the velocity of the gas flow increases sufficiently, the thickness of the liquid film becomes more uniform around the pipe's circumference. The slightly increased thickness of the liquid film at the lower side of the pipe differentiates vertical and the horizontal annular flows. However, when the gas has a very high velocity, the liquid is entrained in the gas as a fine mist and the

liquid travels as random drops in a "flow fog". The film on the pipe wall disappears entirely. Annular and the mist flow regimes are commonly grouped together and known as annular flow fog. Horizontal annular flow is very similar to vertical annular flow, provided allowance is made for gravity which affects the slippage of each phase in the vertical flow and density variations across the pipe for horizontal flow.

For oil-water flows the same phenomena are observed, see Figure 2-6 though Conan et al., (2009) have recently observed that for very light oils a third layer of pure oil may appear at the top of the pipe, but they suggest this may have been a result of the manner in which they injected the oil into the water flow.
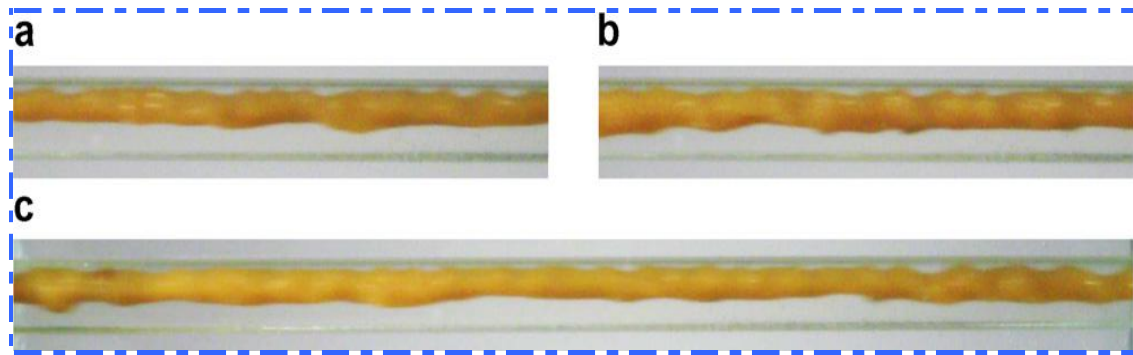
Figure 2-6: Core annular flow oil in water, Grassi et al., (2008) (pipe ID 21mm, water superficial velocity 1ms^{-1}, gas superficial velocity 0.5ms^{-1})

McKibben et al., (2000) performed a laboratory study on heavy-oil-water flows in a horizontal steel pipe of 53mm ID with a transparent working section. Five oils were used with densities varying from 884 – 985kgm^{-3} and viscosities from 620 – 11200mPa.s. In these experiments the oil flow was established and the water gradually introduced. They found that for low water-to-oil ratios, up to about 20% in a total flow of about 6 l/min (a bulk velocity of less than 0.05ms^{-1}), the water took the form of slugs within the oil. The velocity of these slugs was found to be about twice the superficial velocity of the oil. As the water flow increased it was observed that a layer of streamlined oil flow could be sitting on a turbulent layer of water. For all the bulk flow velocities used, up to about 0.12ms^{-1}, the water appeared to be concentrated in the lower side of the pipe but water was occasionally detected along the axis of the pipe and even at the top of the pipe.

McKibben et al., (2000) considered that viscosity and density differences between the oil and the water were insufficient to explain all the results obtained, particularly the flow patterns obtained with the heavier oils, and so introduced a new factor "wettability" of the pipe wall. This was used to explain the fact that, even at low velocities the heavier oils were present as a bottom layer on the pipe wall. The heavier oils preferentially wet the steel of the pipe wall.

2.4.3 Fluid-fluid inclined flow

Prediction of flow patterns in inclined pipes is important if the operator is to avoid formation of a stationary deposit which causes a partial blockage of the pipe, increasing system losses and reducing system efficiency. One of the first to study two-phase upflow patterns in inclined pipes was Scott (1985) who observed that for low flow rates the water close to the oil-water interface moves with the oil as it flows up the pipe but that close to the lower side of the pipe gravitational effects could cause a layer of water to flow backwards. As the angle of inclination increased segregated flow patterns were replaced with wavy flow where the size of the waves increased as the angle of inclination increased, at least up to about 30°.

Vigneaux et al., (1988) investigated oil-water upflows in pipes at between 5° and 65° from the vertical for two pipes, one 100mm ID and the other 200mm ID. The emphasis of their research was on the effect of the angle of inclination and mixture velocity on the radial distribution of the volume fraction. For flows at 15° to the horizontal, where the water volume fraction was about two-thirds and oil propagated as droplets in the water, they found that the diameter of the pipe made a difference to the volume fraction distribution, with a much higher gradient found in the smaller diameter pipe. Here the mean superficial velocity was 0.235ms^{-1} and the concentration of water ranged from 80% near the lower side of the inclined pipe to 30% at the top of the 100mm ID pipe and 50% at the top of the 200mm ID pipe. For lower flows the pattern is more stratified with the water gathering in the lower side of the pipe. As the slope of the pipe increased to 55°, a continuous oil flow appears at the top of the pipe and the water volume fraction as a function of distance from the pipe axis approximates an **S** shaped curve: 100% at the lower side of the inclined pipe to zero at the upper side of the inclined pipe. However, the S shape was much steeper for the smaller diameter pipe.

For inclined two-phase flows the degree of inclination will affect the flow patterns observed. Because of net gravitational forces on the different components there is a tendency for stratification. The heavier components tend to sink to the lower side of the pipe wall, while the lighter components do the opposite. Different levels of stratification occur, which depend on the realative density of the materials and the degree of inclination. Studies on this type of flow condition can be read in Lucas et.al (2001) , G. Oddie, H et.al (2003) and Hing-De Jin Wang et.al (2003) . For example, if the gas velocity is greater than the liquid, slippage takes place and liquid holdup occurs. The steeper the angle of inclination the more important is hold-up. At angles of inclination of about 30° to the horizontal large slugs of liquid could be generated and the appearance is of backward flow of the liquid. This effect is at its maximum between about 20° and about 70° to the horizontal (Carpentero-Rogero et.al (2009). However, while qualitative information is available reliable quantitative data on the effects of change in angle of inclination is very difficult to come across (Rodriguez and Oliemans, 2006).

Flores (1997) and Flores et al., (1998) carried out experimental and theoretical studies on oil-water flow in vertical and inclined pipes to better characterize flow patterns and develop models to predict flow pattern transitions, holdup and pressure drops. Studies were carried out in a 50mm ID pipe using mineral oil and water for angles of inclination of 90°, 75°, 60°, and 45° from the horizontal. He found that the slippage decreased as the angle of inclination increased, and that for the moderate oil and water flow rates used the flow was dominated by dispersed oil-in-water. Grassi et al., (2008) have suggested that the flow patterns change little with small changes in the angle of inclination of the pipe, but in inclined gas-liquid flows the different phases tend to separate from each other because of gravitational effects, and this does depend on the angle of inclination and the flow regimes will range from those found with vertical flow to those found for horizontal flow. Nevertheless, it is possible to say there are four main types of flow regimes for co-current gas-liquid flow in inclined pipes: Stratified and wavy flow, Plug/slug flow, Atomization and Annular flow. A brief explanation for each of these flow regimes is provided in the following subsections.

2.4.3.1 Stratified and wavy flow

For relatively low gas and liquid flow rates the gas and liquid phases separate into two distinct layers with the liquid at the lower side of the inclined pipe below the gas phase but this depends on the slope of the pipe. At low flow rates, the two phases have a smooth boundary, and each phase occupies a more or less constant proportion of the pipe. For uphill flow, if the superficial velocity of either or both phases increases waves appear on the liquid surface. Rodriguez and Oliemans (2006) investigated oil in water flows for horizontal flow and flow at 1°, 2° and 5° above the horizontal. They found significant changes in the flow patterns even for these small angles of inclination, but the largest changes were limited to low, stratified flows. In particular, the disappearance at 5° of stratified flow separated by a clearly defined interface. By 5° there was mixing at the interface for all the flow rates investigated. Kumara et al., (2009) also found flow pattern to be sensitive to the angle of the pipe and confirmed that even for slight pipe inclinations, 5° or less above the horizontal, established smoothly stratified flows in horizontal pipes disappeared.

For the case where the flow of the liquid is downhill while the gas continues to flow uphill the increased relative speed of the two phases generate waves in the interface. However, should the liquid be flowing downhill there is the possibility of be transition from laminar to turbulent liquid flow so that, even without gas flow present, natural instability of the interface occurs (Lioumbas et al., 2005).

2.4.3.2 Plug/slug flow

As the liquid flow rate passes a certain critical value waves in the liquid at gas-liquid boundary touch the upper side (top) of the pipe creating gas plugs and liquid slugs. Some authors term these slugs rather than plugs because the gas phase remains to some extent continuous and the actual slugs contain large gas bubbles. This is probably the most frequently encountered flow regimes during co-current gas–liquid flow in inclined pipes and over the last decades has attracted the interest of many researchers (e.g. Grolman and Fortuin, 1997; Rodriguez and Oliemans, 2006, Poesio, et al., 2007).

2.4.3.3 Dispersed "bubble" flow

If, for gas-water flows, the superficial velocity of the water is further increased, and remains greater than that of the gas, dispersed bubble flow occurs. Here, gas bubbles are scattered throughout the body of the liquid just as with vertical bubble flows. Because of their lower density, the gas bubbles tend to gather at the upper wall of the inclined pipe, however, and when the velocity of the liquid is high enough, turbulence effects disperse the gas bubbles into the liquid along the pipe. In the case of uphill flow the gas bubbles maintain their separate identity to a higher velocity than for horizontal flow.

Dispersion is observed with oil-in-water flows, from very dilute oil-in-water dispersions to more concentrated dispersions of larger oil drops. Lucas and Jin (2001) in their investigation of homogeneous velocity present results for oil-in-water but their figures also present regions of high oil flows and small water flows which are described as dispersion of oil in water.

2.4.3.4 Dispersed or atomised flow

This type of flow is encountered at very high gas flow rates, where the liquid forms a thin film around the pipe circumference while the gas travels in the centre of the pipe. However, a part of the liquid continues to travel as drops in the centre of the pipe with the gas. For both horizontal and vertical flows if the gas velocity increases sufficiently, liquid is entrained into the gas and dispersed throughout the gas phase as a fine mist so that the liquid travels as random drops in a "flow fog". The film on the pipe wall disappears entirely.

The flow rates at which at the transition to atomised flow takes place for oil-water flows will depend on the angle of inclination of the pipe. Kumar et al., (2009) have found that for upflow the steeper the pipe the lower the superficial velocities at which the dispersed flow pattern emerged. Rodriguez and Oliemans (2006) had reported similar findings in terms of a narrowing of the transition region between different flow regimes, and an extension of the range of flow rates at which dispersed flow could be found.

2.5   Solids-fluid flow regimes

Essentially, slurry is a mixture of solid and liquid, its physical characteristics depends on many factors such as the concentration and size distributions of the solids in the liquid phase, whether or not the flow is turbulent and the degree of turbulence, viscosity of the fluid, and the dimensions of the pipe carrying the flow. As would be expected the size and shape of the particles will have an effect on the flow patterns. Henthorn at al (2005) claim to have shown that even variation in particle shape can greatly affect the flow. Mica flakes, non-spherical sand particles and spherical glass beads of much the same density and equivalent volume diameters were used. The greater drag forces exercised by the less spherical particles, is believed to dissipate energy through turbulence effects, and significantly slow the flow.

Particles carried by a liquid and moving in a pipe will experience forces due to being submerged in the liquid, due to particle-particle interaction and may also interact with the pipe wall. Assuming a sufficiently dilute solution so that the particle-particle interactions can be ignored (at least to a first degree) the forces on a particle will be the body forces of weight, buoyancy and drag. Should the fluid flow be turbulent there will be additional forces on the particle due to its interaction with turbulence eddies. Sand slurries contain particles up to a few millimetres diameter with a relatively high density and are considered settling slurries since the solid particles tend to accumulate at the bottom of the pipe.

The flow of solid-liquid slurries in pipes differs from the flow of homogeneous liquids in a number of ways. With liquids the nature of the flow (i.e., laminar, transitional, or turbulent) can be characterized from a knowledge of the physical properties of the fluid and the pipe system. Characterization of slurry flow is not as simple as that because superimposed on the properties of the liquid are the properties of the solid particles and the effect of the particles on the mixture properties (Coiado and Diniz, 2001). Suppose a two-phase solid-liquid mixture flows in a horizontal pipe. If the slurry flow rate is high enough, all the solid particles will be suspended. If the flow rate is reduced, the solid particles whose density is higher than that of the carrier liquid tend to settle out and agglomerate at the lower side of the pipe, forming a moving deposit, above which flows a heterogeneous mixture. Decreasing the flow rate further causes the moving bed height to increase while its mean velocity

decreases. At some stage in the development of the bed, the forces on the particles at the base of the bed resisting motion become greater than the forces acting to move the particles. That is three, layers exist in the pipe (Doron and Barnea, 1993).

Doron, et al., (1997) have shown that with inclined pipes a fourth layer is possible. At the lower side of the inclined pipe there may be slippage of the solids deposited on the pipe under gravitational forces. They found that as the pipe tilted the bed height initially increased and reached a maximum with upward tilt of the pipe between 20° to 40°. For angles of inclination greater than this the gravitational effect becomes more pronounced and the bed height is reduced.

The limit deposition velocity (sometimes the suspending velocity) is the minimum fluid flow required to suspend a solid particle in the pipe. Below this velocity particles will settle out to form a bed on the lower side of the pipe, above this velocity particles on the lower side of the pipe will be taken up by the flow and all the particles are fully suspended in the pipe. It will depend on particle diameter, particle concentration and angle of inclination of the pipe carrying the flow. For angles of inclination from 0° to about 30° it was found that for a given solid concentration the limit deposition velocity remained more or less constant – about 3ms^{-1} for a 13% concentration of particles of density 2650kg/m^3, and mean diameter 0.36mm in a 100mm ID pipe. Of course, the less dense the particles and the lower their concentration, the lower the limit deposition velocity.

Homogeneous flow, or a close approximation to it, is encountered in slurries of high solids concentrations and fine particle sizes. The heterogeneous suspension regime is the most important mode of transport of granular materials by pipelines, because the maximum amount of solids is transported per unit energy input. There is in the literature a considerable number of publications about heterogeneous suspension regime in horizontal pipe. On the other hand, the number of articles concerning heterogeneous regime in non-horizontal pipeline is limited, and there is a substantial lack of information about the development of equations which permit computation of head loss (Coiado and Diniz, 2001).

2.5.1 Solids-fluid vertical flow

When considering vertical flow of solids in a fluid it is easy to see why there cannot be stratified flow or slug/plug flow. Also because the gravitational force is parallel to the pipe wall and there will be radial symmetry in the flow there cannot be an asymmetric distribution of particles in the flow. Thus vertical flow of solids in a fluid, whether gas or liquid must be suspended axi-symmetric. Not all solids have a density greater than that of water, so we would expect there to be instances when the solid particle velocity was greater than the fluid velocity due to the action of buoyancy forces. In vertical pipes the velocity of solids for upward flow is less than the fluid velocity and it is greater for downward flow. The difference is approximately the value of the settling velocity, approximately, (Raudkivi, 1989).

2.5.1.1 Suspended axi-symmetric flow

Velocity profiles

Lee and Durst (1982) considered upward vertical flow of spherical glass beads in air of mean velocity of between 5.60ms^{-1} and 5.84ms^{-1}, in a 20.9mm diameter pipe. Four different diameter particles were used: 0.1mm, 0.2mm, 0.4mm and 0.8mm. The volume ratio of particles to air ranged from 0.058% to 0.112%. They made three practical observations; (i) That the profile of the mean particle velocity was more or less-constant (flat) across the pipe, especially for the larger particles, (ii) The mean particle velocity was always less than the mean air velocity, and the larger the particle the slower its velocity, and (iii) There was a narrow layer at the pipe wall, larger than the viscous sub-layer of the air flow, into which the particles did not intrude. The larger the particle the wider the particle-free region near the wall.

Tsuji et al., (1984) measured the mean and fluctuating velocities of the particles in a gas-solid flow in a vertical pipe. They used polystyrene spheres (1020kgm^{-3}, 0.2mm to 3mm diameter) in a vertical glass pipe of ID 30.5mm. In agreement with Lee and Durst they found that the smaller the particle size, the more uniform was the mean air velocity distribution across the pipe, all other things being equal. They also found that large particles increased air turbulence throughout the pipe section, while small particles reduced it. Medium sized particles tended to increase turbulence in the

vicinity of the pipe centre and reduced it near the pipe wall. Lee and Durst (1982) had found that the presence of the 0.8mm diameter glass particles increased the measured turbulence intensities for the air flows they used. This phenomenon has been confirmed more recently by Yerrumshetty (2007) who has shown that for mean solids concentrations greater than about 0.1% the presence of the solid particles alters the turbulence patterns, and that the larger the particles the greater the effect. The presence of larger particles, where particle Reynold number is greater than about 70, caused the production of additional turbulence, while particles with smaller Reynold number increased the rate of dissipation of turbulent energy.

Louge et al., (1991) investigated "relatively dilute" flows of particles of 0.2mm and 0.5mm diameter in fast flowing air (as high as 18.9ms^{-1}) in a vertical pipe. The diameter of the pipe does not appear to be given in the paper. This paper is primarily concerned with the effect of the particles on the airflow, but the authors confirm that velocity fluctuation for the air increased with increase in particle diameter, that the velocity profiles for both air and particles are fairly flat across the pipe, and there is a clear decrease in particle velocity close to the wall.

The work of Sumner et al., (1990) and Bartosik and Shook (1995) can be seen as an extension of the work of Lee and Durst to the upward flow of fine, medium and coarse sand particles (respective diameters about 0.2mm, 0.5mm and 0.8mm) in water of mean velocity from about 2.5ms^{-1} to about 7 ms^{-1} in a 25.8mm ID pipe. Three solid concentrations were investigated: 10%, 30% and 40% by volume. The particle density was 2650kgm^{-3}. Their reported data agrees well with the mean particle velocity patterns found by Lee and Durst (1982), (i) That the profile of the mean particle velocity was more or less-constant across the pipe, especially for the larger particles, (ii) The mean particle velocity was less than the mean fluid velocity, (iii) There was a narrow layer at the pipe wall, into which the particles did not intrude. They suggest this is about the width of one half the particle diameter.

Alajbegovic et al., (1994) investigated solid-water upflow in a vertical pipe of ID 30.6mm. Two solids were used; ceramic spheres of mean diameter 2.23mm and density 2450kgm^{-3}, and expanded polystyrene of mean diameter 1.79mm and density 32kgm^{-3}. For the ceramic particles the particle velocity was generally less than that of the fluid, but the velocity of the polystyrene particles was – as expected - everywhere

greater than the fluid velocity. The diameters of both the ceramic and polystyrene spheres were larger than those reported above and the velocity profiles, while fairly uniform across the pipe were less so than those observed for smaller diameter particles. The measured axial velocities for both particles and all flow rates examined did, in fact show a broad but shallow peak centred on the pipe's axis, with the peak for the polystyrene particles more distinct than for the ceramic, see Figures 2-7 and 2-8 below.
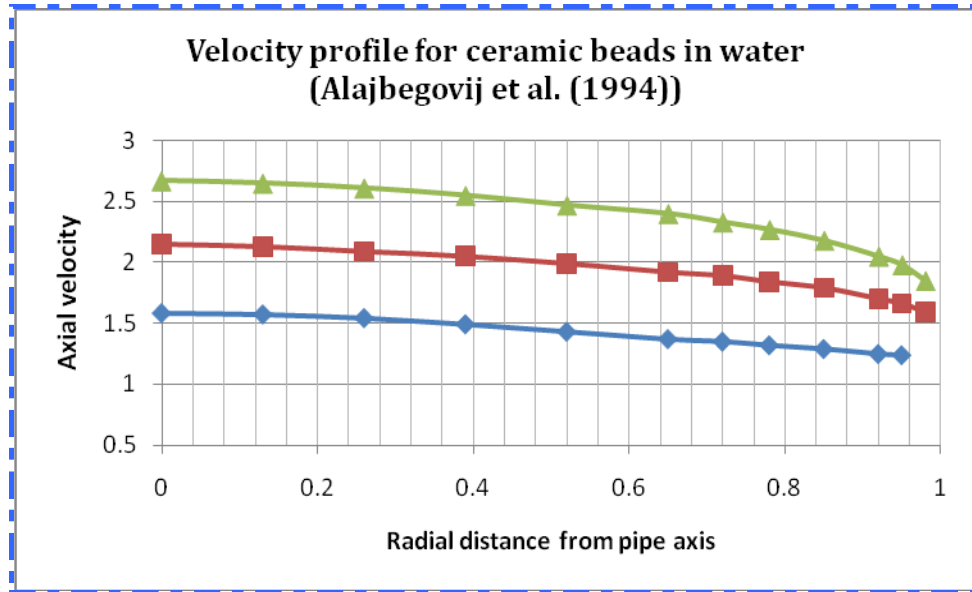
Figure 2-7: Velocity profiles of ceramic beads in water
Top line: superficial water velocity (U_{WS}) = 2.20ms^{-1},
middle line: U_{WS} = 1.89ms^{-1}, bottom line; U_{WS} = 1.41 ms^{-1}
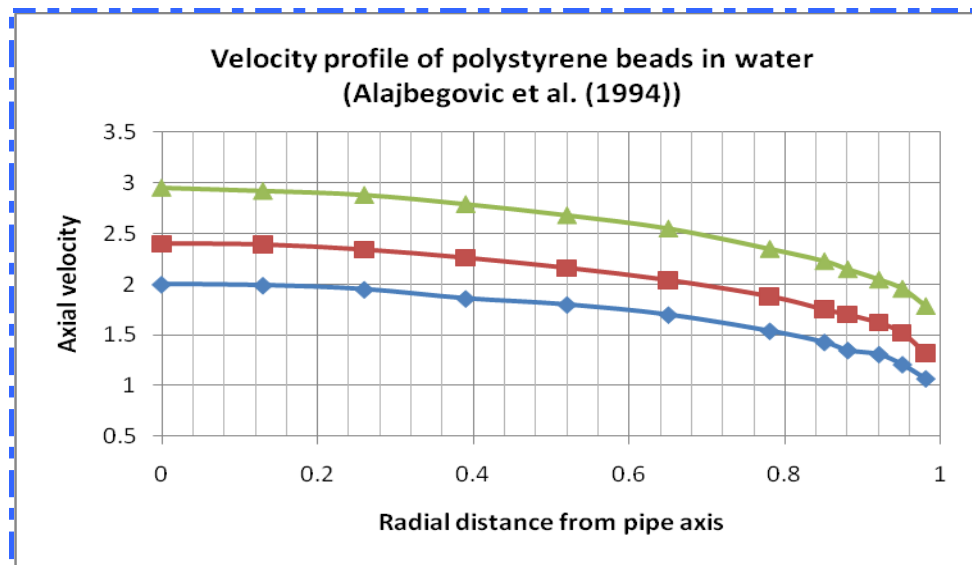
Figure 2-8: Velocity profiles of polystyrene beads in water
Top line: superficial water velocity (U_{WS}) = 2.22ms^{-1}, middle line: U_{WS} = 1.77ms^{-1}, bottom line; U_{WS} = 1.44ms^{-1}

It was also noticed that in the case of the ceramic particles only, close to the pipe wall, the fluid velocity fell below that of the particles. The cross-over point moved away from the wall the higher the flow velocity, from about one tenth the radius to three-quarters the radius as the superficial liquid velocity rose from 1.42ms^{-1} to 2.20ms^{-1}.

Particle concentration/volume fraction

Alajbegovic et al., (1994) presented measured volume fraction distributions for the ceramic beads for a number of flow conditions. The data presented confirmed that for low liquid flows the volume fractions for the ceramic particles showed an almost uniform distribution cross the pipe, but as the fluid velocity increased the volume fraction at the centre of the pipe increased. Alajbegovic et al., presented the results of Sakaguchi et al., (1991), to confirm their findings that the higher the superficial liquid velocity the more the solid particles shift towards the pipe's centreline. Though, of course, the degree and extent will depend in the size, shape and density of the solid particles and the pipe diameter. Both sets of authors agreed that there exists a particle free region close to the pipe wall for all the flow velocities and particles tested. The particle free zone can be seen in the figure below which represents the data of Alajbegovic et al.
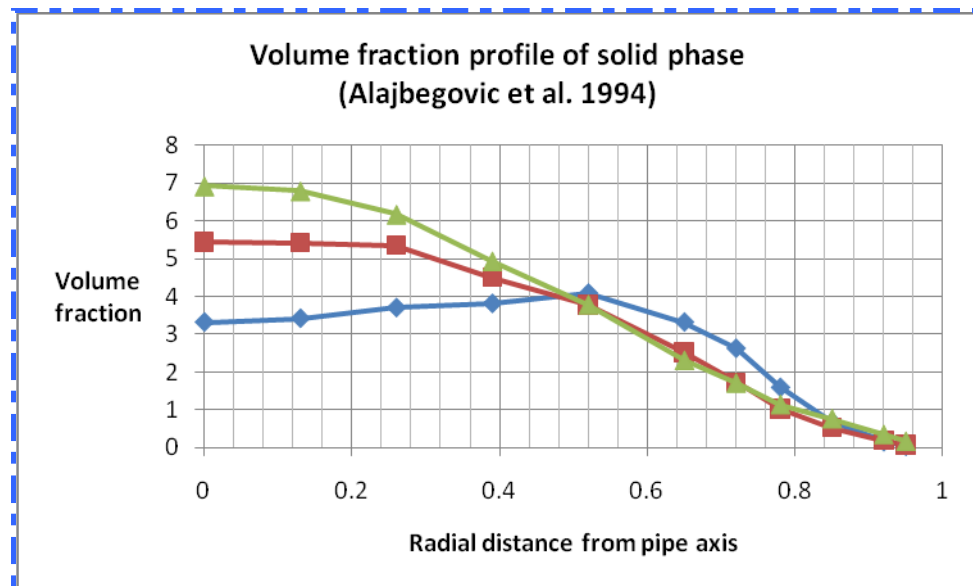
Figure 2-9: Volume fraction profiles, ceramic beads in water
Green line: superficial water velocity $(U_{WS}) = 2.22\text{ms}^{-1}$,
Brown line: $U_{WS} = 1.77\text{ms}^{-1}$, Blue line; $U_{WS} = 1.44\text{ ms}^{-1}$

Sumner et al., (1990) and Bartosik and Shook (1995) found the finer the sand particles in sand-water flows the more uniform the concentration across the pipe. As with Alajbegovic et al., at smaller particle diameters (d=0.2mm) the particle concentration was uniform almost to the wall, but for larger particle diameters (d=0.8mm) there was a clear tendency for the particles to travel nearer the centre of the pipe. Both papers found that, all other things equal, the lower the particle concentration the more even was the particle distribution across the pipe.

Yerrumshetty (2007) attempted an explanation: Very fine particles would follow the small-scale motions of the fluid so that the action of turbulent diffusion would produce a uniform concentration distribution over the pipe cross-section. Given the small scales involved this could be to within the immediate vicinity of the wall. However, he claimed that there was insufficient information available in the literature to quantitatively test the hypothesis.

2.5.2 Solids-fluid horizontal flow

A horizontal solids-fluid flow is asymmetric. The distribution will depend on the density of the solids; the more dense the solids the less the net upward buoyancy force on its particles. The more dense the particles the quicker they sink to the lower side of the inclined pipe – all other things being equal – which can cause a layer of solid particles to develop. If more than one solid was being transported the density and size of the particles would both vary and the layer of particles on the lower side of the inclined pipe would also be non-uniform.

2.5.2.1 Stratified (stationary and/or moving bed)

An introduction to the flow patterns in a solids-liquid two-phase flow is given in Akagawa et al., (1989) and shown in Figure 2-10. Although Figure 2-10 is for flow in an annulus it is considered relevant here because the flow regimes it depicts are, essentially, those that occur for solid-in-fluid flows in all horizontal pipes. The four regimes may be classified as: Stratified (Figure 2-10 d) – for horizontal pipes a two-phase sand-water flow will generally consist of two layers when the water flow velocity is below a so-called limit deposition velocity, there will be a stationary bed of sand at the lower side of the pipe and the upper side of the pipe is filled with a relative

weak heterogeneous mixture. For a small increase in water flow, particles in the top of the sand bed are moved by the flow and the sand bed now consists of two layers; a stationary base, above which is a moving layer and the upper side of the pipe is filled with a heterogeneous mixture. For very low liquid velocities the solid particles may pile up in the pipe to such an extent that a blockage may occur but this is rarely observed in real situations. The limit deposit velocity increases with pipe diameter and thus so does the critical velocity that will keep the suspended coarse particles in motion (Doron and Barnea, 1996).

As the liquid flows upwards over the surface of the solid particles it entrains particles from the top of the layer back into the liquid flow, taking them further up the pipe. We may therefore see a kind of recycling process with particles being carried upstream sinking to the lower side of the inclined pipe being carried a distance downstream before being caught up by the fluid and carried upstream again. Of course, some solid particles could, depending on the fluid forces they experience, be carried up the pipe without ever sinking onto the solid layer. Yerrumshetty (2007) has pointed out that a packed bed is most likely to result when superficial velocities are very low and when the solid particles are very dense, and gives the example of lead, 10 838 kgm^{-3}.

2.5.2.2 Moving bed

Further increase in the superficial velocity of the fluid will cause the particles in all of the sand bed to move with the flow, see Figure 2-10 c. Matousek (2002) has shown that the size of the sand particles is important, the finer the particles the lower the limit deposition velocity. Matousek drew two conclusions: that the layer which first forms on the bottom of the pipe is likely to consist of predominantly course sand, and concentration profiles for finer sands are more likely to be uniformly distributed over the cross-section of the pipe.

2.5.2.3 Suspended asymmetric

If the fluid superficial velocity increases further to above the so-called suspending velocity (the minimum velocity for which the flow is fully suspended in the pipe) all the sand particles will be suspended in the pipe, see Figure 2-10 b. However, as with

dispersed and annular flows for two-phase gas-liquid flows the sand is not uniformly dispersed throughout the pipe cross-section.

2.5.2.4 Suspended symmetric

For the highest flow rates the sand particles become uniformly distributed throughout the pipe cross-section, see Figure 2-10 a.

a. suspended symmetric   b. suspended asymmetric

c. moving bed   d. stationary – moving bed
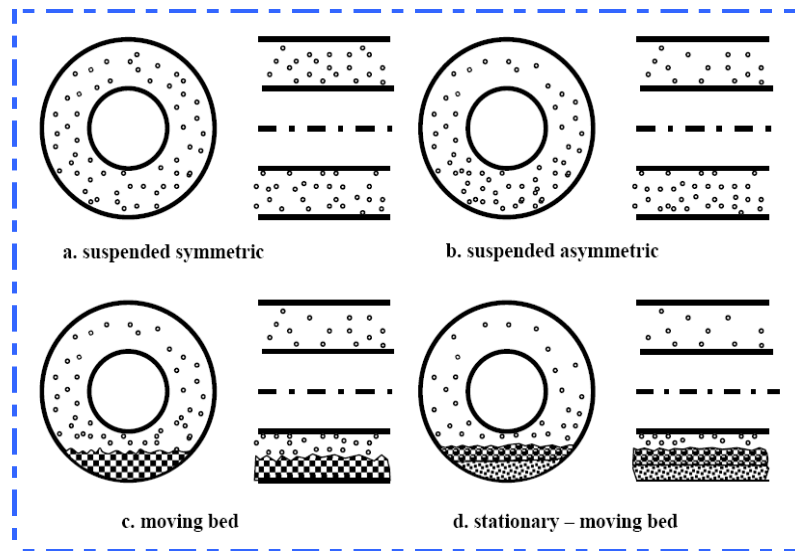
Figure 2-10: Two-phase flow patterns for horizontal solids-liquids flows. The liquid velocity decreases from high in (a) to low in (d) (Akagawa et al., 1989)

2.5.3 Solids-fluid inclined flow

Horizontal solids-fluid flow is very different from vertical and inclined flow is even more complex. For example, as stated above, vertical flow in a pipe is axi-symmetric for both velocity and concentration for both phases, while for horizontal flow these quantities are asymmetric. But with inclined flow an important additional complication occurs with the sand bed. For vertical flow there can be no sand bed, with horizontal flow there can be a two layer sand bed, the bottom layer stationary and the top layer moving with the flow, but with a sand bed in an inclined pipe the bed can consist of three layers, as shown schematically in Figure 2-11, where the distribution of the solids across the pipe cross-section is highly non-uniform.

If the layer of solid on the lower side of the inclined pipe becomes thick enough, it can slip/slide down the pipe against the fluid flow. Such reverse flow may be episodic or, under suitable circumstances, continuous (Doron et al., 1997). If the process of

entrainment is strong enough it will ensure that there is a net upwards solids flow despite the downward motion of the solids bed at the lower side of the pipe.
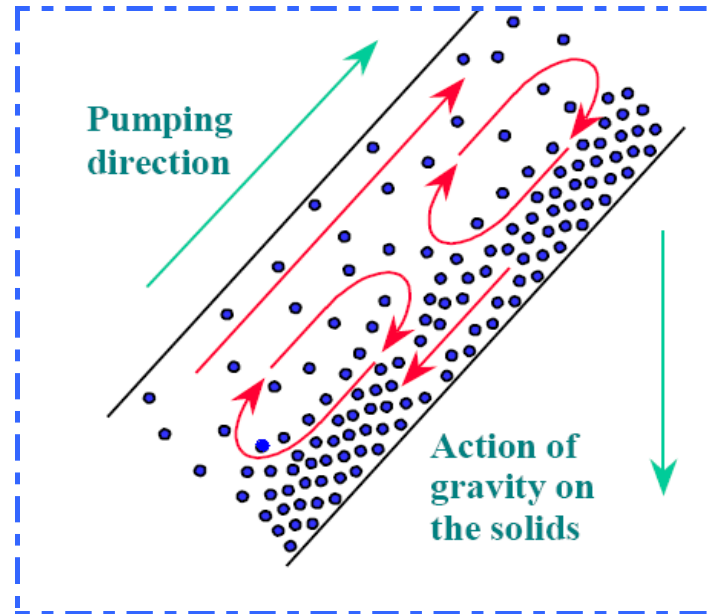
Figure 2-11: A solids-liquid flow in an inclined pipe

Lucas et al., (1999) investigated solids volume fraction and velocity distributions for 4mm diameter plastic beads of density 1341kgm^{-3} in water flowing upwards in an 80mm ID pipe. Measurements were made with a local conductivity probe with the pipe vertical and at 5° to the vertical. The vertical distributions of both the local solids fraction and the axial velocity distribution were very similar to those reported above.

The distributions measured for the 5° angle for water superficial velocity about 0.21ms^{-1} and solids superficial velocity about 0.021ms^{-1} were skewed, as would be expected. The local solids volume fraction is higher on the lower side of the inclined pipe and decreases towards the top of the pipe. The local axial velocity distribution was also skewed, but inversely so to the local solids volume fraction. At the bottom of the pipe the local axial velocity distribution was at its minimum, with some indication that there was possible reverse flow adjacent to the pipe wall, gradually increasing to a maximum value at the top of the pipe.

Using a 27.8mm ID glass pipe Yakubov et al., (2006) investigated solid-liquid flows for various angles of inclination between 0° and 90°. Three sets of solid light particles of mean diameters 1.5mm, 2.5mm and 3.2mm were used with water as the fluid

medium. The solid material was not specified but the densities claimed were very low: 1.25kgm^{-3} and 2.65kgm^{-3}. These cannot be correct given that photos and diagrams in the article show the solid particles did not float, so the densities are more likely to be 1250kgm^{-3} and 2650kgm^{-3}. The purpose of this project was to determine the effect of angle of inclination on the solids bed formed on the bottom of the pipe, so the range of water flow velocities was limited. Yakubov et al., (2006) claimed to have had beds formed in the pipe for slopes as great as 70° for superficial water velocities of less than about 0.05ms^{-1}.

For angles of inclination of less than about 40°, a solids layer was formed on the bottom of the pipe for superficial water velocities below about 0.13ms^{-1}. At this flow rate the water began to move particles in the surface while leaving a motionless layer at the bottom of the pipe. As the water velocity increased saltation occurred (the lift exerted by the water on a particle is sufficient to pull it away from the surface and into the flow; as the particle moves into the water away from the bed, the lift decreases and the particle sinks back towards the surface). For slopes of greater than 20°, very little further increase in water flow rate was required for the break-up of the bed.

Yakubov et al., (2006) found that the critical superficial water velocity required to remove particles from the bed increased with particle diameter, particle density, with angle of inclination up to about 45° and inversely with height of the bed.

Doron et al., (1997) found that for a given solid concentration (13% by weight for particles of density 2650kgm^{-3} and diameter 0.36mm), all other things being equal, the limit deposition velocity remained more or less constant (about 3ms^{-1}) for an angle of inclination between 0° and about 30°. Above that angle the limit deposition velocity increased and the likelihood of the bottom layer of particles slipping down the inside of the pipe also increased. Generally, Doron et al., (1997) found that the greater the density of the particles and the higher the concentration the higher the limit deposition velocity.

2.6   Solids-liquid flow measurement methods

A number of detailed reviews of multiphase flow measurement devices already exist in the literature. For this investigation only methods which can take a local

measurement in a pipe cross-section are considered, thus techniques such as gamma ray attenuation, which gives measurements averaged along the length of a chord of the cross-section are not discussed. Similarly global measurement techniques are not discussed. Any literature review of reasonable length can provide only a brief discussion of the theoretical and practical basis of some of the wide range of techniques used to take local measurements in multiphase flows. Applications of each are presented and the suitability of each technique for the particular solids-liquid flow proposed for this investigation is then critically discussed. The reader is referred to referenced sources for more information. In conclusion this section will show why one particular technique was chosen for development and application to the current investigation.

2.6.1 Optical methods

A variety of techniques can be included within the general classification of optical methods which could be applied to the flow conditions of the current investigation. Applications in which each technique has been used are then described. Finally the possible application of each method to the current investigation is critically examined. Experimental studies of two-phase flows such as slurries are hindered because even solids fractions as low as 10%, the mixtures are becoming optically opaque. Acoustical scattering and magnetic resonance imaging techniques are used for measuring some aspects of the flows, but it is desirable that the powerful techniques of laser Doppler velocimetry and particle image velocimetry should be used (Adrian 1991). This has led to the well-known technique of matching the refractive indices of the solids and the liquid by careful choice of both to achieve maximum optical transparency of solids/liquid mixtures. However, in practice the depth to which one can "see" into the mixture is limited by seemingly random variations of the refractive index of the liquid caused by changes in its temperature, by variation of the refractive index of the material of the solids due to imperfections and some reflection from the particle surfaces. For example, Chen and Kadambi (1994) achieved only about 25mm penetration through 50% concentrations of 40 lm silica sand particles in a sodium iodide solution. Yianneskis, M. and Whitelaw, J.H. (1984) successfully used ID2 lm silica gel particles at 14% volume concentration in a 51 mm diameter pipe, but reported that other brands of silica gel particles gave limited penetration at high

concentrations due to refractive index variations within the particles. However, work is continuing and Wei, F.et.al. (1998) has described new refractive index-matched systems for solid particles in liquids which significantly extended penetration depths and maximum concentrations by improving transparencies, making experimental investigations in relatively large scale pipes possible, possibly up to 100mm ID.

2.6.1.1 Velocimetric methods

This method involves tracking the paths of individual particles or bubbles. A good review of previous research on measurement techniques for multiphase flow is reported by Chaouki et al (1997). The simplest velocimetric measuring technique is photography. Cinematographic techniques have been used by Scarlett and Grimley (1974) in solids-liquid flows and by Gunn and Al-Doori (1985) and Polonsky et al (1998) in gas-liquid flows.

In a solids-liquid flow, cinematography is used to follow the path of tracer particles within the flow; but to visualise the tracer particles the rest of the flow must be invisible to the camera. To achieve this, the liquid and the majority of the solid particles must have matched refractive indices and be translucent to the wavelength of light used. If the measurements are to be carried out on flow in a cylindrical pipe – the usual case – then measures must be taken to eliminate refraction effects due to the round pipe. This usually involves constructing a liquid filled rectangular box round the pipe. To visualise the motion of the tracer particles in 3 dimensions, images must be acquired at two mutually perpendicular positions and then recombined, see Figure 2-3 Scarlett and Grimley (1974). Using this system the probability of tracer particles passing through designated pixels in the pipe cross-section can be measured.
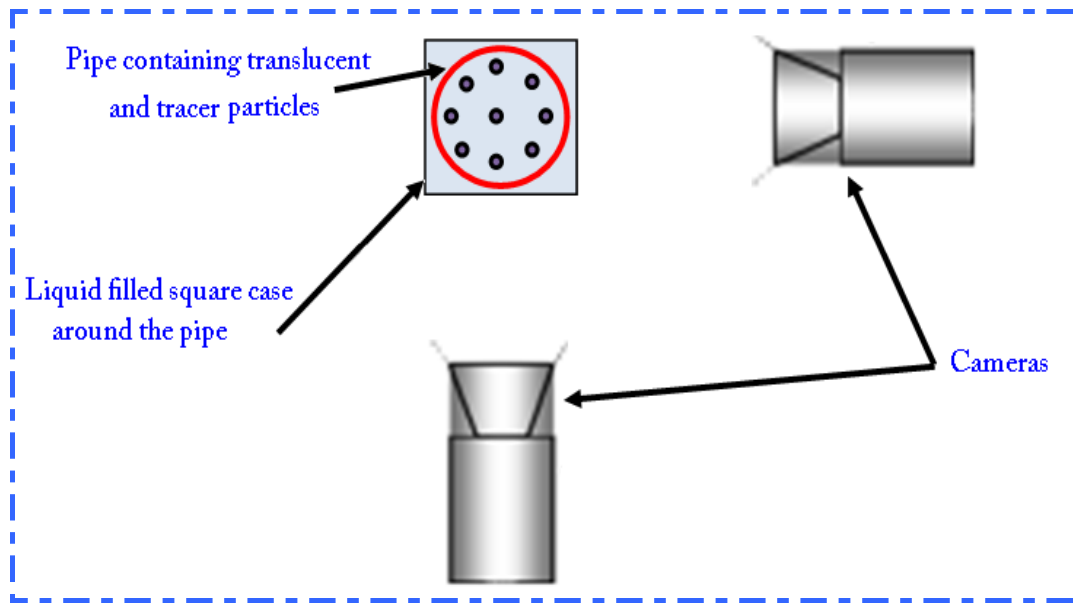
Figure 2-12: The optical method of Scarlett and Grimley (1974).

For gas-liquid flow measurements, Yamamoto et al., (1998) incorporated sophisticated image analysis into their system. Using two perpendicular images, like those in the method of Scarlett and Grimley (1974) they were able to track individual bubbles in three dimensions, as they rose through a liquid column in flows with much higher volume fractions than previously achieved. In the case of Scarlett and Grimley (1974), the total gas volume fraction had to be low in order that individual bubbles could be imaged clearly. Gunn and Al-Doori (1985) used high speed video cameras to record the passage of bubbles through a column of water. Polonsky et al., (1998) used video cameras to record the movement of large Taylor bubbles which covered almost the entire cross-section of the pipe. In these applications the possibility of capturing more than one bubble in the direct line of sight of the camera was low. The system of Gunn and Al-Doori (1985) was also used to record the interaction of an intrusive probe with rising bubbles.

Obviously photographic methods cannot be applied directly to industrial applications as they require expensive equipment and the analysis of the data can be extremely time-consuming. Additionally, in order to achieve a reasonable level of accuracy, high speed cameras must be used operating at speeds of up to 3000 frames per second (Scarlett and Grimley, (1974)). Because of these disadvantages, photographic methods were not considered suitable for the current investigation.

Another form of velocimetry is laser velocimetry. Here a sheet of laser light is shone across the flow and particles, or bubbles, in the flow appear to shine as they cross the light sheet and reflect the light. A camera aimed perpendicularly at the light sheet can record the instant these particles cross the light sheet, assuming that the flow between the camera and the sheet is relatively transparent. This technique generally uses translucent particles which, if the material is chosen carefully, are generally invisible to the camera but reflect the laser light. A variation of this technique is streak velocimetry where the laser light is pulsed twice for each exposure on the camera (Hassan and Blanchat, 1991). This results in each image appearing as a streak showing the path of each particle. The length of each streak is directly proportional to the velocity of the particle. A second variation of this technique is Particle Image Velocimetry (PIV), where each image records the instantaneous position of the particle (Jones and Delhaye, (1976)). Analysis of a series of these images allows the particle tracks to be determined and the velocity calculated. In both of these variations the solids volume fraction is measured using a counting technique.

The advantage of laser velocimetry over conventional velocimetry is that higher volume fraction flows can be used without having to introduce tracers. However the technique still requires a relatively translucent flow, and a large quantity of specialist hardware and software. Again it is also not easily applicable in an industrial environment. For these reasons it was decided that this technique was also not suitable for the current investigation.

2.6.1.2 Laser Doppler Anemometry

Laser Doppler Anemometry (LDA) relies on the Doppler effect. Here a laser beam is focussed onto a control volume in the cross-section of the multiphase flow, see Figure 2-13. The bubbles or particles in the flow scatter the beam and the frequency of the scattered light is measured. The frequency of the scattered light is different from that of the incident beam and the difference in frequency is proportional to the velocity of the object which caused the scattering. This method also allows calculation of the solids volume fraction by counting the number of particles which pass through the control volume (Chaouki et al., 1997; Jones and Delhaye 1976; Chen and Kadambi, 1994).

Because an important requirement for LDA is a clear optical path to the control volume it is usually limited to flows of low dispersed phase concentrations and may have difficulties if the particle size were to exceed 4mm diameter (Sheng and Irons, 1991). A number of researchers have attempted to circumvent the low concentration condition. Wei et al (1998) optimised the tip of a local LDA probe in order to reduce the distance between the measuring window and the control volume. This reduced the chance of particles passing between the two. In solids-liquid flow, both Chen and Kadambi (994) and Yianneskis and Whitelaw (1984), successfully used a matched refractive index system and a small number of tracer particles.
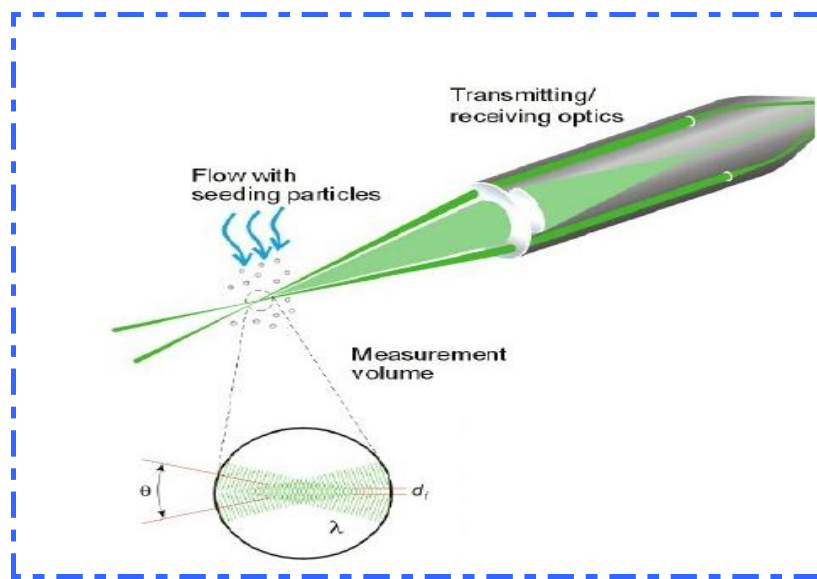
Figure 2-13: Local LDA probe (Sheng and Irons, 1991)

Marié (1983) has proposed LDA for the measurement of the flow rate of a liquid. Here a transmitter sends a laser beam into the liquid flow. The beam is reflected to a receiver by particles seeded into the flow. The reflected beam laser will be modulated by the flow rate and by combining/comparing initial and reflected beams a Doppler shift will be observed. To reflect the laser beam seeding particles have to be inserted into the liquid and this might affect on the flow rate of the liquid.

In conclusion LDA suffers from many of the problems identified with velocimetric techniques. Again, specialist, high cost, equipment is required, and there is no real possibility of developing the technique for industrial use in rugged conditions. For these reasons it was decided that LDA was not a suitable technique for the current investigation.

2.6.1.3 Fibre-optic probes

By inserting probes into the flow it is possible to make local measurements in a two-phase flow, using optical methods, regardless of the disperse phase volume fraction (Moura and Matvillet, 1996). Here light is transmitted down an optical fibre to an open tip situated within the flow. Some of the light is reflected, either back up the same fibre or up a parallel fibre. The remainder of the light is transmitted out into the flow. The relative proportion of light which is reflected depends on the refractive index of the material surrounding the tip of the probe. Generally, these intrusive probes determine which phase the tip of the device is immersed in at a given time and because the flow must be fluid-fluid this type of device is unsuitable for the current investigation.

An intrusive optical probe that can be used in a solids-liquid flow has been reported by Akagawa et al., (1989). Light was transmitted into the flow through an optical fibre as before. However a receiving fibre was positioned near to the first fibre in such a way that particles passing close to the pair reflected light into it. Two sensors of this type separated by a known axial distance were used to measure the solids velocity. This type of device would be applicable to the current investigation although it requires relatively complex equipment and analysis. However, the probes were intrusive and in order to minimise the flow disturbance, research has been carried out into the optimum shape of probe, see Moura and Marvillet (1996), Cartellier and Achard (1991), and Jones and Delhaye (1976). If the method selected for this investigation were to be intrusive, then this work would be useful.

2.6.2 Tracer methods

Tracers are the most commonly used method to measure the mean solids velocity. Radioactive tracers are injected into a flow and the time taken for them to reach a downstream detector measured. This gives a measure of the mean tracer velocity along the length of travel. Making the properties of the tracer similar to the properties of the solids component, was a method used by Tallon et al., (1998) to measure the mean flow of solids in a pneumatic transport application. However, this method has been adapted by some researchers to allow local measurements. Tracer particles are mixed with the solid component of the flow as if a mean estimate was to be made but

instead of using only one downstream detector, a carefully positioned array of detectors is used. This allows the local position and trajectory of each tracer particle to be measured at a given cross-section of pipe, so the solids velocity and the solids volume fraction can be measured using a counting method, see Chaouki et al., (1997). It was decided that it was unsuitable for this investigation due to the high cost and complexity of the necessary equipment.

2.6.3 Sampling methods

Sampling involves removing some of the flowing mixture from the pipe. The simplest way is to put a small pitot tube into the flow at a relevant position, as has been done successfully by Miller and Gidaspow (1992) for gas-solids flows. However, researchers such as Nasr-El-Din and Shook (1985) claim that the presence of the pitot tube affects the flow and that solids will tend to be deflected around the probe rather than entering it. These researchers recommended the use of isokinetic sampling to ensure that the flow enters the pitot. Here fluid is drawn out through the rear of the isokinetic sampling probe in such a way that the static pressure at the mouth of the tube is identical to that which would exist at the same point in the flow in the absence of the tube. Whichever method is used to acquire the sample, the analysis is the same. The withdrawn sample is separated and measured off-line allowing the local volumetric flow rate of each phase to be measured.

However, this method does not allow the local solids volume fraction or the local solids velocity to be directly determined because the volumetric solids flow rate at a point is proportional to the product of these properties, and the velocity cannot be independently determined without additional information. Rao and Dukler (1971) acquired this extra information using an isokinetic-momentum probe. The sampling tube was mounted on a sensitive strain gauge. It was then possible to measure the force applied by the solids as they struck the sampling tube. This extra information allowed both the solids volume fraction and solids velocity to be measured.

An important factor in accurate sampling is the diameter of the sampling tube which must be large enough to ensure that a relatively undisturbed flow enters it, but small enough not to significantly disturb the overall flow pattern. Rao and Dukler (1971) used solid particles 0.065mm in diameter with a sampling tube 1.6mm diameter. They

claimed that this ensured that a representative flow of solids entered the tube. Miller and Gidaspow (1992) claimed accurate results using a 0.47mm diameter tube with 0.075mm diameter solid particles. If the solid particles were to be as large as, say, 4mm in diameter then to achieve the same ratio of sampling tube diameter to solids diameter as Rao and Dukler (1971) and Miller and Gidaspow (1992) the tube would have to be between 25mm and 100mm in diameter. In laboratory conditions where the working section of a flow loop is likely to be less than 100mm in diameter these sizes make this method unsuitable.

2.6.4 Electrical methods

Electrical measurement methods applied to two-phase flows rely on the electrical properties of the phases being measurably different. The electrical properties most frequently used are the conductivity and permittivity of the different phases. In this research the solid particles may be assumed to be insulators, i.e. their electrical conductivity is negligible. The permittivity of the solids and water are not relevant because in the present investigation the measurement technique employed differences between the conductivity of the solids particles and the water. Thus, only electrical conductivity measurement techniques are discussed here. In order to make direct local electrical measurements in a two-phase flow an intrusive local device may be used.

In the present investigation the conductivities of the two phases differ significantly. The conductivity for university tap water at 20°C is approximately 150μScm^{-1}. As stated above the conductivity of the solids is, for all particles present is effectively zero.

2.6.4.1 Local conductivity probes for fluid-fluid flows

The majority of research that has been carried out on local conductivity measurement probes for flow measurement has been in the area of fluid-fluid flows. These devices may use a penetration principle similar to that employed by local optical probes as described in Section *2.6.1.3*. Such probes consists of a conducting needle tip supported by, but insulated from, a conducting holder, see Figure 2-14. Current is sourced at the needle electrode and the conducting casing (which forms a second electrode) is earthed. If the probe tip is immersed in a non-conducting medium current does not flow. If the probe tip is immersed in a conducting medium current flows. The

measured potential difference across the two electrodes is low if the probe is immersed in the conducting phase and high if the probe is immersed in the non-conducting phase. It is thus quite simple, theoretically, to measure the relative time that the probe is immersed in each phase and hence to estimate the volume fraction of each phase (Lucas et al., 2004). This technique has been extended to obtain bubble velocities by mounting two needle electrodes axially separated, and cross-correlating the two signals. Cross-correlation applied to flow measurement is described in Section 2.11.
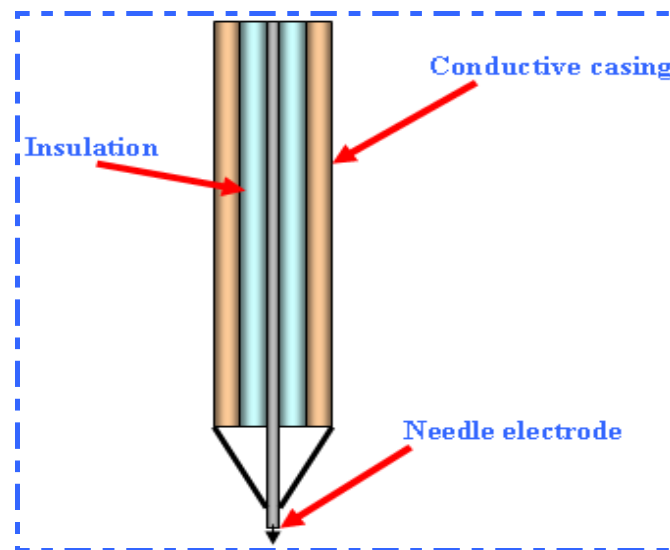
Figure 2-14: General representation of a penetration type conductivity probe tip (Lucas et al., 2004)

Obviously this technique cannot be applied directly to solids-liquid flow measurement. However researchers have investigated the disturbance to flows caused by the presence of local probes in two-phase flow fields, the properties of electrical fields in two-phase flows, the optimal probe parameters for cross-correlation flow measurement, and also methods of constructing local probes. This research could be applicable to the current investigation and therefore it is briefly reported here.

Ceccio and George (1996) have reported finding considerable disturbance of the flow by local probes, and Jones and Delhaye (1976) and Moura and Marvillet (1996) have reviewed penetration type local probe techniques. Cartellier and Achard (1991) have presented an assessment of the relative accuracies of local disperse phase volume fraction measurement using a wide variety of local penetration probes. As errors in all local probe measurements will be introduced by probe intrusion, the latter is an

interesting reference. Probes are reported as having relative accuracies of between ±5% and ±20% which suggests that this type of probe could achieve the accuracy needed for useful industrial application.

Many of the probes reported used only single sensors (Vigneaux, et al., 1988; Clark et al, 1992). Angeli and Hewitt (1996) reported the use of a probe 0.86mm in diameter in a pipe 25.4mm in diameter. Sheng and Irons (1991) reported the use of a 1.5mm diameter probe in a model of a large steel making ladle. Teyssedou et al., (1998) reported more detailed tests on a 1mm diameter probe used in a 19mm pipe. They varied the sharpness of the probe tip which changed the distance between the needle electrode and the earthed casing, and discovered that with a large electrode separation the probe gave an artificially high reading when positioned near the pipe wall. They concluded that the large electrode separation caused the electric field around the probe to penetrate further into the flow and this allowed the pipe wall to affect the field and therefore alter the reading.

The literature also contains reports of penetration probes with two sensors, designed to estimate the local dispersed phase velocity using cross-correlation. However these velocity estimates are compared with reference measurement see Lucas et. al., (2005). Thang and Davis (1979) reported using a 1.6mm diameter probe in a 50mm diameter pipe with an axial distance between the two sensors of about 5mm. Van der Welle (1985) reported using a dual sensor probe with a sensor separation of 10mm although the other dimensions of the probe were not given. Revankar and Ishii (1993) reported the use of a probe 0.7mm in diameter in a 5mm diameter pipe with an axial distance between the sensors of 4mm. Serizawa et al., (1975) used a 1.8mm diameter probe in a 60mm diameter pipe with an axial distance between the sensors of 5mm. Some authors such as Castello-Branco and Schwerdtfeger (1994) and Sun et al., (1998) have reported using a dual sensor probe where the probe diameter is much the same magnitude as the sensor separation. Castello-Branco and Schwerdtfeger (1994) used a 1.8mm diameter penetration probe, with a 2mm sensor separation, for measuring large bubble plumes in casting ladles. Sun et al., (1998) reported the use of a sensor separation of 2mm although the overall diameter of the device was not given.

Gunn and Al-Doori (1985) investigated the effect of intrusive probes on the flow field by photographing the flow around the probe. They used two 4mm diameter probes

separated by an axial distance of 11mm. The experiments were carried out in a 15mm deep slot so that the probe was visible to the camera at all times. Their conclusions were that bubbles in the flow were deformed as they struck the probe. However they concluded that the overall flow was not affected by the probe.

In conclusion, probes with diameters of between 0.7mm and 4mm have been used by researchers in this field. The ratio of probe diameter to pipe diameter varied between 0.03 and 0.14, suggesting a range of opinion on the ideal ratio of probe/pipe diameter to minimise flow disturbance. The sensor separations used in these devices varied from 2mm to 11mm, with no authors reporting substantial errors in their velocity estimates. This literature review suggests that although probes affect those bubbles which they actually penetrate, they do not affect the overall flow field. Finally, the majority of the probes examined had been constructed by bonding the components together with an epoxy resin. This gave the necessary strength whilst also insulating the components from each other.

2.6.4.2 Local conductivity probes for solids-liquid flows

Compared to the research carried out into penetration probes for fluid-fluid flows, little has been done involving local conductivity measurement probes for solids-liquid flows. Possibly because in solids-liquid applications the probe cannot penetrate the particles, it is usually designed to measure the conductivity of the mixture, σ_m, in a small volume around itself. A known electrical current, I, is established between two electrodes and the potential difference, V, is then measured either between these two electrodes, or between two other electrodes in the vicinity.

The conductivity of a two phase mixture is a function of the electrical conductivity of each phase and the relative volume fractions of each phase. If the conductivity of each of the two phases and of the mixture is known, the dispersed phase volume fraction can be estimated. Many relationships have been developed to give this estimate (MacTaggart R.S. et.al (1993)).

Nasr-El-Din et al (1985) developed a 4.8mm diameter probe for use in these types of pipe flows. The probe used a four electrode configuration with current injected between two "field" electrodes and the resulting potential difference measured across

two "sense" electrodes, see Figure 2-15. Using this configuration the author claimed that electro-chemical effects were eliminated. He also claimed that this configuration eliminated variations in the conductivity reading due to varying mixture velocity. The "field" electrodes were areas of the casing whilst the "sense" electrodes were the ends of 0.3mm diameter wire. The two "sense" electrodes were 1mm apart. The components were bonded together, and insulated from each other, with an epoxy resin.
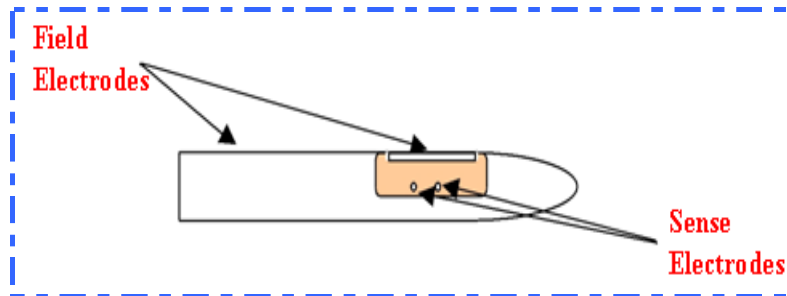
Figure 2-15: Local conductivity probe of Nasr-El-Din et al (1985)

Using this probe Nasr-El-Din et al took measurements in a 50mm diameter pipe, and obtained profiles of the solids volume fraction across the pipe. Whilst the results were not validated against any reference measurements, some factors were noted which could be applicable to the present investigation: the conductivity measurement varied with the orientation of the probe relative to the pipe wall, and as the particle diameter increased above the separation of the sense electrodes the probe began to underestimate the solids volume fraction.

The wall effect mentioned above has also been noted by Teyssedou et al (1988), and such results are not surprising given the asymmetrical nature of the probe design. As the conductivity of the liquid varies with temperature it is also not surprising that variations in measured values were observed as the temperature of the system changes. No explanation was given for the observation that as the particle diameter increased there was drop in measured solids volume fraction close to the pipe wall, but it was suggested that it be taken as a guide for the design of this type of probe.

MacTaggart et al (1993) extended the work of Nasr-El-Din et al (1985) by developing a probe for measuring the solids volume fraction in a tank containing a solids-liquid mixture. The probe design had strong similarities with that of Nasr-El-Din: the probe

was 4.8mm in diameter, used a four electrode measurement technique and the "sense" electrodes were 1mm apart. Using this device profiles of local solids volume fraction were made for a large mixing vessel. As might be expected most of the conclusions reached were similar to those of Nasr-El-Din (1985). MacTaggart also reported a wall effect, that the solids volume fraction estimate varied depending on which field electrode was facing the wall, and it was concluded that the area of the field electrode closest to the wall had an effect on the measurement. No explanation for this was given, it was merely presented as a guideline for the design of this type of probe.

Asakura et al (1992) reported a probe that did not use a four electrode measurement technique. It was claimed that the 3mm diameter probe could be used to measure solids velocity as well as solids volume fraction. However, few details of the device, or the measurement technique, were given. The probe possessed three "ring shaped" electrodes formed from 0.3mm diameter wire arranged as shown in Figure 2-16. Adjacent electrodes were separated by 10mm.
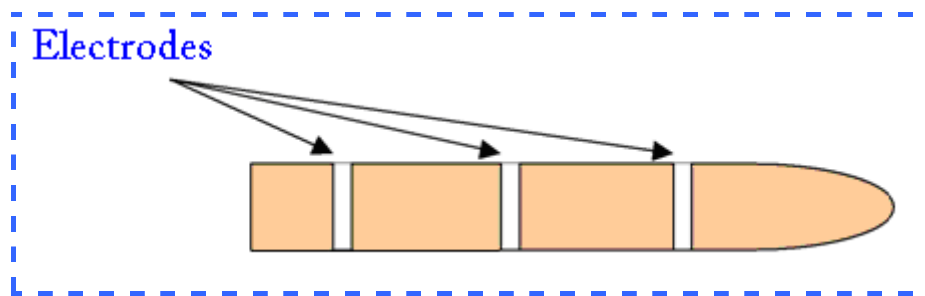
Figure 2-16: The local conductivity probe of Asakura et al (1992)

The most obvious measurement technique for use with this device would be to inject current from the centre electrode to each of the outer electrodes. This would result in two measurable potential differences which could be cross-correlated to give a solids velocity estimate. The signal from either of these two "sensors" might also be used to give a solids volume fraction measurement. Using this device Asakura et.al (1992) measured profiles of solids volume fraction and solids velocity across a 51mm diameter pipe. However the measurements were not tested against any reference devices nor was there any discussion of possible errors.

A six electrode probe was developed by Xie et al (1998) to measure the velocity of a flow of blood, which can be considered a solids-liquid flow. While details of the

dimensions of this device were not reported, its general configuration is shown in Figure 2-17.
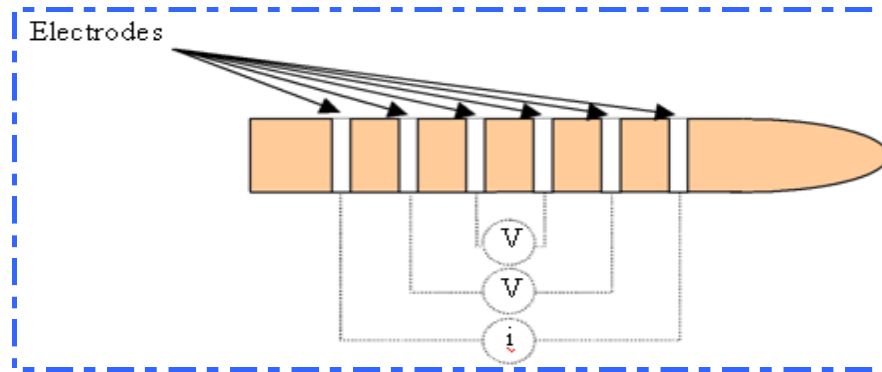
Figure 2-17: The local conductivity probe of Xie et al (1998)

Xie et.al (1998) claimed that by establishing an alternating current across the outermost electrode pair, and measuring the resulting potential differences as shown in Figure 2-17, measurement of the resistivity of the blood could be made. However a number of assumptions were made in order to justify this, in particular that the resistivity was proportional to the velocity of the blood due to the changing alignment of the blood cells. Results were referred against an unspecified "speedometer" but clearly such an effect would not be present in the investigations proposed for this project.

2.6.4.3 Six-electrode local probe for solids-liquid flow

Lucas et.al (1999) designed and built a six-electrode conductivity probe of diameter 4mm which can be used in solids-water pipe flow (see Figure 2-18).
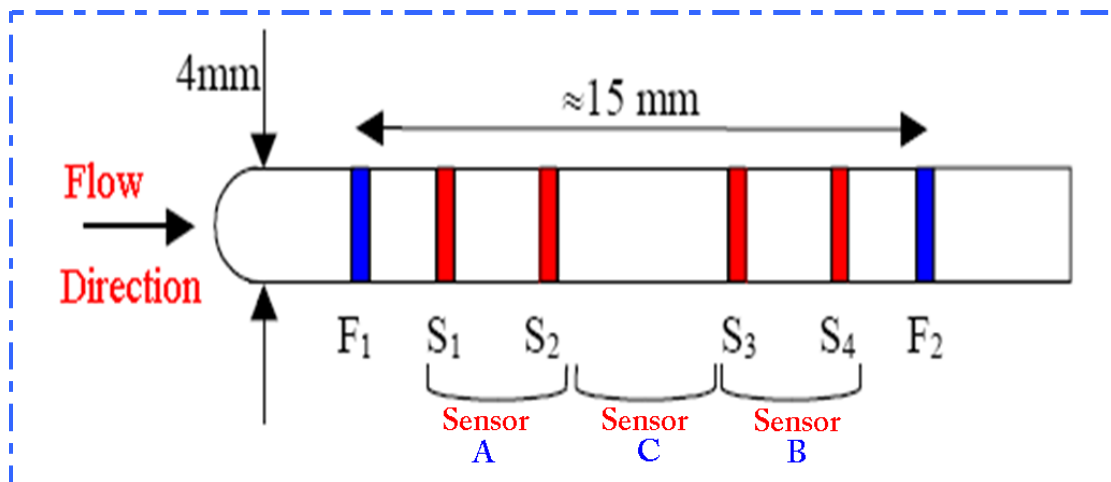
Figure 2-18: Six-electrode local probe of Lucas al (1999)

This probe was used in conjunction with a computer controlled traversing mechanism, to obtain the distributions of the local solids volume fraction and the local solids axial velocity both in vertical upwards and inclined solids-water flows. Inserting an intrusive measuring device into the pipeline is generally not acceptable with multiphase flows containing solids since it will be liable to damage by abrasion, and blockages may build up around it. So it was decided that it was unsuitable for this investigation. The results obtained by Lucas and his colleagues were obtained using an obtrusive technique but will help to confirm the results obtained by the author of this thesis.

2.6.4.4 Electrical Impedance Tomography Systems

Electrical Resistance Tomography (ERT), also known as Electrical Impedance Tomography (EIT), is a technique that uses conduction currents for imaging the structure of the solids-liquid flow (Hua Li et.al (2008), Wang, M. et.al (2005), Wu, Y. et.al (2005), E Fransolet et.al (2002) and Wang, M. et.al (1999). From a number of electrodes, a d.c or high frequency electrical current is injected into the flow and the resulting potential distribution is measured. The larger the number of sources and receivers the higher the spatial resolution of the image produced. From the measured data, a computer model of the electrical conductivity distribution is found from which, to within some predetermined tolerance, the phase volume fraction can be found. ERT measurements do not require a probe that intrudes into the flow, all the electrodes are mounted around the inside of the flow pipe, see Figure 2-19.

Figure 2-19: Dual plane Electrical Resistance Tomography system

The ERT device in Figure 2-19 had 16 stainless steel electrodes spaced equidistantly around the internal circumference of an 80m diameter pipe in each of two planes. Each electrode measured 5mm in the axial direction and 10mm circumferentially. For water-continuous multiphase flows, for which the dispersed phase is non-conducting, the pipe is surrounded by a number of electrodes which are in contact with the water. Current is successively injected between pairs of electrodes and voltages measurements are made between other electrode pairs see Figure 2-20. The relationship between conductivity σ and potential φ is

$$\nabla \cdot (\sigma \nabla \varphi) = 0 \qquad\qquad 2\text{-}12$$
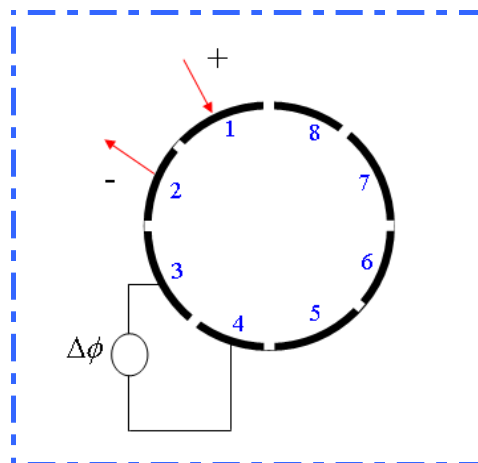
Figure 2-20: Single plan Electrical Resistance Tomography system

It is possible to determine the conductivity distribution in the flow cross-section from the measured boundary voltages. For a conducting continuous phase and non-conducting dispersed phase the local dispersed phase volume fraction can be determined from the measured local conductivity using:

$$\alpha = \frac{2\sigma_w - 2\sigma_m}{\sigma_m + 2\sigma_w} \qquad\qquad 2\text{-}13$$

The flow cross-section is divided into P 'pixels'. N measurement configurations are used to obtain N boundary voltage measurements (where typically N=P)

For small $\Delta\sigma$

$$\Delta\Phi_j = \sum_{i=1}^{P} - S_{i,j}\Delta\sigma_i \qquad (j=1,2,\ldots N) \qquad 2\text{-}14$$

where: $S_{i,j}$ is a normalised sensitivity coefficient relating changes in the jth boundary voltage measurement to changes in the conductivity in the ith pixel. The minus sign is present in Equation 2-14 because boundary voltage measurement will reduce as pixel conductivity increases. Following the example of Lucas et.al (1999), Equation 2-14 is re-written in matrix form so that it can be solved by standard software packages.

$$[\Delta\varphi] = -[S]_n^{-1}[\Delta\sigma] \qquad\qquad 2\text{-}15$$

Hence

$$[\Delta\sigma] = -[S]_n[\Delta\varphi] \qquad\qquad 2\text{-}16$$

where: n is an iteration number, $[\Delta\sigma]$ is the conductivity matrix, $[S]$ is the sensitivity matrix and $[\Delta\varphi]$ is the potential difference matrix.

The above matrix equation is solved iteratively, each step towards the solution being obtained using the conjugate gradients method. For each iteration a new set of values for $[S]$ are found because the sensitivity coefficients $S_{i,j}$ are affected by the conductivity distribution ('soft field' effect) their values have to be updated at each step see Lucas et.al (1999). These are substituted back into the original equation to

give a new S matrix (S is updated) and the process is repeated. The process stops either after a specified number of iterations (not used here) or when the change in the value of $[S]$ is sufficiently small and convergence is reached. The dispersed phase volume fraction in each pixel is then calculated.

Balasubrammaniam in an unpublished thesis (2008/2009) has reported on a somewhat similar investigation to this research but using EIT to investigate mean velocity of oil-water mixtures and volume fraction oils of two-phase oil and water flows in a pipe of circular cross-section. Of particular interest here is the comparison Balasubrammaniam made between the values obtained using EIT and his reference values.

Balasubrammaniam measured the mean volume fraction of oil for constant flow rates (water $3.5m^3/h$ and oil $1.0m^3/h$) in an 80mm ID pipe inclined at 0°, 15°, 30°, 45° and 60° to the vertical. He used a dp cell to provide a reference measure $\overline{\alpha}_{ref}$ in order to compare with the results obtained using an EIT system with 16 electrodes $\overline{\alpha}_{EIT}$. His results appear in Table 2-2.

Table 2-2: Volume Fraction Values at Different inclinations obtained by Balasubrammaniam (2008/2009)

θ^0 (angle of inclination to vertical)	Mean volume fraction of oil using EIT, $\overline{\alpha}_{EIT}$	Mean volume fraction of oil using dp cell, $\overline{\alpha}_{ref}$	% error
0	0.0568	0.1837	-69%
15	0.0517	0.1134	-54%
30	0.0408	0.0978	-58%
45	0.0489	0.0771	-36%
60	0.0858	0.0473	81%

It can be seen that there is a considerable difference between the reference mean volume fraction, α_{ref}, and the measured mean volume fraction using the EIT system, α_{EIT}.

Balasubrammaniam (2008/2009) himself concluded that his results clearly revealed a problem with his EIT system: in particular he emphasised that the volume fraction values found by EIT do not follow the accepted pattern. That for his results, as the angle of inclination to the vertical steadily increases, the value of α_{ref} first decreases, then increases. Balasubrammaniam concluded that this is a quite different trend from that normally observed whereby α_{ref} steadily decreases with increasing inclination. He also commented on the obvious differences in values of α_{ref}, is and α_{EIT}.

However, before commenting on the measured values of α_{ref} and α_{EIT}, it is worthwhile observing that the volume fraction distributions across the pipe, obtained by Balasubrammaniam, behaved in an apparently strange manner. If the pipe were divided by a vertical line passing through the centre of the pipe one would expect the volume fraction distribution to be symmetrical about that line. With the EIT measurements this was the case only for 0°. In all other flow conditions investigated by Balasubrammaniam the oil appeared either well to the left or to the right of the vertical line. Nor did the volume fraction distribution obtained by EIT always show the lighter oil to be in the top half of the pipe. Referring to the values of the mean volume fraction that is actually calculated two comments are necessary. Comparing Balasubrammaniam's results for the volume fraction distribution obtained using the EIT for an angle of inclination of 30°, even allowing for the obvious error in symmetry (the oil flow appears in the bottom half of the pipe on the right hand side) there are clear differences with values measured using the dp cell, which give the pattern that would be expected, see Figure 2-21 and Figure 2-22. This puts a question mark over the image reconstruction software. Note that this software used by Balasubrammaniam was supplied by a commercial vendor of EIT systems- who also supplied the hardware used by Balasubrammaniam.
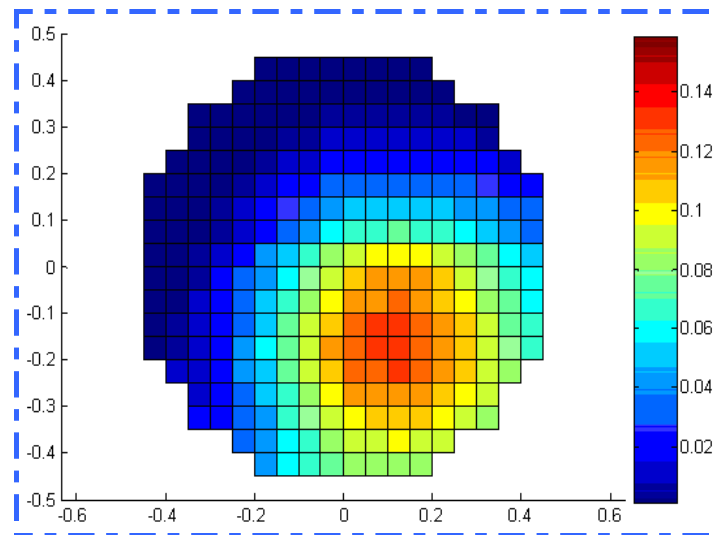
Figure 2-21: Volume fraction distribution at 30° inclination as found by EIT, water 3.5 m^3/hr and oil 1.5 m^3/hr.

.
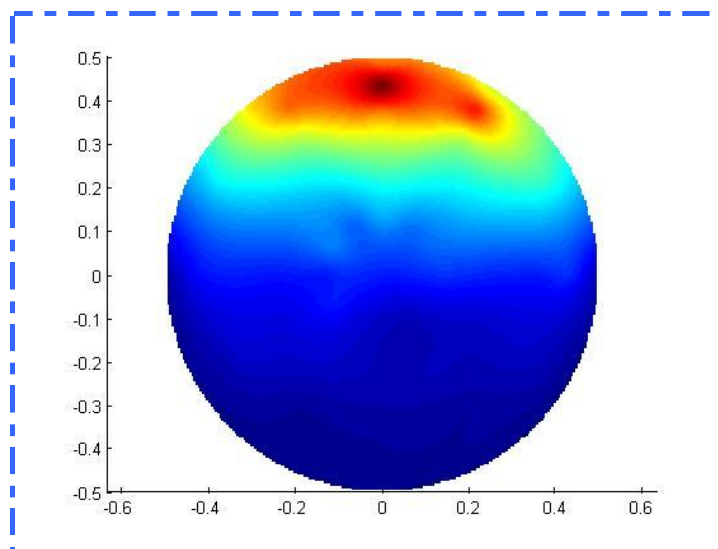
Figure 2-22: Reference volume fraction distribution at 30° inclination as obtained by local probe, water 3.5m^3/hr and oil 1.5 m^3/hr

Another point needs to be included here. Quite apart from distribution of volume fraction over the cross-section there is the question of the actual values measured by the EIT. In some distributions that Balasubrammaniam obtained (the one for 0° is the most obvious) the <u>maximum</u> measured value of the local volume fraction (from the EIT) is well below the <u>average</u> value obtained by the dp cell. That is the EIT method seriously underestimates the actual volume fraction. Balasubrammaniam did compare his results with the volume fraction distribution obtained by Lucas and Panagiotopoulos (2009) using dual sensor probes (Figures 2-23 and 2-24) and

reported that while those authors found a volume fraction which was more or less constant over the pipe cross-section he found a bell shaped pattern with a well-defined maximum on the pipe centre-line. This puts a second question mark over the image reconstruction software. It is known that the complicated and advanced digital signalling processing software inherent in the EIT system can lead to inaccurate estimates of the local solids volume fraction as has been noted previously (E Fransolet et.al (2002)).
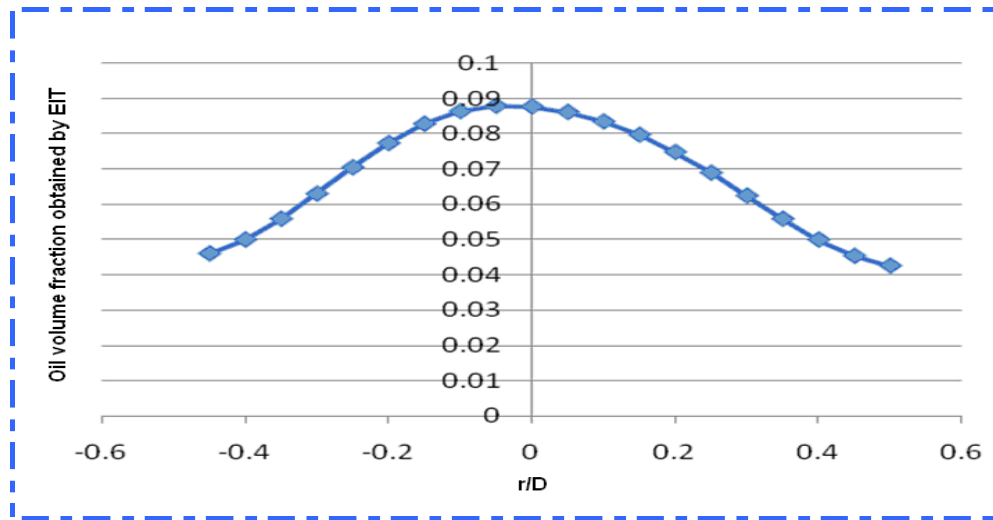
Figure 2-23: Volume fraction as a function of radial distance from centre of pipe measured using EIT system for reference oil fraction 0.15, after Balasubrammaniam (2008/2009)
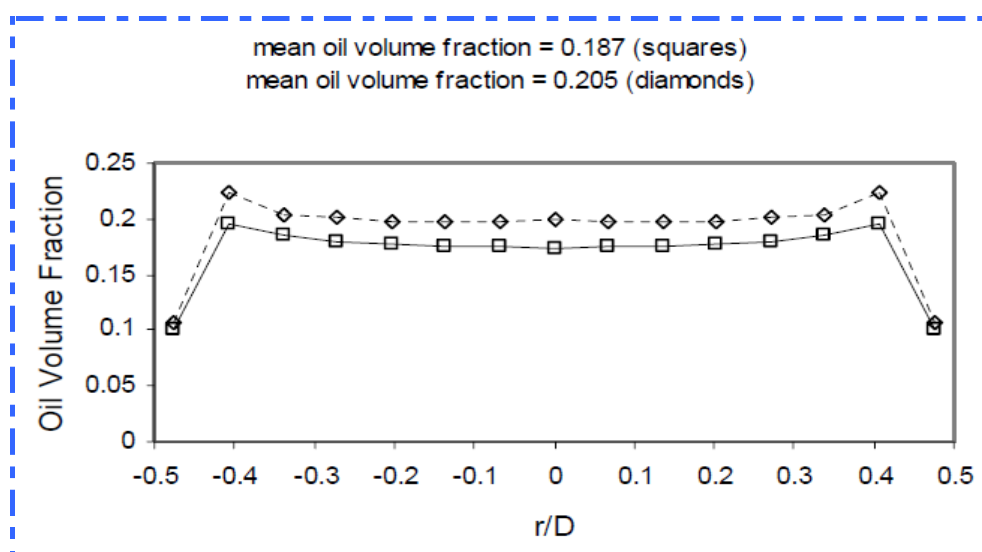
Figure 2-24: Volume fraction as a function of radial distance from centre of pipe, after Lucas and Panagiotopoulos (2009)

Balasubrammaniam also reports the measured velocity of bubbles obtained using a cross-correlation technique. The cross-correlograms are just what would be expected. Assuming the same volume flow rates as used for the measuring the volume fractions would expect a minimum bubble velocity of about 0,25ms^{-1} (the mean flow of the oil-water mixture). The velocities Balasubrammaniam reports, about 0.36ms^{-1}, are what one would expect in an inclined pipe where the bubbles travel much faster.

Balasubrammaniam attempted to measure the mean flow velocity (U_{CC}) across the pipe cross-section using a cross-correlation technique where the planes of the electrodes were 30mm apart. Simultaneously he calculated the mean flow velocity (U_h) by dividing the total volume flow rate by the cross-sectional area of the pipe.

Generally he found that the smaller the angle of inclination the less good the correlation. For a flow rate of 6.5m^3/h of water and 2.0m^3/h of oil the correlograms for inclinations of 0° and 60° are shown in Figures 2-25 and 2-26 respectively.

The first thing that is obvious is that for 0° inclination the trace shows a signal with a lot of background noise (broader peak) while the trace for the 60° inclination shows a very narrow peak. The second very noticeable point is that the magnitude of the correlation coefficient at inclination of 60° is about ten times as great as the other (in some cases the ratio was thirty-five). This tends to indicate that the disturbances in the flow preserved their identities much better for a pipe that was not vertical.

As would be expected there was greater agreement between the mean velocities determined for sharper peaks of larger amplitudes and the mean velocity found from the total volume flow rate. This was true even though flow patterns are less symmetrical for more horizontal pipes.
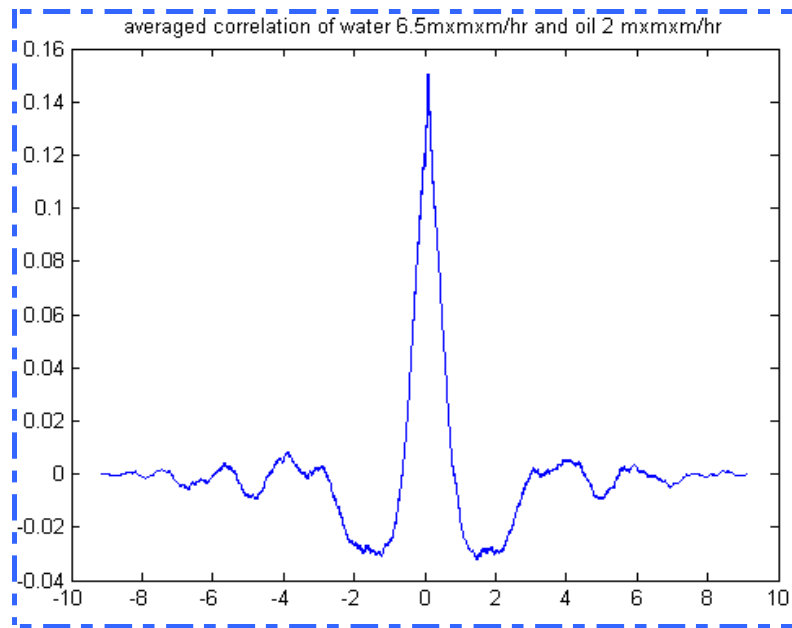
Figure 2-25: (a) Correlogram for pipe at 0° to vertical: water 6.5 m^3/hr and oil 2.0m^3/hr hr, averaged time delay 0.0959 sec, calculated mean flow velocity, 0.313 ms^{-1}, reference flow velocity 0.470 ms^{-1}
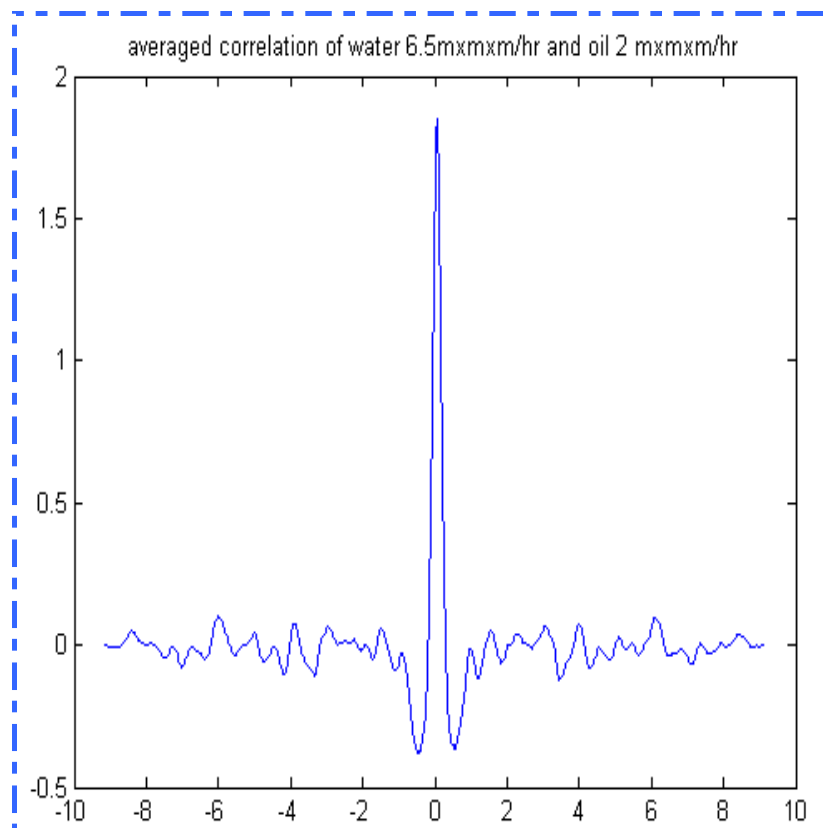
Figure 2-26: (b) Correlogram for pipe at 60° to vertical: water 6.5 m^3/hr and oil 2.0m^3/hr hr, averaged time delay 0.0625 sec, calculated mean flow velocity, 0.480 ms^{-1}, reference flow velocity 0.470 ms^{-1}

A rather strange feature of the mean velocities can be seen when the measured results for U_{CC} are plotted against the calculated values for U_h (Figure 2-27). For each inclination of the pipe, U_{CC} is plotted against U_h and for each set of points the best fit straight line has a slope about $0.6 - 0.7$. Thus it appears that for small inclinations (pipe nearly vertical) the correlation device is more accurate for low flow rates, while for the larger inclinations this device is more accurate for faster flows. Balasubrammaniam does not comment on this and an explanation does not spring to mind.
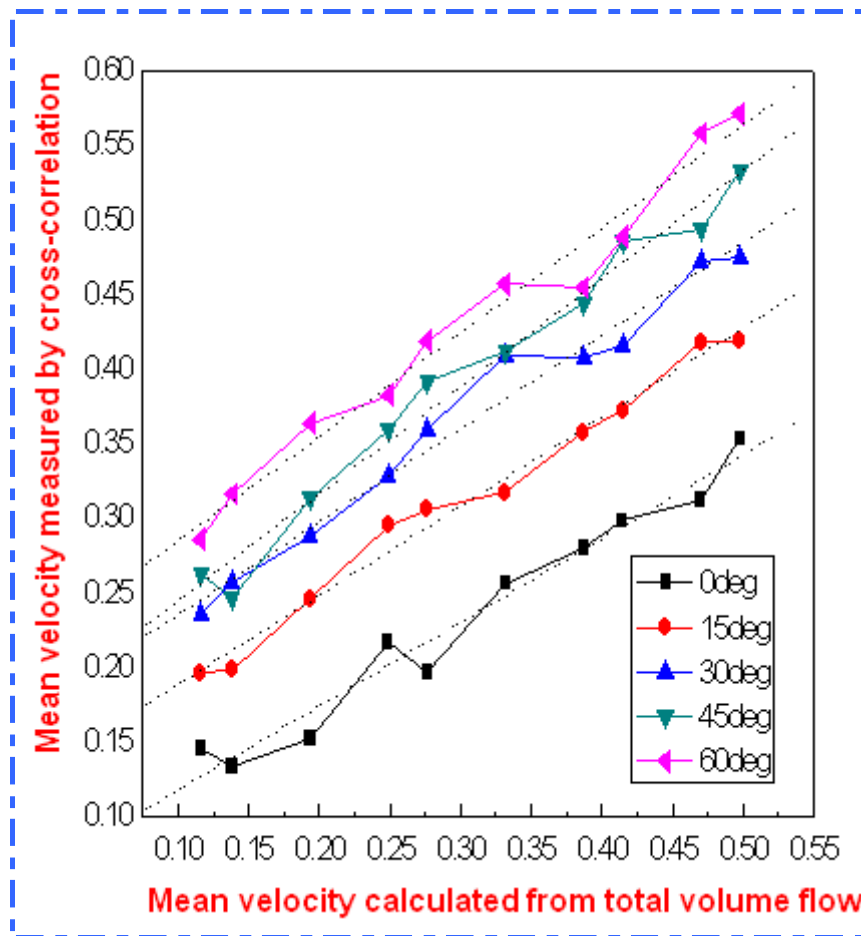
Figure 2-27: Mean velocity obtained by cross-correlation verses mean velocity calculated from total volume flow rate divided by cross-sectional area of pipe.

In the present study the proposed ICC system is intended to overcome the disadvantages of the dual-plane ERT system including a major disadvantages of the ERT system - its high initial and maintenance costs.

2.7   Conductivity measurement device

Apart from its use in two-phase flow, electrical measurement conductivity has been used in a variety of other fields. It was decided that research carried out in these other areas could be applicable to the present investigation as it was important to identify any other fields in which the current research could be applied. Therefore a brief review of conductivity measurement in other fields was carried out and is presented below.

2.7.1   Electrolyte conductivity measurement devices

The area of application most closely related to two-phase flow measurement is the measurement of the conductivity of electrolytes and other liquids. Volanschi et al.,(1992) have reported the use of a two electrode solid state instrument used for measuring pH but there appear to have been considerable electro-chemical effects and drifting of measurements with this device (Volanschi et al.,(1994)).

Ncube et al.,(1991) reported the use of a two electrode probe with one electrode having an area $0.001mm^2$ and the other having an area $500mm^2$. They claimed that this caused the measurement to be localised at the small electrode. However they reported substantial drift over time using this system which Nasr-El-Din et al.,(1985) and Volanschi et al., (1992) have suggested is caused by electro-chemical effects which could be negated by using a four electrode system.

2.8   Comments on conductivity methods

Local conductivity probes that measure local values of solids volume fraction and solids velocity are reported in the literature. These devices appear to be relatively inexpensive, and their simple and robust construction allows them to be made with a variety of different geometries for different industrial applications. The probes varied in diameter from 3mm to 4.8mm giving ratios of probe diameter to pipe diameter of between 0.06 and 0.1.

The major disadvantage of these devices is that they are intrusive, despite the opinions of Gunn and Al-Doori (1985) which suggest that such effects are negligible. Inserting an intrusive measuring device into the pipeline is generally not acceptable with solids-

water flows since it will be liable to damage by abrasion, particularly in small ID pipes, and blockages may build up around it Consequently, recent advances in water-solids measurements based on non-intrusive techniques are generally given priority, in particular optical, ultrasound, nuclear, conductivity and electrostatic transducers. This thesis concentrates on non-intrusive conductivity measurement.

2.9   Relating mixture conductivity to the solids volume fraction

Estimating the local solids volume fraction α_S by measuring the local mixture conductivity σ_m is a relatively simple and economical method which can yield accurate results. The method relies on the fact that the electrical conductivity of a solids-liquid mixture depends on the conductivity and the relative volume of each of the phases. In the proposed investigation the liquid, water, is conductive whilst the solids assumed to have a conductivity of zero. Therefore as α_S increases σ_m will fall.

In order to obtain an accurate estimate of α_S it is necessary to accurately relate it to σ_m. Many expressions have been developed for this relationship, of which Maxwell's [1873] was one of the earliest, see Equation 2-17. A review of these relationships is given by Nasr-El-Din et al.,(1985) and also in MacTaggart et al., (1993). Experimental testing of some of their relationships has been reported by De La Rue and Tobias (1959).

$$\frac{\sigma_m - \sigma_w}{\sigma_m + 2\sigma_w} = \alpha_s \frac{\sigma_s - \sigma_w}{\sigma_s + 2\sigma_w} \qquad \text{2-17}$$

Here α_S is the local solids volume fraction. σ_m, σ_w and σ_s are the conductivities of the mixture, the continuous phase (water), and the dispersed phase (solids) respectively. Maxwell's relationship assumes that the particles are evenly sized spheres and that they are in an ordered arrangement at a low volume fraction. This low volume fraction condition allowed Maxwell to assume that the electrical field around any one particle was unaffected by any other particles. In the current investigation the assumption is made that σ_s is effectively zero. Therefore Maxwell's

relationship reduces to Equation 2-18.

$$\sigma_m = \sigma_w \frac{2(1-\alpha_s)}{(2+\alpha_s)}$$

2-18

Nasr-El-Din et al(1985) and De La Rue and Tobias (1959) reported that a number of other researchers have independently developed theoretical relationships that reduce to this simplified form of Maxwell's relationship. Turner (1973) and Neale and Nader as reported by Nasr-El-Din et al (1985) have demonstrated that Maxwell's relationship accurately fits experimental data for solids volume fractions up to 0.55, and de la Rue and Tobias (1959) have reported experimental work by a number of researchers that confirm that Maxwell's relationship can be relied upon.

Bruggeman (1935), in deriving Equation 2-19, extended Maxwell's relationship to solid spheres of random size and distribution, and so the equation should apply to mixtures with solids volume fractions approaching 1.

$$(\sigma_m - \sigma_s)\left(\frac{\sigma_m}{\sigma_w}\right)^{\frac{-1}{3}} = (1-\alpha_s)(\sigma_w - \sigma_s)$$

2-19

2.10   Cross-correlation flow velocity measurement

As a solid particle passes an upstream sensor it causes a momentary change in its output signal. The same particle then travels to a downstream sensor and causes a similar change in the output signal as it passes. The time delay between these changes in output signal will be approximately equal to the time taken for the particle to travel the distance between the sensors. This is inversely proportional to the particle mean velocity. To calculate the solids mean velocity, the time lag between the changes in output signal measured at the upstream and downstream sensors must be found. This is done by cross-correlation.

Cross-correlation can be considered as the process of matching two signals as a function of the time delay between them (Beck. M.S. et.al (1987)). Consider two time signals $x(t)$ from upstream sensor X and $y(t)$ from the downstream sensor Y. The cross-correlation function $R_{xy}(\tau)$ of $x(t)$ and $y(t)$ is defined in Equation 2-20. If

the signals are unrelated $R_{xy}(\tau) = 0$ for all values of τ. However, a very important property of the cross-correlation function is that if $x(t)$ and $y(t)$ are the output signals of a cross-correlation flow meter, $R_{xy}(\tau)$ will have a maximum values when $\tau = \tau_p$, where τ_p is equal to the time taken for particles to travel from the first to second sensor.

$$R_{xy}(\tau) = \lim_{T \to \infty} \frac{1}{T} \int_0^T x(t)\, y(t + \tau)dt \qquad\qquad 2\text{-}20$$

In Equation 2-20 T is the time period over which the signals $x(t)$ and $y(t)$ are sampled. Note T must be greater than the time taken for the particle to pass between the sensors.

Because the cross-correlation function $R_{xy}(\tau)$ has a maximum value when $\tau = \tau_p$ the mean transit time of particles in the flow to pass between sensors X and Y, τ_p can be found by determining the value of τ at which $R_{xy}(\tau)$ is at maximum. In a uniform two phase flow where all disperses particles travel with velocity V_p then since $\tau_p = L/V_p$ where L is the distance between sensors X and Y, the particle velocity V_p can be calculated. Unfortunately, researchers have demonstrated that in vertically upward, bubbly flows, the characteristic flow velocity obtained using impedance cross-correlation techniques does not correspond to either the velocity of the continuous phase or the velocity of the discontinuous phase. Rather, it corresponds to the propagation velocity of naturally occurring void fraction waves also known as kinematic waves, in the flow see Beck et.al (1987).
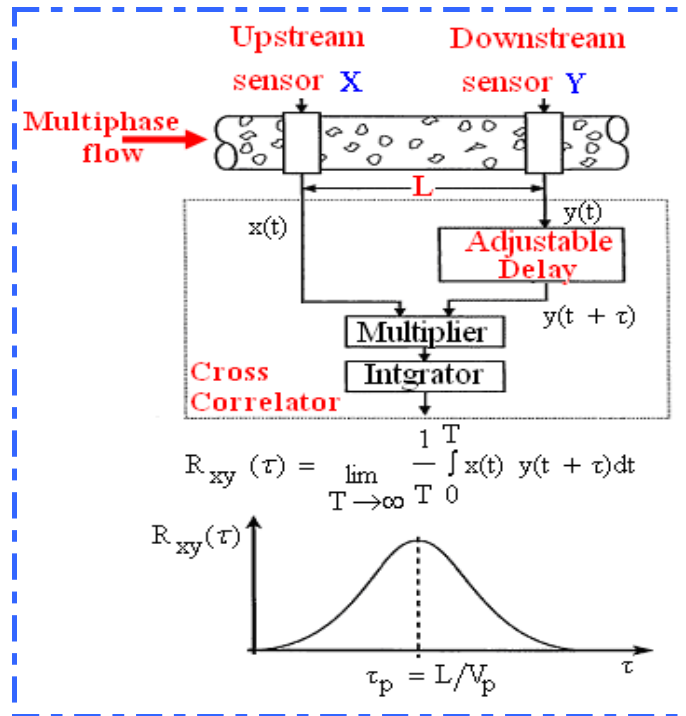
Figure 2-28: Schematic diagram of cross-correlation flow meter Beck et.al (1987).

Nevertheless, Lucas et.al (2001) has also shown that it is possible to use impedance cross-correlation techniques to measure the velocity of Taylor bubbles in the slug flow regime and but that by using the conventional cross-correlation technique it is not possible to measure the velocity of the liquid phase in the slug regime. Lucas et.al (1997) has also demonstrated however, for that bubbly flows, the mean velocities of the dispersed and continuous phases can be derived from the kinematic wave velocity.

In cross-correlation flow measurement two linked design parameters of the device are critical. These are the axial separation of the two sensors, L, and the sampling frequency of the device f_s. When computing the cross-correlation function the accuracy of the estimate of the time delay associated with the peak of the cross-correlation function is approximately equal to $\tau_p \pm \delta\tau$ where $\delta\tau = \dfrac{1}{f_s}$. Thus the higher the sampling frequency f_s, the greater the accuracy with which τ_p is measured. However, τ_p will reduce as L reduces, so the smaller the value of L the greater will be the error to a given value of f_s. In this way the accuracy of the cross-

correlation velocity estimate is dependent on both L and f_s. This relationship is discussed in detail by Beck et.al (1987).

Generally, when deciding upon the value for L, a compromise between maintaining the similarity of the flow patterns between the upstream and downstream sensors, and the accuracy of resolution of measurement of the transit time will have to be made. The smaller the separation the greater the similarity of the signals obtained from the two sensors and the easier it is to obtain a distinct and obvious maximum for $R_{xy}(\tau)$. On the other hand, the relatively slow process of data acquisition, and possible interference of the electrical fields between the two sensor arrays requires a longer distance L. Both the similarity of signals and the dynamic behaviour of the system must be considered.

However, in general terms given that what is required is a low-cost, non-intrusive device it appears obvious that a cross-correlation technique should be used to determine the particle velocity. Such a method has the added advantages that it is readily understandable and reasonably easy to apply. Therefore, the speed of data collection plays a dominant role in the use of cross-correlation algorithm.

2.11   Conclusions from the literature review

As described in Chapter 1, the aim of this investigation is to measure the local solids volume fraction and the local axial solids velocity, α_s and u_s respectively, in upward solids-liquid flows in pipes inclined at different angles to the vertical. In this investigation measurements are intended to be made at 0°, 15° and 30° to the vertical and it is intended to use these measurements to calculate the solids volumetric flow rate and area averaged values of the solids volume fraction and the axial solids velocity, $Q_{s,meas}$, $\overline{\alpha}_{s,meas}$, and $\overline{u}_{s,meas}$, respectively, see Chapter 6 for the experimental details. It is expected that there will be a dynamic balance and a flow will be established where the time-averaged local solids volume fraction shows a variation across the pipe from a high value at the "lower side " to a much lower value at the upper side of the pipe. Naturally, the time-averaged axial velocity profile for solids carried in multi-phase flow in an inclined pipe will be correspondingly complex, with an axial solids velocity in the forward direction at the upper side of the

inclined pipe and smaller axial solids velocity at the bottom with the possibility of reverse flow adjacent to the lower face of the pipe.

At present, there are few commercially available devices for measuring the local solids volume fraction and velocity distributions in water-solids flows in inclined pipes. These devices include ERT, however that method presently suffers from a number of drawbacks. It is relatively costly in terms of the equipment itself, the high quality technical support required and the computing time necessary to adequately process the necessary information. The greater accuracy required the greater the number of electrodes required, but the accompanying processing goes up as the square of the number of electrodes. Thus a 16 electrodes arrangement has 104 possible combinations while an eight electrode arrangement has only 20 combinations. While a laptop PC running Windows and equipped with 2 serial ports may be used to control the ERT system, the data sets needed to generate conductivity images requires sophisticated inversion software. A fully 3-D imaging technique is presently impractical on a PC, the computer processing power required for detailed resolution of in-pipe velocities and distributions is still outside the capabilities of even modern PCs.

ERT is unable to measure the flow rate of the continuous phase and in its current form has difficulties in presenting an absolute value. Some have argued that the only measure of data quality is the degree to which reciprocal measurements agree. Reciprocal measurements are measurements in which the transmitter electrodes and the receiver electrodes have been interchanged. Thus the electrode geometry remains the same. Ideally, reciprocal measurements should be identical. Other more rigorous calibration and referencing techniques are required.

In addition, the algorithms required to interpret the measured voltages into a description of, say, solids fraction in a flow are complex so that different algorithms can give slightly different results, and the resolution will be limited by the spatial smoothing necessary in the imaging algorithm. In addition, the flow patterns produced are a function of electrode position, so mis-alignment will introduce systematic errors in addition to any random errors. The clarity and definition of the patterns will be a related to electrode size and the fact that they have to be positioned at the boundary (pipe wall) of the flow. Thus the resolution will be sharpest in the region of the pipe

wall and in the centre may be limited to 5%-10% of the pipe diameter for smaller numbers of electrodes.

Nevertheless accurate determination of the mean values of both local solids volume fraction and the local axial solids velocity require local measurements to be made inside the pipe at a sufficiently large number of locations on the given pipe cross-section, this is particularly true for inclined flows where particle velocity and local solids volume fraction can be highly skewed. This will require a non-intrusive method. The above review of the literature shows that the only non-intrusive devices that can give reliable results are laser methods or conductance/correlation techniques. Laser equipment is not readily available, is relatively expensive and unlikely to be acceptable for industrial application, not to mention that on-site flows are highly likely to contain oils and so be opaque. Conductance methods combined with cross-correlation techniques look very promising, and with the present rate at which processing power is increasing it is to be hopes that certain key problem associated with dual-plane ERT can substantially reduced.

On the basis of the literature review and industrial constraints on the project it is proposed that the measurement system to be adopted will be similar to previous ERT systems used for online monitoring of solids-in-water flows. Impedance Cross-Correlation (ICC) is a device similar in principle ERT. The experimental results obtained from this system will be compared with the ERT results obtained by Lucas et al., (1998) and a six-electrode local probe obtained by Lucas et al., (2000). The design of the ICC device will be given in the next chapter.

Chapter 3   INSTRUMENT DESIGN AND CONSTRUCTION

This chapter describes the measurement principles, design considerations and construction of the Impedance Cross-Correlation flow meter. The conductance measurement electronic circuit that was designed and constructed is explained. The chapter also describes the design and construction of the electrode selection circuitry controlled by computer via a LABJACK data acquisition and control unit. Software was successfully developed to control the selection of the electrode configurations for the two electrode arrays (A and B).

.

3.1 Basic measurement method

As mentioned in Chapter 2, measurements of conductivity have previously been successfully used in a wide variety of applications to multiphase flow measurement (Wei F et.al , 1998). Of course, to measure the local solids volume fraction α_S by measuring the local mixture conductivity σ_m the relationship between α_S and σ_m must be known. In a solids-water flow, with which this project is concerned, the liquid is assumed conducting and its conductivity is σ_w. The solids are assumed to be composed of insulating material with an electrical conductivity of zero. The measured local conductivity, σ_m , of a region of the flow – which is known, or assumed, to contain a representative concentration of the solids particles - can then be used to make an estimate of the local solids volume fraction, α_S, using the simplified form of Maxwell's equation (Maxwell, J.C. (1873)) for conductivity of mixtures, see Section 2.9:

$$\alpha_S = \frac{2\sigma_w - 2\sigma_m}{\sigma_m + 2\sigma_w} \qquad\qquad 3\text{-}1$$

The concept behind the electrical conductivity technique is that the conductivity of a two phase mixture depends on the volume fraction of the disperse phase, the conductivity of the multiphase fluid decreasing with increasing solids volume fraction.

To measure u_S, the local axial solids velocity, fluctuations in the local mixture changes in conductivity which occur as solid particles pass each of two axially separated conductivity sensors, are detected and cross-correlated, see Section 2.10.

3.2 Design considerations of the Impedance Cross-Correlation flow meter for multi-component flow measurement

In this project, the ICC consists of two electrode arrays attached to the inner surface of the pipe carrying the two-phase flow, (see Figure 3-1). In each electrode array there are eight stainless steel electrodes mounted equidistantly around the internal circumference of the pipe. The electronic circuitry was such that any electrode or

combination of electrodes in an array could be selected to be (i) excited by a 10kHz excitation voltage (V^+), or (ii) be earthed (E), or (iii) used as a 'virtual earth' measurement (V_e). For example, if it was desired to measure the solids flow velocity only at the upper side of an inclined pipe, the electrodes which were at the upper side of the pipe were used. It is considered that this arrangement is novel and has not been used before for multiphase flow measurement of solids in liquids. To protect the ICC and provide additional shielding from electronic interference it was enclosed within an earthed stainless steel cover as shown in Figure 3-3(a).
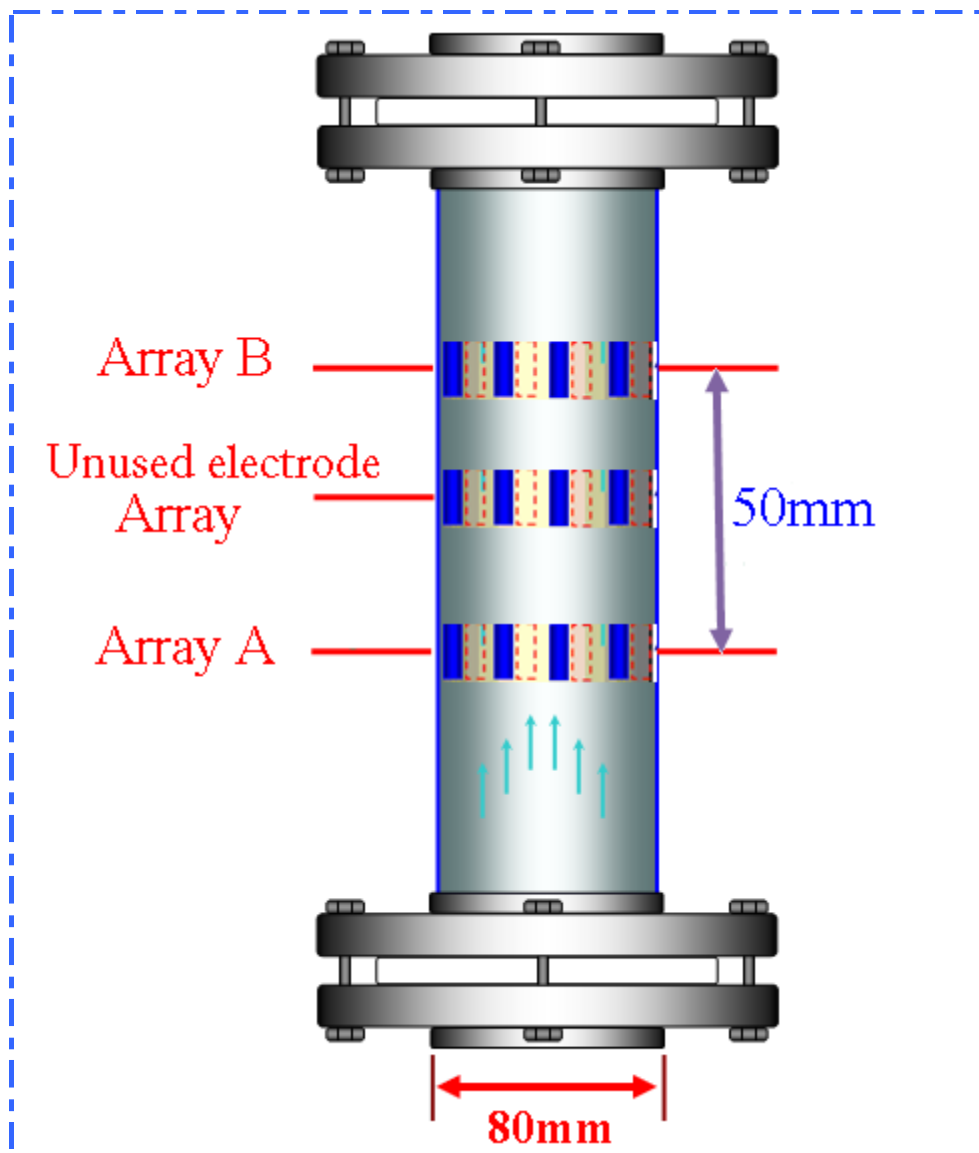
Figure 3-1: Schematic diagram of the Impedance Cross-Correlation device

The essential principle of the instrument is that the electrodes in a given array, on the inner surface of the pipe carrying the multiphase flow, are used to introduce an electric current into the solids-water mixture. An inverting amplifier is used to measure the mixture conductance (and hence the mixture conductivity) at specific locations in the flow cross section at arrays A and B, from which the solids volume fraction at these locations can be calculated. Cross correlation of conductance measurements at corresponding locations in the flow cross section at arrays A and B enables the solids velocity at these locations to be determined.

3.3   Construction of the ICC device

In order to make the necessary measurements using the flow loop system available at the University of Huddersfield, for multiphase flow testing, the instrument had to be designed with the following factors in mind:

❖ To achieve the required cross-correlation in order to determine the velocity of the flow, two separate electrode arrays must be used, (see Figure 3.1). Two arrays are sufficient but a third array was also constructed in case it was found necessary to alter the axial separation of the arrays. The possible axial array separations L that could be achieved using the ICC device that was constructed are 30 mm, 20mm and 50mm (see Figure 3-1) although the value of L that was used in the present investigation was always 50mm.

❖ For highly non-uniform solids distributions, to measure the solids velocity and volume fraction profiles in each part of the pipe, each of the two electrode arrays consisted of eight electrodes mounted around the pipe. The internal circumference of the pipe was 80 mm so the eight electrodes will be some 31mm apart – centre to centre. This is considered a sufficient distance for two reasons, firstly the electrodes are sufficiently far apart for there to be adequate space around each electrode. This ensures that the electrical connections to one electrode do not interfere with the connections to a neighbouring electrode. Secondly the electrodes are close enough together to give an adequately detailed picture of the flow in the pipe.

❖ To select the optimum axial separation L between the two electrode arrays a survey of previous work was carried out. X. Den et al. (2001) found that for an 80mm diameter pipe the optimum distance L between the two electrodes arrays for the purpose of determining the flow velocity by cross-correlation should be 50mm centre to centre, see Figure 3.1. He obtained that result by experimentally varying the distance between two electrode arrays incrementally and observing which separation gave the best results.

❖ 'Cross-talk' between the two electrode arrays had to be eliminated.

❖ To determine the detailed profiles of α_S and u_S, it was necessary to determine the optimum duration of data acquisition from each electrode configuration. The LABJACK data acquisition card which was used could acquire data from multiple channels at a rate of 1 kHz per channel for considerably longer than 60 seconds, but 60 seconds was considered to be sufficient for the purposes of the experiments.

❖ To determine the detailed profiles of α_S and u_S it was necessary to ensure that the positions of each of the eight electrodes in each array was properly identified and clearly matched to the relevant channel of the electronic circuitry.

❖ For each electrode configuration data was acquired from both the ICC and reference measurement devices and the results compared. This is discussed in the next chapter.

3.4   ICC design and construction

The mechanical system of the ICC consisted of the sleeve (flange and ICC casing) the flow tube (pipe element and O rings) and the electrode assembly, see Table 3-1.

Table 3-1: ICC components list

Component designation	Component	Type	Number of items	Component Material	Comment
Sleeve	Flange	BS4504 DN80	2	PVC	3 inch
	ICC casing	Tubular	1	Stainless steel	210mm OD 115mm ID 310mm long
Flow tube	Pipe element	Tubular	1	Peak	110mm OD 80mm ID 310mm long
	'O' rings	M9	4	Rubber	Thickness 2mm
Electrode assembly	Electrodes	E6013	24	Stainless steel	
	Bolts	M8	24	Stainless steel	
	Cable terminals	3.2mm ID	16	Copper	
	Washers	M6	24	Stainless steel	
	Nuts	M8	48	Stainless steel	

3.5   Assembly drawing

Figures 3-2 to 3-4 show the ICC meter, drawn using SolidWorks software.

(a)   (b)
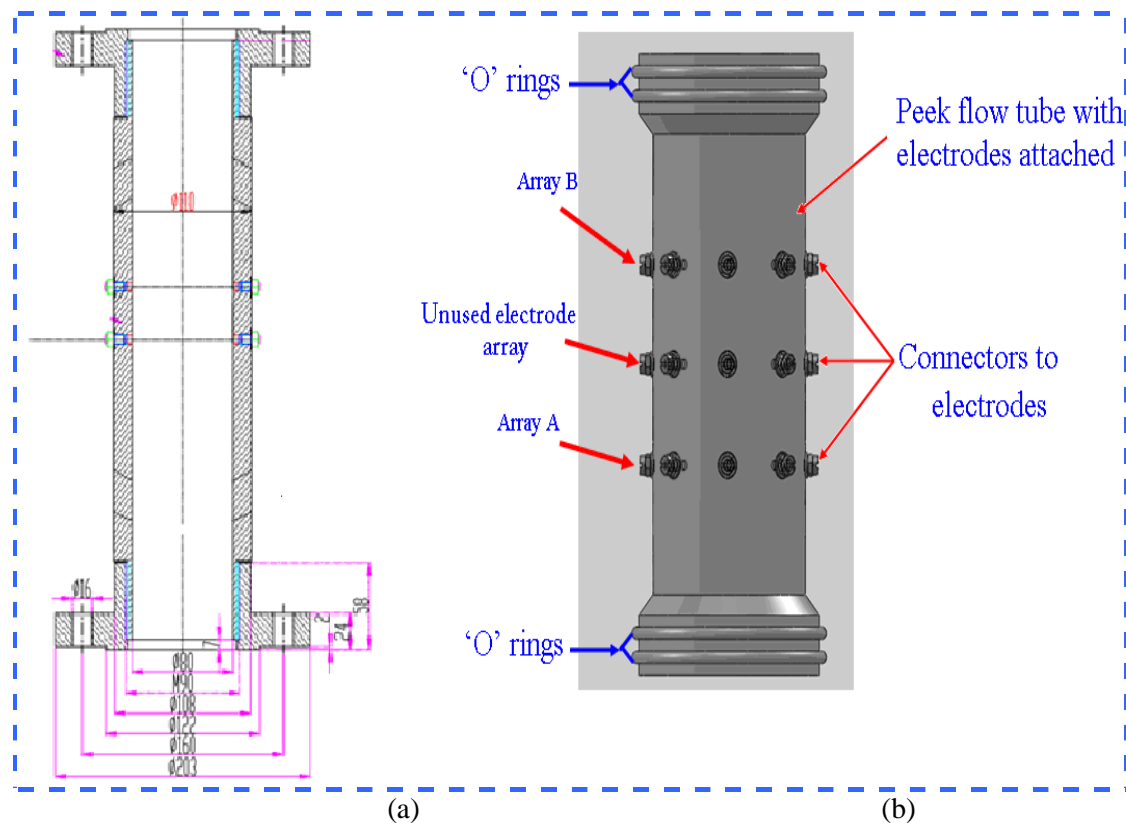
Figure 3-2: ICC body design

123

Figure 3-2 (a) shows the dimensions of the cross-section of the device. Figure 3-2 (b) shows the three arrays of electrodes. In each array, there are eight electrodes around the circumference of the pipe. Array C was not used in the present investigation. The four 'O' rings, with two at the top and two at the bottom are for sealing the flow tube into the stainless steel casing. Flanges were fitted to the ends of the stainless steel casing to enable it to be mounted into the flow loop.

Figure 3-3 (a) shows the casing of the device. It was made of a stainless steel, and was used to protect the inner structure of the ICC, which is common practice in industry. Figure 3-3 (b) shows how the electrodes were mounted in the flow tube wall. At the inner surface of the flow tube wall the electrodes were in contact with the multiphase mixture. At the outer surface of the flow tube wall were connectors enabling the electrodes to be connected to the relevant electronic circuitry.
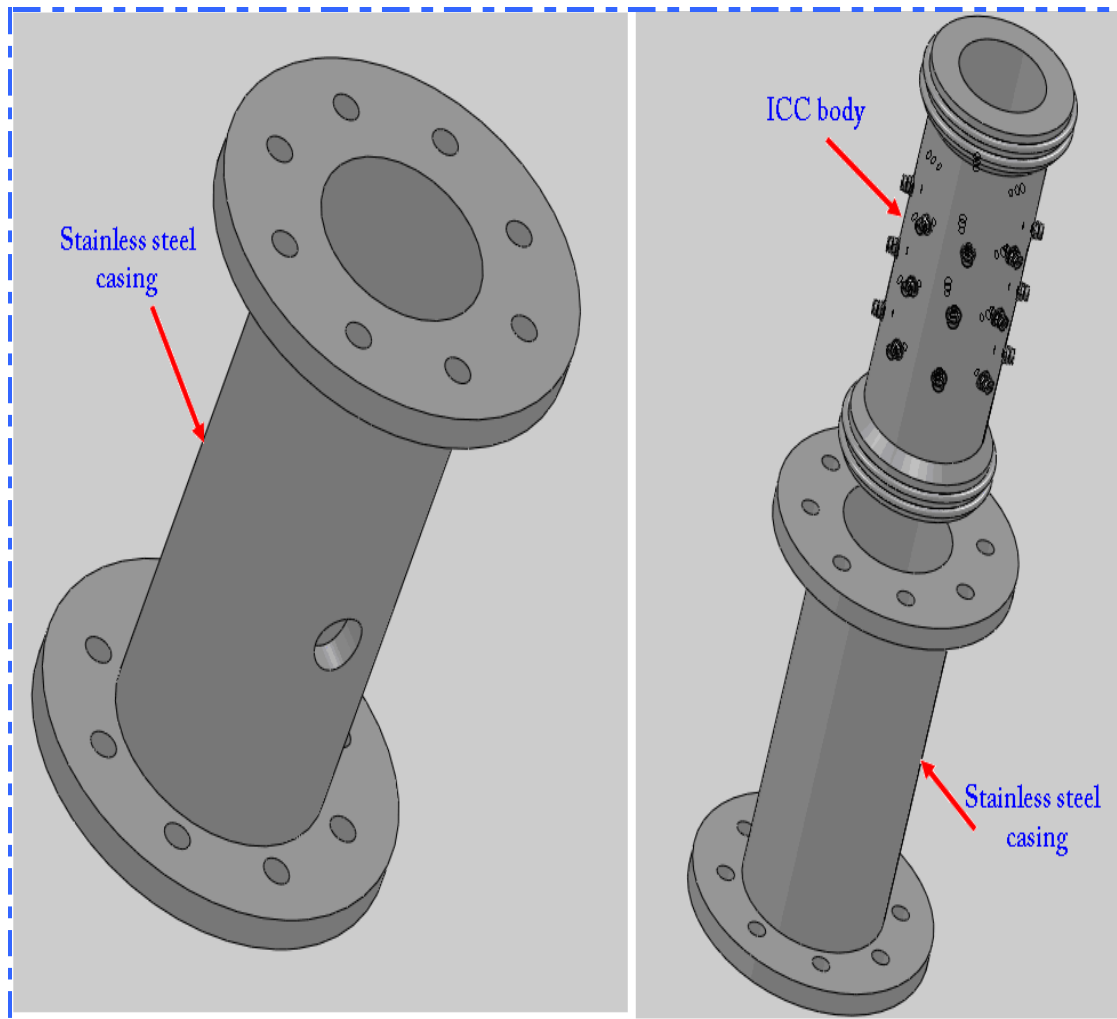
(a)   (b)

Figure 3-3: ICC body and casing
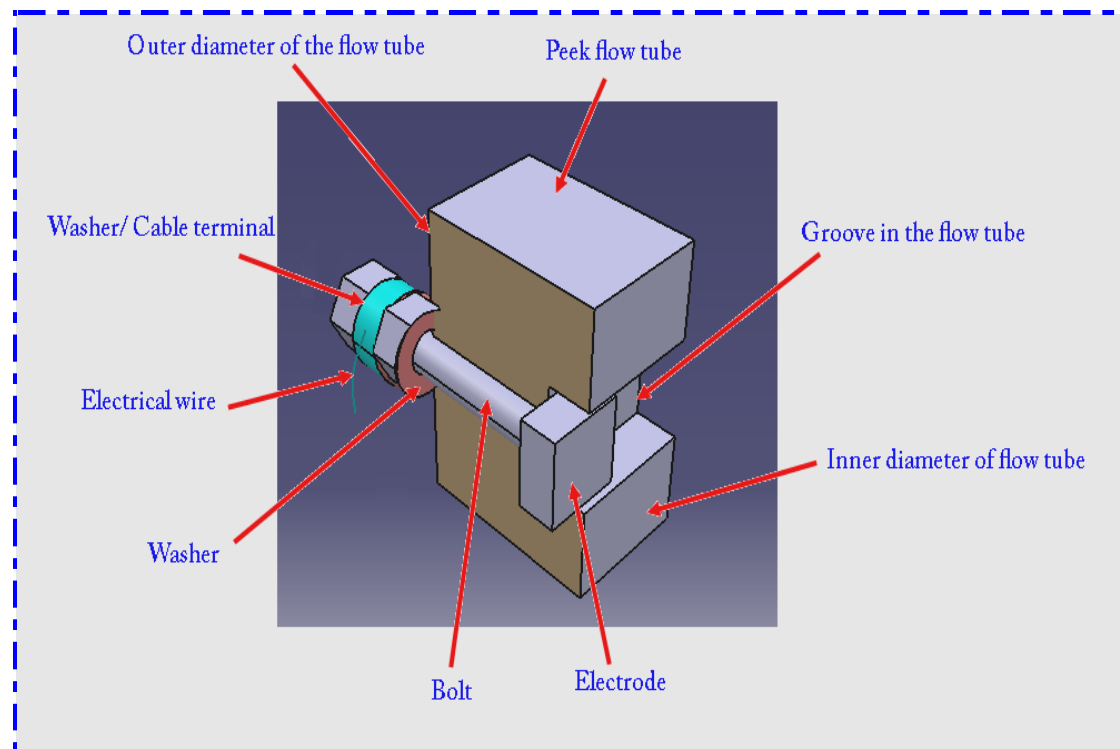
Figure 3-4: Electrode assembly

Figure 3-4 shows the pipe prepared for an electrode, with a hole drilled through the pipe for the electrical connection and a groove cut in the face of the pipe to take the electrode, and also it shows the array with the electrodes in place. Figure 3-5 (a) shows an individual array without the electrodes and Figure 3-5 (b) shows the array with the electrodes in place.
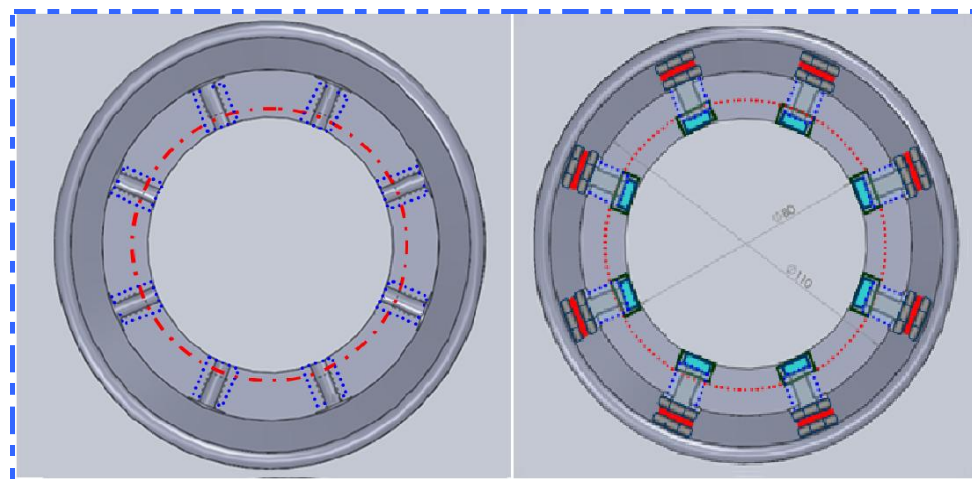
(a) Cross section of ICC device without electrodes in place

(b) Cross section of ICC device with electrodes in place

Figure 3-5: Electrode array
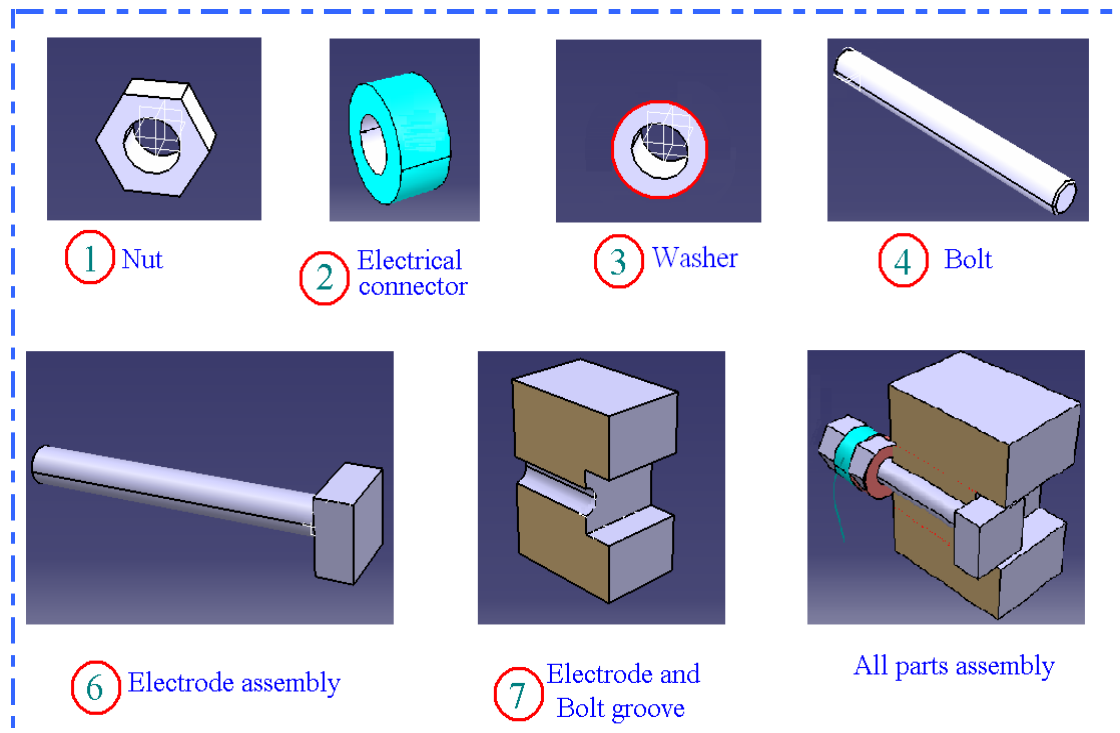
Figure 3-6: Electrode assembly

Figures 3-3, 3-4, 3-5, 3-6 and 3-8 show details of the electrodes and their positions in the ICC. Each array of eight electrodes was arranged on a cross-sectional plane of the pipe. As can be seen a hole is drilled through the tube wall and on the inner face a groove is cut to take the rectangular stainless steel electrode which had dimensions of 2.3mm circumferentially x 2mm longitudinally x 0.4mm radially. The electrodes had a long pin on the back that passed through the wall of the pipe enclosed in an insulating sleeve. The top of the pin was threaded and the copper wires carrying the excitation or measurement signals were attached to the pin, see Figure 3-6, using a washer and double nut arrangement which was used to mechanically hold the electrode firmly in place and to grip the wires. Figure 3-5 (a) shows an array without electrodes and Figure 3-5 (b) shows the array with electrodes in place.

Output data were simultaneously acquired from both electrode arrays A and B. After reconstruction these measurements give profiles of the conductivity distribution within the flow cross-section at the axial positions of the electrode arrays. The level of detail given by each profile is a function of the number and position of the active electrodes in each array.
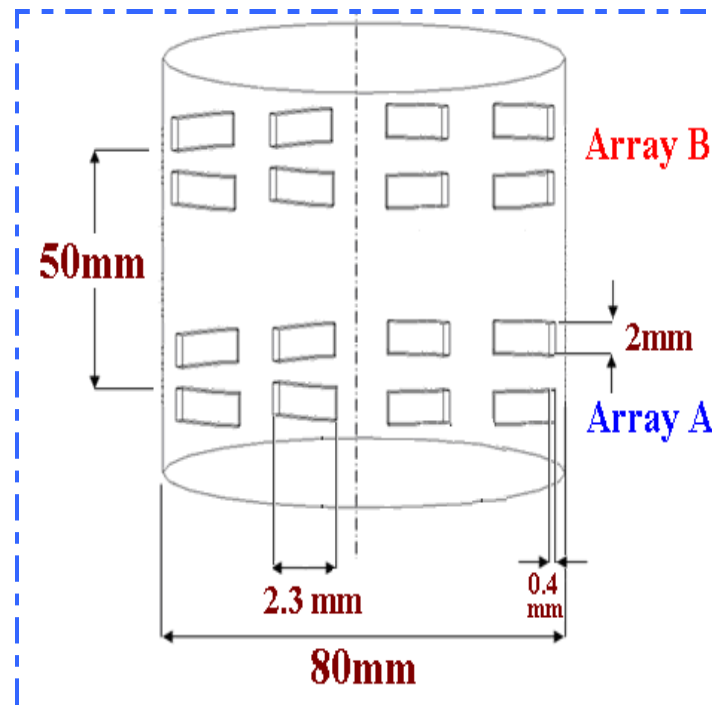
Figure 3-7: Arrangement of electrode array on the pipe
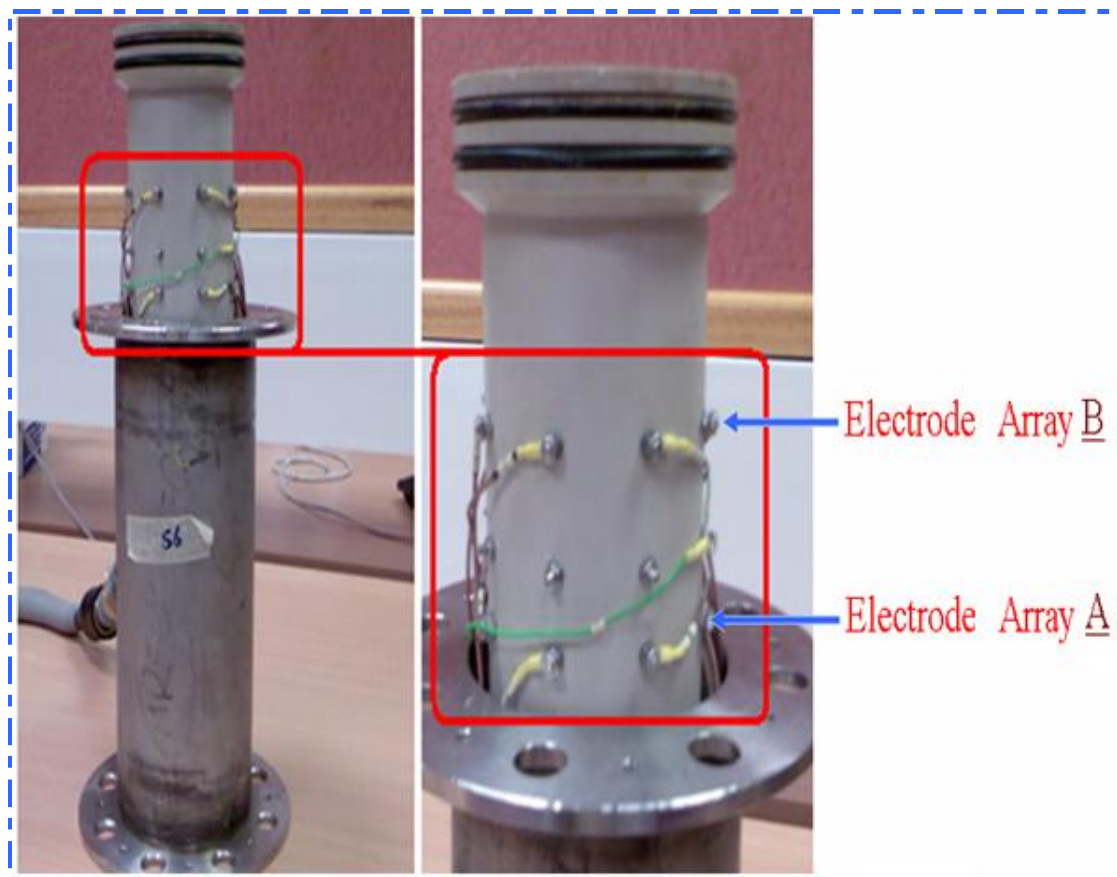
Figure 3-8: Photo of Impedance Cross-Correlation device

Note that, before its use the flow loop the ICC flow meter was subject to a series of bench tests, both static and dynamic. These are described in the next chapter.

3.6   Conductance circuit design

The schematic diagram, Figure 3-9, shows the main components of the circuit for measuring the conductance of the multiphase mixture at each the two electrode arrays. It is made up of six main stages. As channels for both arrays A and B are the same it is only necessary to describe one in detail.
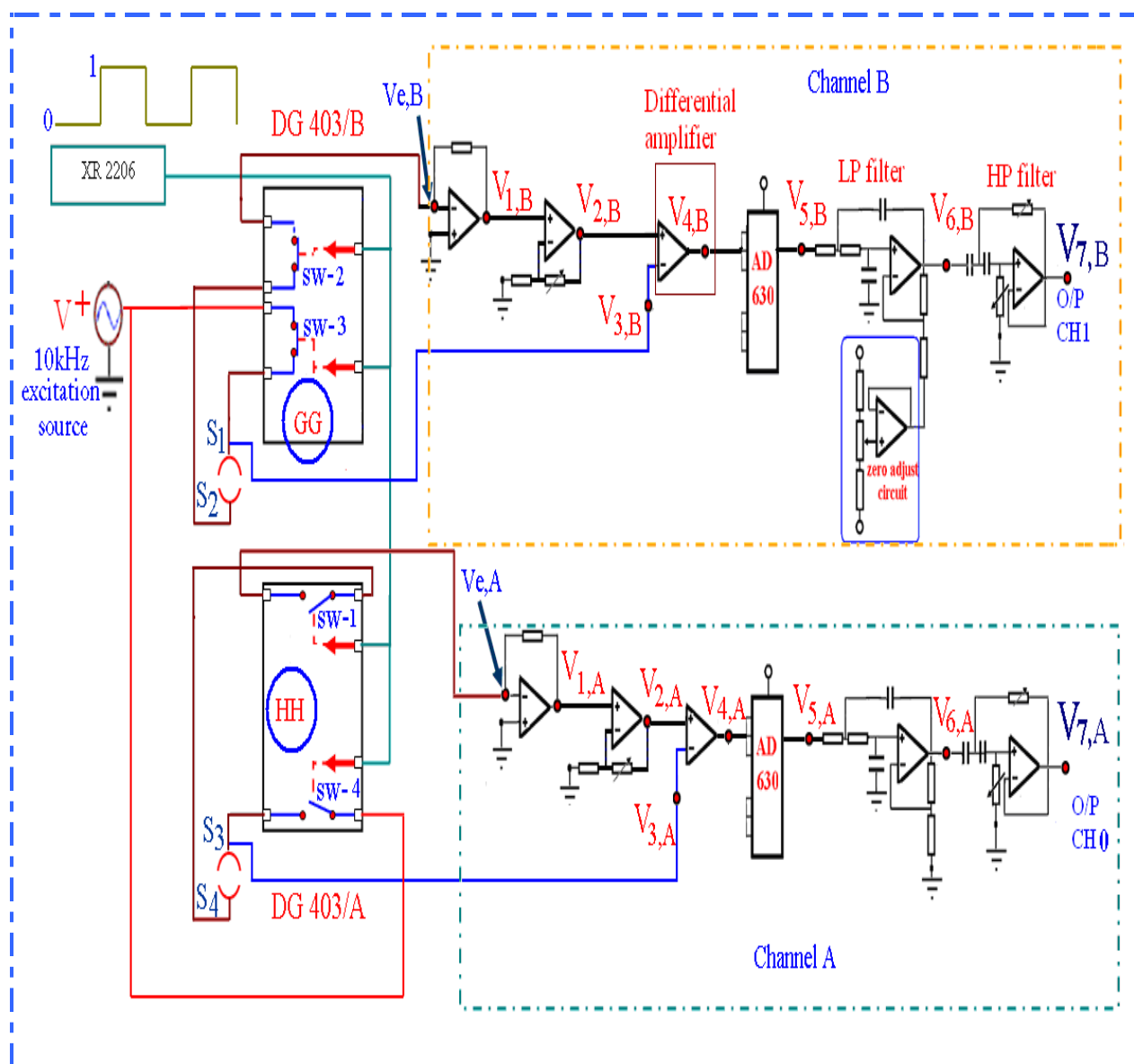
Figure 3-9: Schematic diagram of the conductance measurement circuit
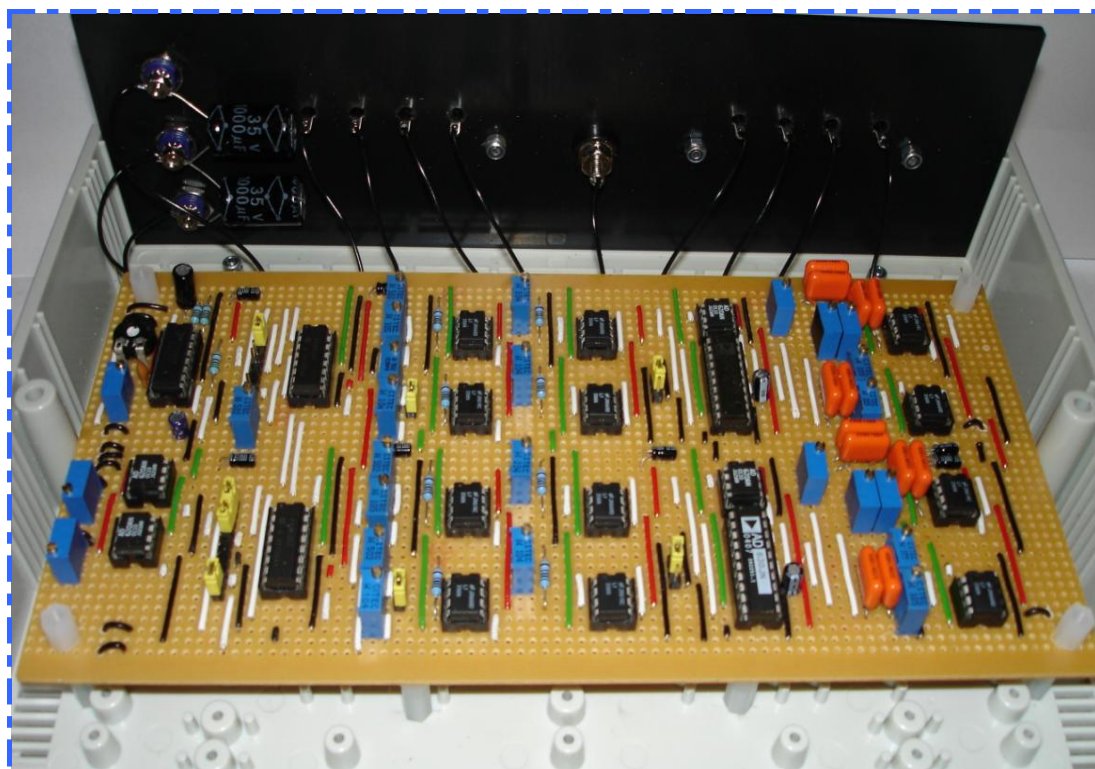
Figure 3-10: Photo of the conductance measurement circuit

In Figure 3-9, the XR-2206 is a monolithic function generator integrated circuit (working in a similar manner to a 555 timer) capable of producing high quality pulse waveforms of high-stability and accuracy. The output waveforms can be both amplitude and frequency modulated by an externally supplied voltage. Frequency of operation can be selected externally over a range of 0.01Hz to more than 1MHz. The excitation signal V^+ was a sine wave of frequency 10kHz of amplitude 2V peak to peak. The purpose of using the XR-2206 is to ensure that the V^+ electrodes in array A and the V^+ electrodes in array B were connected <u>alternately</u> to the excitation source. This meant that arrays A and B were never active at the same time and so cross-talk was prevented between the two arrays. The switching frequency was 100kHz and the excitation signal applied to the V^+ electrodes is 10 kHz and this resulted in the signals shown in Figure 3-11 being applied to the V^+ electrodes in arrays A and B. It can be seen from Figure 3-11 that when array A is active, array B is not , so cross-talk between the two arrays is eliminated.

The switching mechanism is controlled by the XR-2206 (see http://www.jaycar.com- (accessed 04/03/10) for details) which is a generator with two states: low (0) and high (1). Since the ICC has two electrode arrays A and B, there are two corresponding

electronic circuits, channels A and B. Each channel has an analogue switch DG-403 controlled by the XR-2206 (see http://www.intersil.com (access 04/03/10) for details) to enable switching between the two channels. Both channels are connected to an excitation signal (V^+), to channel A via switch 4 (SW-4) which is connected to electrodes in array A. The same signal is also connected to channel B via switch 3 (SW-3) which is connected to electrodes in array B.

For channel A, switches SW-1 and SW-4 in the DG 403/A are normally open but a high state signal from the XR-2206 will close both. This will result in the 10kHz measurement signal V^+ being connected to the electrode set S_{AS} (the set of electrodes in array A connected to V^+) and the measurement circuit being connected to the electrode set S_{AM} (the set of electrodes in array A connected to the input of inverting amplifier $V_{e,A}$) via the conductive fluid.

Channel B is completely isolated from channel A because of the sequencing of the signals by the XR-2206. For channel B, switches SW-2 and SW-3 in the DG 403/B are normally open but a low state signal from the XR-2206 will close both. This will result in the 10kHz measurement signal V^+ being connected to the electrode set S_{BS} (the set of electrodes in array B connected to V^+) and the measurement circuit being connected to the electrode set S_{BM} (the set of electrodes in array B connected to the input of inverting amplifier $V_{e,B}$) via the conductive fluid. At this stage channel A is completely isolated from channel B because of the opposite state of its switches.
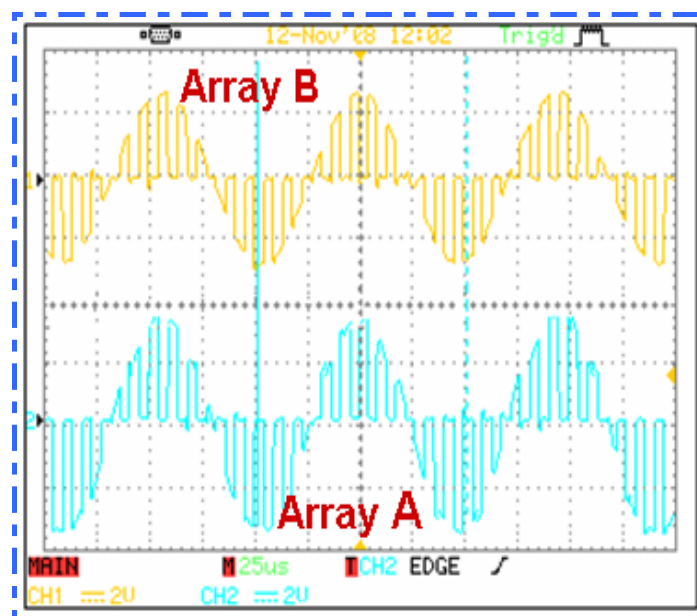
Figure 3-11: Excitation signals applied to the V^+ electrodes of each array

The differential amplifier takes the difference between its two input signals, V_2 and V_3, amplifies the difference, and outputs it as V_4, Figure 3-9. In the current work a technique has been developed to maximise the sensitivity of the system to changes in conductivities measured by arrays A and B. In the new technique the transmitted signal was treated using the initial signal fed into the system to isolate a signal that represents only the disturbance. To do this, a copy of the excitation signal is fed into the system ($V_{3,A}$) and is adjusted in level to match that of the measured signal being fed into the differential amplifier ($V_{4,A}$) when only water is present. The result is that signal $V_{4,A}$ will have an amplitude only when the measured conductivity changes from the conductivity of water and has zero (or very small) amplitude at other times. Similarly for array B. This allowed the use of a high gain amplifier without it getting saturated. Accordingly, a signal with high sensitivity and high amplitude that fully represents the disturbances was attained.

In each channel the voltage V_4 was fed into an AD630 integrated circuit which was configured as a precision rectifier, see Figure 3-9. The main effect of this stage was to perform full wave rectification on voltage V_4 and output the result as V_5. This signal, V_5, was then fed into a low pass Butterworth filter with cut-off frequency of 200Hz. This frequency was determined by iteration. Different frequencies were tried and the best result found. This removed the high frequency carrier wave content from the signal to give a DC output voltage, V_6. The voltage V_6 is proportional to V_4 as in Equation 3-2 where k is the gain of the circuit:

$$V_6 = kV_4 \qquad\qquad\qquad 3\text{-}2$$

The voltage V_6 was fed into a high pass filter to remove the DC components which are unnecessary for cross-correlation. The zero adjustment allows the DC offset of $V_{6,B}$ to be adjusted. During the setting-up procedure, the zero adjust was used to set the output voltage $V_{6,B}$ to zero when air only was present in the pipe and hence the mixture conductivity (σ_m) was effectively zero. For each array separately the output from the high pass filter was used to measure the fluctuating conductance between the V^+ set of electrodes and V_e, set of electrodes. $V_{7,A}$ and $V_{7,B}$ were the voltages used for cross-correlation velocity measurement ($V_{7,A}$ is also known as O/P CH-A and $V_{7,B}$ as O/P CH-B). $V_{6,B}$ was used to measure the mean conductance between S_1 and S_2.

S_1 represent an electrode, or set of electrodes in array B that is to be connected to the excitation source. S_2 is an electrode or set of electrodes in array B that is to be connected to the virtual earth of the inverting amplifier ($V_{e,B}$). S_3 represent an electrode, or set of electrodes in array A that is to be connected to the excitation source. S_4 is an electrode or set of electrodes in array A that is to be connected to the virtual earth of the inverting amplifier ($V_{e,A}$).

3.7 Electrode selection and assignment

This section shows how specific electrodes in array B (say) are connected together to form set S_1 which is connected to V^+, and how electrodes in array B (say) are connected together to form set S_2 which is connected together to $V_{e,B}$ (see Figure 3-9). It also describes how the remaining electrodes in array B are connected to ground. A similar arrangement was used for sets S_3 and S_4 for array A.

Consider array B: one group of electrodes is connected to S_1 and hence to V^+, another electrode group is connected to S_2 and hence to $V_{e,B}$. Another electrode group is connected to ground.

For the mth ($1 \leq m \leq 8$) electrode in array B, whether it is connected to S_1, S_2 or ground is determined using **three** analogue switches (denoted AA_m, BB_m and CC_m, see Figure 3-12). The input signals to AA_m, BB_m and CC_m which determine whether the electrode is connected to S_1, S_2 or ground, come from Q_{1-m}, Q_{2-m} and Q_{3-m} in latches L_1, L_2 and L_3 respectively (see Figure 3-12). In turn the outputs Q_{1-m}, Q_{2-m} and Q_{3-m} are set sequentially using one of **eight** electrode potential signal from the LABJACK data acquisition + control unit and **three** independent ''Latch enable'' signals from the LABJACK.

For array A: The principle of operation is the same as for array B, the only difference is that one electrode group is connected to S_3 and hence to V^+, the second electrode group is connected to S_4 and hence to $V_{e,A}$. Another electrode group is connected to ground.

For the mth ($1 \leq m \leq 8$) electrode in array A, whether it is connected to S_3, S_4 or ground is determined using **three** analogue switches (denoted DD_m, EE_m and FF_m, see

Figure 3-12). The input signals to DD_m, EE_m and FF_m which determine whether the electrode is connected to S_3, S_4 or ground, come from Q_{4-m}, Q_{5-m} and Q_{6-m} in latches L_1, L_2 and L_3 respectively (see Figure 3-12). In turn the output Q_{4-m}, Q_{5-m} and Q_{6-m} are set sequentially using one of **eight** electrode potential signal from the LABJACK data acquisition + control unit and **three** independent ''Latch enable'' signals from the LABJACK.

3.7.1 Electronic switching circuit for arrays A and B

The electronic circuit was designed to be able to select any electrodes from a given array (A or B) and connect them to excitation (V^+), measurement (V_e) or to earth (E) in the corresponding channel (A or B) of the conductance measurement circuit (see Figure 3.9).

Both array A and array B were used to determine the electrical impedance /conductivity of the multiphase flow, but when array A was active, array B was not, and vice versa. The excitation signal V^+ was applied to an electrode or set electrodes (S_3) in array A and the conductance was measured. The measured value would change with changes in the volume fraction of the dispersed phase. Then an exactly similar electrode arrangement would be activated in array B. The signals taken from the two arrays could then be cross-correlated to find the time it took for the solids to travel from one array to the next.

In Figure 3-12, the electrode selection circuit, there are eight main electronic components:

❖ The pulse generator, XR-2206 (see http://www.jaycar.com-(accessed 04/03/10) for details), which is used to switch between arrays A and B and can be seen in the top left hand corner.

❖ An analogue switch, AD403 (for more detail see for details http://www.intersil.com (accessed 04/03/10)), indicated as GG connects S_2 to the input $V_{e,B}$ of the inverting amplifier in channel B, also see Figure 3-9. In addition, the analogue switch GG connects S_1 to the excitation signal ($V+$).

❖ An analogue switch, AD403 (for more detail see http://www.intersil.com (accessed 04/03/10)), indicated as HH connects S_4 to the input $V_{e,A}$ of the inverting amplifier in channel A, also see Figure 3-9. Analogue switch HH also connected S_3 to the excitation signal (V^+).

❖ The six 74AC573 chips in Figure 3-12, are three latches, L_1 to L_3, for Array B and three latches, L_4 to L_6 for array A, (for more detail see http://www.datasheetcatalog.org (accessed 04/03/10)). Each latch is activated separately by **three** independent latch signals from the LABJACK data acquisition and control unit (see Figure 3-12).

❖ Three analogue switches, AA_m, BB_m and CC_m for each electrode in array B and DD_m, EE_m and FF_m for each electrode in array A, details of which are given in http://www.intersil.com (accessed 04/03/10).

It should be noted that Figure 3-12 shows only electrode 1 in array B, so analogue switches AA_1, BB_1 and CC_1 are shown connected for electrode 1 in array B. In fact, the **three** analogue switches AA_m, BB_m and CC_m can be set to connect to any of the mth electrodes in array B, as required. Similarly the **three** analogue switches DD_1, EE_2 and FF_3 can be connected for electrode 1 in array A. In fact, the three analogue switches DD_m, EE_m and FF_m can be set to connect to any of the mth electrodes in array A, as required. The electrode potential selection signals from the LABJACK are shown for electrode 1 in array A and array B. In fact LJ1 to LJ8 are used to select the potential for electrodes 1 to 8 respectively for both array A and array B.
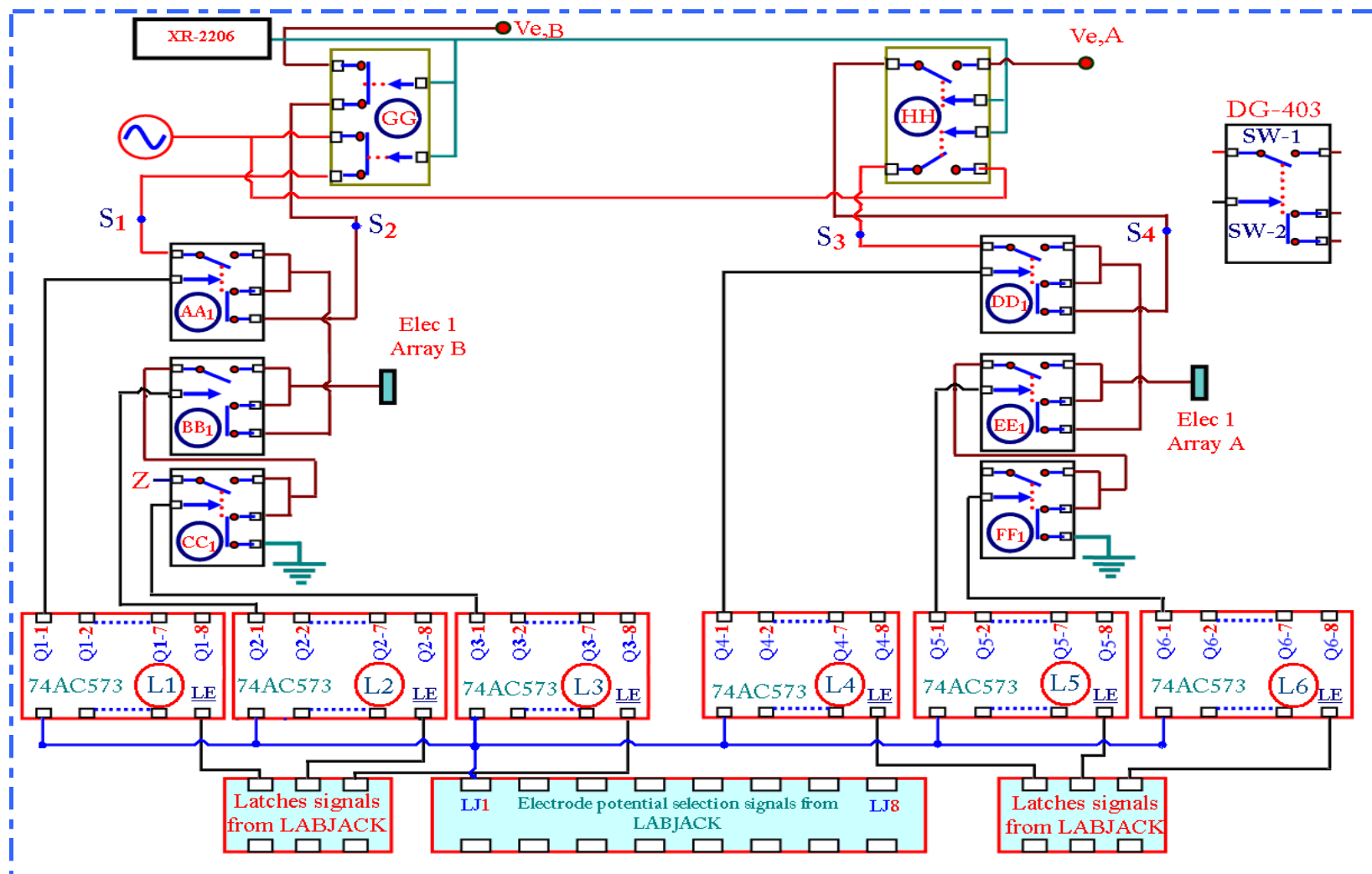
Figure 3-12: A schematic diagram of the electrode selection circuit (for electrode 1 for array A & B)

Figure 3-13: A photo of the electrode selection circuit for array A
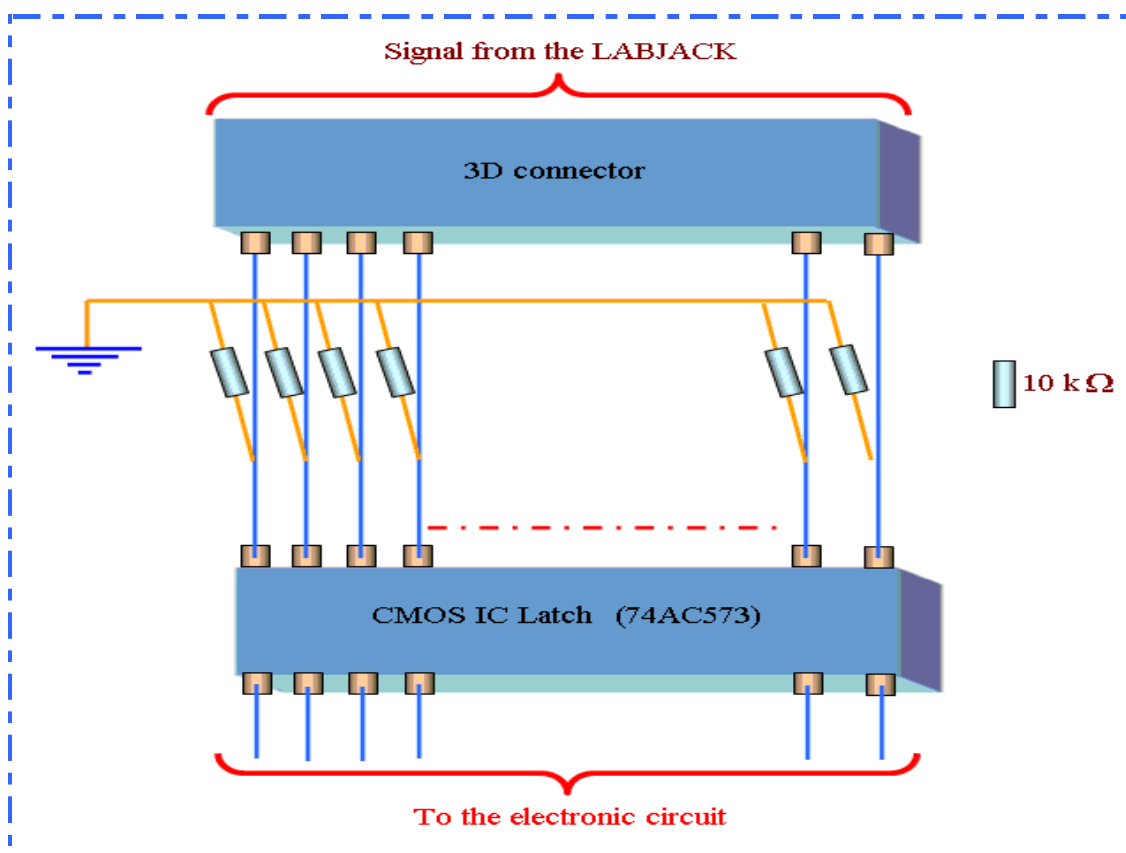
Figure 3-14: Block diagram of the experimental setup

3.7.2 Principle of operation

The circuit used a dedicated MATLAB code. A PC was used to communicate with the LABJACK to set the desired electrode configuration for both arrays A and B. Fourteen signals were sent from the LABJACK to both arrays. Note that for array A, **three** 74AC573 chips were required and each pin of this chip is fed with eight defined signals and one latch signal. A similar arrangement was in place for array B. The latch output response to the received signal depended upon the state of the Latch Enabled input (LE) or pin 11. Each electrode in the ICC meter has an input from each of the three latches. The selection of the electrode configurations is operated by the analogue switches DG-403 (see Figure 3-12). The output of this circuit is connected to the conductance circuit (see Figure 3-9) which was discussed in Section 3.6. The mechanism can be summarised as follows:

For Array B

❖ 8 bits for Latch L_1 to set Q_{1-m} (for m=1 to 8). Then LE bit is used to enable L_1.

❖ 8 bits for Latch L_2 to set Q_{2-m} (for m=1 to 8). Then LE bit is used to enable L_2.

❖ 8 bits for Latch L_3 to set Q_{3-m} (for m=1 to 8). Then LE bit is used to enable L_3.

For Array A

❖ 8 bits for Latch L_4 to set Q_{4-m} (for m=1 to 8). Then LE bit is used to enable L_4.

❖ 8 bits for Latch L_5 to set Q_{5-m} (for m=1 to 8). Then LE bit is used to enable L_5.

❖ 8 bits for Latch L_6 to set Q_{6-m} (for m=1 to 8). Then LE bit is used to enable L_6.

Note that in the present study, if the mth electrode in array B was set to a given potential (V^+, V_e or E) then the corresponding electrode in array A was also set to the same potential. Consequently the electrode potential signal (LJ_1 to LJ_8, see Figure 3-12) from the LABJACK could be used for both arrays A and B.

As mentioned earlier, there are four states to be chosen from to define the electrode status. Tables 3-2 and 3-3 shows the general truth table of the selection of the four states for array B and array A respectively.

Table 3-2: Truth table for mth electrode in array B.

Electrode status	$Q_{1\text{-}m}$	$Q_{2\text{-}m}$	$Q_{3\text{-}m}$
Excitation electrode (V$^+$)	H	L	X
Virtual earth measurement electrode(V$_e$)	L	L	X
Earth electrode (E)	X	H	L
High impedance (Z)	X	H	H

Table 3-3: Truth table for mth electrode in array A.

Electrode status	$Q_{4\text{-}m}$	$Q_{5\text{-}m}$	$Q_{6\text{-}m}$
Excitation electrode (V$^+$)	H	L	X
Virtual earth measurement electrode(V$_e$)	L	L	X
Earth electrode (E)	X	H	L
High impedance (Z)	X	H	H

where: H is state High (1), L is state Low (0) and X is either (0 or 1). m is the electrode number (m=1 to 8).

It is now shown how electrode 1 in each array can be connected to one of three potentials (V$^+$, V$_e$ or E) see Figure 3-12.

For Array B, taking electrode 1 as an example, to set this electrode to excitation (V$^+$), according to the truth table (see Table 3-2), Q$_{1\text{-}1}$ in L1 is set High and Q$_{2\text{-}1}$ in L2 is set Low. This will activate SW-1 to close and SW-2 to open from switch AA1 (see Figure 3-12). This will result in setting electrode 1 to excitation since SW-1 is opened and SW-2 is closed in switch BB1 because Q$_{2\text{-}1}$ in L2 is set Low.

To set the same electrode to virtual earth (measurement, V$_e$), both Q$_{1\text{-}1}$ in L1 and Q$_{2\text{-}1}$ in L2 are set Low (see Table 3-2). This will result in SW-1 and SW-2 from switch AA1 remaining in their normal state (see Figure 3-12). This will result in setting electrode 1 to virtual earth since SW-1 is opened, and SW-2 is closed in switch BB1 because Q$_{2\text{-}1}$ in L2 is set Low.

To set the same electrode to earth (E), according to the truth table (Table 3-2) Q_{2-1} in L2 is set High and Q_{3-1} in L3 is set Low. This will activate SW-1 to close and SW-2 to open from switch BB1. This will result in setting electrode 1 to earth since SW-1 is opened, and SW-2 is closed in switch CC1 because Q_{3-1} in L3 is set Low.

To set the same electrode to high impedance (Z), both Q_{2-1} in L2 and Q_{3-1} in L3 are set High. This will activate SW-1 to close and SW-2 to open from switch BB1. This will result in setting electrode 1 to high impedance since SW-1 is closed and SW-2 is opened in switch CC1 because Q_{3-1} in L3 is set High. Note that, the high impedance (Z) state is usually not used in the current investigation. However, the author has used it as an indication of an unconnected (not being used) electrode.

For Array A, taking electrode 1 as an example, to set this electrode to excitation (V^+), according to the truth table (see Table 3-3), Q_{4-1} in L4 is set High and Q_{5-1} in L5 is set Low. This will activate SW-1 to close and SW-2 to open from switch DD1 (see Figure 3-12). This will result in setting electrode 1 to excitation since SW-1 is opened and SW-2 is closed in switch EE because Q_{5-1} in L5 is set Low.

To set the same electrode to virtual earth (measurement, V_e), both Q_{4-1} in L4 and Q_{5-1} in L5 are set Low (see Table 3-3). This will result in SW-1 and SW-2 from switch DD1 remaining in their normal state (see Figure 3-12). This will result in setting electrode 1 to virtual earth since SW-1 is opened and SW-2 is closed in switch EE1 because Q_{5-1} in L5 is set Low.

To set the same electrode to earth (E), according to the truth table (see Table 3-3) Q_{5-1} in L5 is set High and Q_{6-1} in L6 is set Low. This will activate SW-1 to close and SW-2 to open from switch EE1. This will result in setting electrode 1 to earth since SW-1 is opened and SW-2 is closed in switch FF1 because Q_{6-1} in L6 is set Low.

To set the same electrode to high impedance (Z), both Q_{5-1} in L5 and Q_{6-1} in L6 are set High. This will activate SW-1 to close and SW-2 to open from switch EE1. This will result in setting electrode 1 to high impedance since SW-1 is closed and SW-2 is opened in switch FF1 because Q_{6-1} in L6 is set High. Note that, the high impedance

(Z) state is usually not used in the current investigation. However, the author has used it as an indication of an unconnected (not being used) electrode.

An array of LEDs was used in the circuit. Each column of LEDs represented four states (Excitation, Virtual earth measurement, Earth and High impedance) of each electrode (Figure 3-13). Since there were two electrode arrays, a similar argument applies to each one in terms of circuit design and operation.

3.8   Data acquisition and control system, and data processing

The data acquisition and control system is computer based. All controls were automated using MATLAB software, Figure 3-15.
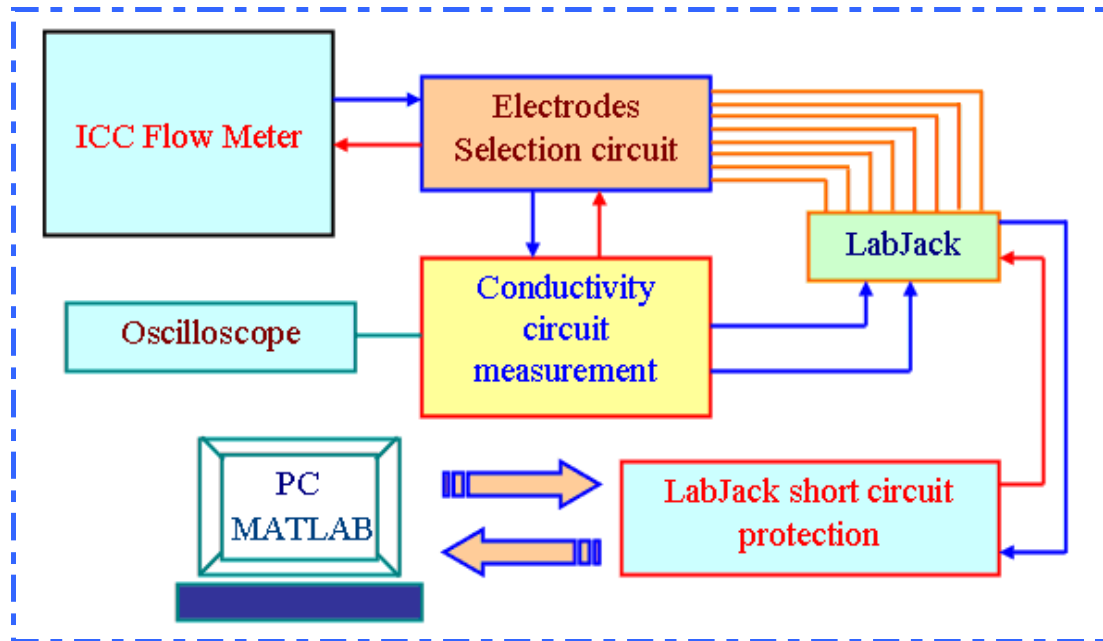
Figure 3-15: Block diagram of the experimental setup

The LABJACK has eight analogue input (AI) channels (see Figure 3-16). At this stage only two channels (AI0 and AI1) are needed to read the voltage signals from $V_{7,A}$ and $V_{7,B}$ (see Figure 3-9). As stated earlier $V_{7,A}$ and $V_{7,B}$ are the signals used for cross correlation but $V_{6,B}$ is used for volume fraction measurement (see Section 3.10). The D-connector of the LABJACK was used to feed the digital electrode selection signals from the PC. These signals were generated using MATLAB code developed by the author (see Appendix Code-1). The reason for using the D-connector instead of the normal output channels (AO) is because the number of channels is not enough to cover 14 digitals electrode selection signals

140

Data were collected at a sampling rate of 1kHz per channel, and the LABJACK data acquisition card was used to record the data. The Analogue Input function as it appears in MATLAB reads a specified number of scans (up to 4096) at a specified scan rate (up to 8192 Hz) from the 0, 1 Analogue Inputs. The actual scan rate was equivalent to 1kHz per channel. First, data is acquired and stored in the LABJACK's 4096 sample RAM buffer. Then, the data was transferred to the PC. The Analogue Input MATLAB function has only 60 seconds of run time. To compensate for this limitation, each data collection was taken ten times then averaged using ensemble averaging.
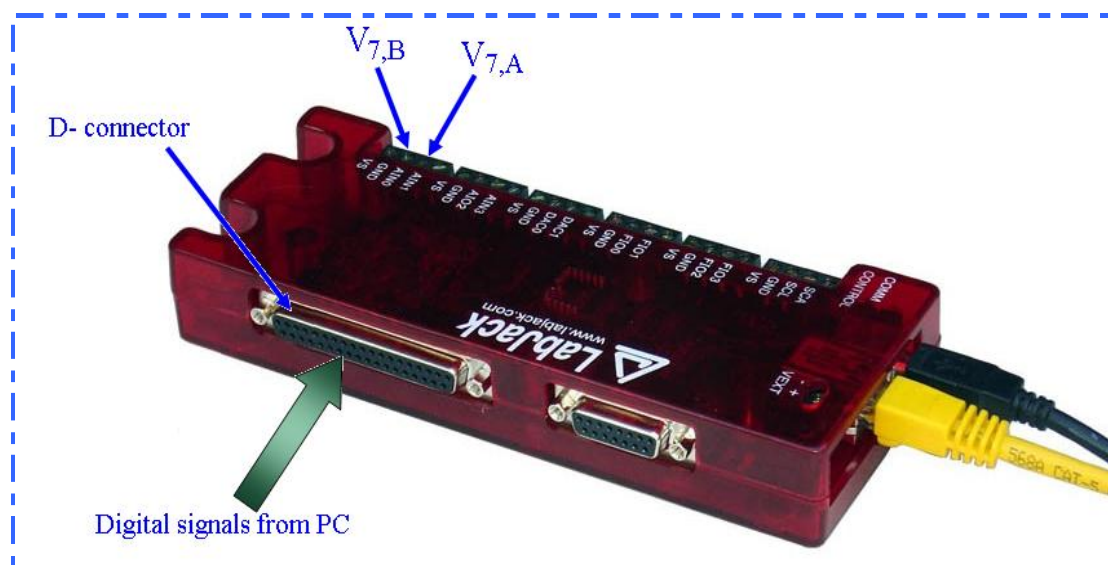
Figure 3-16: Analogue to Digital converter (LABJACK) (http://labjack.com/u12 accessed 02/01/07)

3.8.1 LABJACK short-circuit protection

LABJACK digital outputs have no short-circuit protection. In order to protect the LABJACK outputs from short-circuit it is recommended by the LABJACK company to add a 1.5kΩ serial resistor to the output. However, since the digital outputs operate at 5V a 1.5 k resistor would restrict the maximum digital output current to

5V/1500Ω= 0.0033 A = 3.3 mA

But the maximum current per channel is 20 mA, so a decision was made to use only a 500 ohm resistor and restrict the maximum current per channel to 10 mA. These resistors were installed inside the DB25 plug that connects to the LABJACK (see

Figure 3-14). This decision also allows for the LABJACK limitation of a maximum total current of 200 mA.

3.8.2 Programming the latches

A MATLAB code was created by the author for automatic electrode selection. The code, (see Appendix Code-2,) operates when the "SetRing1" function (controls Array A) or "SetRing2" function (controls Array B) (see Appendix Code-3) are used. The parameters of these two functions are given by:

SetRing1(a,b,c,d,e,f,g,h)
SetRing2(a,b,c,d,e,f,g,h)

where:

a　　　　status of electrode 1

b　　　　status of electrode 2

c　　　　status of electrode 3

d　　　　status of electrode 4

e　　　　status of electrode 5

f　　　　status of electrode 6

g　　　　status of electrode 7

h　　　　status of electrode 8

The status, which can be confirmed by the LED array (see Figure 3-17), is a one digit number as follows:

1　　　　Connected to excitation signal (V^+)

2　　　　Connected to virtual earth measurement (V_e)

3　　　　Connected to earth (E)

4　　　　Not connected i.e. high impedance (Z).

3.8.3 Circuit validation

First, the MATLAB code was set to any electrode configuration, for example, SetRing1 (2, 2, 2, 2, 1, 1, 1, 1). This means that electrodes 1-4 in array A are set as virtual earth electrodes and electrodes 5-8 as excitation electrodes. The first four

electrodes have green LEDs switched on and the other four electrodes have red LEDs set switched on simultaneously.

Figure 3-17: LED circuit

This step was repeated for all the different electrode configurations just to check the signals sent from MATLAB via the LABJACK were lighting the correct LEDs.

Next the ICC flow meter was connected to the switching circuit as shown as in Figure 3-18. This test was to test the continuity of the switching circuit i.e. to make sure that the signal going to each electrode is really the signal from the MATLAB sent through the LABJACK. To do this, a volt-meter was connected between the excitation output signal of the switching circuit and the electrodes in the ICC meter. For example, SetRing1 (1,2,2,2,2,2,2,2) sets electrode 1 in array A as excitation and all other electrodes in array A to virtual earth ($V_{e,A}$). The volt-meter was simply used to show continuity of connection between the excitation output and electrode 1. In every case the resistance measured was within the range 50.3 to 50.5 ohm. The resistance between the excitation output and all other electrodes in array A was essentially infinite. This was then repeated, in turn, for all the other electrodes of array A. The same procedure was followed for array B.

3.9   Measurement of solids velocity

In order to measure the velocity of a solid particle passing through the ICC flow meter the fluctuating output voltage, $V_{7,B}$ between S_1 and S_2 is taken as being the output from array B. Similarly, the fluctuating output voltage, $V_{7,A}$ between S_3 and S_4 is taken as being the output from array A. The conductance between the array A electrodes and between the array B of electrodes vary due to the passage of the non

conducting solids particles and these variations in conductance were measured using the two-channel circuit described in section 3.6 and shown in Figure 3-9. The two signals were then cross-correlated using a program written in MATLAB, and an estimate of the solids velocity, u_S , was made, see Figure 3-18.
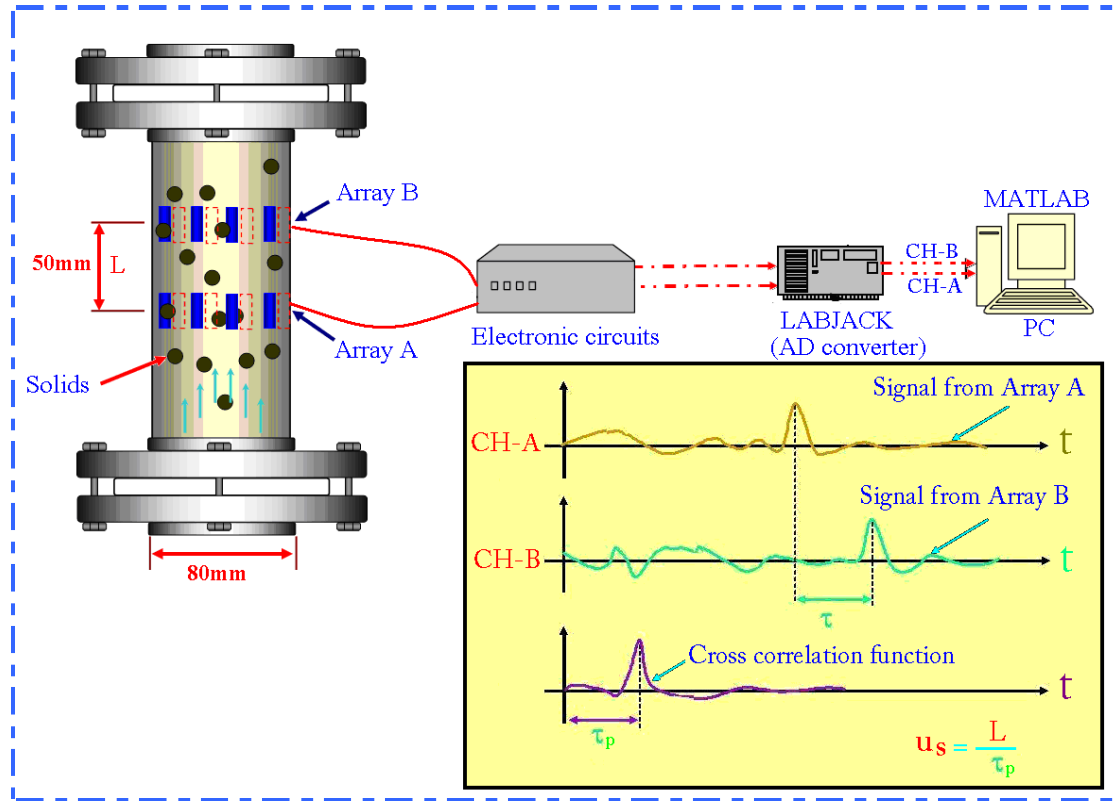
Figure 3-18: Schematic of the cross-correlation flow meter and instrumentation

Figure 3-18 shows a block diagram of the set up of the ICC flow meter. As can be seen, the correlation flow meter consists of two electrode arrays and is used to obtain the mean velocity of the solids between arrays A and B in that part of the flow cross-section preferentially interrogated by the electrode selection for arrays A and B (see Chapter 5) . The outputs from the arrays were fed to the electronic circuits and these outputs were fed to the analogue to digital converter (LABJACK). Both signals were then cross-correlated using software written in MATLAB listed in Appendix Code-5.

3.10   Solids volume fraction measurement

As mentioned in Section 2.9 the local solids volume fraction measured by the ICC meter, α_S , is given by Maxwell's relationship which, see Equation (3-1), can be re-arranged as

$$2\sigma_m - 2\sigma_w = -\alpha_s(\sigma_m + \sigma_w) \tag{3-3}$$

And

$$\alpha_s = \frac{1 - \dfrac{\sigma_m}{\sigma_w}}{0.5\left(1 + \dfrac{\sigma_m}{\sigma_w}\right)} \tag{3-4}$$

For a general understanding of the calculation theory for obtaining α_s the following equations (3-5 to 3-7) can be summarised in general form. This will be followed by a detailed description of calculating α_s involved in this work.

The DC output voltage $V_{6,B}$ (see Figure 3-9) is proportional to the gain of the system so from Equation 3-6 the constant, K, can be found.

$$V_{6,B,w} = K\sigma_w \tag{3-5}$$

where: $V_{6,B,w}$ is the output voltage from array B when water only is present in the flow, so;

$$K = \frac{V_{6,B,w}}{\sigma_w} \tag{3-6}$$

where: σ_w is the water conductivity.

Then, the conductivity of the mixture σ_m can be calculated from the output voltage measured for the two-phase flow, using the equation;

$$V_{6,B,m} = K\sigma_m \tag{3-7}$$

where: $V_{6,B,m}$ is the output voltage when both water and solids are flowing obtained from array B.

Having found K and measured $V_{6,B,m}$, σ_m, can be found. Then by substituting, σ_m and σ_w into Equation 3-5, the solids volume fraction α_S can be calculated. The value of the constant 'K' was found to vary slightly for the eight rotational positions a given configuration. Consequently, 'K' was written as $K_{B,I,n}$ corresponding to the value of 'K' for the nth rotational position of the Ith configuration. The measured value of 'K'(for Config-I,II and III) $K_{B,I}$, $K_{B,II}$ and $K_{B,III}$ respectively. Where $K_{B,I}$, $K_{B,II}$ and $K_{B,III}$ are obtained from:

$$K_{B,I} = \frac{1}{8} \sum_{n=1}^{\infty} K_{B,I,n} \qquad\qquad 3\text{-}8$$

$$K_{B,II} = \frac{1}{8} \sum_{n=1}^{\infty} K_{B,II,n} \qquad\qquad 3\text{-}9$$

$$K_{B,III} = \frac{1}{8} \sum_{n=1}^{\infty} K_{B,III,n} \qquad\qquad 3\text{-}10$$

The values of $K_{B,I}$, $K_{B,II}$ and $K_{B,III}$ are given in Table 3-4

Table 3-4: Definitions and measured values of K for each electrode configuration (Config-I,II and III)

Constant	Definition	Measured value of K
$K_{B,I}$	Config-I Array B	0.0526
$K_{B,II}$	Config-II Array B	0.0592
$K_{B,III}$	Config-III Array B	0.0667

From Equations 3-5 and 3-7 we have that for the nth rotational position of the Ith configuration

$$V_{6,B,w} = K_{B,I,n}\, \sigma_w \qquad\qquad\qquad 3\text{-}11$$

and

$$V_{6,B,m} = K_{B,I,n}\, \sigma_m \qquad\qquad\qquad 3\text{-}12$$

and so,

$$\frac{V_{6,B,m}}{V_{6,B,w}} = \frac{\sigma_m}{\sigma_w} \qquad\qquad\qquad 3\text{-}13$$

$V_{6,B,m}$ is measured (for all rotational positions of a given configuration) for a given set of experimental conditions and $V_{6,B,w}$ is a measured (for all rotational positions of a given configuration) for water only (i.e. the test section is full of "water only") periodically during a give series of test. The quantity $\dfrac{\sigma_m}{\sigma_w}$ obtained for a given rotational position of a given electrode configuration from Equation 3-13 could there be subtitled into Equation 3-4 to find α_S. Because $V_{6,B,w}$ was measured regularly throughout a given series of tests, the measured values of α_S were unaffected by changes in the water conductivity σ_w which have arises due to changes in the water salinity or changes in the water temperature.

Chapter 4 IMPEDANCE CROSS-CORRELATION MODELLING, SIMULATION AND ANALYSIS

In this chapter, a model for a single array of 8 electrodes was developed using a finite element analysis package (COMSOL). The chapter begins by giving the aim and objectives for carrying out this modelling. Then the modelling procedure is presented as is the sensitivity distribution in the flow cross-section for different electrode configurations. The sensitivity distribution and ''Centre of Action'' for all electrode configurations that have been used in this investigation are described.

4.1   Introduction

In order to investigate the characteristics of the impedance cross correlation flow meter (ICC) and how it functions in different flow regimes, it's important to model its performance. This software package chosen for this modeling work is ***FEMLAB*** (COMSOL).

4.2   Modelling aims and objectives:

The main aim of the work presented in this chapter is to model just one of the two arrays of 8-electrodes. The model was produced using two dimensional finite element analysis. This model was used to calculate a sensitivity distribution for different electrode configurations. This aim was achieved by meeting the following objectives:

- ❖ Carrying out a review of the finite element software COMSOL to become familiar with it.

- ❖ To model a single array of 8-electrodes.

- ❖ To investigate which electrode configurations interrogated deepest into the flow cross-section.

- ❖ To measure the sensitivity distribution for given electrode configurations (see Tables 4-2, 4-3 and 4-4).

- ❖ To calculate a Centre of Action (CoA) for each electrode configuration from the sensitivity distribution results. The CoA is discussed in Section 4.9 and its position defined by Equations 4.5 and 4.6.

4.3   FEMLAB software package

Finite Element Method Laboratory (FEMLAB) is a computer software package based on MATLAB that is used for solving various types of Partial Differential Equations (PDEs) (http://www.saw.uwaterloo.ca/femlab (accessed 04/03/10)). In 2005, the FEMLAB software was re-named COMSOL Multiphysics in its later versions, after Version 3.1 (the version used in this project to carry out the ICC flow meter investigation).

The COMSOL Multiphysics package was used. This commercial software package is designed to solve systems of coupled two and three-dimensional PDEs. It can model physical phenomena over a wide range of applications including electromagnetics. Using finite element methods it can easily be set up to model complex problems that cannot readily be solved using analytical techniques. This project used the AC/DC module which can model electrostatic, magnetostatic, and electromagnetic phenomena including the performance of capacitors, inductors, even micro-sensors, and solve for the electromagnetic and electrostatic fields in devices that include anisotropic dielectrics and maeterials with different electric permittivities and/or magnetic permeabilities. It allows the boundary conditions (and mesh parameters) to be entered by the researcher via a graphics interface. The sub-module of particular interest here is the Conductive Media (DC) module which contains the necessary material on electrostatics and conductive media, see Figure 4-1.
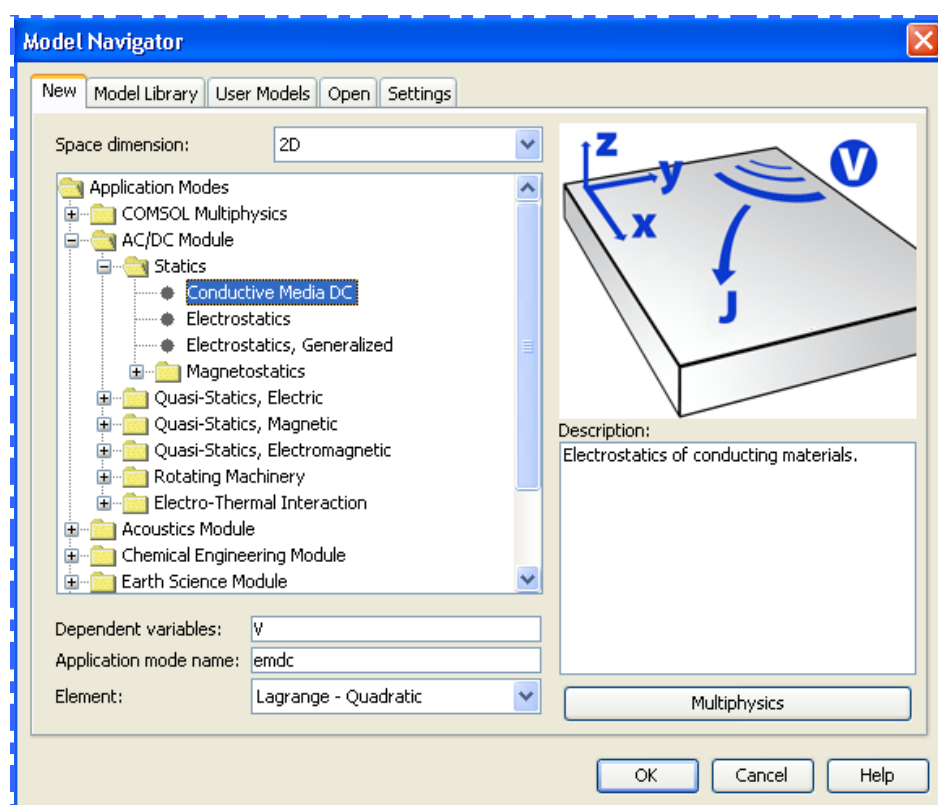
Figure 4-1: FEMLAB modules[http://www.saw.uwaterloo.ca/femlab , accessed on 04/03/10)]

The typical modelling steps of FEMLAB are (http://www.saw.uwaterloo.ca/femlab (accessed 04/03/10):

I. **Defining the geometry:** Here, the model is input as a drawing according to specified dimensions and scales. To achieve this, coordinate axes are defined and a grid is established.

II. **Defining the physics:** Here the relevant equations and boundary conditions are defined. Each element is input and specified individually. Then the model tests the elements for compatability. If any elements are not compatible an error message will appear.

III. **Mesh specification:** The initial parameters of the mesh to be used for the solution to the PDEs are input quite simply by clicking on the mesh button. A refine button may be used to adjust mesh size until it is sufficiently fine. This step will, largely, be a balance between how "fast" is the computer and how complicated is the model. The more complicated the model, the smaller the mesh size, the greater the number of steps required for an acceptable the solution, the higher the computation rate needed.

IV. **Computation:** This requires the solution of the well-known Laplace equation:

$$\nabla \cdot \left(\sigma \nabla \varphi \right) = 0,$$

This equation has been solved many times for numerous boundary conditions and step II defines those applicable here. The COMSOL Multiphysics package then sets up the corresponding electromagnetic equations and energy balances and runs through the required number of steps to obtain the solution(s) of the PDEs for the system entered.

V. **Post-processing:** Selection from the large number of graphical routines in the post-processing menu to obtain the most useful and user friendly form of the results of the computations.

From the above steps we can define a simple and basic flowchart of the computation sequence of FEMLAB, see Figure 4-2.
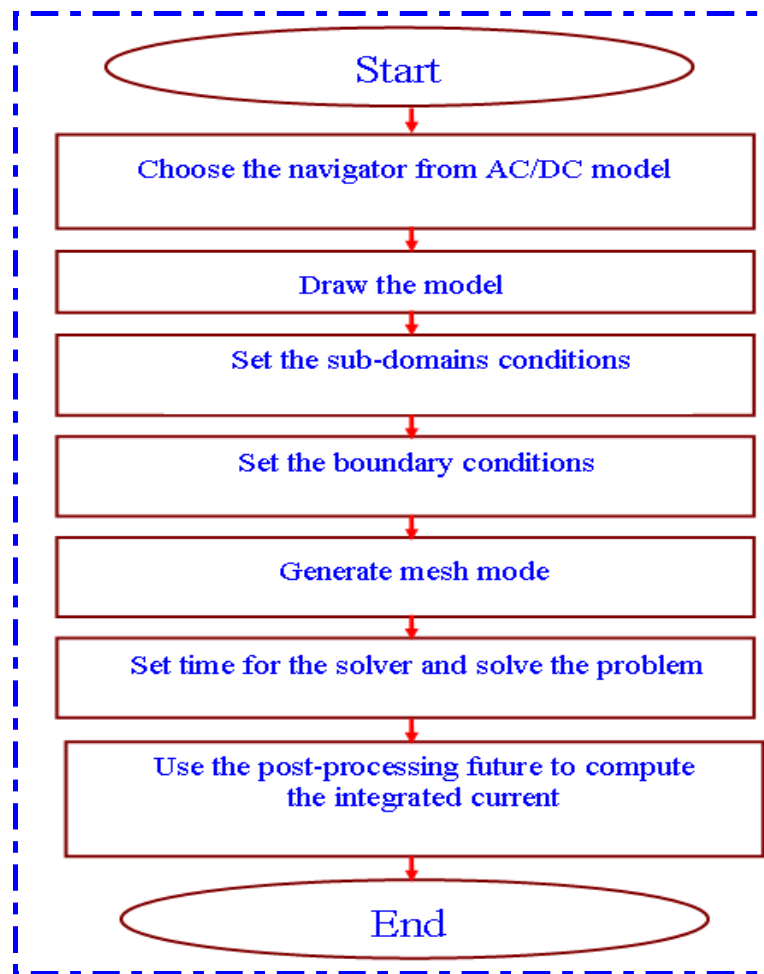
Figure 4-2: FEMLAB flowchart

4.4   Modelling steps

4.4.1 Geometrical design set up

The aim of designing the COMSOL computational model of the flow meter is to calculate the total current through the measurement electrodes (virtual earth electrodes, V_e) of the ICC device. The field sensitivity at a particular location in the flow cross-section (for a given electrode configuration) to the presence of a non-conducting particle, can be measured by the change in the total current through the virtual earth electrodes brought about by the presence of that particle at that particular point. (Compared to the total current through the V_e electrodes when no particles are present in the flow cross-section). Sensitivity variations in the flow cross-section can be tested for by inserting a simulated nylon rod into a simulation of the ICC flow meter at different positions in the flow cross-section.

152

The model was set in a two dimensional modelling (2D) state. The 2D model was preferred to the 3D model in this study because:

- ❖ Fewer mesh elements are involved in the solving process and hence convergence is quicker.

- ❖ 2D takes less computational time than the 3D model.

- ❖ 2D allows investigating more meshing options.

By following the modelling steps below a computational model for the ICC flow meter was achieved. In section 4.5, a description is given of how spatial variations in the sensitivity of the sensing fields associated with different electrode configurations are calculated.

1st step

The ICC design process commenced by drawing a circle on the 2D Gemo1 sheet of FEMLAB. This was done using the draw menu in FEMLAB. By clicking on the ''circle'' button a window appeared allowing the desired position and diameter (80mm) of the circle to be entered, see Figure 4.3. All eight electrode positions in the array and the electrode dimensions (2.3 x 0.4mm) were also entered.
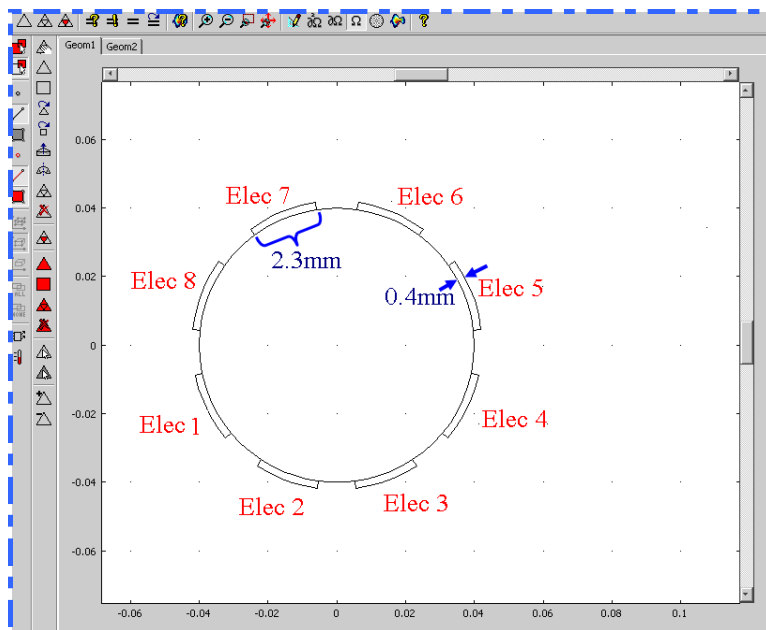
Figure 4-3: 2D single array, 8-electrode sensor

2nd step

There are two sets of data which must be inserted at this stage. The sub-domain boundary conditions must be set for the 8 electrodes (Figure 4-4) and the conducting media (Figure 4-5). This includes: Stainless-steel electrical conductivity = 4.032 (S/m), electrode thickness = 0.4mm and water electrical conductivity = 0.01S/m.

In a dual array system the electrodes are directly in contact with the material inside the vessel. Different models may be used to describe the dual array system based on the required complexity and it might, for example, be necessary to include such phenomena as contact impedance between the electrode and the process material in the equations (http://www.saw.uwaterloo.ca/femlab (accessed 04/03/10). The electrical field distribution associated with the system is determined by solving the Laplace equation (http://www.saw.uwaterloo.ca/femlab (accessed 04/03/10).

$$\nabla \cdot (\sigma \nabla \varphi) = 0, \qquad\qquad 4\text{-}1$$

where: φ is the local electrical potential and σ is the local electrical conductivity.
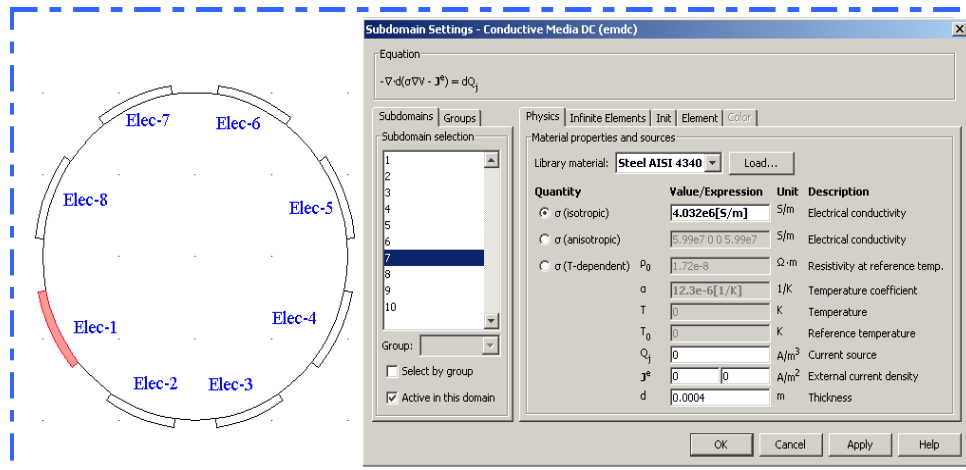
Figure 4-4: Sub-domain conditions for the 8 electrodes
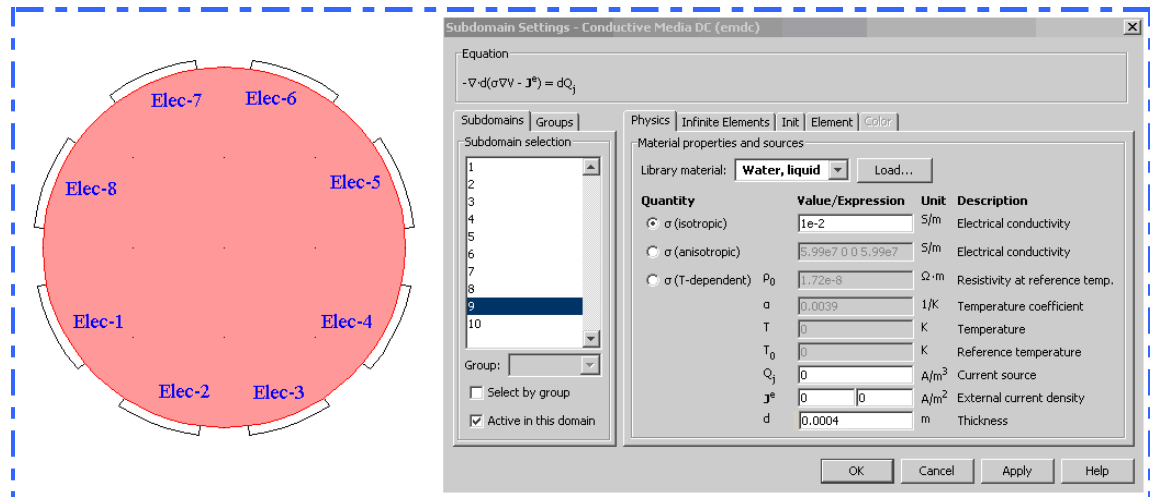
Figure 4-5: Sub-domain conditions for the 8 electrodes

4.4.2 Simulation process

Before the model begins simulation it must be "meshed" by clicking the mesh button. When the mesh operation is run successfully, the model will be ready to "solve" the given problem. This process is begun by pressing the solve button as shown in Figure 4-6, below.
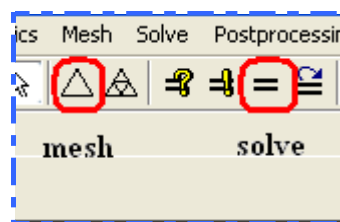
Figure 4-6: Mesh and Solve commands

To get a mesh that satisfactorily balances accuracy and computing resources depends on the problem description, the geometry and what the solution is for. The general approach is to use a technique known as mesh convergence. Here the mesh is incrementally refined and the results obtained are compared with the results obtained for the previous mesh. If the change is greater than a specified percentage value the process is repeated. This technique can fail if the initial mesh size is set too large or too fine.

The mesh size can be adjusted using the mesh menu in FEMLAB. In this particular case, setting the mesh to 7147 elements caused the computation process to fail due to the limited available computer memory. The mesh chosen was "fine" (7040 elements) and this took approximately 3 minutes to arrive at a solution. The FE mesh

is shown in Figure 4-7 together with the numbering of the electrodes in the array.
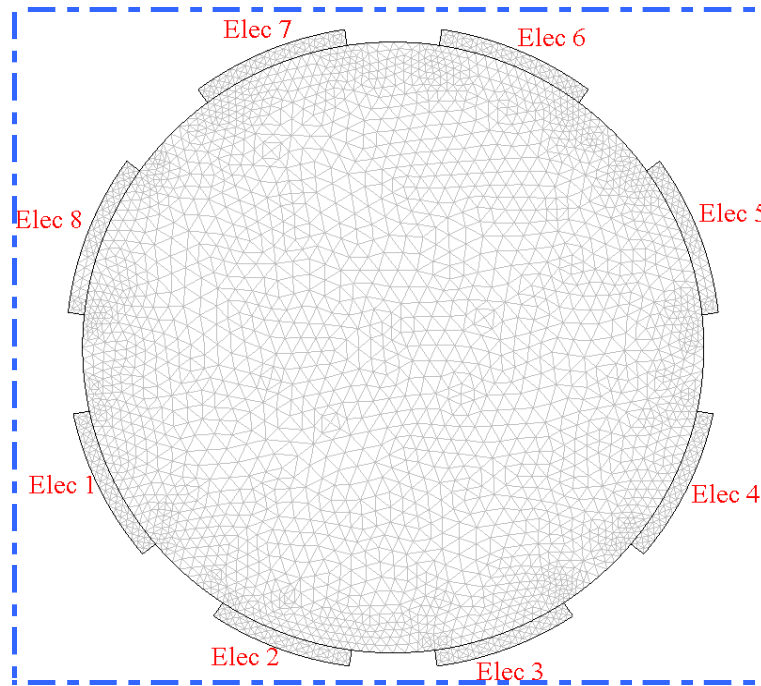
Figure 4-7: Computer display of co-ordinates and electrodes showing finite element mesh

In the following Sections (4.5 and 4.6) the sensitivity distribution is investigated using a simulated nylon rod of external diameter 15mm. The results of this simulation will be compared with the results of corresponding experimental bench tests using a real system and a real nylon rod (see Chapter 5). The simulation results are also used to calculate the position of the CoA of a given electrode configuration.

4.5   Sensitivity distribution and effect of adding a simulated nylon rod

The local sensitivity of the sensing field, that is the change in the measured voltage when a simulated 15mm diameter nylon rod is inserted at a given location, was calculated at twelve positions (denoted 'holes' 1 to 12 in Figure 4-8) within the flow cross-section for the given electrode configuration under investigation. In these simulations, the cross-section was assumed to be filled with water (the conducting medium) and the nylon rod was assumed to be inserted longitudinally at different spatial locations in the flow cross-section to simulate the presence of a non-conducting particle of the dispersed phase. For array B, a sensitivity parameter $\delta V_{6B,i}$ (see Figure 3-9) is defined as

$$\delta V_{6B,i} = V_{6B,i} - V_{6B,0} \qquad\qquad 4\text{-}2$$

where: $V_{6B,i}$ is the value of the output voltage from the detection circuitry associated with array B when the nylon rod is inserted into the ith hole and $V_{6B,0}$ is the value of this output voltage when the nylon rod was absent.
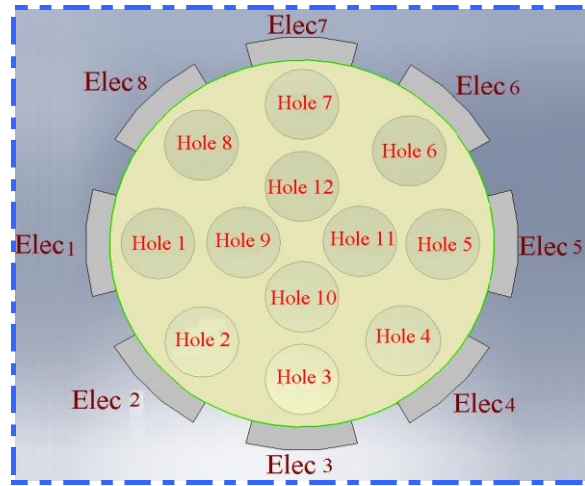
Figure 4-8: The 12 positions at which the sensitivity of the sensing field was calculated
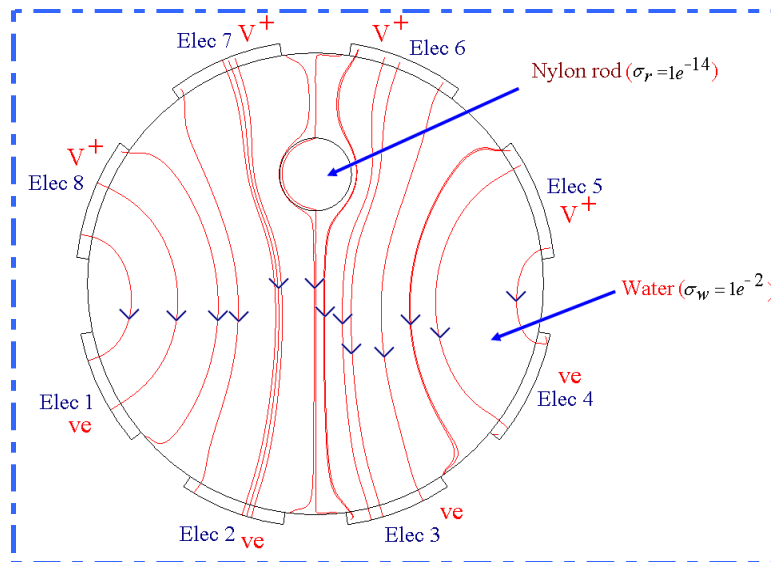
Figure 4-9: Simulated effects on the current flow between electrodes of inserting a nylon rod into hole 12 the ICC when electrodes 5, 6, 7 and 8 are excitation electrodes and remainder are measuring electrodes

COMSOL enables the current density distribution for the model to be predicted. Figure 4-9 shows how the simulated electrical current is distributed in the flowing

media in the presence of a nylon rod. The material surrounding the nylon rod is water of conductivity (σ_w) of 0.01S/m and the conductivity for the nylon rod (σ_r) is effectively zero. The simulated nylon rod was introduced into each 'hole' in turn (see Figure 4-8) and the total or integrated current though all the measurement electrodes (V_e) was calculated. Introducing the nylon rod into the simulated sensing field results in a change in the current density distribution, see Figure 4-9. From this, an effective system resistance, R_f, can be calculated using the equation:

$$R_f = \frac{V^+}{I} \qquad\qquad 4\text{-}3$$

where: I is the total, or integrated, current through all of the measuring electrodes, and V^+ is the voltage between the source electrodes and the measurement electrodes. Once R_f is calculated then, provided that the feedback resistance R_a in the inverting amplifier conductance measurement circuit and V^+ are known (see Figure 4-10), the output voltage $V_{1,B}$, for the circuit in Figure 3-9 and 4-10 may be predicted.
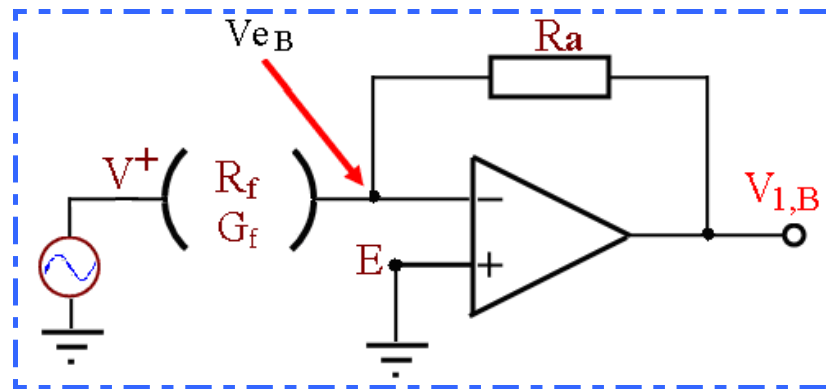
Figure 4-10: Fluid conductance circuit

Once $V_{1,B}$ is known, and the conductance circuit gain k (see Equation 3-2) has been found, the output voltage $V_{6,B}$ (see Figure 3-9) can be found.

4.6   Sensitivity distribution results using nylon rod

This section describes the electrode arrangements used to investigate the sensitivity distribution within the test section to the presence of a nylon rod. The electrode configurations used in the experimental procedures are listed in Tables 4-2, 4-3 and 4-

4 and, as can be seen, the initial electrode arrangements were cyclic – that is, within a given configuration one moves from one rotational position to the next by a simple rotation of 45°. Because there were eight electrodes there were eight possible rotational positions. Thus, in each of the three cases, it was necessary to test only one rotational position. However, in this section, the results presented are for **two** rotational positions for each electrode arrangement.

From Tables 4-2, 4-3 and 4-4 it can be seen that the simple cyclic arrangements of the electrodes can take any one of eight rotational positions. For convenience, and as a form of shorthand, the three given arrangements have been labelled Config-I, II and III, respectively. These will be used in both simulation and bench tests. The CoA, see Section 4.9, for these configurations will be calculated since they will be used in the practical work of the present study.

However, for completeness sake, a number of other, more complex, configurations were initially selected to investigate the proposed technique (see Table 4-1). The electrode configuration, Config-ξ, was chosen to be investigated for both simulation and bench tests, while three electrode configurations, Config-λ, Config-ω and Config-ς were used in the bench tests alone (see Chapter 5).

Table 4-1 contains four different electrode configurations; Config-ξ , Config-λ , Config-ω and Config-ς .

❖ In   Config-ξ the four adjacent electrodes 3, 4, 5 and 6 are excitation electrodes (V^{+}) and the all remaining electrodes (1,2,7,8) are used as measurement electrodes (V_e).

❖ In Config-λ the three adjacent electrodes 4, 5 and 6 are excitation electrodes (V^{+}), electrodes 1, 2, 7 and 8 are the measurement electrodes (V_e) and electrode 3 is earthed (E).

❖ In Config-ω only electrode 5 is an excitation electrode (V^{+}), electrode 1 is set as the measurement electrode (V_e) and the remaining electrodes are earthed (E).

❖ In Config-ς electrodes 1 and 3 are excitation electrodes (V^+), electrodes 5, 6, 7 and 8 are the measurement electrodes (V_e) and electrodes 2 and 4 are earthed (E).

Config-I, contains eight rotational positions (see Table 4-2). In this configuration one electrode is excitation electrode (V^+), and its adjacent electrode is the measurement electrode (V_e). The other six electrodes are earthed (E). For example, in rotational position-1, the electrode 1 is an excitation electrode (V^+) and electrode 2 is the measurement electrode (V_e), and electrodes 3,4,5,6,7 and 8 are connected to ground (E). Seven similar arrangements are possible by simply rotation of the first arrangement, as can be seen from Table 4-2.

Config-II, contains eight rotational positions (see Table 4-3). In this configuration one electrode is an excitation electrode (V^+), and both adjacent electrodes are the measurement electrodes (V_e). The other five electrodes are earthed (E). For example, in rotational position-1, electrode 1 is an excitation electrode, electrodes 8 and 2 are the measurement electrodes and the other five electrodes are connected to ground. Again, seven similar arrangements are possible by simply rotation of the first arrangement, as can be seen from Table 4-3.

Config-III, also contains eight rotational positions (see Table 4-4). In this configuration two adjacent electrodes are the excitation electrodes (V^+), the adjacent electrodes are the measurement electrodes (V_e). The other four electrodes are earthed (E). For example, in rotational position-1 electrodes 1 and 2 are the excitation electrodes, electrodes 3 and 8 are the measurement electrodes and the other four electrodes are connected to the earth (E). Once again, seven similar rotational positions are possible by simply rotation of the first arrangement, as can be seen from Table 4-4.

Table 4-1: Electrode configurations ξ, λ, ω and ς

Electrode Configuration	Excitation Electrodes (V+)	Measurement (Virtual Earth) Electrodes (V_e)	Earth Electrodes (E)
Config-ξ	3,4,5,6	1,2,7,8	none
Config-λ	4,5,6	1,2,7,8	3
Config-ω	5	1	2,3,4,6,7,8
Config-ς	1,3	5,6,7,8	2,4

Table 4-2: Electrode configurations (Config-I)

Electrode Configuration	Electrode Rotational Positions	Excitation Electrodes (V^+)	Measurement (Virtual Earth) Electrodes (V_e)	Earth Electrodes (E)
Config - I	Rotational position-1	1	2	3,4,5,6,7,8
	Rotational position -2	2	3	1,4,5,6,7,8
	Rotational position -3	3	4	1,2,5,6,7,8
	Rotational position -4	4	5	1,2,3,6,7,8
	Rotational position -5	5	6	1,2,3,4,7,8
	Rotational position -6	6	7	1,2,3,4,5,8
	Rotational position -7	7	8	1,2,3,4,5,6
	Rotational position -8	8	1	2,3,4,5,6,7

161

Table 4-3: Electrode configurations (Config-II)

Electrode Configuration	Electrode Rotational Positions	Excitation Electrodes (V^+)	Measurement (Virtual Earth) Electrodes (V_e)	Earth Electrodes (E)
Config - II	Rotational position-1	1	8,2	3,4,5,6,7
	Rotational position -2	2	1,3	4,5,6,7,8
	Rotational position -3	3	2,4	1,5,6,7,8
	Rotational position -4	4	3,5	1,2,6,7,8
	Rotational position -5	5	4,6	1,2,3,7,8
	Rotational position -6	6	5,7	1,2,3,4,8
	Rotational position -7	7	6,8	1,2,3,4,5
	Rotational position -8	8	1,7	2,3,4,5,6

Table 4-4: Electrode configurations (Config-III)

Electrode Configuration	Electrode Rotational Positions	Excitation Electrodes (V^+)	Measurement (Virtual Earth) Electrodes (V_e)	Earth Electrodes (E)
Config - III	Rotational position-1	1,2	3,8	4,5,6,7
	Rotational position -2	2,3	1,4	5,6,7,8
	Rotational position -3	3,4	2,5	1,6,7,8
	Rotational position -4	4,5	3,6	1,2,7,8
	Rotational position -5	5,6	4,7	1,2,3,8
	Rotational position -6	6,7	5,8	1,2,3,4
	Rotational position -7	7,8	6,1	2,3,4,5
	Rotational position -8	8,1	2,7	3,4,5,6

4.7 Sensitivity distribution results for Config-ξ :

The predicted system sensitivity distribution for Config-ξ is shown in Figure 4-11 where the vertical axis represents the sensitivity parameter $\delta V_{6,B}$ in volt, which is also represented by the colour scale to the right of the diagram. Where the red colour in the colour scale represents the maximum value of sensitivity distribution inside the flow cross-section and the blue colour represents the minimum value of the sensitivity distribution on the flow cross-section. The 12 holes indicated in Figure 4-11, indicate the positions of the simulated holes shown in Figure 4-8.
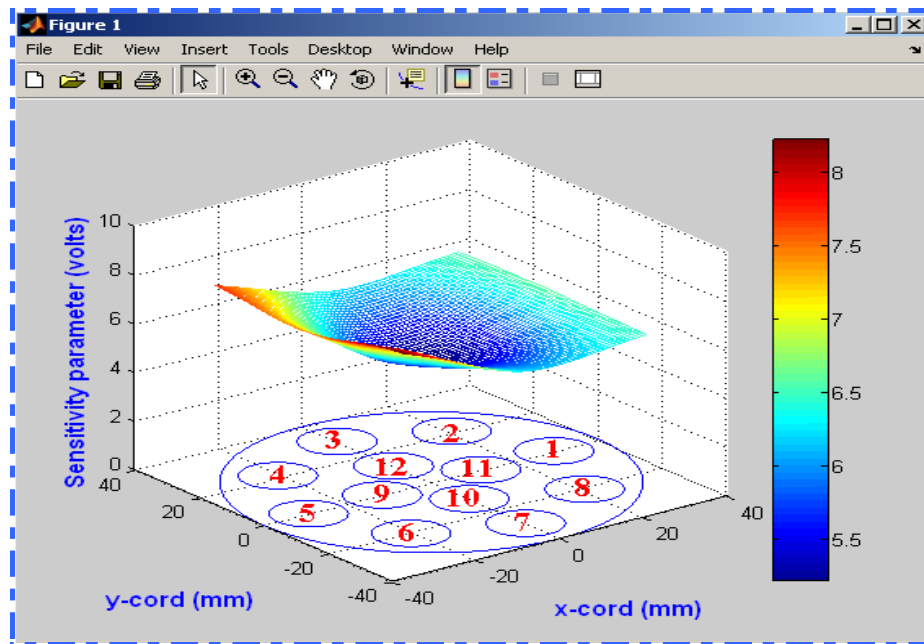
Figure 4-11: Sensitivity distribution for Config-ξ

For Config-ξ, Figure 4-11 shows that the calculated system sensitivity to the simulated insertion of the 15mm OD nylon rod is greater when the rod is inserted in the vicinity of the excitation electrodes (3,4,5,6) than in the vicinity of measurement electrodes (1,2,7,8). The lowest sensitivity was at the middle of the pipe.

4.8 Sensitivity distribution results for Config. I, II and III:

Because of the cyclic symmetry of the electrode arrangements listed in Tables 4-2, 4-3 and 4-4 it is necessary only to calculate the sensitivity distribution for one electrode rotational position for each of Config-I, Config-II and Config-III. Strictly speaking, the sensitivity distribution for each of the other 7 electrode rotational positions could

then be found by simply rotating in steps of 45 degrees the calculated sensitivity distribution. However, to confirm that this is true, the sensitivity distribution for two electrode rotational positions were calculated for each of Configs I,II and III as shown in Figures 4-12 to 4-13.

4.8.1 Sensitivity distribution for Config-I:

The sensitivity distribution profiles shown in Figure 4-12 (a) and (b) are for rotational positions-5 and 8 of Config-I respectively. The vertical axis represents the sensitivity parameter in volt. Also there is a colour scale on the right hand side representing the sensitivity parameter scale. The colour red represents the maximum value of the sensitivity parameter and blue represents the minimum value of the sensitivity parameter. As expected the sensitivity distribution in Figure 4-12 (b) (rotational position-8) is the same as for (a) (rotational position-5) except that it is rotated by 135° (3×45°). From the results shown in Figure 4-12 (a) and (b) the sensitivity to the simulated inserted nylon rod is higher when the rod is inserted near the excitation electrodes and lower when the rod is inserted near the measuring electrodes. Also, as expected the lowest sensitivity was in the vicinity of the grounded electrodes. In addition, for the results shown in Figures 4-12 (a), (b) it is apparent that if we set one electrode as V^{+}, an adjacent electrode as V_e and all of the other electrodes as E, then we will interrogate the flow in a relatively 'local' region adjacent to the excitation electrode.

(a)   (b)
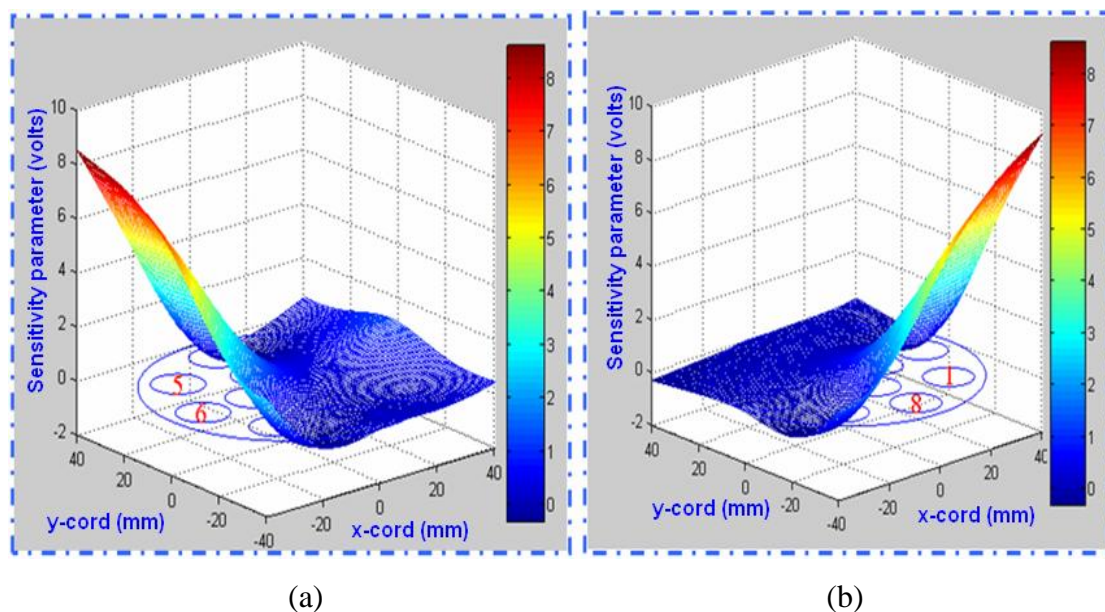
Figure 4-12: Config-I sensitivity distribution for rotational positions-5 and 8

4.8.2 Sensitivity distribution for Config-II:

The sensitivity distribution profiles shown in Figure 4-13 (a) and (b) are for rotational positions 1 and 3 of Config-II respectively. Again, the vertical axis represents the sensitivity parameter in volt and there is the same colour scale on the right hand side to represent the sensitivity parameter scale. As expected the sensitivity distribution in Figure 4-13 (b) (rotational position-3) is the same as for (a) (rotational position-1) except that it is rotated by 180° (4 x 45°). It can be seen from Figure 4-13 (a) and (b) the sensitivity of the system to the simulated insertion of the nylon rod is greatest in the vicinity of the excitation electrode. It should be noted that the sensitivity distribution is different from that obtained using Config-I, as can be seen by comparing Figures 4-12 and 4-13. Also it can be seen from Figures 4-12 and 4-13 that the effective sensing region is larger than for Config-I.

(a)   (b)
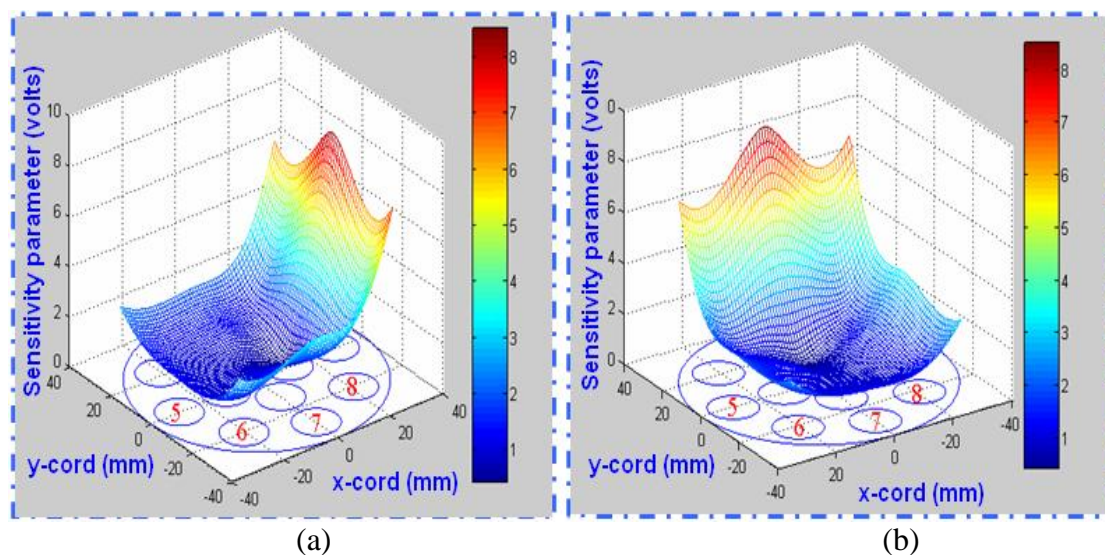
Figure 4-13: Config-II sensitivity distribution for rotational positions-1 and 3

4.8.3 Sensitivity distribution for Config-III:

The sensitivity distribution profiles of Config-III shown in Figure 4-14 (a) and (b) are for rotational positions 1 and 7 respectively. There is the same colour scale on the right hand side as in Figure 4-14 to represent the sensitivity parameter scale. As expected the sensitivity distribution in Figure 4-14 (a) (rotational position-1)   is the same as for (b) (rotational position-7) except that it is rotated by 315° (7 x 45°). Again it was found that the sensitivity is highest close to the excitation electrodes and lowest close to the earthed electrodes. It can be seen from Figure 4-14 that the Config-III

effective sensing region is larger than for Config-I and II. Also it should be noted that sensitivity is higher than for either Config-I or II.

<div align="center">(a)   (b)</div>
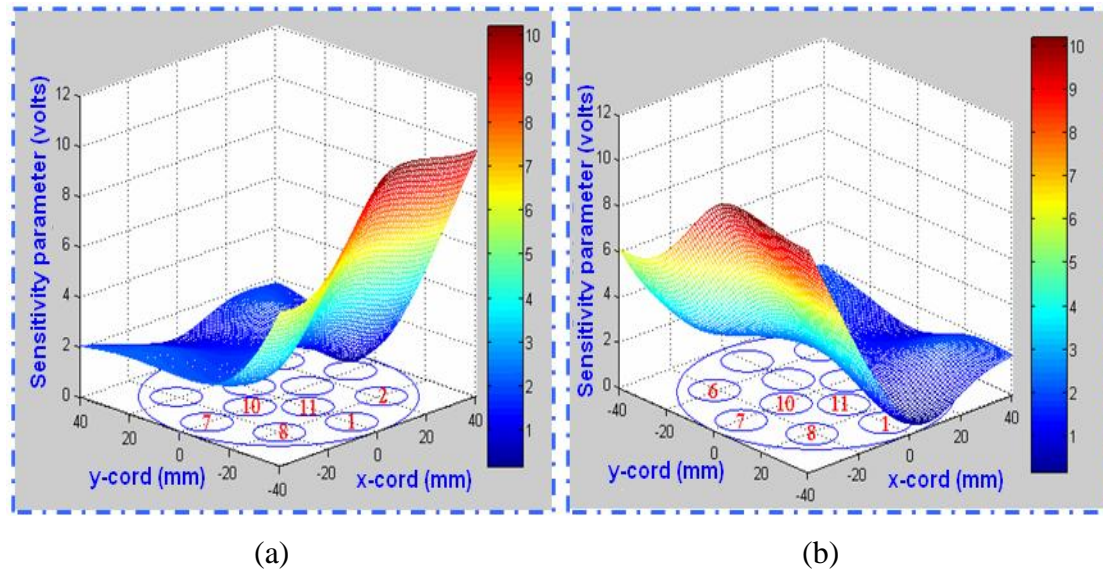
Figure 4-14: Config-III sensitivity distribution for position-1 and position-7

It can be seen that the sensitivities obtained for Config-I, II and III, were a clear maximum confined to the region of the excitation electrode(s), although this could be broadened somewhat by having more than one measurement electrode. However, it is clear that for these limited number of electrodes the system is sensitive at the circumference and lacks sensitivity in the centre of the pipe. With Config ξ there were four excitation and measuring electrodes and it can be seen that the sensitivity was more uniform over the cross-section, but did not reach the same maximum value. Here, then, the electrode arrangement was more sensitive to phenomena in the centre of the pipe but somewhat less sensitive at the periphery.

4.9   Centre of Action

From the sensitivity distribution results obtained in Section 4.6 a boundary can be defined where the sensitivity is 10% of the maximum sensitivity for a given electrode configuration. This enables to define an 'effective sensing region' for each electrode configuration presented in Tables 4-2, 4-3 and 4-4. Also the spatial location of a 'Centre of Action' for each effective sensing region can be defined. For example, for electrode configuration 'j' the x and y co-ordinates of the centre of action are given by the following Equations (4-5) and (4-6):

$$C_{x,j} = \frac{\sum\limits_{i=1}^{N} x_i \, a_i \, s_i}{\sum\limits_{i=1}^{N} a_i \, s_i}$$

4-5

where: $C_{x,j}$ is the x co-ordinate of the CoA for configuration j, x_i is the distance from the origin to the ith element in the COMSOL model, a_i is the area of the ith element, s_i is the sensitivity parameter for the ith element which is equivalent to $\delta V_{6B,i}$ and N is the total number of elements in the flow cross-section. Similarly the y co-ordinate of the Centre of Action for configuration j may be calculated from:

$$C_{y,j} = \frac{\sum\limits_{i=1}^{N} y_i \, a_i \, s_i}{\sum\limits_{i=1}^{N} a_i \, s_i}$$

4-6

where: $C_{y,j}$ is the y co-ordinate of the CoA for configuration j, y_i is the ith element in the COMSOL model, a_i is the area of the ith element, s_i is the sensitivity parameter for the ith element which is equivalent to $\delta V_{6B,i}$ and N is the total number of elements in the flow cross-section.

The equations defining the CoA are identical in form to the equations defining the centre of mass in a two-dimensional system, with the product $a_i \, s_i$ for the ith element replacing the mass m_i for that element. Thus, for example, it can be taken as a measure of how far into the fluid the sensing field extends. For example, if the CoA is close to the perimeter, then the field will not be sensitive to the presence of particles in the centre of the pipe. Conversely, for the sensitivity of the measurement system to extend well into the pipe, the CoA should be near the centre.

In each rotational position the sensitivity parameter for i^{th} element in each pixel a cross the section can be defined. This was done by a MATLAB code which enables the user to define the required sensitivity parameter. The MATLAB code will provide the matrix of x, y and z parameters. For example, to find the coordinate of the CoA, Equations 4-5 and 4-6 can be easily implemented. To find the CoA for other

rotational positions of the electrodes simply rotate in steps of 45°. The same procedure can be adopted for the effective sensing region boundary.

4.9.1 Effective sensing regions and Centre of Action for Config-I, Config-II and Config-III

Figure 4-15, shows calculated effective sensing regions and CoA for electrode rotational positions-5 and 8 for Config-I. Figure 4-16 shows the calculated effective sensing regions and CoA for electrode rotational positions-1 and 3 for Config-II. Figure 4-17 shows the calculated effective sensing regions and CoA for electrode rotational positions-1 and 7 for Config-III. The square mesh elements used to calculate the CoA had a side of length 2mm. The limit of the effective sensing region is shown in red and the position of the CoA in blue. As expected, in every case rotational symmetry was preserved.

4.10 Conclusions

Figure 4-18 combines information from Figures 4-15 to 4-17 and shows the predicted CoAs for each of the three electrode configurations listed in Tables 4-2, 4-3 and 4-4 for all eight electrode rotational positions for each configuration. Obviously different electrode configurations and electrode rotational positions interrogate different regions of the cross-section of the pipe. This is important because the velocity of dispersed phase will vary from top to the lower side of the pipe in inclined flow.

Table 4-5 shows the x and y co-ordinates of the Centre of Action of each effective sensing region for each electrode rotational position for each of Config-I, II and III.

It can be seen that as the electrode arrangement moves from Config-I to Config-II and Config-III the CoA moves deeper into the pipe and the depth of interrogation increases. That is, the average calculated distance of the CoA from the centre of the pipe is about 34mm for Config-I, about 25mm for config-II and about 18mm for Config-III. This is because the electrode arrangement changes from a single excitation and measurement electrode, to one excitation and two measurement and then to two excitation and two measurement electrodes. This suggests that with more advanced and more complex electrode arrangements it should be possible to interrogate deep into the pipe.
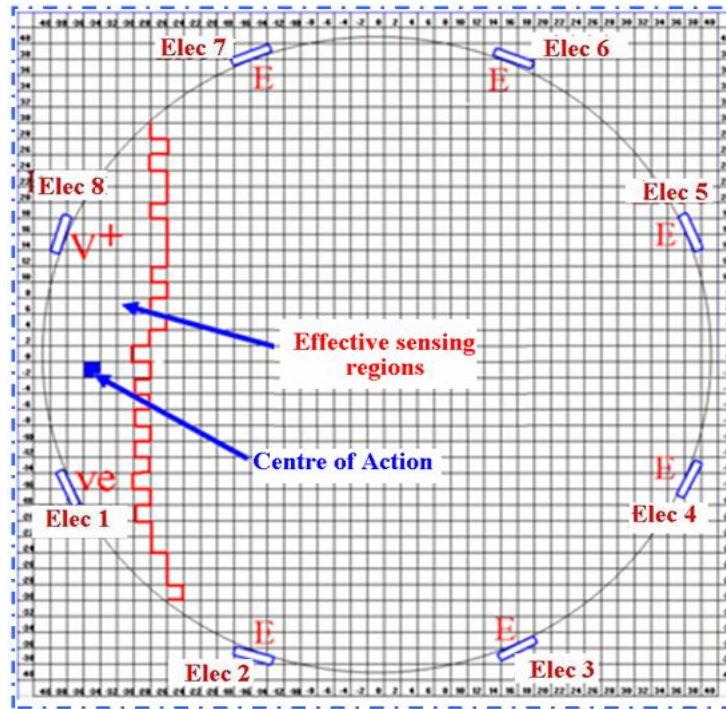
(a)
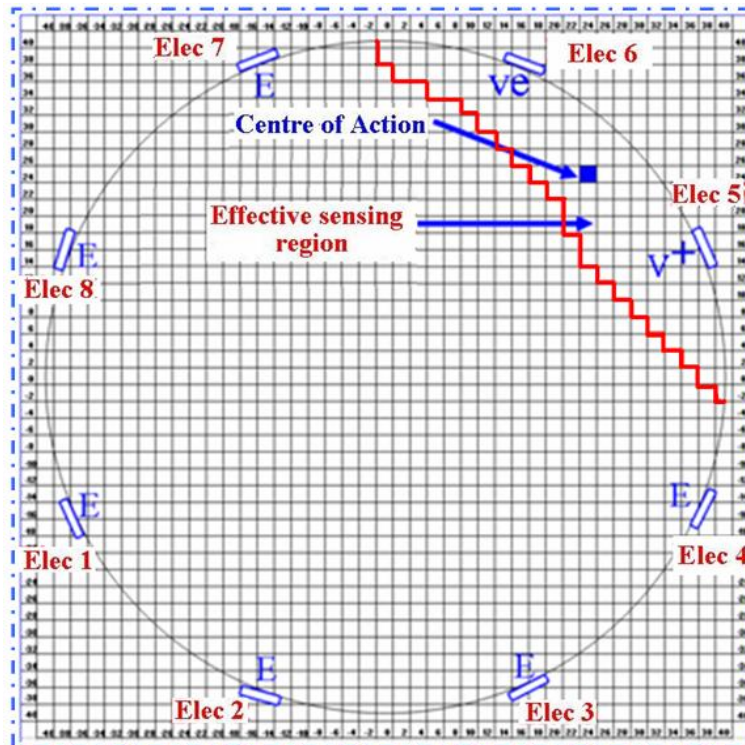
(b)

Figure 4-15: Effective sensing regions associated with electrode position-5 and position-8, Config-I
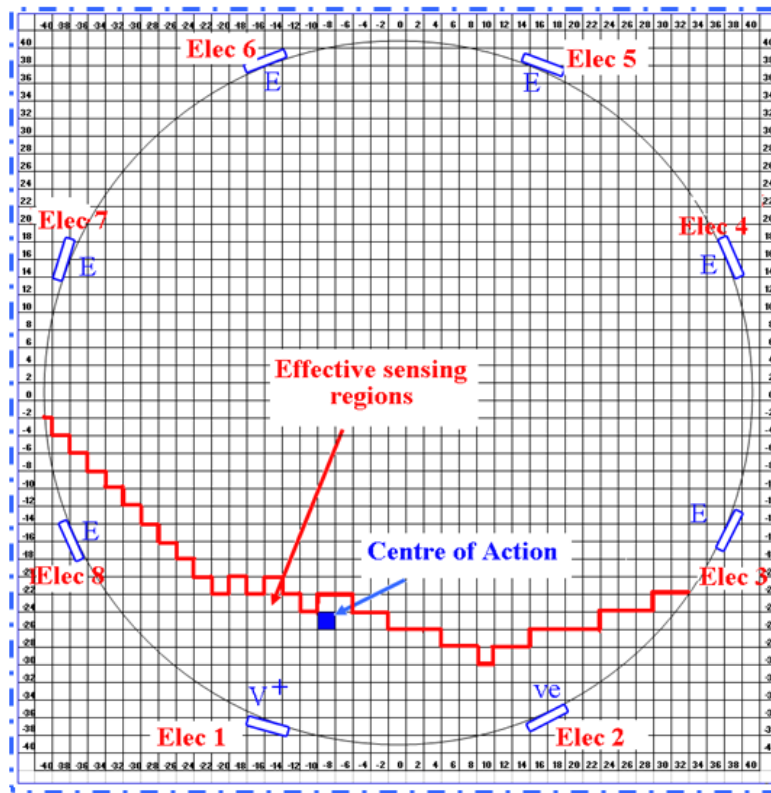
(a)
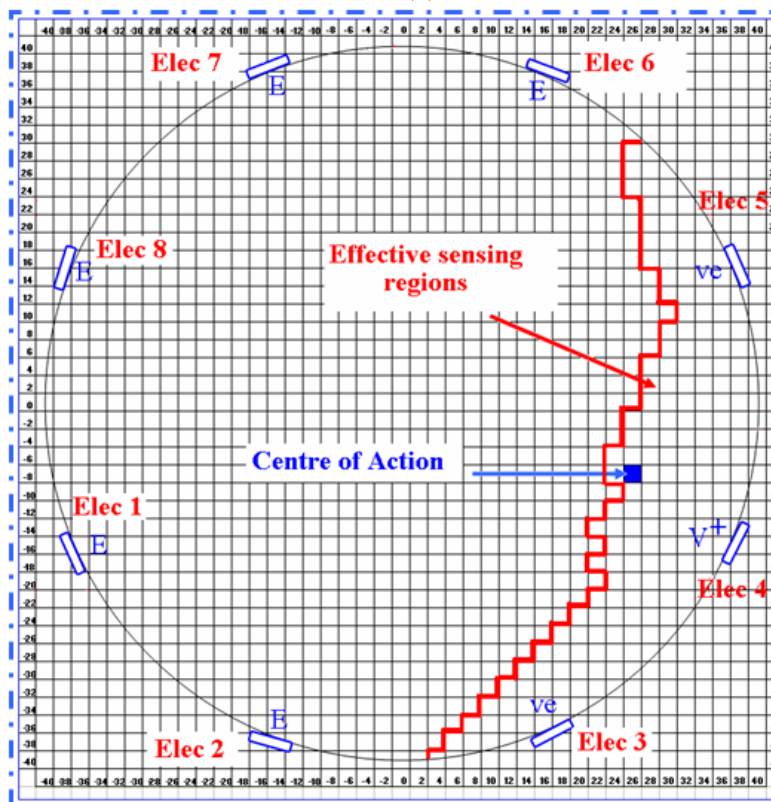
(b)

Figure 4-16: Effective sensing regions associated with electrode position-1 and position-3, Config-II
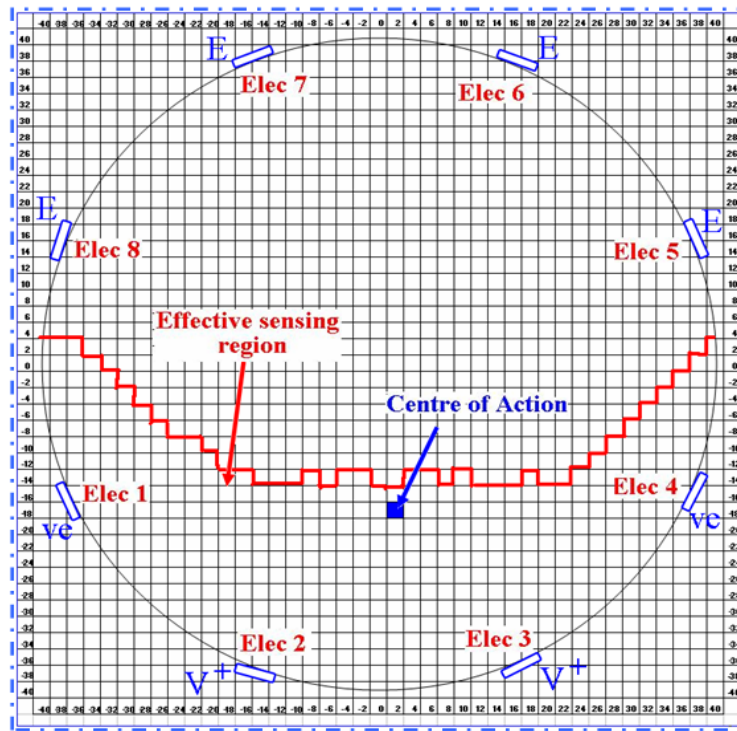
(a)
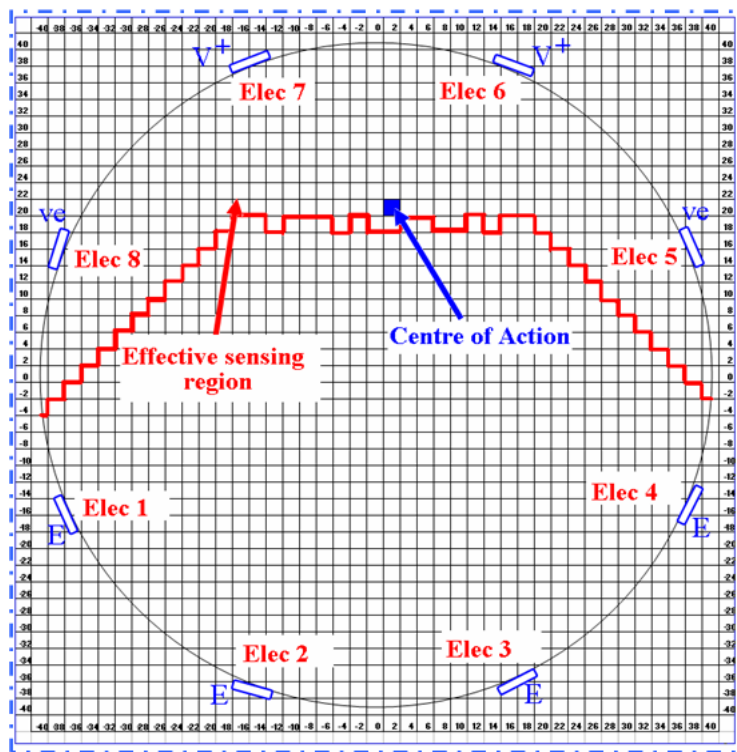
(b)

Figure 4-17: Effective sensing regions associated with electrode position-1 and position-7, Config-III
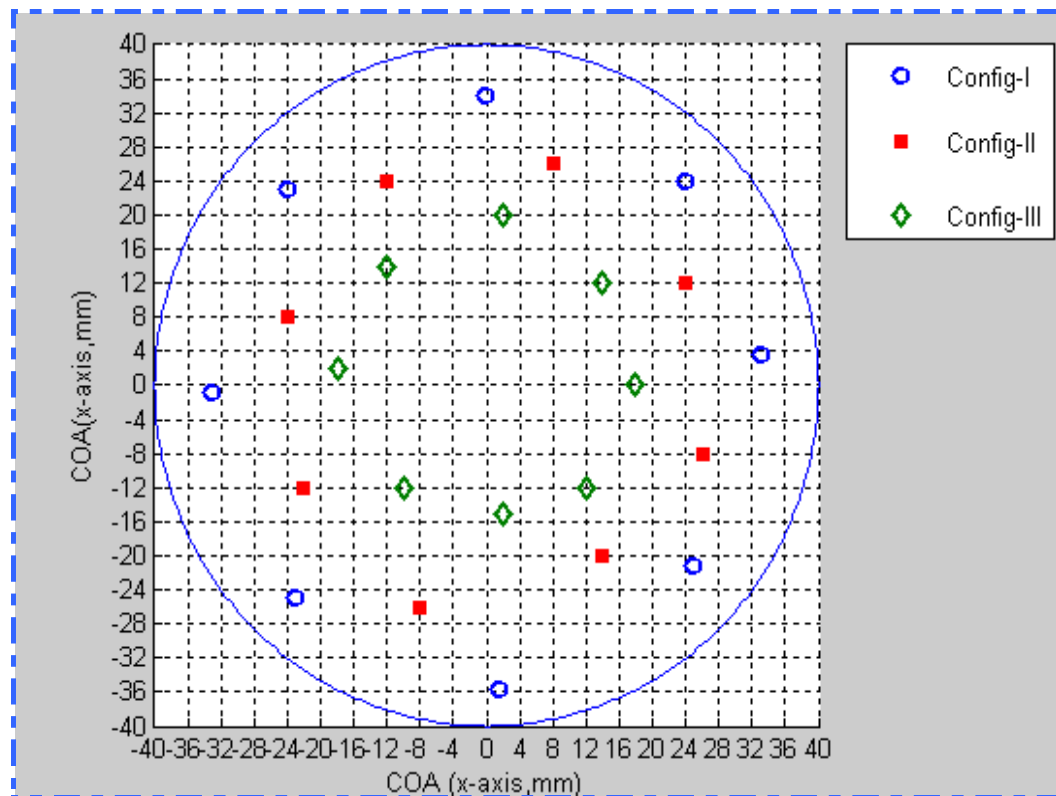
Figure 4-18: Location of CoA for Config-I, II and III for each of the eight possible electrode rotational positions per configuration.

Table 4-5: CoA coordinates for Config-I, II and III for each of the eight possible electrode rotational positions per configuration.

	Electrode Configuration	CoA x-coordinate (mm)	CoA y-coordinate (mm)
Config-I	rotational position-1	-23	-24.9
	rotational position-2	1.5	-35.6
	rotational position-3	25	-21.1
	rotational position-4	33	3.7
	rotational position-5	24	24
	rotational position-6	-0.1	34.1
	rotational position-7	-24	23
	rotational position-8	-33	-0.8
Config-II	rotational position-1	-22	-12
	rotational position-2	-8	-26
	rotational position-3	14	-20
	rotational position-4	26	-8
	rotational position-5	24	12

	rotational position-6	8	26
	rotational position-7	-12	24
	rotational position-8	-24	8
Config-III	rotational position-1	-10	-12
	rotational position-2	2	-15
	rotational position-3	12	-12
	rotational position-4	0.8	18
	rotational position-5	14	12
	rotational position-6	2	20
	rotational position-7	-12.1	14
	rotational position-8	-18	2

Chapter 5   STATIC AND DYNAMIC BENCH TESTS

In this chapter, static and dynamic experimental bench tests are described. The chapter begins by giving reasons for carrying out these tests. After that it describes the experimental apparatus and procedures for the static tests. Next it gives the results obtained. Section 5.6 shows the comparison of results obtained from the static bench tests and the finite element model (COMSOL). The experimental procedure for the dynamic tests is shown in Section 5.8. The last section gives the conclusion drawn from these tests.

5.1　　Reasons for carrying static and dynamic bench tests

Before the ICC flow measuring device was used in the flow loop a number of preliminary experimental static and dynamic bench tests were carried out. These are detailed in this chapter.

The static testing and dynamic tests were carried out to achieve the following objectives:

❖ To calibrate the electronic circuits and to select an appropriate excitation signal to be used.

❖ To experimentally investigate spatial variations in the sensitivity of the electric 'sensing' field for different electrode configurations.

❖ To check that the conductance circuit and electrode selection switches were working as they should, and to make sure that both arrays were excited alternately to prevent cross-talk between the two signals (see Section 3.6).

❖ To ensure the correct functioning of the cross-correlation software developed in MATLAB to calculate time delays between the signals $V_{7,A}$ and $V_{7,B}$ from the two electrode arrays A and B.

5.2　　Static test experimental apparatus

The aim of the static bench tests was to investigate spatial variations in the sensitivity of the electric sensing field for different electrode configurations. These tests were designed to provide the necessary information when, at a later stage, the device is used in the real flows to identify which electrode configuration is most suitable for interrogating a particular area or segment of the flow cross-section. The experimental apparatus consisted of the impedance cross-correlation (ICC) flow meter (see Section 5.3), electronic circuits, a 15mm nylon rod for simulating the presence of a particle of the dispersed phase and a data acquisition system. Two plastic plates, each with 12 holes of equal diameter (15mm) were placed one at each end of the pipe forming the ICC flow meter, see Figure 5.1. The holes in the top plate were through holes while the holes in the bottom plate were "blind" holes. This meant that the ICC could be

filled with water from the top without it leaking. The reason why 15mm was chosen as the diameter of the nylon rod was because this was found to give a measurable change in the output voltage $V_{6,B}$ when inserted anywhere in the cross section. After the ICC was filled with tap water the nylon rod was inserted through one of the holes in the top plate as shown in Figure 5-1. To ensure the rod was vertical and parallel to the walls of the pipe, its lower end sat in the corresponding blind hole of the nylon plate at the bottom of the ICC. The inside surfaces if the two plates were a distance of 470mm apart.
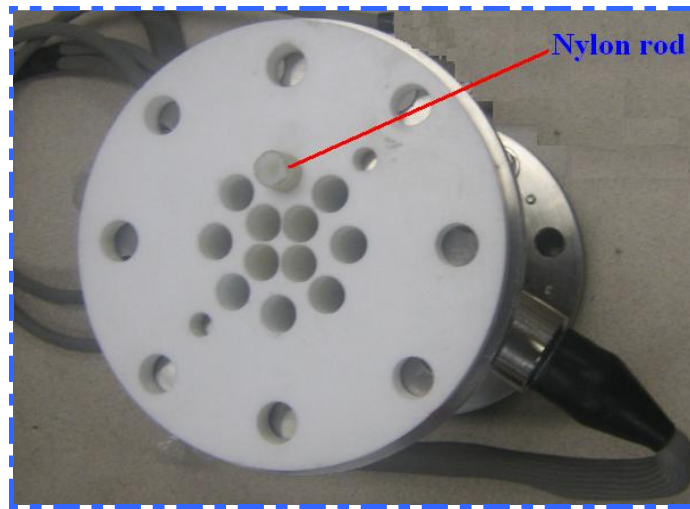
Figure 5-1: ICC flow meter with nylon rod

The holes in the plates were arranged as shown in Figure 5-2 (also shown as Figure 4.8). Since the geometry of the plates and their holes is known accurately, the position of the nylon rod in the flow cross-section is also known. For convenience the numbering of the electrodes is such that the eight outer holes in each plate have the same number as the nearest electrode (see Figure 5-2). The geometry of the system is identical to that used in the COMSOL simulations in Chapter 4.
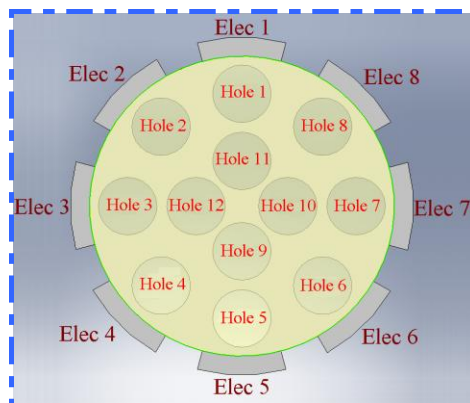
Figure 5-2: Positions of the 12 holes through which the nylon rod was inserted

5.3   Static test experimental setup

Figure 5-3 shows a block diagram of the ICC set-up for both static and dynamic bench tests, with the ICC flow meter connected to two electrode selection circuits which were separately connected to electrode arrays A and B. The two signals from the electrodes (e.g. $V_{7,A}$ and $V_{7,B}$) were fed to the LABJACK which was connected to the PC through a USB port.

Three programmes using the MATLAB's software were developed (see Appendix Codes 1, 2 and 3). The first was to acquire data from each electrode selection circuit, CH-A and CH-B, for 60 seconds, the second and third were used to control the electrode selection circuits for each of arrays A and B so that the desired electrode configuration was selected. From CH-B two measurement were required (e.g. $V_{6,B}$ and $V_{7,B}$, see Figure 3-9) where $V_{6,B}$ was used for volume fraction measurement and $V_{7,B}$ for cross-correlation. From CH-A the corresponding measurement was $V_{7,A}$ which was used for cross-correlation to determine particle velocity. Each of the $V_{6,B}$, $V_{7,B}$ and $V_{7,A}$ measurements were taken over 60 seconds. As explained in Chapter 3 (Section 3.8.3) the LED array for each switching circuit shows the user which electrodes in each array are V^{+}, Ve or earth potential.
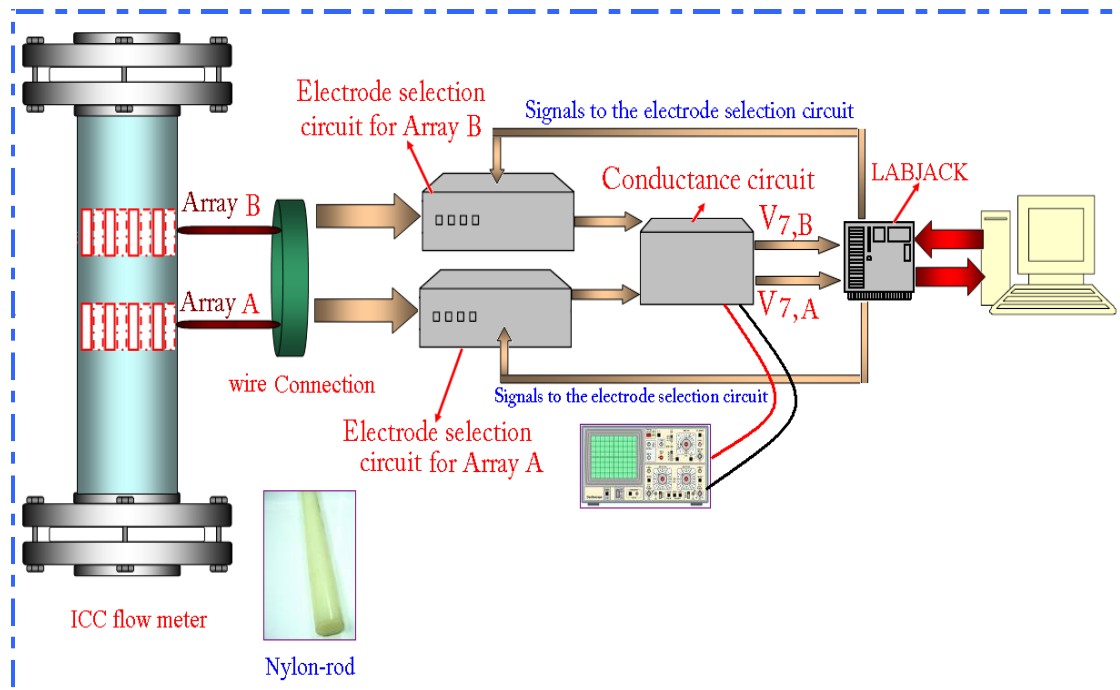
Figure 5-3: Hardware set up of the static and dynamic bench tests

Both conductance circuit and electrode selection circuits were powered by ±15V using a laboratory power supply (with an accuracy of ±0.1V), and the 10kHz sine wave excitation signal, 2V peak to peak, was provided by a laboratory signal generator (again with an accuracy of ±0.1V).

5.4   Static testing procedure

In the static tests, the flow meter was filled with water and a nylon rod was inserted into holes 1 to 12 in turn (see Figures 5-1 and 5-2) in the flow cross-section to simulate the presence of a non-conducting particle of the dispersed phase. The effect on the circuit output voltage $V_{6,B}$ was investigated.

For array B, for all electrode configurations used, twelve sets of data were collected with the nylon rod inserted and one set of data when the nylon rode was absent. For array B, a sensitivity parameter was defined by Equation 4-1 as the change in measured voltage when the nylon rod is inserted:

$$\delta V_{6B,i} = V_{6B,i} - V_{6B,0} \qquad\qquad 4\text{-}1$$

where: $V_{6B,i}$ is the value of the output voltage from the detection circuitry associated with array B when the nylon rod is inserted into the ith hole and where $V_{6B,0}$ is the value of this output voltage when the nylon rod was absent. When the sensitivity parameter is relatively large the nylon rod is located at a position in the cross-section enclosed by array B where the field sensitivity is high. Note that, the COMSOL results were adjusted to take into account the gain of the conductance circuit to give the correct values of $\delta V_{6B,i}$ by using different mesh by iteration.

5.5   Results of the static bench test

As stated in Section 4.6 the present results refer only to two rotational positions for Config-I, II and III, see Tables 4-2, 4-3 and 4-4. However, as shown in Table 4-1, four more complicated electrode configurations Config-ξ, Config-λ, Config-ω and Config-ς were also used to investigate the proposed technique.

5.5.1 Electrode Configurations, Config-ξ, Config-λ, Config-ω and Config-ς

The measured sensitivity distributions of Config-ξ, Config-λ, Config-ω and Config-ς are shown in Figures 5-4 and Figure 5-5. The vertical axis in each figure represents the sensitivity parameter $\delta V_{6B,i}$, which is also represented by the colour scale to the right of the diagram. The colour red in each figure represents the maximum value of sensitivity parameter inside the flow cross section and the colour blue represents the minimum value of the sensitivity parameter in the flow cross section.

(a) Config-ξ **(b)** Config-λ
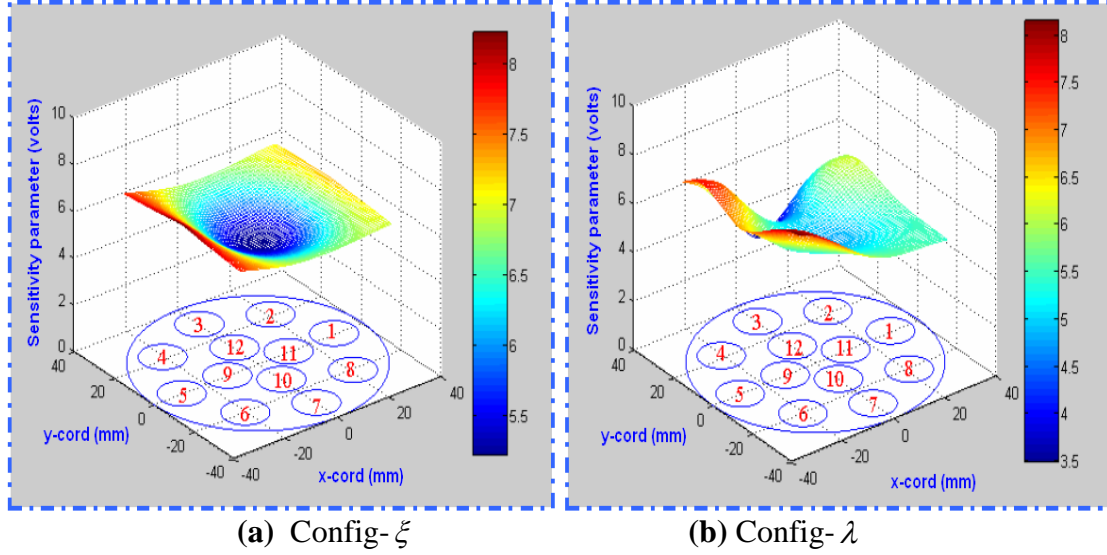
Figure 5-4: Measured sensitivity distributions for Config-ξ and Config-λ

(a) Config-ω **(b)** Config-ς
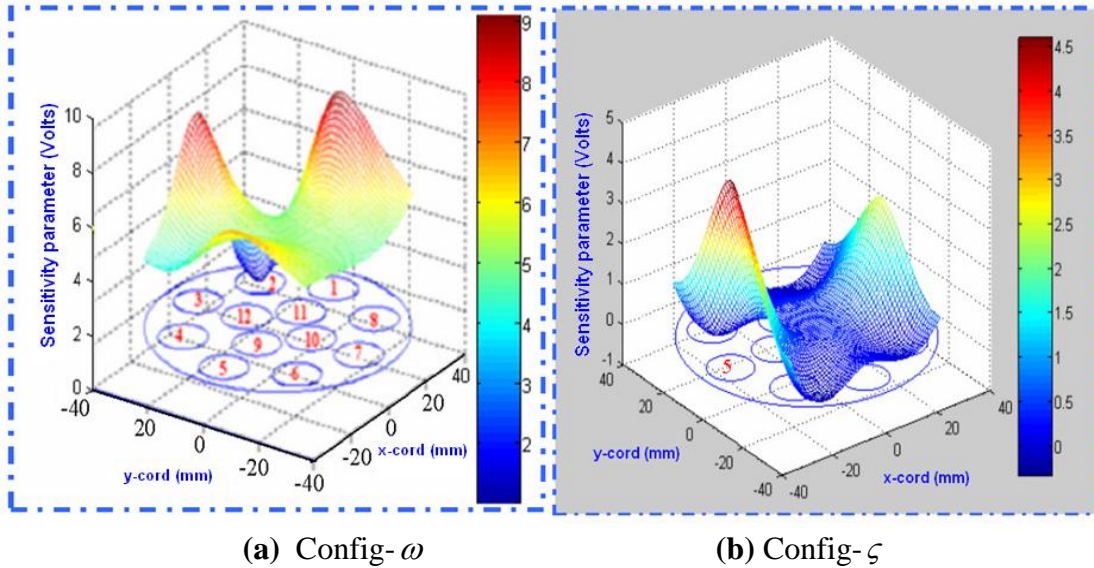
Figure 5-5: Measured sensitivity distributions for Config-ω and Config-ς

It is clear from Figure 5-4 (a) that for Config-ξ the system sensitivity in the vicinity of the excitation electrodes (3,4,5 and 6) is marginally higher than the sensitivity in the vicinity of measurement electrodes (1,2,7 and 8). The lowest sensitivity was in the middle of the pipe. Figure 5-4 (b) shows the sensitivity distribution for Config-λ. In the vicinity of the excitation electrodes (4,5 and 6) the sensitivity is high compared with the sensitivity in the vicinity of the measurement electrodes (1,2,7 and 8). However, the sensitivity dipped in the vicinity of earthed electrode (3) but did not appear as low in the centre of the pipe as with Config-ξ.

It is clear that for Config-ω, Figure 5-5 (a), that the system sensitivity in the vicinity of the excitation electrodes (1 and 3) is higher than in the vicinity of measurement electrodes (5,6,7 and 8). On other hand, the sensitivity in the vicinity of the earth electrodes (2 and 4) was lowest with the sensitivity in the region of electrode 2 lowest of all. The results shown for Config-ς in Figure 5-5 (b) indicate that the system sensitivity in the vicinity of the excitation electrode (5) is again higher than for the other electrodes while the sensitivity at the grounded electrodes was low.

5.5.2 Electrode Configuration Config-I (rotational position-5 and 8)

The measured sensitivity distributions of Config-I, (rotational positions-5 and 8) are shown in Figure 5-6. Again, the vertical axis in each figure represents the sensitivity parameter $\delta V_{6B,i}$, which is also represented by the colour scale to the right of the diagram in the usual way.
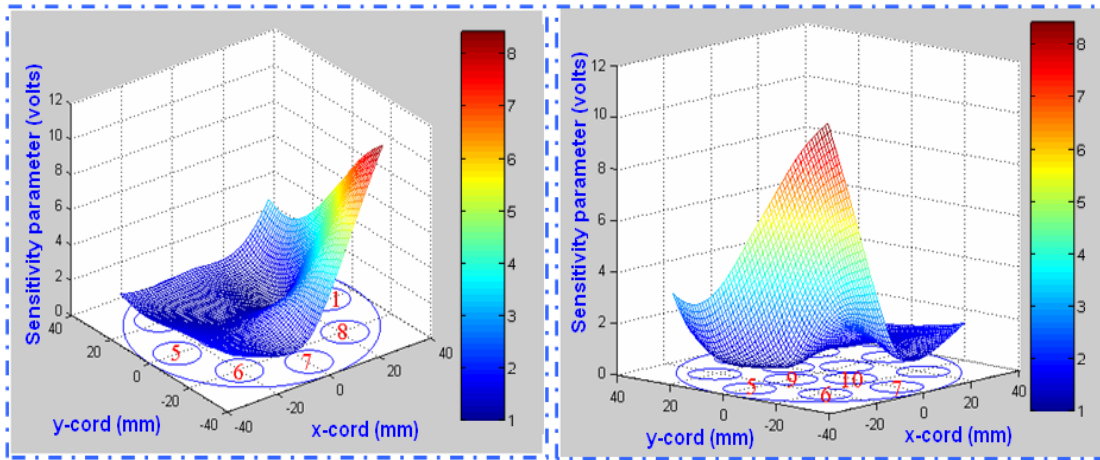
    (a) Rotational position-5   (b) Rotational position-8

Figure 5-6: Measured sensitivity distributions for Config-I

It is clear from Figure 5-6 (a) that the system sensitivity in the vicinity of electrode (8) is much higher than elsewhere in the flow cross section. The lowest sensitivity was in the vicinity of grounded electrodes (2,3,4,5,6 and 7). The sensitivity distribution associated with electrode rotational position-8 is expected to be the same as that for electrode rotational position-5 except that it is rotated clockwise by 135°. The experimental results shown in Figure 5-6 (a) and (b) confirm this expectation. Thus, from Figure 5-6 (a) and (b) it is apparent that if we set one electrode as V^{+}, an adjacent electrode as V_e and all of the other electrodes as E, then we will interrogate the flow in a relatively 'local' region adjacent to the V^{+} electrode.

5.5.3 Electrode Configuration Config-II (rotational position-1 and 5)

The system sensitivity distributions for rotational position-1 and rotational position-5 of Config-II are shown in Figure 5-7 (a) and (b) respectively. The vertical axis represents the sensitivity parameter $\delta V_{6B,i}$, which is also represented by the colour scale to the right of the diagram in the usual way.
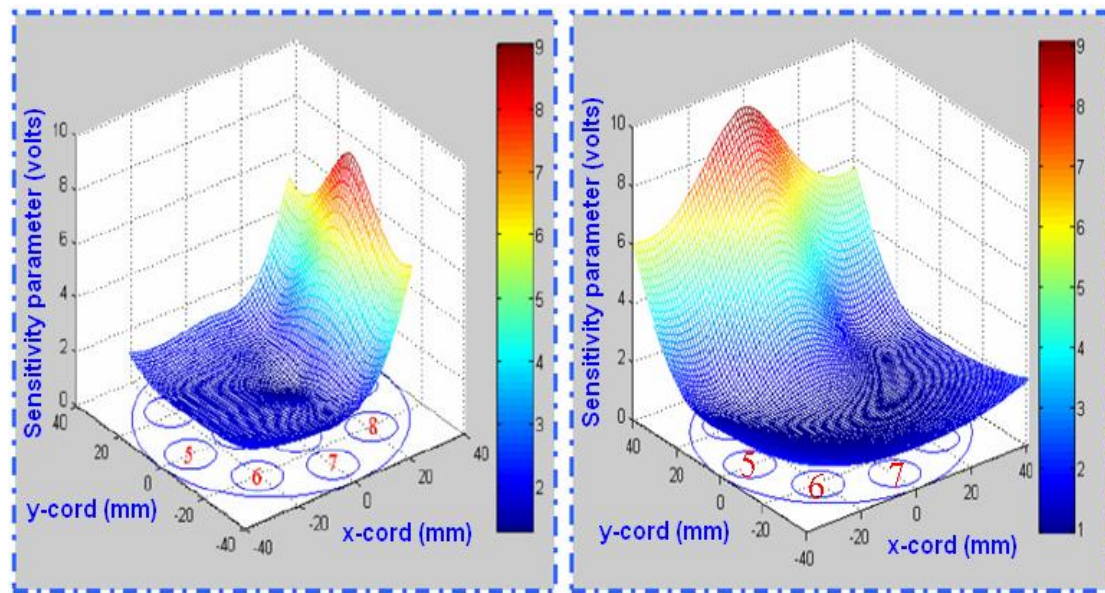
(a) Rotational position-1   (b) Rotational position-3

Figure 5-7: Measured sensitivity distributions for Config-II

From Figure 5-7 (a), for rotational position-1 the lowest system sensitivity was in the vicinity of the ground electrodes (3,4,5,6 and 7). It can be seen that the system sensitivity is much higher in the vicinity of excitation electrode 1 than measurement

electrodes 2 and 8. The sensitivity distribution associated with electrode rotational position-5 is expected to be the same as that for electrode rotational position-1 except that it is rotated clockwise by 180°. The experimental results shown in figure 5-7 (a) and (b) confirm this expectation.

5.5.4 Electrode Configuration Config-III (rotational position-1and 7)

The system sensitivity distributions for rotational position-1 and rotational position-7 of Config-III are shown in Figure 5-8 (a) and (b) respectively. The vertical axis represents the sensitivity parameter $\delta V_{6B,i}$, which is also represented by the colour scale to the right of the diagram in the usual way.
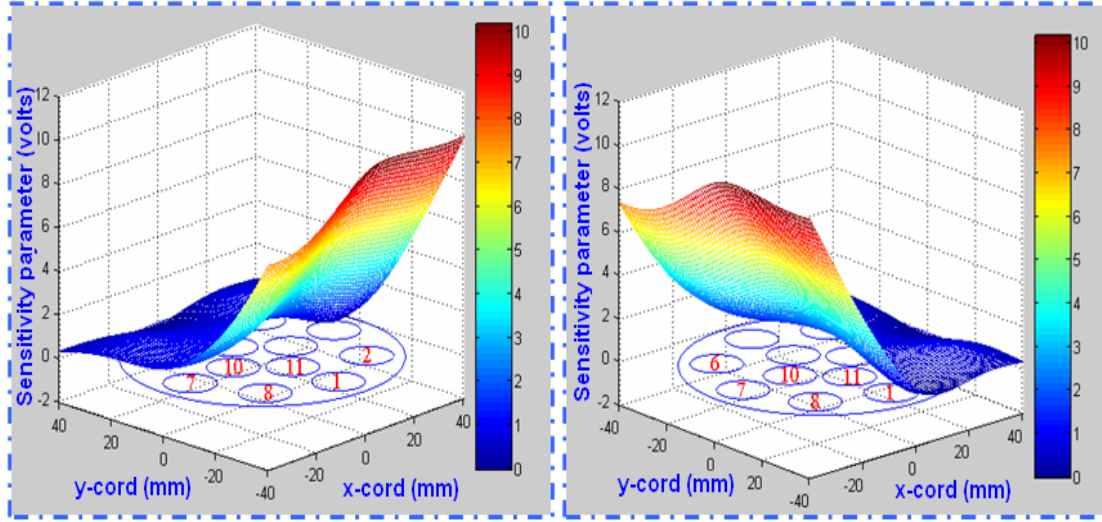
(a) Rotational position-1   (b) Rotational Position-7

Figure 5-8: Measured sensitivity distributions for Config-III

It is clear from Figure 5-8 (a) and 5-8 (b) that the system sensitivity in the vicinity of the excitation electrodes is higher than in the vicinity of the measurement electrodes, and the sensitivity in the vicinity of the earth electrodes was lowest.

5.6   Comparison between modelling and static test results

In this section, the static test results are compared with the modelled results from COMSOL. This involves comparisons for Config-I, Config-II, and Config-III for the selected rotational positions and configuration Config-ξ.
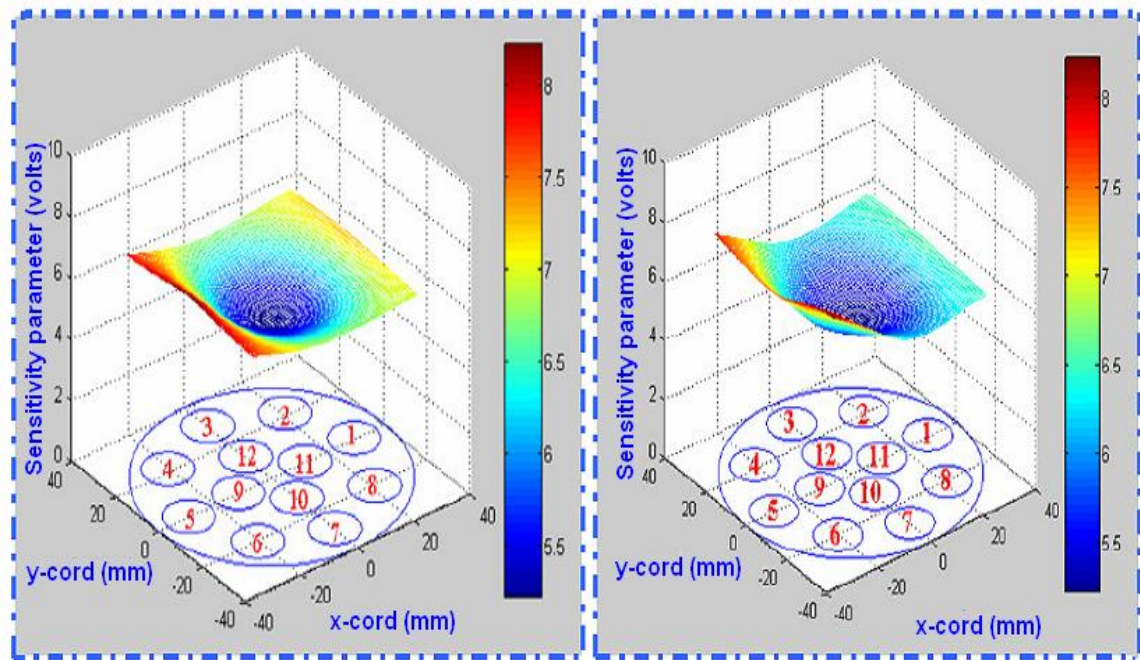
Config-ξ (Static test)   Config-ξ (COMSOL simulation)

Figure 5-9: Comparison of predicted and measured results for Config-ξ
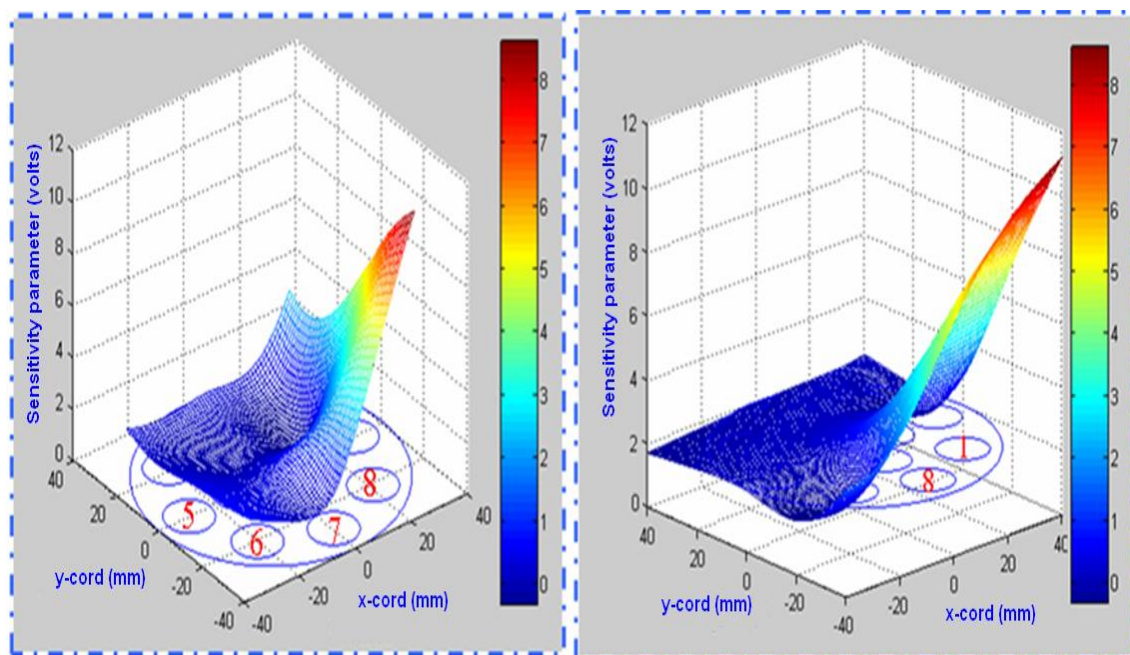
Config-I Rotational position-5   Config-I Rotational position-5
(Static test)   (COMSOL simulation)

Figure 5-10: Comparison of predicted and measured results for Config-I
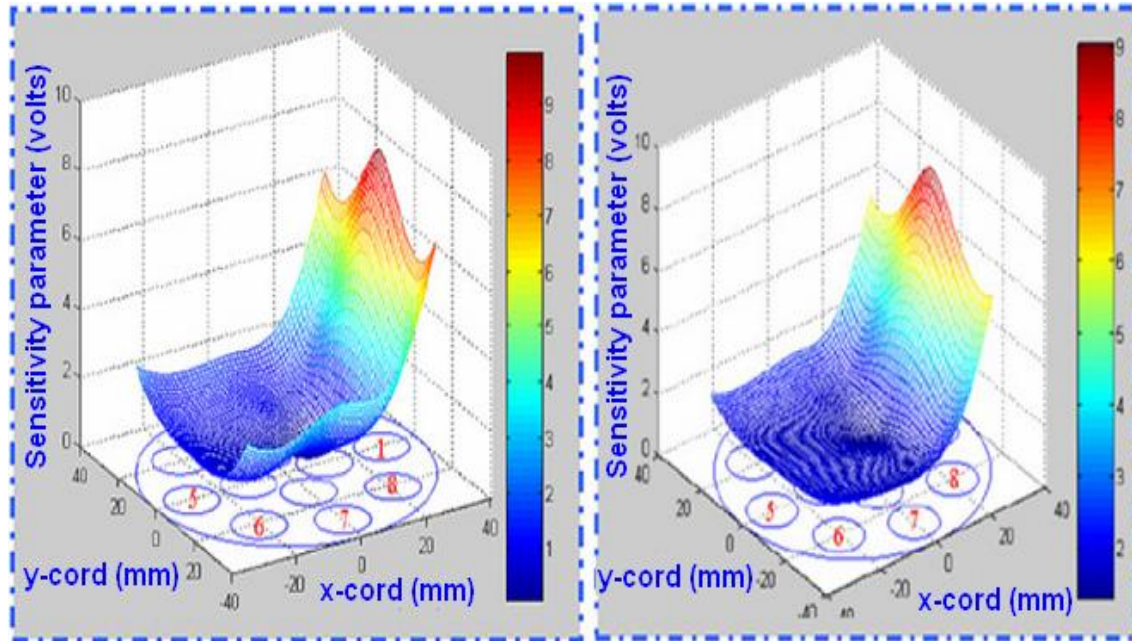
183

<div align="center">
Config-II Rotational position-1   Config-II Rotational position-1

(Static test)   (COMSOL simulation)
</div>

Figure 5-11: Comparison of predicted and measured results for Config-II
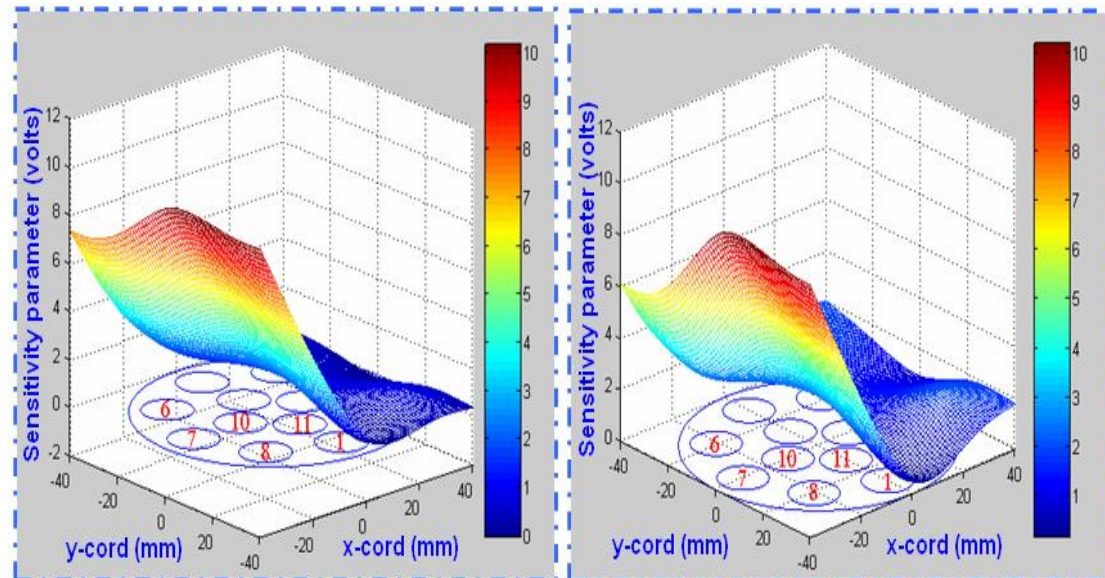
<div align="center">
Config-III Rotational position-1   Config-III Rotational position-1

(Static test)   (COMSOL simulation)
</div>

Figure 5-12: Comparison of predicted and measured results for Config-III

As an explanatory example, consider Config-ξ (see Table 4-1 and Figure 5-9), the excitation electrodes are (3,4,5 and 6) and the measurement electrodes are (1,2,7 and

8). The predicted and measured values at points corresponding to the twelve holes shown in Figure 5-2 can be determined and the accuracy of the model can be evaluated, see Figure 5-12.
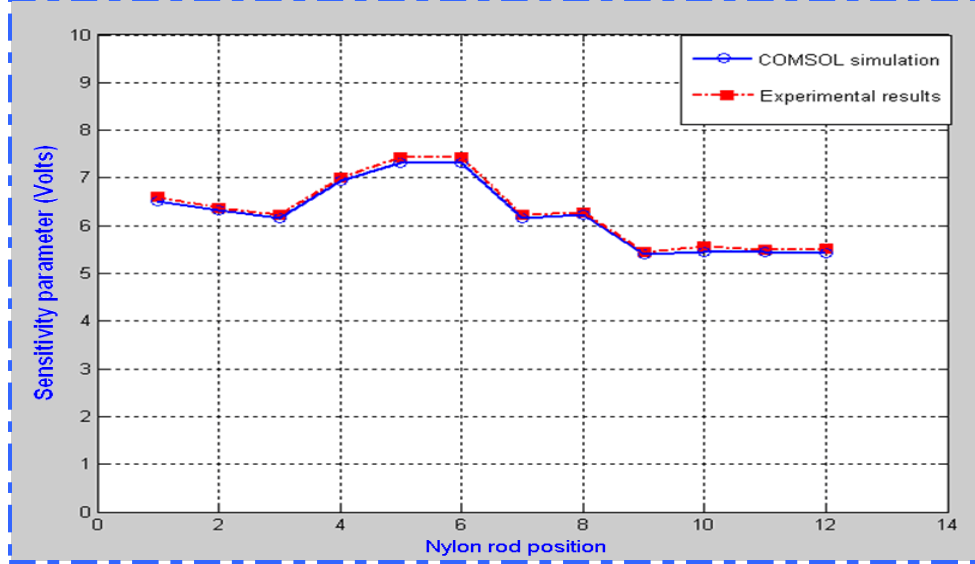
Figure 5-13: Comparison of predicted (COMSOL) and experimental result for Config-ξ

Comparing the measured and predicted sensitivities for Config-ξ, it can be concluded that the differences in the sensitivity parameter $\delta V_{6B,i}$ between the theoretical predictions from COMSOL and from the experimental static bench test is small. Figure 5-13 shows a comparison of the two sensitivity distributions. A percentage error can be calculated using Equation 4-2:

$$\varepsilon = \frac{\delta V_{6B,i,\text{sta}} - \delta V_{6B,i_{\text{model}}}}{\Delta V_{\text{model}}} *100 \qquad 4\text{-}2$$

where: $\delta V_{6B,i,\text{sta}}$ and $\delta V_{6B,i_{\text{model}}}$ are the voltage difference obtained from static test and the voltage difference obtained using COMSOL respectively. The percentage error is shown in Figure 5-14. The differences between the COMSOL predictions and experimental results are within a range of less than 2%.
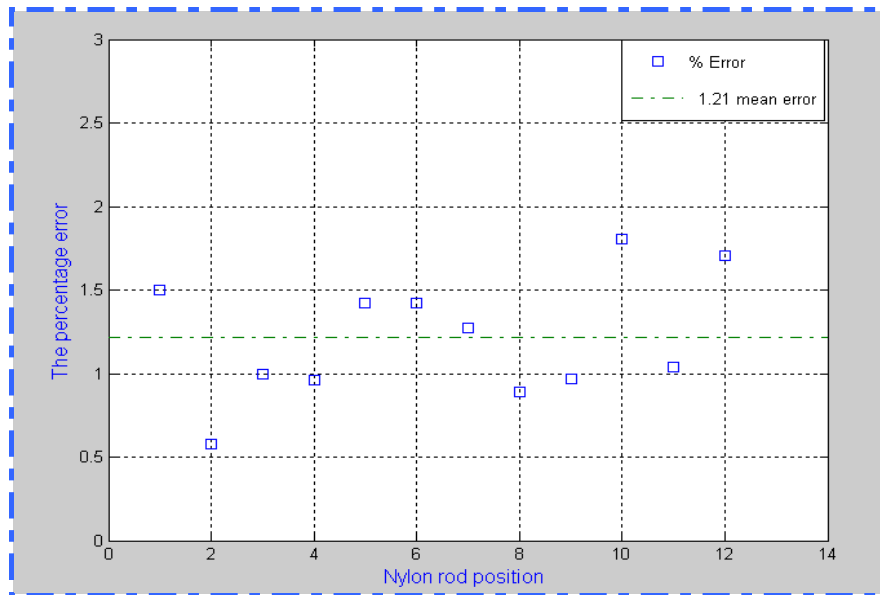
Figure 5-14: The relative percentage error between COMSOL predictions and experimental results for Config-ξ

In Figure 5-14 the horizontal green dotted line represents the mean value of the percentage error, ε, for all 12 data nylon rod positions for Config-ξ. The error between measured and predicted sensitivities for Config-II and III can be evaluated similarly and Table 5-1, shows the electrode configuration and its corresponding mean relative percentage error.

Table 5-1: Mean relative percentage error for differences between measured and predicted sensitivities for Config-I, II and III

Electrode Configuration	Mean value of the percentage error between measured and predicted sensitivities
Config-I Rational position 5	1.21%
Config-II Rational position 1	1.24%
Config-III Rational position 1	1.65%

5.7 Dynamic test experimental apparatus

The dynamic tests were to check the performance of the ICC flow meter and to test how well the electronic circuit prevented cross-talk between the two electrode arrays. For the dynamic tests the hardware used was the same as that for the static tests

described in Section 5.4 (see Figure 5-3). Cross-correlation software to obtain the time it took for particles in the flow to pass from one electrode array to the other was developed (see Appendix Code-4).

5.8 Experimental procedure and results for the Dynamic test

In this experiment two balls P and Q were used which have the same diameter of 29mm but slightly different densities (1200kg/m^3, 1164.7kg/m^3 for balls P and Q respectively). The balls were dropped vertically so that they passed between the two electrode arrays and their velocities determined using the ICC flow meter. Firstly, we set the electrode configuration (Config-I) for arrays A and B to rotational position-8 (see Table 4-2). The choice of Config-I (rotational positions 5 and 8) were to ensure minimum or no interference between the two sensing regions. The balls were dropped at the same time but in different parts of the pipe; ball P was dropped between electrodes 1 and 8 and ball Q was dropped between electrodes 5 and 6 as shown in Figure 5-15. Then, the signals $V_{7,A}$ (blue) and $V_{7,B}$ (red) from the two arrays were measured and cross-correlated as shown in Figure 5-17.
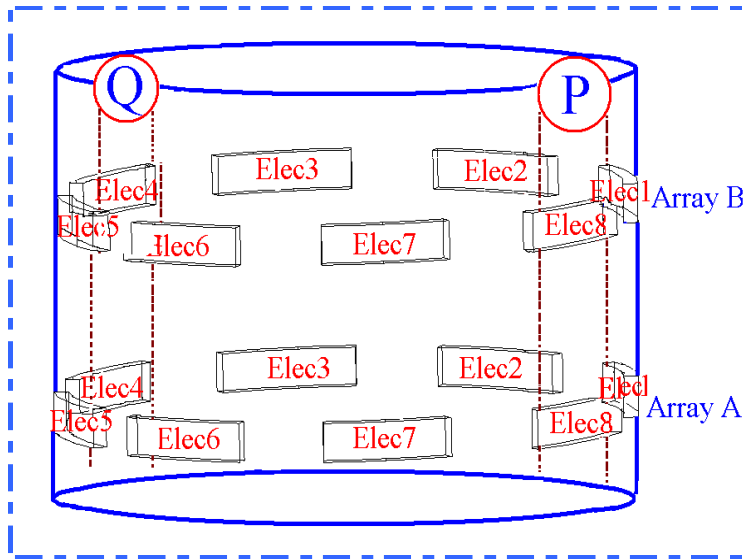
Figure 5-15: Arrangement of electrode array on the pipe

Figure 5-16 shows the output signals from the two arrays ($V_{7,A}$ and $V_{7,B}$, see also Figure 3-9). The signal from array A is coloured blue, while the red signal is from array B. The presence of only one peak in each of the red and blue signals makes it clear that this system was only sensing ball P, and ball Q produced no noticeable

effect on the output voltages $V_{7,A}$ and $V_{7,B}$. This is because (see Figure 5-6 (a)), for electrode rotational position-8 , the sensitivity of the electric sensing field close to electrodes 1 and 8 (the location of ball P) is much higher than the sensitivity close to electrodes 5 and 6 (the location of ball Q). Thus, we see that for electrode rotational position-5 (see Table 4-2) the ICC system preferentially detects velocities in that part of the flow cross section close to electrodes 1 and 8.

Cross-correlating $V_{7,A}$ and $V_{7,B}$ gives rise to the single peaked correlogram shown in Figure 5-17 with the peak value at a time delay of 0.042 seconds. Given that the axial separation of the arrays is 0.05m, this corresponds to a measured velocity of 1.19ms^{-1}. The velocities for the balls were assumed to be their terminal velocities V_T given by the expression (Govier G et.al. 1972):

$$V_T = \left[\frac{4}{3}d\left(\frac{\rho_B - \rho_W}{\rho_W} \right)\frac{g}{C_D} \right]^{0.5} \qquad \text{4-3}$$

Where C_D is a drag coefficient for the ball, and depends upon its shape and surface roughness properties, ρ_W is the density of the water, ρ_B is the ball density and g is the acceleration of gravity. It can be seen from Equation (4-3) that V_T is dependent upon the ball diameter, d. A good discussion of the terminal settling velocity of a spherical particle is given by Govier G et.al. 1972, who suggest that $C_D = 0.059$. Thus:

$$V_T = \left[\frac{4}{3} * (29 \times 10^{-3})\left(\frac{200}{1000} \right)\frac{9.81}{0.059} \right]^{0.5} = 1.28\text{m/s}$$

This is in reasonably good agreement to the measured velocity of 1.19ms^{-1}. The measured value is less than the predicted value but agreement is good enough to confirm the effectiveness of the cross-correlation method for the detection of velocity of particles travelling within the fluid.

This is summarised in this section. The terminal settling velocity V_T of the particles is defined as the velocity at which a single particle will settle due to gravity alone. This requires that no other particles interact with it and that no external force is applied.

The theory applied in this section (Govier G et.al. 1972) also assumes that the particles are smooth, regular, rigid spheres. Whilst this is not strictly the case in this investigation it is a reasonable assumption. Under these conditions two forces act on the particles. These are a downward gravitational force, F_g, given by Equation 4-4 and the drag force resisting the motion of the particles, F_D, which is given by Equation 4-5.

$$F_g = \frac{\pi d^3}{6}(\rho_p - \rho_w)g \qquad\qquad 4\text{-}4$$

$$F_D = C_D \frac{\rho_w u_p^2}{2} \frac{\pi d^2}{4} \qquad\qquad 4\text{-}5$$

In Equation (4-4) and Equation (4-5) ρ_p and ρ_w are the densities of the particles and the water respectively. C_D is the drag coefficient; d is the particle diameter and u_p is the particle velocity with respect to the fluid. At the terminal settling velocity these forces become equal so that no acceleration takes place. At this point $u_p = V_T$. In order to calculate V_T it is necessary to calculate C_D, the drag coefficient. The value of C_D is a function of the particle Reynolds number, Re_p. This is given by Equation 4-6 where μ_w is the viscosity of the water.

$$Re_p = \frac{d\, u_p\, \rho_w}{\mu_w} \qquad\qquad 4\text{-}6$$

In the current investigation a value of C_D equal to 0.059 was employed for both balls P and Q (Govier G et.al. 1972). Equation (4-3) is obtained by combining and re-arranging Equations (4-4) and (4-5) for the special case $u_p = V_T$.
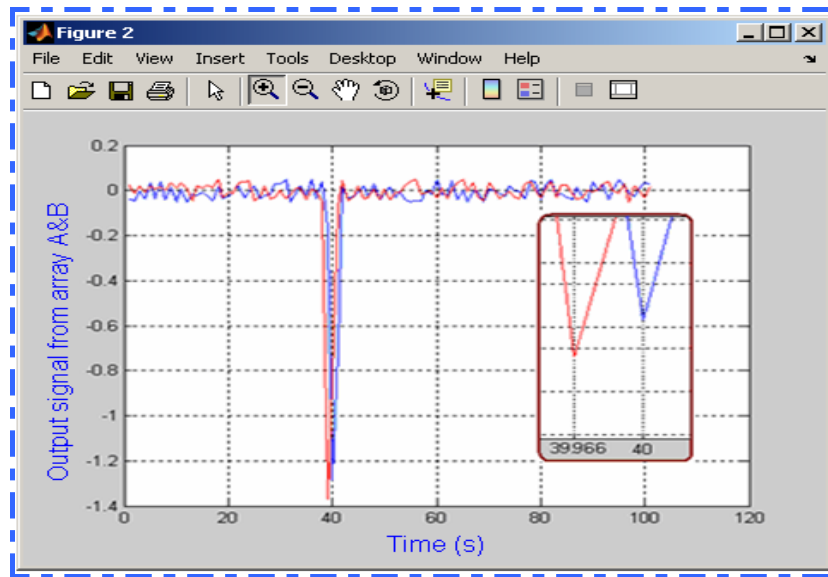
Figure 5-16: The output signals from arrays A and B($V_{7,A}$ - blue and $V_{7,B}$ – red) for ball P.
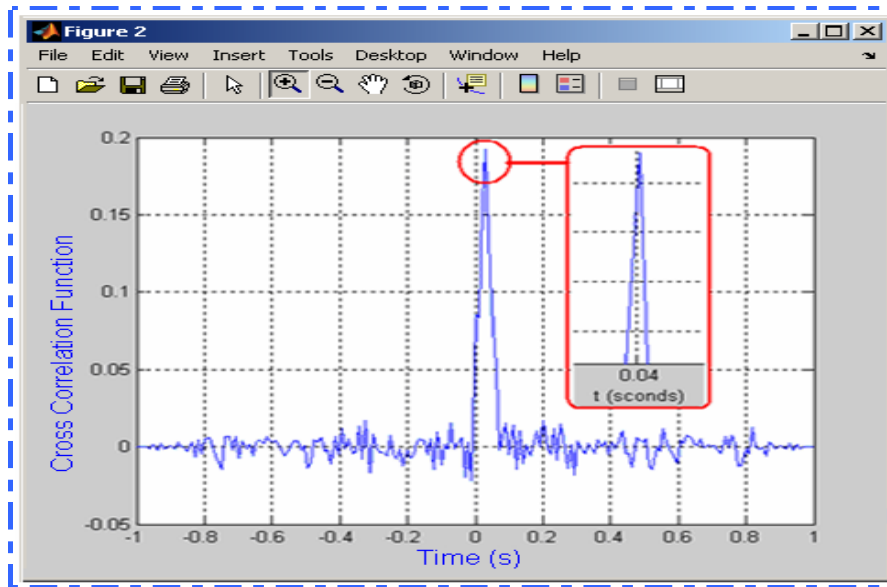
Figure 5-17: Cross-correlation of the two signals ($V_{7,A}$ and $V_{7,B}$) for ball P

Next the electrodes in arrays A and B were set to Config-I rotational position-5 (see Table 4-2) and here the sensitivity of the electric field was much higher in the vicinity of ball Q than in the vicinity of ball P (see Figure 5-6 (b)). The test was repeated as above and again a single peaked correlogram was produced with the peak value at a time delay of 0.0505 seconds (see Figure 5-19) giving a measured velocity for ball Q of 0.99 ms^{-1}. For this test the density of the ball was 1164.7kg/m^3, so the theoretical velocity of ball Q is:

$$V_T = \left[\frac{4}{3} * (29 \times 10^{-3}) \left(\frac{164.7}{1000} \right) \frac{9.81}{0.059} \right]^{0.5} = 1.02 \text{m/s}$$

Again this is in reasonable agreement with the velocity predicted by Equation (4-3), 1.02 ms^{-1}. The single peak also confirms, as expected, that for electrode rotational position-5, the ICC system only senses flow velocities in the vicinity of electrodes 5 and 6 (see Figure 5-18).
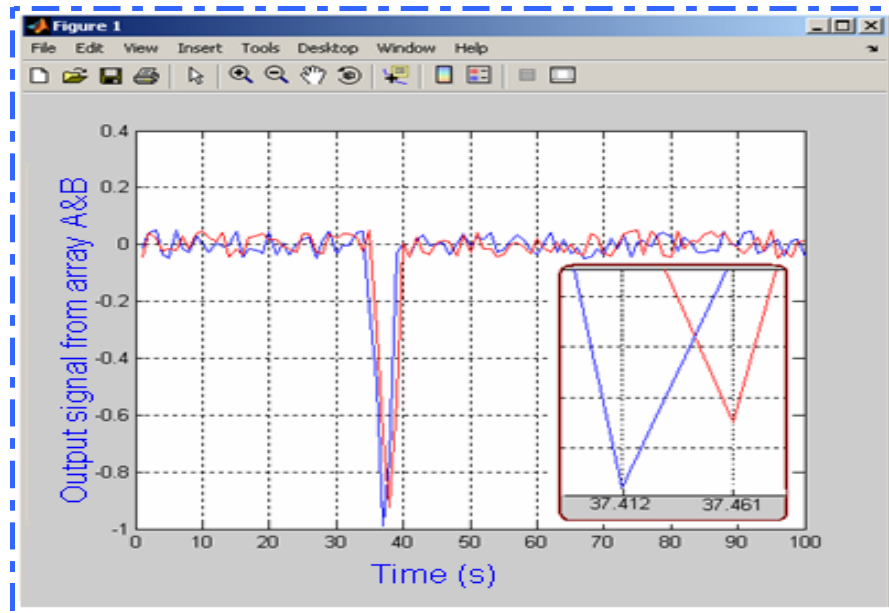
Figure 5-18: The output signals from arrays A and B (V7,$_A$ - red and V$_{7,B}$ - blue) for ball Q
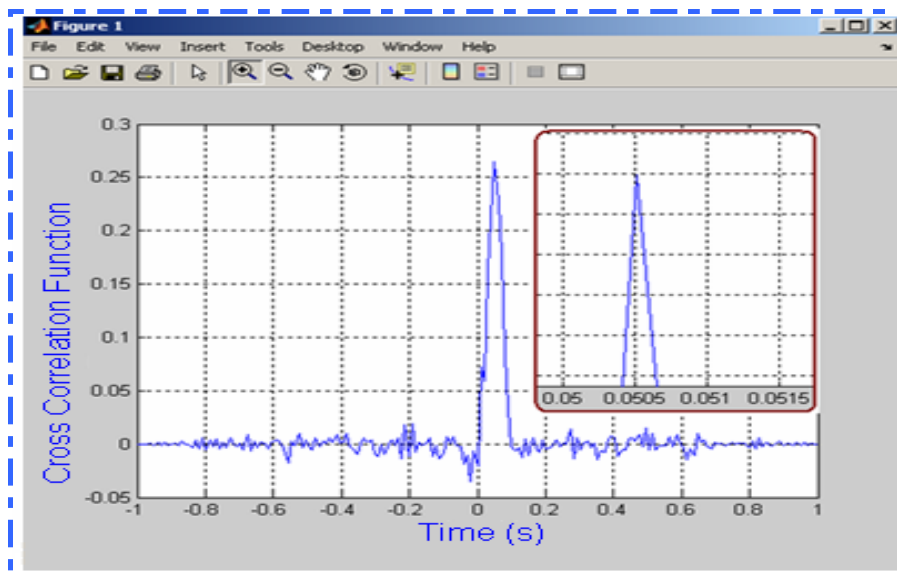
Figure 5-19: Cross-correlation for the two signals (V$_{7,A}$ and V$_{7,B}$) for ball Q

Finally, the electrode configuration for arrays A and B was set to Config-ξ (Table 4-1), which gives rise to a relatively uniform sensing field (see Figure 5-4). Again, the balls were dropped at the same time, with ball P dropped between electrodes 1 and 8

and ball Q dropped between electrodes 5 and 6. Voltages $V_{7,A}$ (blue) and $V_{7,B}$ (red) were obtained from arrays A and B respectively as shown in Figure 5-20.
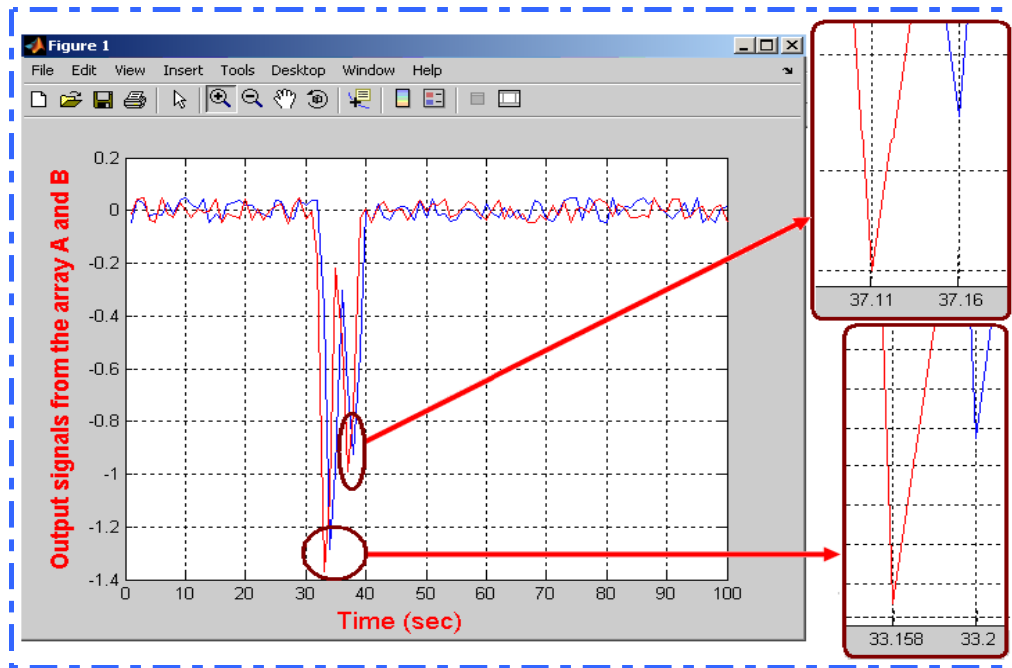
Figure 5-20: The output signals from arrays A and B V7,A (blue) and V7,B (red) for balls P and Q

Here it can be seen from Figure 5-20 that two spikes occur in both $V_{7,A}$ and $V_{7,B}$ traces. The peak was first associated with ball P and the second associated with ball Q. By zooming in, the time taken by each of the two balls to travel between the two electrode arrays (A and B) can be found. The balls were dropped close to the pipe wall, where this configuration is most sensitive.

Table 5-2: Delay time obtained from cross-correlation function for simultaneaous measurements of velocities for balls P and Q using Config-ξ

	Time (s)	Velocity (m/s)
Ball P	0.042	1.19
Ball Q	0.051	0.99

The simultaneous velocities in Table 5-2 correspond closely to the velocities for P and Q when they were sensed individually. It is therefore apparent that, for Config-ξ, the electric field is sensitive to the presence of the balls in all parts of the flow cross-section.

5.9   Conclusions

❖ Config ξ, Config λ, Config ω, Config-ς and Config-I, II and III have been tested to find the configurations which best interrogate different part of the cross-section of the pipe. The likely sensitivity distributions were predicted using the COMSOL software, see Section 4.7. Experimental tests were then carried out which showed that the experimental and predicted results were very close, within 2% of each other for all tests and all configurations, see Figures 5-9 to 5-12 and Table 5-1.

❖ Config ξ, with four excitation and four measurement electrodes had a sensitivity distribution that was fairly uniform around the periphery of the pipe but less sensitive in the centre, see Figure 5-21 (a). Nevertheless this electrode arrangement was capable of detecting the passage of two balls dropped simultaneously through the ICC flow meter, see Figure 5-20.

❖ Config-I, II and III, because of the limited number of electrodes used for excitation and measurement, and also because the electrodes were adjacent to each other, tended to interrogate the flow close to the boundary of the pipe where the excitation and measurement electrodes were located. As the number of excitation and measurement electrodes increased the CoA moved closer to the centre of the pipe. With two excitation and two measurement electrodes, Config-III interrogated a section of the pipe that covered about half the cross-section and extended close to the centre, see Figures 4-17 and 5-12. By suitable rotation of the electrode arrangement Config-III could be used to interrogate almost the full cross-section of the pipe.

❖ Config ξ, was chosen for dynamic testing of the ICC system as this was the electrode arrangement that gave best coverage of the pipe cross-section. It was found experimentally that the ICC flow meter, with this electrode arrangement, could detect and differentiate between two balls with slightly different densities dropped simultaneously through the ICC system. It was also found that both velocities determined by the meter were close to the predicted values. It can be concluded that that particles flowing in one part of the pipe do not adversely affect the measured cross-correlation velocity determined for particles flowing in another part of the pipe.

Chapter 6   EXPERIMENTAL APPARATUS

This chapter begins by describing the multiphase flow loop on which all the experiments were carried out. Following this is a description of the instruments used for making reference measurements; including a Hoppers and load cells used in the process of making reference measurement of the flow rates of both solids and water, a differential pressure transmitter for measuring the mean solids volume fraction and a turbine meter for measuring the liquid flow rate. The Chapter also covers the range of solids-liquid flow conditions used for the experimental tests. Finally, it gives a description of the experimental procedures that were used.

6.1 Multiphase flow loop

To test the performance of the ICC flow meter with an actual multiphase flow through it, a flow loop was used. This is a facility capable of carrying solids-water flows of a type relevant to the present research investigation at different flow rates (for both solids and water) and different solids volume fractions. In addition, the working section of the flow loop could be positioned at varying inclinations to the vertical including, $0^o, 15^o$ and 30°, to enable the non-uniform flows described in Section 1.2 to be established. The loop was also instrumented for providing reference measurements of the following flow parameters:

1. Mean solids volume fraction in the working section, $\bar{\alpha}_{s,ref}$

2. Mean solids velocity in the working section, $\bar{u}_{s,ref}$.

3. Solids volumetric flow rate, $Q_{s,ref}$.

4. Water volumetric flow rate, $Q_{w,ref}$.

The equipment used to make these reference measurements, to which the measurements taken with the ICC will be related, is described in Section 6.3. The flow loop system used in this study was already in existence at the University of Huddersfield. This system was taken and enhanced for the present project, extending its capabilities to multi-phase flows which included solids in water flows, and flows at different angles to the vertical. Also the devices for making reference measurement were incorporated into the new system, see Figures 6-1 and 6-2 for a schematic diagram and photograph of the flow loop system respectively.
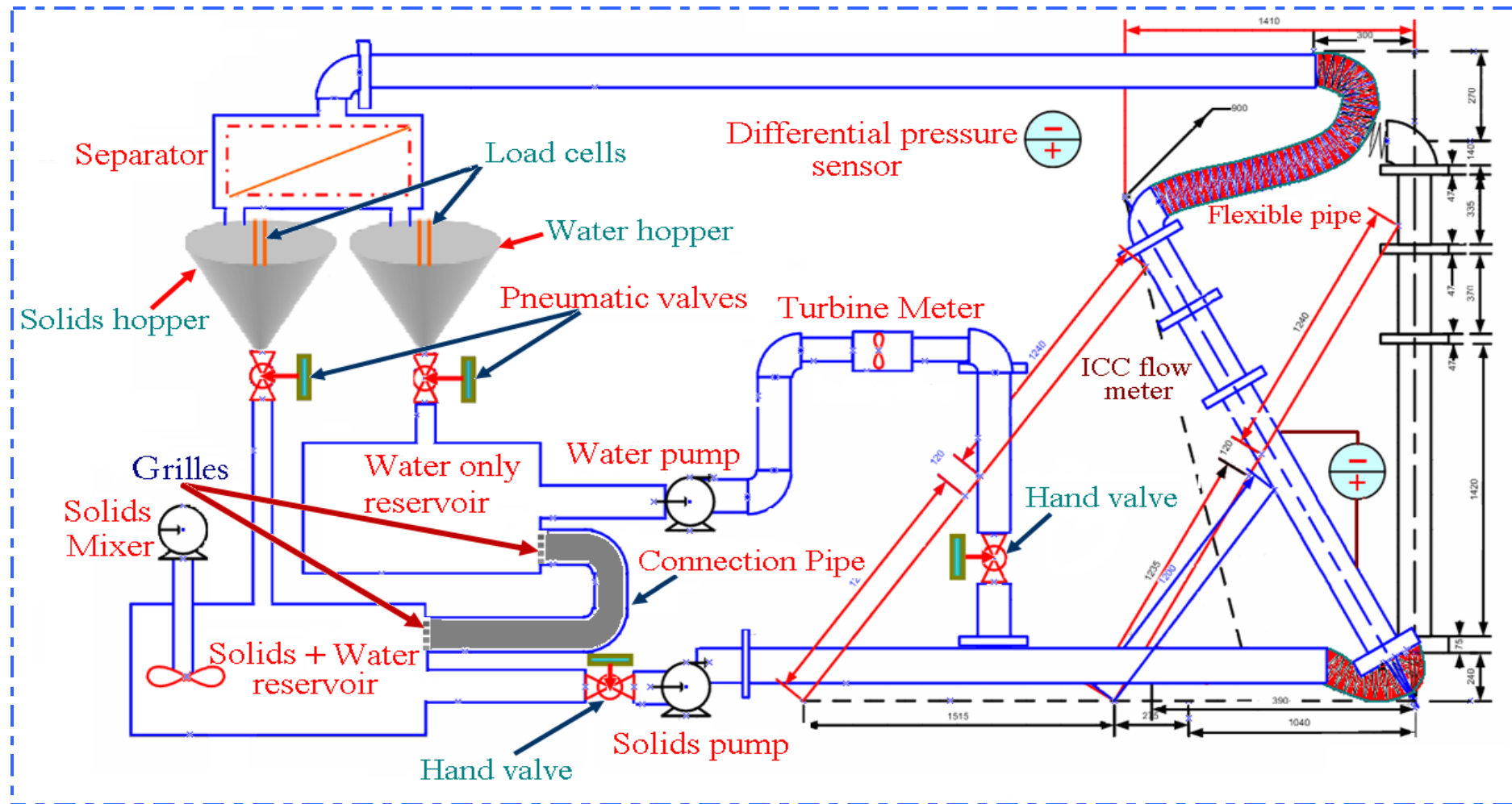
Figure 6-1: Schematic diagram of the University of Huddersfield flow loop system for multiphase flow (the working section is shown at two angles of inclination)
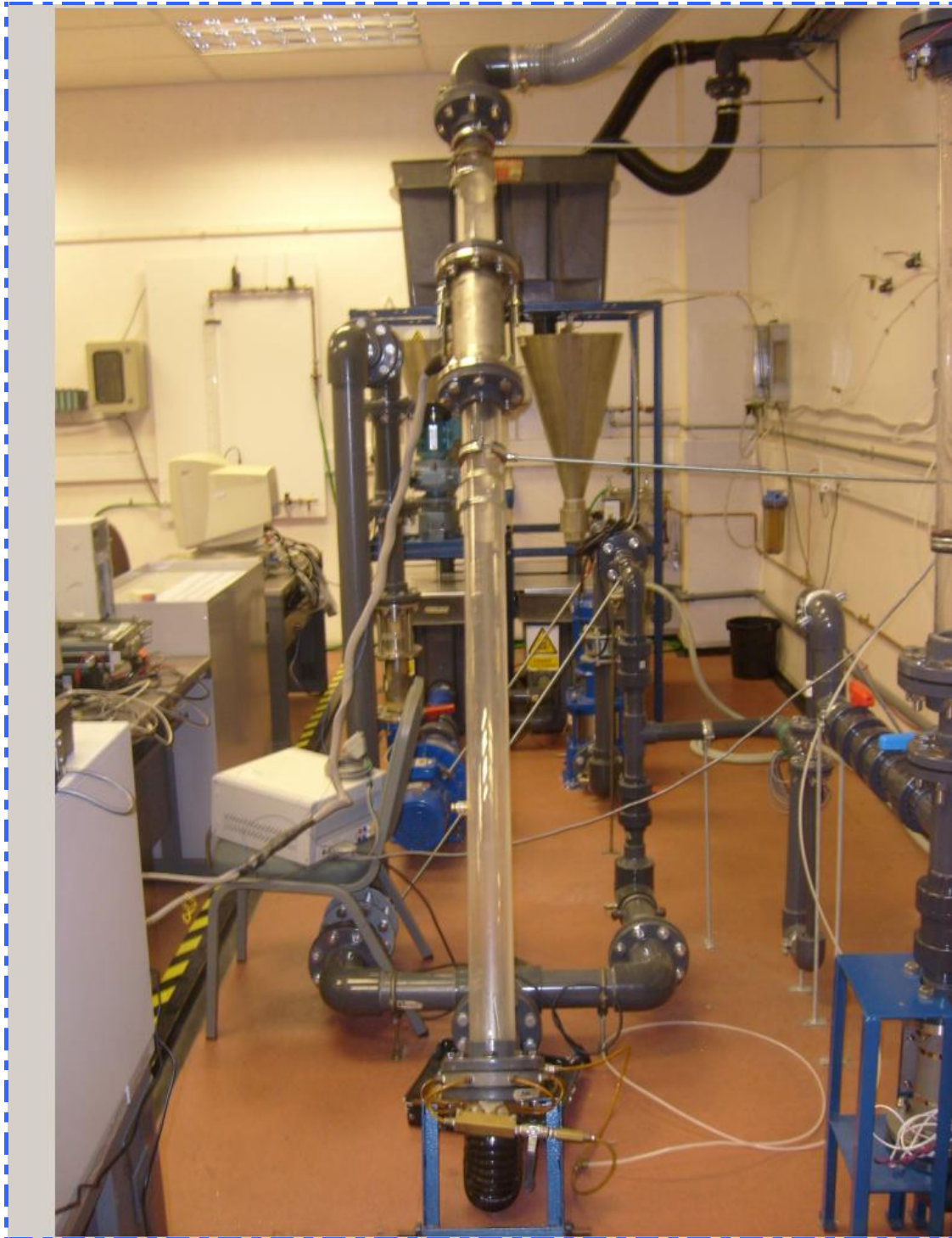
Figure 6-2: Photograph of the University of Huddersfield flow loop system for multiphase flow.

6.2   Flow capabilities of the multiphase flow loop

The flow loop is designed to provide flows with water as the continuous phase. In this work the dispersed phase consisted of solid plastic spheres of 5mm diameter and density of 1340.8 kg m^{-3}. The working section is so arranged that it can be positioned to give upward flows which are either vertical or inclined at an angle to the vertical. For the current investigation inclinations of $30^o, 15^o$ and 0° degrees to the vertical were used. However, it is possible to set the system for other inclinations if required.

For the current investigation the total length of the working section in which the ICC was installed was1.68m distance from inlet. The working section had an 80 mm inside diameter. The ratio of pipe length to pipe diameter meant that fully developed flow were not established at the ICC. However fully developed inclined solids-water flow is not well define in the literature. The flow never actually stabilizes because of the presence of intermittent K-H structures. The average flow properties at any point in the cross section were averaged over a period of about 1 minute without varying the position of the ICC. But this is not important because the intention is for the ICC device to be able to accurately meter whatever solids-liquid flow passes through it. The ICC section was attached near to the top of the pipe as shown in Figure 6-2. The electrode assembly was configured as shown in Figures 3-1 and 3-2 so that the axial separation of the electrode arrays, was 50 mm.

A Honeywell ST-3000 differential pressure (ΔP) sensor was included in the flow loop working section to provide a reference measurement of the solids volume fraction $\overline{\alpha}_{s,ref}$. The device measures the differential pressure across a 1m length of the working section (see Section 6.3.3).based on the pressure difference across a piezoelectric membrane, and is shown in Figure 6-1. A flushing system ensures that no air can become trapped in either the transducer or the measurement lines.

The solids particles are pumped from a reservoir, containing water and solids, using a multiphase pump which pumps the required mixture of solids and water through the system. The solids-water mixture in the solids reservoir is maintained in a homogeneous condition by a mixer which was switched on whenever the multiphase solids-liquid flow was circulating. After flowing upwards through the working

section, the multiphase mixture is conveyed to a separator where the water and solids are separated. The solids pass, via a conical hopper, to the solids holding tank, and the water passes via a second conical hopper, to the water tank. Each of the hoppers has a pneumatically actuated ball valve at its base. Each hopper was suspended by a load cell which measured the mass of the hopper and its contents. The load cells and the valve control system are interfaced to a PC. By closing the valves at the base of the hoppers and recording the time taken for a given mass of material to collect in the hopper the mass flow rate of that material can be calculated. Provided the solids and water densities are known, reference values $Q_{s,ref}$ and $Q_{w,ref}$ of the volumetric flow rates of the solids and the water respectively are readily calculated from the mass flow rates of solids and water. The grey shaded pipe section (see Figure 6-1) between the two reservoirs is to ensure the water level is the same in both reservoirs, thus ensuring that the water from the water hopper could flow into the solids-water reservoir. Separation grilles prevented solid particles from passing into the water reservoir.

In order to increase the range of water volumetric flow rates that can be used, and also to vary the solids volume fraction in the flow loop working section, water could also be pumped separately through the working section using a vertical multistage in-line centrifugal pump from a second reservoir containing water only. This water flow passes through a turbine meter to give the additional water flow rate. By using the two pumps together both the solids flow rate $Q_{s,ref}$ and the water flow rate $Q_{w,ref}$ can be independently set in the working section. Note that when both pumps and both reservoirs are used together reference values of the water and solids volumetric flow rates are obtained from the hopper valve/load cell systems described above.

6.3   Reference measurement devices

On this flow loop reference measurement devices were used including hopper/load cells for measuring the solids and water volumetric flow rates, a differential pressure sensor for measuring the global dispersed phase volume fraction and a turbine meter for measuring volumetric liquid flow rate from the "water only" reservoir. The turbine meter was used to calculate the working section fraction factor (see Section 6.3.2).

These reference measurement devices had to be calibrated. The following sections describe in detail the calibration procedure.

6.3.1 Hopper load cell system

$Q_{s,ref}$ and $Q_{w,ref}$ are measured gravimetrically. The multiphase flow passes through a separator, see Figure 6-1, which separates the different phases into conical stainless steel hoppers, each with a pneumatic ball valve at the bottom. Each hopper is suspended by a load cell which measures the total mass of the hopper and its contents. Both the load cells and the valves at the base of each hopper are interfaced with a PC. At suitable times the valves in the bases of the hoppers are shut and the load cell readings taken to obtain the weight of each hopper and its contents. After a convenient time, the weight of each hopper was measured again and, by simple subtraction, the mass of material which had flowed into each hopper could be calculated. For a given hopper the volumetric flow rate Q of the material into that hopper is given by:

$$Q = \frac{M}{T\rho} \qquad\qquad 6\text{-}1$$

where: M is the mass of material flowing into hopper in time T, and ρ is the density of the material.

For the water hopper the water volumetric flow rate is given by:

$$Q_{w,ref} = \frac{M_w}{T\rho_w} \qquad\qquad 6\text{-}2$$

For the solids hoper the volumetric flow rate is given by:

$$Q_{s,ref} = \frac{M_s}{T\rho_s} \qquad\qquad 6\text{-}3$$

where: M_w and M_s is the mass water flow rate and mass solids flow rate respectively.

A control program was used to control the pneumatic valves at the bases of the hoppers, to automatically obtain readings from the load cells, and to calculate $Q_{s,ref}$ and $Q_{w,ref}$ at intervals during the experimental testing. After time T had elapsed, the

valves at the bases of the hoppers were opened again to release the material into the appropriate reservoirs.

The load cells were calibrated twice during this project, firstly before the experimental testing began and secondly after the experimental testing was complete. This gave a check on drift in the calibration. The calibration procedure was to incrementally add known masses of water to each of the hoppers, and to record the resulting output from each hopper load cell. For each hopper the mass was added in equal increments for the full range of the load cells, 0kg to 40kg. To ensure better accuracy the procedure was carried out three times for each hopper and the results averaged.
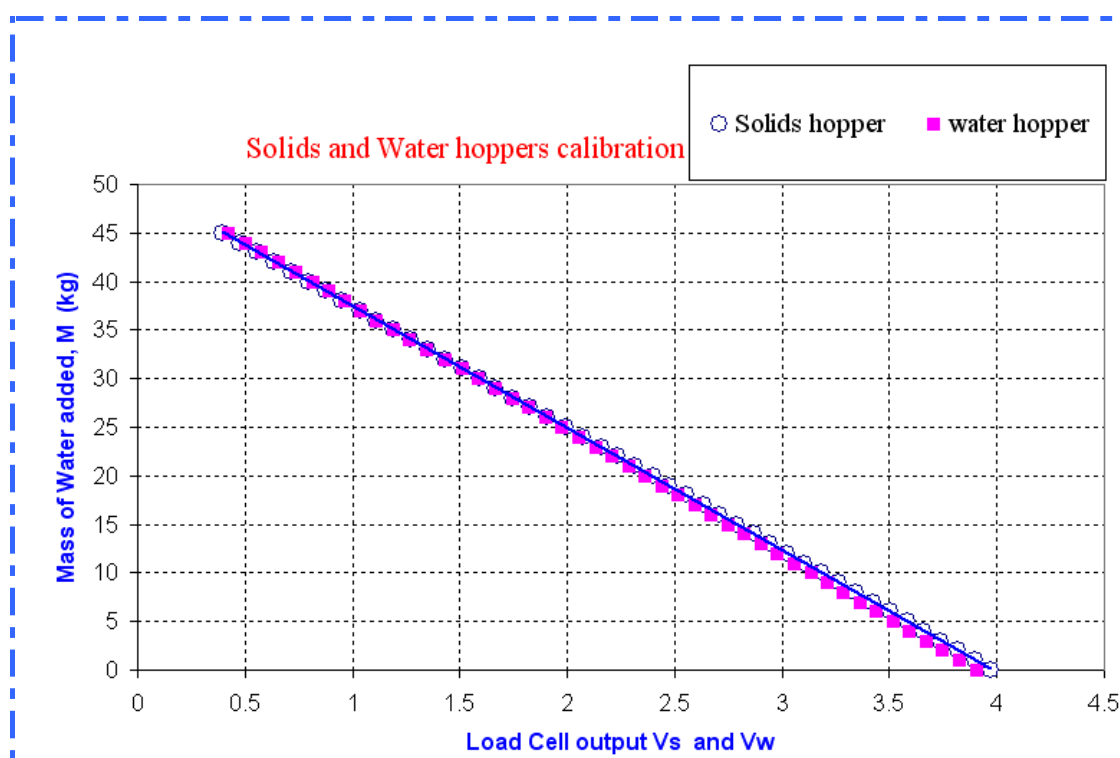
Figure 6-3: Solids and water hoppers calibration

Figure 6-3 shows the hopper calibration curves obtained (note that the output voltage from each load cell decreased as the hopper mass increased). Both load cells showed excellent linearity with minimal differences between the three tests. Simple linear regression using MATLAB gave the first order relationships between the mass in each hopper and the recorded voltages from the appropriate load cell. These equations were integrated into the gravimetric flow measurement control program procedures used during the flow loop tests (see Section 6.3.2).

Calibration was checked at intervals by adding a known mass of water to each hopper and checking that the response of the load cell fell on the calibration curve in Figure 6-3. Equation 6-4 shows the relationship between the mass M_S of material in the solids hopper and the load cell output voltage V_S. Whilst Equation 6-5 shows the relationship between the mass of material M_W in the water hopper and the load cell output voltage V_W from the water hopper load cell.

$$M_S = 50.464 - 12.921\,V_S \qquad\qquad 6\text{-}4$$

$$M_W = 49.974 - 12.553\,V_W \qquad\qquad 6\text{-}5$$

The load cell systems were set up in such a way that Equations 6-4 and 6-5 enabled the masses M_S and M_W of material inside the solids and water hoppers to be determined independent of the mass of each hopper and the mass of the valve at the base.

6.3.2 Turbine meter

The turbine meter is installed in the liquid line of the flow loop (see Figure 6-1). It can be used to give the reference volumetric water flow rate measurement, $\overline{Q}_{w,t,ref}$, delivered by the centrifugal pump from the "water only" reservoir and this was used to calculate the pipe friction factor (see Section 6.3.4). The readings of the turbine meter itself were checked by comparing them to measurements taken using the water gravimetric hopper (when water only was flowing). The purpose of measuring the pipe fraction factor is to compensate the reference measurement of the solids volume fraction from the dp cell, see section 6.3.3.

The water volumetric flow rate, $\overline{Q}_{w,t,ref}$, from the turbine meter was obtained by determining the speed of rotation of the turbine. With turbine meters, the rotational frequency f is directly proportional to the water flow rate over a specified range of operation see Equation 6-6.

$$\overline{Q}_{w,t,ref} = Kf \qquad\qquad 6\text{-}6$$

where $\overline{Q}_{w,t,ref}$ is the water volumetric flow rate, f is the rotational frequency of the turbine meter, and K is the turbine meter factor. K is known to vary over the life of the meter, for example if the meter begins to wear. However, it can be said that over

the duration of this project there was no detectable change in K due to wear. It is also known that the meter factor is specified constant over only a specified range of flow rates, but the device was always used within this specified flow rate range.

The method used for the calibration of the turbine meter was a simple comparison with the mean reference water flow rate $Q_{w,ref}$ recorded by the gravimetric flow measurement system. The turbine meter was calibrated at both the start and end of the project and no noticeable change in K was found. The calibration curve for the full range of flow rates used in the flow loop system is shown in Figure 6-4. This curve gave good agreement with the factory supplied meter factor over the specified range for the turbine meter.
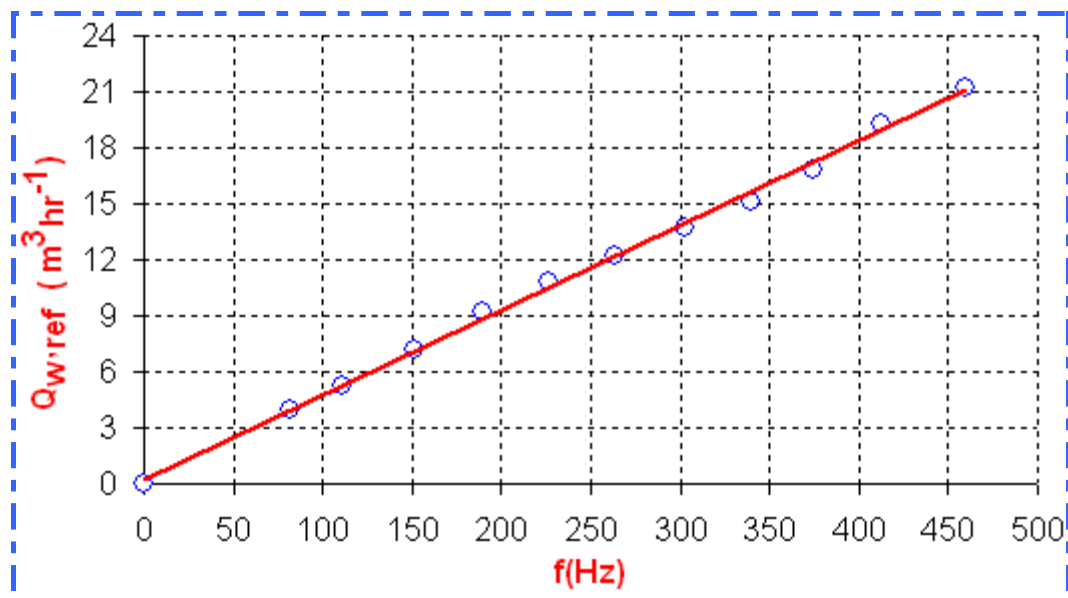
Figure 6-4: Turbine meter calibration

In determining the best straight line for the measured points the observed physical reality must be the important consideration. It was quite clear from the measurement procedure that when no flow passed through the meter (f = 0) the reading on the meter was zero. That is there was no "zero error". Thus the best fit straight line had to pass through the point (0,0). This is quite easy to achieve and there are any number of software packages readily available that can achieve this. Using [www.savetman.com (accessed 21/01/10)] it was shown that the best fit straight line passing through the measurement points and (0,0) had K= 0.0455m^{3}h^{-1}Hz^{-1}. The equation for the line is:

$$Q_{w,ref} = 0.0455 \, f \ m^3 h^{-1} Hz^{-1}$$

Figure 6-4 shows a clear linear relationship between f and $Q_{w,ref}$, as the flow rate increased. The factory supplied meter factor for this meter was $0.0455 m^3 h^{-1} Hz^{-1}$ over a design range of $3.41 m^3 h^{-1}$ to $40.88 m^3 h^{-1}$. The best fit line calculated from the calibration experiments gave a meter factor of $0.0455 m^3 h^{-1} Hz^{-1}$. Then the calculated turbine meter factor from the calibration experiment agreed with the factory calibration to four decimal places.

6.3.3 Differential pressure sensor

A schematic representation of the differential pressure cell (dp cell) is shown in Figure 6-5.
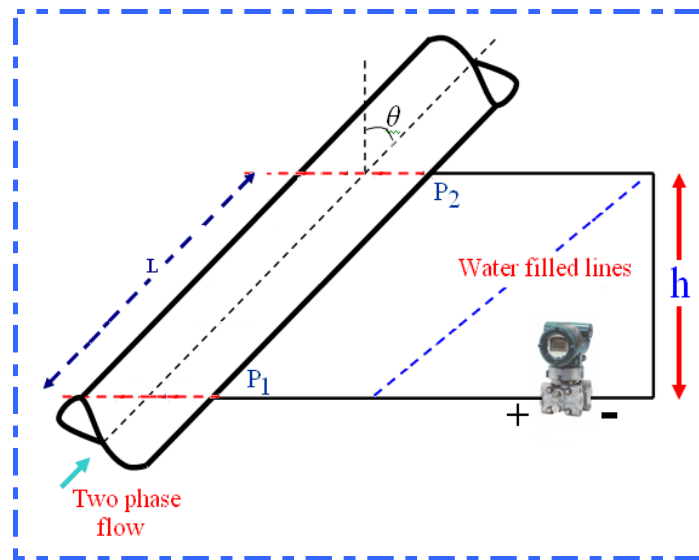
Figure 6-5: Schematic of the differential pressure cell installation

With reference to Figure 6-5, if the time averaged properties of the multiphase flow in the pipe are steady then it is possible to write;

$$P_1 = P_2 + \rho_m g \, L\cos\theta + F \qquad\qquad 6\text{-}7$$

where: P_1 and P_2 are the upstream pressure and downstream pressures respectively, L is the length of pipe under consideration, F is the frictional pressure loss along the length of pipe, ρ_m is the mean density of the flowing fluid (which is assumed

constant) and g is 9.81ms^{-2}. Since the pipe is inclined at an angle θ to the vertical, and the length of the pipe is L the corresponding vertical height between the pressure tapping is $h = L\cos\theta$

Consider the case where only water flows; we have Equation 6-7

$$\Delta P = P_1 - P_2 - \rho_w g\, L\cos\theta \qquad\qquad 6\text{-}8$$

where: ΔP is the differential pressure drop along the length of the pipe due to frictional losses in the water flow measured by the dp cell, and ρ_w is the water density.

The density of the mixture can be expressed as:

$$\rho_m = \overline{\alpha}_{s,\,ref}\; \rho_s + (1 - \overline{\alpha}_{s,\,ref})\,\rho_w \qquad\qquad 6\text{-}9$$

where: $\overline{\alpha}_{s,\,ref}$ is the mean solids volume fraction obtained by the dp cell.

Combining Equations 6-7 and 6-8 , gives:

$$\Delta P + \rho_w g\, L\cos\theta = \rho_m g\, L\cos\theta + F \qquad\qquad 6\text{-}10$$

Equation 6-10 can be re-arranged to give Equation 6-11:

$$\rho_m - \rho_w = \frac{\Delta P - F}{g\, L\cos\theta} \qquad\qquad 6\text{-}11$$

From 6-9 and 6-11

$$\overline{\alpha}_{s,\,ref}\; \rho_s + \rho_w - \overline{\alpha}_{s,\,ref}\; \rho_w - \rho_w = \frac{\Delta P - F}{g\, L\cos\theta} \qquad\qquad 6\text{-}12$$

Equation 6-12 can be re-arranged to give Equation 6-13:

$$\overline{\alpha}_{s,\,ref} = \frac{\Delta P - F}{g\, L\cos\theta\, (\rho_s - \rho_w)} \qquad\qquad 6\text{-}13$$

Before discussing frictional losses in multiphase flows it is necessary to discuss frictional losses in single-phase liquid flow. For the well-known case of viscous laminar flow shear resistance is the cause of frictional pressure losses. Of course, the higher the viscosity the greater the shear forces (Benedict, 1980; Massey, 1990).

In a turbulent flow the energy needed to create eddies and vortices results in a so-called eddy viscosity which causes the frictional pressure losses in turbulent flow to be much greater than for laminar flow. These eddies interact with the surface of the pipe causing additional pressure losses. In a solids-liquid flow other interactions such as particle-particle, particle-fluid, and particle-wall interactions occur (Roco, et. al., 1983). With upward vertical flow the turbulent eddy patterns will be modified which, in turn modifies the shear stresses in the flow.

There is a wide range of opinion on the effect of the addition of solids to the flow. Govier and Aziz (1972) have reported that for vertical flow the addition of small particles of diameter of less than one hundredth of a mm has minimal effect. They claim that in such circumstances a reasonable approximation of the pressure losses can be obtained the friction factor for the carrier fluid alone. Mizukami, et. al., (1992) reported the same findings for solids-gas flow. Durand and Newitt (see Govier and Aziz, 1972) found the same effect with inclined flows provided the particles did not settle out, but remained suspended in the flow. Interestingly, it has been found for two-phase flow of gas in liquid and fine particles in liquid that frictional pressure losses are lower than in a single-phase flow, Serizawa, et, al., (1975). Roco and Shook (1983) have reported that the settlement of solid particles onto the pipe wall in inclined flow will decrease the pressure drop in the flow.

However, a number of authors have reported that frictional pressure losses in two-phase flow as higher than for single-phase flows provided the solids volume fraction >0.15 (Chen and Kadambi, 1994; Turian and Yuan 1977; Akagawa, et. al., 1989). Beggs and Brill (1973) reported that such frictional pressure losses could be up to three times those in single-phase flow but that that the pressure loss decreased as the mixture velocity increased. It was generally agreed that the pressure drop due to frictional losses is much less than pressure losses due to the change in potential energy of the flow see Akagawa, et. al., (1989).

On the basis of the brief literature review above it was decided that, to a first approximation, it would be acceptable to assume that a single-phase friction factor could be used to represent the frictional losses in the present investigation. The frictional losses in both laminar and turbulent single-phase flow were quantified by Darcy, and the Darcy-Weisbach equation is now considered the best empirical relation for pipe-flow resistance. The pressure loss according to the Darcy-Weisbach as reported by Massey (1990) for a circular pipe carrying only water is:

$$F = \frac{2\rho_W L R \bar{u}_w{}^2}{D} \qquad\qquad 6\text{-}14$$

Here R is an empirical friction factor which will depend largely on whether the flow is turbulent or not and the surface roughness of the wall of the pipe, $\bar{u}_w$ is the mean flow velocity, D is the pipe diameter (80mm), ρ_W is the density of the fluid (ρ_{water} = 1000kgm^{-3}), L is the length of the pipe and θ is the angle the pipe makes with the vertical. A number of practical methods have been developed to estimate R, see Massey (1990). But these are not easy to use because it is difficult to quantify such factors as the pipe roughness. It is usually advisable to determine the friction factor experimentally for each flow condition and each application. This is what was done in the current investigation.

Here R is an empiric friction factor which will depend largely on whether the flow is turbulent or not and the surface roughness of the wall of the pipe, u is the mean flow velocity, D is the pipe diameter (80mm), and ρ_W is the density of the fluid (ρ_{water} = 1000kgm^{-3}). A number of practical methods have been developed to estimate R, see Massey (1990). But these are not easy to use because it is difficult to quantify such factors as the pipe roughness. It is usually advisable to determine the friction factor experimentally for each flow condition and each application. This is what was done in the current investigation.

In a single-phase liquid flow:

$$\Delta P = F \qquad\qquad 6\text{-}15$$

Rearranging Equation 6-14 and using Equation 6-15 gives:

$$R = \frac{D\,\Delta P}{2\rho_W L\,(\bar{u}_W^{\,2})}$$

6-16

Using Equation 6-16 it is now possible to experimentally determine the relationship between R and $\bar{u}_W$ for the flow loop working section in the present investigation. Single-phase water flows were set up with known $\bar{Q}_{W,t,ref}$ measured using the turbine meter described in Section 6.3.2. From $\bar{Q}_{W,t,ref}$ it is possible to calculate $\bar{u}_W$ the mean water velocity in the pipe using Equation 6-17 where A is the cross-sectional area of the working section. The value of R was calculated using Equation 6-16 and using the measured differential pressure ΔP from the dp cell.

$$\bar{u}_W = \frac{\bar{Q}_{W,t,ref}}{A}$$

6-17

Equation 6-16 enables the relationship between R and $\bar{u}_W$ to be determined experimentally for the flow loop working section. The first step was to use only water in the system and to measure a volume flow rate, $\bar{Q}_{W,t,ref}$, using the turbine meter. $\bar{u}_W$, the mean water velocity in the pipe could be calculated immediately.

By combining the measured pressure difference in the working section, ΔP, with Equation 6-16 it was possible to calculate the value of R for these flow conditions. The resulting curve is shown in Figure 6-6. A least squares fit sixth order polynomial approximation, Equation 6-16, was used to relate R to $\bar{u}_W$.

$$R = 0.597\,\bar{u}_W^{\,6} - 2.8708\,\bar{u}_W^{\,5} + 5.4995\,\bar{u}_W^{\,4} - 5.3911\,\bar{u}_W^{\,3} + 2.8645\,\bar{u}_W^{\,2} - 0.791\,\bar{u}_W + 0.0976$$

6-18
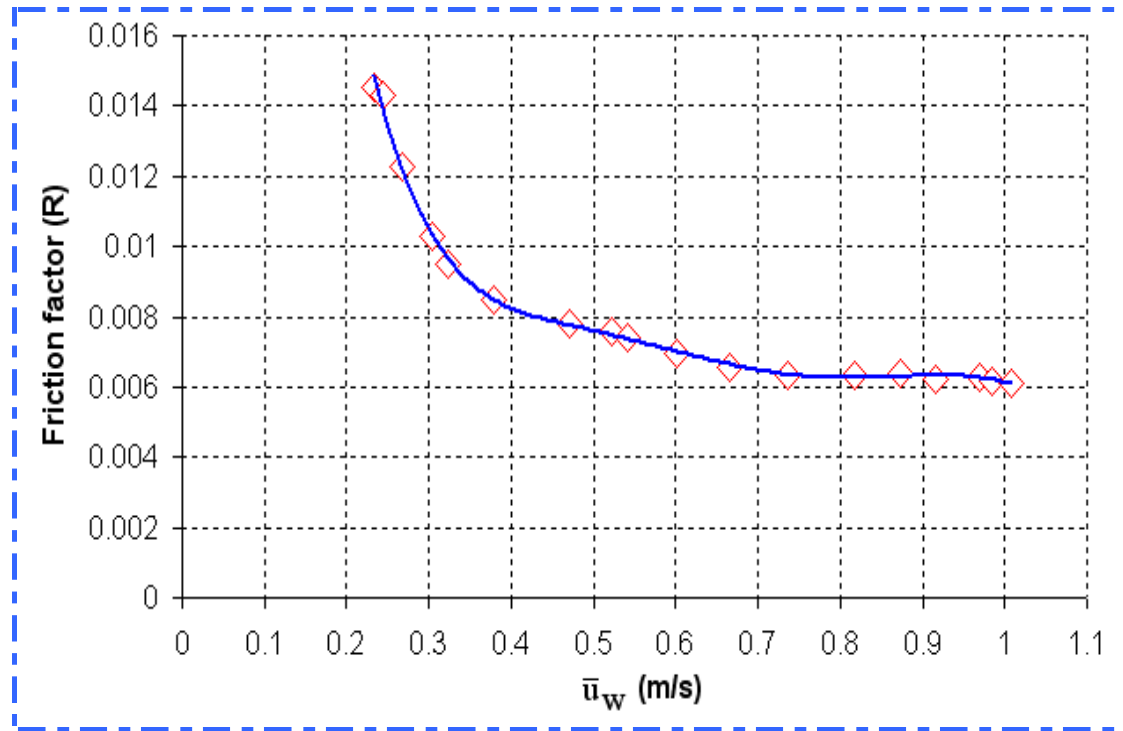
Figure 6-6: Variation of friction factor, R, with $\bar{u}_w$

Figure 6-6 shows the experimentally determined values of R. The shape of the curve shows the accepted increase in friction factor R as the flow velocity decreases $\bar{u}_w$, see Massey (1990) and Cory, PhD thesis (1999).

For two phase solids water flows F was obtained using

$$F = \frac{2\rho_w\, L\, R\, u_h^{\ 2}}{D} \qquad\qquad 6\text{-}19$$

where;

$$u_h = \frac{Q_{w,\,ref} + Q_{s,\,ref}}{A} \qquad\qquad 6\text{-}20$$

And the value of R that was used was obtained from Equation 6-18 by subtitling u_h for $\bar{u}_w$. The value of F obtained from Equations 6-19 and 6-20 above was used in Equation 6-13 to enable $\bar{\alpha}_{s,\,ref}$ to be calculated in two phase solids liquid flows.

6.4   Experimental procedure

The experimental procedure used in the present investigation can be divided into three sections. These are the initial data acquisition, followed by initial and secondary data analysis.

6.4.1 Experimental data acquisition

The ICC device was installed in the solids-water multiphase flow loop at the University of Huddersfield as shown in Figure 6-2. In the current investigation measurements were acquired from the ICC using appropriate electrode configurations (see Tables 4-2, 4-3 and 4-4). This operation was carried out using the ICC control switching circuits and data acquisition software described in Chapter 3. The spatial locations of the centre of action for each rotational position for Config-I, II and III are listed in Tables 4-5 and were arranged as shown in Figure 4-17. In this study, data were collected for many different flow conditions. These flow conditions were based on various water and solids flow rates (see Table 6-1). Nine flow conditions were used for each of **three** different pipe inclination ($0^\circ, 15^\circ$ and 30°). Table 6-1 shows the range of solids-liquid flow conditions for the three inclination angles. Each of these flow conditions were applied for each rotational position of each of electrode configurations I,II and III as listed in Tables 4-2, 4-3 and 4-4.

Table 6-1: Flow rates used in the current investigation

Flow condition no:	Angle of inclination of test pipe	Solids volumetric flow rate, $Q_{s,ref}$ (m³h⁻¹)	Water volumetric flow rate, $Q_{w,ref}$ (m³h⁻¹)
1	0°	0.696	4.25
2	0°	0.750	5.49
3	0°	0.724	6.12
4	0°	1.188	6.18
5	0°	1.225	6.45
6	0°	1.183	6.51
7	0°	2.229	5.87
8	0°	1.998	7.98
9	0°	1.974	9.35
10	15°	0.613	9.45

11	15°	0.731	10.91
12	15°	0.704	12.43
13	15°	1.187	12.82
14	15°	1.104	13.94
15	15°	1.010	15.43
16	15°	1.631	14.05
17	15°	1.587	15.26
18	15°	1.623	16.94
19	30°	0.360	7.218
20	30°	0.591	10.79
21	30°	0.549	12.13
22	30°	0.951	12.47
23	30°	1.010	14.06
24	30°	0.959	15.66
25	30°	1.410	14.10
26	30°	1.651	15.96
27	30°	1.623	17.12

The ICC device was configured as a dual-plane system. Measurements were simultaneously acquired from the two electrode arrays. After analysis the measurements gave profiles of the conductivity distribution within the flow cross-section. Variations in conductivity recorded for a given electrode arrangement in the first array were cross-correlated with variations in conductivity recorded for the same electrode arrangement at the second array. This allowed a profile of the solids velocity to be calculated for each flow condition. Selection of the region of flow to be interrogated was performed by an electrode selection mechanism for both electrode arrays A and B (see Section 3.7).

In order to obtain a profile of the solids volume fraction the conductivity measurements acquired from **one** array of electrodes were reconstructed using the technique described in sections 3.10 and 6.4.3.2.

6.4.2 Initial data analysis

As described in Section 3.7 the ICC flow meter is controlled by an electrode selection switch circuit which allow selection of each rotational position listed in Tables 4-2, 4-3 and 4-4. For each rotational positions selected (for Configs-I, II and III), a data set

was collected for 60 seconds. These data sets were then written to a text file in MATLAB. This text file contain two sets of data, the first set was the data obtained from the first array and in the second set the data obtained from second array (see Section 3-9). A series of MATLAB codes were written to carry out some initial analysis on this data (see Appendix Code-1).

The measurement signals obtained by the ICC using the eight rotational positions for each electrode configuration listed in Tables 4-2, 4-3 and 4-4 were then cross-correlated using a cross-correlation function in MATLAB. The time delay, t_p, of the peak of the resulting cross correlation function of the signals obtained from the sensor arrays at A and B, was then written to a text file. This procedure was repeated for each different rotational position listed in Tables 4-2, 4-3 and 4-4 during the experimental testing.

6.4.3 Secondary data analysis

6.4.3.1 Local solids axial velocity

In order to calculate the local axial solids velocity, u_S, it is necessary to measure the time taken for the particles to pass between array A and array B of the ICC. u_S can be obtained by Equation 6-21 where L is the distance between the two arrays.

$$u_S = \frac{L}{t_p} \hspace{4cm} \text{6-21}$$

The local axial solids velocity profiles results obtained by ICC are presented for the test pipe inclined angles at 0°, 15° and 30° to the vertical, eight different rotational positions were set individually for both arrays A and B using Config-I,II and III as listed in Tables 4-2, 4-3 and 4-4. For each rotational position data were collected for 60 seconds. This process was repeated for twenty seven flow conditions (see Table 6-1).

6.4.3.2 Local solids volume fraction

In order to calculate the local solids volume fraction α_S using Maxwell's relationship (Maxwell, J.C. (1873)) it is necessary to use the measured values of the local solids-

212

water mixture conductivity obtained from the ICC device σ_m and the water conductivity σ_w as shown in Equation 6-22 which is reproduced here.

$$\alpha_S = \frac{1 - \dfrac{\sigma_m}{\sigma_w}}{0.5 \left(1 + \dfrac{\sigma_m}{\sigma_w}\right)} \qquad\qquad 6\text{-}22$$

In the current investigation, the solids volume fraction profiles were obtained from **one** electrodes array only (Array B) see Figure 3-9. The technique presented in Section 3-10 was performed for each configuration listed in Tables 4-2, 4-3 and 4-4, eight different rotational positions for each Config-I, II and II were defined and data were collected for 60 seconds for each rotational position.

6.4.3.3 Integrated global measurements of solids volume fraction, solids axial velocity and solids volumetric flow rate from the local probe

The distributions of the local solids volume fraction and local axial velocity obtained by the ICC device can be used to estimate $\overline{\alpha}_{s,meas}$, $\overline{u}_{s,meas}$ and $Q_{s,meas}$: the mean solids volume fraction, the mean solids axial velocity and the solids volumetric flow rate respectively. In order to calculate the mean global values of these flow parameters it is necessary to integrate the local values determined in the previous two sections. This is done using Equations 6-23, 6-24 and 6-25:

$$\overline{\alpha}_{s,meas} = \frac{1}{A} \int_A \alpha_s dA \qquad\qquad 6\text{-}23$$

$$\overline{u}_{s,meas} = \frac{\int_A \alpha_s u_s dA}{\int_A \alpha_s dA} \qquad\qquad 6\text{-}24$$

$$Q_{s,meas} = \int_A \alpha_s u_s dA \qquad\qquad 6\text{-}25$$

where: A represents the cross section area of the pipe.

6.4.3.4 Reference measurement

Reference measurements of $Q_{s,ref}$ and $Q_{w,ref}$ were obtained as described in Section 6.3.1. To calculate reference measurements of $\overline{\alpha}_{s,ref}$ see Section 6.3.3 it was necessary to use the differential pressure data. It is also now possible to calculate the reference solids axial velocity, $\overline{u}_{s,ref}$.

$$\overline{u}_{s,ref} = \frac{Q_{s,ref}}{A\overline{\alpha}_{s,ref}} \qquad\qquad 6\text{-}26$$

It should be noted at this point that these reference measurements of $\overline{\alpha}_{s,ref}$, $\overline{u}_{s,ref}$ and $Q_{s,ref}$ are global values and can only be compared with the integrated values of the ICC device measurements as shown in Section 6.4.3.3.

Chapter 7   EXPERIMENTAL RESULTS

This chapter reports the test results obtained using the ICC flow meter and the experimental methodology described in Section 6.4. The ICC was used to measure the velocity of the solids volume fraction using cross-correlation over the 'effective sensing regions' associated with the different electrode configurations described in Tables 4-2, 4-3 and 4-4. The range of solids-liquid flow measurement conditions are described in Section 7.1. Section 7.2.2 presents the local axial solids velocity profiles obtained by the ICC meter. Sections 7.2.3 and 7.2.4 show the 3D profiles of the local axial solids velocity and discuss the local axial solids velocity obtained by the ICC respectively. Section 7.2.5 shows the results of the local axial solids volume fraction results obtained by the ICC system. Sections 7.2.6 and 7.2.7 show the 3D profiles of the local axial solids volume fraction obtained by the ICC and discuss the local axial solids volume fraction profiles respectively. Finally, In Section 7.3, the results have been compared with the values obtained from the reference measurement devices.

7.1 Flow conditions tested with the ICC meter

For each flow condition tested with the ICC meter, the time averaged reference values obtained ($Q_{s,ref}$, $Q_{w,ref}$, $\overline{\alpha}_{s,ref}$ and $\overline{u}_{s,ref}$), their definitions and the methods of measurement are shown in Table 7-1.

Table 7-1: Measured parameters and measurement nomenclature

Parameter	Definition	Method of measurement
$Q_{s,ref}$	Reference solids volumetric flow rate	The time average solids volumetric flow over the experimental test run measured using the gravimetric hopper system as described in Sections 6.3.1.
$Q_{w,ref}$	Reference water volumetric flow rate	The time average water volumetric flow rate over the experimental test run measured using the gravimetric hopper system as described in Section 6.3.1.
$\overline{\alpha}_{s,ref}$	Reference solids volume fraction	The time average solids volume fraction over the experimental test run measured using pressure gradient method corrected for frictional pressure loss as described in Section 6.3.3.
$\overline{u}_{s,ref}$	Reference solids velocity	The time average solids velocity over the experimental test run measured by combining the solids volumetric flow rate and solids volume fraction measurements as described in Section 6.4.3.4.

Table 7-2 shows the reference flow conditions that were used in the experimental tests. Each experimental test took place on a separate occasion. Table 7-2 also shows the reference solids and water volumetric flow rates obtained from the reference devices (see Table 7-1) and the reference value of the mean solids volume fraction $\overline{\alpha}_{s,ref}$, obtained using the differential pressure measurement technique described in Section 6.3.3.

Table 7-2: Flow conditions used in the experimental study

Flow condition no:	Angle of inclination of test pipe	Solids volumetric flow rate, $Q_{s,ref}$ (m^3h^{-1})	Water volumetric flow rate, $Q_{w,ref}$ (m^3h^{-1})	Solids volume fraction $\overline{\alpha}_{s,ref}$ (ms^{-1})	Solids velocity $\overline{u}_{s,ref}$ (ms^{-1})
1	0°	0.696	4.25	0.16	0.244
2	0°	0.750	5.49	0.132	0.289
3	0°	0.724	6.12	0.121	0.33

4	0°	1.188	6.18	0.181	0.37
5	0°	1.225	6.45	0.171	0.4
6	0°	1.183	6.51	0.162	0.41
7	0°	2.229	5.87	0.29	0.43
8	0°	1.998	7.98	0.211	0.53
9	0°	1.974	9.35	0.18	0.61
10	15°	0.613	9.45	0.12	0.29
11	15°	0.731	10.91	0.13	0.31
12	15°	0.704	12.43	0.12	0.33
13	15°	1.187	12.82	0.19	0.35
14	15°	1.104	13.94	0.16	0.39
15	15°	1.010	15.43	0.15	0.41
16	15°	1.631	14.05	0.21	0.42
17	15°	1.587	15.26	0.20	0.44
18	15°	1.623	16.94	0.22	0.34
19	30°	0.360	7.218	0.09	0.22
20	30°	0.591	10.79	0.15	0.21
21	30°	0.549	12.13	0.09	0.34
22	30°	0.951	12.47	0.19	0.28
23	30°	1.010	14.06	0.15	0.37
24	30°	0.959	15.66	0.17	0.32
25	30°	1.410	14.10	0.19	0.41
26	30°	1.651	15.96	0.21	0.46
27	30°	1.623	17.12	0.18	0.51

7.2 Experimental results using the ICC meter

This section presents the local axial solids velocity and local solids volume fraction profiles results of the solids water flows as determined using the ICC meter, see Sections 7.2.1 and 7.2.2. The profiles are shown for vertical upward flows and upward flows inclined at 15° and 30° to the vertical. These profiles are presented for each of the twenty-seven flow conditions shown above in Table 7-2, using each of the eight different rotational positions of Configs-I, II and III, listed in Tables 4-2, 4-3 and 4-4. The profiles obtained of the local solids velocity and the solids volume fraction will be discussed in Sections 7.2.2 and 7.2.4 respectively.

7.2.1 Experimental procedure

The ICC flow meter was used in the solids-water multiphase loop, see Figures 6.1 and 6.2. In chapter 4, three electrode configurations are described: Config-I, Config–II and Config-III, see Tables 4-2, 4-3 and 4-4. The experimental procedure was as follows: Config-I, see Table 4-2, is the electrode arrangement where one electrode is excited, an adjacent electrode is the measurement electrode and the other six electrodes are earthed. There are thus eight different rotational positions that can be used to interrogate the flow for each of arrays A and B, see Figure 7-1. This configuration was used to measure the local solids velocity distribution by cross-correlating fluctuations in the measured conductivity at corresponding regions of the flow cross-section. The local solids volume fraction was measured using the conductivity of the mixture as measured by the ICC using the Maxwell equation (Maxwell, J.C. (1873)). The region of flow to be interrogated was selected by the choice of electrodes, which were the same for both array A and B. For example, to measure the solids velocity in the top of an inclined pipe, area H in Figure 7-1, electrode 6 was set as excitation, electrode 7 as measurement and the remaining electrodes were connected to ground. Similarly, to measure the solids velocity on the lower side, area A, electrode 2 was set as excitation and electrode 3 as measurement, and the remaining electrodes were set to ground. To be precise it is the areas of A and H near the circumference which would be interrogated, see Figure 4-15. By cyclic rotation of the excitation and measurement electrodes, **eight** rotational position were produced which interrogated the eight areas of the pipe in order. For each rotational positional in Config-I the measured solids velocity or volume fraction is plotted against the location of the centre of action (CoA) for that rotational position see Figures 7-3 to 7-29.
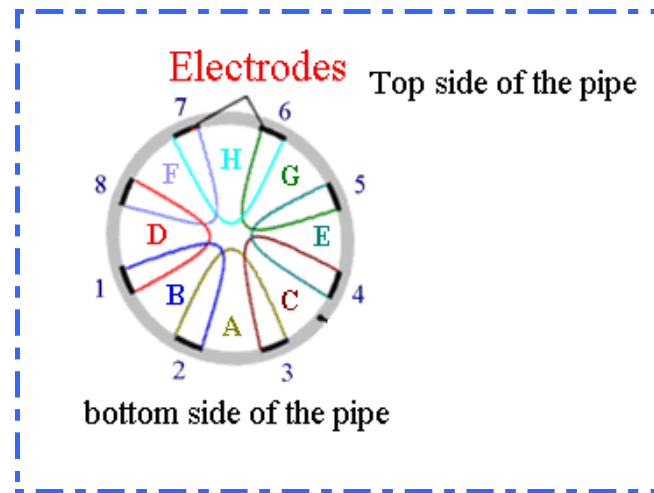
Figure 7-1: Single 8 electrodes array

Config-II, see Table 4-3 is where one electrode is excited, both adjacent electrodes are set as the measurement electrodes and the other five electrodes are earthed. Again there are thus eight different rotational positions that can be used to interrogate the flow for each of arrays A and B. With Config–II, the experimental procedure was similar to that for Config-I except that this electrode configuration increases the area of the region being interrogated (see Figure 4-16 (a) and (b)). Note the area being interrogated is twice that with Config-I. If we wanted to measure the local solids velocity in the lower side of the pipe electrode 2 was set as excitation and electrodes 1 and 3 as measurement, with all other electrodes set to ground for both arrays A and B. Here areas the outer portions of areas A and C will be interrogated, see Figure 4-16 (a and b). Once again by cyclic rotation of the excitation and measurement electrodes 8 rotational positions were produced which interrogated eight areas of the pipe in order.

Config-III, see Table 4-4 is where two adjacent electrodes are excited, the adjacent electrodes are set as the measurement electrodes and the other four electrodes were earthed. To measure the local solids velocity and local solids volume fraction in the lower side of the pipe electrodes 2 and 3 were set as excitation, and electrodes 1 and 4 as a measurement, and the remaining four electrodes were set to ground for both arrays A and B. Here those portions of the areas A, B and C nearest the circumference will be interrogated, see Figure 4-17 (a and b). Again there are 8 rotational positions.

Config-ψ represents a combination of Configs-I, II and III with the aim of overcoming the problem of insufficient definition of the flow in the cross-section. As explained earlier in Section 4.7, the CoA was calculated for Config-I, II and III for

each rotational position using the sensitivity distribution described in Chapter **four**. For each of Configs-I,II and III local solids velocity and local volume fraction at eight spatial locations, corresponding to the CoA of the eight rotational positions for the given configuration were determined. For Config-ψ we determine the solids velocity and the volume fraction at **twenty four** spatial locations corresponding to the CoA of the eight rotational positions for each of Config-I, II and III.

7.2.2 Local axial solids velocity profiles from the ICC

In this section the results measured using the ICC meter are presented for the test pipe inclined at 0°, 15° and 30° to the vertical. For all these results the y-coordinate lies along the longitudinal axis of the pipe from the lowest point on the pipe a cross a diameter to the opposite side (see Figure 7-2) and the x-axis is horizontal. A study of previous literature showed that the both local velocity and local volume fraction are principally a function of the y co-ordinate (and are essentially constant as the x co-ordinate varies for a fixed value of y). For this reason it was decided to plot volume fraction and velocity profiles against the y-coordinate of the Centre of Action. Figures 7-3 to 7-29 show the distribution of the measured solids velocity obtained from the ICC against the y-coordinate of the Centre of Action.
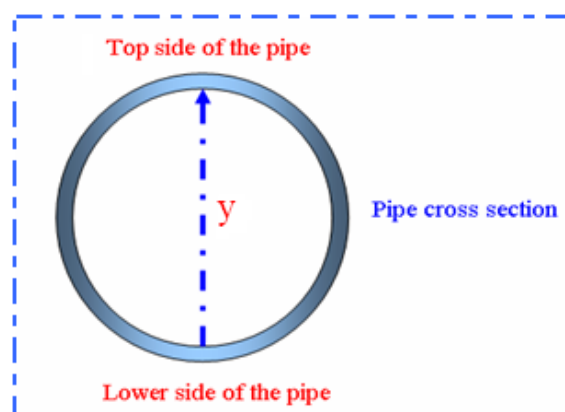
Figure 7-2: The position of the y axis relative to the pipe cross-section.

Figures 7-3 to 7-11 show the results obtained for flows in a vertical pipe. Figures 7-12 to 7-20 show the results for flows obtained when the pipe is inclined at an angle of 15° to the vertical. Finally, Figures 7-21 to 7-29 show the results for flows obtained when the pipe is inclined at an angle of 30° to the vertical. These results presented in this section show the measured local axial solids velocity plotted against Centre of

Action y-coordinate. Note that, for every flow condition reference values are given of (i) the mean solids volume fraction obtained by the differential pressure measurement technique (see section 6.3.3) (ii) the solids and water volumetric flow rates obtain by hoppers load cell (see section 6.3.1) (iii) the mean solids velocity(see section 6.4.3.4).

For each rotational position data were collected for 60 seconds. Data from both arrays were cross correlated to obtain the local axial solids velocity for a defined rotational position using the MATLAB code listed in Appendix (Code-6). This process was repeated for the twenty seven flow conditions listed in Table 7-1.

7.2.2.1 Local solids velocity profiles for upward flow in a vertical pipe

In each figure three sets of data are presented for Configs-I, II and III. Note that, in the vertical flow results (Figures 7-3 to 7-11) the plots also include the calculated reference solids velocity and reference water flow velocity, $\bar{u}_{s,ref}$ and $\bar{u}_{w,ref}$ respectively, and which are given by:

$$\bar{u}_{s,ref} = \frac{Q_{s,ref}}{A\bar{\alpha}_{s,ref}} \tag{7-1}$$

$$\bar{u}_{w,ref} = \frac{Q_{w,ref}}{A\left(1-\bar{\alpha}_{s,ref}\right)} \tag{7-2}$$

The vertical red dotted line represents $\bar{u}_{s,ref}$ and the vertical brown dotted line $\bar{u}_{w,ref}$. It can be seen from Figure 7-3 to 7-11 that the local axial solids velocity profiles appear flat across the pipe cross-section. Lucas et.al (1999, 2000) and Cory PhD thesis 1999 show a similar finding, that the local axial solids velocity profiles in vertical solids and water flows is flat across the cross the pipe section. This is an acceptable result because in the vertical flow the solids distribution over the pipe cross-section would be expected to be uniform, and this is what was visually observed. There is a small variation between the three defined configurations (Configs-I, II and III), however, the variation is within an acceptable range. Obviously, there are differences in the results obtained for Configs-I, II and III as indicated in Figures 7-3 to 7-11 for the vertical flow. This is due to the following reasons:

❖ Random variations in the liquid/solid flows, which are likely to be small.

❖ Experimental errors inherent in the system, which are investigated and reported in this chapter.

❖ The interrogated area being investigated is different for each configuration, but this would not be expected to be significant here as the solids velocity profile would be expected to be uniform.
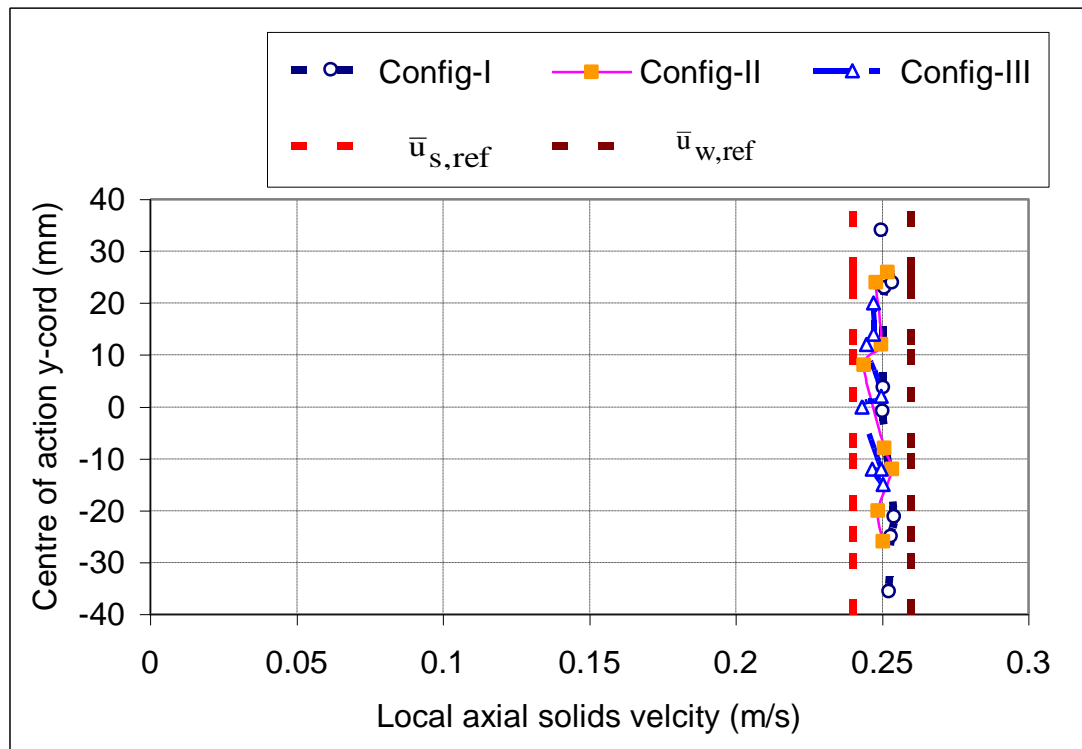
Figure 7-3: Local solids velocity profiles for vertical flow, flow condition 1($Q_{s,ref}$ =0.696 m^{3}h^{-1}, $Q_{w,ref}$ = 4.25 m^{3}h^{-1})
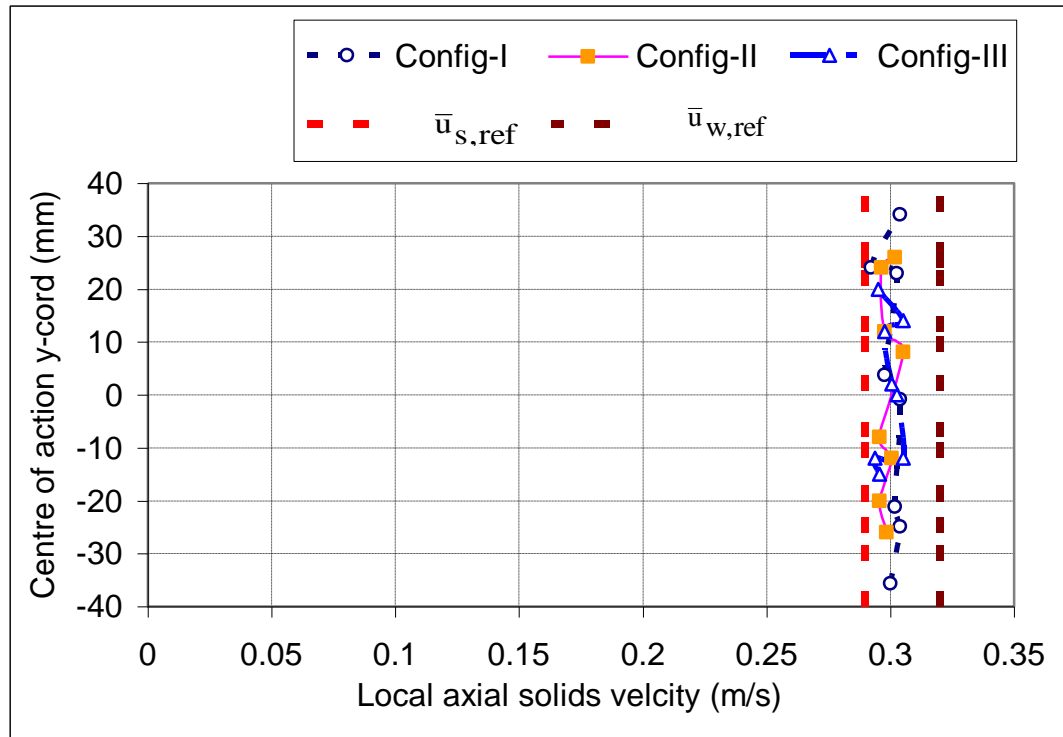
Figure 7-4: Local solids velocity profiles for vertical flow, flow condition 2
($Q_{s,ref}$ =0.750 m^{3}h^{-1}, $Q_{w,ref}$ = 5.49 m^{3}h^{-1})
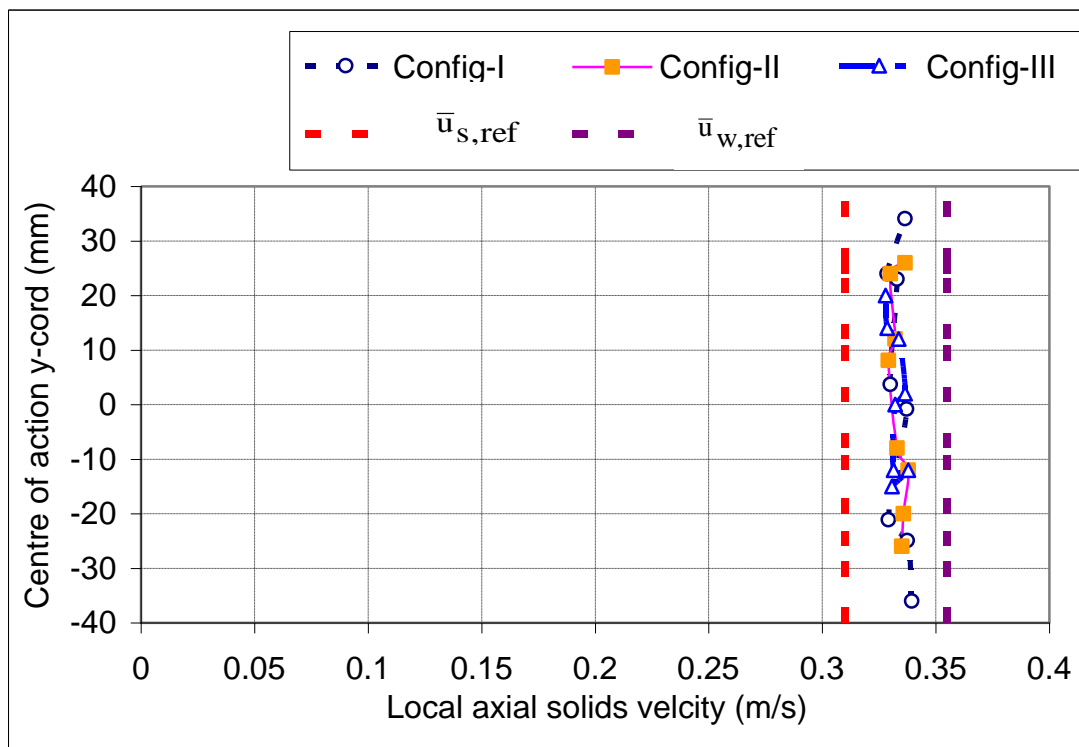
Figure 7-5: Local solids velocity profiles for vertical flow, flow condition 3($Q_{s,ref}$ =0.724 m^{3}h^{-1}, $Q_{w,ref}$ = 6.12 m^{3}h^{-1})
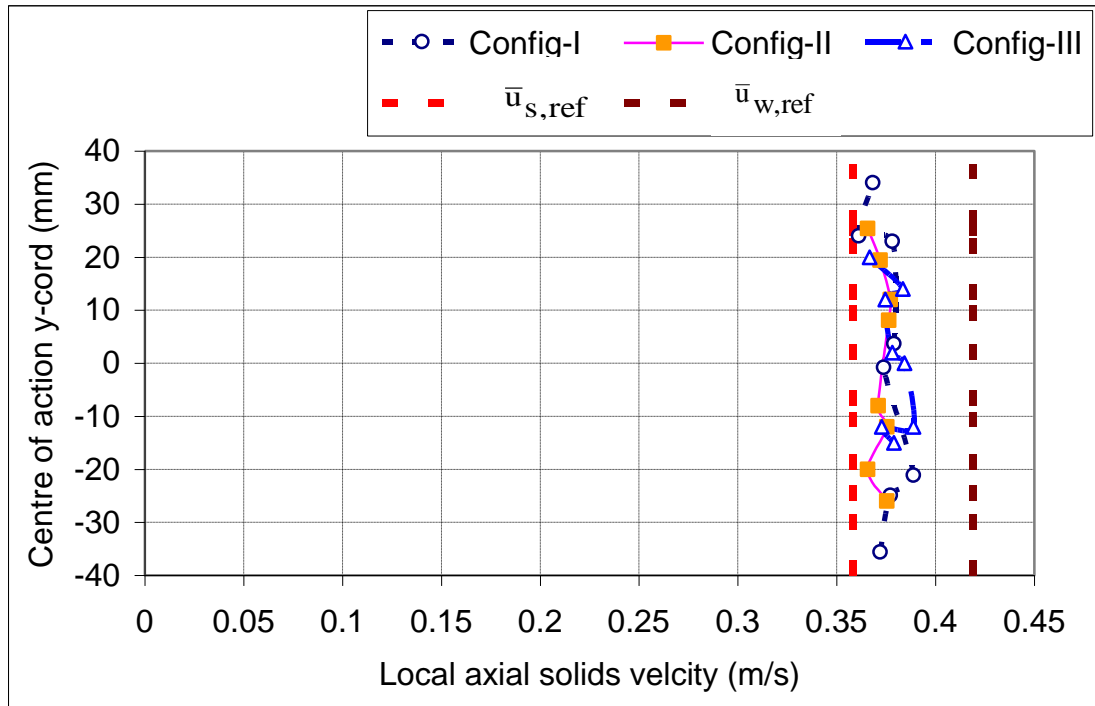
Figure 7-6: Local solids velocity profiles for vertical flow, flow condition 4($Q_{s,ref}$ =1.188 m^{3}h^{-1}, $Q_{w,ref}$ = 6.18 m^{3}h^{-1})
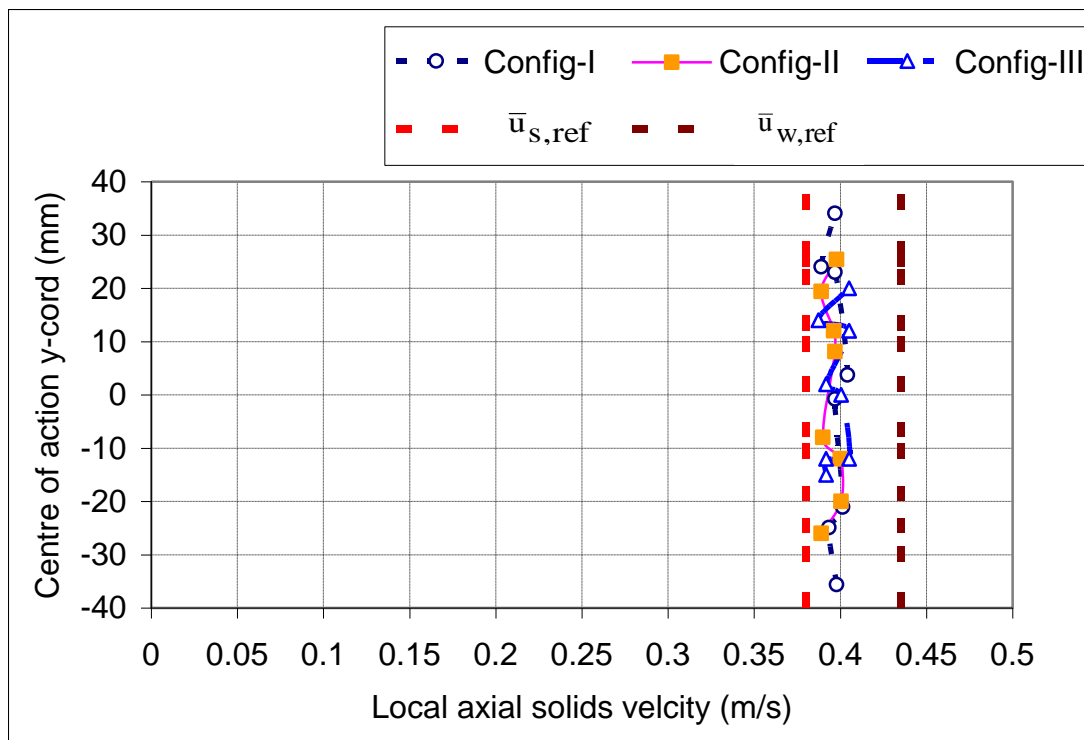
Figure 7-7: Local solids velocity profiles for vertical flow, flow condition 5 ($Q_{s,ref}$ =1.225 m^{3}h^{-1}, $Q_{w,ref}$ = 6.45 m^{3}h^{-1})

224
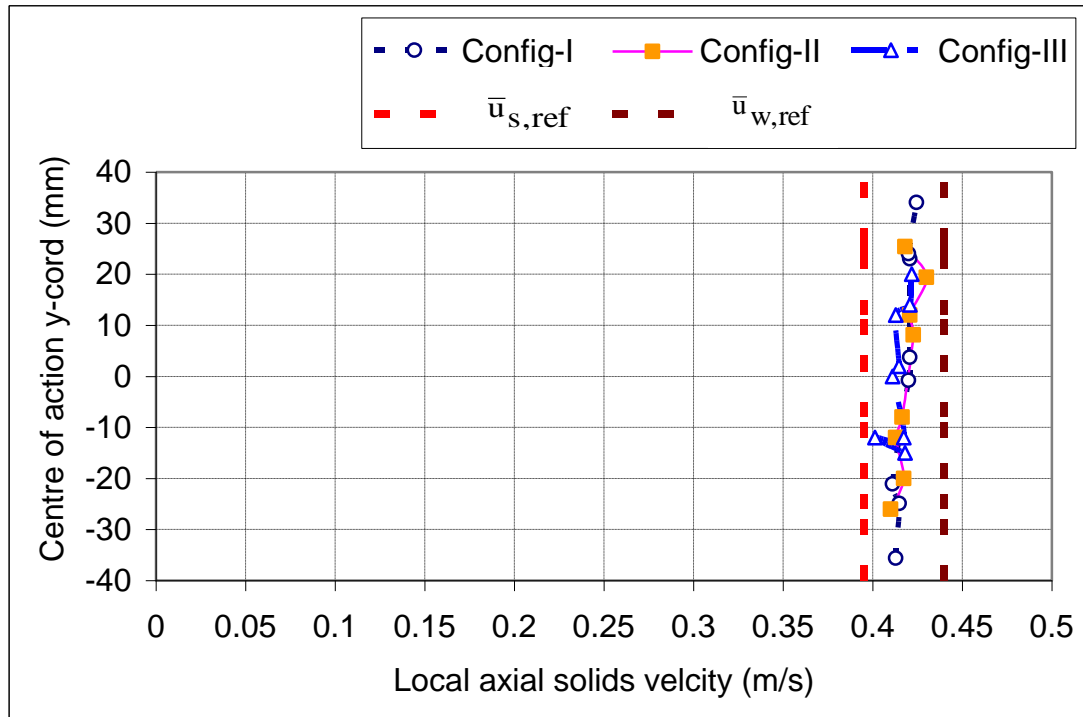
Figure 7-8: Local solids velocity profiles for vertical flow, flow condition 6 ($Q_{s,ref}$ =1.183 m^{3}h^{-1}, $Q_{w,ref}$ = 6.51 m^{3}h^{-1})
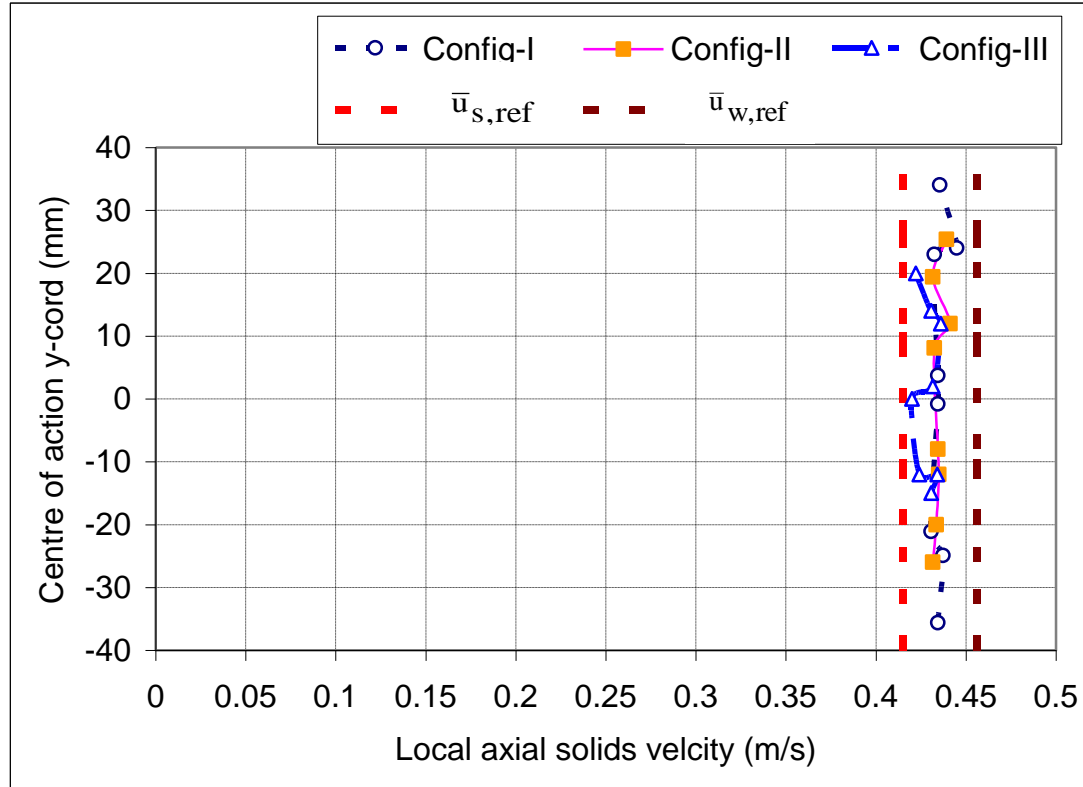
Figure 7-9: Local solids velocity profiles for vertical flow, flow condition 7($Q_{s,ref}$ =2.229 m^{3}h^{-1}, $Q_{w,ref}$ = 5.87 m^{3}h^{-1})
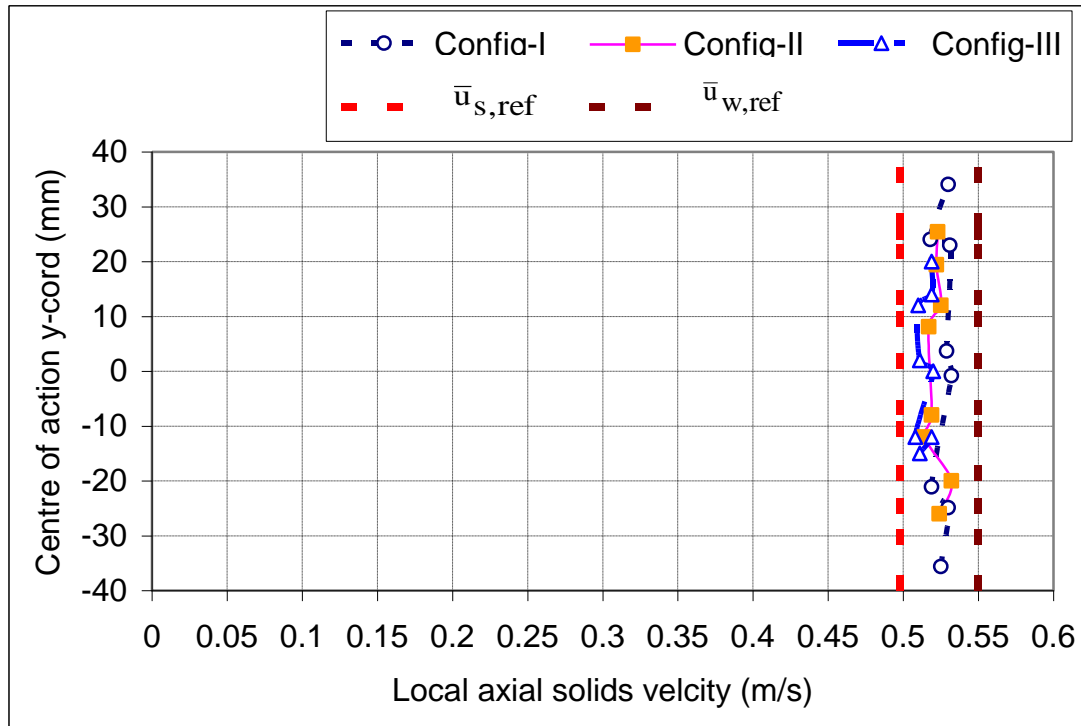
Figure 7-10: Local solids velocity profiles for vertical flow, flow condition 8($Q_{s,ref}$ = 1.998 m^{3}h^{-1}, $Q_{w,ref}$ = 7.98 m^{3}h^{-1})
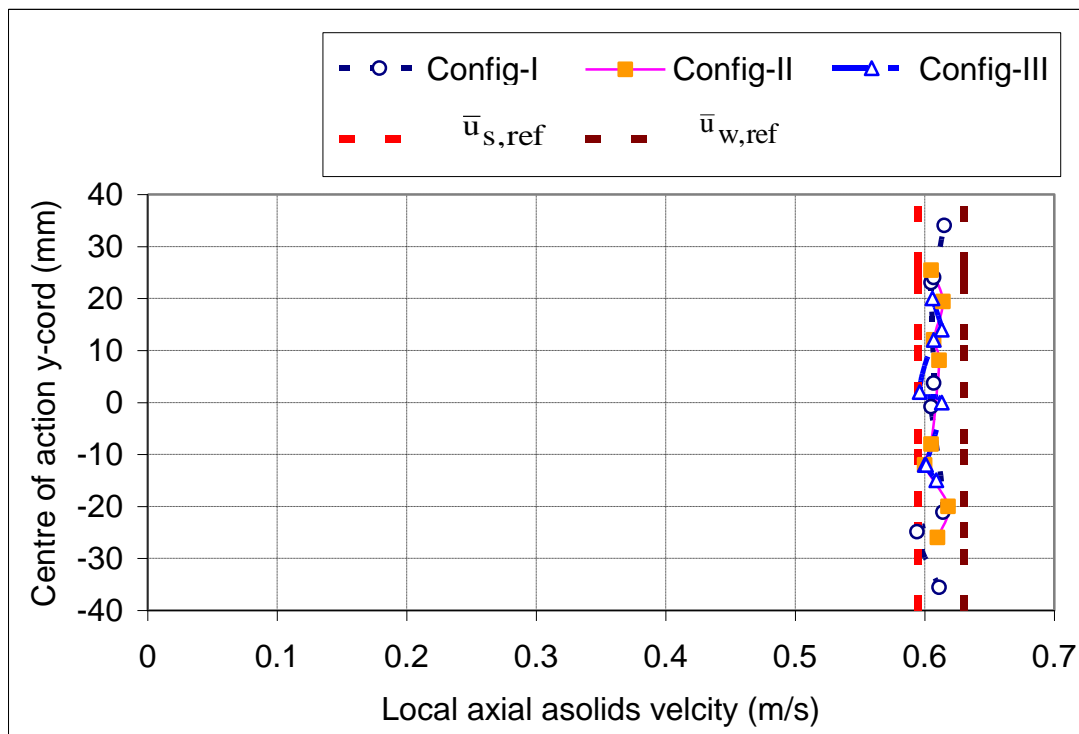
Figure 7-11: Local solids velocity profiles for vertical flow, flow condition 9($Q_{s,ref}$ =1.974 m^{3}h^{-1}, $Q_{w,ref}$ = 9.35 m^{3}h^{-1})

7.2.2.2 Local solids velocity profiles for flow inclined 15° from vertical

It should be remembered that the area of the pipe being interrogated is different for each electrode configuration, so for inclined pipes where the flows are non-symmetrical and the solids velocity varies rapidly with spatial locations in the pipe, the results will show consistent differences. This is the major cause of the different results obtained for Configs-I, II and III.

The results for Config-I refer to an electrode configuration where one electrode is excited, an adjacent electrode is the measurement electrode and the other six electrodes are earthed. The CoA for each rotational position for Config-I is about 6mm from the pipe wall, see Figure 4-15. Config-II is where one electrode is excited and both adjacent electrodes are set as the measurement electrodes and the other five electrodes are earthed. The CoA for for each rotational position for Config-II is about 15mm from the pipe wall, see Figure 4-16. The electrode configuration for Config-III is where two adjacent electrodes are excited, the adjacent electrodes are set as the measurement electrodes and the other four electrodes were earthed. The CoA for each rotational position for Config-III is about 20mm from the pipe wall, see Figure 4-17.

The sensitivity distribution profiles and effective sensing regions presented and defined in Sections 4.8 and 4.9, are different for Configs-I,II and III, see Figures 4-15, 4-16 and 4-17. For Config-I the sensing region covers just the two electrodes concerned and extends about seven squares (14mm) into the pipe. For Config-II the sensing region expands to cover three electrodes and extends about eight squares (16mm) into the pipe. For Config-III the sensing region expands further to include four electrodes and extends about thirteen squares (26mm) into the pipe. It can be seen that the effective area over which the measurement is made is different for each configuration.

Obviously that there are differences in the results obtained for Configs-I, II and III as indicated in Figures 7-12 to 7-20 and Figure 7-21 to 7-29 when the pipe is inclined at an angle to the vertical and the flow velocity varies with spatial location in the flow cross section. For instance, for the rotational position where Config-I measures the velocity at the top of the pipe, because the effective area over which the measurement is taken is small, the measurement corresponds closely to the maximum value of the

solids velocity. Config-II will measure the velocity averaged over a greater area, but because the maximum value is at the top and decreases as you move diametrically across the pipe, Config-II will measure a slightly smaller velocity. Config-III will measure the velocity over an even greater area and so the value measured should be smaller than for either Config-I or II. Thus Config-I should consistently gives the highest velocity at the top of the pipe for all flow conditions, and consistently give the lowest value (possibly even negative for backward flow) at the lower side of the inclined pipe. Config-III should consistently give the lowest velocity at the top of the pipe and is very unlikely to give a negative velocity at the lower side of the pipe. It is also predictable that the measured velocity from each of Configs-I, II and III should be approximately equal towards the centre of the pipe (CoA = 0). These predictions are confirmed by the measurement of flows shown in Figures 7-12 to 7-29 (Figure 7-18 does not conform to this trend and is discussed in more detail later).

Figures 7-12 to 7-20 present results for the pipe inclined at 15°. It is clear from the results obtained that the local axial solids velocity is significantly greater at the upper side of the inclined pipe than at the lower side. Also, for inclined upward flow, the distribution of the measured local solids velocity u_S is highly non-uniform. Once again Lucas et al (1999, 2000) and Cory (1999) reported similar findings using six local probes and ERT.

Figure 7-12 shows there is an evidence of a negative local solids velocity on the lower side of the inclined pipe of about -0.19ms^{-1} for Config-I, flow condition number 10. This means that, in this region, the solids particles were actually flowing backwards down the pipe and this agreed with the visual observation of the flow. The local axial solids velocity on the upper side of the inclined pipe for the same flow condition was 0.8ms^{-1}. Similarly, for Config-II, there was a negative local axial solids velocity at the lower side of the inclined pipe, about -0.045 ms^{-1} (see Figure 7-12). Here, at the upper side of the inclined pipe there was a local axial velocity of about 0.75 ms^{-1}. For Config-III, the local axial solids velocity was about 0.01 ms^{-1} at the lower side of the inclined pipe and about 0.71 ms^{-1} at the upper side of the inclined pipe (see Figure 7-12). A somewhat similar pattern of results can be seen in Figure 7-13 for flow condition number 11.

For flow conditions numbered 12 to 18, none of Configs-I, II or III detected negative local axial solids velocities at the lower side of the inclined pipe, see Figures 7-14 to 7-20. However, all three electrode arrangements detected higher local solids velocity at the upper side of the inclined pipe than the lower side. These results agree with visual observations of the flow. In Figure 7-18 (flow condition 25), Config-I shows a negative local axial solids velocity in the centre of the pipe. The author did observe this phenomenon at other times and attributed it to some unsettled solid particles in the cross-section associated with the behaviour of the solids pump when it had being running for a long time.
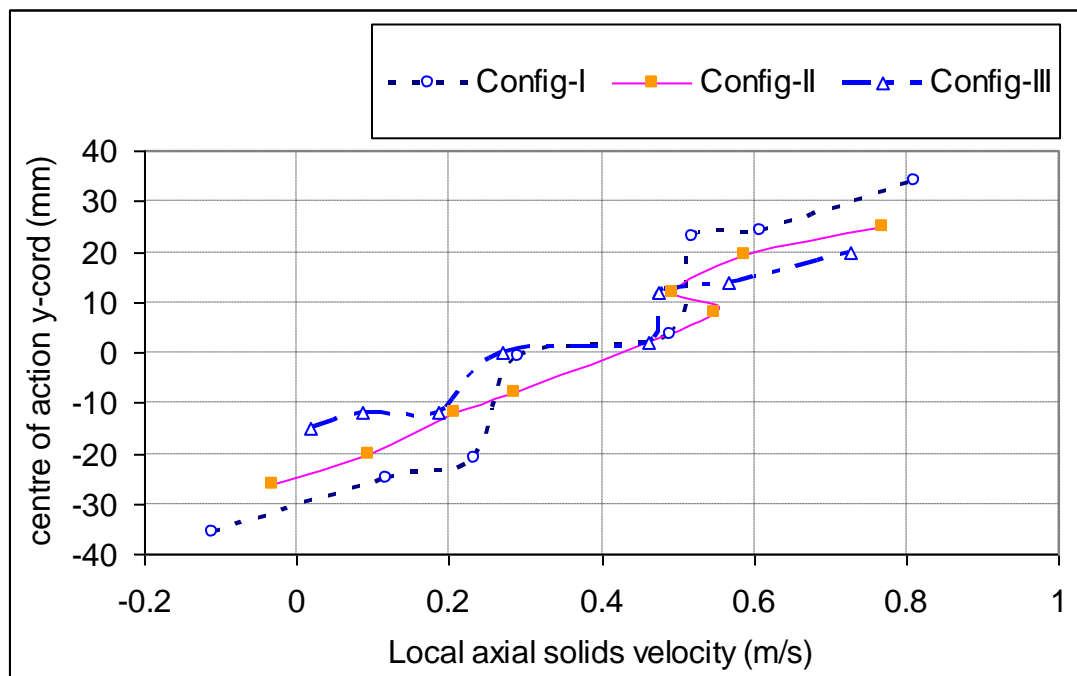
Figure 7-12: Local solids velocity profiles for flow inclined 15° from vertical, flow condition 10 ($Q_{S,ref}$ = 0.613 m³h⁻¹, $Q_{W,ref}$ = 9.45 m³h⁻¹)
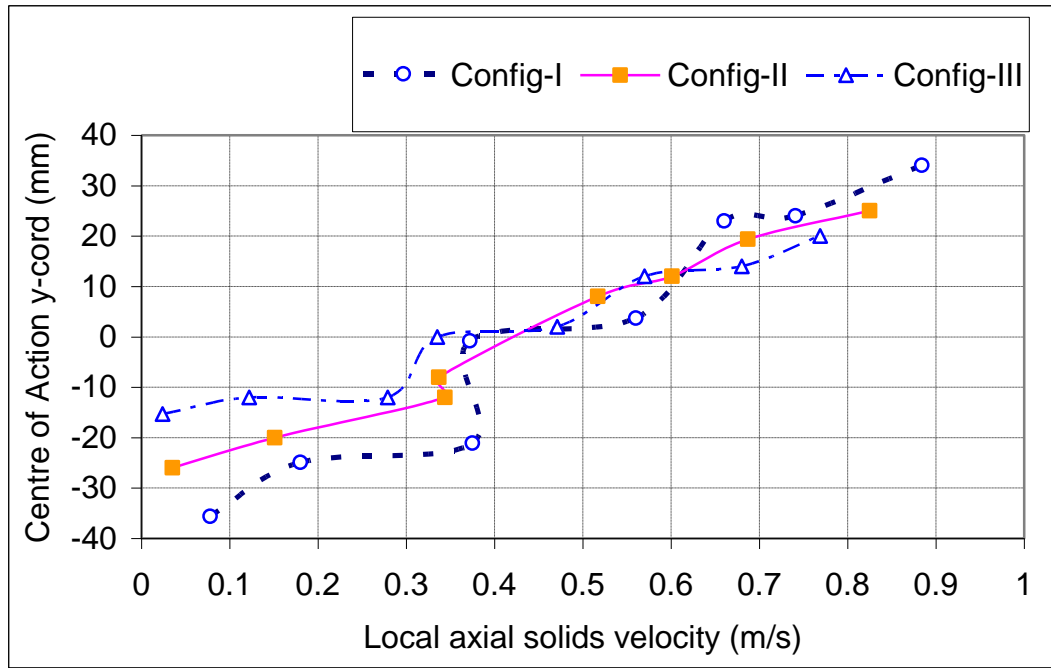
Figure 7-13: Local solids velocity profiles for flow inclined 15° from vertical, flow condition 11($Q_{s,ref}$ =0.731 m³h⁻¹, $Q_{w,ref}$ = 10.91 m³h⁻¹)
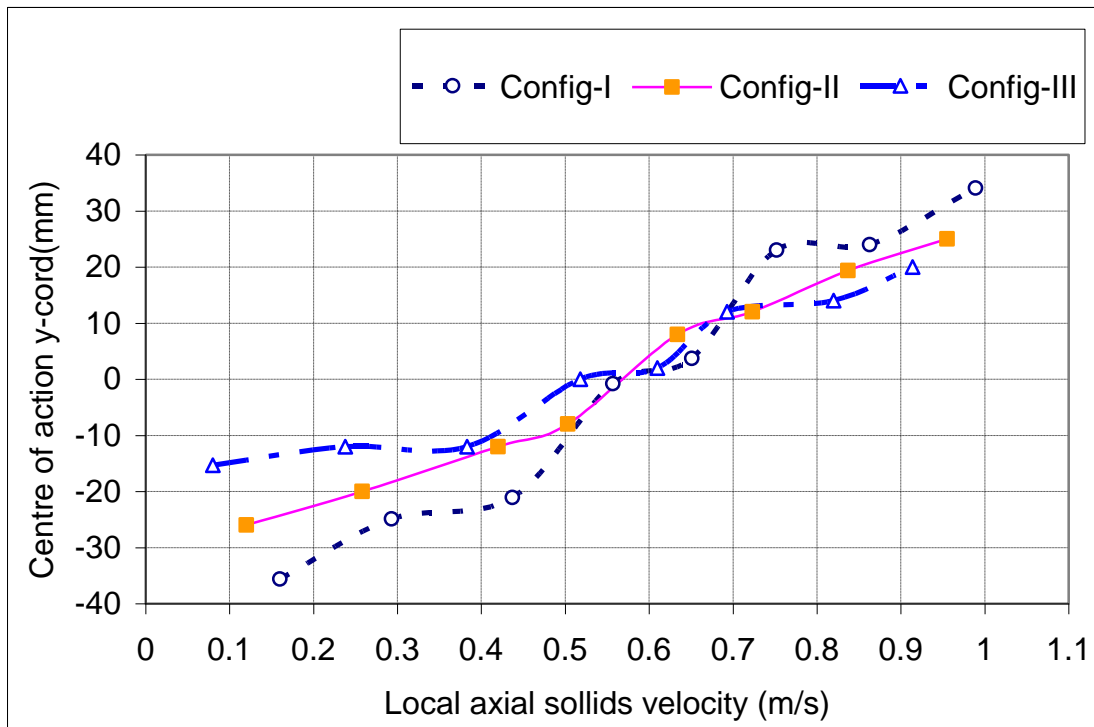
Figure 7-14: Local solids velocity profiles for flow inclined 15° from vertical, flow condition 12($Q_{s,ref}$ =0.704 m³h⁻¹, $Q_{w,ref}$ = 12.43 m³h⁻¹)
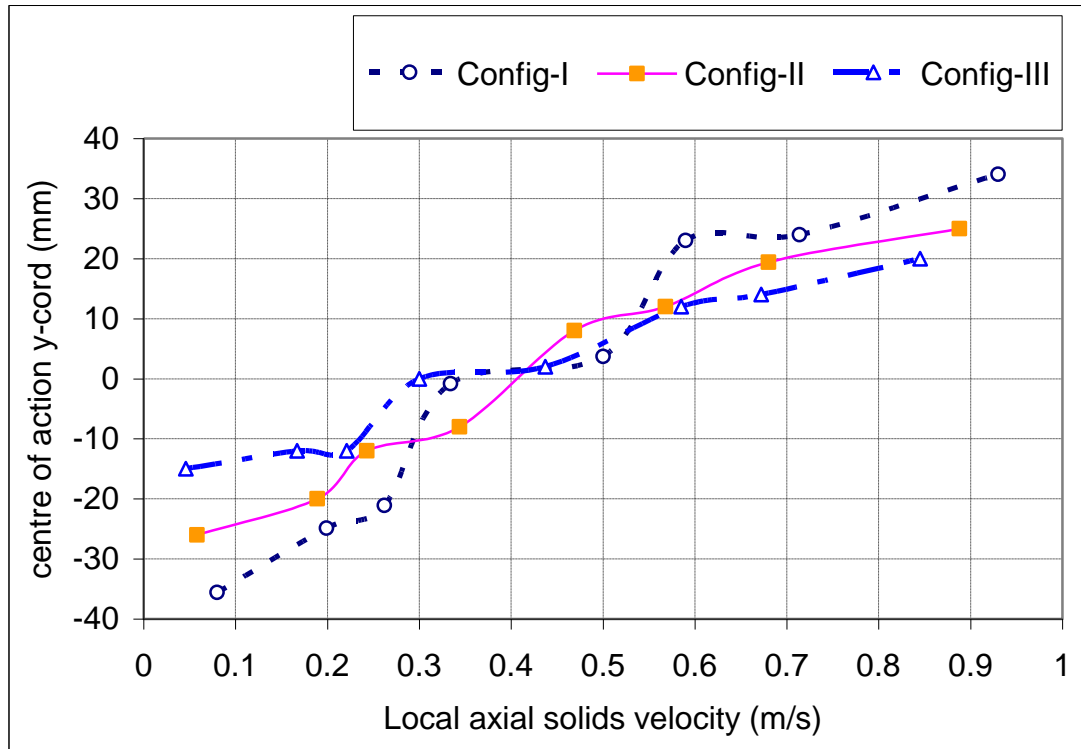
Figure 7-15: Local solids velocity profiles for flow inclined 15° from vertical, flow condition 13($Q_{s,ref}$ =1.187 m³h⁻¹, $Q_{w,ref}$ = 12.82 m³h⁻¹)
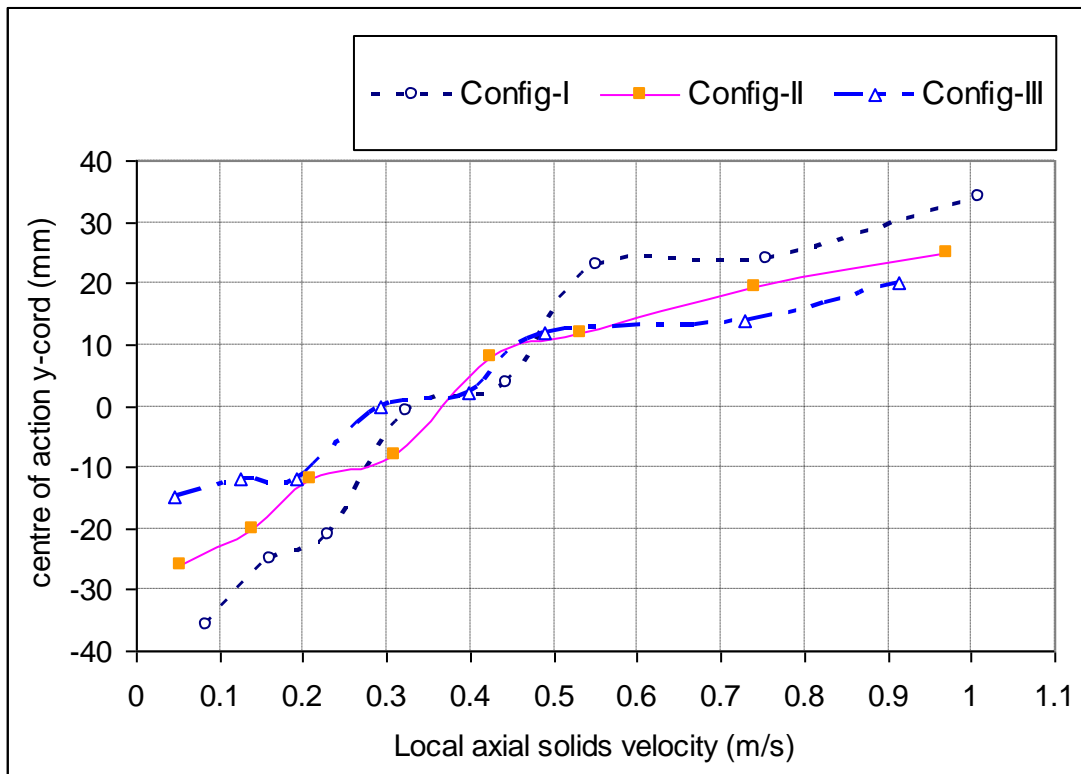
Figure 7-16: Local solids velocity profiles for flow inclined 15° from vertical, flow condition 14($Q_{s,ref}$ =1.104 m³h⁻¹, $Q_{w,ref}$ = 13.94 m³h⁻¹)

231
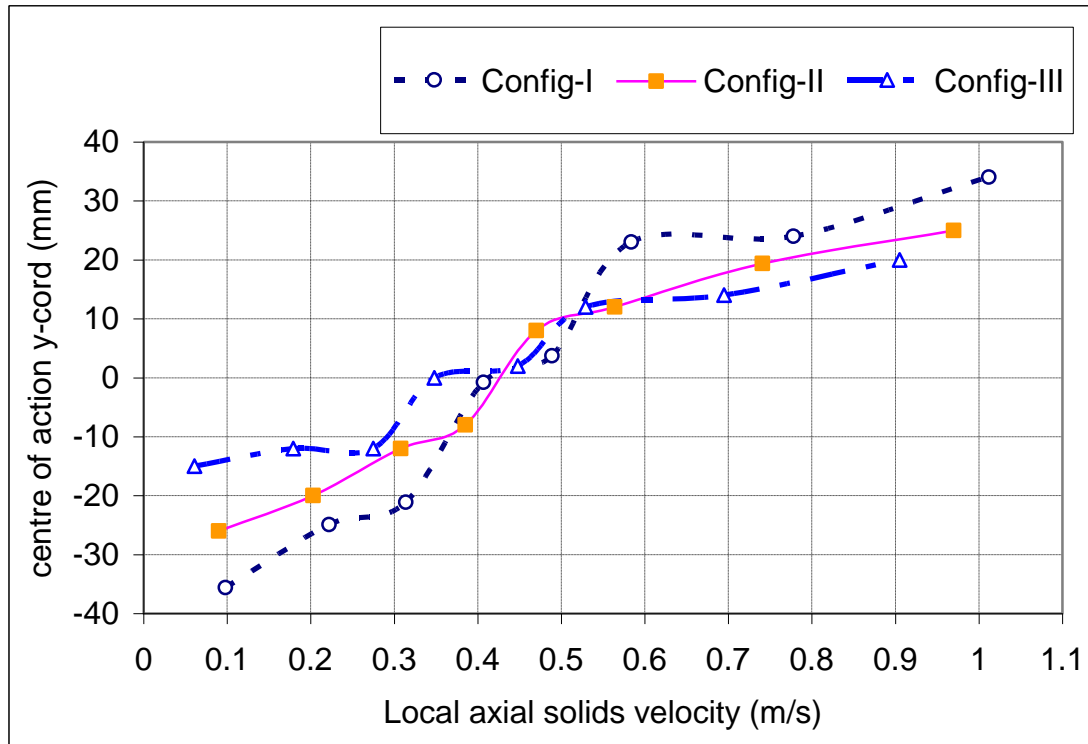
Figure 7-17: Local solids velocity profiles for flow inclined 15° from vertical, flow condition 15($Q_{s,ref}$ =1.010 m^{3}h^{-1}, $Q_{w,ref}$ = 15.43 m^{3}h^{-1})
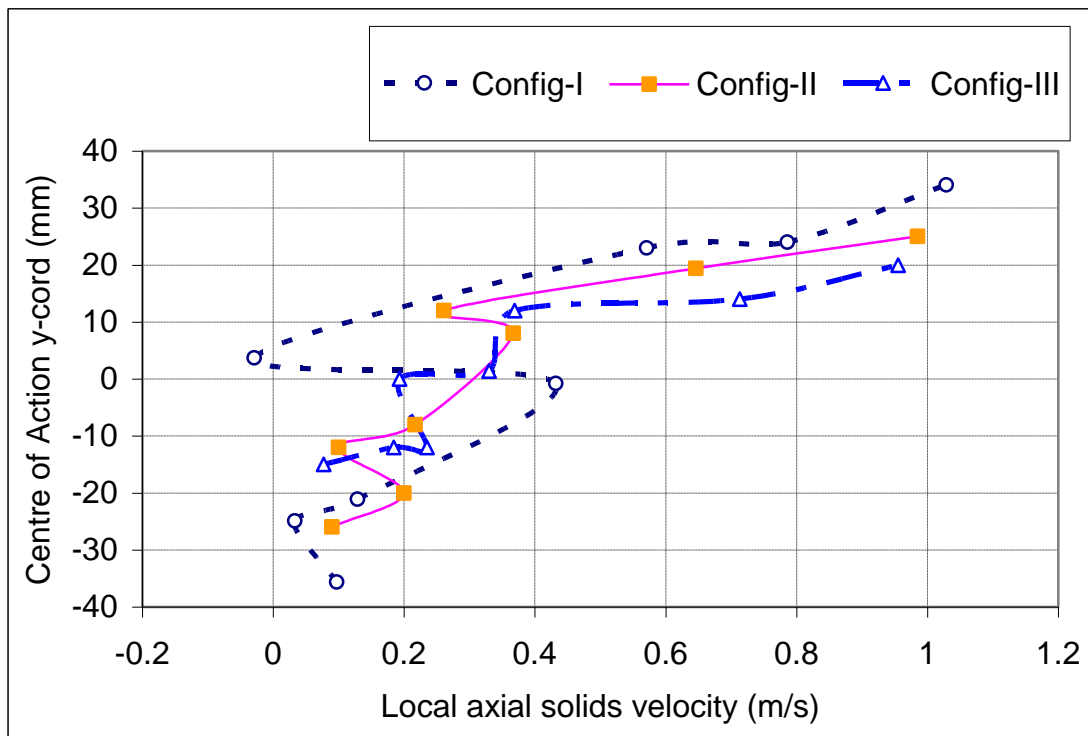
Figure 7-18: Local solids velocity profiles for flow inclined 15° from vertical, flow condition 16($Q_{s,ref}$ =1.631 m^{3}h^{-1}, $Q_{w,ref}$ = 14.05 m^{3}h^{-1})
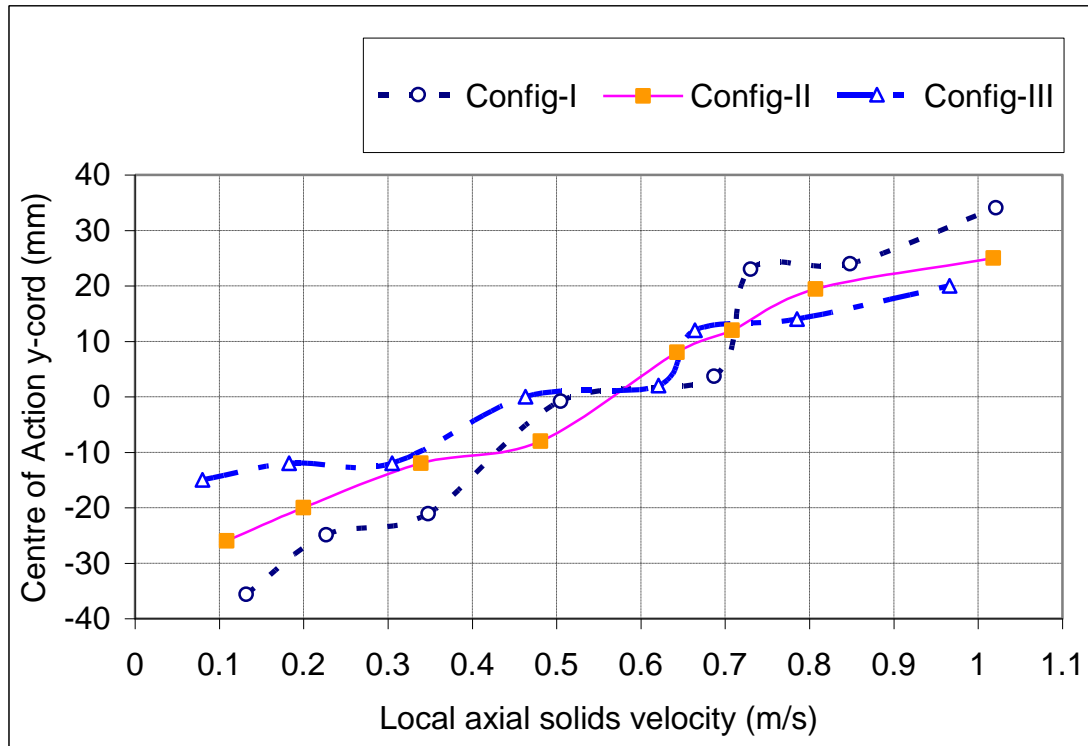
Figure 7-19: Local solids velocity profiles for flow inclined 15° from vertical, flow condition 17($Q_{s,ref}$ =1.587 m^{3}h^{-1}, $Q_{w,ref}$ = 15.26 m^{3}h^{-1})
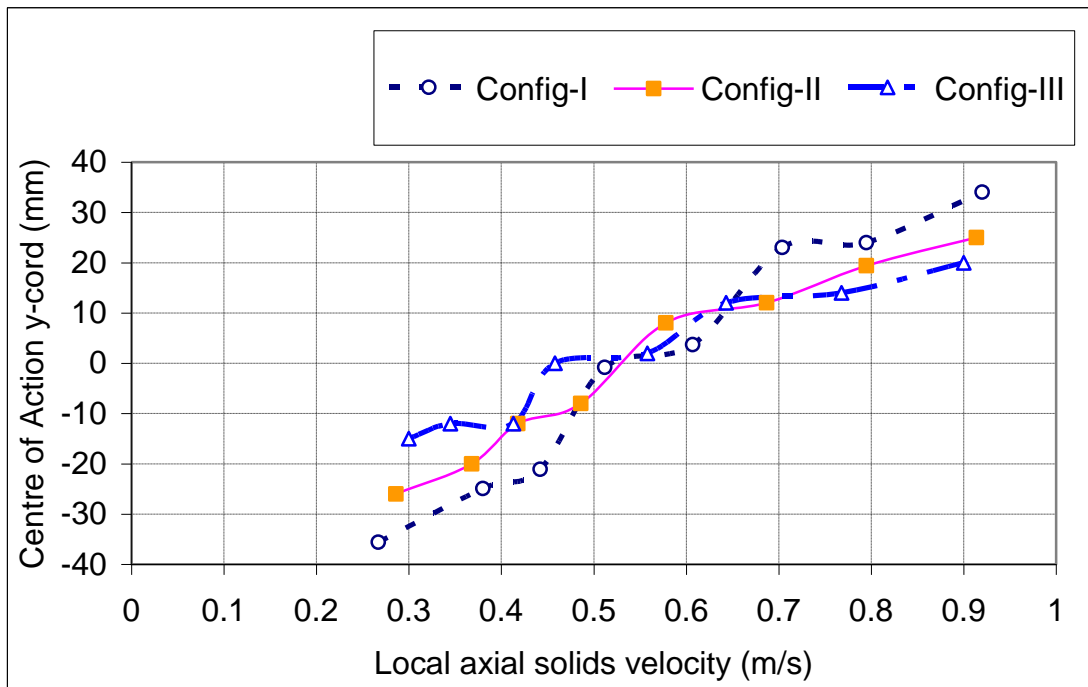
Figure 7-20: Local solids velocity profiles for flow inclined 15° from vertical, flow condition 18($Q_{s,ref}$ =1.623 m^{3}h^{-1}, $Q_{w,ref}$ = 16.94m^{3}h^{-1})

7.2.2.3 Local solids velocity profiles for flow inclined 30° from vertical

In Figures 7-21, 7-22, 7-24 and 7-25 (corresponding to flow conditions 19, 20, 22 and 23) Configs-I and II show negative local axial solids velocities at the lower side of the inclined pipe. For all four flows conditions the rotational position for Config-I corresponding to where the effective sensing region is closest to the lower side of the inclined pipe consistently measured the most negative local axial solids velocity (compared to the Configs-I and II). There "most negative" axial velocities for Config-I about -0.17ms^{-1}, -0.3 ms^{-1}, -0.25 ms^{-1} and -0.25 ms^{-1} respectively.

For Figure 7-21, at the upper side of the inclined pipe Configs-I and II show local solids velocities of about 0.98ms^{-1} and 0.85ms^{-1} respectively while Config-III shows 0.80ms^{-1}. The differences between these values are attributed to the averaging effects of the different rotational position, see discussion above. Similar results are observed in Figures 7-22, 7-24 and 7-25.

In Figures 7-23 and 7-26 to 7-29 Configs-I, II and III all show positive local solids velocity at both upper and lower side of the inclined pipe. However, as expected for all flows there was a higher local solids axial velocities at the upper side of inclined pipe than the lower side of the inclined pipe. Visual observations were consistent with this finding.
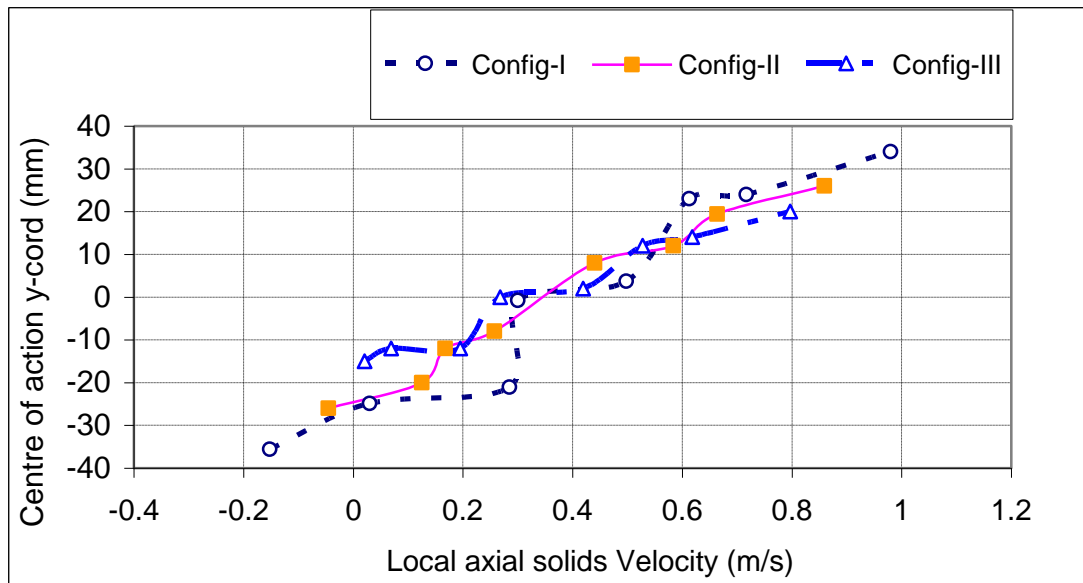
Figure 7-21: Local solids velocity profiles for flow inclined 30° from vertical, flow condition 19($Q_{s,ref}$ =0.360 m^{3}h^{-1}, $Q_{w,ref}$ = 7.218 m^{3}h^{-1})
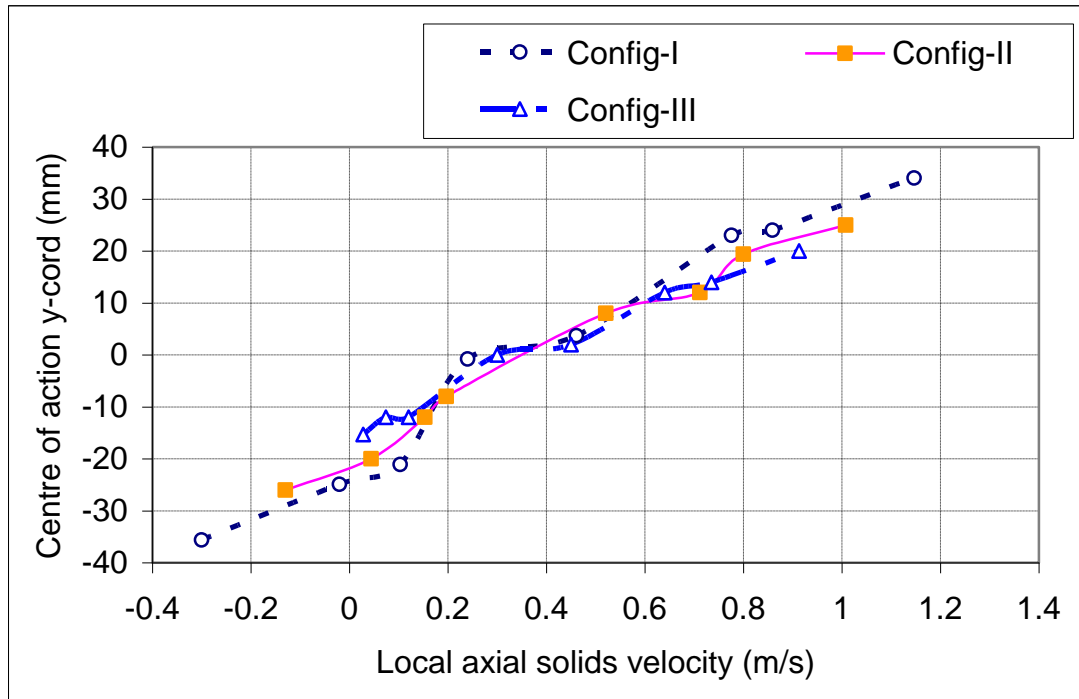
Figure 7-22: Local solids velocity profiles for flow inclined 30° from vertical, flow condition 20($Q_{s,ref}$ =0.591 m^{3}h^{-1}, $Q_{w,ref}$ = 10.79 m^{3}h^{-1})
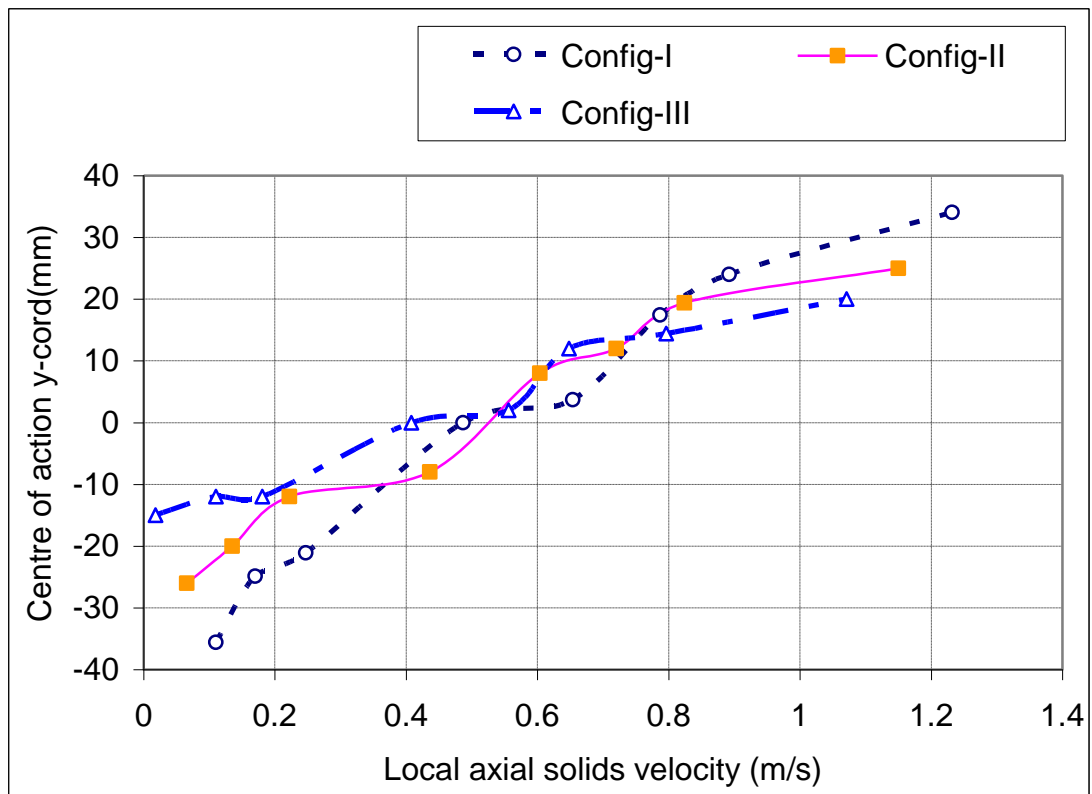
Figure 7-23: Local solids velocity profiles for flow inclined 30° from vertical, flow condition 21($Q_{s,ref}$ =0.549 m3h-1, $Q_{w,ref}$ = 12.13 m3h-1)
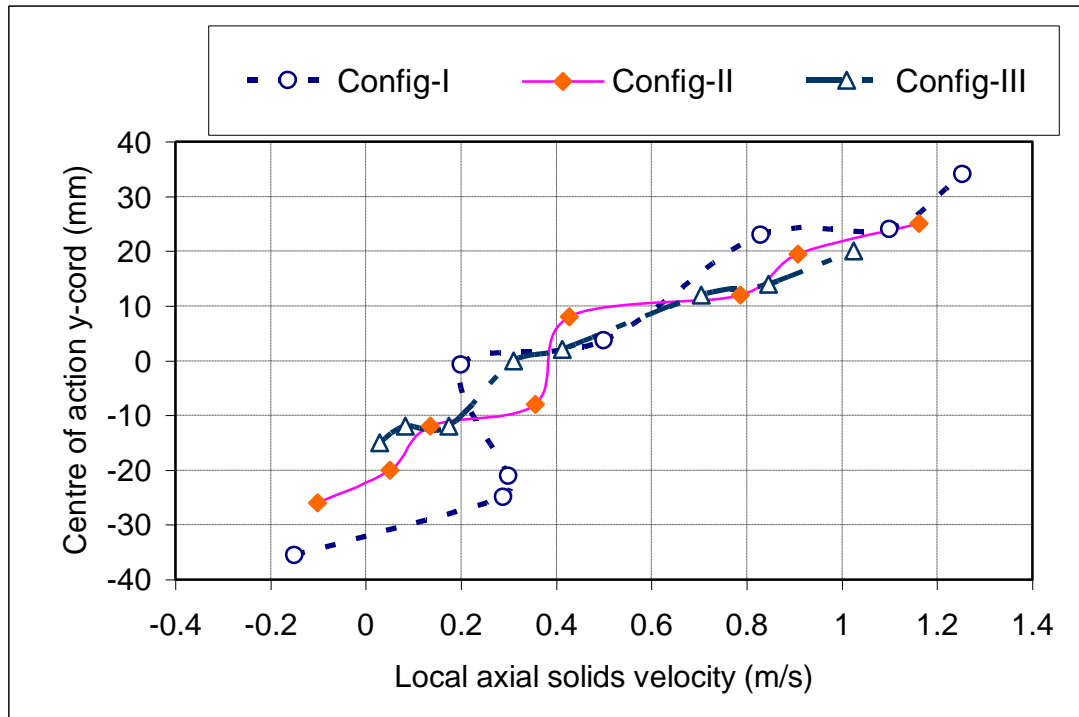
Figure 7-24: Local solids velocity profiles for flow inclined 30° from vertical, flow condition 22($Q_{s,ref}$ =0.951 m^{3}h^{-1}, $Q_{w,ref}$ = 12.47 m^{3}h^{-1})
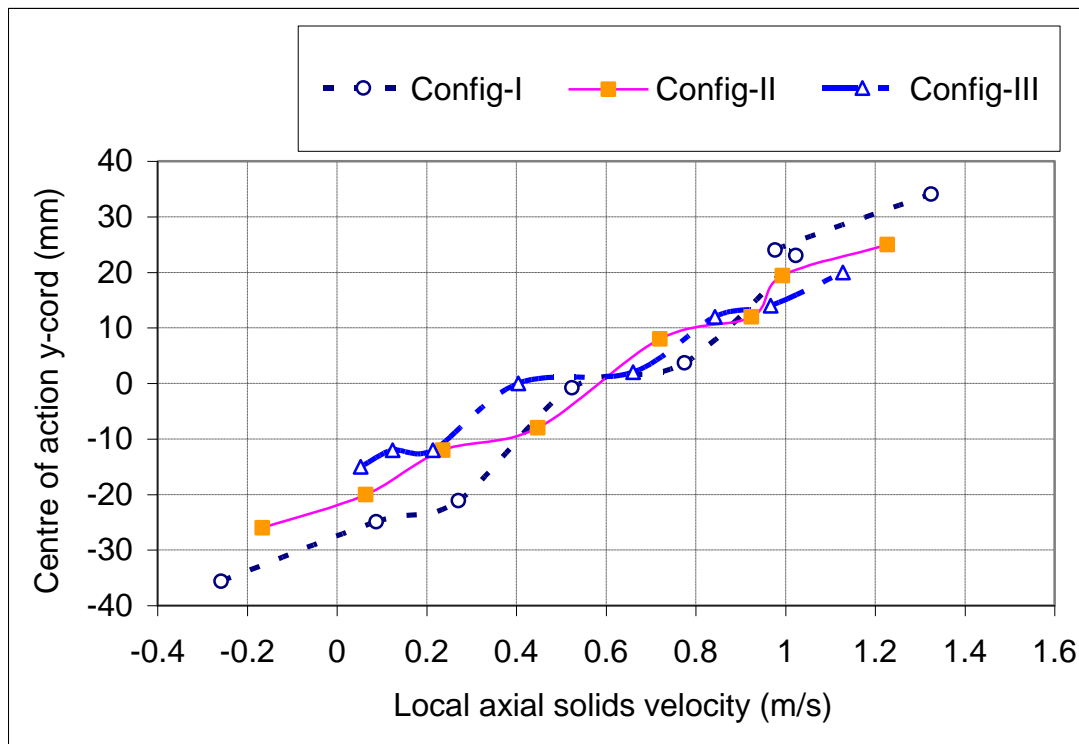
Figure 7-25: Local solids velocity profiles for flow inclined 30° from vertical, flow condition 23($Q_{s,ref}$ =1.010 m^{3}h^{-1}, $Q_{w,ref}$ = 14.06 m^{3}h^{-1})
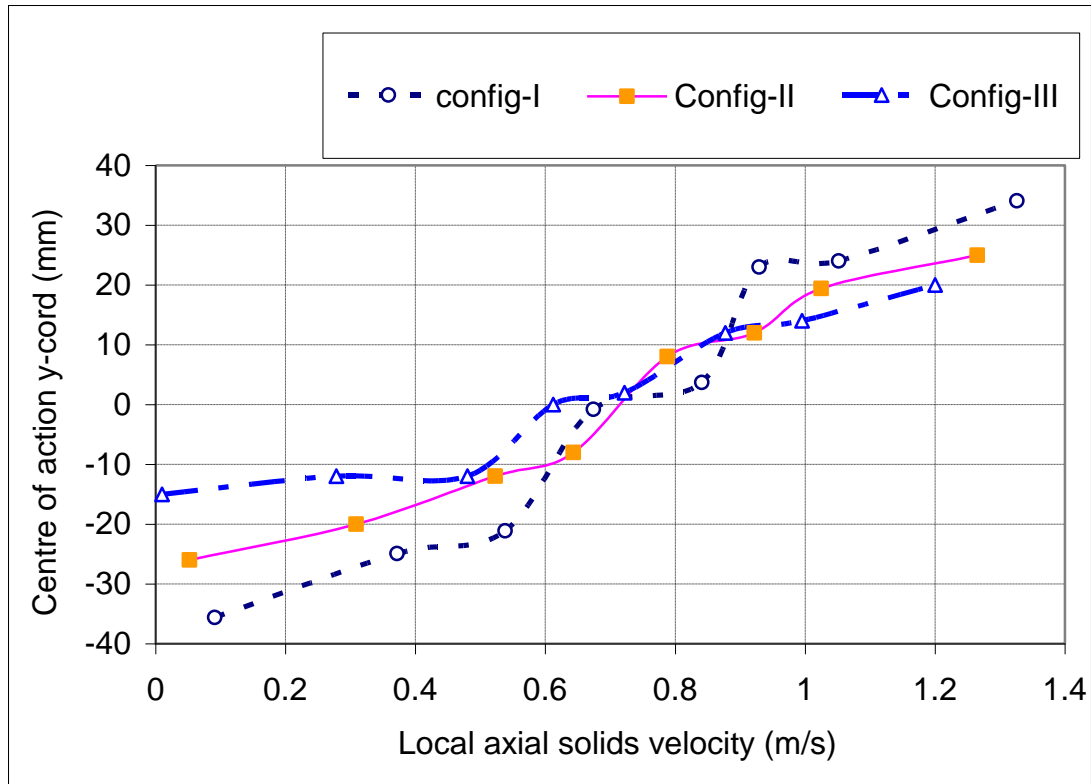
Figure 7-26: Local solids velocity profiles for flow inclined 30° from vertical, flow condition 24($Q_{s,ref}$ =0.959 m^{3}h^{-1}, $Q_{w,ref}$ = 15.66 m^{3}h^{-1})
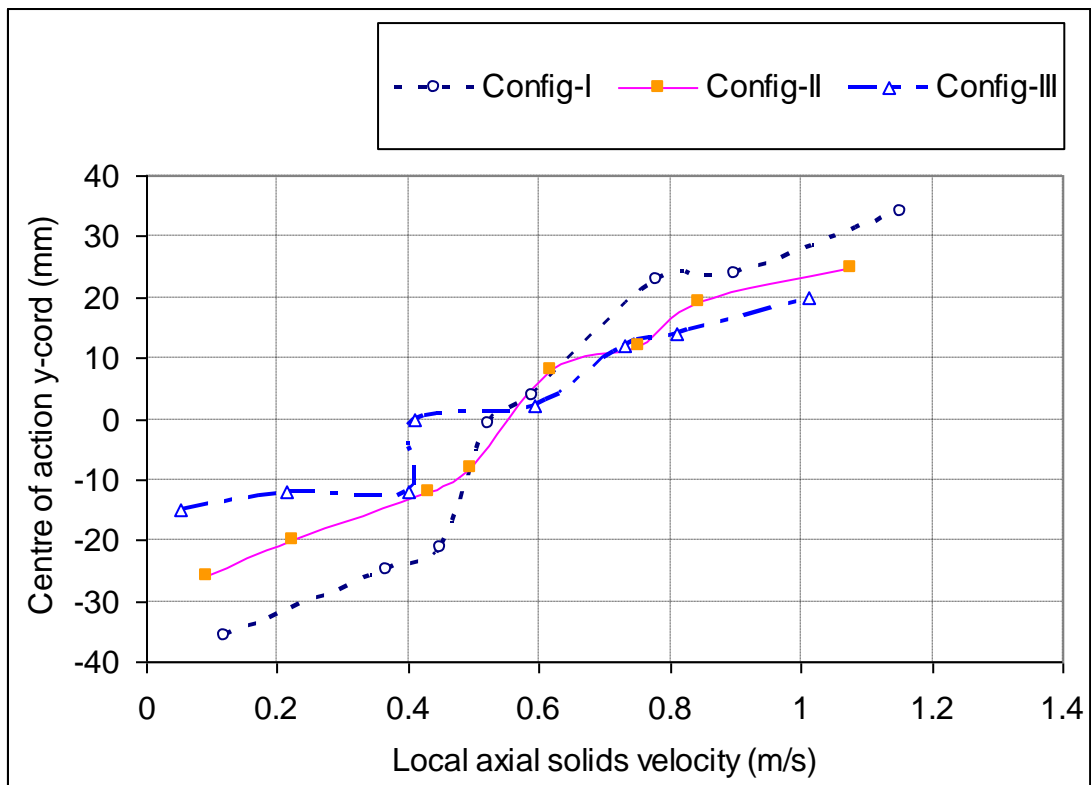
Figure 7-27: Local solids velocity profiles for flow inclined 30° from vertical, flow condition 25($Q_{s,ref}$ =1.41 m^{3}h^{-1}, $Q_{w,ref}$ = 14.10 m^{3}h^{-1})
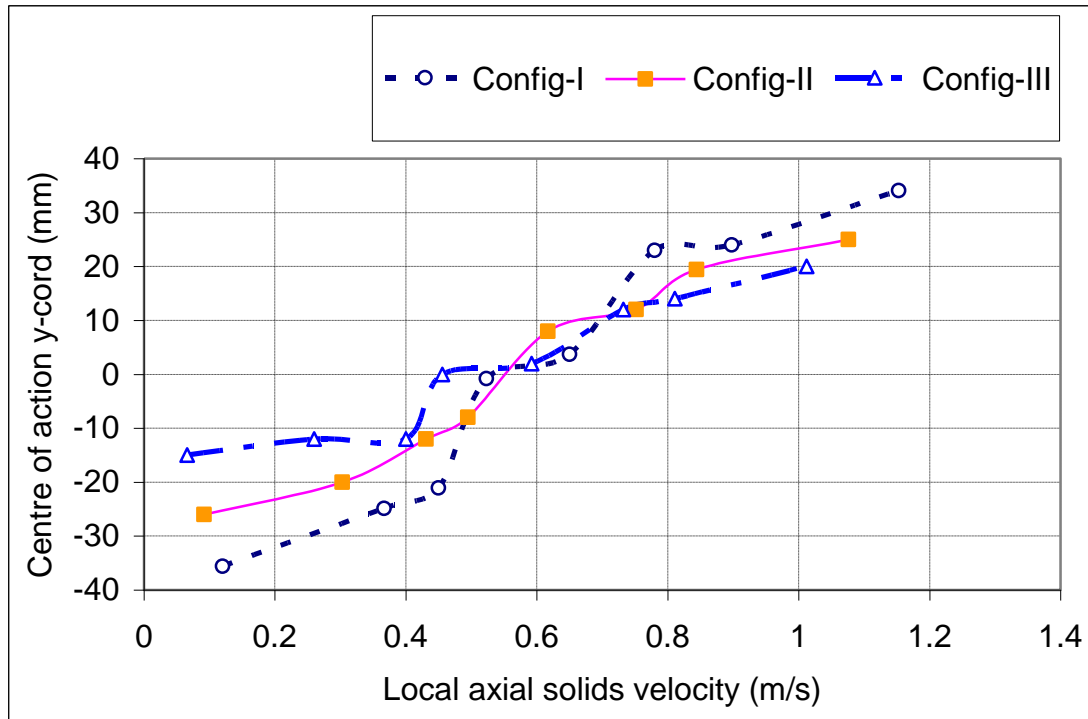
Figure 7-28: Local solids velocity profiles for flow inclined 30° from vertical, flow condition 26($Q_{s,ref}$ =1.651 m³h⁻¹, $Q_{w,ref}$ = 15.96 m³h⁻¹)
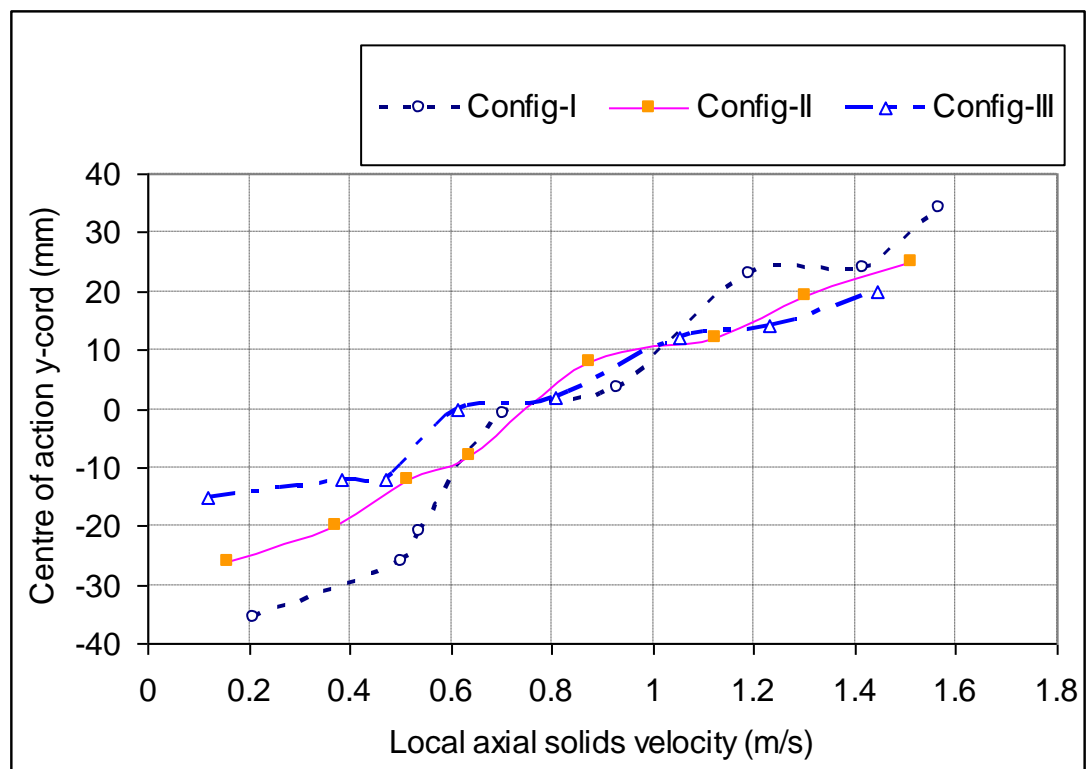
Figure 7-29: Local solids velocity profiles for flow inclined 30° from vertical, flow condition 27($Q_{s,ref}$ =1.623 m³h⁻¹, $Q_{w,ref}$ = 17.12 m³h⁻¹)

7.2.3 3D Profiles of the local axial solids velocity from ICC

The local axial solids velocity profiles (0°, 15° and 30°) were plotted in 3D using an interpolation routine within MATLAB to show these profiles as a function of spatial location in the flow cross-section as defined by the x and y coordinates of the CoA see Table 4-5. The author developed software listed in Appendix (Code 6) in MATLAB to obtain the 3D plot profiles. Also, the results have been integrated to give overall measurement values as described in Section 6.4.3.3. In each of the 3D figures, there is a colour scale which represents the value of the local solids velocity (u_S) at particular measuring point. The red colour represents maximum value of the solids velocity and colour blue represent the minimum value of (u_S) at particular flow conditions. Config-ψ represents a combination of Configs-I, II, III which is used to overcome the problem of the insufficient number of points in the flow cross section (see Section 7.2.1).

7.2.3.1 3-D Local solids velocity profiles for upward flow in a vertical pipe

Config-I

Config-II

Config-III

Config-Ψ
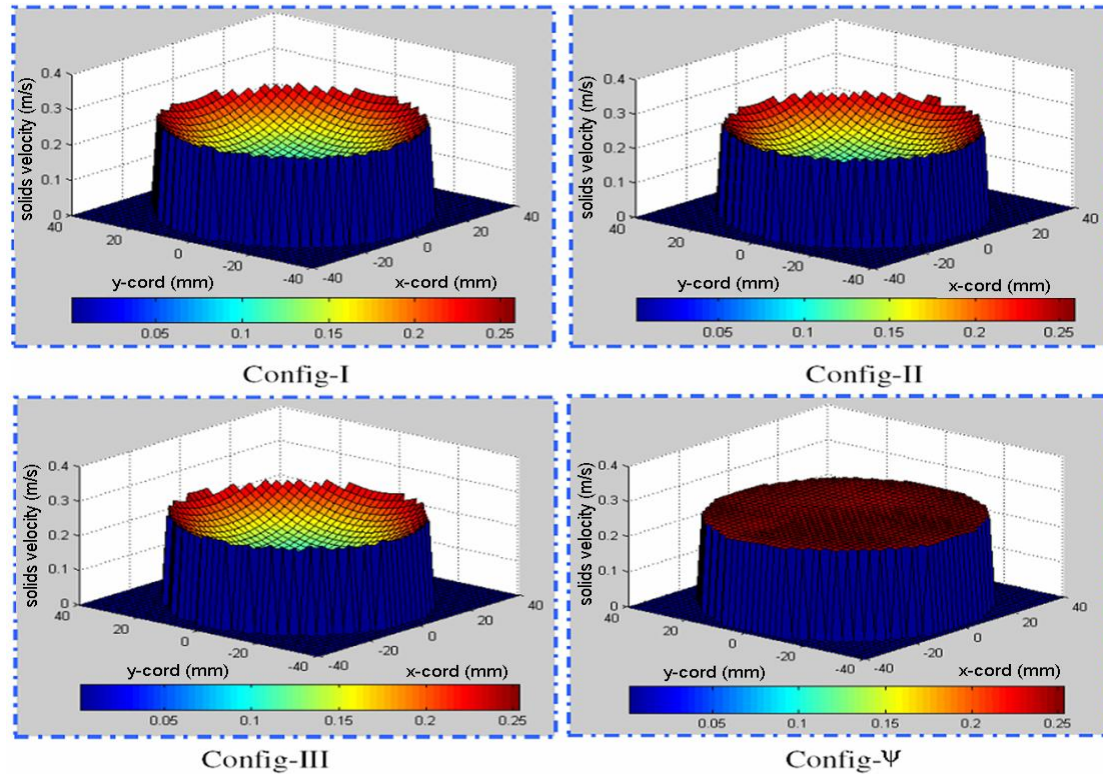
Figure 7-30: Local solids velocity profiles for flow in vertical pipe, flow condition 1($Q_{s,ref}$ =0.696 m^{3}h^{-1}, $Q_{w,ref}$ = 4.25m^{3}h^{-1})

239
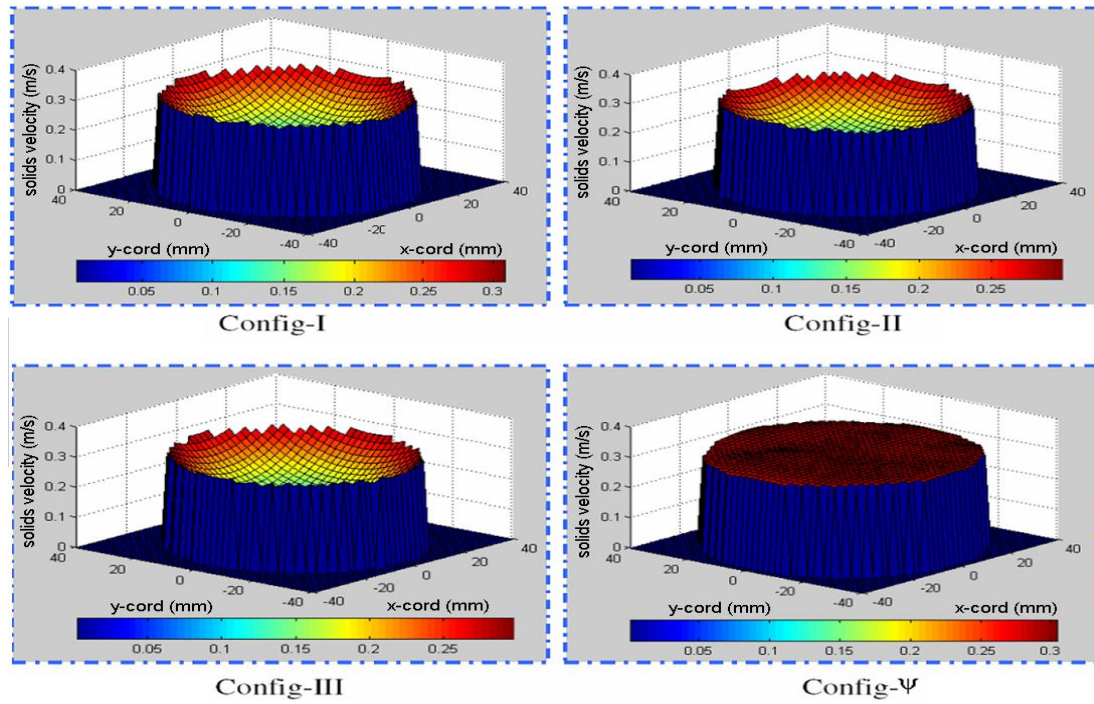
Figure 7-31: Local solids velocity profiles for flow in vertical pipe, flow condition 2($Q_{s,ref}$ =0.750 m³h⁻¹, $Q_{w,ref}$ = 5.49 m³h⁻¹)
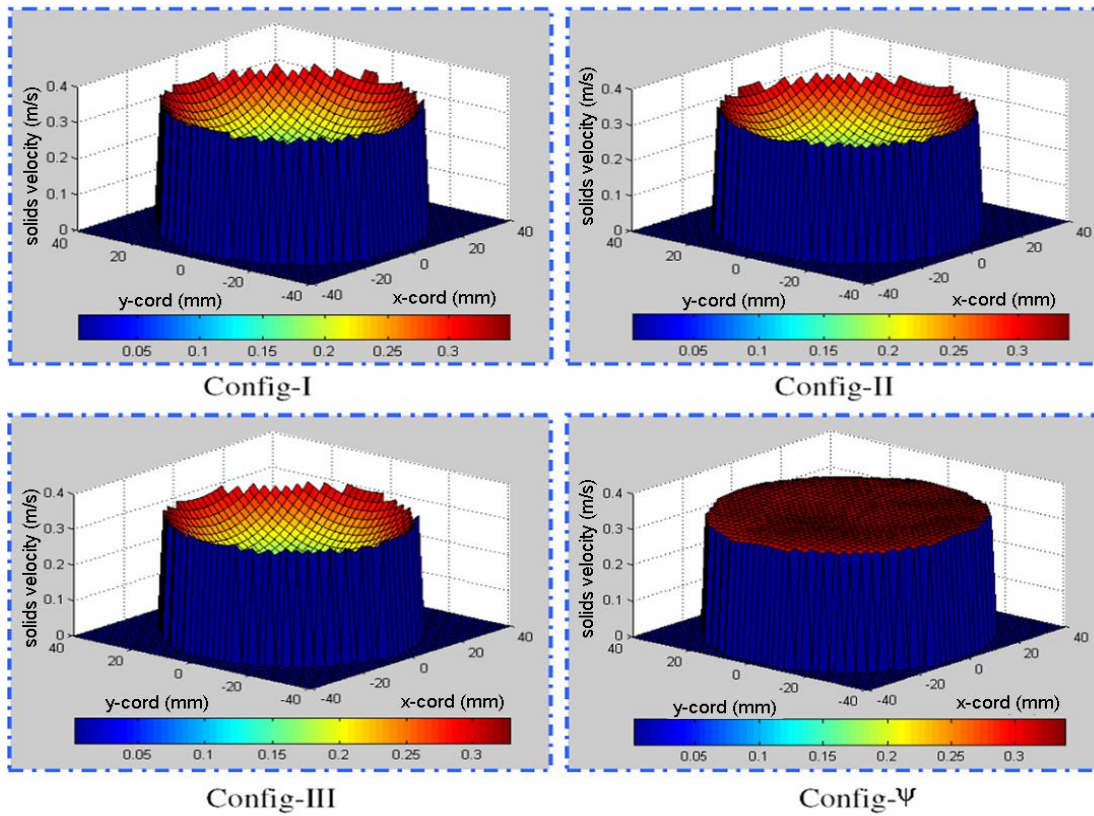
Figure 7-32: Local solids velocity profiles for flow in vertical pipe, flow condition3 ($Q_{s,ref}$ =0.724 m³h⁻¹, $Q_{w,ref}$ = 6.12 m³h⁻¹)
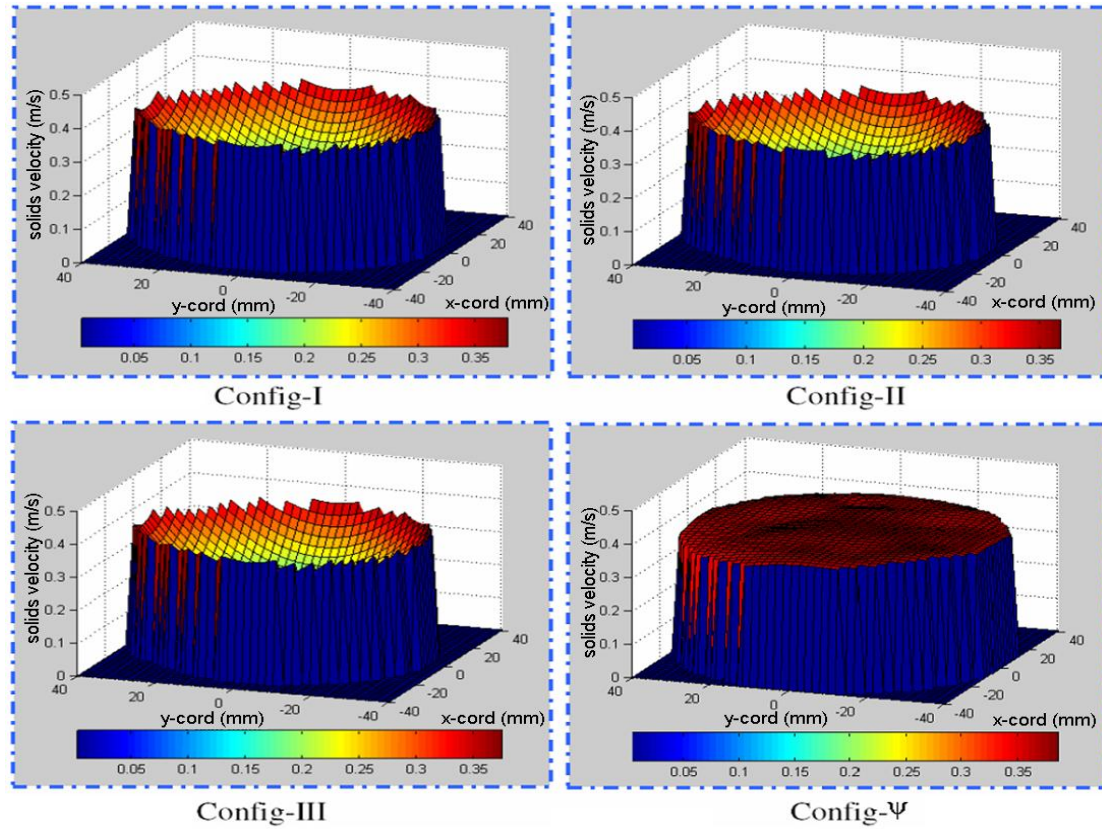
Figure 7-33: Local solids velocity profiles for flow in vertical pipe, flow condition 4($Q_{s,ref}$ =1.188 m^{3}h^{-1}, $Q_{w,ref}$ = 6.18 m^{3}h^{-1})
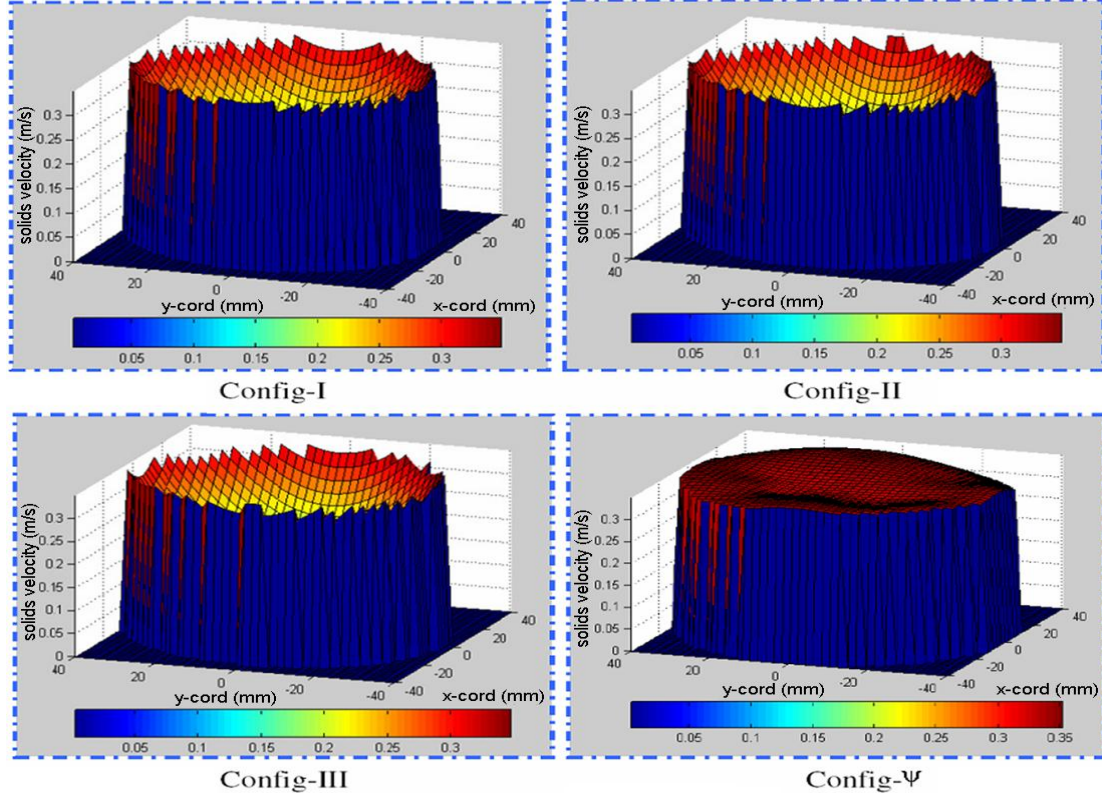
Figure 7-34: Local solids velocity profiles for flow in vertical pipe, flow condition 5($Q_{s,ref}$ =1.225 m^{3}h^{-1}, $Q_{w,ref}$ = 6.45 m^{3}h^{-1}).

241
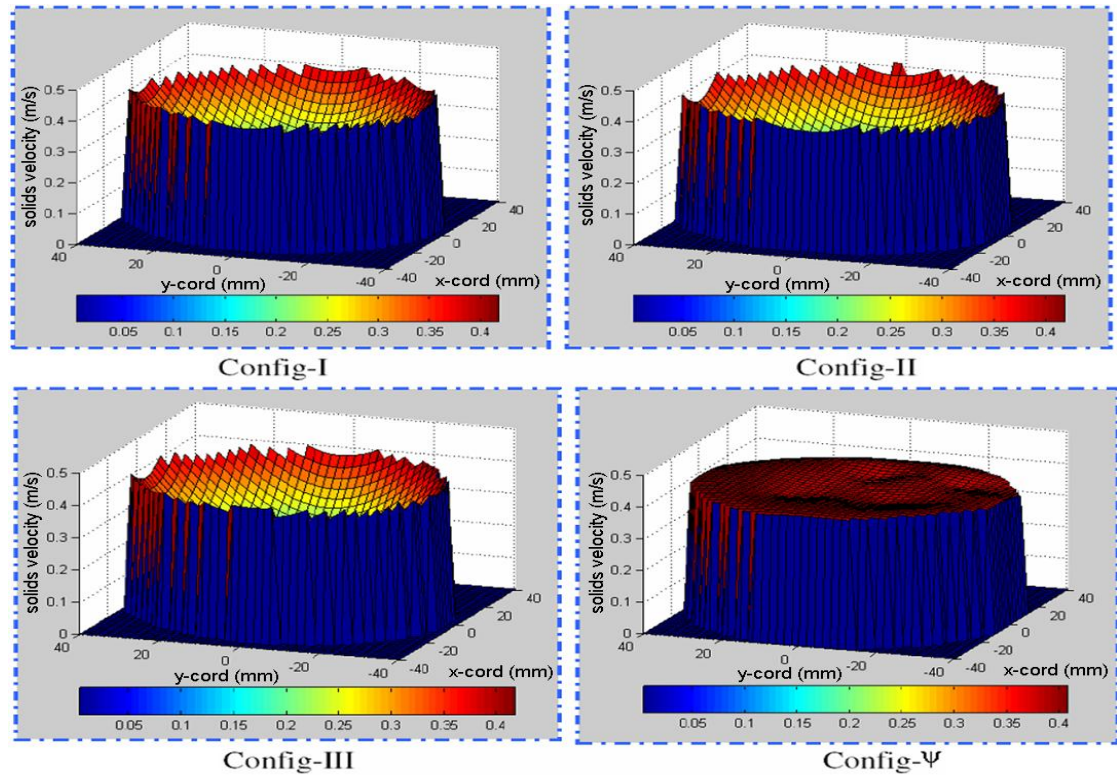
Figure 7-35: Local solids velocity profiles for flow in vertical pipe, flow condition 6($Q_{s,ref}$ =1.183 m^{3}h^{-1}, $Q_{w,ref}$ = 6.51 m^{3}h^{-1})
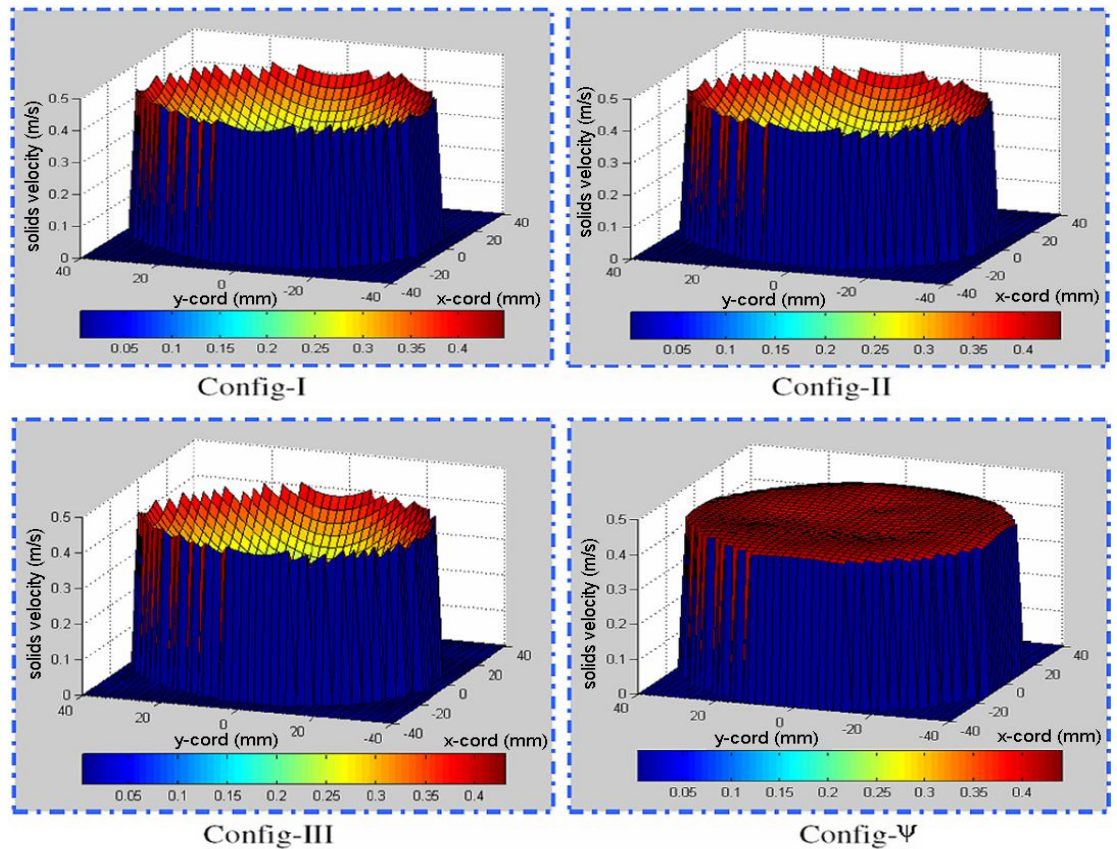
Figure 7-36: Local solids velocity profiles for flow in vertical pipe, flow condition 7($Q_{s,ref}$ =2.229 m^{3}h^{-1}, $Q_{w,ref}$ = 5.87 m^{3}h^{-1})
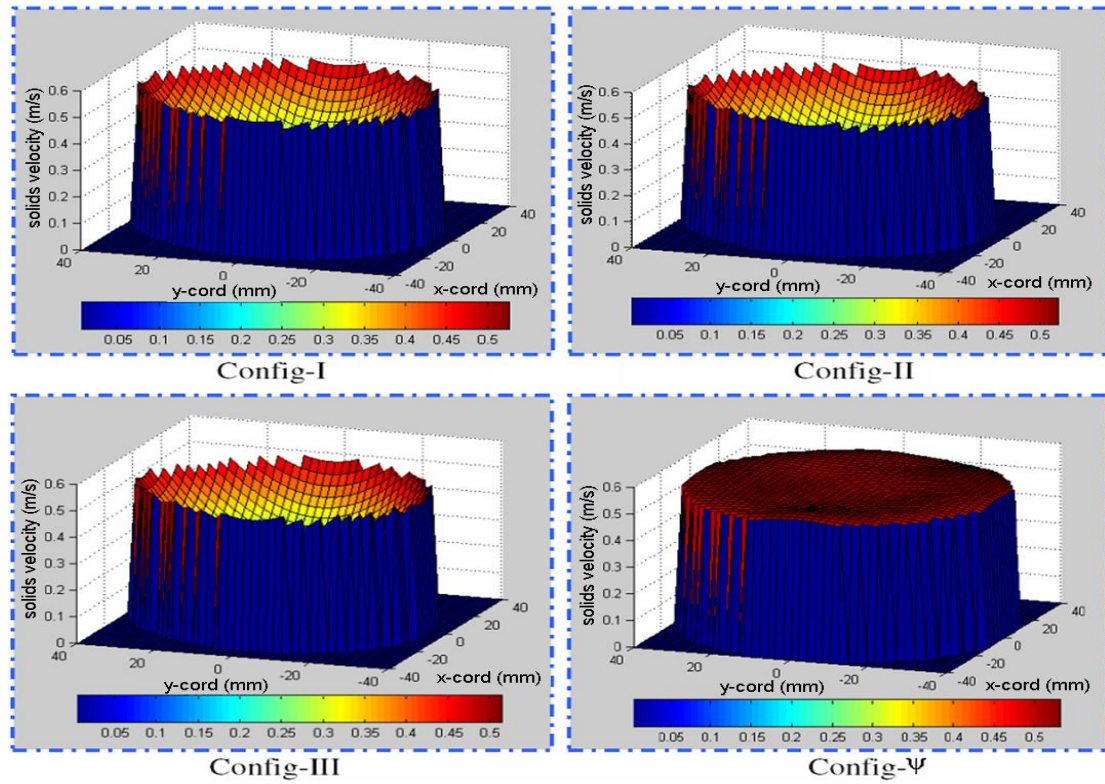
Figure 7-37: Local solids velocity profiles for flow in vertical pipe, flow condition 8($Q_{s,ref} = 1.998$ m^{3}h^{-1}, $Q_{w,ref} = 7.98$ m^{3}h^{-1})
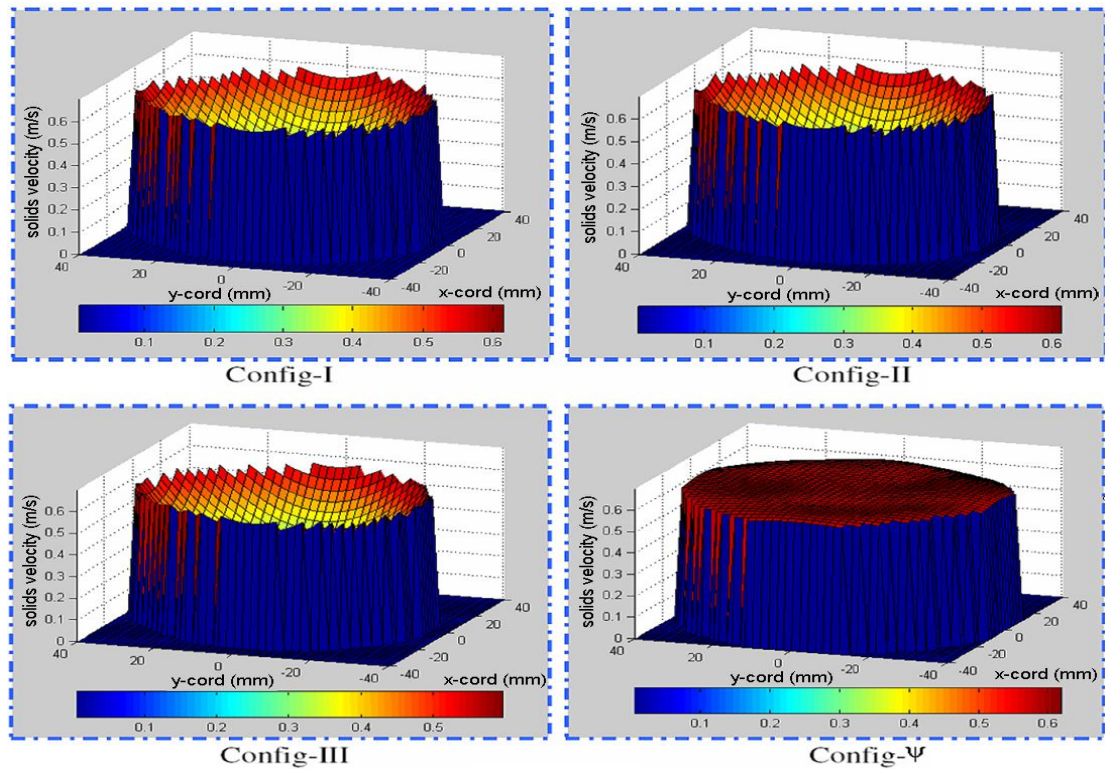
Figure 7-38: Local solids velocity profiles for flow in vertical pipe, flow condition 9($Q_{s,ref} = 1.974$ m^{3}h^{-1}, $Q_{w,ref} = 9.35$ m^{3}h^{-1})

7.2.3.2 3-D Local solids velocity profiles for upward flow in a pipe inclined at 15° to the vertical
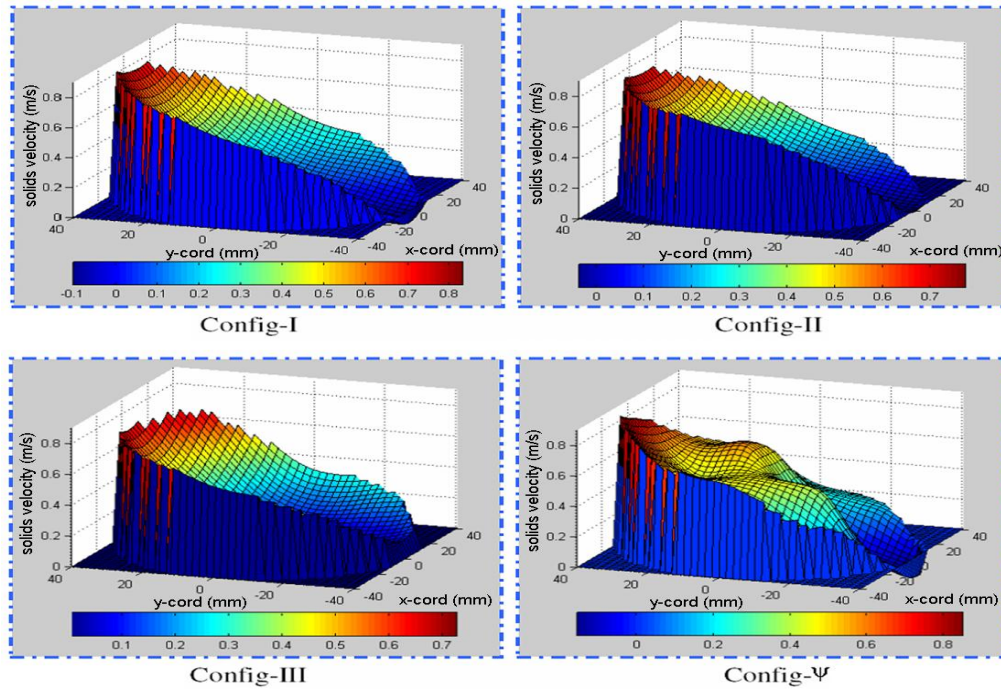
Figure 7-39: Local solids velocity profiles for flow in pipe inclined at 15° to the vertical, flow condition 10($Q_{s,ref} = 0.613$ m^{3}h^{-1}, $Q_{w,ref} = 9.45$ m^{3}h^{-1})
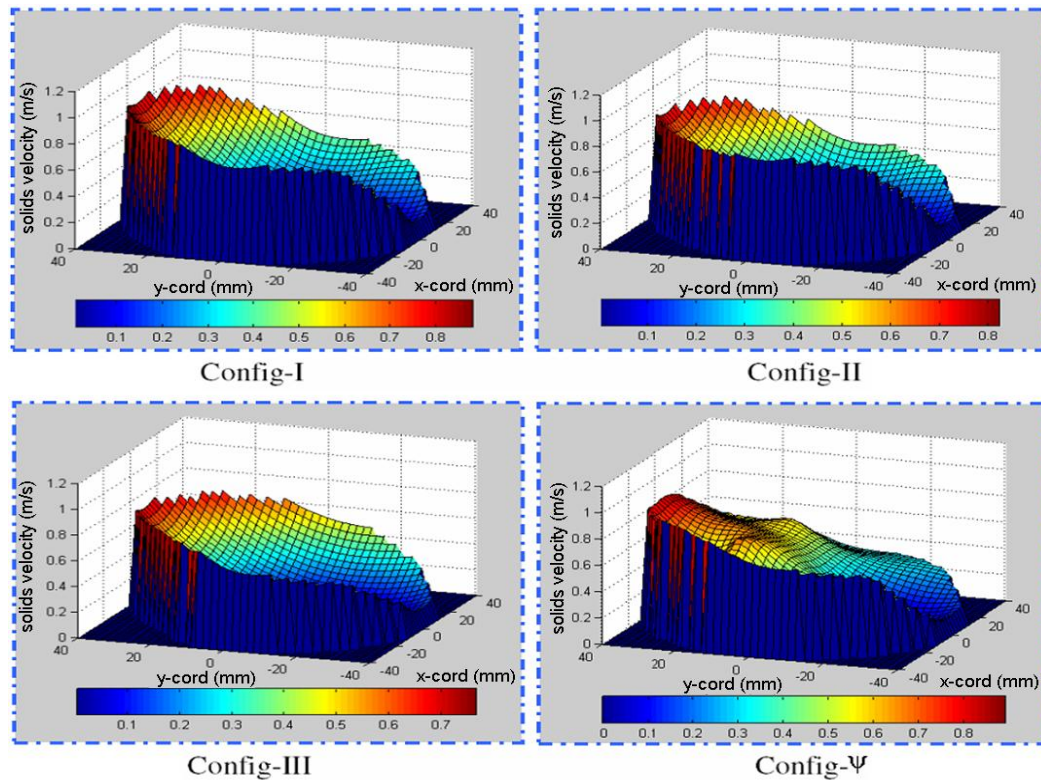
Figure 7-40: Local solids velocity profiles for flow in pipe inclined at 15° to the vertical, flow condition 11($Q_{s,ref} = 0.731$ m^{3}h^{-1}, $Q_{w,ref} = 10.91$ m^{3}h^{-1})

244
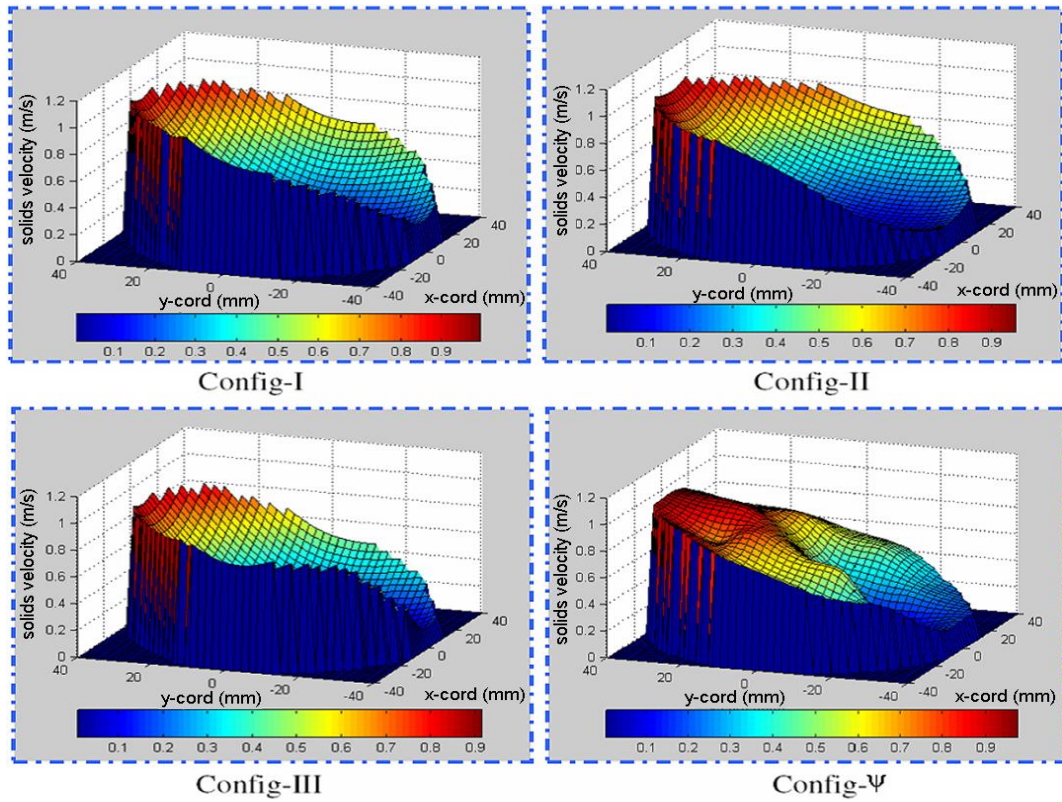
Figure 7-41: Local solids velocity profiles for flow in pipe inclined at 15° to the vertical, flow condition 12($Q_{s,ref}$ =0.704 m³h⁻¹, $Q_{w,ref}$ = 12.43 m³h⁻¹)
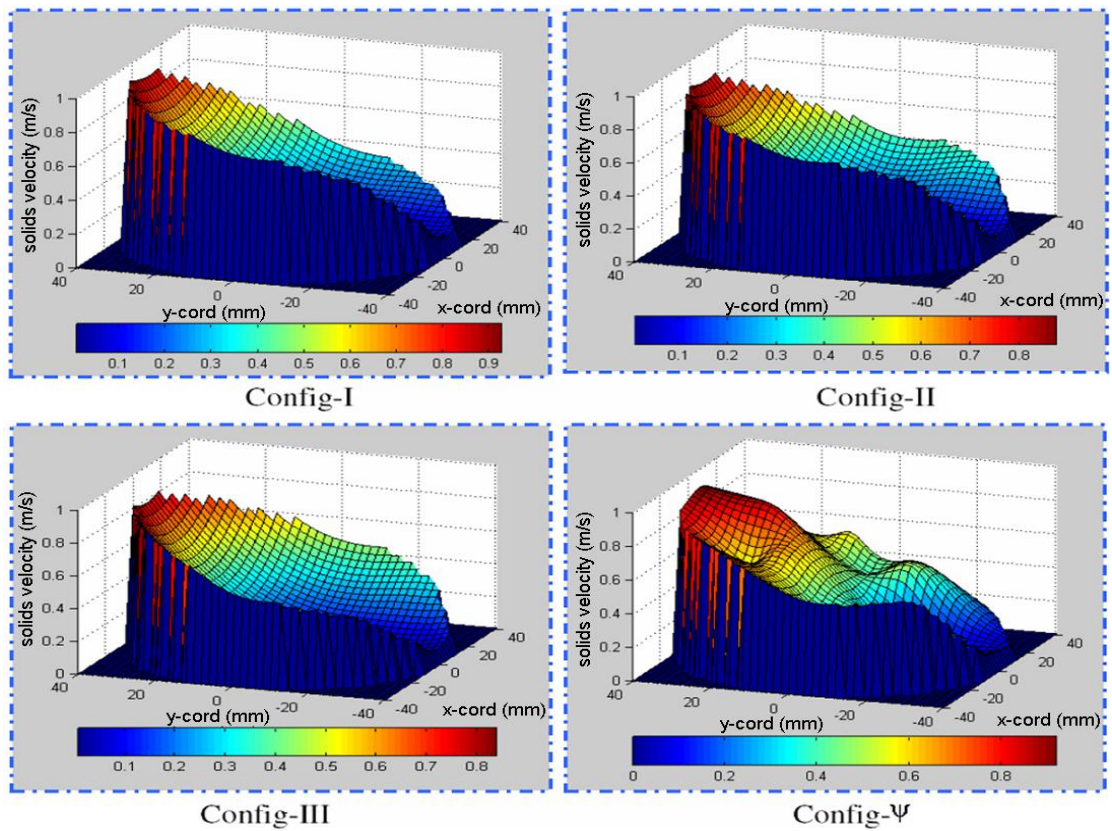
Figure 7-42: Local solids velocity profiles for flow in pipe inclined at 15° to the vertical, flow condition 13($Q_{s,ref}$ =1.187 m³h⁻¹, $Q_{w,ref}$ = 12.82 m³h⁻¹)

245
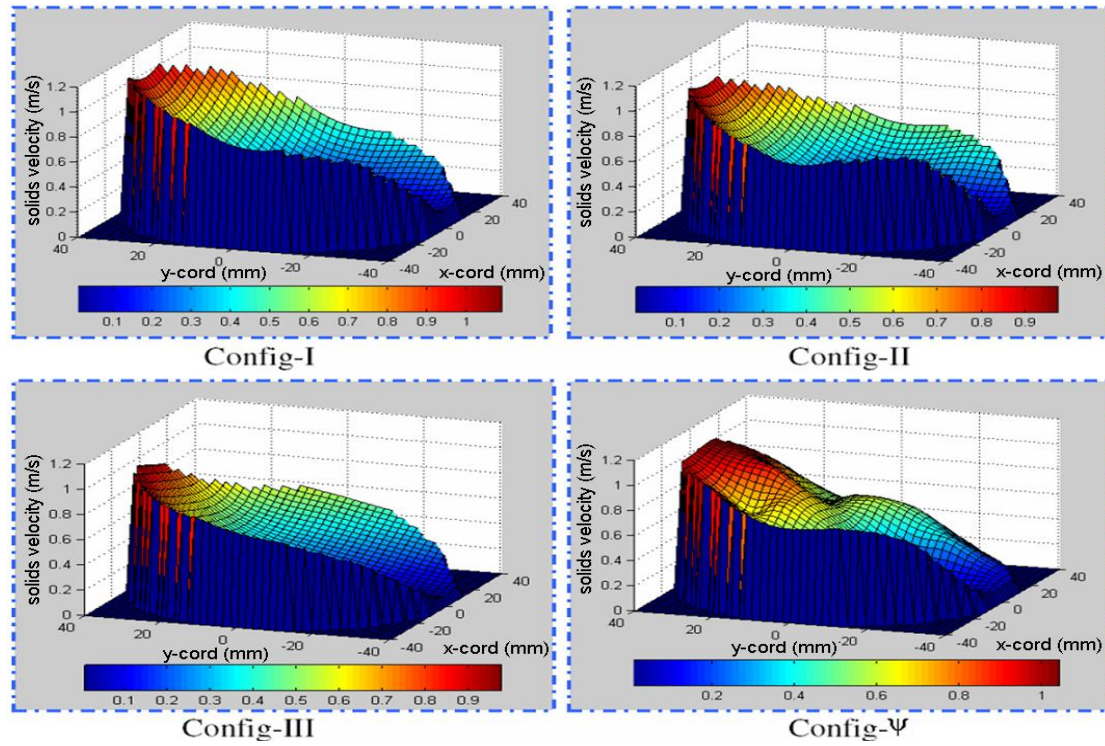
Figure 7-43: Local solids velocity profiles for flow in pipe inclined at 15° to the vertical, flow condition 14($Q_{s,ref}$ =1.104 m^{3}h^{-1}, $Q_{w,ref}$ = 13.94 m^{3}h^{-1})
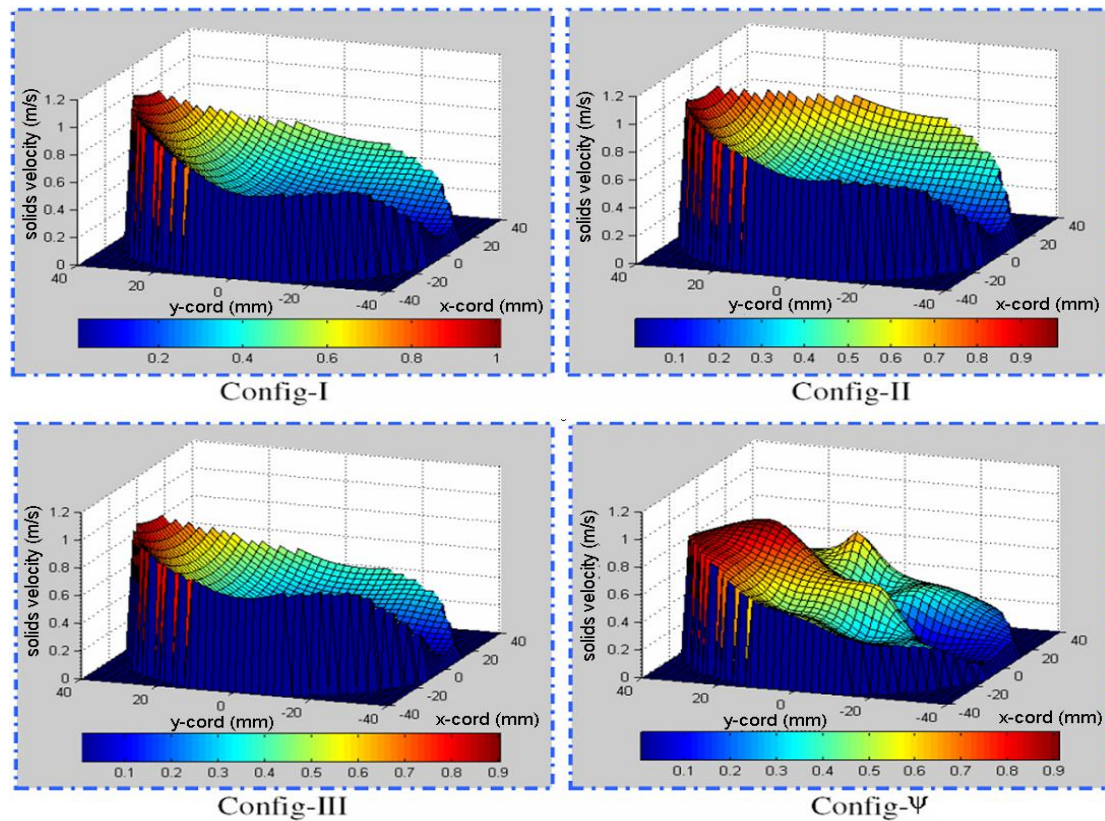
Figure 7-44: Local solids velocity profiles for flow in pipe inclined at 15° to the vertical, flow condition 15($Q_{s,ref}$ =1.010 m^{3}h^{-1}, $Q_{w,ref}$ = 15.43 m^{3}h^{-1})
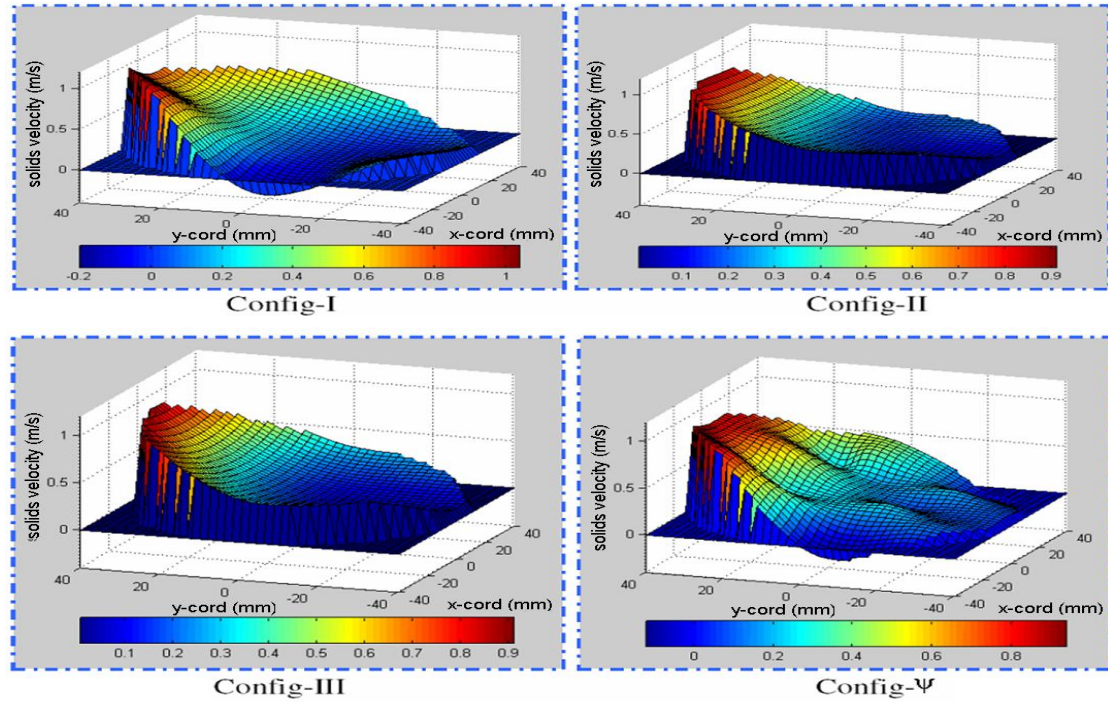
Figure 7-45: Local solids velocity profiles for flow in pipe inclined at to the vertical, flow condition 16($Q_{s,ref}$ =1.010 m^{3}h^{-1}, $Q_{w,ref}$ = 15.43 m^{3}h^{-1})

7.2.3.3 3-D Local solids velocity profiles for upward flow in a pipe inclined at 30° to the vertical
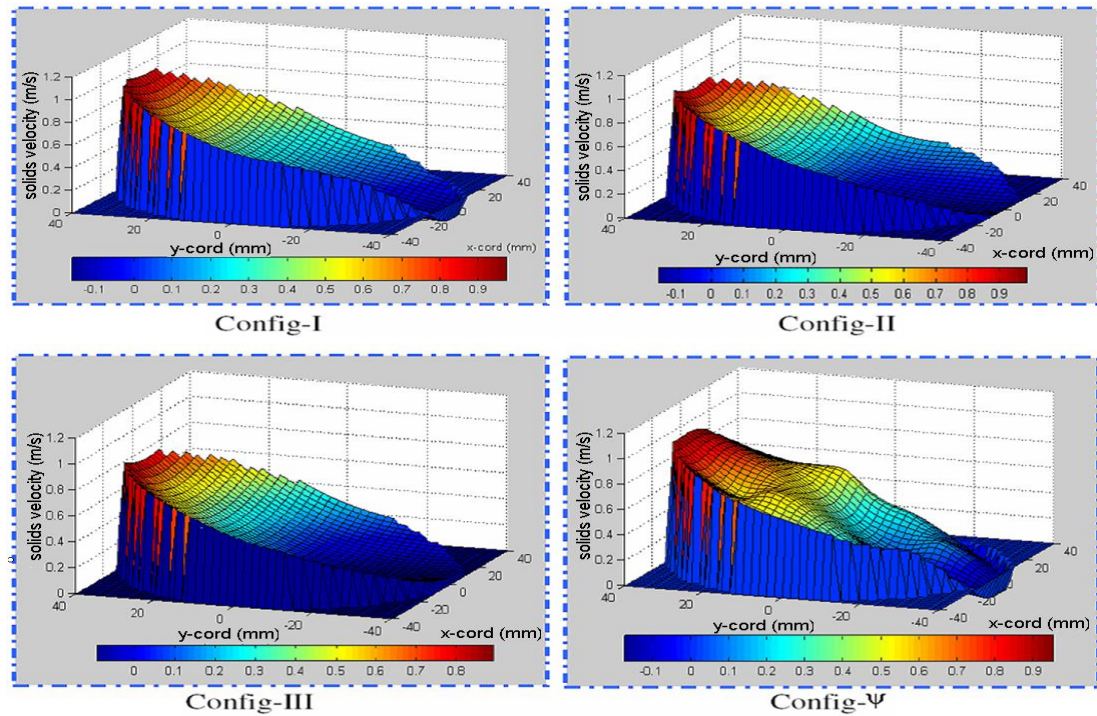
Figure 7-46: Local solids velocity profiles for flow in a pipe inclined at 30° to the vertical, flow condition 19($Q_{s,ref}$ =0.360 m^{3}h^{-1}, $Q_{w,ref}$ = 7.218 m^{3}h^{-1})
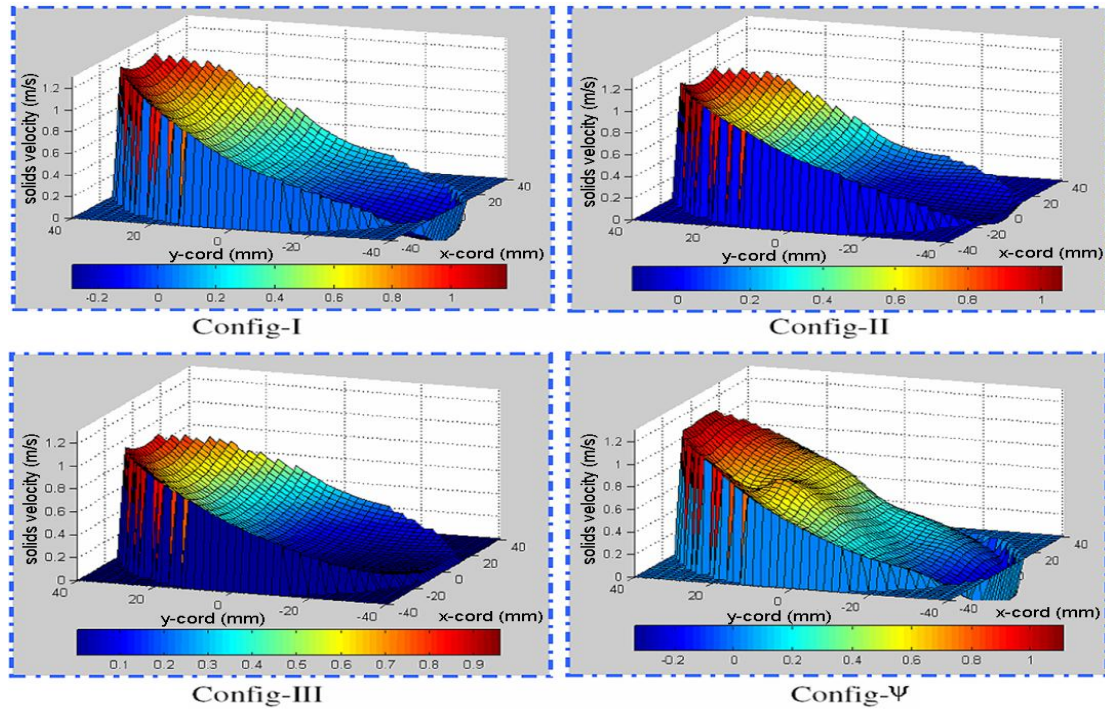
Figure 7-47: Local solids velocity profiles for flow in a pipe inclined at 30° to the vertical, flow condition 20($Q_{s,ref}$ =0.591 m^{3}h^{-1}, $Q_{w,ref}$ = 10.79 m^{3}h^{-1})
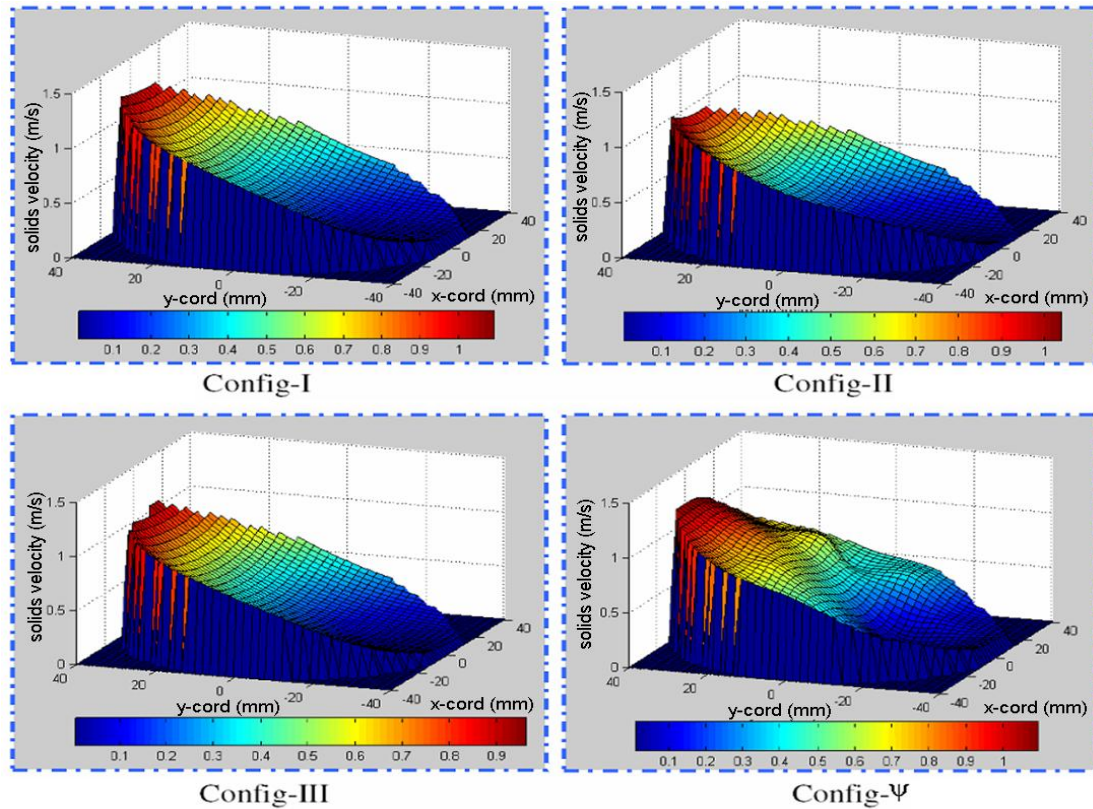
Figure 7-48: Local solids velocity profiles for flow in a pipe inclined at 30° to the vertical, flow condition 21($Q_{s,ref}$ =0.549 m^{3}h^{-1}, $Q_{w,ref}$ = 12.13 m^{3}h^{-1})
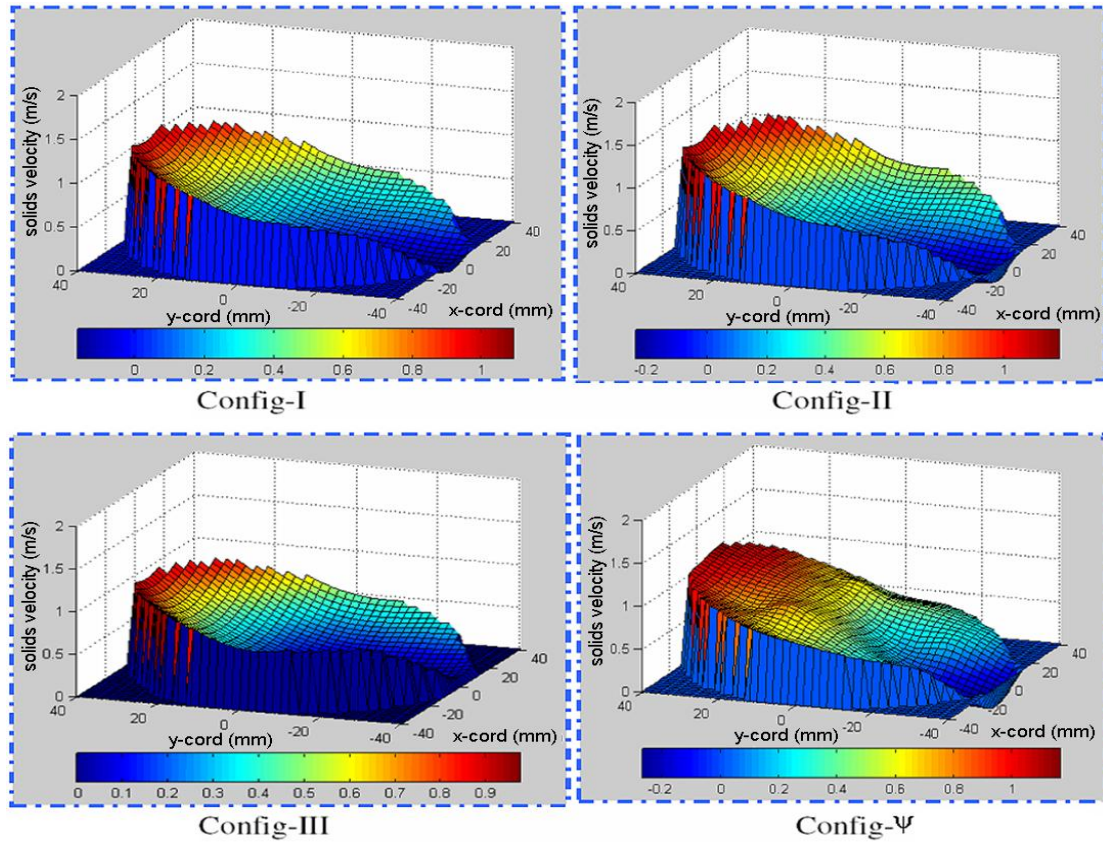
Figure 7-49: Local solids velocity profiles for flow in a pipe inclined at 30° to the vertical, flow condition 22($Q_{s,ref}$ =0.951 m³h⁻¹, $Q_{w,ref}$ = 12.47 m³h⁻¹)
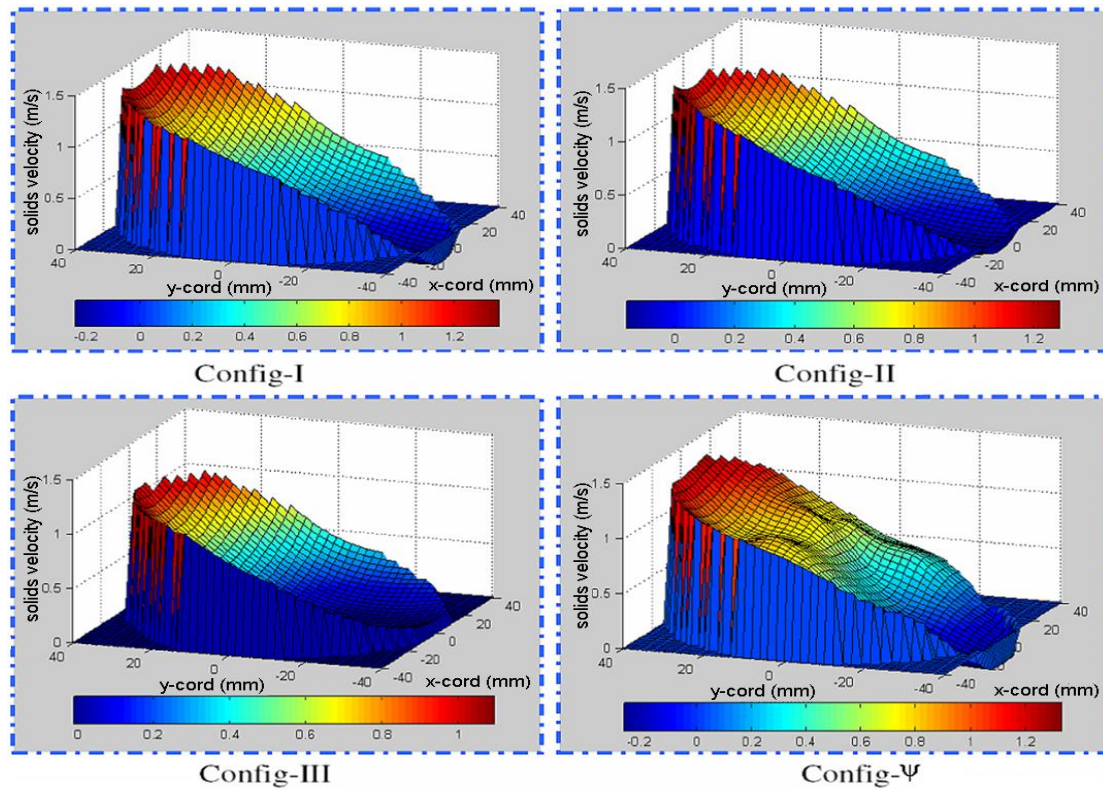
Figure 7-50: Local solids velocity profiles for flow in a pipe inclined at 30° to the vertical, flow condition 23($Q_{s,ref}$ =1.010 m³h⁻¹, $Q_{w,ref}$ = 14.06 m³h⁻¹)
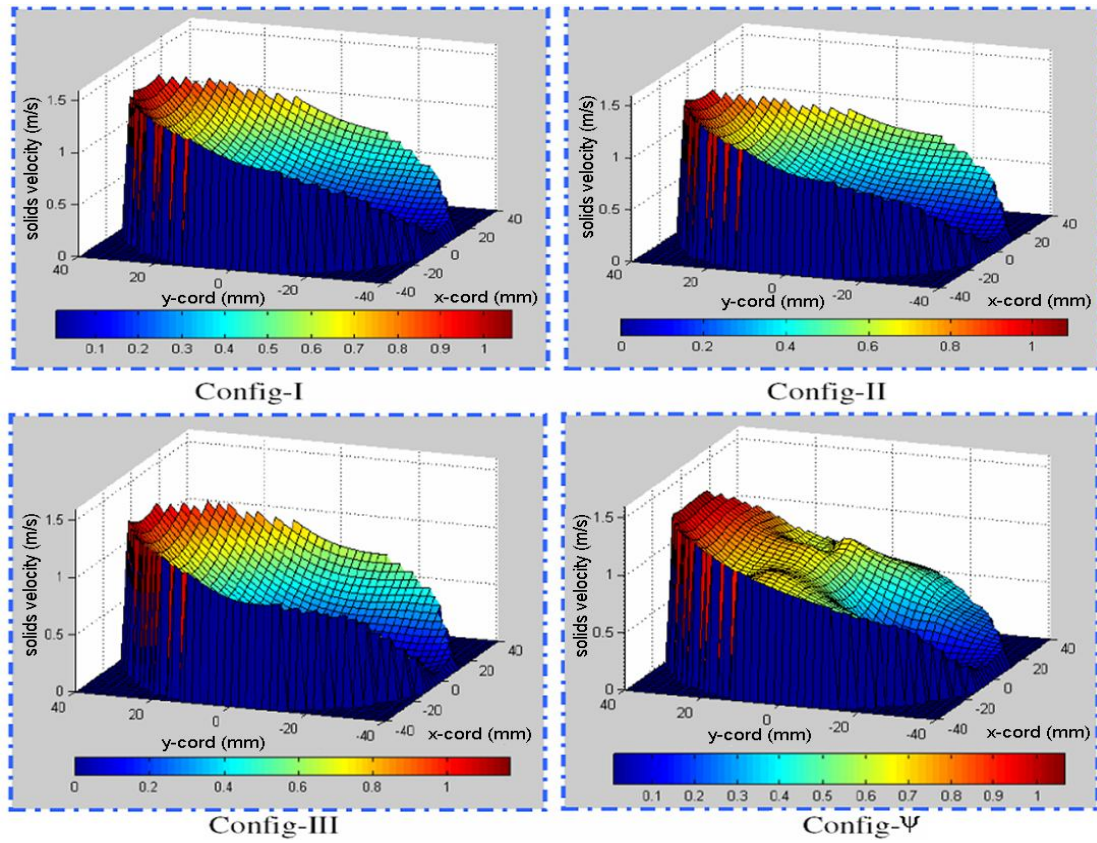
Figure 7-51: Local solids velocity profiles for flow in a pipe inclined at 30° to the vertical, flow condition 24($Q_{s,ref}$ =0.959 m^{3}h^{-1}, $Q_{w,ref}$ = 15.66 m^{3}h^{-1})
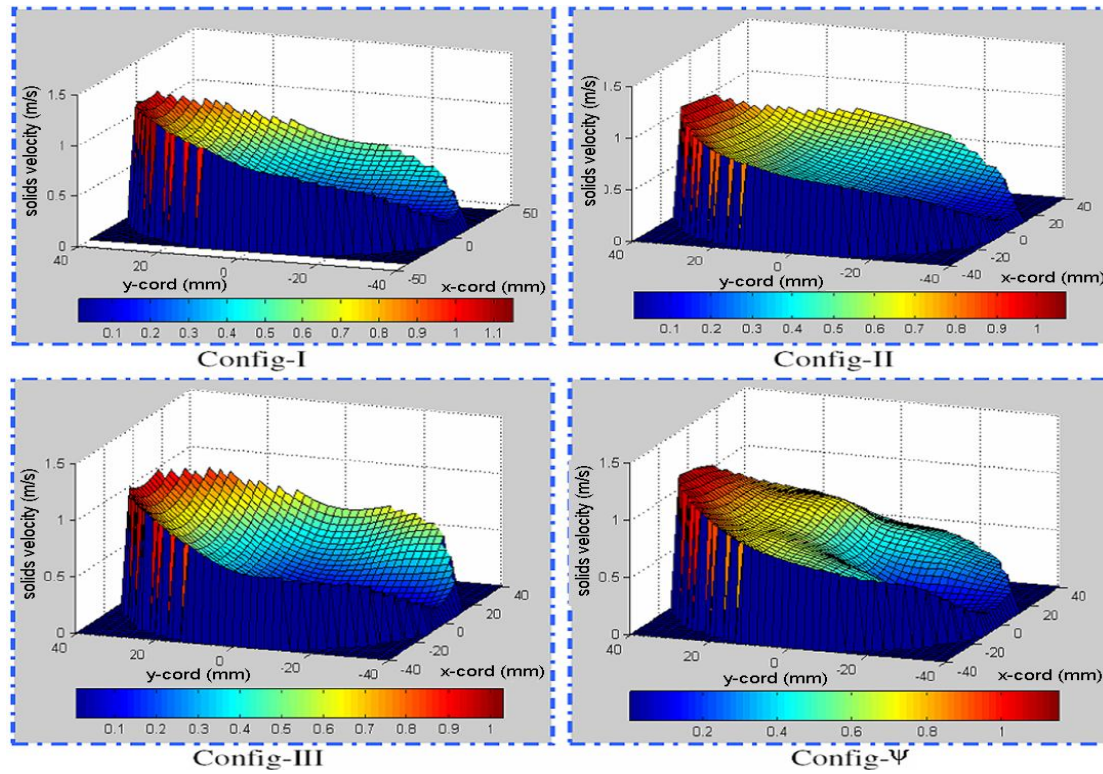
Figure 7-52: Local solids velocity profiles for flow in a pipe inclined at 30° to the vertical, flow condition 25($Q_{s,ref}$ =1.41 m^{3}h^{-1}, $Q_{w,ref}$ = 14.10 m^{3}h^{-1})
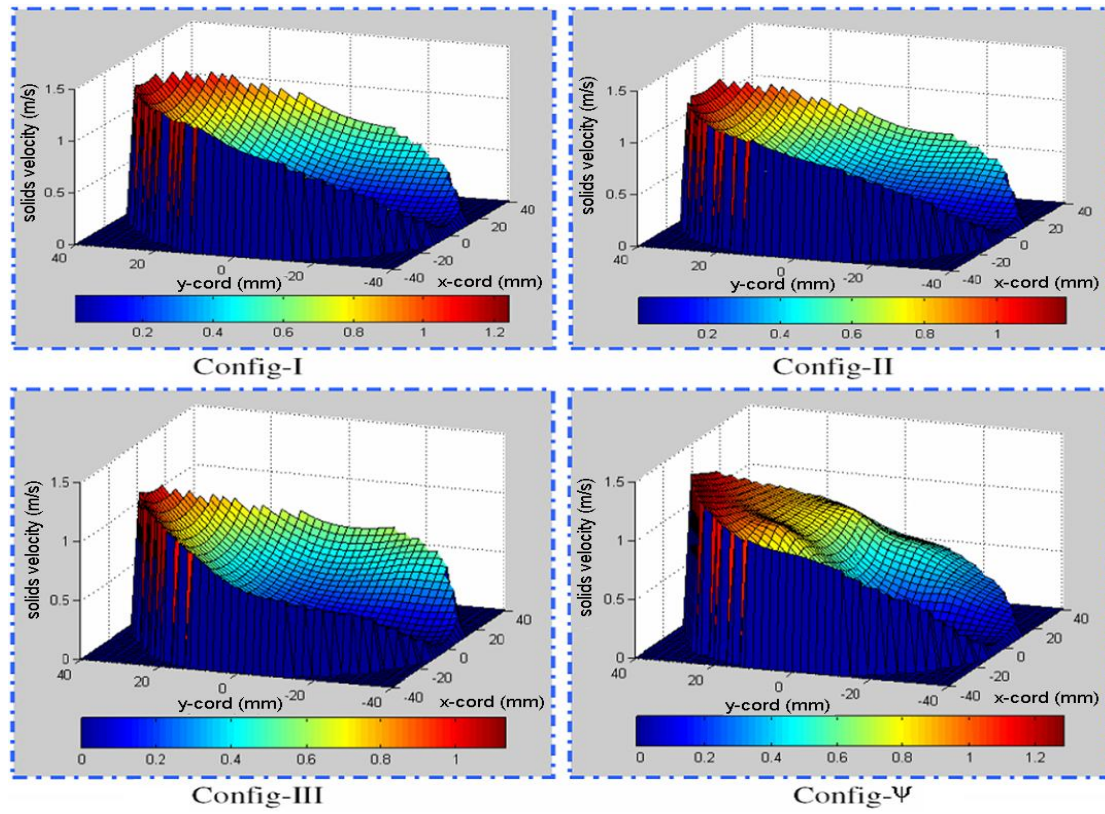
Figure 7-53: Local solids velocity profiles for flow in a pipe inclined at 30° to the vertical, flow condition 26($Q_{s,ref}$ =1.651 m³h⁻¹, $Q_{w,ref}$ = 15.96 m³h⁻¹)
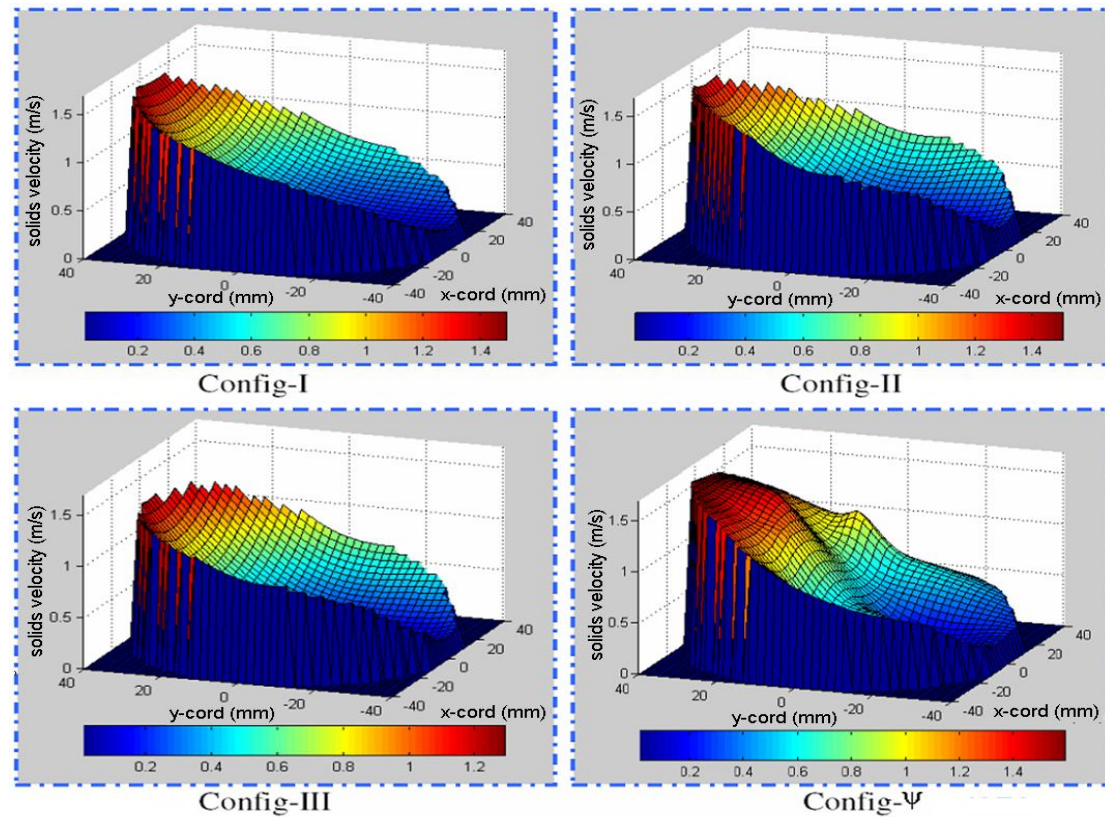
Figure 7-54: Local solids velocity profiles for flow in a pipe inclined at 30° to the vertical, flow condition 27($Q_{s,ref}$ =1.623 m³h⁻¹, $Q_{w,ref}$ = 17.12 m³h⁻¹)

7.2.4 Discussion of the local axial solids velocity profiles

3D profiles of the local solids velocity obtained using Configs-I, II and III for vertical flow (see Figures 7-30 to 7-38) show only small variations of the velocity profiles between the different configurations. The velocity profiles are concave, which may seem to imply that the solids velocity is lower in the centre of the pipe and greater nearer the pipe wall. However, this effect is due the fact that the figures for Configs-I, II and III show the measurements made for the eight separate electrode arrangements. Thus, individually, they have an inbuilt sensitivity bias for solids close to the pipe wall. It could be said that there are an insufficient number of measuring points in the flow cross-section. Thus, as explained in Section 7.2.1 the separate measurements are combined so that, in effect, instead of eight separate measurements in each figure we obtain a measure of the local solids velocity profile corresponding to twenty-four simultaneous measurements. This has been named Config-ψ. Consider Figure 7-30, when the 24 data points are combined the velocity profile becomes flatter over the entire pipe cross-section. This is welcome because the profiles obtained for turbulent flow in a vertical pipe correspond well with accepted flow patterns.

It is clear from Figures 7-39 to 7-45 that, for inclined upward flow, the distribution of the measured local axial solids velocity u_S is highly non-uniform. At the lower side of the pipe, due to the higher local solids volume fraction (the solids accumulate due to gravitational effects) the axial velocity of the solids was lowest.

When the pipe was inclined at 15° to the vertical the four flows with lowest values of the mean solids velocity produced a value of the local solids velocity u_S which was negative at the lower side of the pipe (see Figure 7-39, 7-40 and 7-45). Figure 7-39 (Configs-I, II and ψ) which show evidence of negative local axial solids velocity on the lower side of the inclined pipe indicate that, in this region, the solid particles were actually flowing backwards down the pipe Towards the upper side of the inclined pipe, the local axial velocity of the solid particles was relatively high and positive, indicating that the particles were flowing upwards through the working section.

Figure 7-40 shows that for flow condition 11 there is a negative local axial solids velocity at the lower side of the inclined pipe. Figure 7-42 shows that for flow with

the pipe inclined at 15°, u_S had a maximum value of 0.85ms^{-1} for flow condition 13. Note that, for flows inclined at 15° from the vertical the profiles all show qualitative agreement except for flow condition 16 (see Figure 7-45). Figure 7-45 shows a negative value of solids velocity u_S at the lower side of the pipe. It should be noted that Config-ψ also shows a clear and distinct reversal of flow at the lower side of the pipe, which agreed with visual observation of the flow.

During experimental testing both $Q_{s,ref}$ and $Q_{w,ref}$ varied slightly but these small variations were not the cause of the substantial fluctuations to be seen in Figure 7-18 for flow condition 16 ($Q_{s,ref}$ = 1.631 m^3h^{-1}, $Q_{w,ref}$ = 14.05 m^3h^{-1}) with the pipe at 15° to the vertical. It is more likely that for flow condition 16 in some parts of the pipe the presence of the solids caused fluctuation which occasionally caused $\bar{u}_w$ to fall below the critical velocity, u_c, and the liquid was unable to suspend the solids. This caused significant fluctuations and in some cases flow reversal as shown in Figure 7-45. Secondly, it was observed that at low values of u_S, e.g at flow condition 16, as some solid particles settled out their motion had a radial component which was sufficient to corrupt the cross-correlation function. In order to achieve an accurate measurement of u_S the peak of the cross-correlation function must be accurately located and any degradation of the function results in errors in the velocity measurement.

Figures 7-46 to 7-54 present results when the pipe was inclined angle at 30° to the vertical. Figure 7-46, flow condition 19, shows that at the lower side of the pipe (where the mean density of the solids–water mixture was relatively high due to the high local solids volume fraction) the axial velocity of the solids was low. Indeed, there is evidence of a negative local axial solids velocity on the lower side of the inclined pipe, indicating that, in this region, the solid particles were again flowing backwards down the pipe (this result agrees with visual observation of the flow). Towards the upper side of the inclined pipe, the local axial velocity of the solid particles was relatively high and positive, indicating that the particles were flowing

rapidly upwards through the working section in this region. In all cases for the pipe inclined at 30° to the vertical, where Config-I detected reversal of flow this was also found in Config-ψ, and was confirmed by visual observation.

Figure 7-47, flow condition 20, shows that there is a negative local axial solids velocity of about -0.23ms^{-1} at the lower side of the inclined pipe and the local axial velocity reached 1.1ms^{-1} at the upper side of the inclined pipe. Also, Figure 7-49, flow condition 22, shows that there is a negative local axial velocity of about -0.20ms^{-1} at the lower side of the inclined pipe and the local axial solids velocity reached 1.2ms^{-1}.

Figure 7-50, flow condition 23, shows that there is a negative local axial solids velocity of about -0.20ms^{-1} at the lower side of the pipe, which agrees with the visual observation through the cross section of the pipe, and the maximum at the upper side of the inclined pipe is 1.3 ms^{-1}. Figures 7-51 to 7-54 shows that there is no negative local solids velocity at the lower side of the inclined pipe, but that solids moved more slowly in the upward direction at the bottom of the pipe than at the top and this again agreed with visual observation. Figure 7-53 shows that at the top of the pipe u_S reached 1.2ms^{-1} for flow condition 17. However, on the lower side of the inclined pipe the local axial solids velocity was 0.1ms^{-1}. The results obtained using the ICC meter agreed with Lucas et.al (1999, 2000) and Cory (1999) who measured solids in water flows using six electrode local probe and an ERT system.

A search of the literature found no profiles for the local solids velocity, u_S, in inclined solids-liquid flow. However, Tabeling, et al., (1991) and Lucas (1995) have reported that for liquid-liquid flow in an inclined pipe, a steep gradient can occur in the velocity of the more dense phase with possible negative flow at the lower side of the pipe. Lucas et.al (1999, 2000) reported a negative flow for solids in solids-water flow in an inclined pipe. Scarlett and Grimley (1974) and Hsu, et al., (1989) have published complete cross-sectional profiles of u_S for horizontal solids-liquid flow but since the pipe was horizontal no reverse flow was observed. Both Scarlett and Grimley (1974) and Hsu, et al., (1989) reported a steep gradient of u_S as a function of the y-coordinate which can be attributed to gravitational effects. This suggests that the profile shapes

obtained during the current investigation are reliable. The profiles obtained from the ICC system also show good qualitative agreement with Lucas, et al., (1999, 2000).

7.2.5 Local solids volume fraction profiles from ICC

Solids volume fraction profiles were obtained using one electrodes array only (Array B) see Figure 3-9. The technique presented in Section 3-10 was used for each configuration listed in Tables 4-2, 4-3 and 4-4. Eight different rotational positions were again used for each of Configs-I, II and III. Data were collected for 60 seconds for each rotational position. The profiles are shown for vertical upward flows and upward flows inclined at 15° and 30° from the vertical, using the flow condition given in Table 7-2.

The available literature shows that the local volume fraction profiles are principally a function of the y co-ordinate (and are essentially constant as the x co-ordinate varies for a fixed value of y), see Section 7.2.2. It was initially decided to plot solids volume fraction against the y-coordinate of the CoA (see Figure 7-2). Figures 7-55 to 7-81 show the distribution of the measured solids volume fraction obtained from the ICC against the y-coordinate of the CoA.

7.2.5.1 Local solids volume fraction profiles for upward flow in a vertical pipe.

Figures 7-55 to 7-81 show the local axial solids volume fraction for upward flow in the pipe for three angles of inclination (0°, 15° and 30°). In each figure the y-axis represent the y-coordinate of the CoA and the x-axis represents the local axial solids volume fraction measured at each of the eight rotational positions for Configs-I, II and III, as listed in Tables 4-2, 4-3 and 4-4. Thus in each figure there are eight data points for each of Configs-I, II and III. In Figures 7-55 to 7-63, for vertical flow, the plots also include the measured volume fraction reference values obtained from the dp cell, $\overline{\alpha}_{s,ref}$, and is shown as a red dotted red line.

As has been discussed in Sections 7.2.2.1 and 7.2.2.2 for inclined flows, there were consistent differences in the measurements made of the volume fraction as obtained from Configs-I,II and III. This is because they represent different electrode configurations so that the CoA of each rotational position is a different distance from

the pipe wall and the effective sensing region covers a different area. The resulting differences in the measured values are more pronounced the more the pipe carrying the flow is inclined to the vertical.

It can be seen from Figures 7-55 to 7-63 that for vertical flow, the local axial solids volume fraction appears more-or-less constant across the pipe cross-section. Lucas, et al., (1999, 2000) and Cory (1999) found similar results using the six-electrode local probe and ERT system for the local axial solids volume profiles in vertical flows. As mentioned in Section 7.2.2.1 this is an acceptable result because in the vertical flow the solids distribution would be expected to be uniform across the pipe section and the result agreed with visual observation of the flow pattern.

Figure 7-55: Local solids volume fraction profiles for flow in vertical pipe, flow condition 1($Q_{s,ref}$ =0.696 m^{3}h^{-1}, $Q_{w,ref}$ = 4.25 m^{3}h^1).

Figure 7-56: Local solids volume fraction profiles for flow in vertical pipe, flow condition 2($Q_{s,ref}$ =0.750 m³h⁻¹, $Q_{w,ref}$ = 5.49 m³h⁻¹)

Figure 7-57: Local solids volume fraction profiles for flow in vertical pipe, flow condition 3($Q_{s,ref}$ =0.724 m³h⁻¹, $Q_{w,ref}$ = 6.12 m³h⁻¹)

Figure 7-58: Local solids volume fraction profiles for flow in vertical pipe, flow condition 4($Q_{s,ref}$ =1.188 m^{3}h^{-1}, $Q_{w,ref}$ = 6.18 m^{3}h^{-1})
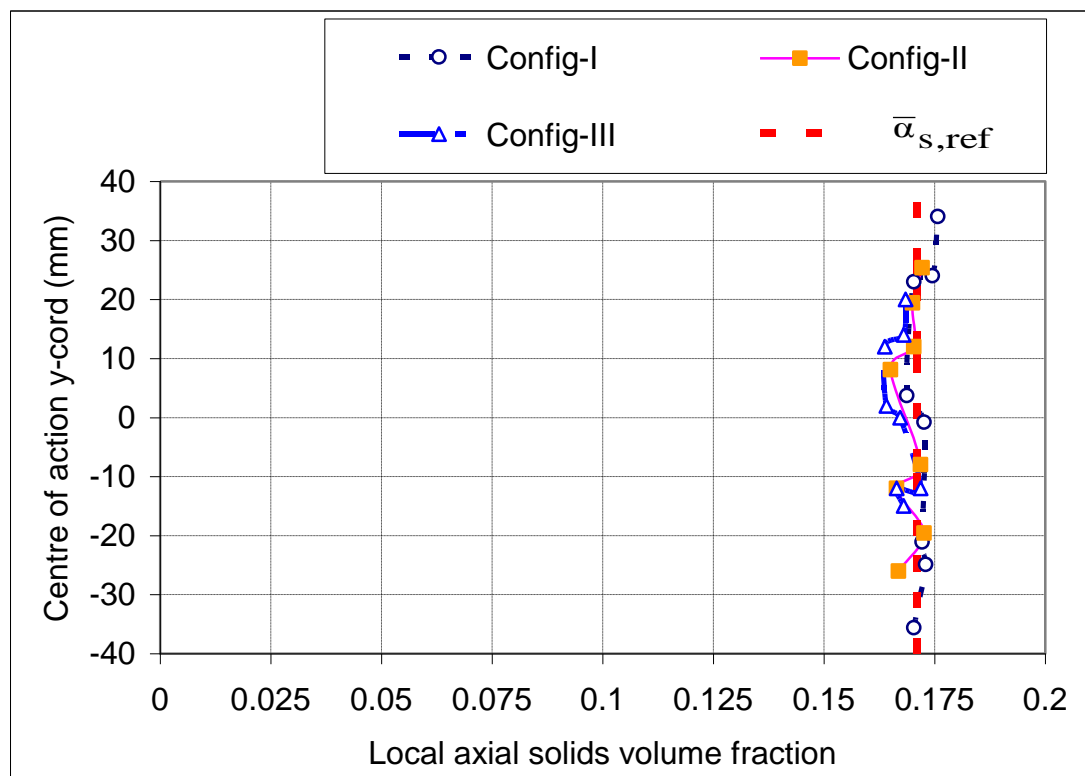
Figure 7-59: Local solids volume fraction profiles for flow in vertical pipe, flow condition 5($Q_{s,ref}$ =1.225 m^{3}h^{-1}, $Q_{w,ref}$ = 6.45 m^{3}h^{-1})
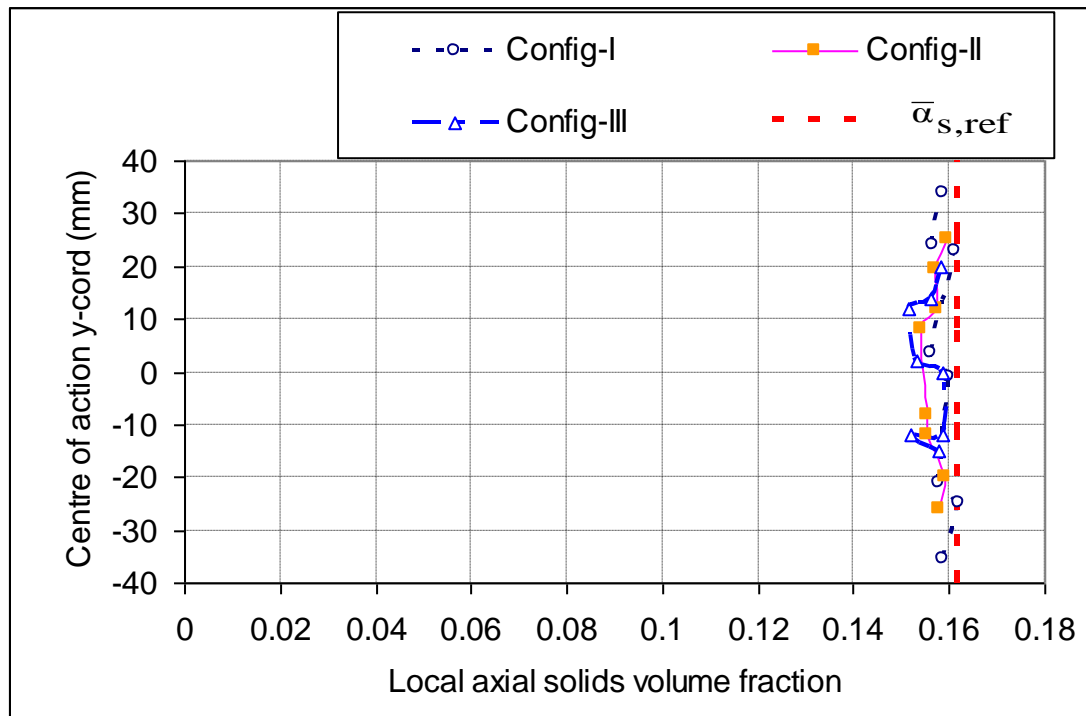
Figure 7-60: Local solids volume fraction profiles for flow in vertical pipe, flow condition 6($Q_{s,ref}$ =1.183 m³h⁻¹, $Q_{w,ref}$ = 6.51 m³h⁻¹)
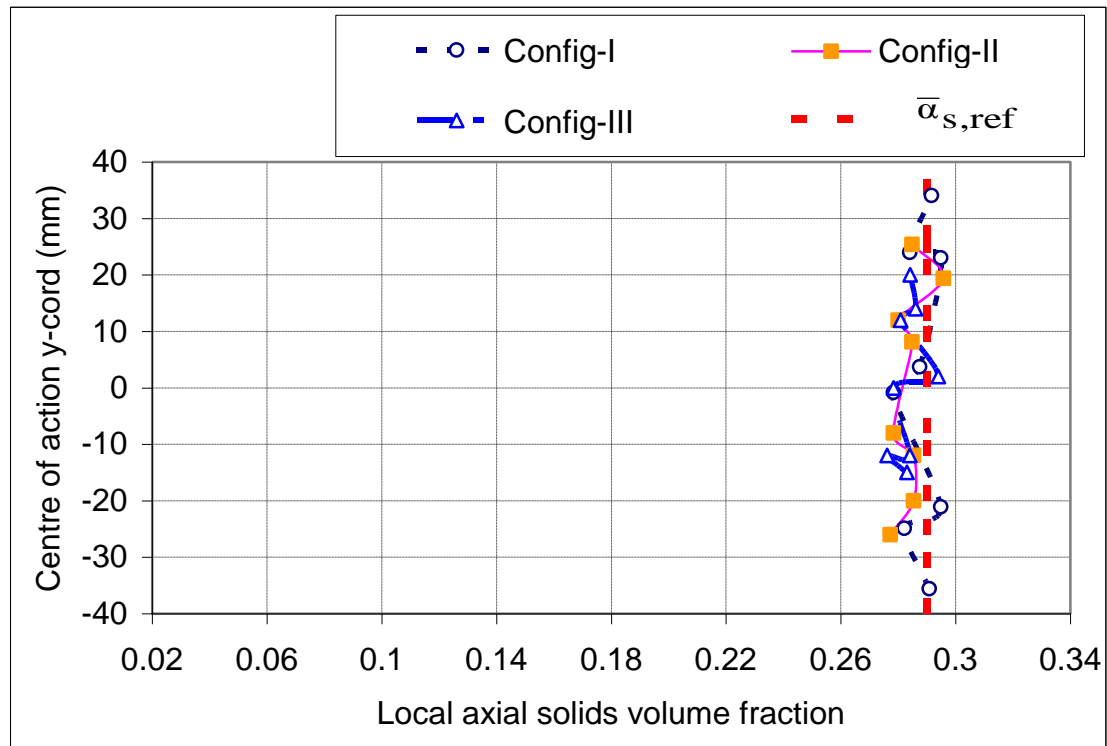
Figure 7-61: Local solids volume fraction profiles for flow in vertical pipe, flow condition 7($Q_{s,ref}$ =2.229 m³h⁻¹, $Q_{w,ref}$ = 5.87 m³h⁻¹)
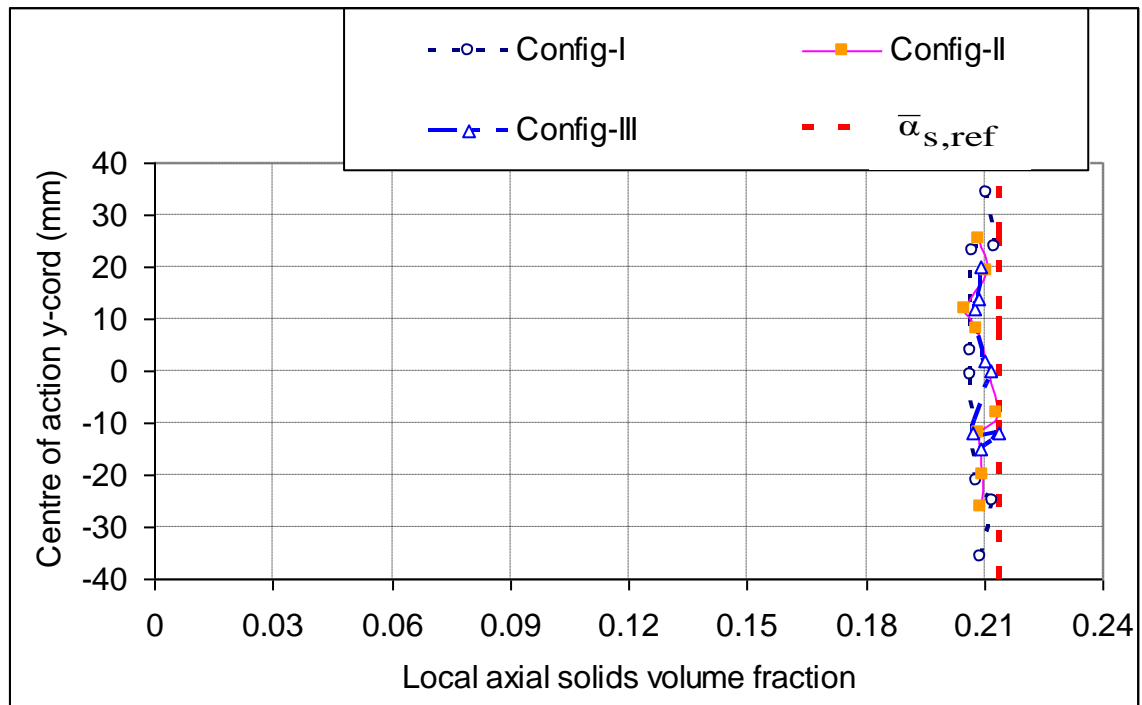
Figure 7-62: Local solids volume fraction profiles for flow in vertical pipe, flow

condition 8($Q_{s,ref}$ =1.998 m^{3}h^{-1}, $Q_{w,ref}$ = 7.98 m^{3}h^{-1})
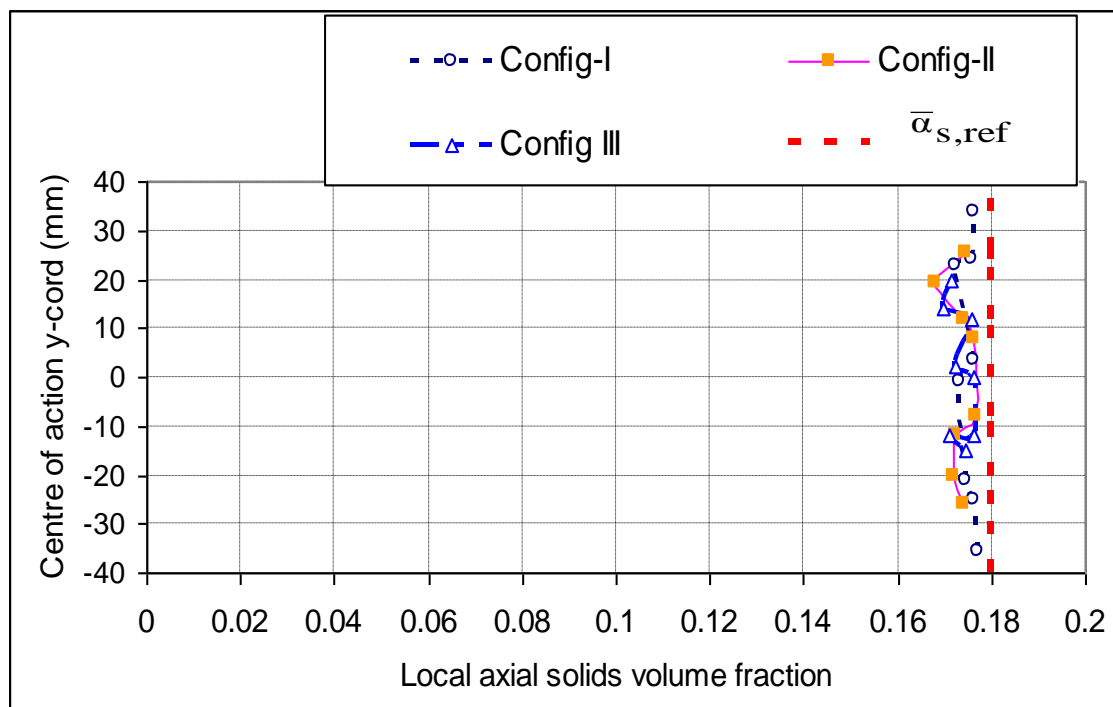
Figure 7-63: Local solids volume fraction profiles for flow in vertical pipe, flow

condition 9($Q_{s,ref}$ =1.974 m^{3}h^{-1}, $Q_{w,ref}$ = 9.35 m^{3}h^{-1})

7.2.5.2 Local solids volume fraction profiles for upward flow in a pipe inclined at 15° to the vertical

For 15° inclined flow there are some consistent differences in the readings obtained for Configs-I, II II and III as indicated in Figures 7-64 to 7-72 when the pipe is inclined at an angle to the vertical and the local solids volume fractions varies rapidly with spatial location in the flow cross section. The area over which Config-I measures the axial solids volume fraction is small so for the rotational position of Config-I where the is CoA closest to the wall of the pipe it is expected that Config-I will give an accurate measurement of the local solids volume fraction at the wall of the pipe. Config-II will measure the axial solids volume fraction averaged over a greater area and Config-III will measure the axial solids volume fraction over an even greater area. Since the CoA is closest to the wall for Config-I and furthest from the wall in Config-III it is to be expected that for flow in inclined pipes, the values of solids volume fraction obtained for Config-I will have a steeper negative average gradient than those obtained using Config-II or III. And Config-II will have a steeper gradient than Config-III.

General speaking, for inclined upward flow, the distribution of the measured local solids volume fraction α_S is highly non-uniform. It is clear from the results obtained for 15° inclination from the vertical that the local axial solids volume fraction is significantly greater at the lower side of the inclined pipe than at the upper side. This is confirmed by visual observation. Once again Lucas, et al., (1999, 2000) and Cory (1999) showed a similar finding using six local probe and ERT.

Figures 7-64 to 7-72 show results for pipe inclination of 15°. In all cases there was an increase in the local axial solids volume fraction the nearer to the bottom of the pipe. However, the rate of increase was not uniform and Figure 7-64, for example, shows variations in the rate of increase as the point of observation moved from the upper to lower side of the pipe, for each of the defined configurations Configs-I, II and III. For Config-I the maximum measured local volume fraction was 0.24, while for Config-II and Config-III it was 0.23 and 0.21 respectively. The minimum measured local solids volume fraction at the upper side of the inclined pipe was 0.05 for Config-I, while for Config-II and Config-III it was 0.047 and 0.04 respectively. Generally, except for the

261

slightly anomalous case of Config-II in Figure 7-66, Figures 7-64 to 7-72 show that the three electrode configurations listed in Tables 4-2, 4-3 and 4-4 (Configs-I,II and III) gives a nearly monotonic line where the local axial solids volume fraction increases the lower the point of observation within the pipe cross-section. This agreed with the author's visual observation of the solids water distribution during the experimental tests.
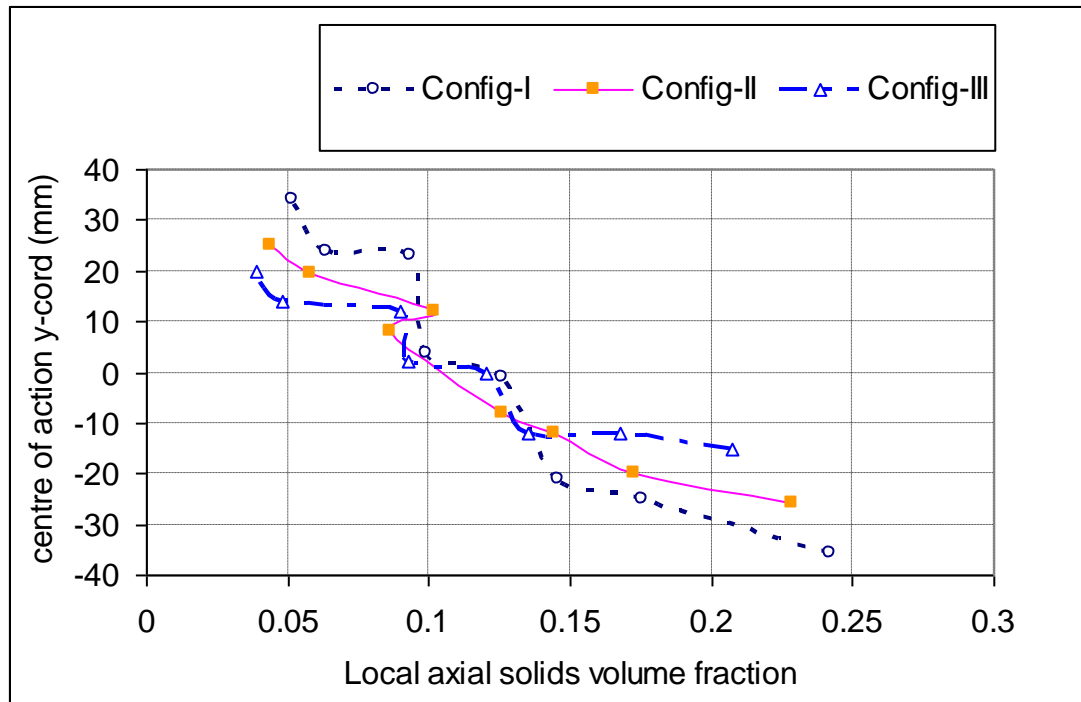
Figure 7-64: Local solids volume fraction profiles for pipe inclined at 15° to the vertical, flow condition 10($Q_{s,ref}$ =0.613 m^{3}h^{-1}, $Q_{w,ref}$ = 9.45 m^{3}h^{-1})
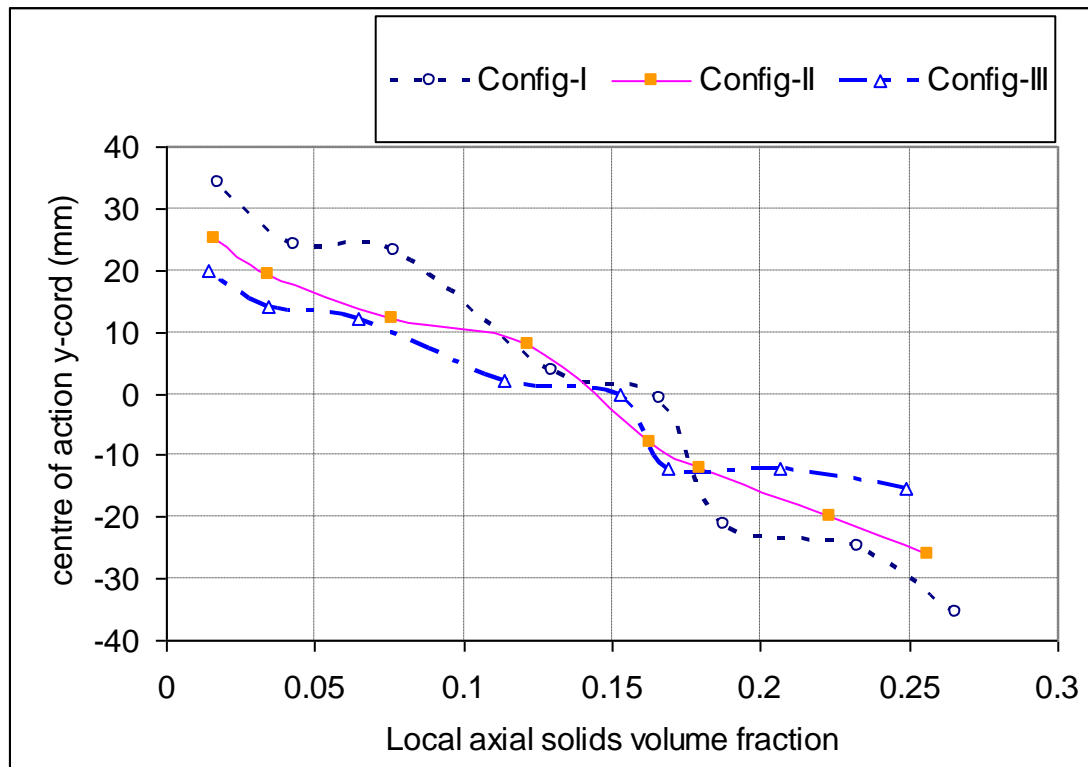
Figure 7-65: Local solids volume fraction profiles for pipe inclined at 15° to the vertical, flow condition 11($Q_{s,ref}$ =0.731 m^{3}h^{-1}, $Q_{w,ref}$ = 10.91 m^{3}h^{-1})
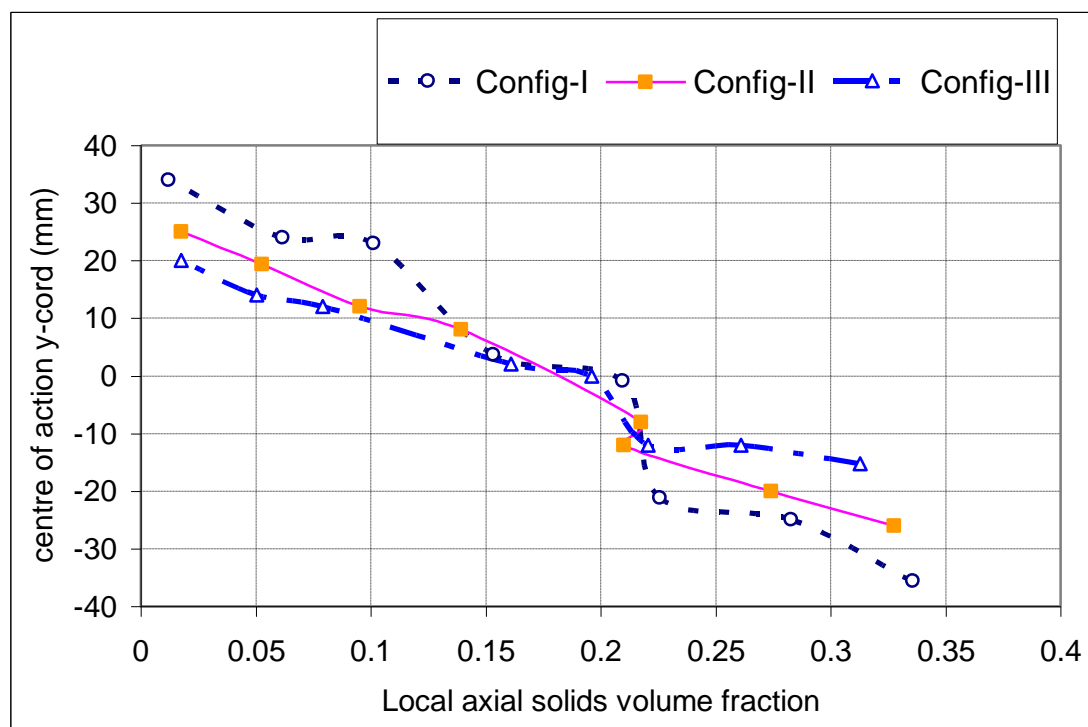
Figure 7-66: Local solids volume fraction profiles for pipe inclined at 15° to the vertical, flow condition 12($Q_{s,ref}$ = 0.704 m^{3}h^{-1}, $Q_{w,ref}$ = 12.43 m^{3}h^{-1})
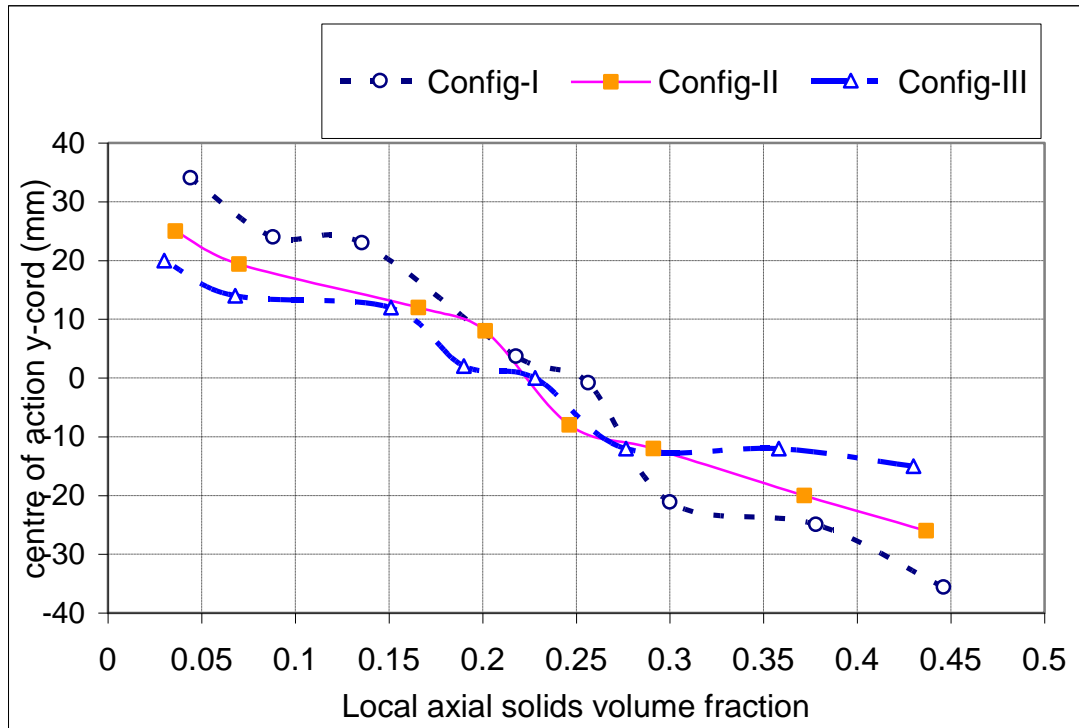
Figure 7-67: Local solids volume fraction profiles for pipe inclined at 15° to the vertical, flow condition 13.($Q_{s,ref}$ =1.187 m^{3}h^{-1}, $Q_{w,ref}$ = 12.82 m^{3}h^{-1})
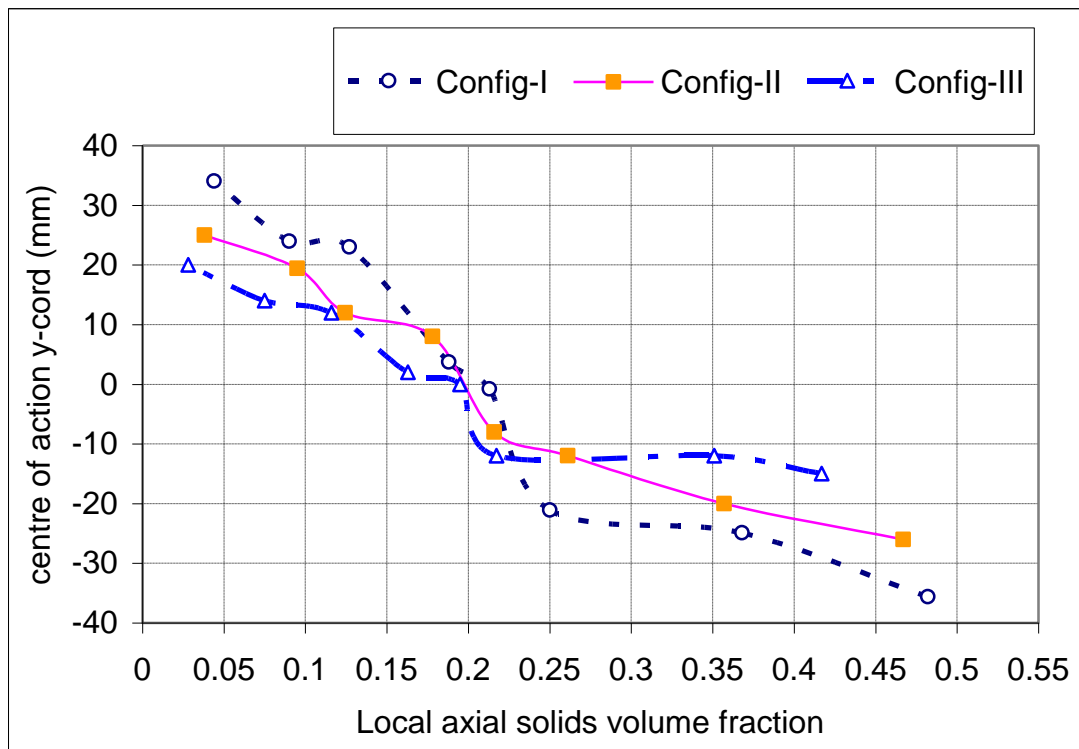
Figure 7-68: Local solids volume fraction profiles for pipe inclined at 15° to the vertical, flow condition 14($Q_{s,ref}$ =1.104 m^{3}h^{-1}, $Q_{w,ref}$ = 13.94 m^{3}h^{-1})

264
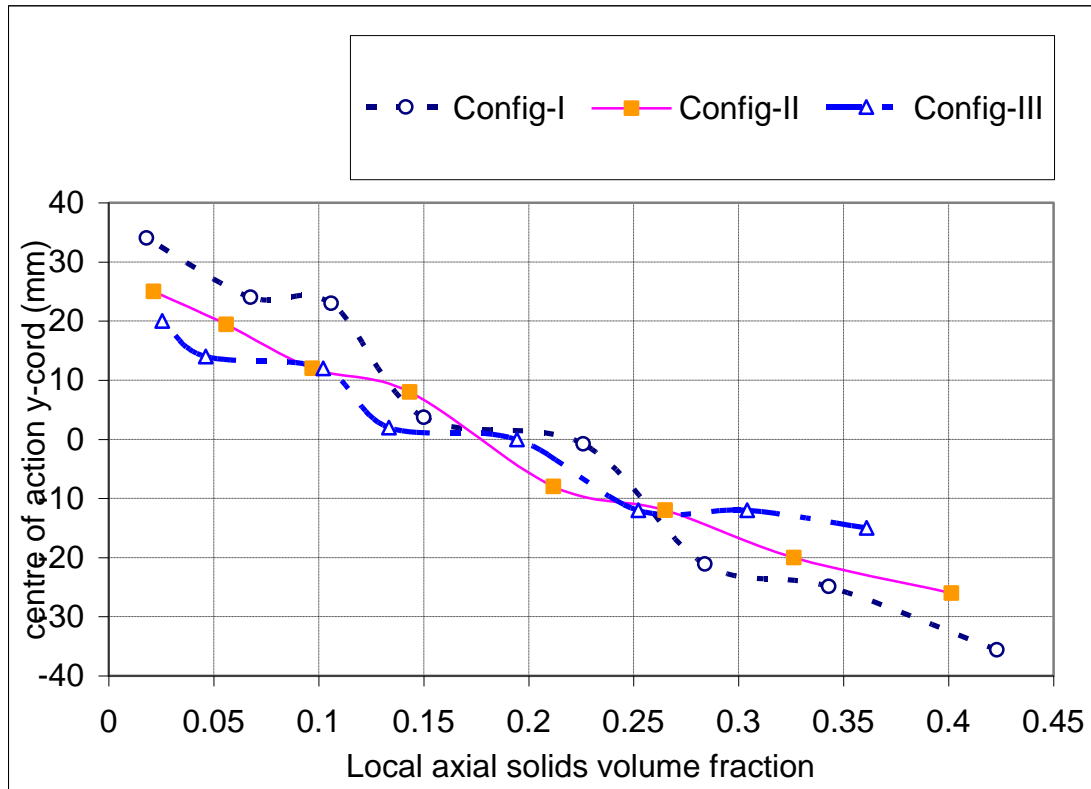
Figure 7-69: Local solids volume fraction profiles for pipe inclined at 15° to the vertical, flow condition 15($Q_{s,ref}$ =1.010 m^{3}h^{-1}, $Q_{w,ref}$ = 15.43 m^{3}h^{-1})
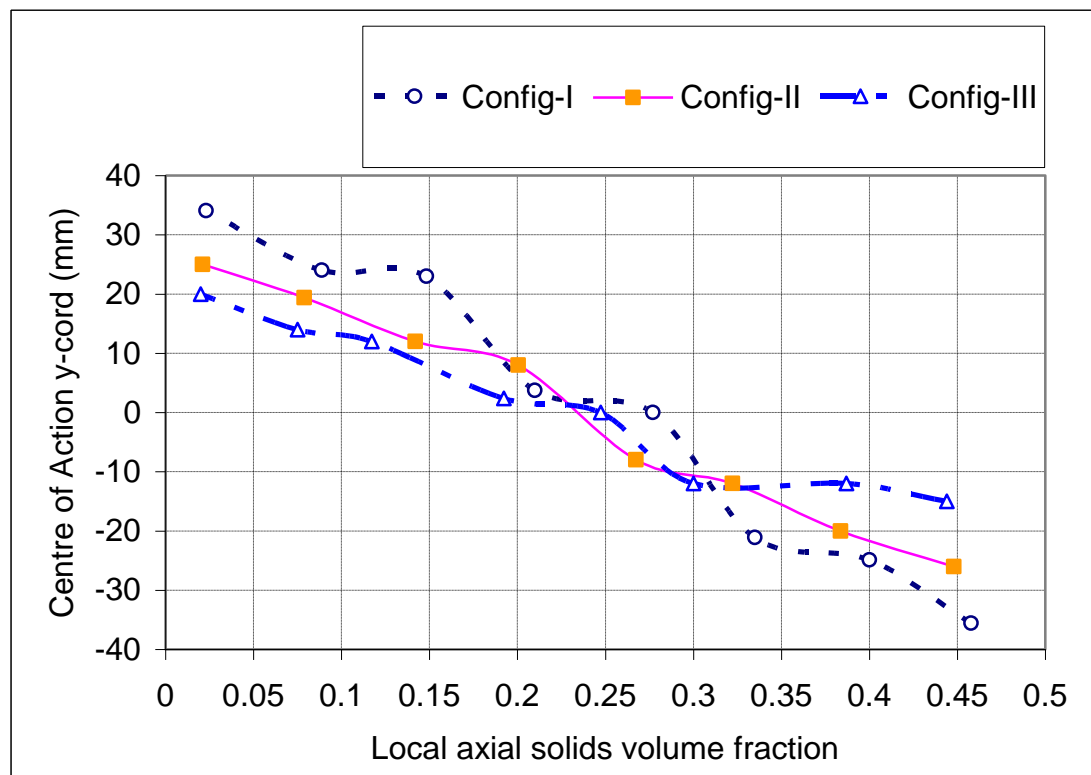
Figure 7-70: Local solids volume fraction profiles for pipe inclined at 15° to the vertical, flow condition 16($Q_{s,ref}$ =1.631 m^{3}h^{-1}, $Q_{w,ref}$ = 14.05 m^{3}h^{-1})
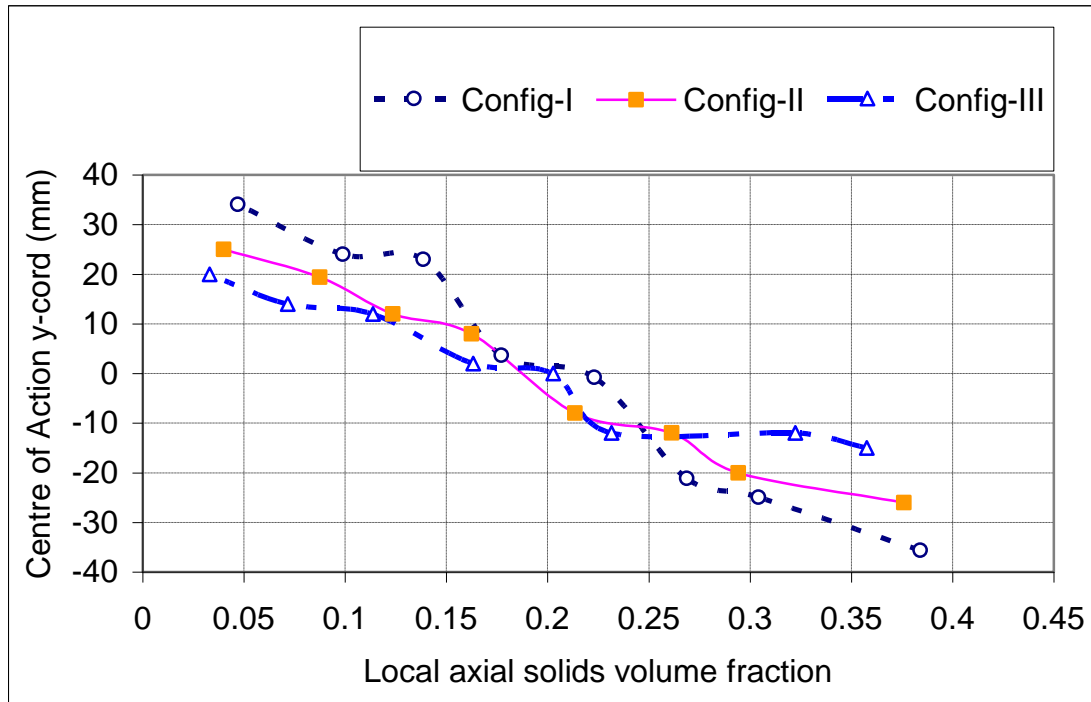
Figure 7-71: Local solids volume fraction profiles for pipe inclined at 15° to the vertical, flow condition 17($Q_{s,ref}$ =1.587 m^{3}h^{-1}, $Q_{w,ref}$ = 15.26 m^{3}h^{-1})
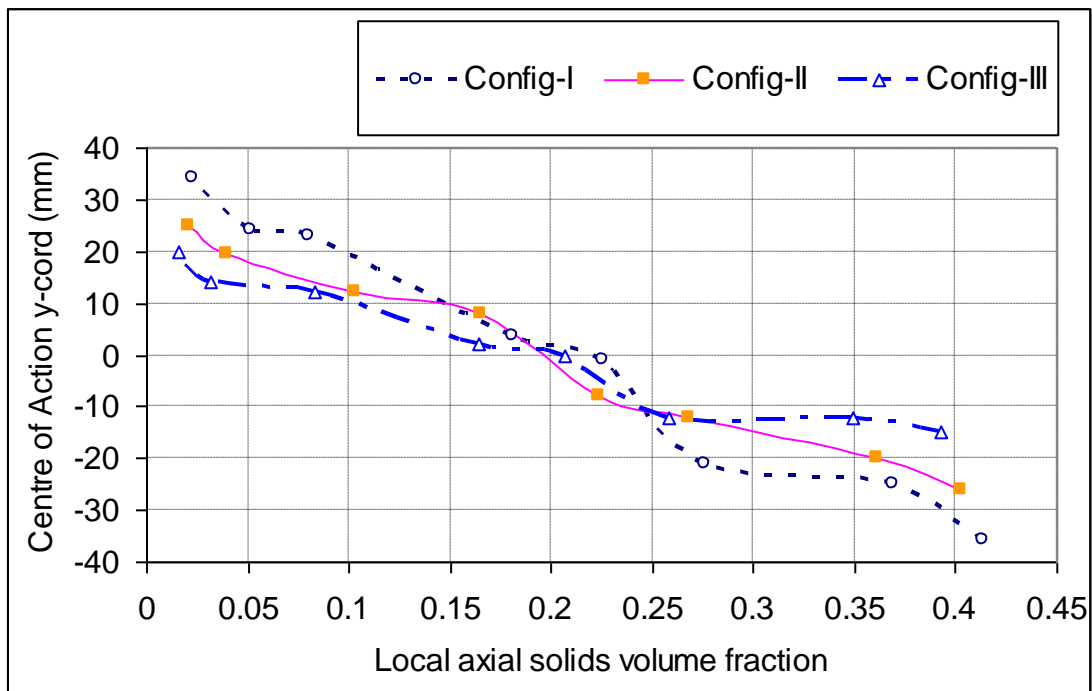
Figure 7-72: Local solids volume fraction profiles for pipe inclined at 15° to the vertical, flow condition 18($Q_{s,ref}$ =1.623 m^{3}h^{-1}, $Q_{w,ref}$ = 16.94 m^{3}h^{-1})

7.2.5.3 Local solids volume fraction profiles for upward flow in a pipe inclined at 30° to the vertical

Figures 7-73 to 7-81 present the results obtained for local solids volume fraction profiles for upward flow in a pipe inclined at 30° to the vertical. The results obtained show similar trends for each of the electrode configurations (Configs-I, II and III). At the lower side of the inclined pipe the local solids volume fraction is higher than at the upper side of the inclined pipe and this was confirmed by the author's visual observations during the experiments. The results show the same monotonic trend as for Figures 7-64 to 7-72. In Figure 7-73, for example, the maximum measured local solids volume fraction at the bottom of the inclined pipe was 0.25 and the minimum measured value at the top was 0.01 as measured by electrode configuration Config-I. For Config-II and Config-III, the maximum and minimum measured local solids volume fractions were 0.23 and 0.215, and 0.0015 and 0.0014 respectively.
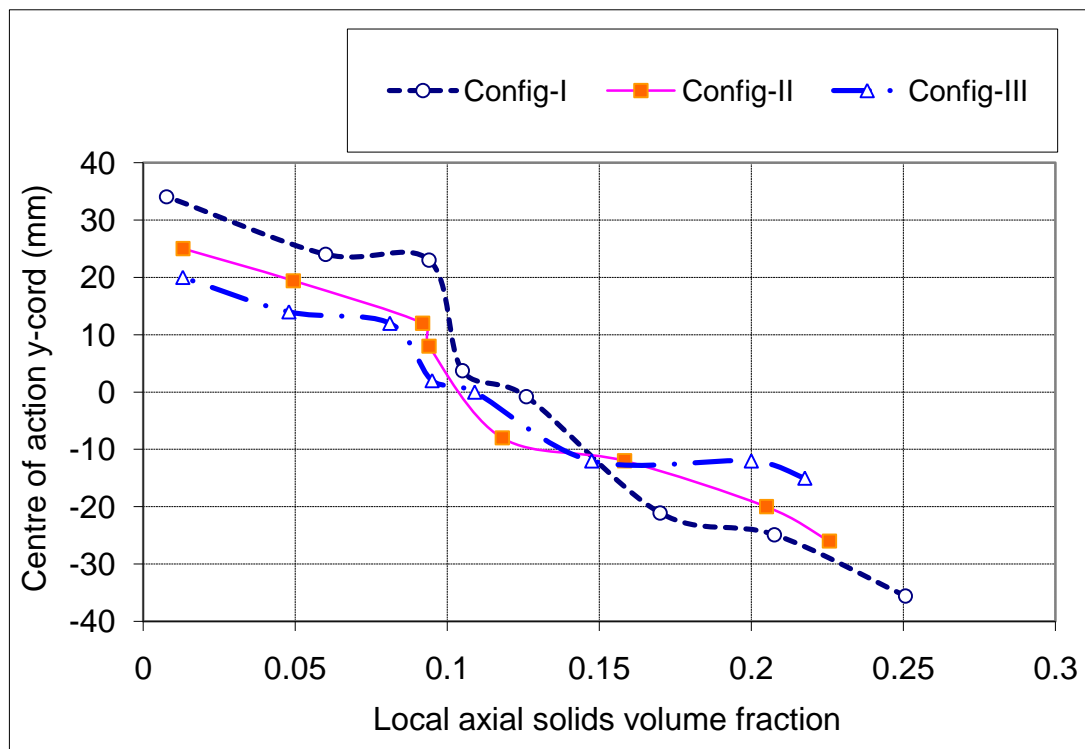
Figure 7-73: Local solids volume fraction profiles for pipe inclined at 30° to the vertical, flow condition 19($Q_{s,ref}$ =0.360 m^{3}h^{-1}, $Q_{w,ref}$ = 7.218 m^{3}h^{-1})
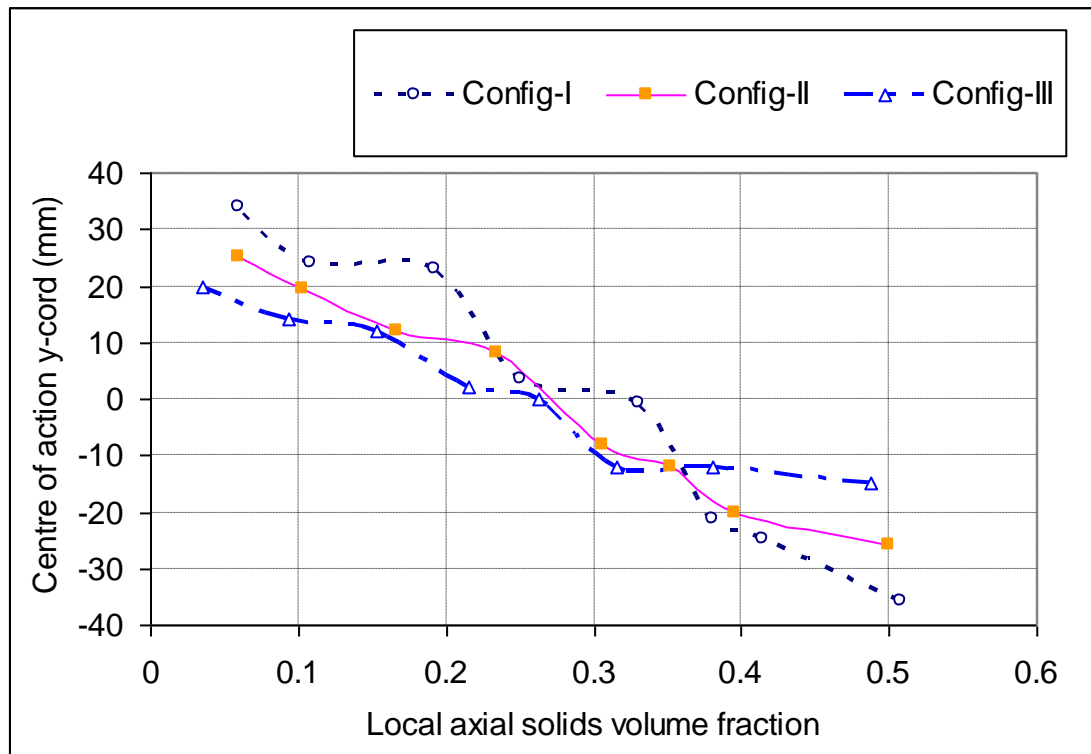
Figure 7-74 Local solids volume fraction profiles for pipe inclined at 30° to the vertical, flow condition 20($Q_{s,ref}$ = 0.591 m^{3}h^{-1}, $Q_{w,ref}$ = 10.79 m^{3}h^{-1})
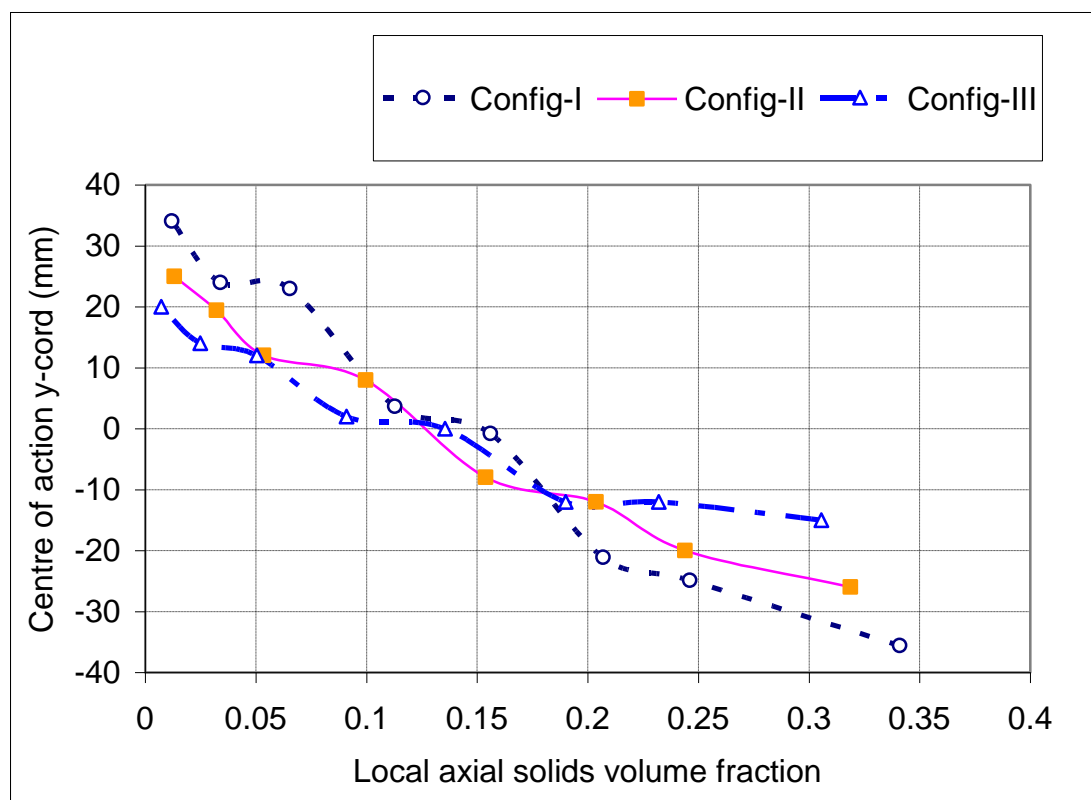
Figure 7-75: Local solids volume fraction profiles for pipe inclined at 30° to the vertical, flow condition 21($Q_{s,ref}$ =0.549 m^{3}h^{-1}, $Q_{w,ref}$ = 12.13 m^{3}h^{-1})
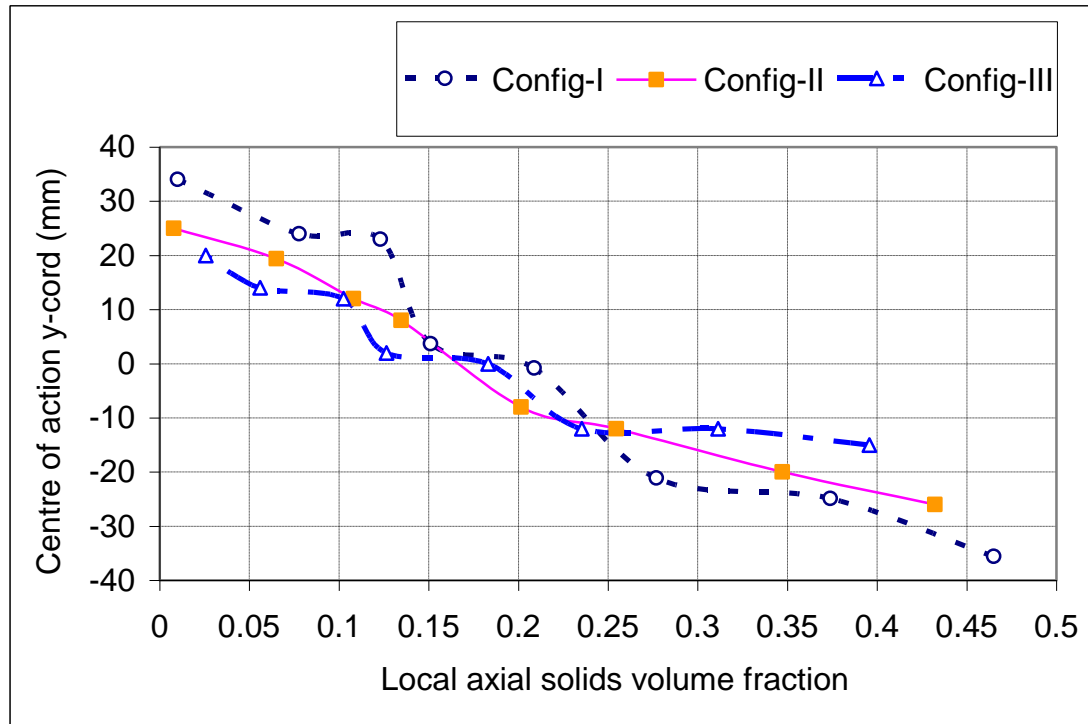
Figure 7-76: Local solids volume fraction profiles for pipe inclined at 30° to the vertical, flow condition 22($Q_{s,ref}$ =0.951 m^{3}h^{-1}, $Q_{w,ref}$ = 12.47 m^{3}h^{-1})
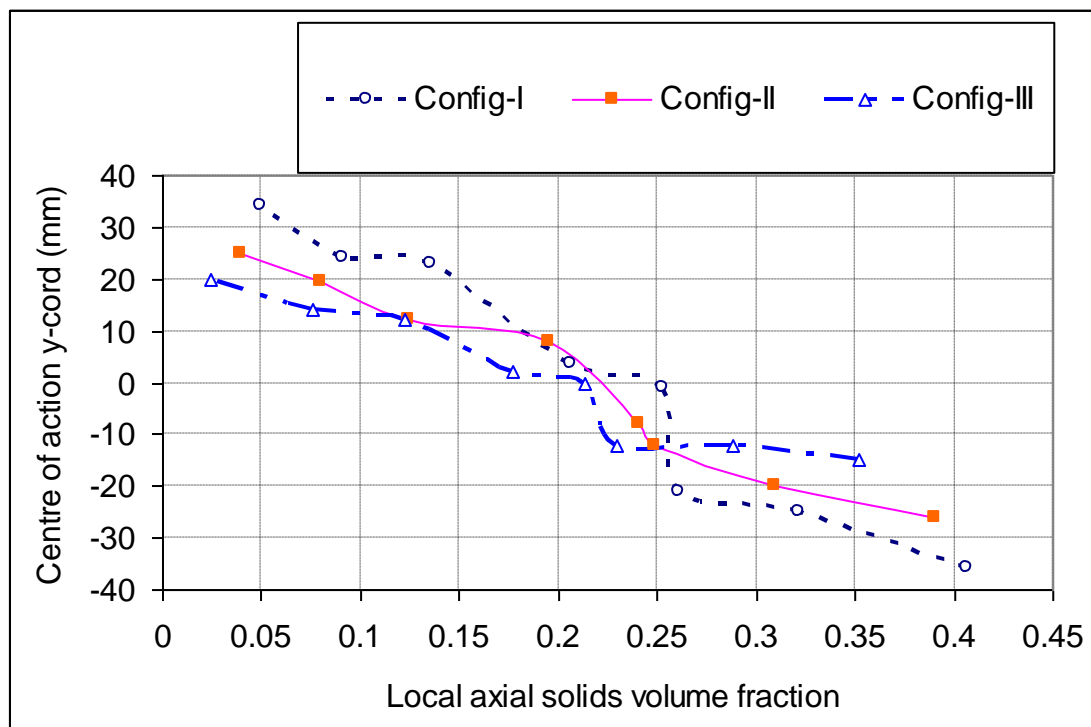
Figure 7-77: Local solids volume fraction profiles for pipe inclined at 30° to the vertical, flow condition 23($Q_{s,ref}$ =1.010 m3h-1, $Q_{w,ref}$ = 14.06 m3h-1)
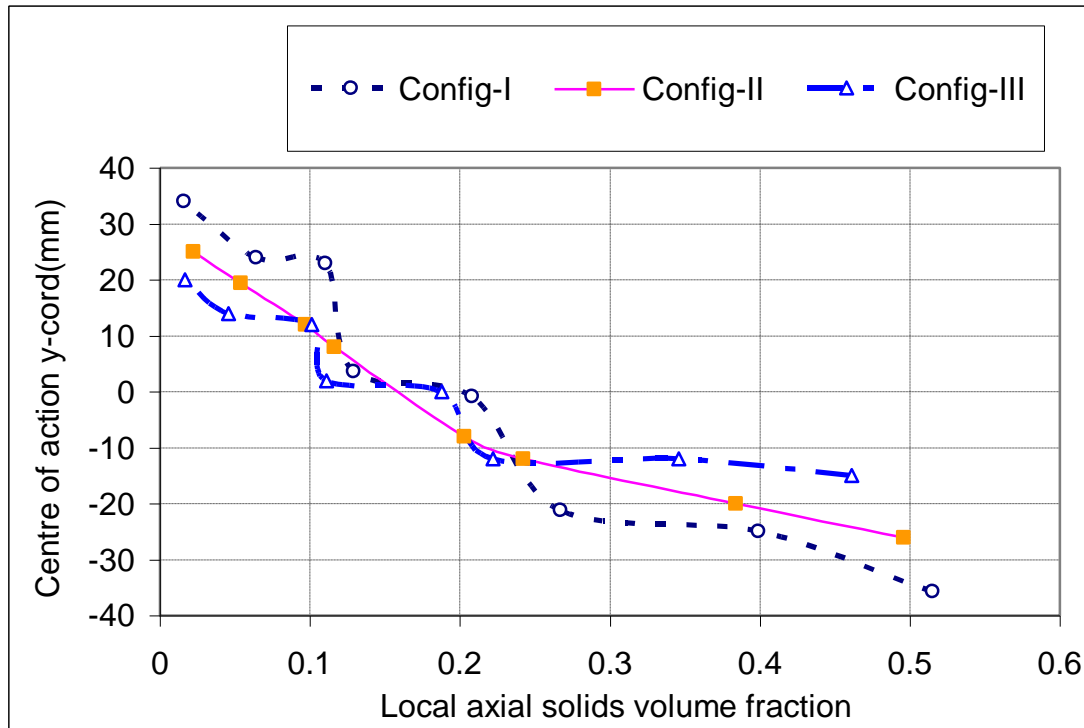
Figure 7-78: Local solids volume fraction profiles for pipe inclined at 30° to the vertical, flow condition 24($Q_{s,ref}$ =0.959 m^{3}h^{-1}, $Q_{w,ref}$ = 15.66 m^{3}h^{-1})
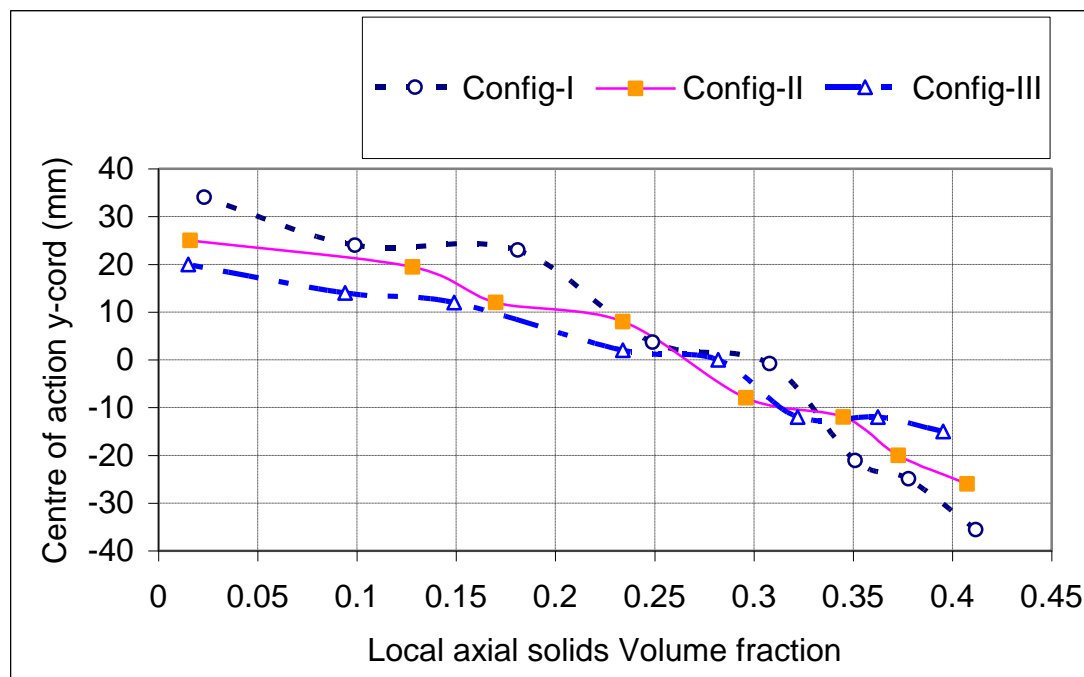
Figure 7-79: Local solids volume fraction profiles for pipe inclined at 30° to the vertical, flow condition 25($Q_{s,ref}$ =1.410 m^{3}h^{-1}, $Q_{w,ref}$ = 14.10 m^{3}h^{-1})
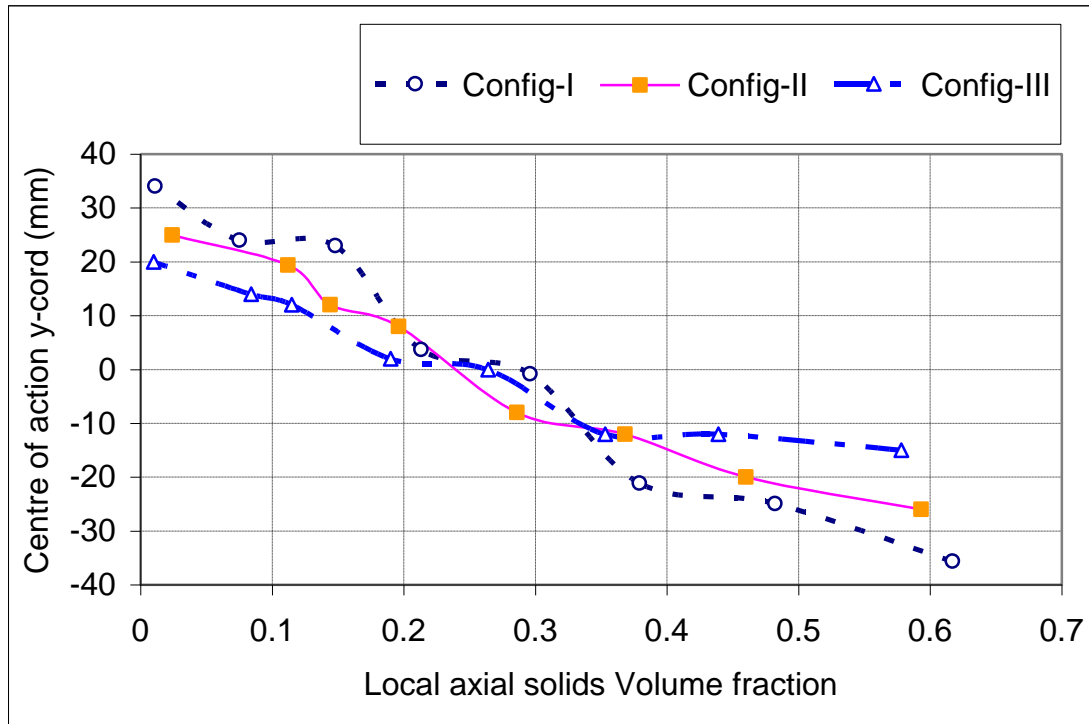
Figure 7-80: Local solids volume fraction profiles for pipe inclined at 30° to the vertical, flow condition 26($Q_{s,ref}$ =1.651 m^{3}h^{-1}, $Q_{w,ref}$ = 15.96 m^{3}h^{-1})
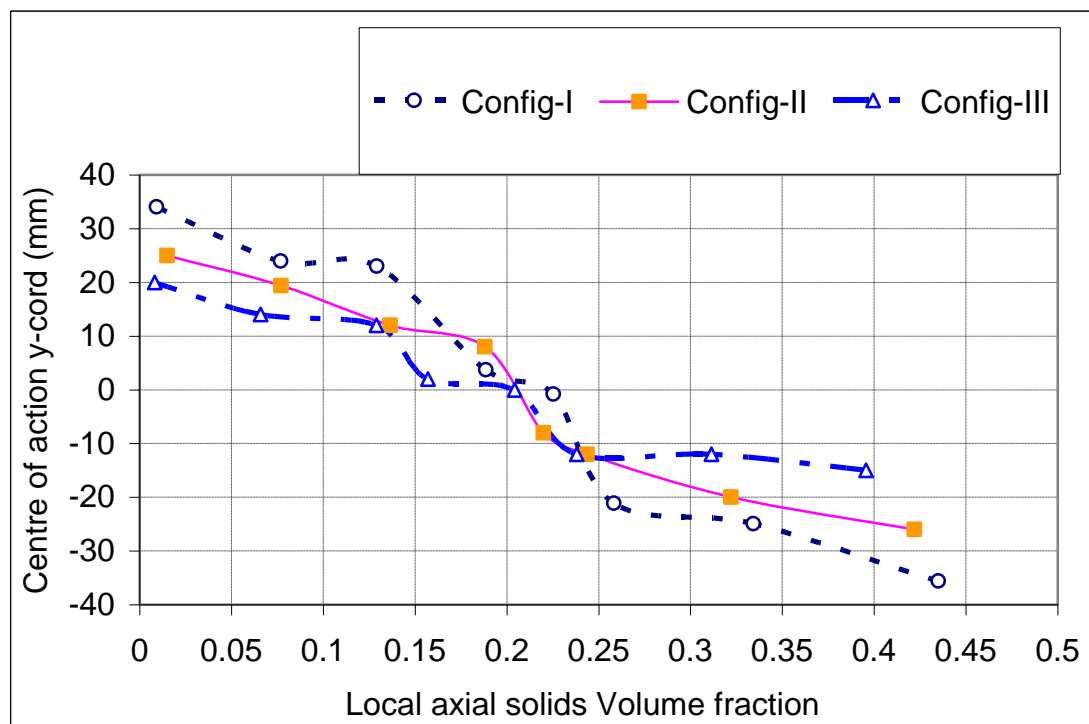
Figure 7-81: Local solids volume fraction profiles for pipe inclined at 30° to the vertical, flow condition 27($Q_{s,ref}$ =1.623 m^{3}h^{-1}, $Q_{w,ref}$ = 17.12 m^{3}h^{-1})

271

7.2.6 3D Profiles of the local solids volume fraction from ICC

In this section 3D plots of the solids volume fraction profiles are presented. These 3D volume fraction profiles were plotted using an interpolation routine within MATLAB to show these profiles as a function of spatial location of the CoA in the flow cross-section as defined by x and y coordinates (see Table 4-5). The author developed software in MATLAB in order to obtain the 3D plots profiles (see appendix (Code-7)). In each of the 3D Figures, again there is a colour scale which represents the value of the local solids volume fraction (α_S) at particular measuring point. The red colour represents maximum value of the local solids volume fraction and colour blue represent the minimum value of α_S at particular flow conditions. Config-ψ represents a combination of Configs-I, II, III. Again Config-ψ represents a combination of Configs-I, II, III and determines the local solids volume fraction for 24 electrode arrangements. That this was again successful is used to overcome the problem of the insufficient number of points in the flow cross section (see Section 7.2.1)

7.2.6.1 3-D profiles of local solids volume fraction for upward flow in a vertical pipe
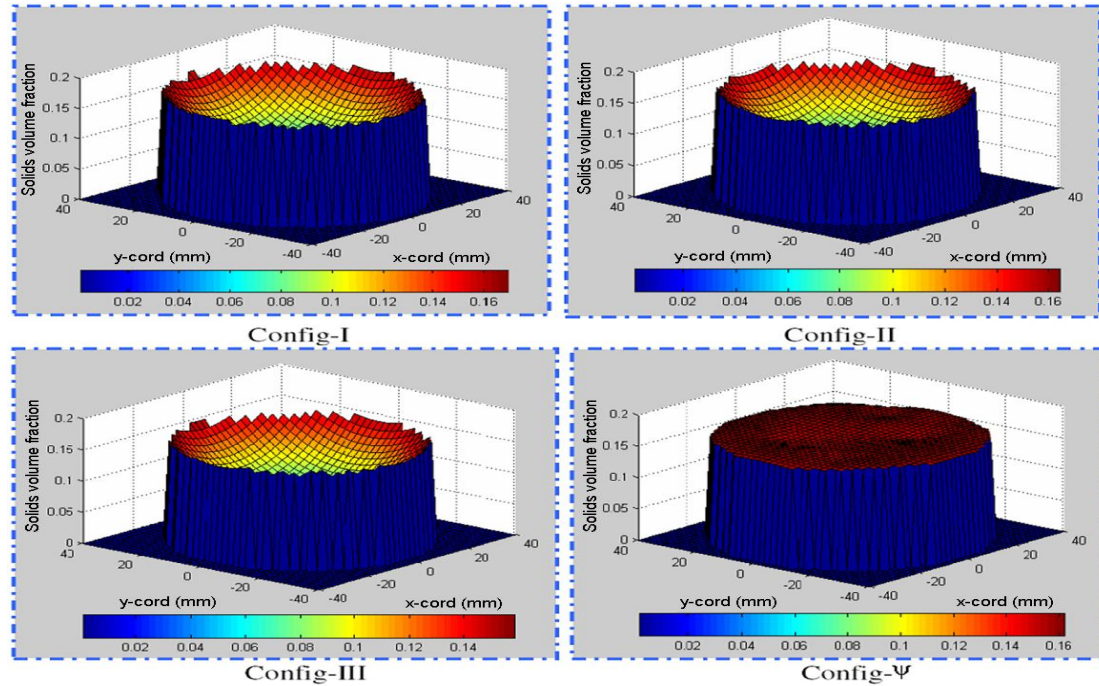
Figure 7-82: Local solids volume fraction profiles for flow in a vertical pipe, flow condition 1($Q_{s,ref}$ =0.696 m^{3}h^{-1}, $Q_{w,ref}$ = 4.25 m^{3}h^{-1}).
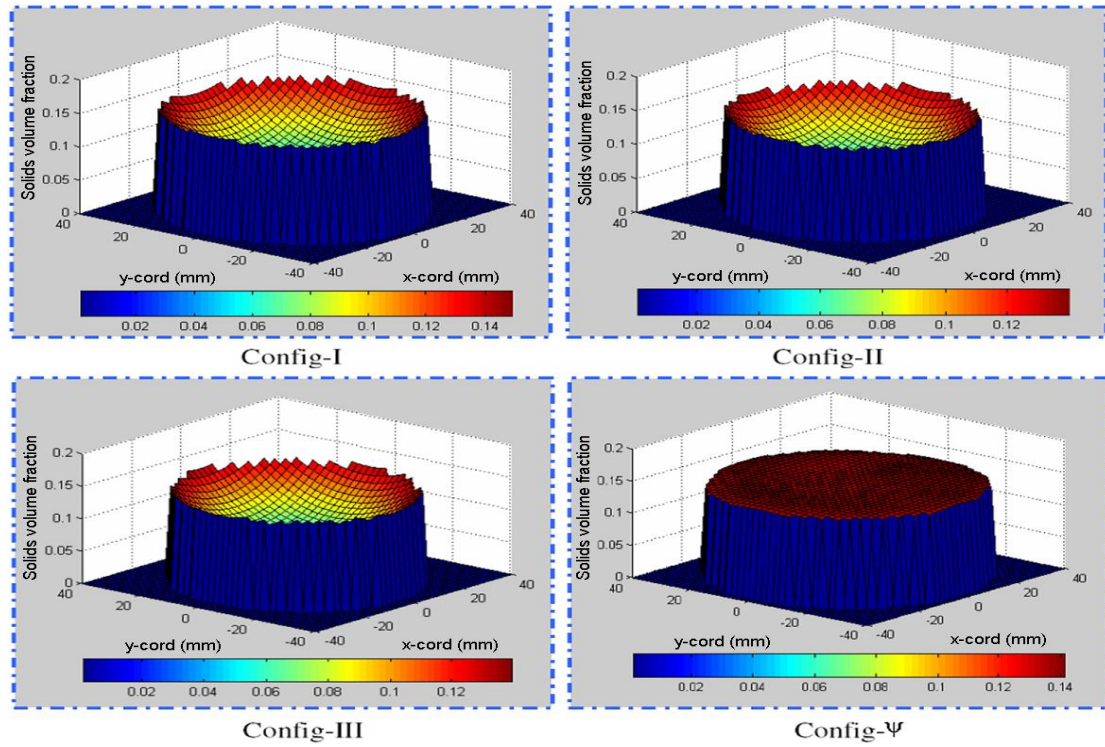
Figure 7-83: Local solids volume fraction profiles for flow in a vertical pipe,, flow condition 2($Q_{s,ref}$ =0.750 m^{3}h^{-1}, $Q_{w,ref}$ = 5.49 m^{3}h^{-1})
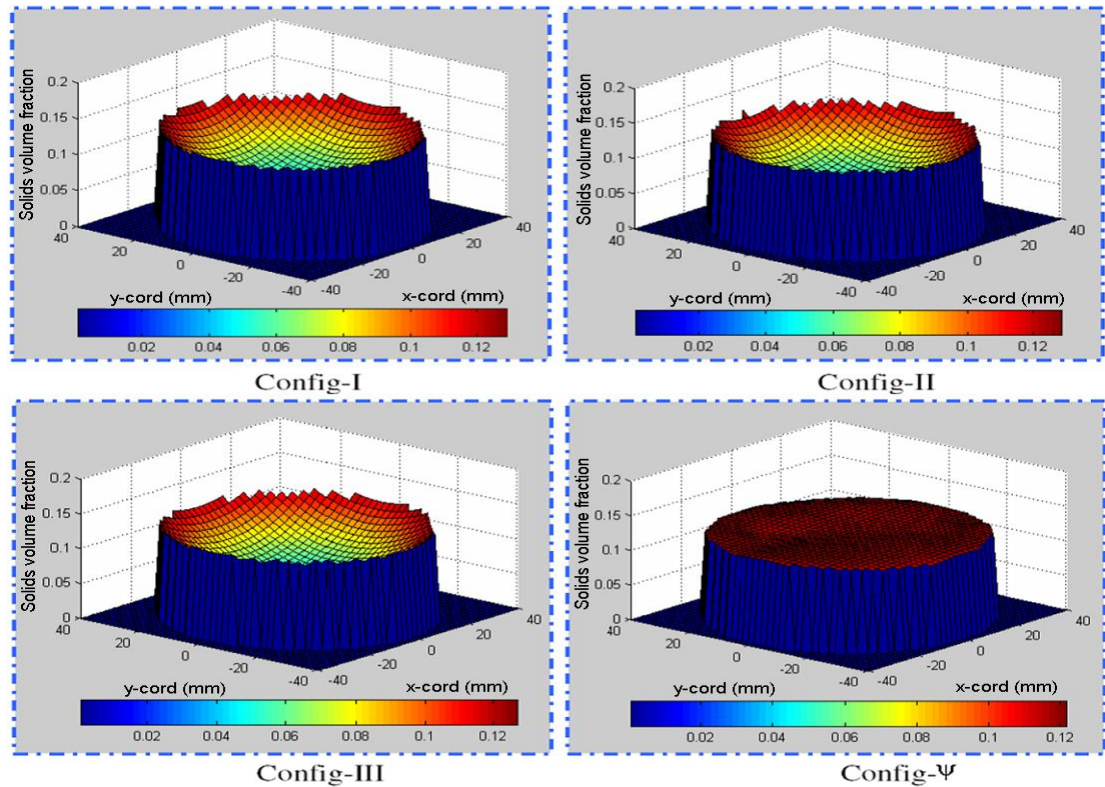
Figure 7-84: Local solids volume fraction profiles for flow in a vertical pipe, flow condition 3($Q_{s,ref}$ =0.724 m^{3}h^{-1}, $Q_{w,ref}$ = 6.12 m^{3}h^{-1})

273
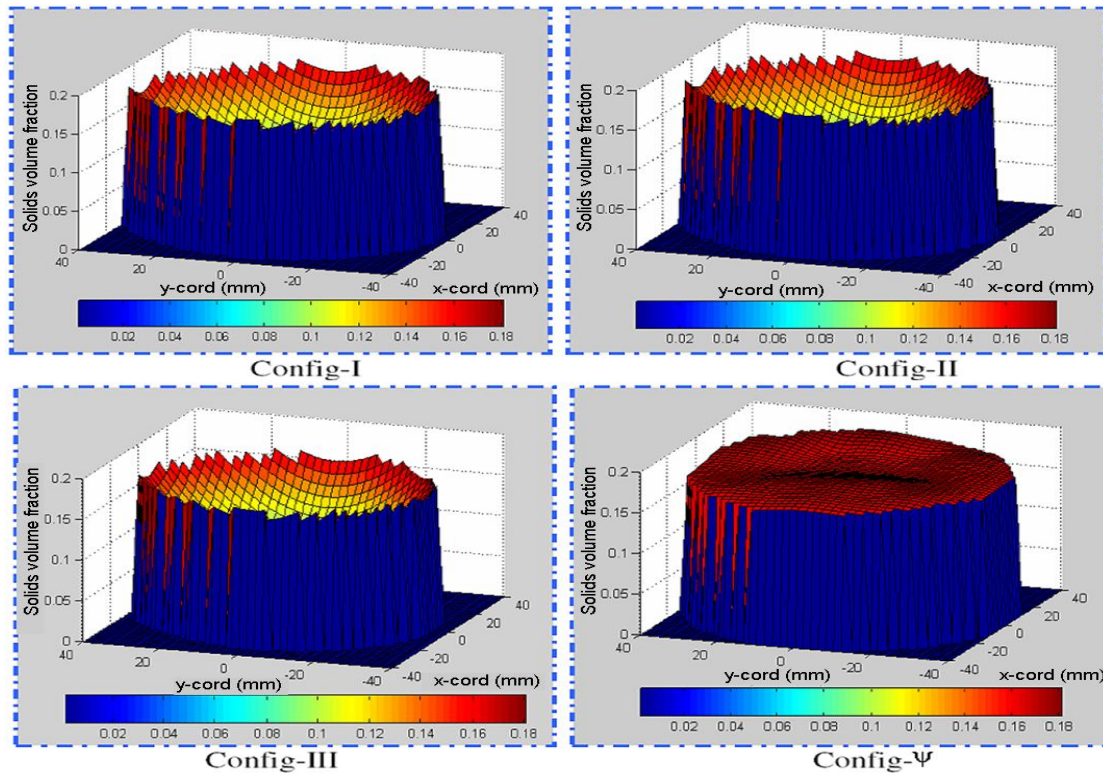
Figure 7-85: Local solids volume fraction profiles for flow in a vertical pipe, flow condition 4($Q_{s,ref}$ =1.188 m^{3}h^{-1}, $Q_{w,ref}$ = 6.18 m^{3}h^{-1})
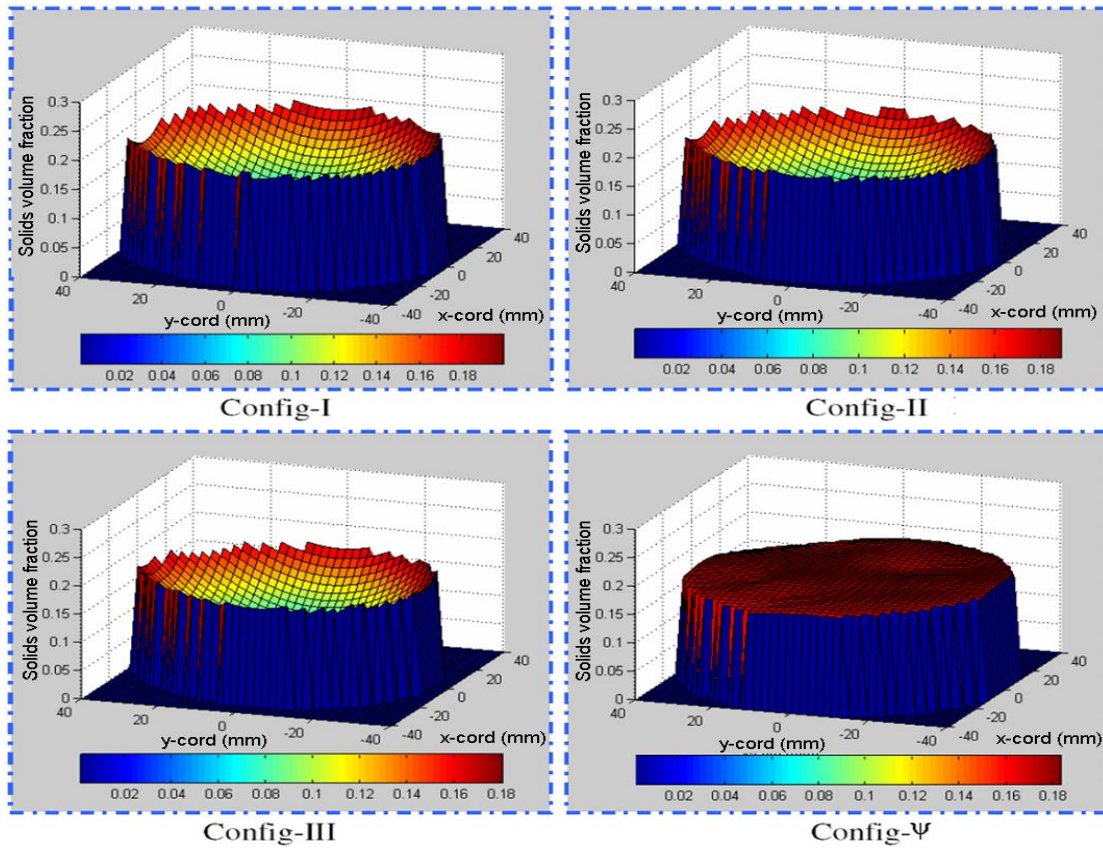
Figure 7-86: Local solids volume fraction profiles for flow in a vertical pipe, flow condition 5($Q_{s,ref}$ =1.225 m^{3}h^{-1}, $Q_{w,ref}$ = 6.45 m^{3}h^{-1})

274
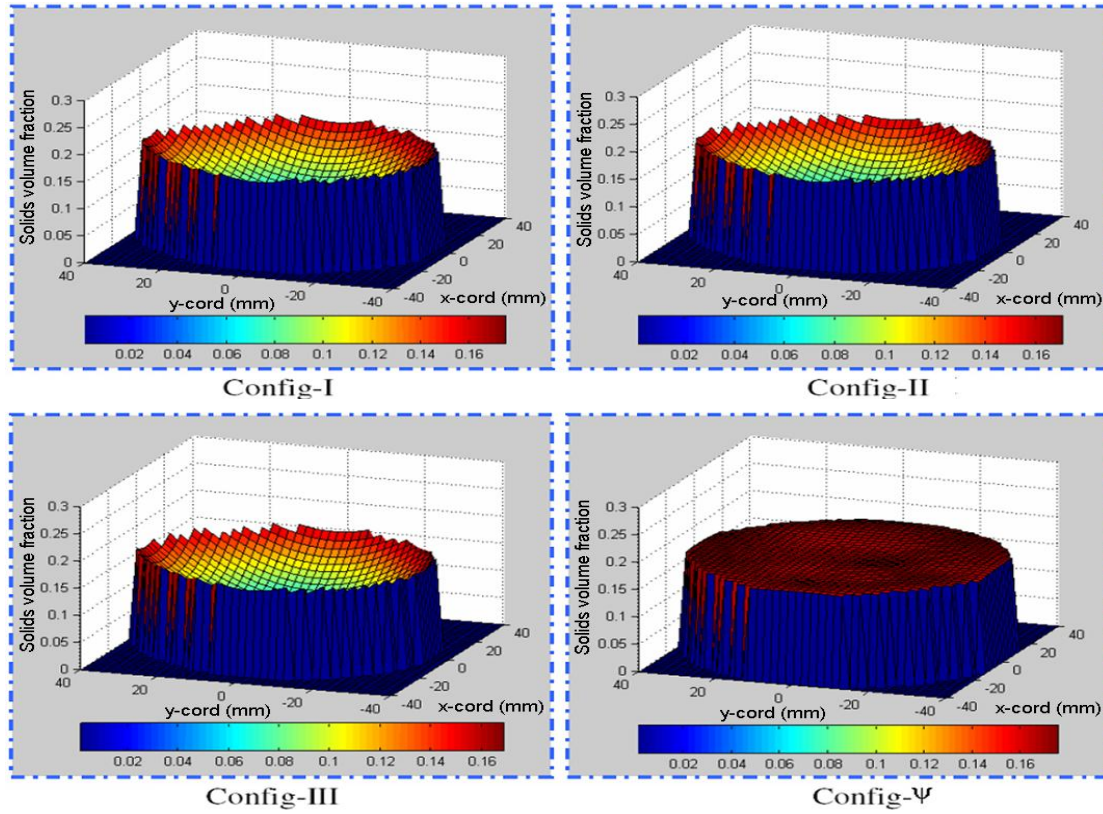
Figure 7-87: Local solids volume fraction profiles for flow in a vertical pipe, flow condition 6($Q_{s,ref}$ =1.183 m^{3}h^{-1}, $Q_{w,ref}$ = 6.51 m^{3}h^{-1})
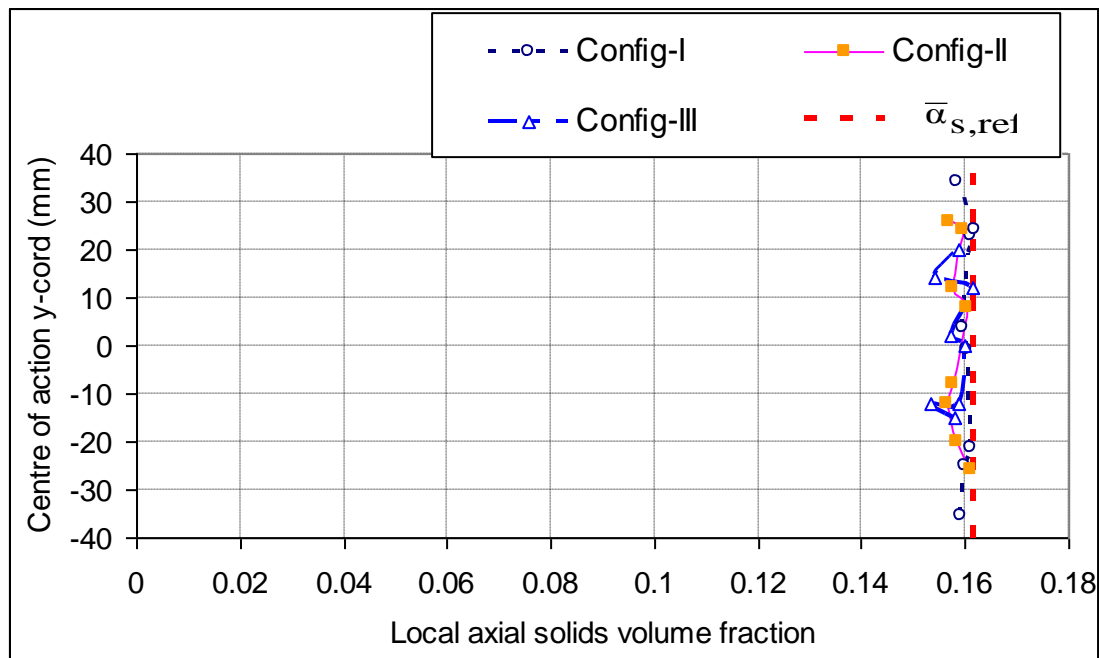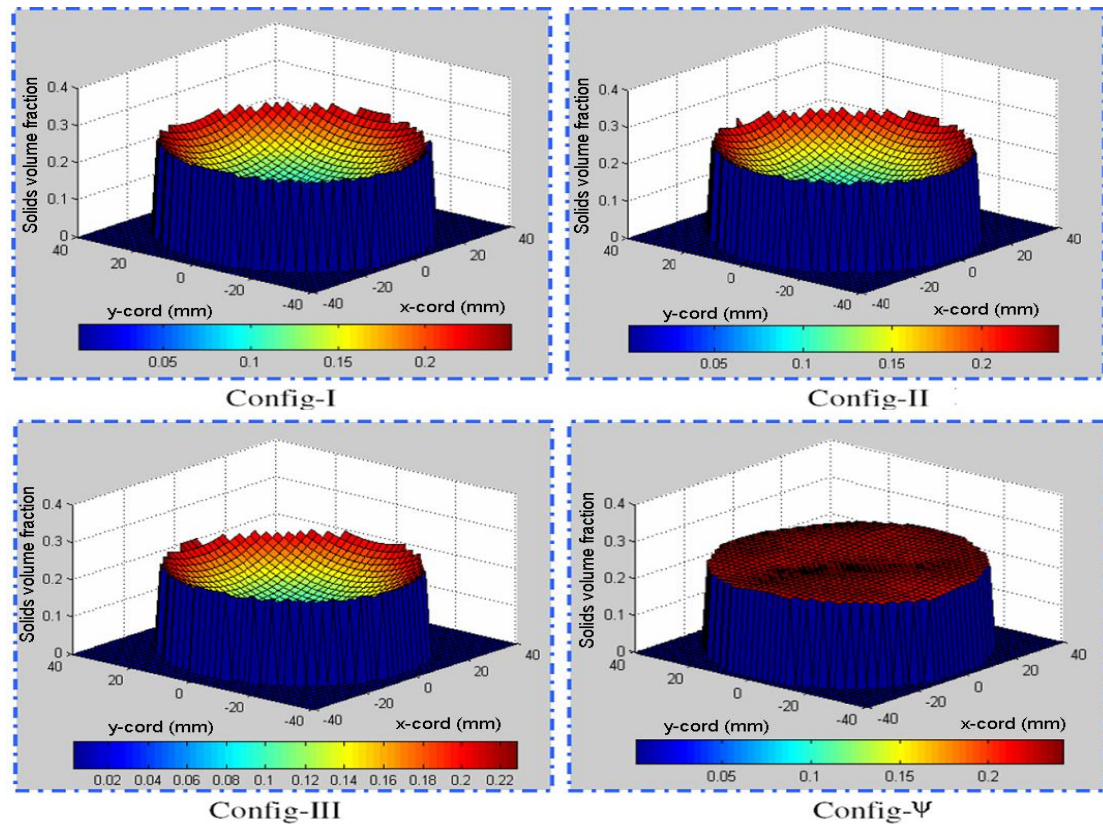

Figure 7-88: Local solids volume fraction profiles for flow in a vertical pipe, flow condition 7($Q_{s,ref}$ =2.229 m^{3}h^{-1}, $Q_{w,ref}$ = 5.87 m^{3}h^{-1})
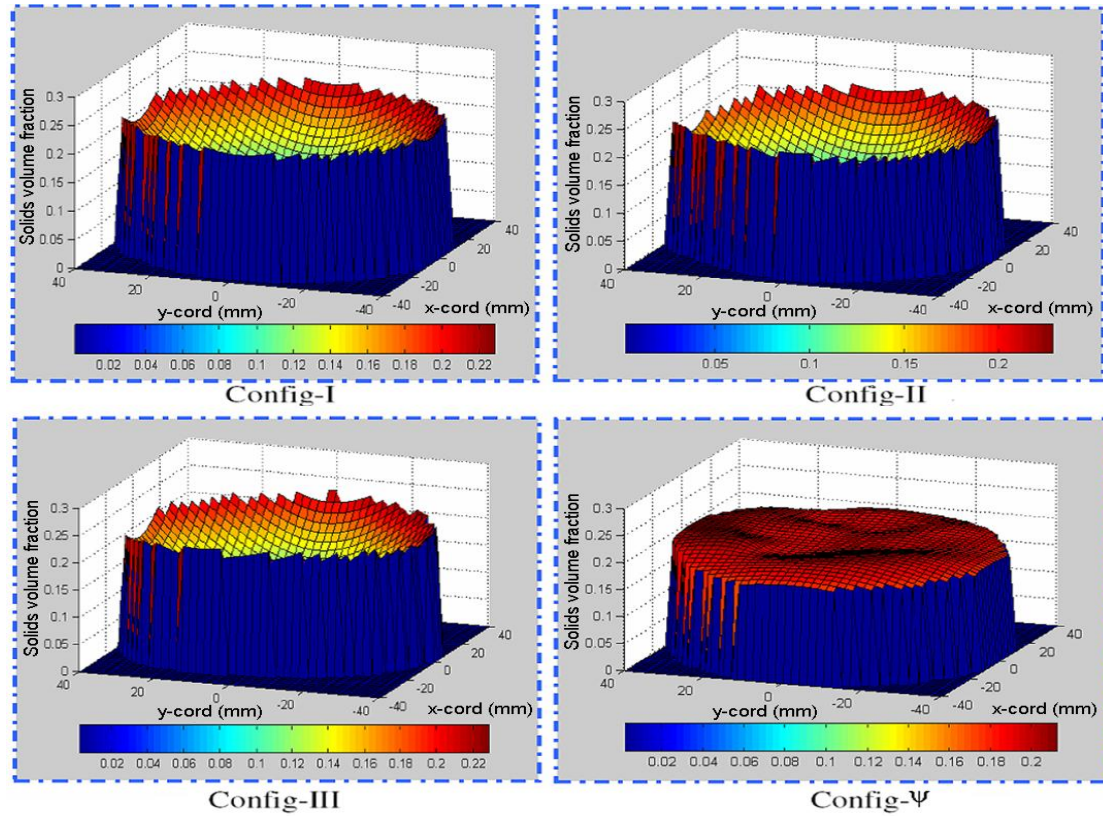
Figure 7-89: Local solids volume fraction profiles for flow in a vertical pipe, flow condition 8($Q_{s,ref}$ =1.974 m^{3}h^{-1}, $Q_{w,ref}$ = 7.98 m^{3}h^{-1})
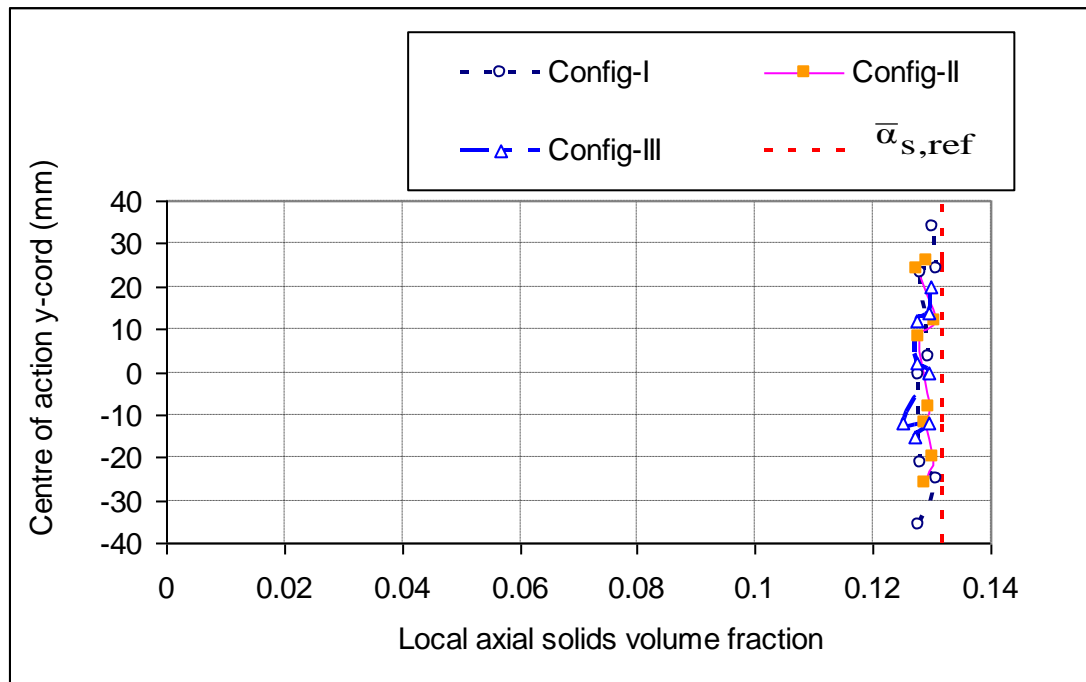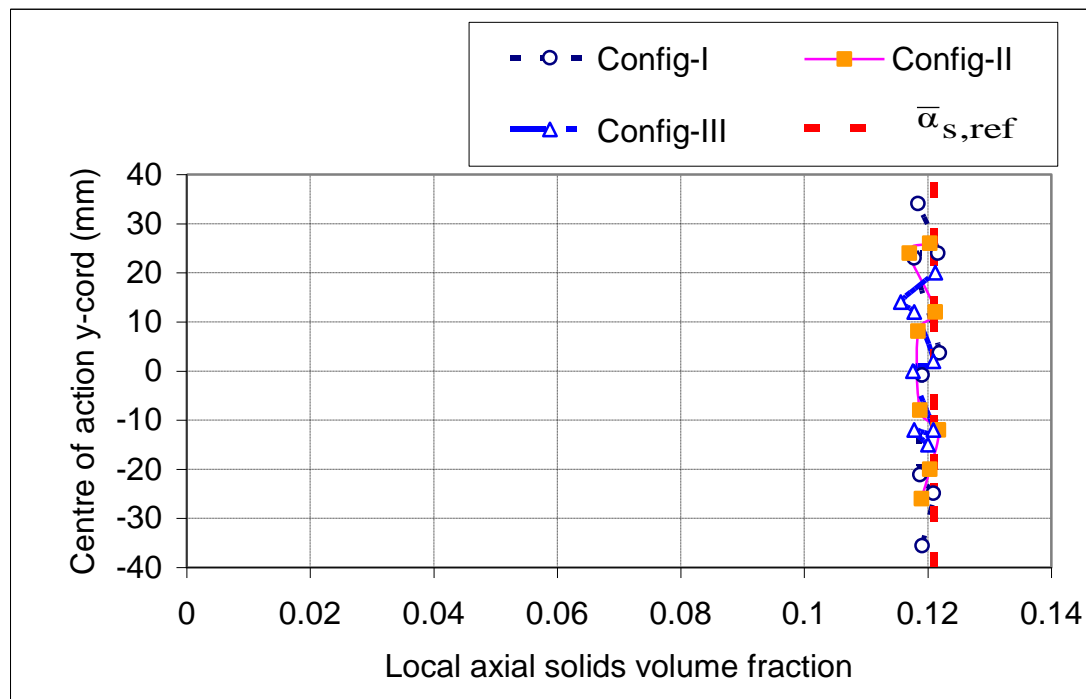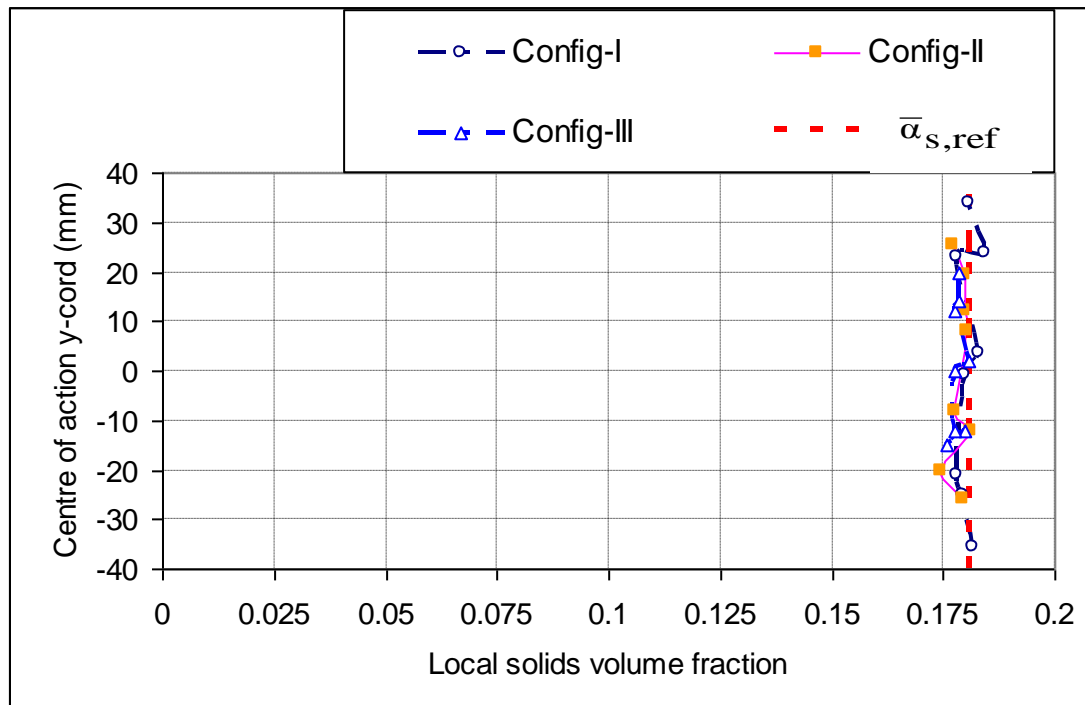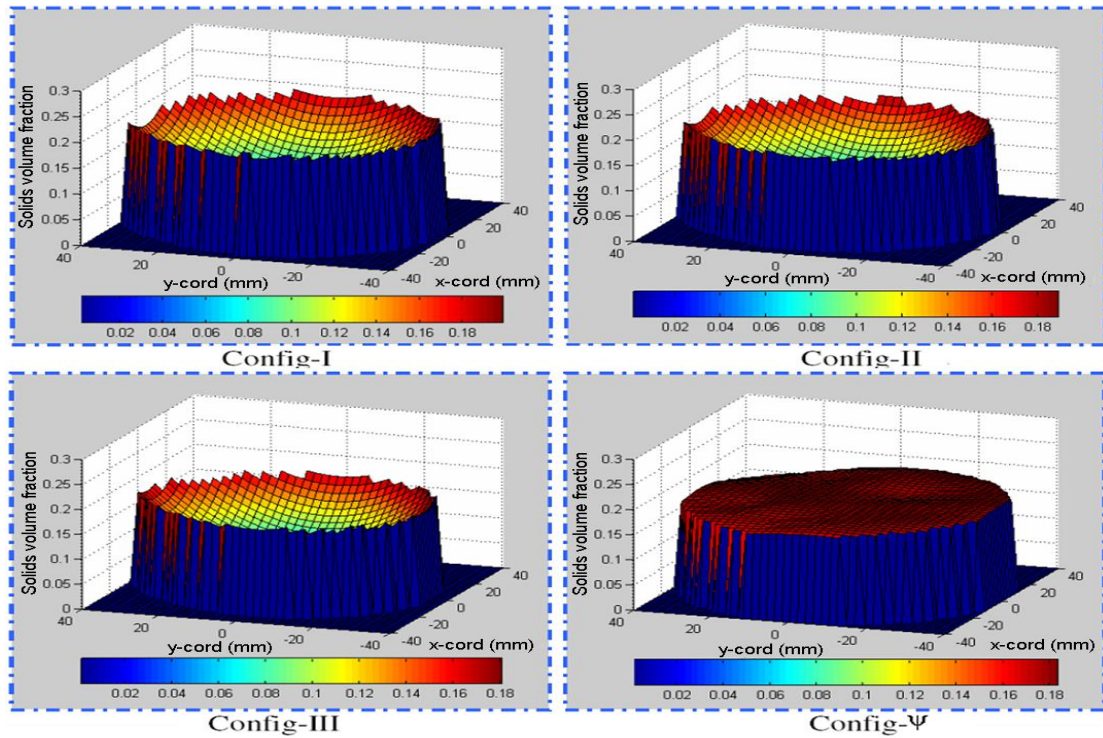

Figure 7-90: Local solids volume fraction profiles for flow in a vertical pipe, flow condition 9($Q_{s,ref}$ =1.974 m^{3}h^{-1}, $Q_{w,ref}$ = 9.35 m^{3}h^{-1})

7.2.6.2 3-D profiles of local solids volume fraction for upward flow in a pipe inclined at 15° to the vertical
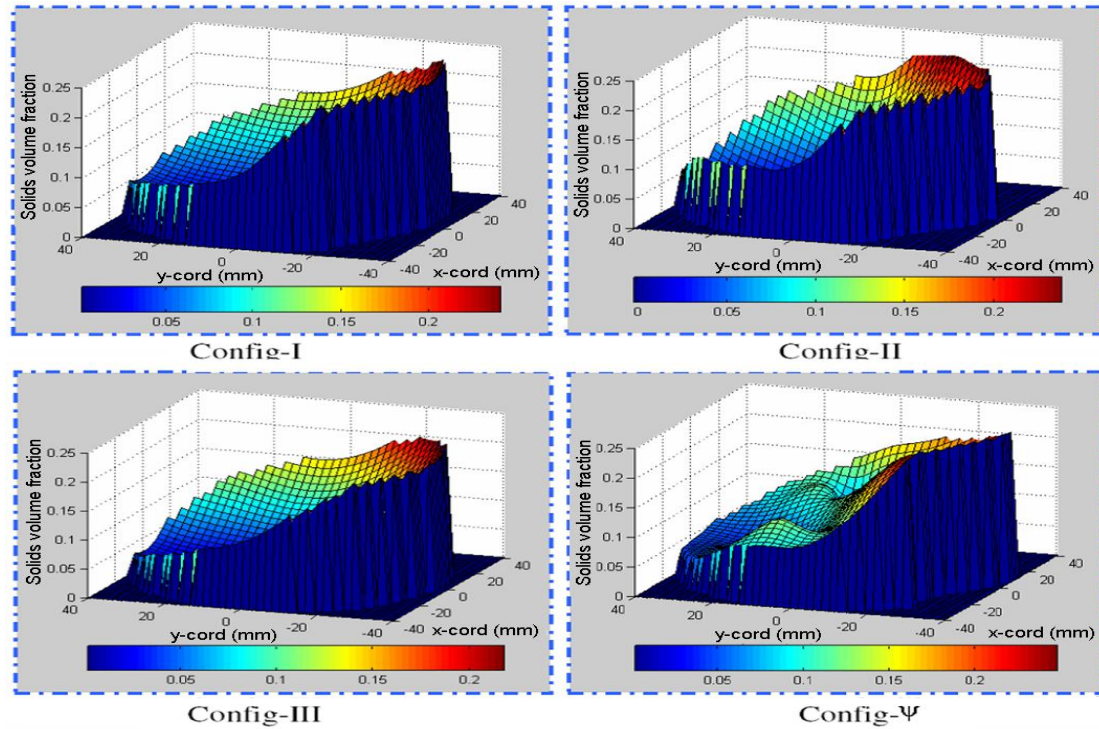
Figure 7-91: Local solids volume fraction profiles for flow inclined 15° from vertical, flow condition 10($Q_{s,ref}$ =0.613 m³h⁻¹, $Q_{w,ref}$ = 9.45 m³h⁻¹)
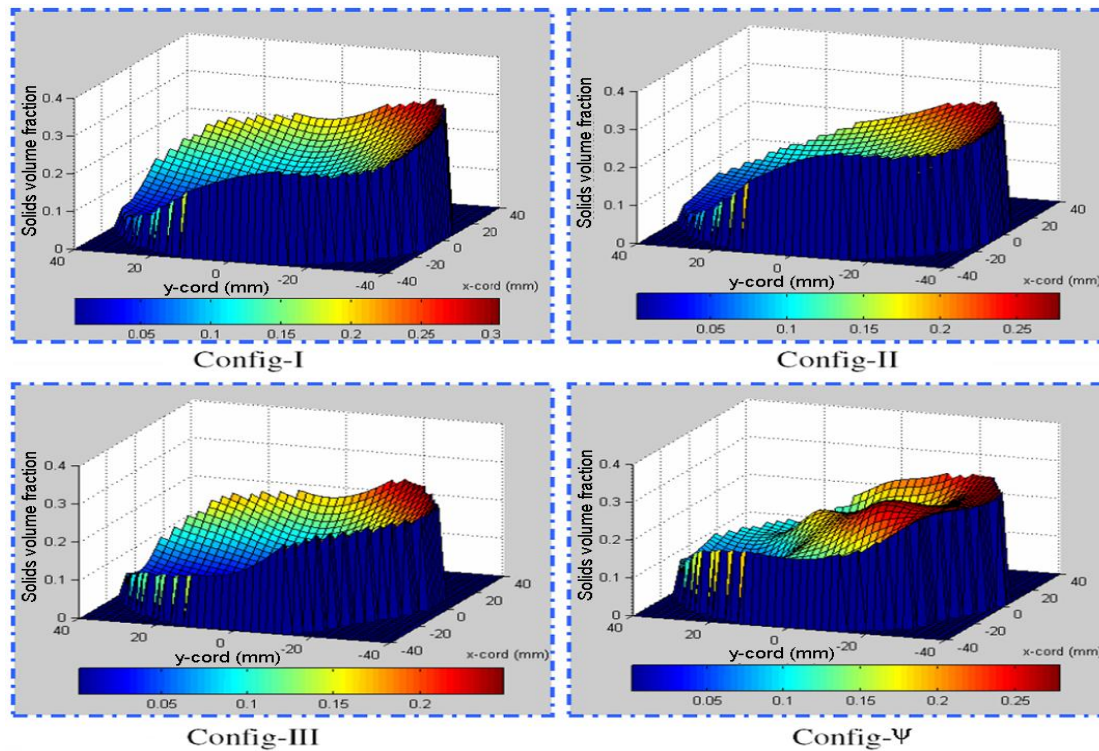
Figure 7-92: Local solids volume fraction profiles for flow inclined 15° from vertical, flow condition 11($Q_{s,ref}$ =0.731 m³h⁻¹, $Q_{w,ref}$ = 10.91 m³h⁻¹)
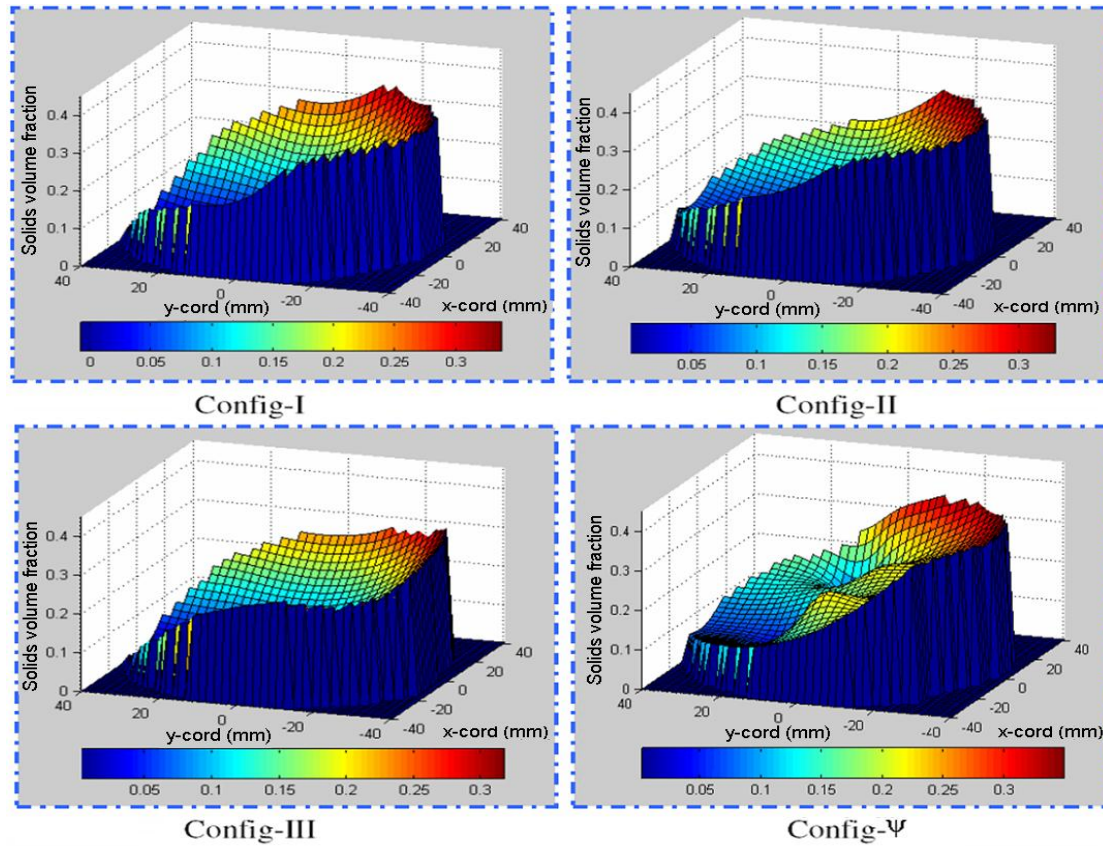
Figure 7-93: Local solids volume fraction profiles for flow inclined 15° from vertical, flow condition 12. ($Q_{s,ref}$ = 0.704 m^{3}h^{-1}, $Q_{w,ref}$ = 12.43 m^{3}h^{-1})
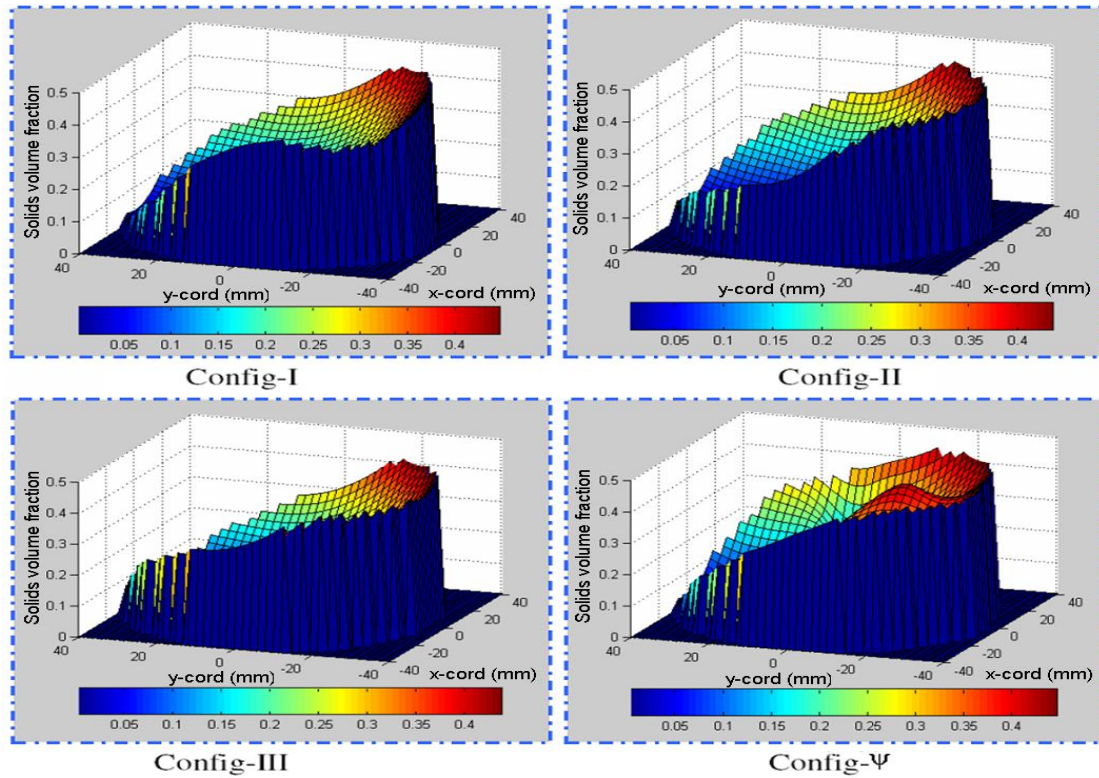
Figure 7-94: Local solids volume fraction profiles for flow inclined 15° from vertical, flow condition 13. ($Q_{s,ref}$ =1.187 m^{3}h^{-1}, $Q_{w,ref}$ = 12.82 m^{3}h^{-1})
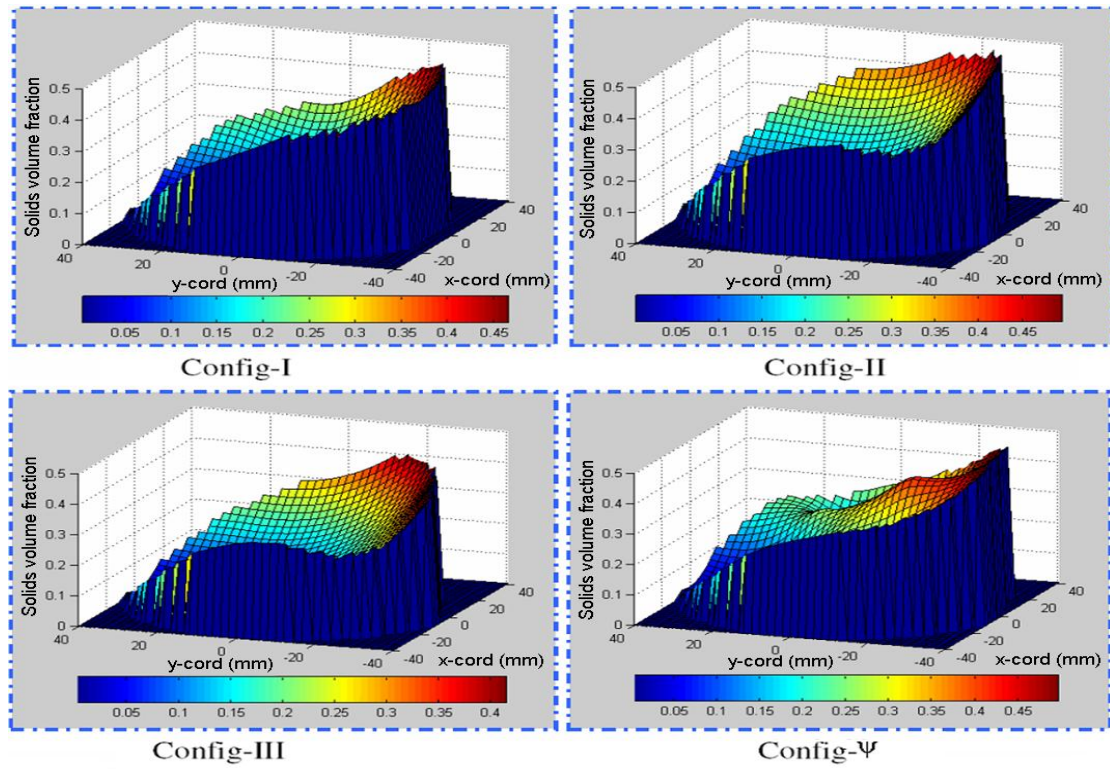
Figure 7-95: Local solids volume fraction profiles for flow inclined 15° from vertical, flow condition 14. ($Q_{s,ref}$ =1.104 m³h⁻¹, $Q_{w,ref}$ = 13.94 m³h⁻¹)
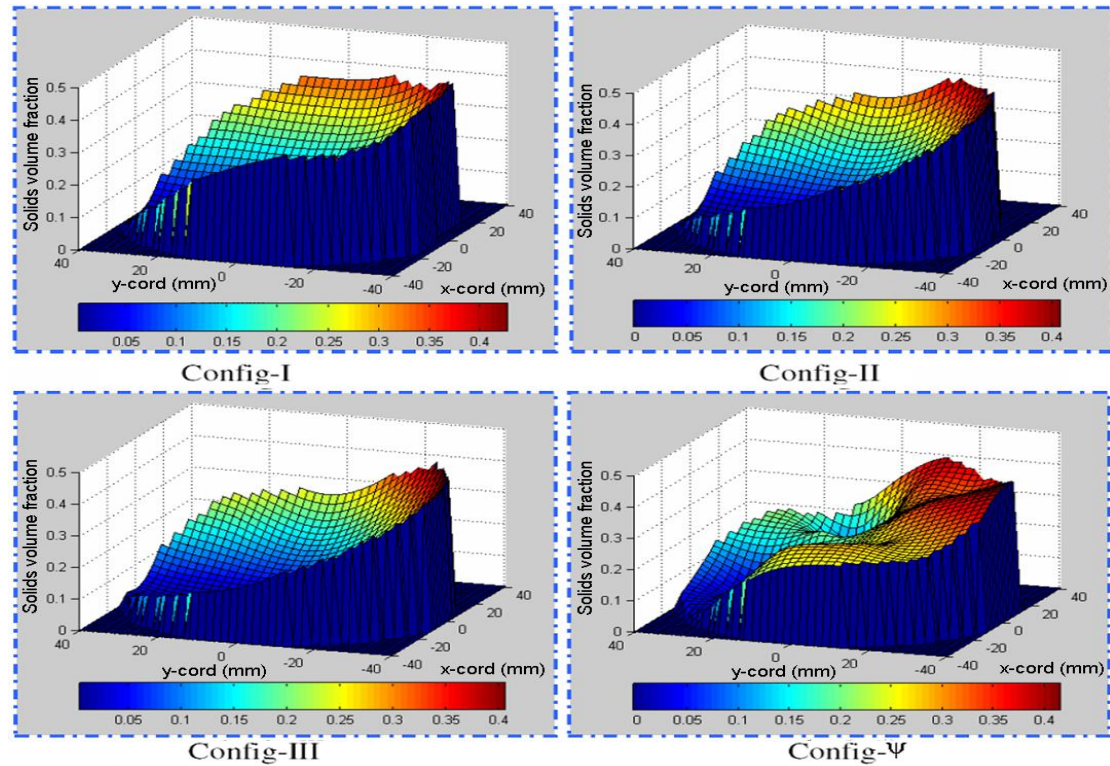
Figure 7-96: local Solids volume fraction profiles for flow inclined 15° from vertical, flow condition 15. ($Q_{s,ref}$ =1.010 m³h⁻¹, $Q_{w,ref}$ = 15.43 m³h⁻¹)

7.2.6.3 3-D profiles of local solids volume fraction for upward flow in a pipe inclined at 30° to the vertical
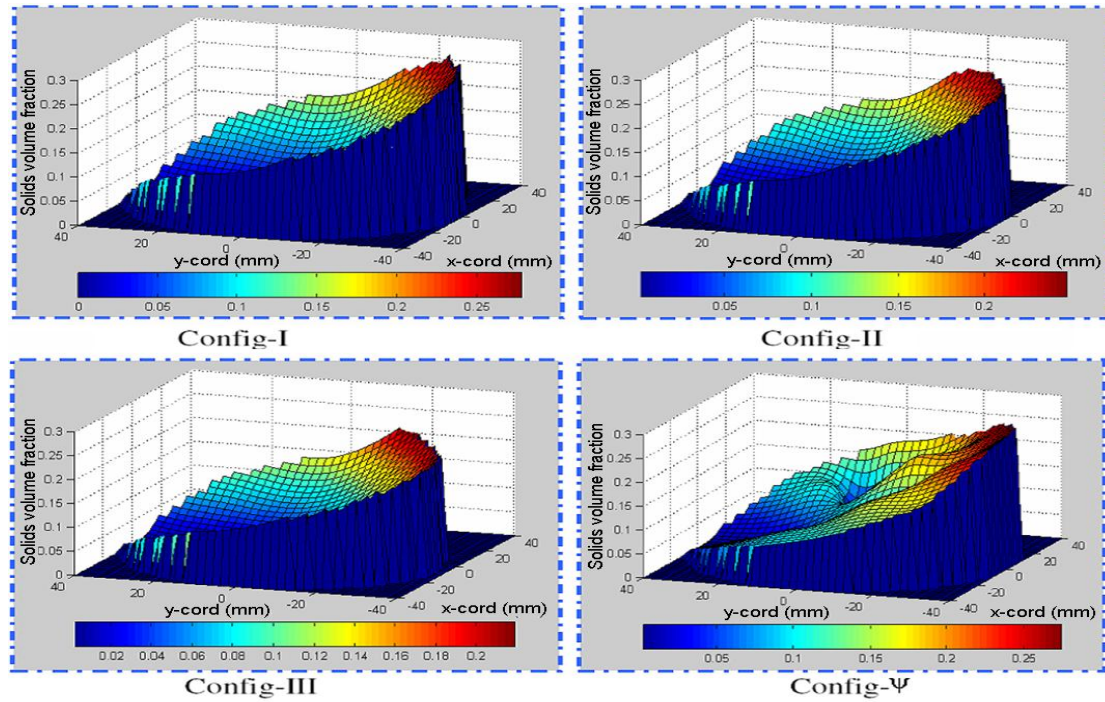
Figure 7-97: Local solids volume fraction profiles for flow in a pipe inclined at 30° to the vertical, flow condition 19($Q_{s,ref}$ =0.360 m^{3}h^{-1}, $Q_{w,ref}$ = 7.218 m^{3}h^{-1})
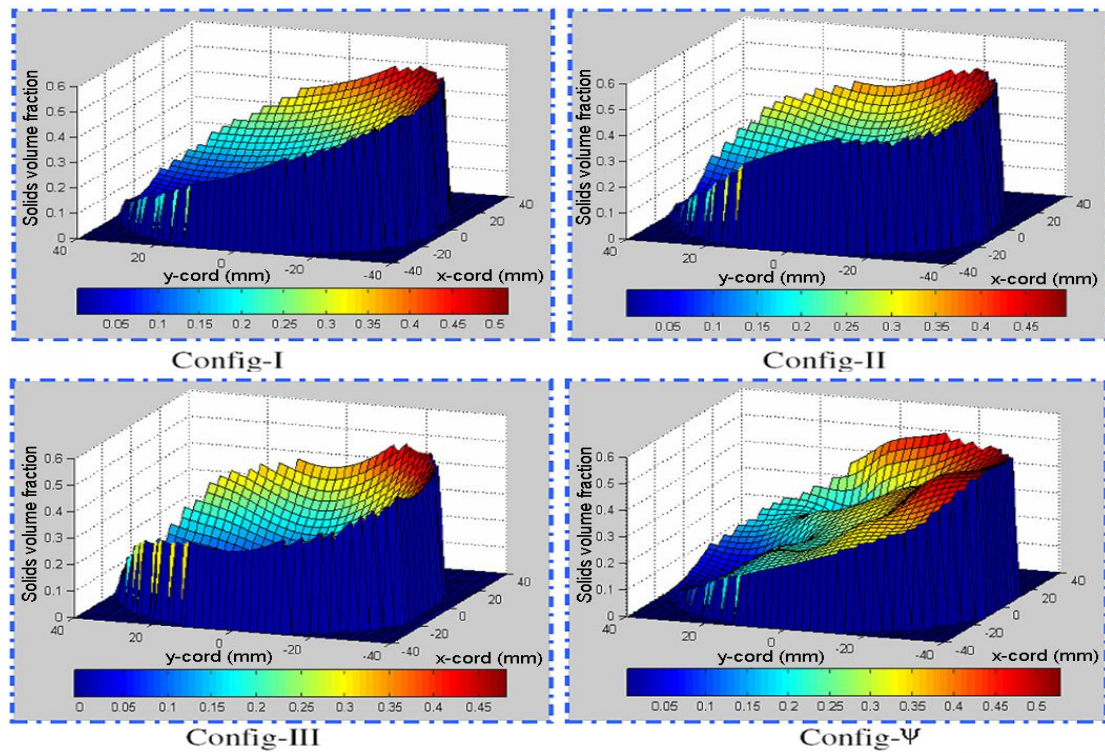
Figure 7-98: Local solids volume fraction profiles for flow in a pipe inclined at 30° to the vertical, flow condition 20($Q_{s,ref}$ = 0.591 m^{3}h^{-1}, $Q_{w,ref}$ = 10.79 m^{3}h^{-1})

280
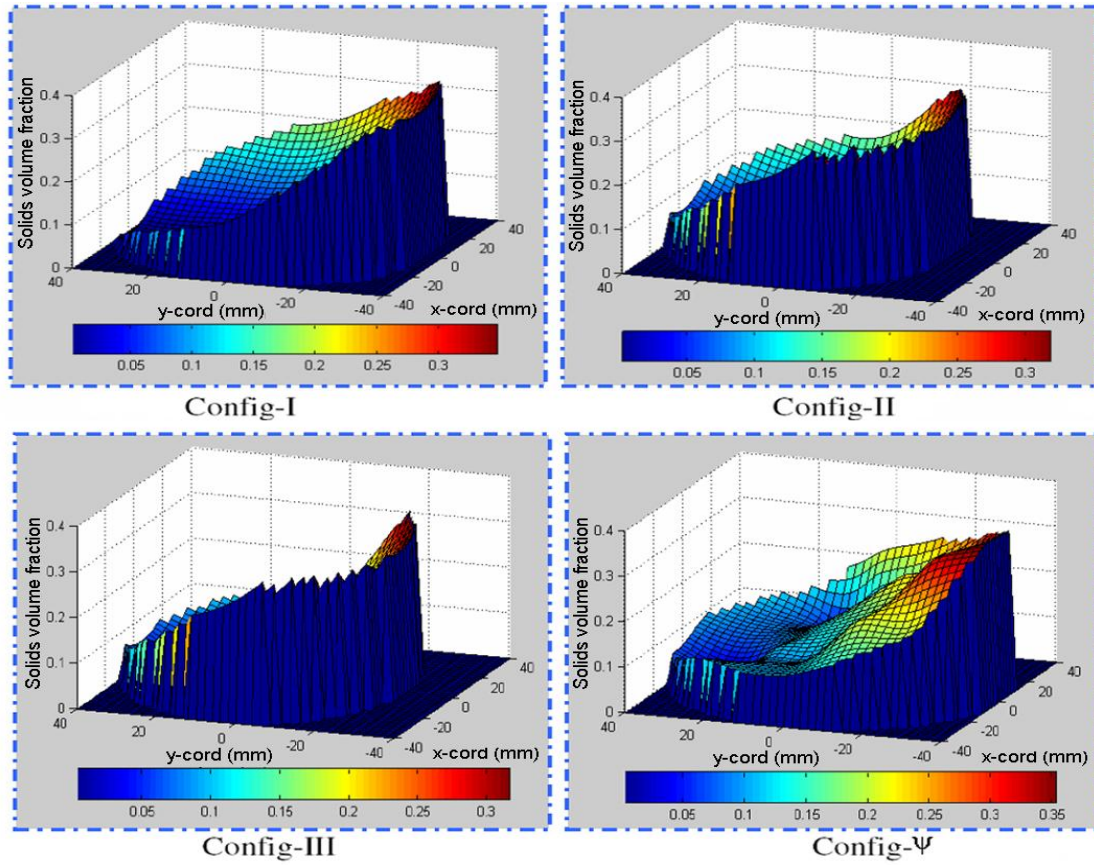
Figure 7-99: Local solids volume fraction profiles for flow in a pipe inclined at 30° to the vertical, flow condition 21($Q_{s,ref}$ =0.549 m^{3}h^{-1}, $Q_{w,ref}$ = 12.13 m^{3}h^{-1})
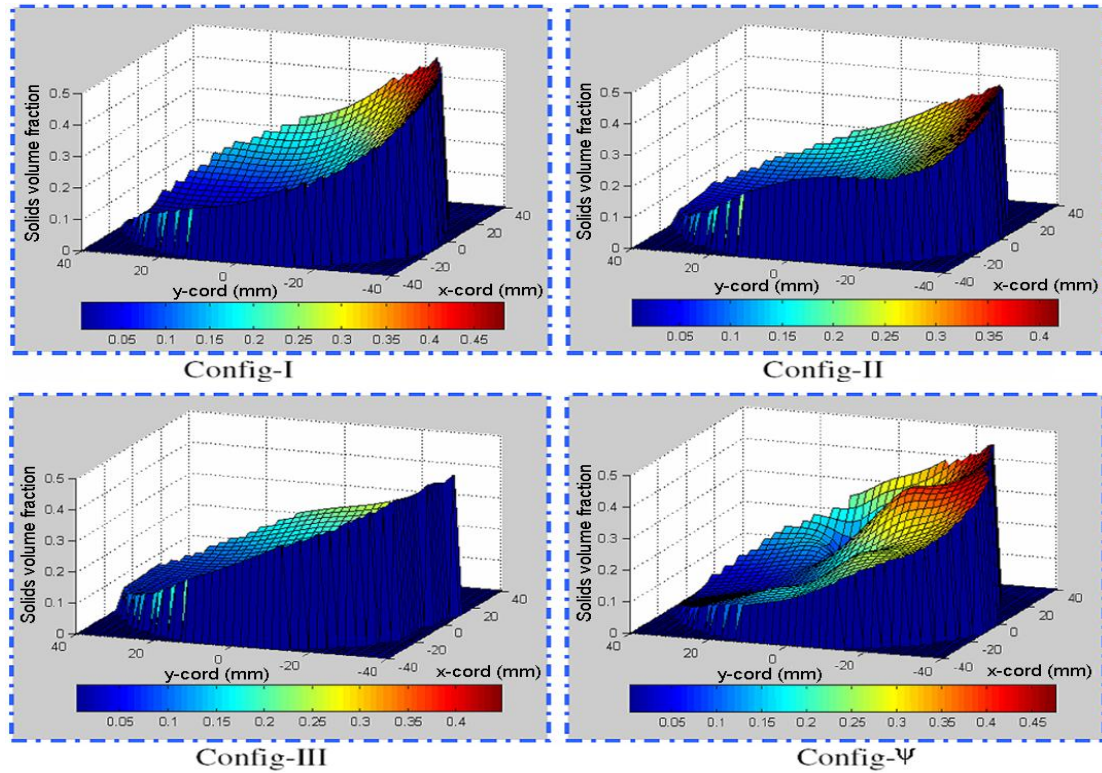
Figure 7-100: Local solids volume fraction profiles for flow in a pipe inclined at 30° to the vertical, flow condition 22($Q_{s,ref}$ =0.951 m^{3}h^{-1}, $Q_{w,ref}$ = 12.47 m^{3}h^{-1})
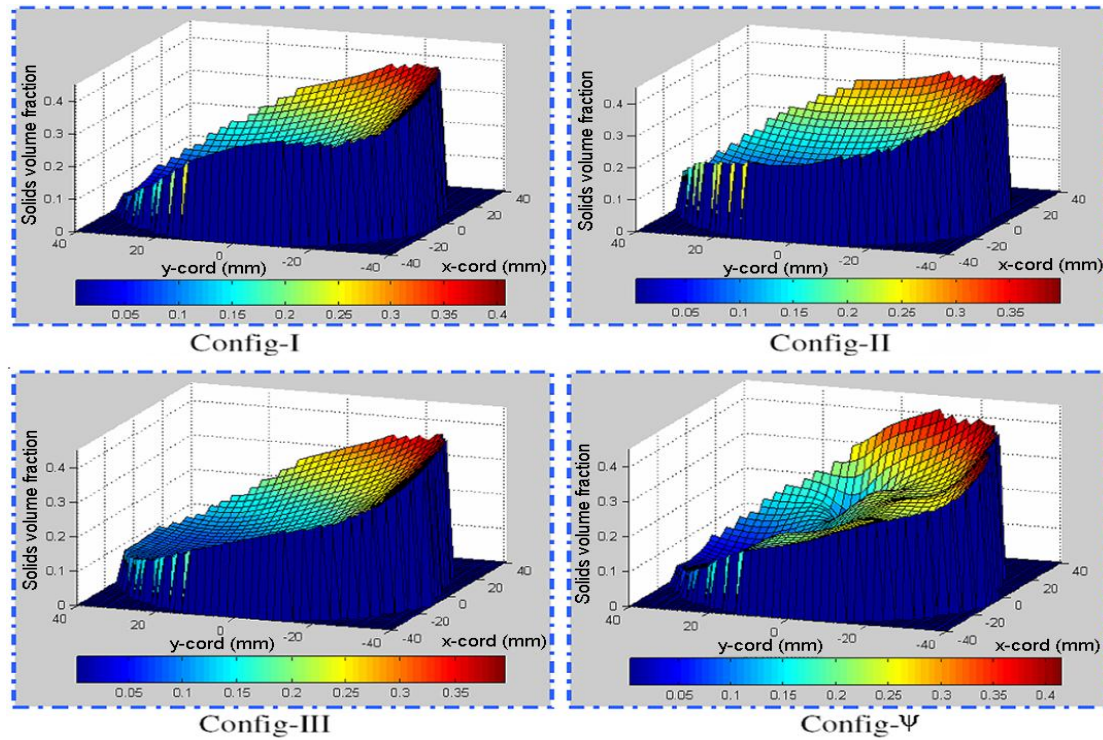
Figure 7-101: Local solids volume fraction profiles for flow in a pipe inclined at 30° to the vertical, flow condition 23($Q_{s,ref}$ =1.010 m^{3}h^{-1}, $Q_{w,ref}$ = 14.06 m^{3}h^{-1})
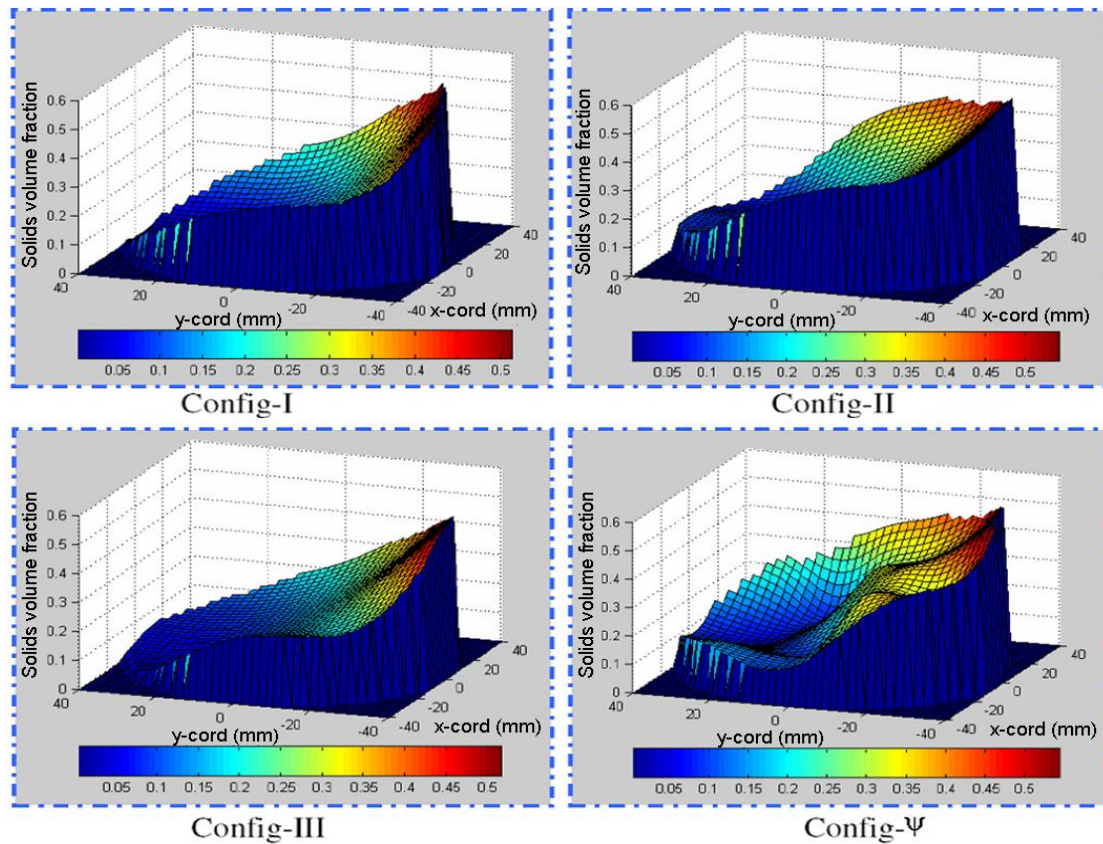
Figure 7-102: Local solids volume fraction profiles for flow in a pipe inclined at 30° to the vertical, flow condition 24($Q_{s,ref}$ =0.959 m^{3}h^{-1}, $Q_{w,ref}$ = 15.66 m^{3}h^{-1})
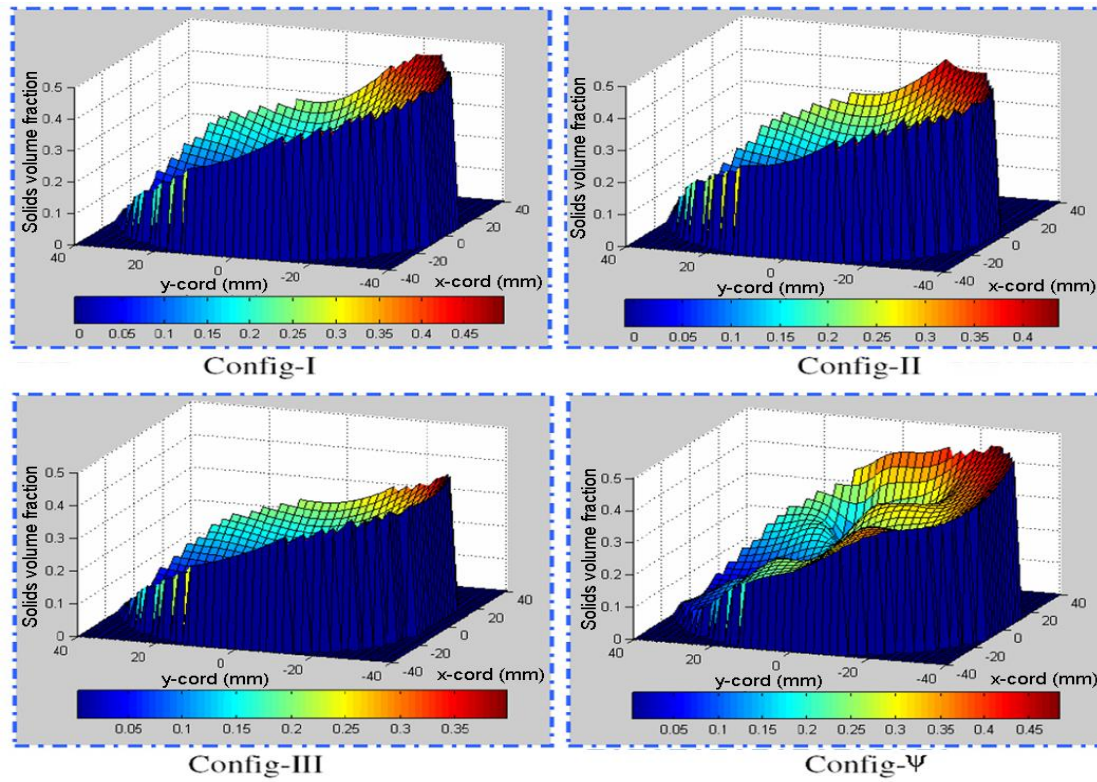
Figure 7-103: Local solids volume fraction profiles for flow in a pipe inclined at 30° to the vertical, flow condition 25($Q_{s,ref}$ =1.410 m^{3}h^{-1}, $Q_{w,ref}$ = 14.10 m^{3}h^{-1})
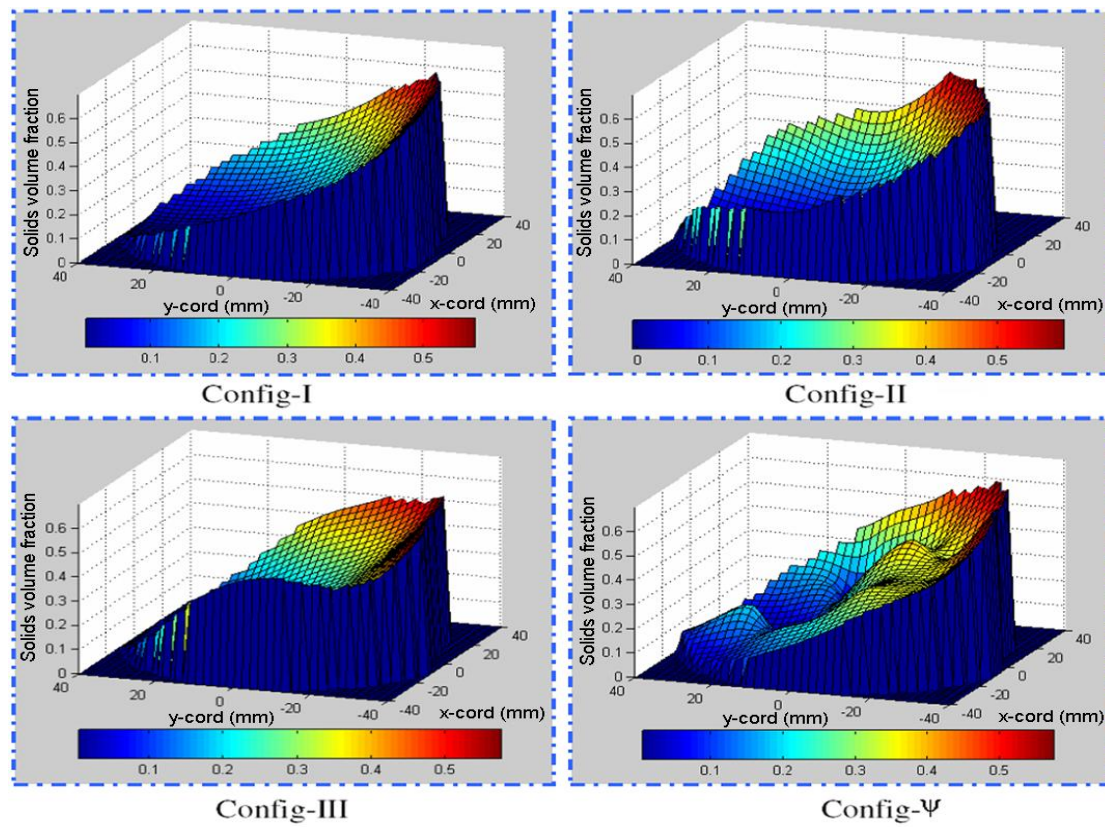
Figure 7-104: Local solids volume fraction profiles for flow in a pipe inclined at 30° to the vertical, flow condition 26($Q_{s,ref}$ =1.651 m^{3}h^{-1}, $Q_{w,ref}$ = 15.96 m^{3}h^{-1})
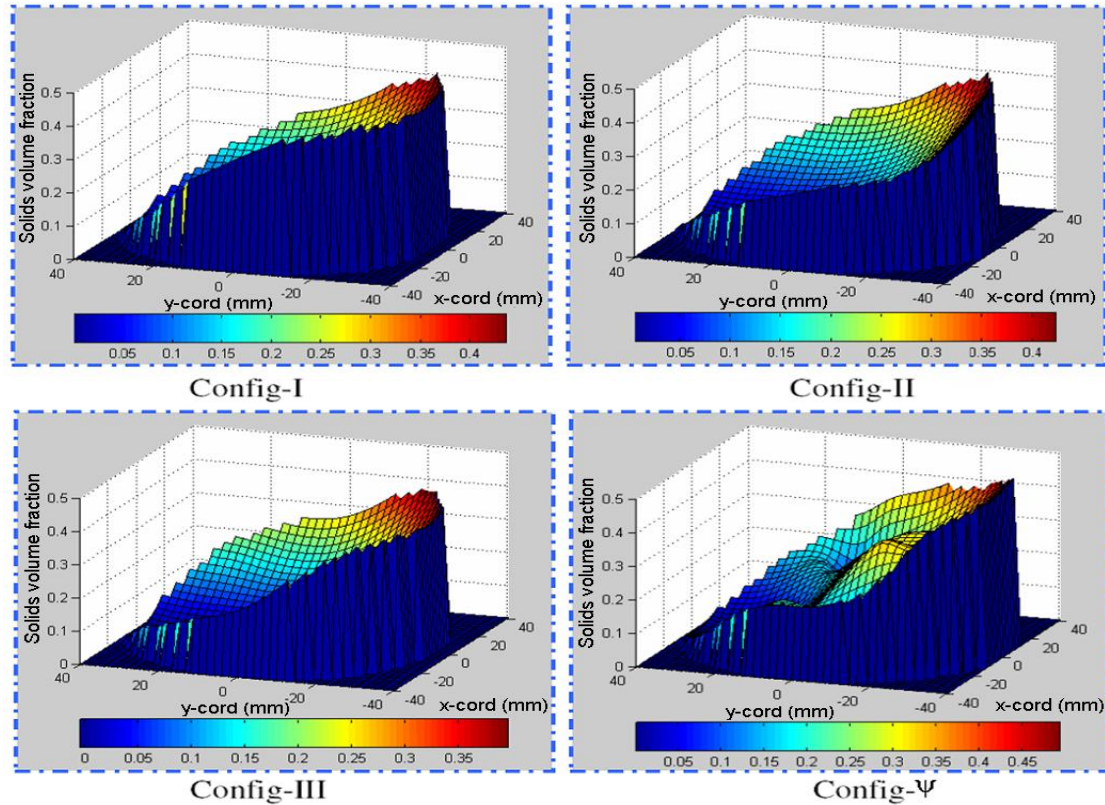
Figure 7-105: Local solids volume fraction profiles for flow in a pipe inclined at 30° to the vertical, flow condition 27. ($Q_{s,ref}$ =1.623 m^{3}h^{-1}, $Q_{w,ref}$ = 17.12 m^{3}h^{-1})

7.2.7 Discussion of the local solids volume fraction profiles

It can be seen that profiles obtained using Configs-I, II and III of local solids volume fraction for vertical flow (see Figures 7-82 to 7-90) show only small variations of the solids volume fraction between the different configurations (Configs-I,II,and III). The solids volume fraction profiles are concave, which may seem to imply that the solids volume fraction is lower in the centre of the pipe and greater nearer the pipe wall. However, when the 24 measurements are combined the solids volume fraction profile becomes flatter over the whole cross-section as shown in Config- ψ (Figures 7-82 to 7-90). The results obtained by the ICC agree with results from Lucas, et al., (1999, 2000) and Cory (1999).

No complete cross-sectional profiles of $α_S$ in vertical upward flow were found in the literature see Cory (1999). However, a number of researchers have claimed to show $α_S$ as relatively constant across the pipe, see Lucas, e al., (1999 2000), Cory (1999),

Akagawa, et al., (1989), Asakura, et al., (1992), Alajbegovic, et al., (1994) and Bartosik and Shook (1995).

Profiles of the local solids fraction for upward flows in inclined pipes (see Figures 7-91 to 7-105) all show a clear decrease in α_S as one moves from the low point on the pipe across the diameter to the other side. At the low point of the pipe α_S is high, reaching close to $\alpha_S = 0.55$, see Figure 7-102 for flow condition 15 (solids and water flow rates of $0.959 m^3 s^{-1}$ and $15.66 m^3 s^{-1}$, respectively). This would appear a high value, since largest proportion of a volume that uniform spheres can occupy is 74% (Steinhaus, H. (1999).

At the higher side of the pipe α_S has its lowest value, sometimes reducing to zero, as shown in Figures 7-103 and 7-105. A similar variation of α_S was also reported by Matousek (1996). Similar profile shapes have been reported by Lucas (1995) and Tabeling, et al., (1991) for the water volume fraction in oil-water flows in inclined pipes.

The most significant aspect of the data shown in Figures 7-91 to 7-105, that the local solids volume fraction is significantly higher at the lower side of the inclined pipe than at the upper side, is due to the simple fact that the solids particles have a higher density than water and preferentially accumulate on the lower side of the inclined pipe. This result agrees with visual observation of the flow through the Perspex working section of the flow loop. The solids volume fraction profiles obtained by the ICC show qualitative agreement with cross-sectional profiles in vertical and inclined angles from vertical (15° and 30°) agreed with Lucas, et al., (1999, 2000) and Cory (1999). Also, the flow profiles reported here also show qualitative agreement with cross-sectional profiles of horizontal solids-liquid flow reported by Scarlett and Grimley (1974), Chen and Kadambi (1994), Roco and Shook (1983) and Hsu et al. (1989) for horizontal solids-liquid flow. The causes of this profile shape are described in Section 1.3.

For the upward vertical flows investigated, the local solids volume fraction and axial velocity distributions were axi-symmetric. As the angle of inclination angle of the

pipe away from the vertical was increased, the solids tended to migrate towards the lower side of the inclined pipe, but symmetry about the y-axis was maintained. The lower density of the solids-liquid mixture at the upper side of the inclined pipe gave rise to relatively high axial velocities in this part of the flow cross section. The effect of pipe inclination on the maximum axial solids velocity must be taken into consideration, when designing pipelines which hydraulically convey solids - because the maximum solids velocity can greatly exceed the mean solids velocity.

7.3 Comparison of experimental results acquired by the ICC device with reference measurements

The aim of this section is to compare the values of $\bar{\alpha}_{s,meas}$ and $\bar{u}_{s,meas}$ obtained by integration with reference data. The data acquired using the ICC device was integrated using the methods described in Section 6.4.3.3 to give global average values of $\bar{\alpha}_{s,meas}$, $\bar{u}_{s,meas}$ and $Q_{s,meas}$. The reference data was acquired using the reference data devices as described in chapter 6.

It should be noted at this point that the data integrated was the actual data acquired by the ICC device. In the profiles presented in Section 7.2 data was interpolated and plotted as profiles to allow a better qualitative comparison to be made between the profiles acquired by the ICC device and different systems reported in the literature (ERT and six local probe obtained by Lucas, et al., (1999; 2000) and Cory (1999)).

For the purposes of quantitative comparison a percentage error term, ε_{ICC} was evaluated from the difference between the reference value obtained from the hopper cell and the value obtained from integrated ICC measurements is defined in Equation 7-1:

$$\varepsilon_{ICC} = \frac{Y_{meas} - Y_{ref}}{Y_{ref}} \times 100 \qquad 7\text{-}1$$

where: Y_{meas} and Y_{ref} represents the values obtained from integrated local measurements obtained by the ICC and the reference measurement obtained from the reference devices respectively.

7.3.1 Mean solids velocity from integrated local measurements from the ICC device

The integrated solids axial velocity values obtained from the ICC device for each pipe inclination angle (0°, 15° and 30°), and the relevant reference data, are presented in Tables 7-3 to 7-6 (where Table 7-3 is for Config-I, Table 7-5 is for Config-II and Table 7-6 is for Config-III).

Table 7-3: Integrated solids axial velocity data from the ICC device and reference for Config-I

Electrodes Configuration	Angle of inclination of test pipe	Solids velocity $\overline{u}_{s,ref}$ (ms^{-1})	Solids velocity $\overline{u}_{s,meas}$ (ms^{-1})	Percentage error ε_{ICC}
Config-I	0°	0.244	0.257	5.3
		0.31	0.324	4.5
		0.33	0.342	3.6
		0.37	0.357	-3.5
		0.4	0.416	4.0
		0.41	0.428	4.4
		0.43	0.453	5.3
		0.53	0.534	0.8
		0.61	0.635	4.1
	15°	0.29	0.305	5.2
		0.31	0.289	-6.8
		0.33	0.348	5.5
		0.35	0.331	-5.4
		0.39	0.411	5.4
		0.41	0.426	3.9
		0.42	0.398	-5.2
		0.44	0.459	4.3
		0.34	0.354	4.1
	30°	0.22	0.23	4.5
		0.21	0.2	-4.8
		0.34	0.323	-5.0
		0.28	0.264	-5.7
		0.37	0.353	-4.6
		0.32	0.299	-6.6

		0.41	0.433	5.6
		0.46	0.484	5.2
		0.51	0.534	4.7

It is important to note the method used to integrate the local measurements of ICC device u_s over the pipe cross-section to obtain an estimate of $\bar{u}_{s,meas}$ (see Section 6.4.3.3). $\bar{u}_{s,meas}$ is given by Equation 7-2.

$$\bar{u}_{s,meas} = \frac{\int_A \alpha_s u_s \, dA}{\int_A \alpha_s \, dA} = \frac{Q_{s,ref}}{A\bar{\alpha}_{s,meas}} \qquad 7\text{-}2$$

It is clear from Equation 7-2 that the value of $\bar{u}_{s,meas}$ is dependent upon the value of $\bar{\alpha}_{s,meas}$. Any errors in the value of $\bar{\alpha}_{s,meas}$ will have an effect on the value of $\bar{u}_{s,meas}$.

Figures 7-106, 7-108 and 7-110 represent the relationship between the reference solids velocity $\bar{u}_{s,ref}$ and the measured solids velocity $\bar{u}_{s,meas}$ as measured by the ICC, for Config-I, II and III respectively. Each figure contains data for the pipe vertical, and inclined at 15° and 30° to the vertical. Each of the three figures shows a good linear relationship between the two quantities. The best fit straight lines have gradients of 1.07, 1.1 and 1.03 respectively. There are 27 sets of data (points) on each of the figures and their respective Pearson correlation coefficients are R=0.98, 0.99 and 0.98 which implies that for all three configurations the linear relation between $\bar{u}_{s,ref}$ and $\bar{u}_{s,meas}$ is highly significant.

Figure 7-107, 7-109 and 7-111 shows the relationship between the percentage error (ε_{ICC}) and the reference solids velocity $\bar{u}_{s,ref}$ for Config-I,II and III respectively. Each figure contains data for the pipe vertical and inclined at 15° and 30° to the vertical. Comparative data is shown in Table 7-4.

Table 7-4: Comparison of the relative % error between reference solids velocity $\bar{u}_{s,ref}$ and the measured solids velocity $\bar{u}_{s,meas}$

	Mean % error			Range of % error			Standard deviation of % error		
	Angle of inclination			Angle of inclination			Angle of inclination		
Config	0°	15°	30°	0°	15°	30°	0°	15°	30°
I (Table 7-3)	3.2	2.2	-2.7	5.5 to -3.5	5.5 to -6.8	5.6 to -6.6	2.8	5.3	5.5
II (Table 7-5)	2.8	3.8	3.5	6.7 to -4.3	7.2 to -7.1	5.9 to -6.6	4.1	5.8	5.8
III(Table7-6)	3.5	4.5	3.6	5.1 to -7.0	6.0 to -6.7	6.4 to -5.2	4.9	5.7	5.2

The data presented in Table 7.4 shows no significant differences in the measurement errors between the three configurations (whether mean, range or standard deviation) for any of the angles of inclination.
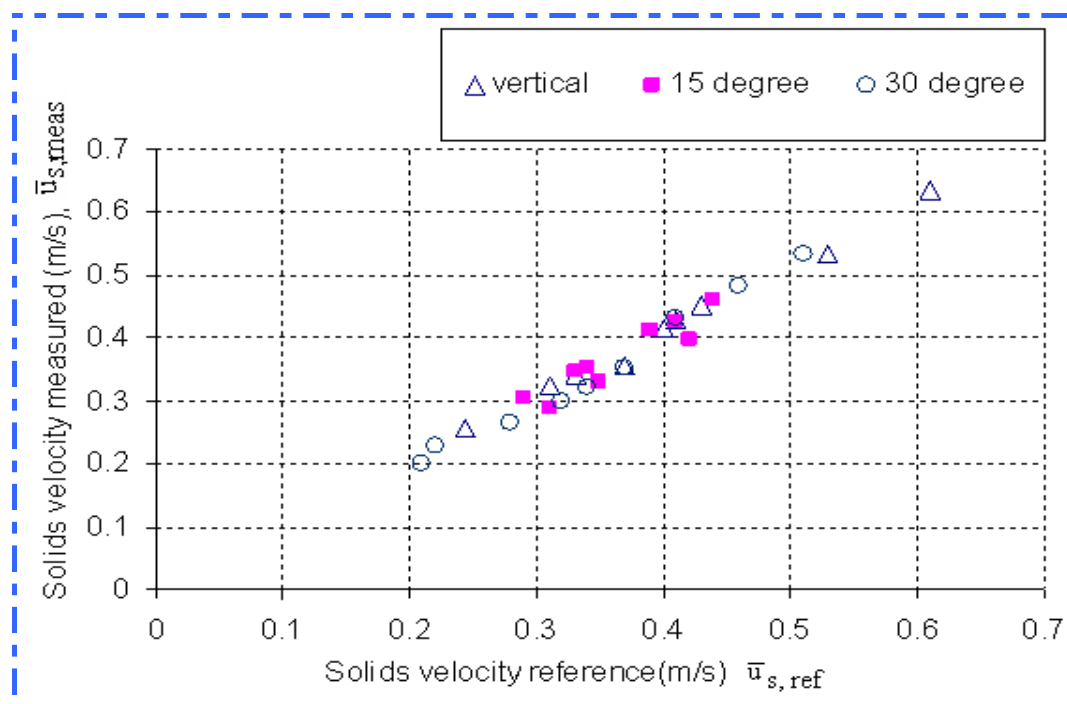
Figure 7-106: The relationship between $\bar{u}_{s,meas}$ and $\bar{u}_{s,ref}$ for Config-I
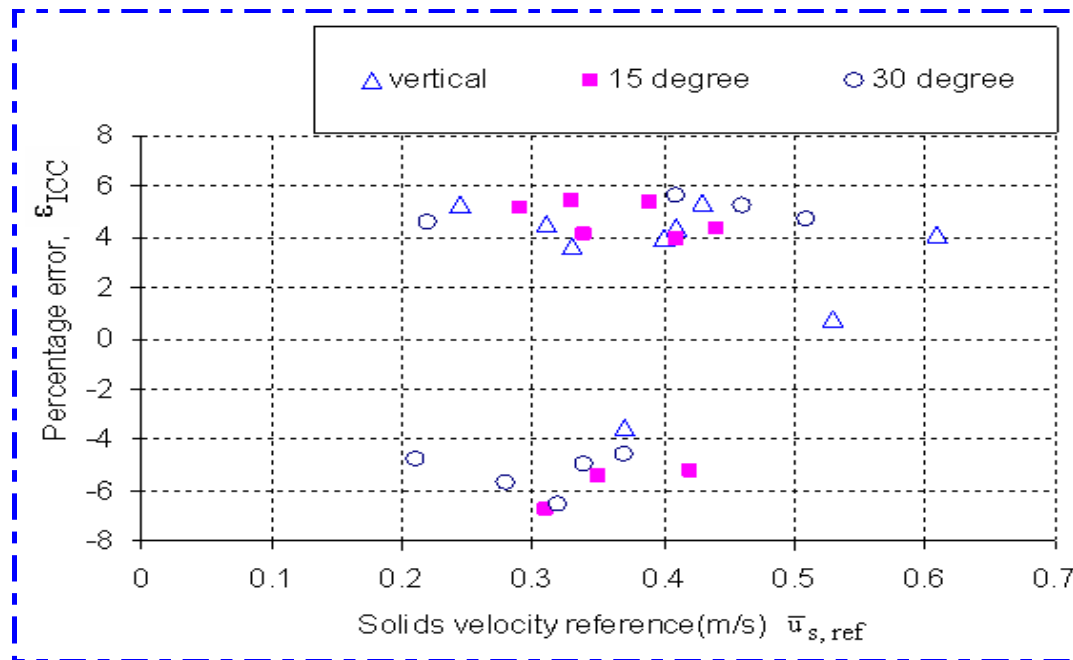
Figure 7-107: Percentage error versus $\overline{u}_{s,ref}$ for Config-I for different inclined angles $0^{o}, 15^{o}$ and 30°

Table 7-5: Integrated solids axial velocity data from the ICC device and reference for Config-II

Electrodes Configurations	Angle of inclination of test pipe	Solids velocity $\overline{u}_{s,ref}$ (ms^{-1})	Solids velocity $\overline{u}_{s,meas}$ (ms^{-1})	Percentage error ε_{ICC}
Config-II	0°	0.24	0.26	5.3
		0.31	0.32	4.5
		0.33	0.32	-4.2
		0.37	0.38	3.5
		0.40	0.38	-4.3
		0.41	0.43	4.6
		0.43	0.45	5.4
		0.55	0.56	3.5
		0.61	0.65	6.7
	15°	0.29	0.31	5.5
		0.31	0.29	-7.1
		0.33	0.31	-5.8
		0.35	0.37	5.7
		0.39	0.42	7.2
		0.41	0.39	-4.6
		0.42	0.45	6.0

		0.44	0.46	5.2
		0.34	0.36	4.4
		0.22	0.21	-4.6
		0.21	0.22	5.7
		0.34	0.32	-4.7
		0.28	0.26	-5.7
30°		0.37	0.39	4.6
		0.32	0.30	-6.6
		0.41	0.43	5.9
		0.66	0.70	6.4
		0.51	0.54	5.3
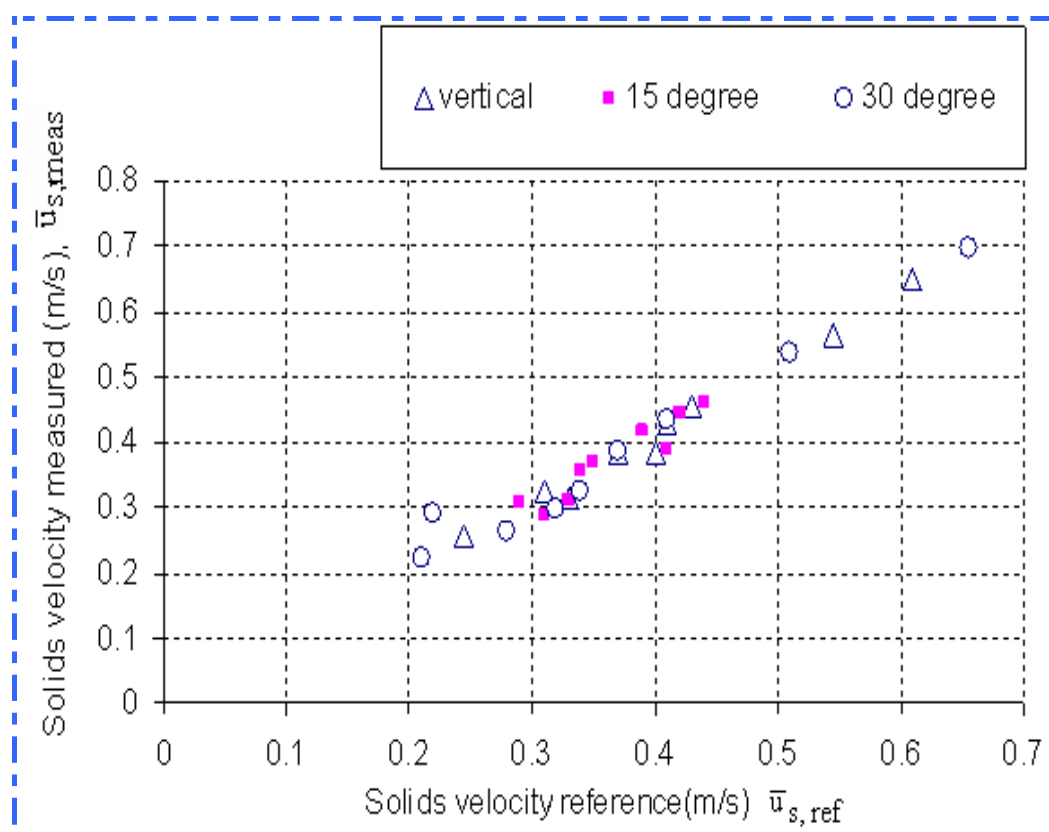
Figure 7-108: The relationship between $\bar{u}_{s,meas}$ and $\bar{u}_{s,ref}$ for Config-II
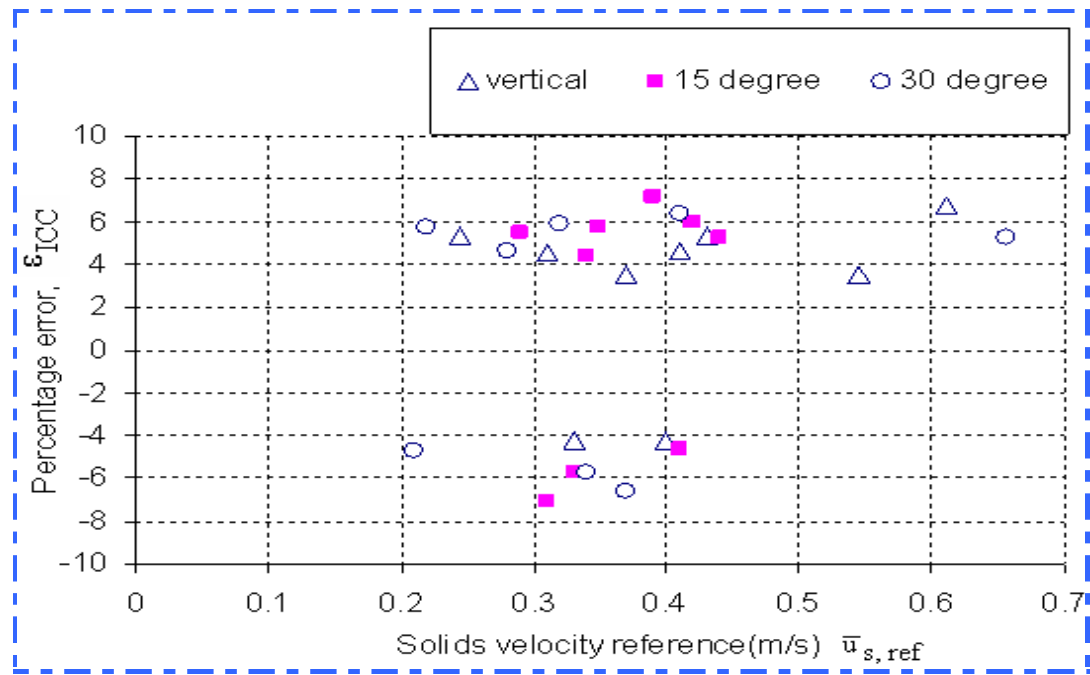
Figure 7-109: Percentage error versus $\overline{u}_{s,ref}$ for Config-II for different inclined

angles 0°, 15° and 30° for all flow conditions listed in Table 7-2

Table 7-6: Integrated solids axial velocity data from the ICC device and reference for Config-III

Electrodes Configurations	Angle of inclination of test pipe	Solids velocity $\overline{u}_{s,ref}$ (ms^{-1})	Solids velocity $\overline{u}_{s,meas}$ (ms^{-1})	Percentage error ε_{ICC}
Config-III	0°	0.244	0.252	3.3
		0.228	0.217	-4.8
		0.471	0.438	-7.0
		0.37	0.382	3.2
		0.4	0.381	-4.8
		0.41	0.429	4.6
		0.43	0.452	5.1
		0.53	0.551	4.0
		0.61	0.634	3.9
	15°	0.29	0.272	-6.2
		0.31	0.325	4.8
		0.33	0.348	5.5
		0.35	0.371	6.0
		0.39	0.41	5.1
		0.41	0.394	-3.9

		0.493	0.46	-6.7
		0.44	0.417	-5.2
		0.34	0.356	4.7
		0.22	0.234	6.4
		0.21	0.199	-5.2
		0.34	0.356	4.7
		0.277	0.265	-4.3
	30°	0.37	0.353	-4.6
		0.32	0.34	6.3
		0.41	0.432	5.4
		0.46	0.482	4.8
		0.51	0.541	6.1
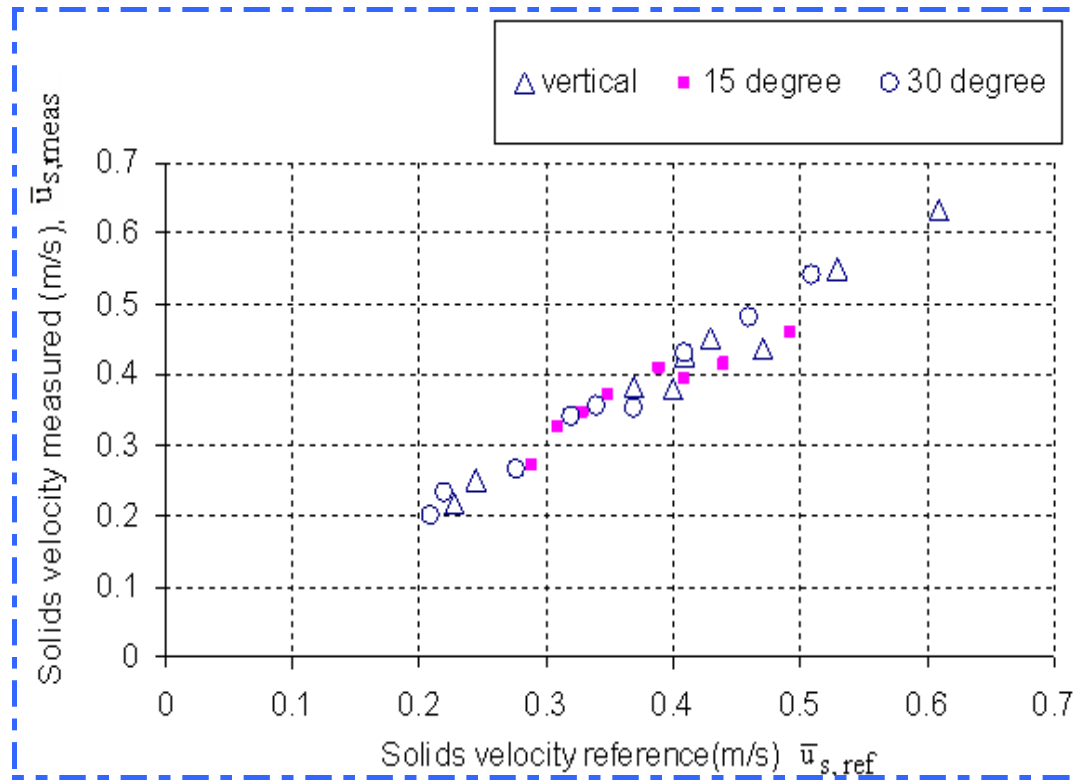
Figure 7-110: The relationship between $\bar{u}_{s,meas}$ and $\bar{u}_{s,ref}$ for Config-III
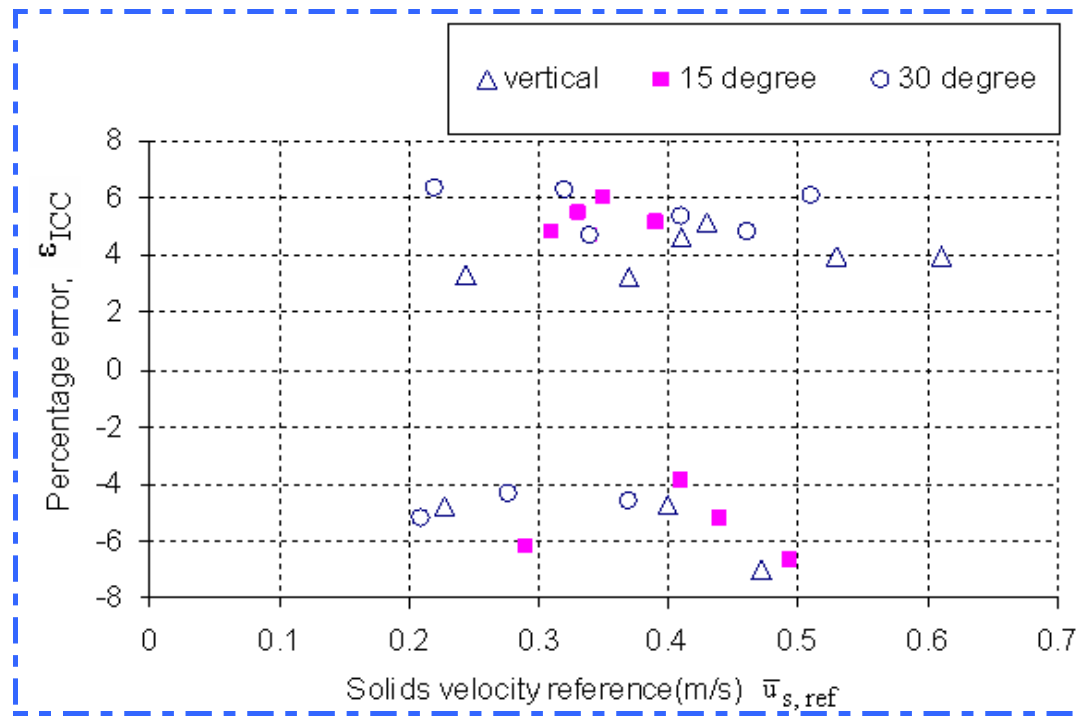
Figure 7-111: Percentage error versus $\overline{u}_{s,ref}$ for Config-III for different inclined angles $0^o, 15^o$ and 30° for all flow conditions listed in Table 7-2

7.3.2 Comparison of reference measurements of solids volume fraction with integrated measurements from the ICC device

The integrated solids volume fraction $\overline{\alpha}_{s,meas}$ obtained from the ICC device using Equation 6-22, for the three pipe inclinations, $0^o, 15^o$ and 30° the relevant reference data, are presented in Tables 7-7, 7-9 and 7-10 (where Table 7-7 is for Config-I, Table 7-9 is for Config-II and Table 7-10 is for Config-III).

Table 7-7: Integrated solids volume fraction data from the volume fraction and reference for Config-I

Electrodes Configurations	Angle of inclination of test pipe	Solids volume fraction $\overline{\alpha}_{s,ref}$	Solids volume fraction $\overline{\alpha}_{s,meas}$	Percentage error ε_{ICC}
Config-I	0°	0.16	0.17	6.3
		0.13	0.135	3.9
		0.12	0.124	3.3
		0.18	0.19	5.6
		0.17	0.16	-5.9
		0.16	0.17	6.3

		0.29	0.28	-3.5
		0.21	0.22	4.8
		0.18	0.19	5.6
	15°	0.12	0.127	5.8
		0.1313	0.138	5.1
		0.12	0.13	-5.3
		0.19	0.195	2.6
		0.16	0.17	6.3
		0.15	0.155	3.3
		0.21	0.22	4.8
		0.2	0.21	5.0
		0.22	0.21	-4.6
	30°	0.09	0.093	3.3
		0.15	0.155	3.3
		0.09	0.098	8.9
		0.19	0.18	-5.3
		0.15	0.159	6.0
		0.17	0.16	-5.9
		0.19	0.2	5.3
		0.21	0.22	4.8
		0.18	0.174	-3.3

<u>Figures 7-112, 7-114 and 7-116</u> show the relationship between the reference solids volume fraction $\bar{\alpha}_{s,ref}$ and the solids volume fraction $\bar{\alpha}_{s,meas}$ measured by the ICC device, for Configs-I, II and III respectively, for the pipe vertical, and inclined at $15°$ and $30°$ to the vertical. Each of the three figures shows a good linear relationship between the two quantities. The best fit straight lines have gradients of 0.95, 1.05 and 1.05 respectively. The Pearson correlation coefficient for the 27 sets of data (points) on each of the figures are R=0.98, 0.99 and 0.98 respectively which implies that for all three configurations the linear relation between $\bar{\alpha}_{s,ref}$ and $\bar{\alpha}_{s,meas}$ is highly significant.

<u>Figures 7-113, 7-115 and 7-117</u> shows the relationship between the percentage error (ε_{ICC}) and the reference solids volume fraction $\bar{\alpha}_{s,ref}$ for Config-I,II and III

respectively. Each figure contains data for the pipe vertical and inclined at 15° and 30° to the vertical. Comparative data is shown in Table 7-8.

Table 7-8: Comparison of the relative % error between reference solids volume fraction $\bar{\alpha}_{s,ref}$ and the measured solids volume fraction $\bar{\alpha}_{s,meas}$

	Mean % error			Range of % error			Standard deviation of % error		
	Angle of inclination			Angle of inclination			Angle of inclination		
Config	0°	15°	30°	0°	15°	30°	0°	15°	30°
I (Table 7-7)	2.9	2.6	1.9	6.3 to -5.9	6.3 to -4.6	8.9 to -5.6	4.5	4.4	5.4
II (Table 7-9)	3.6	1.3	1.9	7.0 to -3.4	3.4 to -5.3	6.3 to -4.7	3.0	2.7	3.5
III(Table7-10)	0.6	1.6	1.1	6.3 to -6.7	7.9 to -7.5	8.2 to -6.7	5.5	6.2	6.0

The data presented in Table 7.8 shows no differences at any meaningful level of significance in the measurement errors between the three configurations (whether mean, range or standard deviation) for any of the angles of inclination. Using the Fisher T-test the difference between mean errors for Config-I and Config-III at 0° inclination (0.6% as compared to 2.9%) has a significance of less than 70%. This is well below the accepted standard of 95%, and the hypothesis that there is a real difference between the mean errors of Config-I and Config-III is rejected.
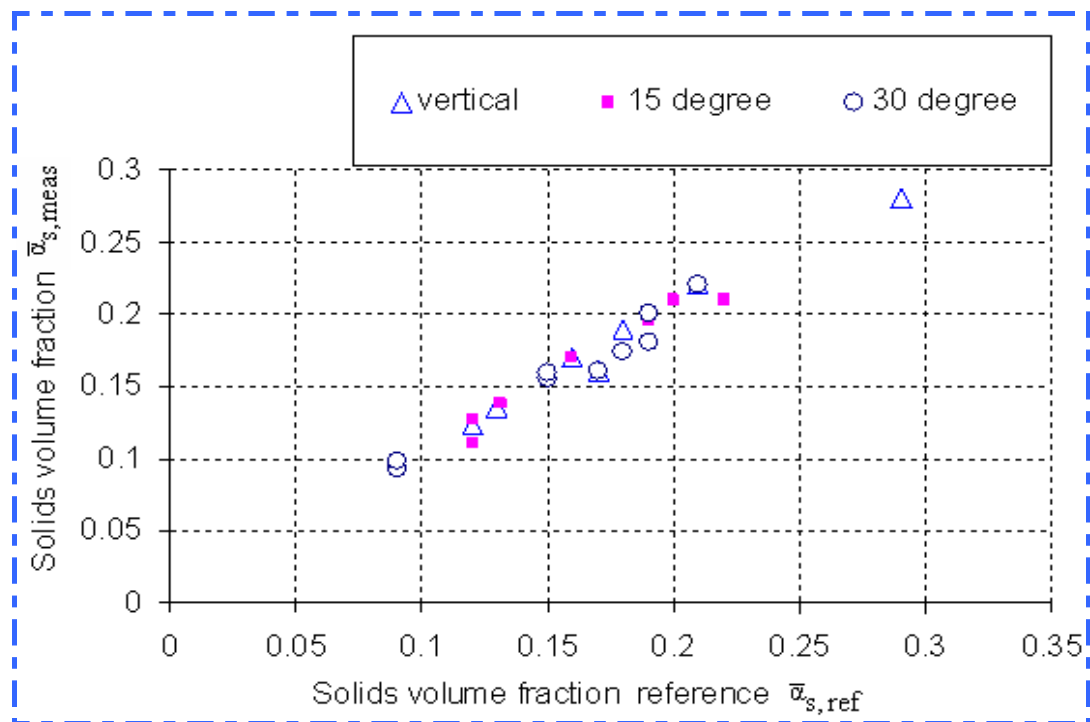
Figure 7-112: The relationship between $\bar{\alpha}_{s,meas}$ and $\bar{\alpha}_{s,ref}$ for Config-I
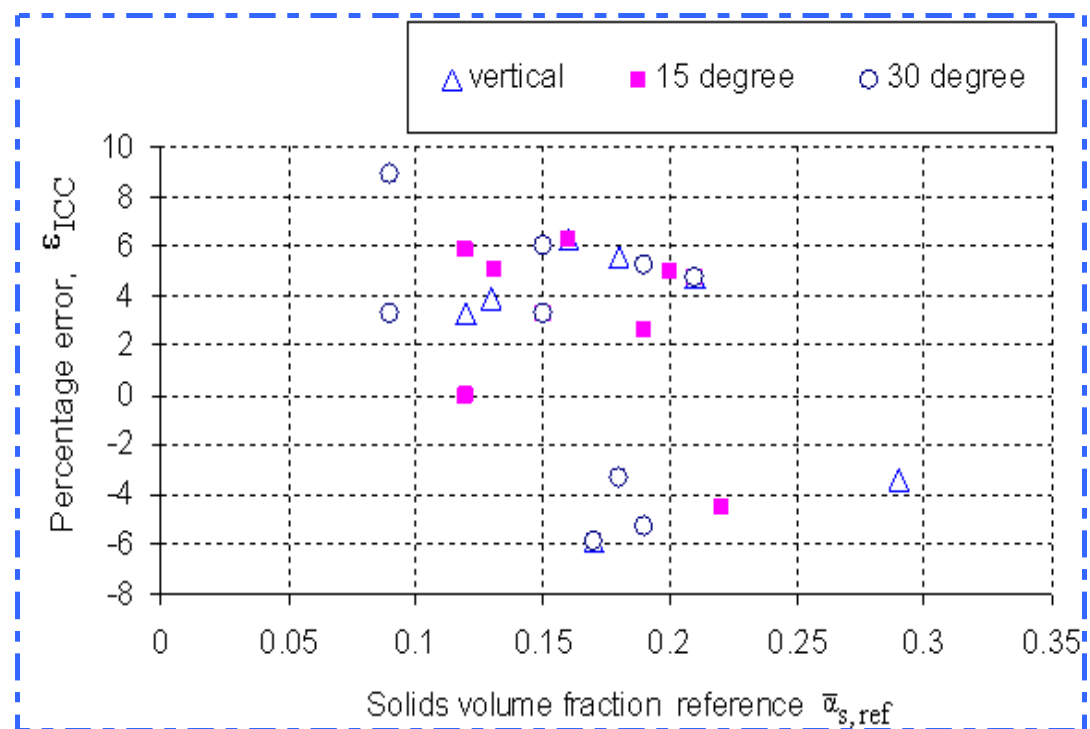
Figure 7-113: Percentage error versus $\bar{\alpha}_{s,ref}$ for Config-I for different inclined angles $0^{\circ}, 15^{\circ}$ and 30° for all flow conditions listed in Table 7-2.

Table 7-9: Integrated solids volume fraction data from the local probe and reference for Config-II

Electrodes Configurations	Angle of inclination of test pipe	Solids volume fraction $\overline{\alpha}_{s,ref}$	Solids volume fraction $\overline{\alpha}_{s,meas}$	Percentage error ε_{ICC}
Config-II	0°	0.16	0.172	7.0
		0.13	0.135	3.7
		0.12	0.128	6.3
		0.18	0.174	-3.4
		0.17	0.178	4.5
		0.16	0.164	2.4
		0.29	0.305	4.9
		0.21	0.22	4.5
		0.18	0.185	2.7
	15°	0.12	0.125	4.0
		0.1313	0.133	1.3
		0.12	0.114	-5.3
		0.19	0.191	0.5
		0.16	0.163	1.8
		0.15	0.154	2.6
		0.21	0.214	1.7
		0.2	0.207	3.4
		0.22	0.223	1.3
	30°	0.09	0.086	-4.7
		0.15	0.148	-1.4
		0.09	0.096	6.3
		0.19	0.193	1.6
		0.15	0.151	0.7
		0.17	0.176	3.4
		0.19	0.202	5.9
		0.21	0.214	1.9
		0.18	0.186	3.2
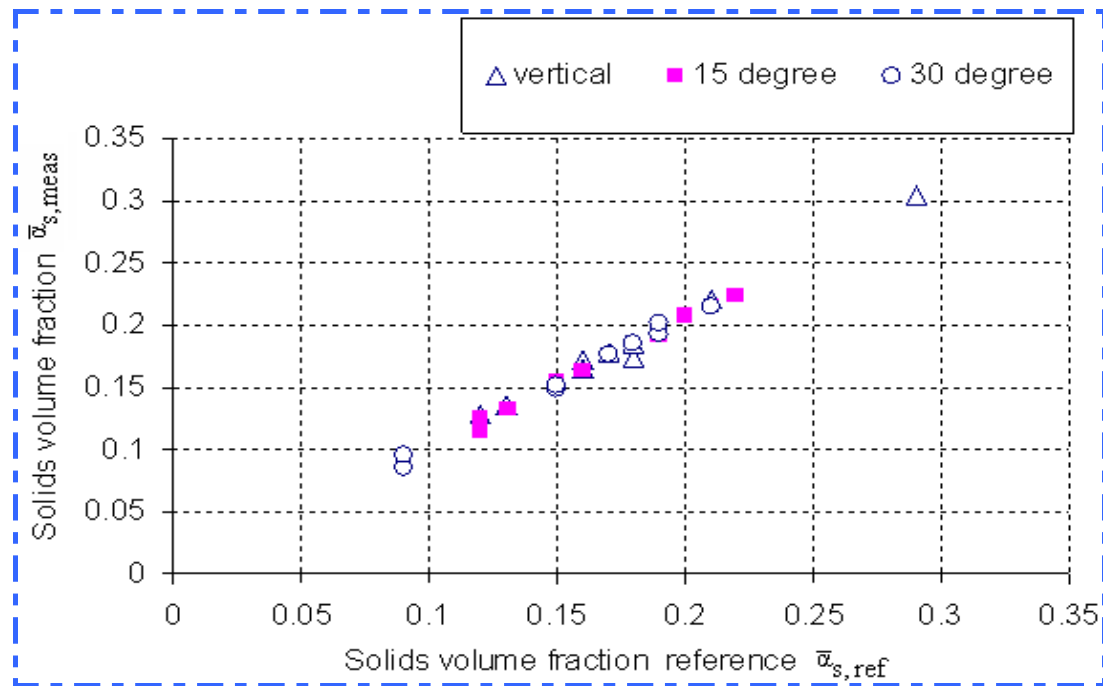
Figure 7-114: The relationship between $\bar{\alpha}_{s,meas}$ and $\bar{\alpha}_{s,ref}$ for Config-II
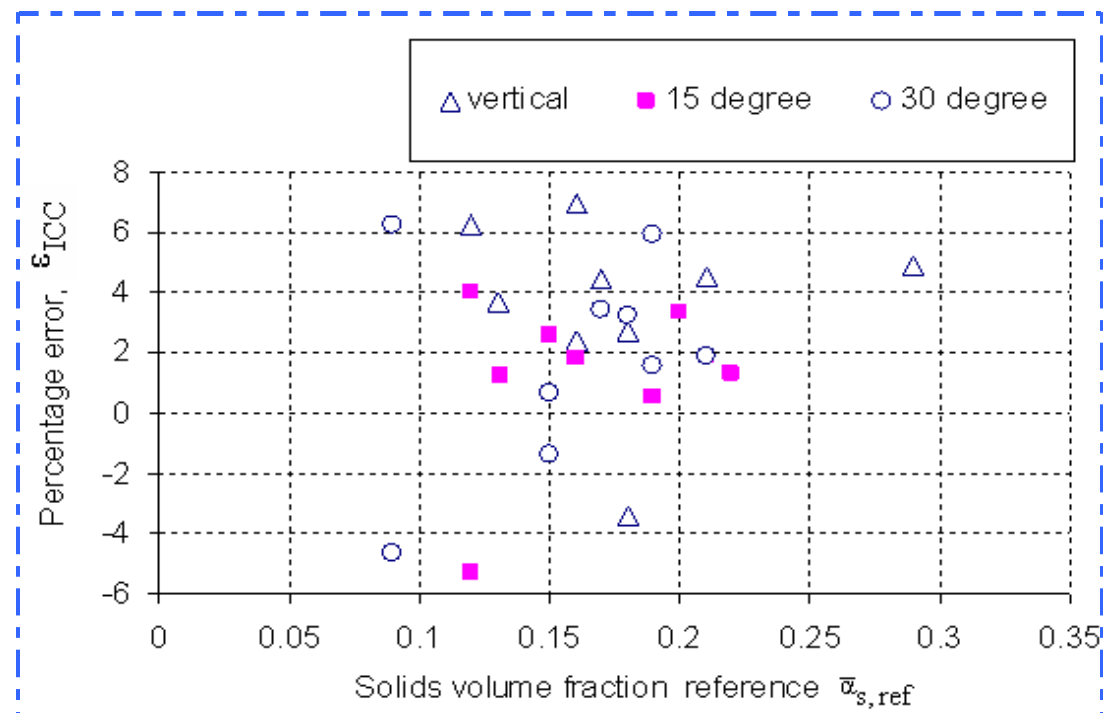
Figure 7-115: Percentage error versus $\bar{\alpha}_{s,ref}$ for Config-II for different inclined

angles $0^{o}, 15^{o}$ and 30° for all flow conditions listed in Table 7-2

Table 7-10: Integrated solids volume fraction data from the local probe and reference for Config-III

Electrodes Configuratio ns	Angle of inclination of test pipe	Solids volume fraction $\overline{\alpha}_{s,ref}$	Solids volume fraction $\overline{\alpha}_{s,meas}$	Percentage error ε_{ICC}
Config-III	0°	0.16	0.17	6.3
		0.13	0.134	3.1
		0.12	0.114	-5.0
		0.18	0.168	-6.7
		0.17	0.167	-1.8
		0.16	0.15	-6.3
		0.29	0.305	5.2
		0.21	0.221	5.2
		0.18	0.19	5.6
	15°	0.12	0.111	-7.5
		0.13	0.136	4.6
		0.12	0.129	7.5
		0.19	0.205	7.9
		0.16	0.165	3.1
		0.15	0.159	6.0
		0.21	0.219	4.3
		0.2	0.19	-5.0
		0.22	0.205	-6.8
	30°	0.09	0.085	-5.6
		0.15	0.14	-6.7
		0.09	0.094	4.4
		0.19	0.18	-5.3
		0.15	0.147	-2.0
		0.17	0.184	8.2
		0.19	0.198	4.2
		0.21	0.22	4.8
		0.18	0.194	7.8
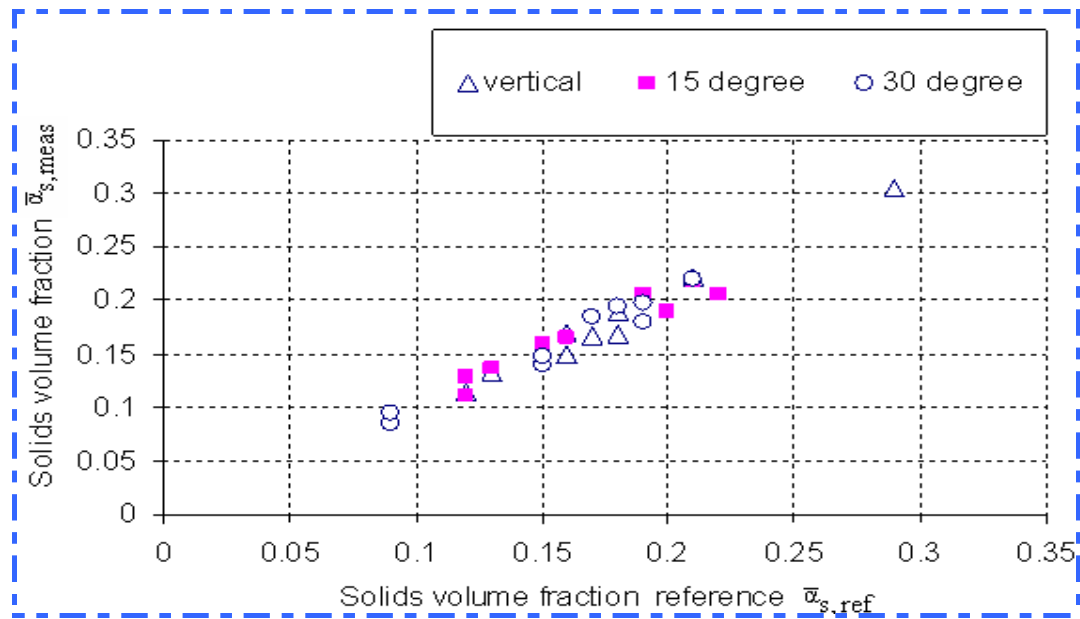
Figure 7-116: The relationship between $\bar{\alpha}_{s,meas}$ and $\bar{\alpha}_{s,ref}$ for Config-III
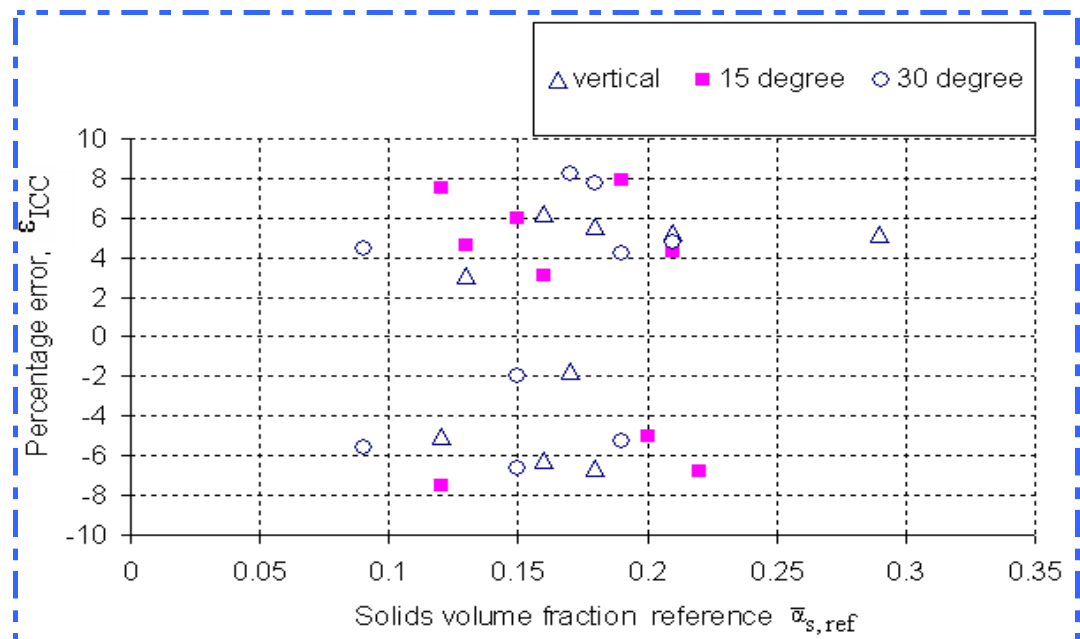
Figure 7-117: Percentage error versus $\bar{\alpha}_{s,ref}$ for Config-III for different inclined angles 0°, 15° and 30° for all flow conditions listed in Table 7-2.

7.3.3 Comparison of reference measurements of solids volumetric flow rate with integrated measurements from the ICC device

Section 6.4.3.3 explains the measurement of the integrated solids volumetric flow rate $Q_{s,meas}$ and how it is determined using Equation 6-24. Tables 7-12, 7-13 and 7-14 show the solids volumetric flow rates measured by the ICC device for the **three**

inclination angles ($0^o, 15^o$ and 30° from vertical) and the Solids reference volumetric flow rates, $Q_{s,ref}$ for each electrode configurations, Config-I, Config-II and Config-III. The percentage error in values obtained for the ICC device are also shown.

Figures 7-118, 7-120 and 7-122 show the relationship between the reference solids volumetric flow rate $Q_{s,ref}$ and the solids volumetric flow rate $Q_{s,meas}$ measured by the ICC device, for Config-I, II and III respectively, for the pipe vertical, and inclined at 15° and 30° to the vertical. Each of the three figures shows a good linear relationship between the two quantities. The best fit straight lines in each case had a gradient of 1.02, and the Pearson correlation coefficient for each line was 0.99, which implies that for all three configurations the linear relation between $Q_{s,meas}$ and $Q_{s,ref}$ is highly significant.

Figures 7-119, 7-121 and 7-123 show the relationship between the percentage error (ε_{ICC}) and the reference solids volumetric flow rate $Q_{s,ref}$ for Configs-I,II and III respectively. Comparative data is shown in Table 7-11.

Table 7-11: Comparison of the relative% error between reference solids volumetric flow rate $Q_{s,ref}$ and the measured solids volumetric flow rate $Q_{s,meas}$

	Mean % error			Range of % error			Standard deviation of % error		
	Angle of inclination			Angle of inclination			Angle of inclination		
Config-	0°	15°	30°	0°	15°	30°	0°	15°	30°
I (Table 7-12)	2.2	1.4	-3.7	4.0 to -2.4	5.7 to -3.1	-2.1 to -6.9	1.8	3.1	1.7
II (Table 7-13)	1.1	2.0	-2.6	3.3 to -2.8	6.0 to -3.0	-1.8 to -4.9	2.6	3.2	1.2
III(Table 7-14)	1.1	-2.1	-0.2	4.0 to -3.3	7.4 to -6.6	4.8 to-3.1	2.9	4.7	3.6

Examination of Table 7-11 shows that for solids volumetric flow rate a significant difference arises within Config-I and within Config-II. When the pipe inclination moves from 15° and 30°, the measured values from these configurations, $Q_{s,meas}$,

fall slightly but significantly below $Q_{s,ref}$. There is a hint that the same phenomenon is beginning to occur in Config-III, but it is not statistically significant at 30°. This difference between $Q_{s,meas}$, and $Q_{s,ref}$ at these angles could be due to beginning of the deposition of particles on the lower side of the pipe and Config-I and II are more sensitive than Config-III to flow patters at the wall of the pipe.

There are no significant differences between any of the means for pipe inclinations of 0° and 15°. However, the difference between Config-I and ConfigIII for the pipe inclined at 30° is significant at a 95% level of confidence. It is possible to say for this one reading that the mean error for Config-III is significantly less than the mean error for Config-I. Unfortunately, it is not possible to be so definite for Config-II and Config-III.

Table 7-12: Integrated solids volumetric flow rate data from the ICC device and reference devices for vertical upward flow for Config-I

Electrodes Configurations	Angle of inclination of test pipe	Solids volumetric flow rate, $Q_{s,ref}$ (m^3h^{-1})	Solids volumetric flow rate, $Q_{s,meas}$ (m^3h^{-1})	Percentage error ε_{ICC}
Config-I	0°	0.696	0.72	2.85
		0.75	0.779	4
		0.73	0.748	2.73
		1.188	1.213	1.68
		1.225	1.2	-2.44
		1.183	1.218	3.38
		2.229	2.276	2.24
		1.998	2.05	2.49
		1.974	2.022	2.53
	15°	0.613	0.626	3.27
		0.731	0.713	-2.74
		0.704	0.74	5.71
		1.187	1.211	1.68
		1.104	1.141	3.63
		1.096	1.076	-1.82
		1.587	1.636	3.14

		1.631	1.58	-3.07
		1.623	1.66	2.46
	30°	0.36	0.346	-2.78
		0.591	0.561	-5.09
		0.549	0.526	-3.64
		0.951	0.924	-3.16
		1.01	0.941	-6.94
		0.959	0.94	-2.09
		1.41	1.372	-2.84
		1.651	1.624	-1.82
		1.395	1.332	-5
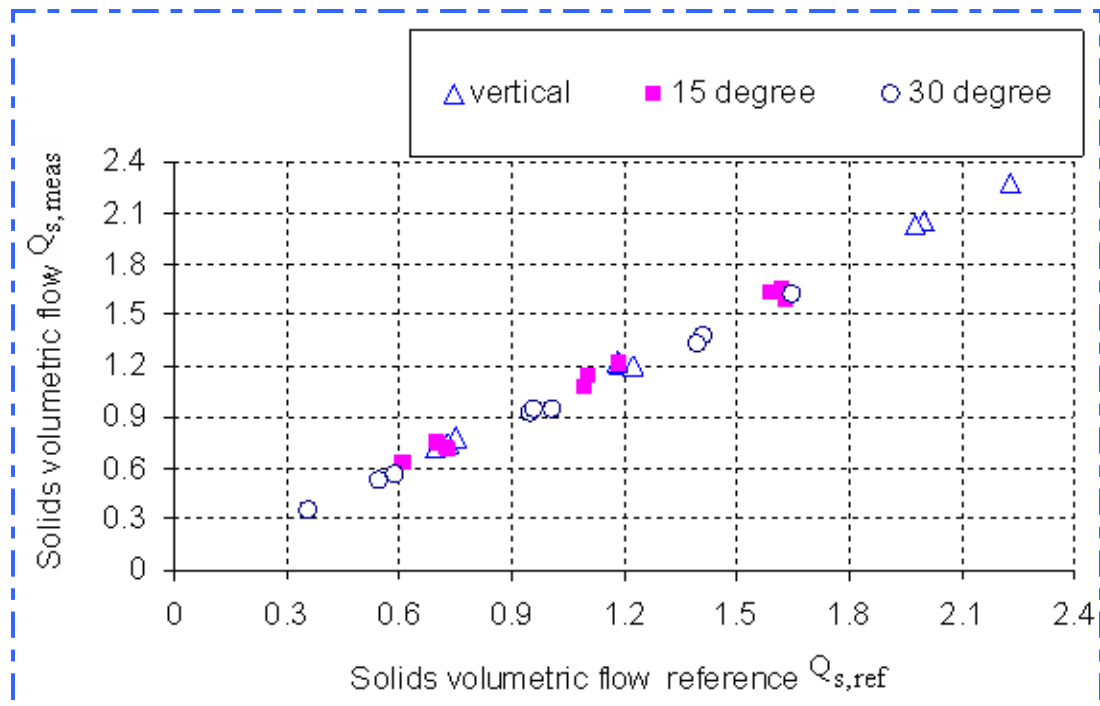
Figure 7-118: The relationship between $Q_{s,ref}$ and $Q_{s,meas}$ for Config-I
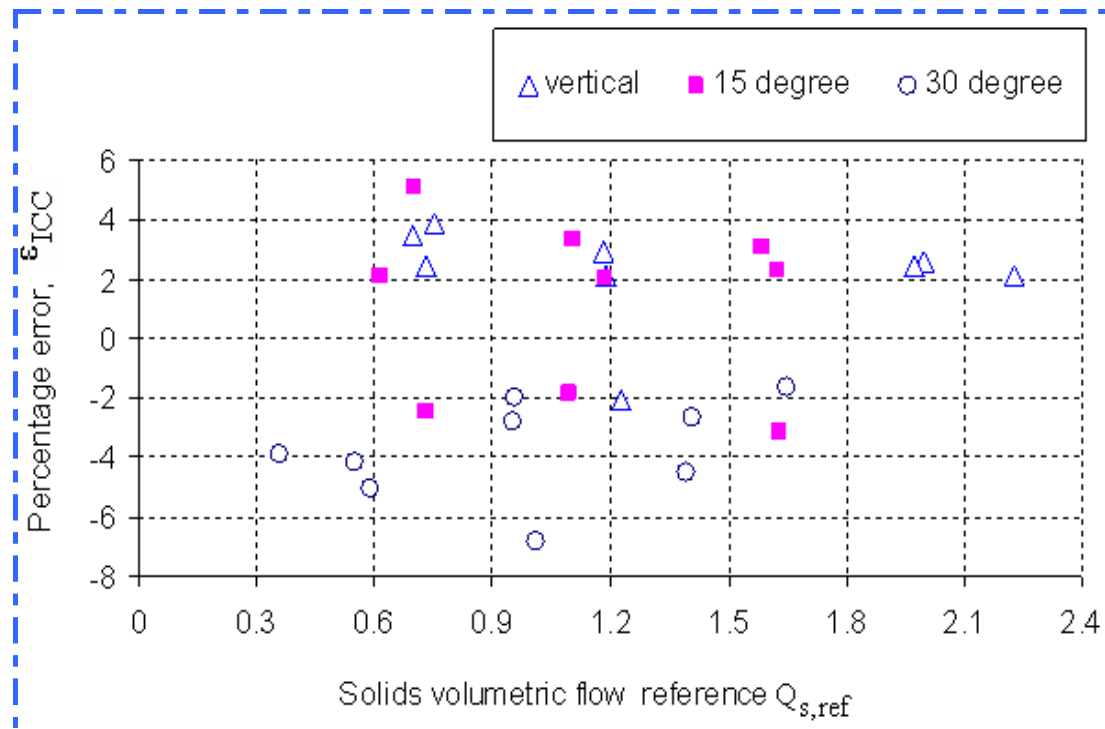
Figure 7-119: Percentage error versus Qs (m^{3}h^{-1}) reference for Config-I for different inclined angles $0^o, 15^o$ and 30° for all flow conditions listed in Table 7-2.

Table 7-13: Integrated solids volumetric flow rate data from the ICC device and reference devices for vertical upward flow for Config-II

Electrodes Configurations	Angle of inclination of test pipe	Solids volumetric flow rate, $Q_{s,ref}$ (m^{3}h^{-1})	Solids volumetric flow rate, $Q_{s,meas}$ (m^{3}h^{-1})	Percentage error ε_{ICC}
Config-II	0°	0.696	0.721	2.85
		0.75	0.774	2.66
		0.73	0.754	2.73
		1.188	1.158	-2.36
		1.225	1.198	-2.05
		1.183	1.153	-2.79
		2.229	2.283	2.28
		1.998	2.062	3.10
		1.974	2.039	3.34
	15°	0.613	0.647	6.03
		0.731	0.716	-1.51
		0.704	0.685	-1.99
		1.187	1.224	2.78

		1.104	1.154	4.16
		1.096	1.144	4.01
		1.587	1.538	-2.97
		1.631	1.675	3.00
		1.623	1.694	4.12
	30º	0.36	0.352	-2.78
		0.591	0.577	-1.87
		0.549	0.538	-1.64
		0.951	0.906	-4.32
		1.01	0.987	-1.99
		0.959	0.941	-1.99
		1.41	1.383	-2.13
		1.651	1.567	-4.91
		1.395	1.368	-1.80
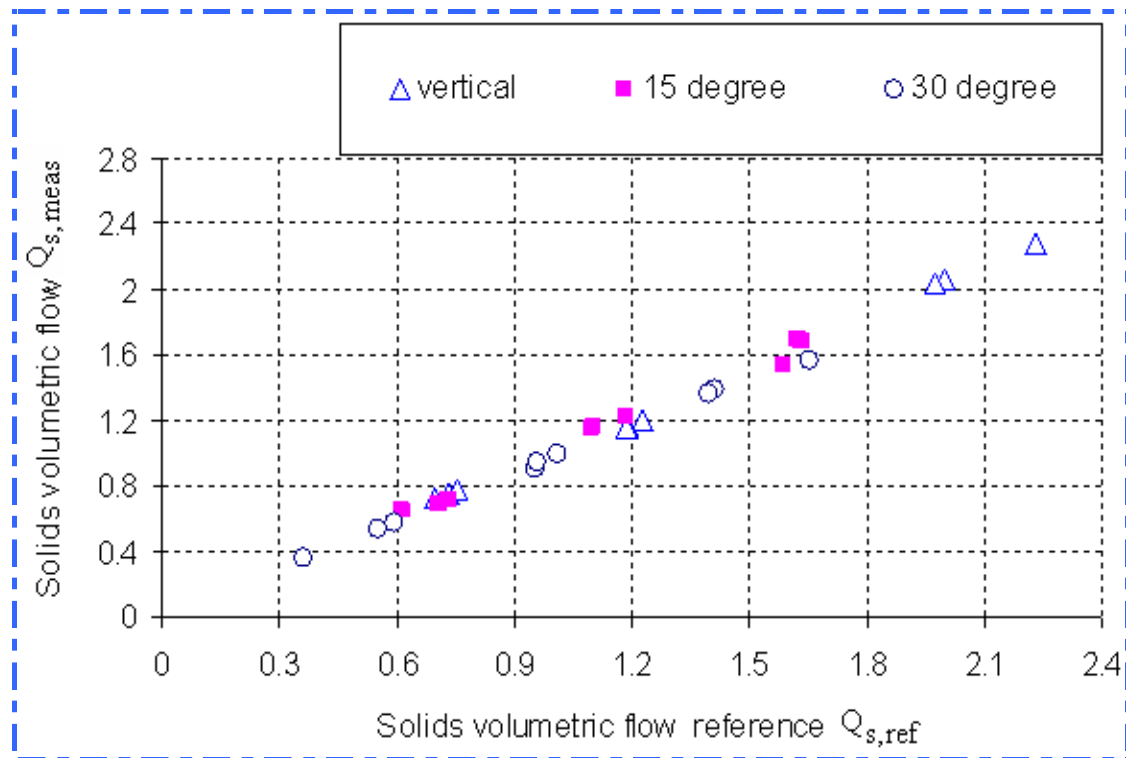
Figure 7-120: The relationship between $Q_{s,ref}$ and $Q_{s,meas}$ for Config-II
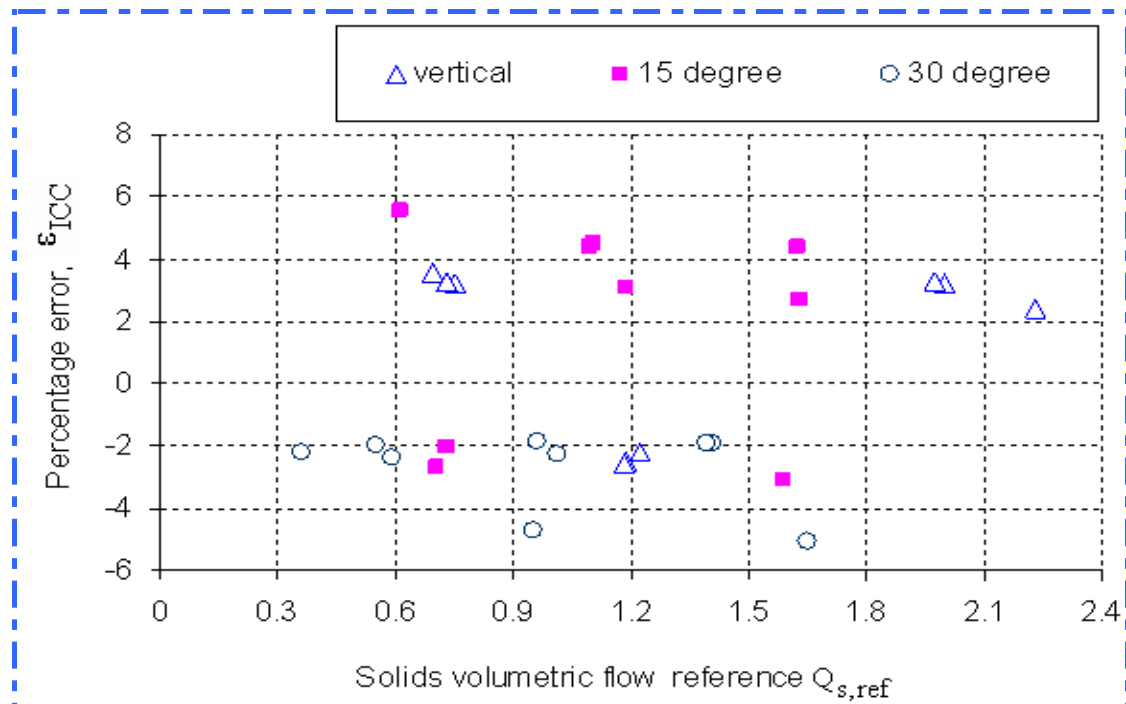
Figure 7-121: Percentage error versus Qs (m^3h^{-1}) reference for Config-II for different inclined angles $0°, 15°$ and $30°$ for all flow conditions listed in Table 7-2.

Table 7-14: Integrated solids volumetric flow rate data from the ICC device and reference devices for vertical upward flow for Config-III

Electrodes Configurations	Angle of inclination of test pipe	Solids volumetric flow rate, $Q_{s,ref}$ (m^3h^{-1})	Solids volumetric flow rate, $Q_{s,meas}$ (m^3h^{-1})	Percentage error ε_{ICC}
Config-III	$0°$	0.696	0.724	2.85
		0.75	0.773	2.66
		0.73	0.709	-2.74
		1.188	1.22	2.52
		1.225	1.185	-3.26
		1.183	1.221	3.38
		2.229	2.276	2.24
		1.998	2.08	4.00
		1.974	1.931	-2.04
	$15°$	0.613	0.573	-6.56
		0.731	0.695	-4.11
		0.704	0.731	4.28

		1.187	1.143	-4.21
		1.104	1.051	-4.55
		1.096	1.051	-4.55
		1.587	1.533	-3.78
		1.631	1.577	-3.07
		1.623	1.737	7.40
	30º	0.36	0.349	-2.78
		0.632	0.656	4.76
		0.549	0.538	-1.82
		0.951	0.928	-2.11
		1.01	1.052	3.96
		0.959	0.928	-3.13
		1.41	1.373	-2.84
		1.651	1.605	-2.43
		1.395	1.467	5.00
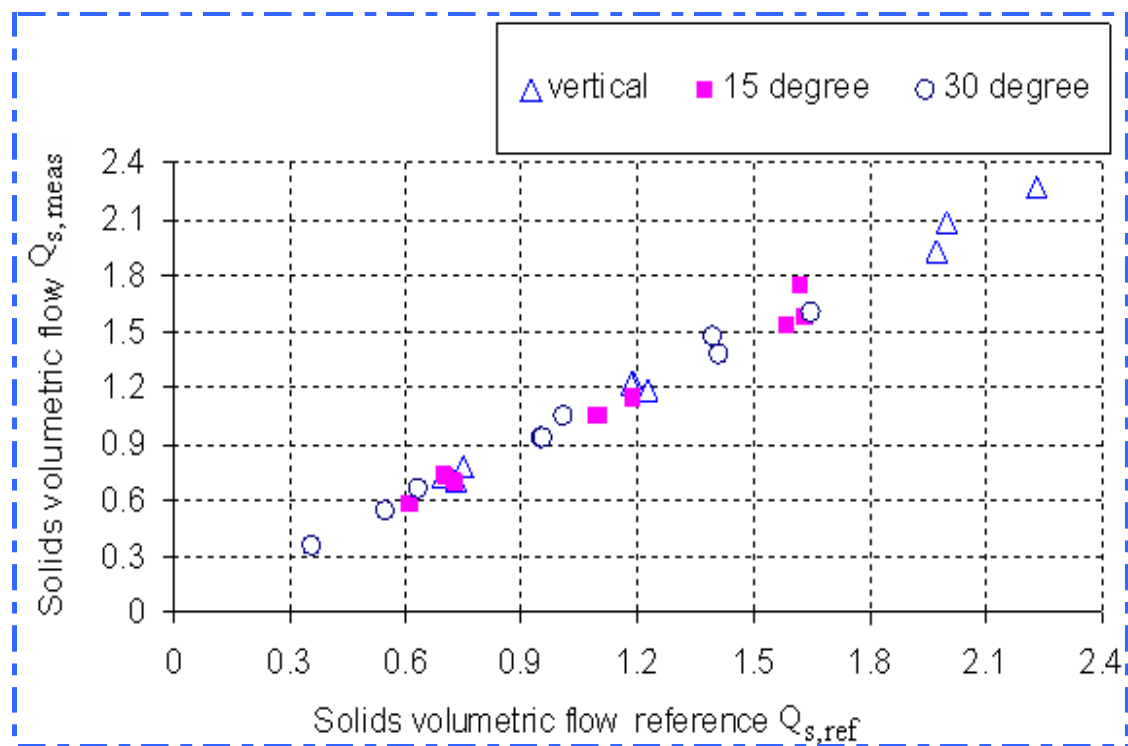
Figure 7-122: The relationship between $Q_{s,ref}$ and $Q_{s,meas}$ for Config-III
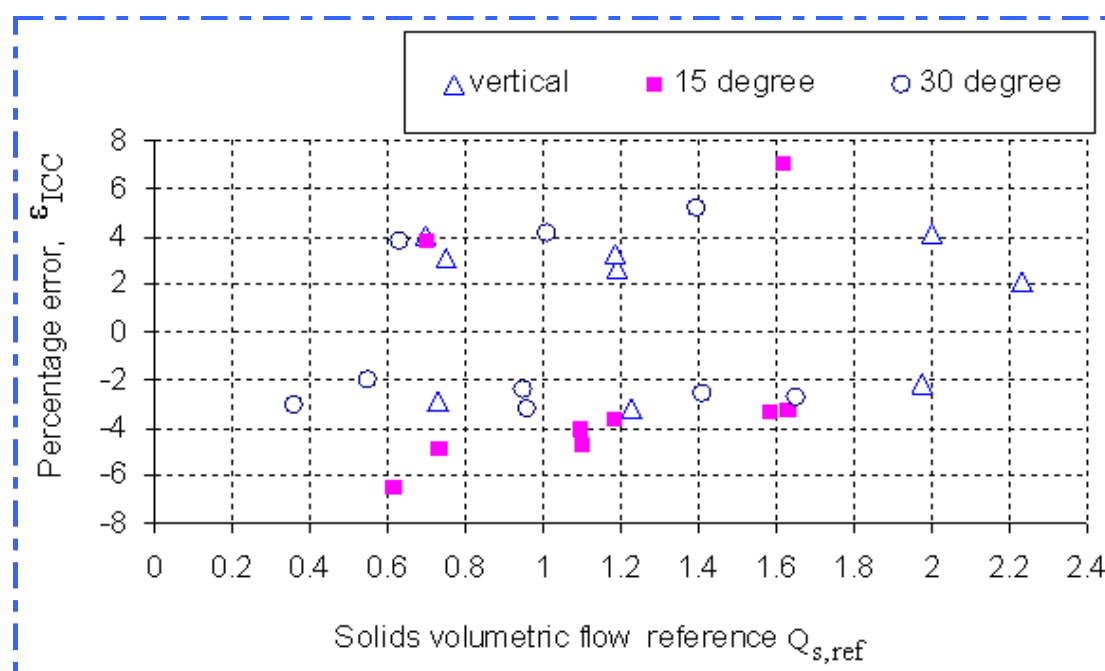
Figure 7-123 : Percentage error versus Q_s (m³h⁻¹) reference for Config-III for different inclined angles $0°, 15°$ and $30°$ for all flow conditions listed in Table 7-2.

7.3.4 Comparison of percentage error with other researchers

This section compares the percentage error between the measurements obtained using the ICC meter and the error obtained by Balasubrammaniam (2008/2009). Balasubrammaniam used an EIT system with a cross-correlation technique to study the mean velocity of oil-water mixtures at five different angles of inclination from the vertical ($0°, 15°, 30°, 45°$ and $60°$). Balasubrammaniam also found the volume fraction distributions for particular flow conditions for different inclination angles and compared the mean oil volume fraction from EIT with the oil volume fraction obtained from reference measurements.

Balasubrammaniam found a large error between the mean oil volume fraction obtained from EIT and by reference measurements particularly when the pipe carrying the oil-water flow was inclined. The mean volume fraction value obtained using the EIT system and the reference values obtained using a dp cell are substantially different. The average percentage, or error in the oil volume fraction measurement using EIT was around 55 %, see Table 7-15 below.

Table 7-15: Volume Fraction Values at Different inclinations obtained by Balasubrammaniam(2008/2009)

θ^0 (angle of inclination to vertical)	Mean volume fraction of oil using EIT, α_{EIT}	Mean volume fraction of oil using DP cell, α_{ref}	% error
0	0.0568	0.1837	-69%
15	0.0517	0.1134	-54%
30	0.0408	0.0978	-58%
45	0.0489	0.0771	-36%
60	0.0858	0.0473	81%

According to Balasubrammaniam the errors in the EIT system were to be expected because of an improper image reconstruction algorithm. This demonstrates a real disadvantage of the EIT, not only is it expensive but even after paying out large sums there can still be substantial errors in the software which are difficult to remedy. Indeed, from the experience of Balasubrammaniam these are not only difficult to remedy but time consuming. On the other hand, as things stand, the ICC meter presented in this thesis had a maximum error (8.9% at angle of inclination 30° see Table 7-8) which was substantially less than the mean error reported by Balasubrammaniam (58%).

Chapter 8   MATHEMATICAL MODEL FOR PREDICTING THE VELOCITY PROFILE IN INCLINED TWO PHASE FLOW

In this Chapter a mathematical model is described which was developed to understand the behaviour of two phase flow in an inclined pipe. In section 8.3 a comprehensive velocity profile model review is presented. This model goes on to describe how the volume fraction data can be used to obtain the velocity profile measurements. The mathematical model can also be used to provide an on-line validation of velocity profile measurements.

8.1   General Concept

To develop a mathematical model for the velocity profile of an inclined two phase flow the important simplifying assumption is that the continuous phase and dispersed phase are well-mixed and have the same local axial velocity i.e there is no **<u>local</u>** slip between the phases. Most research into inclined dispersed phase flows has had a strong experimental bias with little attempt to model the underlying fluid mechanics (see, for example, Vigneaux, et al., 1988). Lucas (1995) developed a mathematical model for dispersed phase flow in an inclined pipe which predicted the velocity distribution from the volume fraction distribution data. According to Lucas the velocity profile in inclined oil-water flows can be obtained from knowledge of the local volume fraction distribution of the flowing components and a measurement of either the axial pressure gradient or of the total flow rate. The author of this thesis has extended Lucas' model and used that model to investigate solids-water flow in inclined pipes.

8.2   Model aim and objectives

Two-phase flow measurement can be achieved by simultaneously using two different devices: a device sensitive to the flow of phase A to measure the velocity of phase A, and a second device to measure the velocity of phase B, see below. One or other or both of these devices is used also to provide the volume fraction of each phase. In a flow consisting of non-conducting solids dispersed in a conducting liquid, (e.g. water) appropriate devices could be a conductivity measurement device, and an electromagnetic flow meter (EFM). The conductivity measurement device could be used to measure solids volume fraction and solids velocity. Meanwhile an electromagnetic flow meter, such as reported by Wang, et al., (2006) could be used to measure the water velocity. Combining the measurements would give full two-phase flow measurement.

However, in order to calculate accurate total volumetric flow rates, accurate values for both the local volume fraction distribution and the axial velocity distribution are required (see Equation 1-3). The former have been successfully obtained using tomography and the ICC flow meter developed by the author of this thesis (see Chapter 7) but relatively few results have been published concerning axial velocity

distribution profile measurements such as the results obtained by the author of this thesis. This chapter describes a model developed for validating the measured solids velocity profiles data using the measured solids volume fraction distribution from experimental work obtaining by the ICC flow meter.

8.3 Predicting the solids velocity profiles from the volume fraction profiles

Velocity profiles measured by cross-correlation between two axially separated planes are becoming increasingly common in multiphase flow systems. At present, because little or no use is made of the constraints imposed by the physics of the flow, high powered computers are required to implement this technique. In the oil industry, it is frequently required to measure volumetric flow rates of different components in liquid-liquid flows in both horizontal and inclined pipes. This thesis will investigate a mathematical model to ascertain if it can be used to predict the velocity profiles obtained using the ICC flow meter, i.e. to validate the measured solids velocity profile data using the measured solids volume fraction distribution.
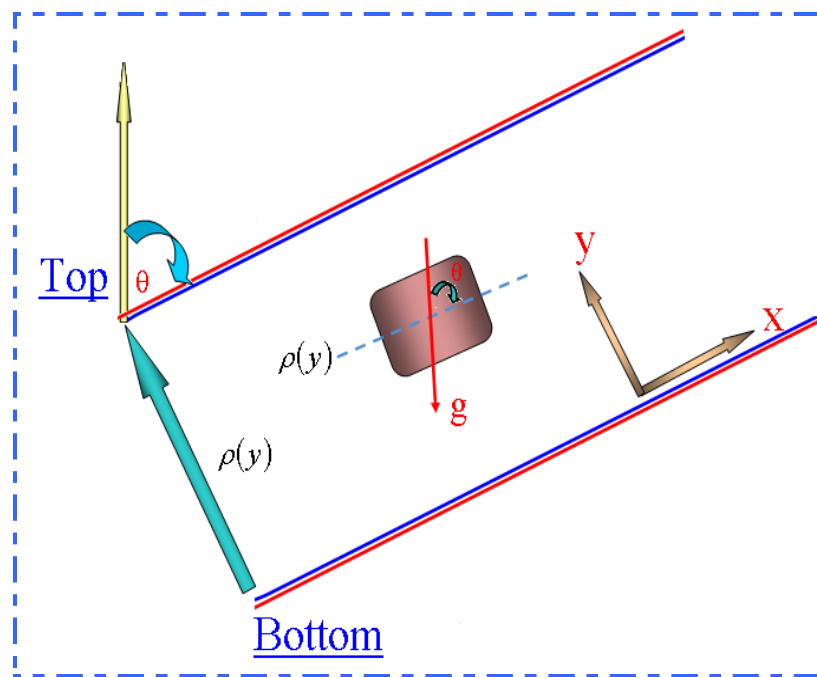
Figure 8-1: Model of flow of molecules in an inclined pipe

8.4 Background

Lucas (1995) has developed a model to predict velocity profiles of oil-water flow in inclined pipes. Figure 8-1 shows a small region of the flow assumed to consist of a

mixture of both flowing components in an inclined pipe. The following assumptions have been made and the experimental data obtained indicated that the resulting model was accurate enough to predict 1-D velocity profiles in oil-water flows.

- ❖ The mean local flow velocity in the x-direction does not vary with time.

- ❖ The mean properties of the flow are steady.

- ❖ The influence of the "two-phase eddy viscosity" (see Lucas, 1995) is much more important than the molecular viscosity of the flow.

- ❖ As this is a 1-D flow model, the flow velocity is determined only by the distance from one wall of the pipe, and the velocity at the walls is assumed be zero.

From Sabersky, et.al., (1989), we may write down the Navier-Stokes equation as:

$$\frac{du}{dt} + u\frac{du}{dx} + v\frac{du}{dy} + w\frac{du}{dz} = -\frac{1}{\rho(y)}\frac{dp}{dx} + \frac{1}{\rho(y)}\frac{d}{dx}\left(\mu\frac{du}{dx} - \rho\,\overline{u'}\right) + \frac{1}{\rho(y)}\frac{d}{dy}\left(\mu\frac{du}{dy} - \rho\,\overline{u'v'}\right)$$

$$+ \frac{1}{\rho(y)}\frac{d}{dz}\left(\mu\frac{du}{dz} - \rho\,\overline{u'w'}\right) - g\cos\theta \qquad\qquad 8\text{-}1$$

where: u is the mixture velocity in x direction, v is the mixture velocity in y direction and w is the mixture velocity in z direction, μ is the laminar viscosity, $\frac{dp}{dx}$ is the axial pressure gradient and $\rho(y)$ is the mixture density which is assumed to vary in the y direction due to stratification of the inclined two phase flow.

For steady flow which is fully developed, the left hand side of Equation (8-1) reduces to zero, and the right hand side of Equation (8-1) can be simplified to give;

$$0 = -\frac{1}{\rho(y)}\frac{dp}{dx} + \frac{1}{\rho(y)}\frac{d}{dy}\left(\mu\frac{du}{dy} - \rho\,\overline{u'v'}\right) - g\cos\theta \qquad\qquad 8\text{-}2$$

Let us now consider the term, $\left(\mu\frac{du}{dy} - \rho\,\overline{u'v'}\right)$ in Equation (8-2). From Sabersky, et al., (1989), we have:

$$-\rho\,\overline{u'v'} = \rho\,\upsilon_T\,\frac{du}{dy}$$

where; υ_T is a kinematic ''eddy viscosity'' term.

We know that in turbulent flows, particularly multiphase turbulent flows that we are attempting to model here, the laminar viscosity terms, $\mu\dfrac{du}{dy}$ is much smaller than the eddy viscosity term (see Lucas, 1995) and may be ignored, and Equation (8-2) can be written;

$$0 = -\frac{1}{\rho(y)}\frac{dp}{dx} + \frac{1}{\rho(y)}\frac{d}{dy}\left(\rho\,\upsilon_T\,\frac{du}{dy}\right) - g\cos\theta \qquad\qquad \text{8-3}$$

Multiplying both sides by $\rho(y)$ gives

$$0 = -\frac{dp}{dx} + \frac{d}{dy}\left(\rho_m\,\upsilon_T\,\frac{du}{dy}\right) - \rho(y)\,g\,\cos\theta \qquad\qquad \text{8-4}$$

Based on the given assumptions, the simplified form of the Navier-Stokes equation can be expressed as follows for a well-mixed two phase flow in an inclined pipe:

$$\rho_m\,\frac{d}{dy}\left\{\upsilon_T\,\frac{du(y)}{dy}\right\} = \frac{dp}{dx} + \rho(y)g\cos\theta \qquad\qquad \text{8-5}$$

where: ρ_m is a weighted mean density of the dispersed phase mixture in the pipe and the term $\rho(y)$ denotes the density of the dispersed phase expressed by:

$$\rho(y) = \rho_d C(y) + \rho_c\,(1 - C(y)) \qquad\qquad \text{8-6}$$

where: C(y) represents the dispersed phase volume fraction in the y direction obtained from the experimental work, that is C(y) is a function of the distance from the wall of the pipe. ρ_d and ρ_c are the dispersed and continuous phases densities respectively.

The weighted mean fluid density, ρ_m, for a circular pipe with cross-sectional area A, is given by (see Lucas, 1995):

$$\rho_m = \frac{1}{A} \int_0^D \left\{ \rho_d C(y) + \rho_c (1 - C(y)) \right\} 2\sqrt{y(D - y)} \qquad \text{8-7}$$

where: D is diameter of the pipe cross-section.

The dispersed phase volume fraction C(y), which can be obtained experimentally, (for example by using the ICC device described in this thesis) is the most significant element in determining the local density of the dispersed phase mixture as well as the two-phase eddy viscosity. Unfortunately, however, the experimental data are usually not enough to cover the entire distance from the upper side to the lower side of the inclined pipe. To overcome this problem a curve fitting technique is introduced. Such an approach simplifies the integration calculation because the expression of the dispersed phase volume fraction is known. In this model, the curve used is a third order polynomial obtained using a MATLAB least squares technique. This fitting method is applied to generate a monotonic curve based on the eight real experimental data points obtained from the ICC device.

To solve the simplified Navier Stokes equation (Equation 8.5), it is first necessary to know the two-phase kinematic eddy viscosity υ_T. Unfortunately no "correct" answer has been found so far to fit the dispersed phase model. Consequently, two expressions of υ_T have been introduced for use in the model. These are (a) a constant; $\upsilon_T = \upsilon_1$, and (b) a linear function of the dispersed phase volume fraction; $\upsilon_T = \upsilon_2 + kC(y)$. Lucas (1995) suggested values for υ_1, υ_2 and k which were successfully used to obtain the velocity profiles for inclined oil-water flows. Lucas also suggested that the values υ_2 and k might be applied to other inclined two phase flows. What is being suggested however is that there is a relatively small range of values which these parameters take for most inclined two phase flows of practical interest.

Case 1 $\upsilon_T = \upsilon_1$

In this case, υ_T is constant, and can be taken outside the bracket in Equation (8-5).
This reduces the simplified form of Navier-Stokes into an ordinary partial differential
equation. The analytical expression of the 1-D velocity profiles can now be obtained.

The procedure for solving the equation is as follows. Integrate both two sides of
equation (8-5) from the bottom to the upper wall of the pipe y =0 to y =D

$$\rho_m \frac{du(y)}{dy} = \left[\frac{1}{\upsilon_T} \frac{dp}{dx} \right] y + \frac{g\cos\theta}{\upsilon_T} \int_0^D \rho(y)\, dy + C_1 \qquad 8\text{-}8$$

where: C_1 is the constant of integration and will be found from the boundary
conditions that the velocity at the pipe wall is zero; that is u(0) = 0 and u(D) = 0.
Integrating Equation (8-8) again gives

$$\rho_m u(y) = C_2 + \frac{C_1(y)}{\upsilon_T} + \left(\frac{dp}{dx} \right) \frac{y^2}{2\, \upsilon_T} + \frac{g\cos\theta}{\upsilon_T} \int_0^D \left[\int_0^{\bar{y}} \rho(y)dy \right] d\bar{y} \qquad 8\text{-}9$$

where: C_2 is a second constant of integration which will also be found from the
boundary conditions u(0) = 0 and u(D) = 0. u(y) is the axial fluid velocity at
coordinate y.
Substituting the boundary conditions into Equation 8-9 gives:

$$C_2 = 0 \qquad 8\text{-}10$$

$$\frac{C_1(y)}{\upsilon_T} + \left(\frac{dp}{dx} \right) \frac{y^2}{2\, \upsilon_T} + \frac{g\cos\theta}{\upsilon_T} \int_0^D \left[\int_0^{\bar{y}} \rho(y)dy \right] d\bar{y} = 0 \qquad 8\text{-}11$$

Substitute the boundary condition into Equation (8-5) and if the axial pressure

gradient $\dfrac{dp}{dx}$ is known, the constants of integration can be found by solving two

equations simultaneously (Equations 8-11 and 8-13). The analytical expression of the
velocity profile can now be solved. However, the usual measured variable is the total

flow rate Q_T rather than the axial pressure gradient $\dfrac{dp}{dx}$, we therefore need to

establish the relationship between Q_T and the integration constants as well as $\dfrac{dp}{dx}$.
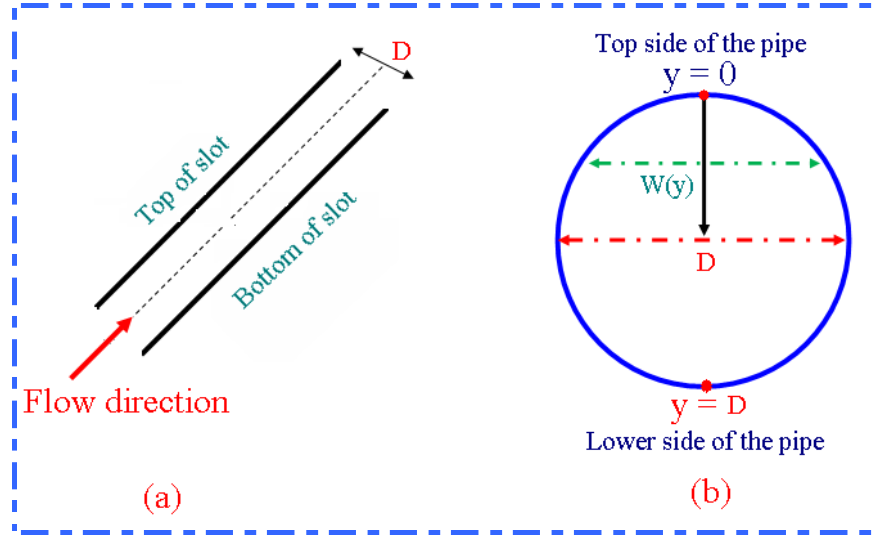
Figure 8-2: (a) Diagram of inclined slot; (b) coordinate system for inclined pipe

The distance $W(y)$ in Figure 8-2 is given by

$$W(y) = 2(y(D - y))^{0.5}$$

The total flow rate through the pipe cross-section is defined as

$$Q_T = \int_0^D u(y)2\sqrt{y(D - y)}dy \qquad\qquad 8\text{-}12$$

Where $u(y)$ the axial fluid velocity is at coordinate y. D is the pipe diameter.

Substituting for $\rho_m u(y)$ from Equation (8-9) and using the value of, $C_2 = 0$ gives:

$$\rho_m Q_T = \int_0^D \left(\frac{C_1 y}{\upsilon_T}\right) 2\sqrt{y(D - y)}dy + \int_0^D \left[\left(\frac{dp}{dx}\right)\frac{y^2}{2\upsilon_T}\right] 2\sqrt{y(D - y)}dy$$

$$+ \frac{g\cos\theta}{\upsilon_T} \int_0^D \left[\int_0^y \left[\int_0^{\bar{y}} \rho(y)dy\right]d\bar{y}\right] 2\sqrt{y(D - y)}dy \qquad\qquad 8\text{-}13$$

Solving Equations (8-11) and (8-13) together, allows the axial pressure gradient $\dfrac{dp}{dx}$ and the constant of integration to be found. Substituting those parameters back into Equation (8-9), the analytical solution of velocity profile can be obtained.

Case 2 $\qquad\qquad v_T = v_2 + kC(y)$

Generally speaking, if the two-phase kinematic eddy viscosity v_T is considered as a constant, then the consequent output from the 1-D model may not predict the mixture velocity profile accurately. Consequently an alternative expression was introduced whereby v_T is a linear function of the dispersed phase volume fraction.

$$v_T = v_2 + kC(y) \qquad\qquad 8\text{-}14$$

Where v_2 and k are constants, and C(y) represents the dispersed phase volume fraction. By simply re-arranging Equation 8-5 we obtain:

$$\rho_m\left\{\frac{dv_T}{dy}\frac{du(y)}{dy} + v_T\frac{d^2u(y)}{dy^2}\right\} = \frac{dp}{dx} + \rho(y)g\cos\theta \qquad\qquad 8\text{-}15$$

Further re-arranging gives:

$$\rho_m v_T\frac{d^2u(y)}{dy^2} = \frac{dp}{dx} + \rho(y)g\cos\theta - \rho_m\frac{dv_T}{dy}\frac{du(y)}{dy} \qquad\qquad 8\text{-}16$$

Dividing both sides of equation 8-16 by $\rho_m v_T$:

$$\frac{d^2u(y)}{dy^2} = \frac{1}{v_T}\frac{1}{\rho_m}\left(\frac{dP}{dx}\right) + \frac{1}{v_T}\frac{1}{\rho_m}\rho(y)\,g\cos\theta - \frac{1}{v_T}\frac{dv_T}{dy}\frac{du(y)}{dy} \qquad\qquad 8\text{-}17$$

8.5 Comparison of MATLAB model predictions with those of Lucas

In the first part of this section the results obtained from the MATLAB model, as represented by Equations 8.1 to 8.17, are compared with the results obtained by Lucas (1995) where the continuous phase was water and the dispersed phase was oil. It is now possible to predict the velocity profile of multiphase flow in an inclined tube using MATLAB to solve the differential Equations 8-9, 8-12 and 8-17.

The first task was to produce a MATLAB code for the solution of these equations (see the code in Appendix-Code8-9). The predictions of this MATLAB model were then compared to the results of Lucas. It was thus necessary to have the same flow conditions as Lucas, and the relevant parameters are listed in Table 8-1.

Table 8-1: Flow condition parameters

Diameter of the pipe	D=200mm
Density of the oil	$\rho_{oil} = 0.78 \times 10^3 \, kg/m^3$
Density of the water	$\rho_{water} = 1.00 \times 10^3 \, kg/m^3$
Inclination of tube to the vertical	$\theta = 25°$
Total flow rate	$Q_T = 26.5 m^3 h^{-1}$

Two expressions of the two-phase eddy viscosity have been used in the model:

(a) $\upsilon_T = \upsilon_1$ and (b) $\upsilon_T = \upsilon_2 + kC(y)$.

Case 1 $\upsilon_T = \upsilon_1$

First a curve fitting technique is applied to obtain an expression for the measured water volume fraction data obtained from Lucas' work and given in Table 8-2.

Table 8-2: Volume fraction data from Lucas (1995)

y	0.00	0.02	0.04	0.06	0.08	0.10	0.12	0.14	0.16	0.18	0.20
C(y)	0.30	0.35	0.375	0.40	0.425	0.45	0.50	0.55	0.58	0.67	0.813

Using a least squares fit, the 3rd order polynomial expression for the water volume fraction data is:

$$C(y) = 108y^3 - 23y^2 + 2.7y + 0.30 \qquad\qquad 8\text{-}17$$

The local fluid density is expressed as:

$$\rho(y) = \rho_{water}C(y) + \rho_{oil}(1 - C(y))$$

$$\rho(y) = (\rho_{water} - \rho_{oil})C(y) + \rho_{oil}$$

$$\rho(y) = 23y^3 - 4.8y^2 + 0.57y + 0.85 \qquad \text{8-18}$$

The weighted mean fluid density of the inclined tube with a circular cross-sectional area A, can be found from:

$$\rho_m = \frac{1}{A}\int_0^D \left\{\rho_{water}\,C(y) + \rho_{oil}\,(1-C(y))\right\}2\sqrt{y(D-y)}dy$$

$$= 0.89 \text{ kg/m}^3$$

In order to obtain the axial pressure gradient, $\dfrac{dp}{dx}$, and the integration constant, Equations (8-9), (8-10) and (8-12) are solved simultaneously using the MATLAB function *Solve*:-

$$C_1 = 0.013$$

$$\frac{dp}{dx} = -7.92 \qquad \text{8-19}$$

Substituting these values into Equation (8-9) and the expression obtained for the velocity gives:

$$u(y) = 13y - 4000y^2 + 9100\left(1.1y^5 - 0.40y^4 + 0.095y^3 + 0.43y^2\right) \qquad \text{8-20}$$

Case 2 $\qquad \upsilon_T = \upsilon_2 + kC(y)$

When considering two-phase eddy viscosity as a first order equation in terms of water volume concentration, the resulting form of the Navier-Stokes equation is much more complicated than when considering the two-phase eddy viscosity as constant.

In MATLAB the function used to solve two-point boundary value problems for ordinary differential equations is called 'bvp4c'. This integrates a system of first order ordinary differential equations on the interval [a, b] subject to general two-point boundary conditions. 'bvp4c' is a finite difference code that implements the 3-stage Lobatto formula (www.matlab.com, accessed on 05/07/09).

The collocation technique uses a mesh of points to divide the interval of integration into sub-intervals. The solver determines a numerical solution by solving a global system of algebraic equations resulting from the boundary conditions, and the collocation conditions are imposed on all the sub-intervals. The solver then estimates the error of the numerical solution on each sub-interval. If the solution does not satisfy the tolerance criteria, the solver adapts the mesh and repeats the process. The user must provide the points of the initial mesh as well as an initial approximation of the solution at the mesh points.

The numerical output of Equation (8-14) will change when different values of υ_2 and k are input, and will produce different velocity profiles. Compared with the first case in which only one parameter could be changed, we have more choices to adjust the simulation result. The experimental data below also shows it would be more suitable for the solid-water velocity profiles prediction in the inclined pipe, while the two-phase eddy viscosity is considered as a function of the solid volume fraction.

A comparison has been produced of the velocity profiles obtained by Lucas (1995) and the predictions of the author's MATLAB model. It can be seen, Figures 8-3 and 8-5, that a trend similar to Lucas's results are obtained (see Figures 8-4 and 8-6).
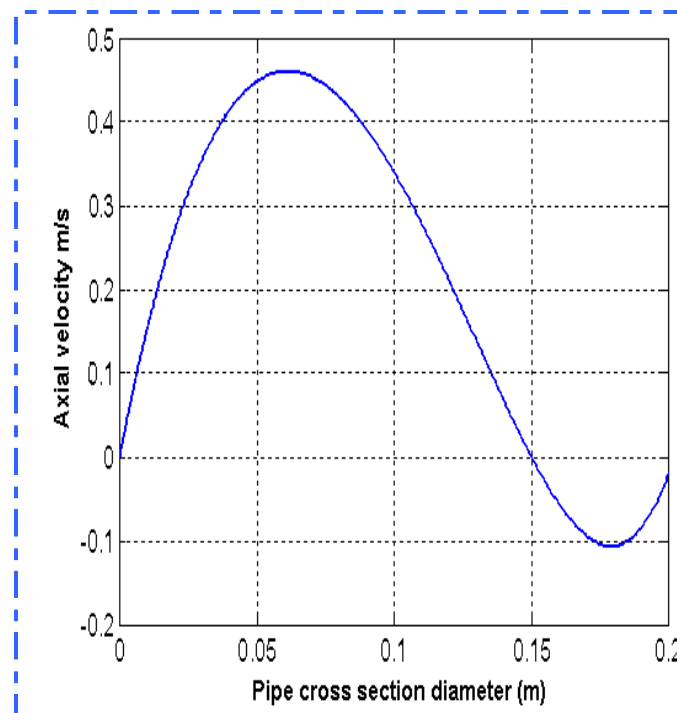
Figure 8-3: Predicted velocity profiles for the two phase oil water flow using MATLAB model devloped in this project. υ_T = constant, (υ_T = 0.0011m^{2}s^{-1})
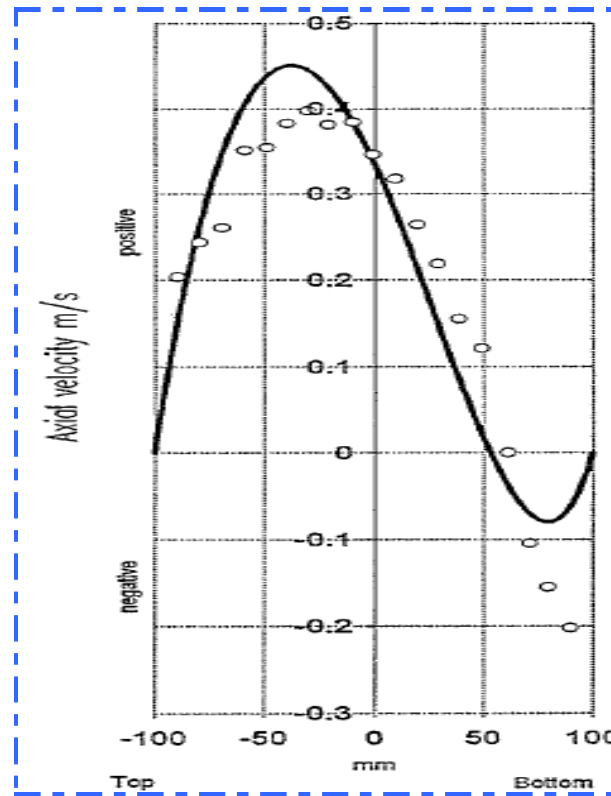
(b)

Figure 8-4: Predicted and measured velocity profiles for the two phase oil water flow results from Lucas model (1995) υ_T = constant, ($\upsilon_T = 0.0011\text{m}^2\text{s}^{-1}$)
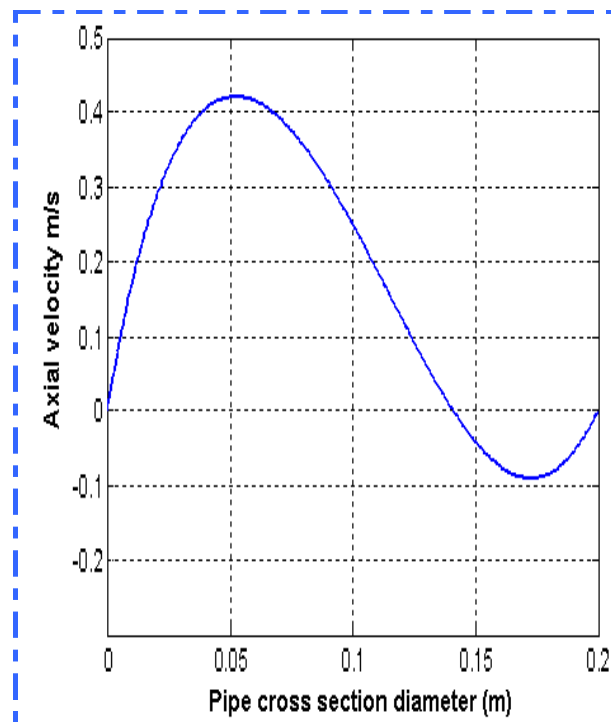
Figure 8-5:Predicted velocity profiles for the two phase oil water flow using MATLAB model devloped in this project. $\upsilon_T = \upsilon_2 + kC(y)$, ($\upsilon_2 = 0.00005\text{m}^2\text{s}^{-1}$, $k = 0.0023\text{m}^2\text{s}^{-1}$)
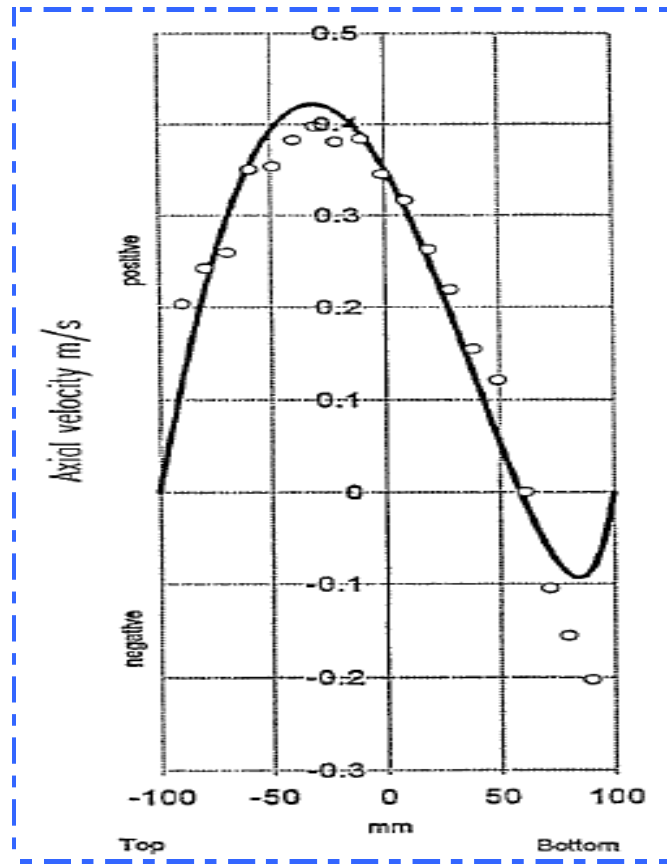
(b)

Figure 8-6: Predicted and measured velocity profiles for the two phase oil water flow results from Lucas model (1995) $\upsilon_T = \upsilon_2 + kC(y)$, ($\upsilon_2 = 0.00005 \text{m}^2\text{s}^{-1}$, $k = 0.0023 \text{m}^2\text{s}^{-1}$)

8.6 Velocity profile prediction of solid-water flow in inclined pipe

In this section, the model is extended to predict the velocity profile of solids-water flows in an inclined pipe, based on the flow model and the method of solving the differential equation already mentioned in Sections 8.3.1 and 8.4. In this section the dispraise phase is solids and the continuous phase is water. It is assumed that the solids and water will mix and travel with the same axial velocity. The relevant flow parameters are shown in Table 8-3; Flow condition 22 was used, see Table 7.2, $Q_{s,ref} = 0.95 \text{m}^3\text{h}^{-1}$, $Q_{w,ref} = 12.47 \text{ m}^3\text{h}^{-1}$ and angle of inclination 30°.

Table 8-3: Solids water flow condition parameters

Diameter of the pipe	D=80mm
Inclination of the pipe to the vertical	$\theta = 30°$
Density of the solid	$\rho_{solid} = 1.34 \times 10^3 \, \text{kg/m}^3$
Reference solids volume velocity $Q_{s,ref}$	$0.95 \text{m}^3 \text{h}^{-1}$
Density of the water	$\rho_{water} = 1.00 \times 10^3 \, \text{kg/m}^3$
Reference water volume velocity $Q_{w,ref}$	$12.47 \, \text{m}^3 \text{h}^{-1}$
Total flow rate	$Q_T = 13.42 \, \text{m}^3 \text{h}^{-1}$

The local solids-volume fraction measurements are for Config-I. As mentioned above, a curve fitting method was used to describe the relationship. Figure 8-5 also shows the local solids volume fraction distribution obtained from the experimental test flow condition-22. It can be seen from Figure 8-7 that for Config-I the solids volume fraction decreases with distance from the lower side of the inclined pipe.
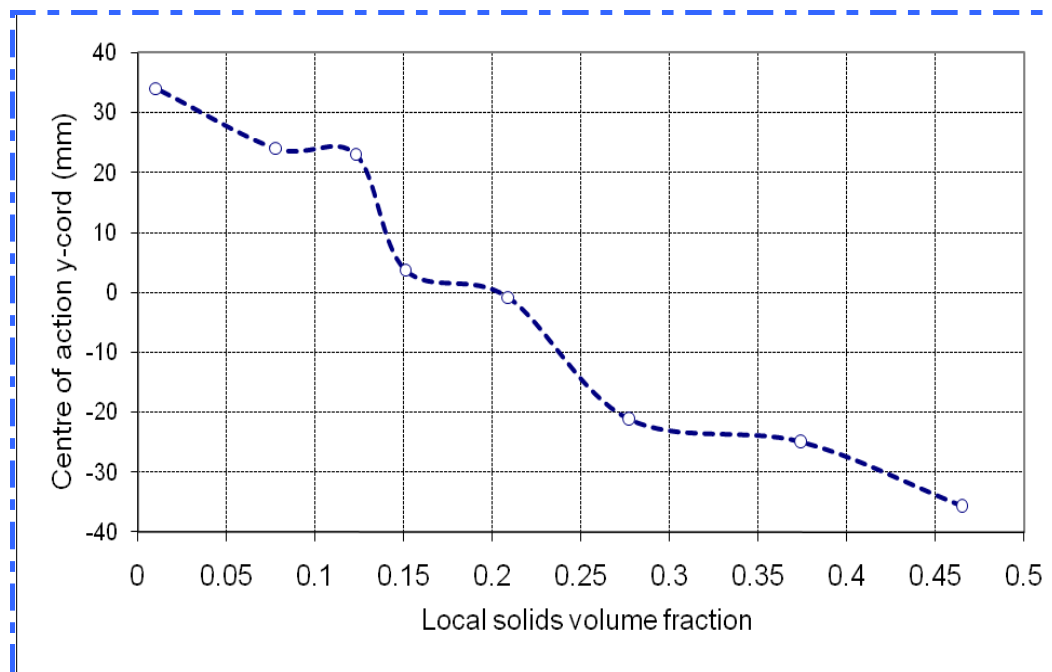
Figure 8-7: Measured local solids volume fraction profiles using Config-I for pipe inclined at 30° to the vertical, flow condition 22 ($Q_{s,ref}$ =0.95 m^{3}h^{-1}, $Q_{w,ref}$ = 12.47 m^{3}h^{-1})

For consistency the y-coordinate of the bottom of the pipe is set to zero and the top is set to 80mm. The best fit expression for the solid volume fraction in terms of the y-coordinate is:

$$C(y) = 829y^3 - 65.6y^2 + 6.43y + 0.0041 \qquad\qquad 8\text{-}21$$

Thus the local fluid density for the solids-water mixture in can be expressed as:

$$\rho(y) = \rho_{solid}C(y) + \rho_{water}(1 - C(y))$$
$$\rho(y) = 278.y^3 - 22.3y^2 + 2.19y + 1.00 \qquad\qquad 8\text{-}22$$

The weighted mean fluid density of the inclined pipe is:

$$\rho_m = \frac{1}{A}\int_0^D \left\{\rho_{solid}\, C(y) + \rho_{water}\,(1 - C(y))\right\} 2\sqrt{y\,(D - y)}\,dy$$

$$= 1.07 \text{ kg/m}^3$$

where: A represent the cross-sectional area of the pipe.

As discussed above the approach to solving the simplified Navier-Stokes equation is determined by the expression representing the two-phase eddy viscosity, υ_T. Once again υ_T was initially considered constant and Figure 8-8 show the simulation velocity profiles with $\upsilon_T = 0.00011$ m^{2}s^{-1}. The range of values of υ_T used to predict the velocity profile changes were found by trial and error. When $\upsilon_T = 0.00011$, the predicted velocity best matches the experimental data. Once υ_T exceeds about 0.00017, the negative velocity at the lower side of the inclined pipe is no longer predicted, which differs significantly from the observed results.
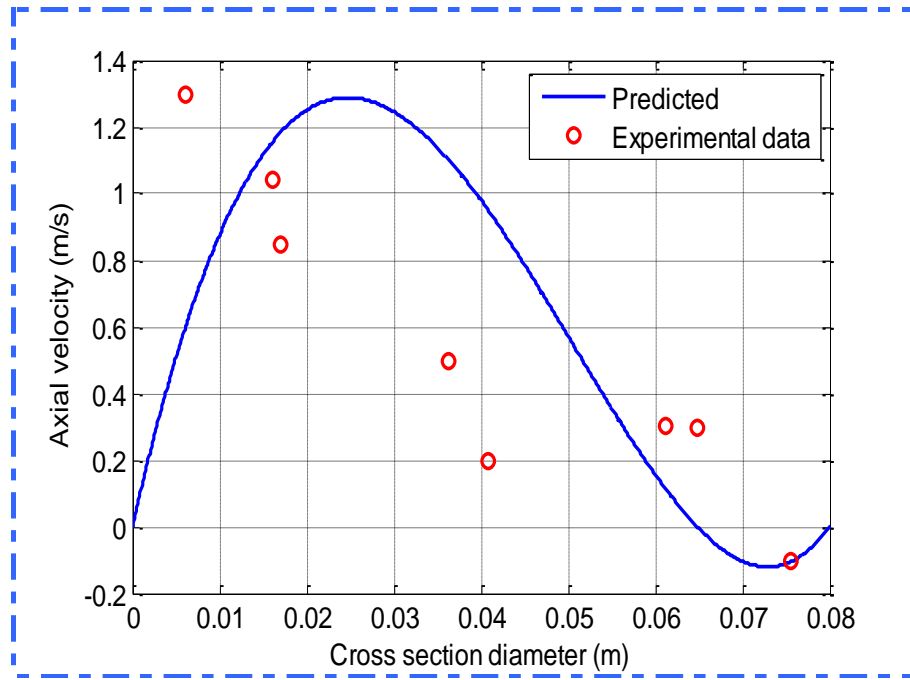
Figure 8-8: A comparison of predicted (-) and measured data (o) using Config-I for two-phase eddy viscosity υ_T =0.00011 m^{2}s^{-1} for pipe inclined at 30° to the vertical, and flow condition 22 ($Q_{s,ref}$ = 0.95m^{3}h^{-1}, $Q_{w,ref}$ = 12.47 m^{3}h^{-1})

For the second case being considered, $\upsilon_T = \upsilon_2 + kC(y)$. The parameters υ_2 and k both affect the shape of the simulated curve. A numerical approach is applied to solve the Navier-Stokes equation with the boundary conditions of zero velocity at the bottom and top of the inclined pipe.

Figure 8-9 shows the simulation results when υ_T = 5x10^{-6} + 9x10^{-4} C(y) and it can be seen that the simulation results are generally close to the experimental velocity data obtained from the ICC using Config-I (flow condition 22 see Table 7-2).
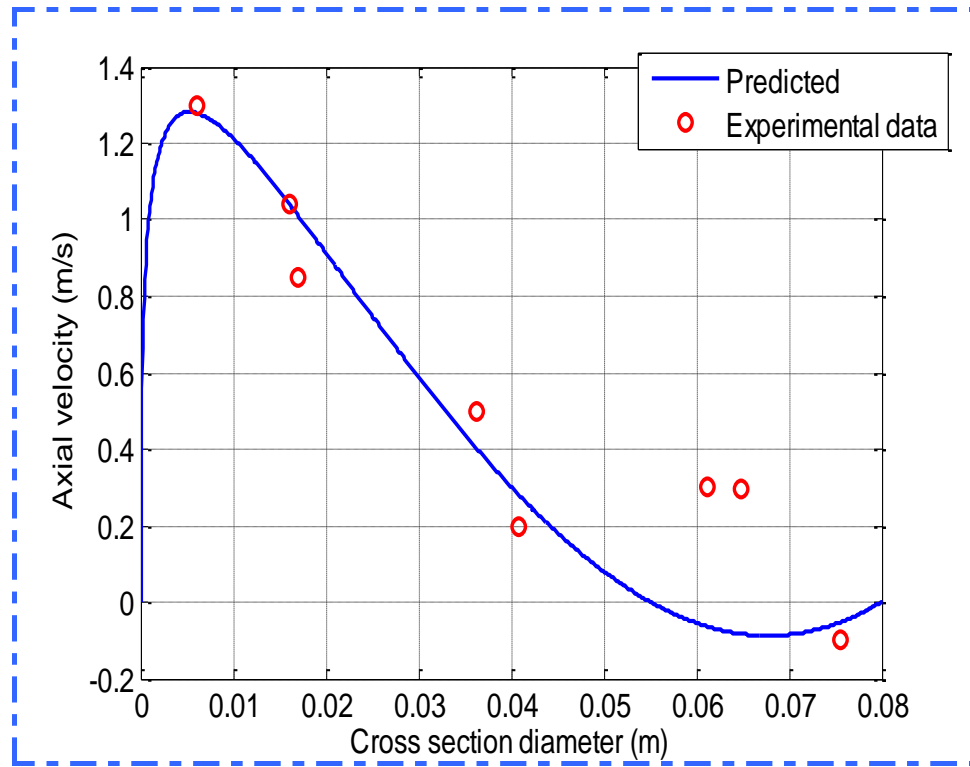
Figure 8-9: A comparison of predicted (-) and experimental data (o) using Config-I for $\upsilon_T = 5\text{x}10^{-6} + 9\text{x}10^{-4}\,C(y)$, for pipe inclined at 30° to the vertical, and flow condition 22 ($Q_{s,ref} = 0.95\text{m}^3\text{h}^{-1}$, $Q_{w,ref} = 12.47\,\text{m}^3\text{h}^{-1}$)

From the comparison between the simulation results and experimental data, it can be concluded that when υ_T is considered as a function of the solid volume fraction, ($\upsilon_T = \upsilon_2 + kC(y)$), the predicted values of the 1-D solid-water velocity profiles in the inclined pipe more accurately represent the measured data than when υ_T is viewed as a constant. Strictly these curves and the values of υ_T and k used cannot be compared to those of Lucas because the curves are for solids liquids while those of Lucas are for liquids-liquids. Also the values of υ_T and k used here were obtained by trial and error to give the best fit.

The results shown in Figure 8-9 are considered to agree with iteration the predicted local axial solids velocity profiles for the solids volume fraction distribution in an inclined pipe. In the author's opinion, the causes of the differences between the output from the model and the experiments include:

❖ The initial simplifying assumptions might mean that some parameters which

have an effect on the measured results are ignored; for example molecular viscosity and forces that might exist between particles.

❖ The assumption of zero fluid of velocity at the wall is key, but solids maybe in contact with wall and be moving.

❖ The precision of the numerical approach may not predict accurately enough. Alternative numerical methods need to be found to check these results and to solve the equations.

❖ The expression of the two-phase eddy viscosity needs to be refined. The expression used for υ_T greatly influences the simulation results and other, better representations of the distribution of the two-phase eddy viscosity would lead to better predicted values.

Chapter 9   CONCLUSIONS AND FUTURE WORK

This chapter contains the main conclusions of the research. It starts by stating the main findings of the current study. Then a summary of the contribution to knowledge made by this research is provided. Finally, the author makes recommendations for future work.

9.1   Conclusions

This section describes how well this research project has met its original aims and objectives, and the new contributions to knowledge that it has made. The major achievements of this research are explained and linked with the original aims and objectives set out in Section 1.5.

A major aim of this thesis was to design a novel non-intrusive Impedance Cross-correlation (ICC) flow meter which is able to accurately measure the mean solids volume fraction, the mean solids velocity and the solids volumetric flow rate in inclined solids in water flows where the local solids volume fraction and velocity distributions are highly non-uniform. This aim has been met with the design, development and successful testing of a non-intrusive ICC flow meter consisting of two electrode arrays separated by an axial distance of 50mm. For this ICC flow meter, the mean percentage errors (for all flow conditions investigated) for the mean solids velocity, the mean solids volume fraction and the solids volumetric flow rate are shown in Tables 9-1, 9-2 and 9-3 respectively.

Table 9-1: The mean percentage errors for the mean solids velocity at different angles of inclination and electrode configurations

	Angle of inclination		
Config	0°	15°	30°
I (Table 7.3)	3.2	2.2	-2.7
II (Table 7.4)	2.8	3.8	3.5
III(Table 7.5)	3.5	4.5	3.6

Table 9-2: The mean percentage errors for the mean solids volume fraction at different angles of inclination and electrode configurations

	Angle of inclination		
Config	0°	15°	30°
I (Table 7.6)	2.9	2.6	1.9
II (Table 7.7)	3.6	1.3	1.9
III (Table 7.8)	0.6	1.6	1.1

Table 9-3: The mean percentage errors for the solids volumetric flow rate at different angles of inclination and electrode configurations

	Angle of inclination		
Config-	0°	15°	30°
I (Table 7-12)	2.2	1.4	-3.7
II (Table 7-13)	1.1	2.0	-2.6
III (Table 7-14)	1.1	-2.1	-0.2

This compares very favourably with quoted errors of up to plus or minus 10% for these measurements using multiphase flow meters which are currently commercially available (Al-Yarubi, 2010). The non-intrusive ICC flow meter has also shown itself capable of measuring the local solids volume fraction (α_S) and the local solids axial velocity (u_S) distributions with good accuracy in vertical and inclined solids-liquid flows.

The electronic measurement hardware of the ICC includes a working conductance circuit (see Section3.6) with two electrode selection circuits for arrays A and B (see Section 3.9) and a data acquisition system and software (see Section 3.8). The author developed software code in MATLAB to select the desired electrode configuration and included LED circuits to check the continuity of the selected electrode circuits and to make sure that the signal going to each electrode was the required signal (as selected from the MATLAB/LABJACK control system). The LEDs gave a visual indication of which electrodes were excited, which electrodes were the measurement electrodes and which electrodes were connected to ground. Cross-talk between the two sensor arrays was eliminated by energizing array A when array B was de-energized, and vice-versa as described in Section 3.6.

A successful 2D COMSOL computational model of the ICC flow meter was achieved to investigate which electrode configurations interrogated deepest into the flow cross-section. The model was a great help in terms of providing comparison data for the bench test results. The model was used to calculate the sensitivity distribution for different electrode configurations (Configs-I, II and III) and to find electrode configurations which can best cover the cross-section of the pipe. For each of the three electrode configuration the 10%, 'effective sensing region' was calculated and a

'Centre of Action' (CoA) for each sensing region was found. The importance of the CoA was that it provided a spatial location for the local volume fraction measurement and the local velocity measurement associated with each rotational position of a particular electrode configuration. The CoA was found for each of the eight different rotational positions for a given electrode configuration using Equations 4-6 and 4-7. The differences in position of the CoA between Configs-I, II and III are due to each of the configurations interrogating different parts of the cross-sectional area of the test pipe.

Config-I one electrode is excitation electrode (V^+), and its adjacent electrode is the measurement electrode (V_e). The other six electrodes are earthed (E). For example, in rotational position-1, the electrode 1 is an excitation electrode (V^+) and electrode 2 is the measurement electrode (V_e), and electrodes 3,4,5,6,7 and 8 are connected to ground (E). Seven similar arrangements are possible by simply rotation of the first arrangement, as can be seen from Table 4-2. For Config-I the CoA is about 6mm from the pipe wall, see Figure 4-15.

Config-II, one electrode is an excitation electrode (V^+), and both adjacent electrodes are measurement electrodes (V_e). The other five electrodes are earthed (E). For example, in rotational position-1, electrode 1 is an excitation electrode, electrodes 8 and 2 are the measurement electrodes and the other five electrodes are connected to ground. Again, seven similar arrangements are possible by simply rotation of the first arrangement, as can be seen from Table 4-3. For Config-II the CoA is about 12mm from the pipe wall.

Config-III, two adjacent electrodes are the excitation electrodes (V^+), the immediately adjacent electrodes are the measurement electrodes (V_e). The other four electrodes are earthed (E). For example, in rotational position-1 electrodes 1 and 2 are the excitation electrodes, electrodes 3 and 8 are the measurement electrodes and the other four electrodes are connected to the earth (E). Once again, seven similar rotational positions are possible by simply rotation of the first arrangement, as can be seen from Table 4-4. For Config-III the CoA is about 22mm from the pipe wall.

A series of static bench tests were performed in order to investigate spatial variations in the sensitivity of the electric 'sensing' field for different electrode configurations

(Configs-I, II and III) and to help determine the regions of flow being interrogated. The tests were carried out and the results showed that the area of the flow cross-section interrogated by the ICC device is highly dependent upon the electrode configuration and that it is possible to have some configurations which interrogate specific localized regions of the flow whilst other configurations interrogate the entire flow cross-section. The spatial resolution of the solids mapping will be the same order of size as the 'effective sensing region' for a given electrode configuration as shown in Figure 5-4(a).

Sensitivity distributions were obtained for the initial electrode configurations Configs-I, II and III (see Tables 4-2, 4-3 and 4-4). From the sensitivity distribution results obtained it is clear that sensitivity is highest near the V^+ electrode(s), lower near the measurement electrode(s) and lowest near the earth electrode(s). The results obtained show that the sensing regions for the three electrode configurations Configs-I, II and III are different.

The static bench test results were compared with the predictions of the COMSOL model (see Section 5.6). The mean relative percentage differences for Configs-I, II and III between the experimental bench tests and the corresponding COMSOL models were 1.21%, 1.24% and 1.65%, respectively (see Figures 5-13 and 5-14) which gave confidence that the device was working as it should.

The ICC meter was successfully installed in the Huddersfield University multiphase flow test rig and experiments were performed at three inclinations of the test pipe (0°, 15° and 30° to the vertical). For the vertical solids in water flows the local solids velocities obtained from the ICC show the well-known flat profile over the cross-section of the pipe for Config-ψ (see discussion below). As expected there was not much difference between the results obtained for Configs-I, II or III (see Chapter 7) for the vertical flow. The local solids velocity profiles were plotted in 3D graphic. The results for Configs-I, II and III showed a drop in velocity in the middle of the cross section pipe (see Figures 7-30 to 7-38) which was entirely due to way in which the results were plotted, with insufficient measurement data at the centre of the cross-section. To overcome this problem, Config-ψ was defined (see below and Section 7.2.1) which gave flat local solids velocity profiles which were nearly identical to

those found by previous researchers such as Lucas et al., (1999, 2000) and Cory (1999), using intrusive local conductance probes, see Sections 7.2.5. [Note that Config-ψ was simply used to determine the local solids velocity and local solids volume fraction at twenty four spatial location corresponding to the CoA of the eight rotational positions for each of Configs-I,II and III in order to overcome the problem of insufficient measurement data in the flow cross-section].

For inclined pipes where the flows are non-symmetrical and the solids velocity varies rapidly with spatial locations in the pipe, the results were expected to show consistent differences for Configs-I, II and III (see Figure7-12 to 7-29). For the inclined solids-water flows when the pipe was inclined at 15° and 30° from vertical, the local axial solids velocity is highest on the upper side of the inclined pipe and lowest at the lower side of the pipe for both angles of inclination. This agreed with visual observation of the flow through the transparent pipe forming the working section of the flow loop. However, on the lower side of the inclined pipe in some flow conditions there was a negative local axial solids velocity, see Figure 7-12 and Figures 7-21, 7-22, 7-24 and 7-25. Under the given conditions, the solids particles were actually flowing backwards down the pipe and this agreed with visual observation.

The accuracy of the local solids velocities obtained using the ICC meter at a given flow condition were investigated by calculating the mean solids velocity $\overline{u}_{s,meas}$ using integration and comparing the result with a reference measurement $\overline{u}_{s,ref}$ of this parameter (obtained from Equation 6-28). No statistically significant differences could be detected between the mean errors in $\overline{u}_{s,meas}$ for any of the electrode configurations (see Table 9-2).

For vertical solids in water flow the local axial solids volume fraction obtained from the ICC shows a flat profile over the cross-section of the pipe for Config-ψ. There were not many differences in the results obtained for Config-I, II and III (see Figures 7-55 to 7-63) for the vertical flow as the solids volume fraction profile would be expected to be uniform. The local solids volume fractions were plotted in 3D graphic. Figures 7-82 to 7-90 show a drop towards the middle of the pipe, this is due to the manner of plotting the results as described above. As mentioned earlier, to overcome

this problem, Config-ψ was defined. It gave flat local solids velocity profiles in the cross section area of the pipe which agrees with results from Lucas et al., (1999, 2000) and Cory (1999).

For the solids-water flows when the pipe was inclined at 15° and 30° from vertical, the distribution of the local solids volume fraction is non uniform, see Figures 7-91 to 7-105. Gravitational effects mean that for the solids, which are more dense than the liquid, the mean density of the solids-water mixture is higher on the lower side of the inclined pipe. Of course, the more horizontal the test pipe the greater this effect, and at the lowest layers the solids can become 'close packed'. Similar volume fraction profiles to those reported for inclined flows in this thesis have been observed by Lucas et al., (1999, 2000) and Tabeling et al., (1991) for the water volume fraction in oil-water flows in inclined pipes.

For the upward vertical flows investigated, the local solids volume fraction and local axial velocity distributions were axi-symmetric. As the angle of inclination angle of the pipe away from the vertical was increased, the solids tended to migrate towards the lower side of the inclined pipe, but symmetry about the y-axis was maintained. The lower density of the solids-liquid mixture at the upper side of the inclined pipe gave rise to relatively high axial velocities in this part of the flow cross-section.

Measured values of the mean solids volume fraction obtained by integrating the ICC local volume fraction data in the cross section, were compared to reference measurements of the mean solids volume fraction obtained using a Honeywell ST-3000 dp cell. Once again, no statistically significant differences could be detected between the errors in the mean solids volume fraction obtained, for all of the electrode configurations investigated.

The ICC measuring system was used to measure the local solids volumetric flow rate for solids liquid flows in vertical and inclined pipes. The ICC measures the local solids volume fraction distribution using array B, and then measures the local solids velocity distribution by cross correlating conductance variations between arrays A and B. The measured solids volumetric flow rate $Q_{s,meas}$ obtained by the ICC is then obtained using Equation 6-2 .The reference solids volumetric flow rate $Q_{s,ref}$ was

determined from the hopper system. Again, no statistically significant differences could be detected between the mean error in $Q_{s,meas}$ for any of the electrode configurations investigated (see Table 9-3).

The profiles of local axial solids volume fraction, α_s, and local axial solids velocity, u_s, as measured by the ICC have a lower spatial resolutions than that of a typical dual-plane Electrical Resistance Tomography (ERT) system such as the system used by Balasubrammaniam (2008/2009) for oil and water flows. However the results obtained by the ICC device were compared with the a dual-plane Electrical Resistance Tomography system and Six-electrode local probes developed by Lucas et al., (1999, 2000) and Cory (1999) for solids and water flows and have shown good general agreement.

Due to the high cost of ERT systems, it may be preferable, in some applications, to use the low cost ICC flow meter for online monitoring of solids-in-water flows and other water continuous multiphase flows. The author believes that the ICC flow meter presented in this thesis can be used to measure the local velocity of the solids and the local solids volume fraction in a wide variety of solids water pipe flows, including horizontal flows. Although the solids particles used in the present investigation were of 4 mm diameter, it is likely that the ICC system can also be used to make local volume fraction and the local velocity measurements in solids and water flows with much smaller particles.

A mathematical model was developed for the numerical simulation of the behaviour of inclined flows of solids in water, see Chapter 8. The main conclusion to be drawn from this model is that the Navier-Stokes equation can be solved, given suitable simplifying assumptions, to give a reasonably good, one-dimensional velocity profile of inclined solids-water flows, provided that the local volume fraction distribution in the flow is known. For the given assumptions there was very close agreement between model predictions and those of Lucas' (1995) model; and quite good agreement with Lucas' experimental results, see Figures 8-3 to 8-6. The model appeared more successful in predicting the local solids velocity profiles observed in the present study. Good agreement was found between the model predictions for solids velocity profile and measured local solids velocity obtained by the ICC system,

see Figure 8.9, for the test pipe inclined at 30° to the vertical (Config-I, flow condition 22).

One of the boundary condition assumptions of the model deserves further consideration. It was assumed that the velocity of the water-solids mixture is zero at the pipe wall. But it was both visually observed and measured by the ICC that there could be solids flow immediately adjacent to the pipe wall - flow which could even be in the opposite direction to the mean flow for certain pipe inclinations and specific solids and water flow rates. In the model developed to predict velocity profiles from the local solids volume fraction profiles obtained by the ICC a number of other important assumptions were made. The velocity distribution of the solids particles has been mentioned above, but another important assumption made in the application of the model was the expressions for the two-phase eddy viscosity. The formulation of this expression needs extensive further investigation. Other assumptions such as the non-existence of buoyancy forces are probably not so significant as the above two.

9.2   Novel Features and Contributions to Knowledge

The research project presented in this thesis incorporated a number of important features that were novel and not previously implemented by other researchers. These are:

One

The author of this thesis success has developed a non-intrusive low cost Impedance Cross-Correlation flow meter to measure the local solids volume fraction distribution and the local axial solids velocity distribution for highly non-uniform solids-water flows and other water continuous multiphase flows. The device has been tested successfully for upward flows in pipes inclined to the vertical.

Two

A control system has been developed consisting of a micro-controller and analogue switches such that, for electrode arrays A and B (each consisting of eight electrodes) any number of the electrodes can be configured as excitation electrodes (V^+), or as virtual earth measurement electrodes (V_e) or earth electrodes (E) enabling different regions of the flow cross-section to be interrogated. By changing the electrode

configuration the electric field sensitivity distribution can be altered, thus changing the region of the flow 'interrogated' by the system. Cross-correlating the output signals from these electrode arrays, in various combinations, measures the velocity of the dispersed phase at different regions within the flow.

Three

The author has developed a switching mechanism to prevent cross-talk between the two arrays of electrodes.

Four

There have been no previous reports on the mathematical model for solids and water flow in inclined pipe.

9.3   Recommendations for Future Work

The results of current investigation and the conclusions reached, suggest a number of avenues for further work:

❖ The axial array separation L between the two electrode arrays A and B is 50 mm (see Chapter 3). The axial separation between the two electrode arrays should be varied to see if any greater accuracy in the measured results are obtained.

❖ The use of more than 2 electrode arrays should be investigated. Using, for example, five arrays, see Figure 9-1, would be expected to give a better analysis of any wave structure of the flow that occurs while measurements are being made. It would also be possible to cross-correlate between each pair of electrode arrays and compare the results obtained to investigate consistency and accuracy of the results.
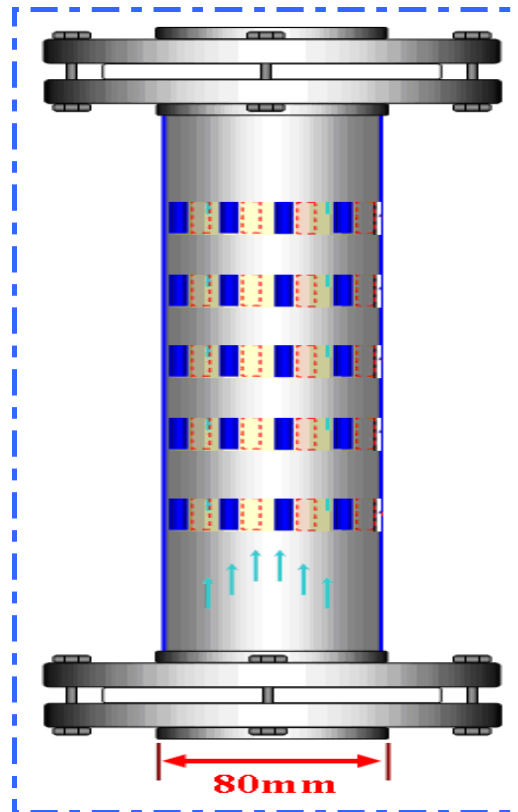
Figure 9-1: Suggested five electrode array flow meter.

❖ In this investigation eight electrodes were used for each electrodes array. Increasing the number of electrode in each array to 16. General speaking, this will increase the number of measuring pointes in the flow cross section. For example in the current investigation each electrode configuration listed in Tables 4-2, 4-3 and 4-4 have 8 different rotational positions. Since the number of electrodes is increased to 16 so a 16 measuring point for each of defined configurations (Config-I, II and III). Obviously, this might will overcome the problem that the author of this thesis phase while plotting the 3D profiles for each defined configuration (Config-I, II and III) and the problem overcome by plotting the all the rotational position listed in Tables 4-2, 4-3 and 4-4 together see Config-ψ .

❖ In this investigation the electrodes were rectangular in shape with dimensions of 2.3mm circumferentially x 2mm longitudinally x 0.4mm radially. Changes the shape of electrodes should be investigated, either by increasing one or more of the dimensions while retaining the same shape, or to use different

shaped electrodes. Wang J.et.al (2006) for example, used circular shaped electrodes.

❖ An ICC flow meter could be combined with an electromagnetic flow meter (EMF) to measure the properties of the multiphase flow. The EMF would be used to measure the continuous phase flow and the ICC meter to measure the dispersed phase. The EMF using the weight function technique to get the continuous phase velocity. For more information about the weight function see Wang J.et.al (2006) which give comprehensive information on the use of the EMF flow meter.

❖ Development of a theoretical model of solids in water flow in inclined pipes for practical flow conditions to predict the velocity of the dispersed phase using the measured volume fraction.

❖ Commercial development of the ICC meter as a low cost flow meter.

References

Abu-Orf M., Dentel S.K. *Polymer dose assessment using the streaming current detector.* Water Environment Research, vol. 69, no. 6, 1997, pp. 1075-1085.

Akagawa, K., Fujii T. and Takenaka N. (1989) *The effects of the density ratio in a vertically rising solid-liquid two-phase flow.* Int. Conf. on the Mechanics of Two-Phase Flows. Taiwan, pp203-208.

Alajbegovic A., Assad, A., Bonetto, F. and Lahey, R. (1994) *Phase distribution and turbulence structure for solid/fluid upflow in a pipe.* Int. J. Multiphase Flow. Vol 20, No3, pp453-479.

Al-Aufi, M. and Al-Hinai, S. (2002) *Petroleum Development Oman Annual Report*, Mina Al-Fahel, Oman.

Al-Yarubi Q.S. (2010) *Phase Flow Rates measurements of Annular Flows* PhD thesis, University of Huddersfield. (unpublished).

Angeli P., Hewitt G.F. *Phase distribution measurements in liquid-liquid pipeline flows using an impedance probe.* Proceedings of the ASME Heat Transfer Division, vol. 334, no. 3, 1996, pp.149-156.

Asakura, K., Ito, M. and Nakajima, I. (1992) *Local mean profiles of velocity, concentration and concentration fluctuations of solid phase in a vertical pipe.* Proc. Int. Conf. on Bulk Materials Storage, Handling & Transportation: Symp. on Freight Pipelines, Australia, Vol1, No 92/7, pp.123-127.

Bannwart, A.C., Rodriguez, O., Carvalho, C., Wang, I. and Vara, R. (2004) *Flow patterns in heavy crude oil-water flow.* J. Energy Resour. Technol. Vol 126, No 3 pp184-190.

Balasubrammaniam. Deepak (2008/9) *"Analysis of oil-water flows using dual-plane EIT system at different inclinations"*, MSc thesis, University of Huddersfield.

Bartosik, A. and Shook, C. (1995) *Prediction of vertical liquid:solid pipe flow using measured concentration distribution.* Particulate Sci. and Tech. Vol 13, pp85-104.

Beck M.S., Plaskowski A. *Cross correlation flowmeters – their design and application.* Adam Hilger, Bristol, 1987.

Beggs, H.D. and Brill, J.P. (1973) *A study of two-phase flow in inclined pipes*. J. Pet. Technol., pp607-617.

Benedict R.P. *Fundamentals of Pipe Flow*. John Wiley & Sons, New York, U.S.A., 1980.

REFERENCES

Binley A., Daily W., Ramirez A. *Detecting leaks from waste storage ponds using electrical tomographic methods.* Proceedings of the 1st World Congress on Industrial Process Tomography, Buxton, U.K., 1999, pp. 6-13.

Bond J., Cullivan J.C., Climpson N., Dyakowski T., Faulks I., Jia X., Kostuch J.A., Payton D., Wang M., Wang S.J., West R.M., Williams R.A. *Industrial monitoring of hydrocyclone operation using electrical resistance tomography. Proceedings of the 1st World Congress on Industrial Process.* Tomography, Buxton, U.K., 1999, pp. 102-112.

Bruggeman D.A.G. *Calculation of different physical constants of heterogeneous substances.* Annalen Physica, vol. 24, 1935, pp. 636-679.

Campbell CS (1990) *Rapid granular flows.* Annu Rev Fluid Mech 22:57-92

Carpentero-Rogero, E., Kross, B. and Sattelmayer, T. (2009) *Simultaneous HS-PIV and shadowgraph measurements of gas-liquid flows in a horizontal pipe.* 13th Int. Symp. in Appl. Laser Techniques to Fluid Mechanics, Lisbon.

Castello-Branco M.A.S.C., Schwerdtfeger K., *Large-scale measurements of the physical characteristics of round vertical bubble plumes in liquids.* Metallurgical and Materials Transactions B, vol. 25, no. 3, 1994, pp. 359-371.

Cartellier, A. and Achard, J.L. (1991) *Local phase detection probes in fluid/fluid two phase flows.* Rev. Sci. Instr., Vol 62, No 2, pp279-303.

Chaouki, J., Larachi, F. and Dudukovic, M.P. (1997) *Non-invasive tomographic and velocimetric monitoring of multiphase flows.* Ind. and Eng. Chem. Research, Vol 36, No 11, pp4476-4503.

Charles, M.E., Govier,G.W. and Hodgson, G.W. (1961) *The horizontal pipe line flow of equal density oil-water mixtures.* Can. J. Chem. Eng., Vol. 39, pp. 27-36.

Ceccio, S.L. and George, D.L. (1996) *A review of electrical impedance techniques for the measurement of multiphase flows.* J. Fluids Eng., Trans. ASME, Vol 118, pp391-399.

Chen R.C. and Kadambi J.R. (1994) *Experimental and numerical studies of solid-liquid pipe flow.* Proc. ASME Fluids Engineering Division, vol. 189, pp123 -135.

Chu C.P., Lee D.J. *Moisture distribution in sludge: Effects of polymer conditioning.* ASCE Journal of Environmental Engineering, vol. 125, no. 4, 1999, pp. 340-345.

Clark, N.N., Seiss, R. and Turton R. (1992) *Probe measurements in gas-liquid systems.* Flow Measurement & Instrumentation, Vol 3, No 1, pp17-23.

Coiado, E.M. and Diniz, V.E. (2001) *Two-phase (solid-liquid) flow in inclined pipes.* J. Braz. Soc. Mech. Sci. Vol 23, No 3

REFERENCES

Conan. C., Decarre, S, Masbernat, O. and Line, A. (2009) *Oil-water flow in a horizontal pipe.* Multiphase Sci. and Tech. Vol 21 Issue 1-2.

Constantini R., Parsons R.H. *The economic and environmental impact of long distance slurry pipelines.* Hydrotransport 3, Proceedings of the 3rd International Conference on the Hydraulic Transport of Solids in Pipes, Golden, Colorado, U.S.A., 1974, pp. K1-K12.

Crilly, J. and Fryer, P. (1993) *New directions in food research: the role of mathematical models.* Inst. of Maths and its Applications. Vol 5, pp265-282.

Dahle, E. (Ed) (2005) *Handbook of Multiphase Flow Metering, Revision 2,* Norwegian Society for Oil and Gas Measurement.

Davies, R.M. and Taylor, G. (1950) *The Mechanics of Large Bubbles Rising Through Liquids and Through Liquids in Tubes.* Proc. Roy. Soc. Series A. 200 pp375-390.

De La Rue R.E., Tobias C.W. *On the conductivity of dispersions.* Journal of the Electrochemical Society, vol. 106, no. 9, 1959, pp. 827-832.

Dong, F., Xiang, J., Qiao, X. and Xu, L. (2003) *Application of Electrical Resistance Tomography to two-phase Pipe Flow Parameters Measurement,* Flow Measurement and Instrumentation Vol 14, pp183-192.

Doron, P. and Barnea, D. (1993) *A three-layer model for solid-liquid flow in horizontal pipes. Int. J. Multiphase Flow.* Vol 19, No 6, pp1029-1043.

Doron, P. and Barnea, D. (1996) *Flow pattern maps for solid-liquid flow in pipes.* Int. J. Multiphase Flow. Vol 22, No 2, pp273-283.

Doron, P., Simkhis, M. and Barnea, D. (1997) *Flow of solid-liquid mixtures in inclined pipes.* Int. J. Multiphase Flow. Vol 23, No 2, pp313-323.

E Fransolet, M Crine , G L'Homme, D Toye and P Marchot, 2002, *Electrical resistance tomography sensor simulations: comparison with experiments,* Meas. Sci. Technol. Vol 13 (1239-1247).

Favelukis, M., Ly, C-H. (2005) *Unsteady mass transfer around spheroidal drops in potential flow.* Chem. Eng. Sci. Vol 60, pp7011- 7021.

Feng, Jianping Wen, Jinghua Fan, Qing Yuan, Xiaoqiang Jia, Yan Sun, *"Local hydrodynamics of gas-liquid-nanoparticles three-phase fluidization.",* Chemical engineering science, volume 60, pages 6887-6898, 2005.

Flores, J.G. (1997) *Oil-water flow in vertical and deviated wells,* PhD. Dissertation, University of Tulsa.

Flores, J.G., Sarica, C., Chen, T.X. and Brill, J.P. (1998) *Investigation of holdup and pressure drop behaviour for oil-water flow in vertical and deviated wells.* J. Energy Resources. Trans. ASME. Vol 120, pp8-14.

REFERENCES

Franca, L., Lahey, R.T., Acikgoz, M., 1992, ''experimental study of three phase flow regimes'' International Journal Multiphase Flow 18, 327-336.

Gao X., , Ma, Y., Zhu, C. and Yu, G. (2006) *Towards the mechanism of mass transfer of a single bubble*, Chinese J. Chem. Eng. Vol 14, pp158-163.

Goharzadeh, A. and Rodgers, P. (2009) *Experimental characterisation of solid particle transport by slug flow using particle image velocimetry.* 6th Int. Symp. Measurement Techniques for Multiphase Flows. J. Physics: Conference Series 147 012069.

Gourich, B., Vial, C., Essadki, A.H., Allam, F., Belhaj, M. and Ziyad, M. (2006) *Identification of flow regimes and transition points in a bubble column through analysis of differential pressure signal – Influence of the coalescence behaviour of the liquid phase.* Chem. Eng. and Processing, Vol 45, Issue 3, pp214-223.

Govier G and Aziz K 1972. *The Flow of Complex Mixtures in pipes*. Van Nostrand Rheinhold, New York.

Grassi, B., Strazza, D. and Poesio, P. (2008) *Experimental validation of theoretical models in two-phase high-viscosity ratio liquid–liquid flows in horizontal and slightly inclined pipes.* Int. J. Multiphase Flow 34:950–965.

Grieve B.D., Dyakowski T., Mann R., Wang M. *Interfacing of EIT into an industrial pressure filter – a practical example. Proceedings of the 1st World Congress on Industrial Process Tomography*, Buxton, U.K., 1999, pp. 113-119.

Grolman, E. and Fortuin, J (1997) *Gas-liquid flow in slightly inclined pipes.* Chem. Eng. Sci. Vol 52, Issue 24, pp4461-4471.

Gunn, D.J. and Al-Doori, H.H. (1985) *The measurement of bubble flows in fluidised beds by electrical probe.* Int. J. Multiphase Flow, Vol 11, No 4, pp535-551.

Gysling D.L. and Loose., D.H. 2005, *Using SONAR-based gas volume fraction meter for improved net oil rate measurement,* CiDRA Corporation Wallingford, CT USA.

Halter R, Hartov A and Paulsen K D 2004. *Design and implementation of a high frequency electrical impedance tomography system.* Physiol. Meas. 25 379-90.

Hassan Y. and Blanchat T. (1991) *Full-field bubbly flow velocity measurements digital image pulsed laser velocimetry.* Experiments in Fluids, Vol. 11, pp.293-301.

Henthorn, K., Park, K. and Curtis, J, (2005) *Measurement and prediction of pressure drop in pneumatic conveying.* Ind. Eng. Chem. Rev 44:5090-5098.

Hewitt, J. M. Delhaye, N. Zuber, "Multiphase Science and technology", volume 2, Hemisphere Publishing Corporation, pages 1-94, 1986.

Holdsworth, S.D. (1992), Aseptic *processing and packaging of food products,* Elsevier Science Publishers. UK.

REFERENCES

Hsu F-L., Turian R.M., Ma T-W. *Flow of noncolloidal slurries in pipelines.* American Institute of Chemical Engineers Journal, vol. 35, no. 3, 1989, pp. 429-442.

Hua Li, Mi Wang, Ying-Xiang Wu and Gary Lucas, *Volume Flow Rate Measurement in Vertical Oil-in-Water Pipe flow using Electrical Impedance Tomography and A Local probe.* Conference on Multiphase Flow in industrial Plants, Palermo, Italy (c) 2008.pp,293-302.

Hulbert M.H., Lambert D.N., Bennett R.H., Freeland G.L., Burns J.T., Sawyer W.B., Field P. *In situ electrical resistivity measurements of calcareous sediments.* ASTM Special Publication STM777, 1982, pp. 414-428.

Jamieson A.W. Multiphase metering – *the challenge of implementation*. Measurement & Control, vol. 32, February 1999, pp.5-9.

Jana, A.K., Das, G. and Das, P.K. (2006) *Flow regime identification of two-phase liquid-liquid upflow through vertical pipe.* Chem. Eng. Sci. 61:1500-1515.

Jim Cory, *"The measurement of volume fraction and velocity profiles in vertical and inclined multiphase flow",* PhD thesis, December 1999.

Jones, O.C. andf Delhaye, J-M. (1976) *Transient and statistical measurement techniques for two-phase flows – a critical review.* Int. J. of Multiphase Flow, Vol 3,pp.89-116.

Jordana J., Gasulla M., Pallás-Areny R. *Leakage detection in buried pipes by electrical resistance imaging. Proceedings of the 1st World Congress on Industrial Process Tomography,* Buxton, U.K., 1999, pp. 28-34.

Kakka R.S. *Review of instruments for measuring flow rate and solids concentration in steelworks slurry pipeline.* Hydrotransport 3, Proceedings of the 3rd International Conference on the Hydraulic Transport of Solids in Pipes, Golden, Colorado, U.S.A., 1974, pp. F81-F92.

Kumara, W.A.S, Halvorsen, B.M. and Melaaen, M.C. (2009) *Pressure drop, flow patterns and local water volume fraction measurements of oil-water in pipes.* Meas. Sci. Technol. Vol 20 Issue 11.

Lagace P.J., Fortin J., Crainic, E.D. *Interpretation of resistivity sounding measurements in N-layer soil using electrostatic images*. IEEE Transactions on Power Delivery, vol. 11, no. 3, 1996, pp. 1349-1354.

Lake, M., Stanley, G. and Podio, A.L. *www.pe.utexas.edu/2phaseweb/flowtwo.html, (accessed 25-09-09)*

Lauer-Leredde C., Pezard P.A., Dekeyser I. Ficus, *a new in-situ probe for resistivity measurements in unconsolidated marine sediments.* Marin Geophysical Researches, vol. 20, no. 2, 1998, pp. 95-107.

REFERENCES

Lee, S. and Durst, F. (1982) *On the motion of particles in turbulent duct flows.* Int. J. Multiphase Flow Vol 8, No 2, pp125-146.

Ling, J., Skudarnov, P.V., Lin, C.X. and Ebadian, M.A. (2003) *Numerical Investigations of liquid-solid slurry flows in a fully developed turbulent flow region. Int*. J. Heat and Fluid Flow, Vol 24, pp389-398.

Ljubicic B., Bukurov Z., Cvijanovic P., Stajner K. *Coal dredging efficiency – The underwater mining experience at Kovin coal mine.* Hydrotransport 13, Proceedings of the 13th International Conference on Slurry Handling and Pipeline

Louge, M.Y., Mastorakos,E. and Jenkins, J.T. (1991) *The role of particle collisions in* pneumatic *transport.* J. Fluid Mech. Vol 231 pp345-359.

Lioumbas, J.S., Paras, S.V. & Karabelas, A.J., 2005 *Cocurrent stratified gas-liquid downflow – Influence of the liquid flow field on interfacial structure*, Int. J. Multiphase Flow Vol 31, No 8, pp869-896.

Lovick, J. and Algeli, P. (2004) *Droplet size and velocity profiles in liquid-liquid horizontal flows.* Chem. Eng. Sci. 59: 3105-3115.

Lucas, D., Krepper, E. and Prasser, H-M. (2001) *Prediction of radial gas profiles in vertical pipe flow on the basis of bubble size distribution.* Int. J. Therm. Sci., Vol 40, pp217-225.

Lucas, G.P., Cory, J., Loh, W.W. and Waterfall, R.C. (1998) *On-line monitoring of drilling cuttings transport using electrical resistance tomography proc.* 2nd Int. Symp. On Measuring Techniques for Multiphase Flows (China) pp 239-244.

Lucas, G.P., Cory, J., Waterfall, R.C., Loh, W.W. and Dickin, F. (1999) *Measurement of the Solids Volume Fraction and Velocity Distributions in Solids-liquid flows Using dual-plane Electrical Resistance tomography.* Flow Measurement and Instrumentation Vol 10, pp.249-258.

Lucas, G.P., Cory, J. and Waterfall, R.C. (2000) *A six-electrode local probe for measuring solids velocity and volume fraction profiles in solids-water flows.* Meas. Sci. Technol. Vol 11 pp1498-1509.

Lucas, G.P. and Lin, N.D. (2001) *Measurement of the homogeneous velocity of inclined oil-in-water flows using a resistance cross correlation flow meter.* Meas. Sci. Technol. Vol 12 pp1529-1537.

Lucas, G.P., Mishra, R. and Panayotopoulos, N. (2004) *Power law approximations to gas volume fraction and velocitry profiles in low void fraction vertical gas-liquid flows.* Flow Meas. and Instr. Vol 15 pp271-283.

Lucas, R. Mishra and N. Panayotopoulos, *"Volume Fraction and Velocity Profile Measurement in Low Void Fraction Gas-Liquid Flows using a Dual- Sensor Conductance Probe"*, Journal of Flow Measurement and Instrumentation Volume 15, Issues 5-6 , October-December 2004, Pages 271-283.

REFERENCES

Lucas, G. and Mishra, R. (2005) *Measurement of bubble velocity components in a swirling gas–liquid pipe flow using a local four-sensor conductance probe.* Meas Sci. and Technology, 16 (3). pp749-758.

Lucas, G.P. and Panagiotopoulos, N. (2009) *Oil volume fraction and velocity profiles in vertically, bubbly oil-in-water flows.* Flow Measurement and Instrumentation Vol 20 pp127-135.

Lucas G P and Walton IC 1997 *Flow rate measurement by kinematics wave detection in vertically upward, bubbly two-phase flows* J. Flow Meas.Instrum. 8 133-43.

Lucas, G., *Modelling velocity profiles in inclined multiphase flow to provide a priori information for flow imaging*, the Chemical Engineering journal, 56 (1995),167-173.

Mactaggart R.S., Nasr-El-Din H.A., Masliyah J.H. *A conductivity probe for measuring local solids concentration in a slurry mixing tank.* Separations Technology, vol. 3, no. 3, 1993, pp. 151-160.

Marié, J.L. (1983) *Investigation of two-phase bubbly flows using laser Doppler anemometry.* Physicochemical Hydrodynamics, Vol 4, No 2, pp103-118.

Marruaz, K., Gonzales, M., Gaspari, E., Ribeiro, G., Franca, F. and Rosa, E. (2001) *Horizontal slug flow in a large-size pipeline.* J. Braz. Soc. Mech. Sci. Vol 23 No 4.

Massey B.S. *Mechanics of Fluids.* Chapman & Hall, London, U.K., 6th edition, 1990.

Matousek, V. (2002) *Pressure drops and flow patterns in sand-mixture pipes.* Expt. Thermal and Fluid Sci. 26:693-702.

Matousek V. *Internal structure of slurry flow in inclined pipe. Experiments and mechanistic modelling.* Hydrotransport 13, Proceedings of the 13th International Conference on Slurry Handling and Pipeline Transport, Johannesburg, South Africa, 1996, pp. 187-210.

Matsui G., *"Identification of flow regimes in vertical gas-liquid two-phase flow using differential pressure fluctuations.",* International journal of multiphase flow, volume 10, pages 711-720, 1984.

Maxwell, J.C. (1873) A treatise on electricity and magnetism, Vol 1. Clarendon Press, Oxford.

McKibben, M.J., Gillies, R.G. and Shook, C.A. (2000) *A laboratory investigation of horizontal well heavy oil-water flows.* Can. J. Chem. Eng. Vol 78 pp743-751.

Miller, A. and Gidaspow, D. (1992) *Dense, vertical gas-solid flow in a pipe.* AIChE Journal, Vol 38, No 11, pp1801-1815.

Mizukami M., Parthasarathy R.N., Faeth G.M. *Particle-generated turbulence in homogeneous dilute dispersed flows.* International Journal of Multiphase Flow, vol. 18, no. 3, 1992, pp. 397-412.

REFERENCES

Moura, L.F. and Marvillet, C. (1996) *Local measurements in gas-liquid twophase flows: A review of different techniques. Experimental and Numerical Flow Visualisation and Laser Anemometry,* Proc. ASME Fluids Engineering Division Conf., Vol 239, No. 4, pp363-370.

Nakanishi, S., Shiomi, Y., Katsuna, H. and Hamaji, M. (1999) *An experimental study of flow pattern and pressure drop of gas-liquid-liquid three-phase flow*. Int. Symp. Two-phase Flow Modelling and Experimentation. Italy.

Nasr-El-Din H. and Shook C.A. (1985) *Sampling from slurry pipelines: Thick walled and straight probes.* Journal of Pipelines, Vol 5, pp113-124.

Ncube F., Kastrinakis E.G., Nychas S.G., Lavdakis K.E. *Drifting behaviour of a conductivity probe*. Journal of Hydraulic Research, vol. 29, no. 5, 1991, pp. 643-654.

Oddie, G., Shi, H., Durlofsky, L., Aziz, K., Pfeffer, B. and Holmes, J. (2003) *Experimental study of two and three phase flows in large diameter inclined pipes.* Int. J. Multiphase Flow. Vol 29, pp527-558.

Poesio, P., Strazza, D. Grassi, B. and M. Margarone, M. (2007) *Statistical measurements in horizontal and slightly inclined pipes of oil-in-water slugs.* 4th Int. Conf. Multiphase Flow, Liepzig (Germany), 9-13 July.

Poesio, P., Sotgia, G. and Strazza, D. (2009) *Experimental investigation of three-phase oil-water-air flow through a pipeline.* Multiphase Sci. and Tech. Vol 21, No1-2, pp107-122.

Pohorecki, R., Moniuk, W., Bielski, P., Sobieszuk, P. and Dąbrowiecki, G. (2005) Bubble *diameter correlation via numerical experiment.* Chem. Eng. Journal, Vol 113, pp35-39.

Polonsky, S., Barnea, D. and Shemer L. (1998) *Experimental study of the motion of an elongated bubble by means of image processing technique.* Development of Measuring Techniques for Multiphase Flows, Proc. 2nd Int. Symp. on Measuring Techniques for Multiphase Flows, China, pp251-256.

Pradhan, S., Lucas, Gary and Zhao, X. (2008) *Measurement of reference velocity vector for four-sensor conductance probes using orthogonal, high speed cameras*. In: 6th North American Conference on Multiphase Technology, 4th-6th June 2008, Banff, Canada. (Unpublished)

Priddy W.J. BP *multiphase meter application experience*. Measurement & Control, vol. 32, February 1999, pp. 9-15.

Pyung Seob Song, Chan Gi Lee, Suk Hwan Kang, Sung Mo Son, Yong Kang, Sang Done Kim, (2005) Drop *properties and pressure fluctuations in liquid-liquid solid fluidized-bed reactors.*, Chem. Eng. and Processing, Vol 44, pp1296-1305.

REFERENCES

Rao, C.S. and Dukler, A.E. (1971) *The isokinetic-momentum probe. A new technique for measurement of local voids and velocities in flow of dispersions.* Industrial and Engineering Chemistry Fundamentals, Vol 10, No 3, pp520-526.

Raudkivi, A.J. (1989) *Loose Boundary Hydraulics.* Pergamon Press, New York.

Revankar S.T., Ishii M. *Theory and measurement of local interfacial area using a four sensor probe in two-phase flow.* International Journal of Heat and Mass Transfer, vol. 36, no. 12, 1993, pp. 2997-3007.

Ridd P.V. *A sediment level sensor for erosion and siltation detection. Estuarine,* Coastal and Shelf Science, vol. 35, 1992, pp. 353-362.

Roco, M.C. & Shool, C.A. (1983). *Modeling of slurry flow: the effect of particle size*, Can. J.Chem.Eng.61, 494-503

Rodriguez, O. and Oliemans, R. (2006) *Experimental study on oil-water flow in horizontal and slightly inclined pipes.* Int. J. Multiphase Flow. Vol 32 pp323-343.

Russel, T.W.F. and Charles, M.E. (1959) *The effect of the less viscous liquid in the laminar flow of two immiscible liquids.* Can. J. Chem. Eng., Vol 37, pp18-24.

Sabersky, R. H.; Acosta, A. J.; Hauptmann, E. G. (1989) *Fluid Flow A First Course in Fluid Mechanics,* MacMillian Publishing Co., New York.

Sakaguchi, T., Shakutsi, H., Tomiyama, A., Minigawa, H. and Kitani, S. (1991) *Microscopic characteristics of multiphses flow using digital image processing.* Proc. Int. Conference on Multiphase Flows, pp357-360. Tsukuba, Japan.

Savage SB (1984) *The mechanics of rapid granular flows.* Adv Appl Mech 24: 289-366.

Scarlett, B. and Grimley, A. (1974) *Particle velocity and concentration profiles during hydraulic transport in a circular pipe.* Hydro-transport 3, Proc. 3rd Int. Conf. on the Hydraulic Transport of Solids in Pipes, Colorado, U.S.A., ppD23-D37.

Schüller R.B., Halleraker M., Engebretsen B. *Advanced profile gauge for multiphase systems. Proceedings of the 1st World Congress on Industrial Process Tomography*, Buxton, U.K., 1999, pp. 126-139.

Scott, G.M. (1985) *A study of two-phase liquid-liquid flow at variable inclinations.* Master's Thesis, University of Texas at Austin.

Seshadri, V., Singh, S.N., Charau, F. and Mishra, R. (2001) *Hold-up in multi-sized particulate solid-liquid flow through horizontal pipes.*, Indian J. Eng. & Materials Sci., Vol 8, pp84-89.

Serizawa A., Kataoka I., Michiyoshi I. *Turbulence structure of air-water bubbly flow – 1.* Measuring techniques. International Journal of Multiphase Flow, vol. 2, no. 3, 1975, pp. 221-233.

REFERENCES

Severin Waelchli, Philipp Rudolf von Rohr, *"Two-phase flow characteristics in gas-liquid microreactors."* International journal of multiphase flow, volume 32, issue 7, pages 791-806, 2006.

Sheng, Y.Y. and Irons, G.A. (1991) *A combined laser doppler anemometry and electrical probe diagnostic for bubbly two-phase flow.* Int. J. Multiphase Flow, Vol 17, No 5, pp585-598.

Steinemann, J. and Buchholz, R. (1984) *Application of an electrical conductivity microprobe for the characterization of bubble behaviour in gas liquid bubble flow.* Verlag Chemie GmbH, D-6940 Weinheim, pp102-107.

Steinhaus, H. (1999) *Mathematical Snapshots*, 3rd ed. New York: Dover, pp. 202-203

Sumner R.J., McKibben, M and Shook, C.A. (1990) *Concentration and velocity distribution in turbulent vertical slurry flow. J. Solid Liquid Flow.* Vol 2, No2, pp33-42.

Sun K.X., Zhang M.Y., Chen X.J. *An investigation of double-sensor resistivity probe techniques for the measurement of gas-liquid bubbly flow.* Development of Measuring Techniques for Multiphase Flows, Proceedings of the 2nd International Symposium on Measuring Techniques for Multiphase Flows, Beijing, China, 1998, pp.111-116.

Tabeling P., Pouliquen O., Theron B., Catala G. *Oil water flows in deviated pipes: experimental study and modelling.* Proceedings of the 5th International Conference on Multiphase Production, Cannes, France, 1991, pp. 292-306.

Takashi Hibiki, Rong Situ, Ye Mi, Mamoru Ishii, *"Local flow measurements of vertical upward bubbly flow in an annulus"*, Heat and Mass Transfer, volume 46, pp 1479-1496, 2002.

Tallon, S., Davies, C.E. and Barry B. (1998) *Slip velocity and axial dispersion measurements in a gas-solid pipeline using particle tracer analysis.* Powder Technology, Vol 99, pp125-131.

Teyssedou, A., Tapucu, A. and Lortie, M. (1988) *Impedance probe to measure local void fraction profiles.* Rev. Sci. Instr., Vol 59, No 4, pp631 639.

Thang, N.T. and Davis, M.R. (1979) *The structure of bubbly flow through venturis.* Int. J. Multiphase Flow, Vol 5, No 1, pp17-37.

Thorn R., Johansen G.A., Hammer E.A. *Three-phase flow measurement in the offshore oil industry - is there a place for process tomography?* Proceedings of the 1st World Congress on Industrial Process. Tomography, Buxton, U.K., 1999, pp. 228-235.

Tsuji, Y., Morikawa Y. and Shiomi, H. (1984) *LDV measurement of an air-solid two-phase flow in a vertical pipe.* J. Fluid Mech., 139:417–434.

REFERENCES

Turner J.C.R. *Electrical conductivity of liquid-fluidised beds.* AIChE Symposium Series, vol. 69, no. 128, 1973, pp. 115-122.

Turian R.M., Yuan T. *Flow of slurries in pipelines.* AIChE Journal, vol. 23, no. 3,1977, pp. 232-243.

Van Der Welle R. Void fraction, *bubble velocity and bubble size in two-phase flow.* International Journal of Multiphase Flow, vol. 11, no. 3, 1985, pp. 317-345.

Varley, J. W. R. Boyd, S. Gallagher, A. K. Brown, P. W. Dodd, *"Correlation between conductivity and liquid hold-up for a multi-segment industrial foam probe for fermentation.",* Biochemical engineering journal, volume 19, pages 199-210, 2004.

Vigneaux P G, Chenais P and Hulin JP 1988 *Liquid-Liquid flow in an inclined pipe.* AIChE J. 34 781-9.

Volanschi A., Olthuis W., Bergveld P. *Design of a miniature electrolyte conductivity probe using ISFETs in a four point configuration.* Sensors & Actuators B, vol. 18-19, 1994, pp. 404-407.

Volanschi A., Olthuis W., Bergveld P. *Electrolyte conductivity measured with an ISFET. Proceedings of Trends in Electrochemical Biosensors Conference*, Trieste, Italy, 1992, pp. 147-154.

Wang, J. Z., Gong, C.L., Lucas, Gary and Tian, Gui Yun (2006) *Numerical Simulation Modelling for Velocity Measurement of Electromagnetic Flow Meter.* Journal of Physics Conference Series, 48. pp. 36-40. ISSN 1742-6588.

Wang, M.,Y.Ma, N.Holiday, Y.Dai, R.A. Williams and G.P. Lucas, 2005, *A High-performance EIT system*, IEEE Sens.J.5,289.

Wang, M., T.F. Jones and R.A. *Williams, 2003, Visualization of Asymmetric Solids Distribution in Horizontal Swirling Flows using Electrical Resistance Tomography*, Trans. IChemE.81,854.

Wang, M., R.Mann and F.J.Dickin,1999, *electrical Resistance Tomographic Sensing System for Industrial Applications*, Chem. Eng. Comm. 175,49.

Wei, F., Lin, H., Cheng, Y., Wang, Z. and Jin, Y. (1998) *Profiles of particle velocity and solids fraction in a high-density riser.* Powder Technology. Vol 100, pp183-189.

Willhoft, E.M.A. (1993) *Aseptic processing and packaging of particulate foods,* Blackie Academic & Professional.

Wu, Y., H. Li, M. Wang and R.A. Williams,2005, *Characterization of Air-water Two-phase Vertical Flow by using Electrical Resistance Imaging*, Can.j.Chem.Eng.83,37.

X Den, F Dong, L J Xu, X P Liu and L A Xu , 2001, *The design of dual-planr ERT system for cross correlation measurement of bubbly gas/ liquid pipe flow*, Meas. Sci. Technol. Vol 12, pp (1024-1031).

REFERENCES

Xie T., Tjin S.C., Yang Q., Ng S.L. *Effect of blood's velocity on blood resistivity.* IEEE Transactions on Instrumentation and Measurement, vol. 47, no. 5, 1998, pp. 1197-1200.

Yakubov, B., Tanny, J., Maron, D.M. and Brauner, N. (2006) *The effect of pipe inclination on a liquid-solid fluidized bed.* HAIT J. Sci and Eng. Vol 3, pp1-19.

Yamamoto, F., Ohta, J., Murai, Y. and Song X. (1998) *PIV Measurement of Multiphase Flows. Development of Measuring Techniques for Multiphase Flows,* Proc. 2nd Int. Symp. on Measuring Techniques for Multiphase Flows, Beijing, China, pp3-20.

Yerrumshetty, A.K., (2007) *Numerical predictions of turbulent gas-solid and and liquid solid flows using two fluid models,* MSc Thesis, Department of Mechanical Engineering at the University of Saskatchewan, Canada.

Yianneskis, M. and Whitelaw, J.H. (1984) *Velocity characteristics of pipe and jet flows with high particle concentration.* Proc. ASME Energy Sources Technology Conference, p12-15.

Zuber and J. A. Fiindlay, *''Average volumetric concentration in two-phase flow systems''*, Journal of Heat Transfer, Vol.87,pp.453-468,1965.

http://science.howstuffworks.com/oil-drilling4.htm, (accessed on 20/02/2008).

http://www.jaycar.com.au/images_uploaded/XR2206V1.PDF, (accessed 04/03/10).

http://www.intersil.com/data/fn/fn3284.pdf, (accessed 04/03/10).

http://www.datasheetcatalog.org/datasheet/SGSThomsonMicroelectronics/mXruyrq.pdf,(accessed 04/03/10)

www.savetman.com/curvefit, (accessed 21/01/10).

http://www.labjack.com/u12, (accessed 02/01/07).

http://www.saw.uwaterloo.ca/femlab/trialintroduction.pdf, (accessed 04/03/10).

http://www.matlab.com, (accessed on 05/07/09).

http://www.savetman.com (accessed 21/01/10).

Appendix

9.4 Code-1

This code used for to record the data for 60 seconds from array A and array B. It starts by selecting the desired electrode configuration.

```
load('electrode-configuration.mat')
endtimes  = length(ringset1(:,1))
volt1 = zeros(2048,length(ringset1(:,1)));
volt2 = zeros(2048,length(ringset1(:,1)));
for  i =1: endtimes
    a = ringset1(i,1);
    b = ringset1(i,2);
    c = ringset1(i,3);
    d = ringset1(i,4);
    e = ringset1(i,5);
    f = ringset1(i,6);
    g = ringset1(i,7);
    h = ringset1(i,8);
 SetRing1(a,b,c,d,e,f,g,h);
 SetRing2(a,b,c,d,e,f,g,h);
%  dgfo = 2;                    % input dgfo == DiGital
Filter Order
                               % 2 = 2nd Order ,...., 10 =
10th Order
 Idnum = -1;                  % LabJack number (-1 for first
LapJack)
 demo = 0;                    % 0 = Working mode  &   1 =
Demo mode
 stateIO = [0];               % State of I/O lines required
- Not used
 updateIO = 0;                % 1 = Wrire I/O states & 0 =
Don't write
 ledon = 1;                   % LapJack indicator led   1 =
on & 0 = off
 numChannels = 2;             % Number of analog chanels
used
 channels = [1 2 3];           % Numbers of the chanels
used
 gains = [0 0 0];              % Gains of the selected
chanels  0 = unity gain
 scanrate = 1000;              % Rate of sampling
sample/second
 disablecal = 0;              % Calibration data   0 = use &
>0 = Don't use
 triggerIO = 0;               % Triger IO port      0=none,
1=IO0, ..., 4=IO3
```

```matlab
 triggerState = 0;          % Trigering state     0=Low
1=High
 numscans = 2048;            % Number of scans     form 1
to 4096 scans 2048
 timeout = 10;              % Maximum nomber of seconds
allowed for operation
 transfermode = 0;          % Always send 0 (LapJack
instructions)
 % data                     % The output array
 % stateIOout               % Array where IO states are
returned - Not used
 % scanRate                 % Actual scan rate used (might
be different)
 % overVoltage              % 1 = Over voltage detected &
0 = every thing ok
 % errorcode                % LabJack error codes or 0 for
no error
 % idnum                    % Local ID number of LabJack,
or -1 if no LabJack is found
 % SampleTime               % Time between any two
consecutive samples
 vsum=0;

 % Feedind instructions into LapJack and receiving the
result array (data)
 [data stateIOout scanRate overVoltage errorcode idnum] =
AIBurst(Idnum, demo, stateIO, updateIO, ledon,
numChannels, channels, gains, scanrate, disablecal,
triggerIO, triggerState, numscans, timeout,transfermode);

 SampleTime = 1/scanRate;       % Calculate actual
sampling time
 for (n=1 : numscans) ;
 time(n,1)= (n-1)*SampleTime;    % create time array for
plotting
 end
 volt1(:,i)= data(:,1);    % create data array for
plotting 1st channel
 volt2(:,i)= data(:,2);    % create data array for
plotting 2nd channel
 volt3(:,i)= data(:,2);    % create data array for
plotting 3rd channel

 vo1=mean(volt1(:,i));          % Average of 1st channel
data
 vo2=mean(volt2(:,i));          % Average of 2nd channel
data
 vo2=mean(volt3(:,i));          % Average of 2nd channel
data
 %------------------------------ Plot of chn1 & chn2 -
------------------
```

```
 subplot(2,2,1)
 plot (volt1(:,1), volt1(:,2));
 title('chn1');
 xlabel('Time(sec)');
ylabel('volt1');
 grid on;
subplot(2,2,2)
 plot (volt2(:,1), volt2(:,2));
  title('chn2');
  xlabel('Time(sec)');
  ylabel('volt2');
  grid on;
%  %------------------------------ Chanel 1 Filter ---
--------------------
%  volt1 = zeros(2048,length(ringset1(:,1)));
% volt2 = zeros(2048,length(ringset1(:,1)));
%  for (m=1:numscans);
%      for (j=0:dgfo);
%          if (m-j>0)
%          vsum = vsum + volt1(m-j, 2);
%          else
%          vsum = vsum + 0;
%        end
%      end
%      volt1f(m,:)=[volt1(i,1) vsum/(dgfo+1)];
%      vsum = 0;
%   end
%
% %  %------------------------------ Chanel 2 Filter -
----------------------
%   for (i=1:numscans);
%      for (j=0:dgfo);
%          if (i-j>0)
%          vsum = vsum + volt2(i-j, 2);
%          else
%          vsum = vsum + 0;
%          end
%      end
%    volt2f(i,:)=[volt2(i,1) vsum/(dgfo+1)];
%      vsum = 0;
%   end
%
%   dataf = [volt1f(:,2) volt2f(:,2)];
%
% %------------------------- Plotting of Filtered chn1
& chn2 ------------
%   subplot(2,2,3)
%   plot (volt1f(:,1), volt1f(:,2));
%   title('Filtered chn1');
%   xlabel('Time(sec)');
%   ylabel('Filtered volt1');
```

```matlab
%    grid on;
%    subplot(2,2,4)
%    plot (volt2f(:,1), volt2f(:,2));
%    title('Filtered chn2');
%  xlabel('Time(sec)');
%    ylabel('Filtered volt2');
%    grid on;
end
hold on
```

9.5   Code-2

This code is used to select the desired electrode configurations for array A.

```matlab
function SetRing1(a,b,c,d,e,f,g,h);

Ring1=[a,b,c,d,e,f,g,h];
Lat1=[0,0,0,0,0,0,0,0];
Lat2=[0,0,0,0,0,0,0,0];
Lat3=[0,0,0,0,0,0,0,0];
%------------------------------- Setting Latches Values
---
for i = 1:8;
    if (Ring1(i)==1);  Lat1(i)=0;  Lat2(i)=0;  Lat3(i)=0;
end
    if (Ring1(i)==2);  Lat1(i)=1;  Lat2(i)=0;  Lat3(i)=0;
end
    if (Ring1(i)==3);  Lat1(i)=0;  Lat2(i)=1;  Lat3(i)=0;
end
    if (Ring1(i)==4);  Lat1(i)=0;  Lat2(i)=1;  Lat3(i)=1;
end
end

%------------------------------- Setting Latch 1 ------
----
for i = 0:7
    EDigitalOut(-1,0,i,1,Lat1(i+1));
end
    EDigitalOut(-1,0,8,1,1);
    EDigitalOut(-1,0,8,1,0);
%------------------------------- Setting Latch 2 ------
----
for i = 0:7
    EDigitalOut(-1,0,i,1,Lat2(i+1));
end
    EDigitalOut(-1,0,9,1,1);
    EDigitalOut(-1,0,9,1,0);
%------------------------------- Setting Latch 3 ------
----
for i = 0:7
```

```
    EDigitalOut(-1,0,i,1,Lat3(i+1));
end
    EDigitalOut(-1,0,10,1,1);
    EDigitalOut(-1,0,10,1,0);
%-------------------------------- Resetting D0-D15 to 0
----
for i = 0:15
    EDigitalOut(-1,0,i,1,0);
end
%-----------------------------------------------------
-------
End
```

9.6   Code-3

This code is used to select the desired electrode configurations for array B.

```
function SetRing2(a,b,c,d,e,f,g,h);

Ring2=[a,b,c,d,e,f,g,h];
Lat4=[0,0,0,0,0,0,0,0];
Lat5=[0,0,0,0,0,0,0,0];
Lat6=[0,0,0,0,0,0,0,0];
%-------------------------------- Setting Latches Values
---
for i = 1:8;
    if (Ring2(i)==1);  Lat4(i)=0;  Lat5(i)=0;  Lat6(i)=0;
end
    if (Ring2(i)==2);  Lat4(i)=1;  Lat5(i)=0;  Lat6(i)=0;
end
    if (Ring2(i)==3);  Lat4(i)=0;  Lat5(i)=1;  Lat6(i)=0;
end
    if (Ring2(i)==4);  Lat4(i)=0;  Lat5(i)=1;  Lat6(i)=1;
end
end
%-------------------------------- Setting Latch 4 ------
----
for i = 0:7
    EDigitalOut(-1,0,i,1,Lat4(i+1));
end
    EDigitalOut(-1,0,11,1,1);
    EDigitalOut(-1,0,11,1,0);
%-------------------------------- Setting Latch 5 ------
----
for i = 0:7
    EDigitalOut(-1,0,i,1,Lat5(i+1));
end
    EDigitalOut(-1,0,12,1,1);
    EDigitalOut(-1,0,12,1,0);
```

```matlab
%------------------------------ Setting Latch 6 ------
----
for i = 0:7
    EDigitalOut(-1,0,i,1,Lat6(i+1));
end
    EDigitalOut(-1,0,13,1,1);
    EDigitalOut(-1,0,13,1,0);
%------------------------------ Resetting D0-D15 to 0
----
for i = 0:15
    EDigitalOut(-1,0,i,1,0);
end
%-----------------------------------------------------
-------
end
```

9.7 Code-4

Cross correlation code for ball

This code is used to cross-correlate the two signals obtained from both arrays A and B to fine the delay time for the two balls crossing arrays A and B.

```matlab
clear all;
clc;
close all;

% this program is meant to measure the time taken by a
ball between two
% planes
%-----------------------------------------------------
-----------
% the aim is to cross correlate plane 1 with plane2 one ,
% similarly other zones
format long
load('test.mat')  % loading the mat file having data
%tt = 0:0.001:0.255; % time period is 1 secs that is
every data is measured at every 0.001 secs
N = length(test(:,1));
T = 0.001*length(test(:,1));
% four zones of plane 1
p1z1 = test(:,1)-1;  % loading first row into plane 1
zone 1
p1z2 = test(:,2)-1;  % loading second row into plane 1
zone 2 similarly others

[C s1] = min(test(:,1));
[C s2] = min(test(:,2));
```

```matlab
% four zones of plane 2

%plotting p1z1
figure(1);
plot(p1z1,'r')
hold on
%plotting p2z1
plot(p1z2)

cor1 = xcorr(p1z1,p1z2); % cross corelating plane 1 zone
1 and plane 2 zone 1
t=linspace(-T,T,2*N-1);  % here just time period is
splitted into 1997 as there is 1997 data (2*999 -1)
figure(2)
plot(t,cor1)  %plotted with t with cor1
[c I] =max(cor1);
I
I_1 = I-999
```

9.8   Code-5

Is used to cross-correlate the two signals obtained from both arrays A and B for each rotational positions for Config-I,II and III in order to find the axial solids velocity.

```matlab
Clear all; % clearing all the previous files opened
clc;       % clearing the screen
close all; % closing all the opened files

load('ch1.mat')   %loading the mat file which has the
measurement data
set = 0;           %initializing an array for storing time
delays
N=4096;            %defining the number of values
T = 0.00223*N;    % defining the total time for taking
the measurements
tt = linspace(0,T,N); %dividing the time scale into equal
intervals
p1 = ch1(:,1)-mean(ch1(:,1)); %storing the plane 1 and
plane 2 values
p2 = ch1(:,2)-mean(ch1(:,2)); %and removing the DC offset
values
cor1 = xcorr(p2,p1); %cross correlating two plane values
t=linspace(-T,T,2*N-1);% defining time interval to plot
cross correlated graph
plot(t,cor1)    % plotting cross correlation graph
title('solids velocity m/s')
[c I] = max(cor1); %storing peak value
```

```matlab
set(1) = t(I);     % storing time of the peak value

% same process as above for second set
p1 = ch1(:,3)-mean(ch1(:,3));
p2 = ch1(:,4)-mean(ch1(:,4));
cor2 = xcorr(p2,p1);
t=linspace(-T,T,2*N-1);
figure
plot(t,cor2)
title('solids velocity m/s')
[c I] = max(cor2);
set(2) = t(I);

%same process as above for third set
p1 = ch1(:,5)-mean(ch1(:,5));
p2 = ch1(:,6)-mean(ch1(:,6));
cor3 = xcorr(p2,p1);
t=linspace(-T,T,2*N-1);
figure
plot(t,cor3)
%axis([-0.5,0.5,-3,8])
title('solids velocity m/s')
[c I] = max(cor3);
set(3) = t(I);

% forth set
p1 = ch1(:,7)-mean(ch1(:,7));
p2 = ch1(:,8)-mean(ch1(:,8));
cor4 = xcorr(p2,p1);
t=linspace(-T,T,2*N-1);
figure
plot(t,cor4)
title('solids velocity m/s')
[c I] = max(cor4);
set(4) = t(I);

%fifth set
p1 = ch1(:,9)-mean(ch1(:,9));
p2 = ch1(:,10)-mean(ch1(:,10));
cor5 = xcorr(p2,p1);
t=linspace(-T,T,2*N-1);
figure
plot(t,cor5)
title(' solids velocity m/s')
[c I] = max(cor5);
set(5) = t(I);

%sixth set
p1 = ch1(:,11)-mean(ch1(:,11));
p2 = ch1(:,12)-mean(ch1(:,12));
cor6 = xcorr(p2,p1);
```

```matlab
t=linspace(-T,T,2*N-1);
figure
plot(t,cor6)
title('solids velocity m/s')
[c I] = max(cor6);
set(6) = t(I);

%seventh set
p1 = ch1(:,13)-mean(ch1(:,13));
p2 = ch1(:,14)-mean(ch1(:,14));
cor7 = xcorr(p2,p1);
t=linspace(-T,T,2*N-1);
figure
plot(t,cor7)
title('solids velocity m/s')
[c I] = max(cor7);
set(7) = t(I);

%eighth set
p1 = ch1(:,15)-mean(ch1(:,15));
p2 = ch1(:,16)-mean(ch1(:,16));
cor8 = xcorr(p2,p1);
t=linspace(-T,T,2*N-1);
figure
plot(t,cor8)
title(''solids velocity m/s'')
[c I] = max(cor8);
set(8) = t(I);

%ninth set
p1 = ch1(:,17)-mean(ch1(:,17));
p2 = ch1(:,18)-mean(ch1(:,18));
cor9 = xcorr(p2,p1);
t=linspace(-T,T,2*N-1);
figure
plot(t,cor9)
title(''solids velocity m/s')
[c I] = max(cor9);
set(9) = t(I);

%tenth set
p1 = ch1(:,19)-mean(ch1(:,19));
p2 = ch1(:,20)-mean(ch1(:,20));
cor10 = xcorr(p2,p1);
t=linspace(-T,T,2*N-1);
figure
plot(t,cor10)
title('solids velocity m/s')
[c I] = max(cor10);
set(10) = t(I);
set
```

```matlab
%finding the averaged cross corelation of all the ten
sets
cor = (cor1 + cor2 + cor3 + cor5 + cor4 + cor6 + cor7 +
cor8 + cor9 + cor10)/10;

%plotting the average chronogram
figure
plot(t,cor)
title(''solids velocity m/s')
[c I] = max(cor);
Avged = t(I)
```

9.9   Code-6

Plot the 3D profile for local axial solids velocity for Config-I,II,III and Config ψ

```matlab
close all;
clear all;
clc;

load('x-cord.mat')    %loading the mat file which has the
x-coordinate of the centre of action.

load('eight-rotational position-solids-velocity-Config-
I.mat') %loading the mat file which has the solids
velocity profile for Config-I.

load('eight-rotational position-solids-velocity-Config-
II.mat') %loading the mat file which has the solids
velocity profile for Config-II.
load('eight-rotational position-solids-velocity-Config-
III.mat') %loading the mat file which has the solids
velocity profile for Config-III.
[xx,yy]=meshgrid(min(-40):2:max(40),min(-40):2:max(40));
zz=griddata(x,y,z,xx,yy,'v4');
zz(xx.^2 + yy.^2>= 1600) = 0;
% surfc(xx,yy,zz,'FaceColor','red','EdgeColor','none')z\
 surf(xx,yy,zz)
%camlight left; lighting phong
%%%%%%%%%%%%%%%
xlabel('x-cord of centre of action');
ylabel('y-cord of centre of action');
zlabel('Solids Velocity (m/s)');
```

9.10 Code-7

Plot the 3D profile for local solids volume fraction for Config-I,II,III and Config- ψ .

```
close all;
clear all;
clc;

load('volume_fraction.mat')   %loading the mat file which
has the x-coordinate of the centre of action.

load('eight-rotational position-solids-volume fraction -
Config-I.mat') %loading the mat file which has the solids
velocity profile for Config-I.

load('eight-rotational position-solids- volume fraction -
Config-II.mat') %loading the mat file which has the
solids velocity profile for Config-II.
load('eight-rotational position-solids- volume fraction -
Config-III.mat') %loading the mat file which has the
solids velocity profile for Config-III.
[xx,yy]=meshgrid(min(-40):2:max(40),min(-40):2:max(40));
zz=griddata(x,y,z,xx,yy,'v4');
zz(xx.^2 + yy.^2>= 1600) = 0;
% surfc(xx,yy,zz,'FaceColor','red','EdgeColor','none')z\
 surf(xx,yy,zz)
%camlight left; lighting phong
%%%%%%%%%%%%%%%
xlabel('x-cord of centre of action');
ylabel('y-cord of centre of
```

9.11 Code-8

To solve Equation 8-5 to obtained the local solids velocity profile.

```
v=0.00012;
S=solve('0.08*x+0.0032*y+0.2844e-
1=0','1.0732*13.2209*1/3600=(0.201e-3)*x/v+(0.503e-
5)*y/v+(0.4406e-4)/v','v=0.0001');
A=double(S.x);
Py=double(S.y);

t=0:0.0001:0.08;
plot(t,(1/1.0732)*A/v*t+(1/1.0732)*Py/(2*v)*t.^2+(1/1.073
2)*9.8*0.866/v*(14.1686*t.^5-
1.9134*t.^4+0.3684*t.^3+0.4992*t.^2));
grid;
```

9.12 Code-9

To solve Equation 8-12 to obtained the local solids velocity profile.

```matlab
function Velocity

solinit=bvpinit(linspace(0,0.2,1000),[1 0]);
sol=bvp4c(@twoode,@twobc,solinit);
x=linspace(0,0.2,1000);
y=deval(sol,x);

plot(x,y(1,:));
grid;
ylim([-0.3,0.5]);
end


function dydx = twoode(x,y)

    Py=-7.93;
    k=0.0023;
    v2=0.00005;
  dydx = [ y(2)
      -1/(k*(107.9303*x^3-
22.6836*x^2+2.7269*x+0.2995)+v2)*(k*(323.7909*x^2-
45.3672*x+2.7269))*y(2)+1/(k*(107.9303*x^3-
22.6836*x^2+2.7269*x+0.2995)+v2)*1.1227*Py+1/(k*(107.9303
*x^3-
22.6836*x^2+2.7269*x+0.2995)+v2)*1.1227*(22.6654*x^3-
4.7636*x^2+0.5726*x+0.8529)*9.8*0.9063];

end

    function res = twobc(ya,yb)
  res = [ ya(1)
          yb(1)];
  end
```